A COMPUTER MODEL FOR THE STUDY OF LIGHT WATER REACTOR FUEL PIN BEHAVIOUR

by

Massoud SAMIEI

B.Sc.(Eng.),M.Sc.,D.I.C.

A Thesis submitted for the
Degree of Doctor of Philosophy
of the
University of London

Nuclear Power Section,
Mechanical Engineering Department,
Imperial College of Science and Technology,
University of London, S.W.7.

March 1980

To my Parents

and to Patricia,

my wife.

ABSTRACT

An integral numerical computer code for the modelling of transient and steady-state thermal and mechanical behaviour of Zircaloy-clad UO_2 fuel pins in water reactors has been developed. The computational technique which determines the stress and deformation state of the fuel pin is based upon an extremely efficient finite difference scheme developed by Wilmore (9).

The non-linear terms in the constitutive equations (generaly owing to creep deformations) produce a non-linear system of equations which has been linearised by using a Taylor expansion technique coupled with a very sophisticated error minimisation algorithm and then solved with great accuracy.

An improved numerical method has also been developed for the fast and efficient solution of the transient heat conduction equation.

In this way a very stable and economical one-dimensional code has been obtained*. The physical processes included are thermo-elastic deformation, thermal and irradiation creep, plasticity, fission gas swelling and release, formation of cracks in the fuel, hot pressing and pore migration. Material properties are all functions of temperature and other relevant variables.

*With appropriate provisions made for its conversion to a quasi-two-dimensional (1½-D) code.

The name given to the code is "SAMURA". In the work presented here, the mathematical basis of SAMURA is described in detail. Some preliminary calculations performed with SAMURA using typical water reactor fuel pin data are also discussed. The main objective has been to validate the accuracy of SAMURA models and assumptions. In this context several benchmarking calculations have been performed using analytical solutions and available experimetnal data. Of particular interest here has been the modelling of a particular Maine Yankee PWR pin and comparison of SAMURA results with those of four major fuel pin modelling codes for this pin. Several other test fuel pins for which the fuel centreline temperature measurements were available have also been modelled.

ACKNOWLEDGEMENTS

I am very grateful to Dr. J.L. Head, my research supervisor, for his invaluable guidance and help in the course of this work; particularly for his support during a period of hard times, when without it, I would have never been able to conclude my work.

I express my gratitude to Professor P.J. Grant for giving me the opportunity to study in the Nuclear Power Section and to Dr. A.J.H. Goddard for his understanding of the extensive computational demands of this work. Miss E. Archer and Mrs. S. Boote have been extremely helpful in trying to provide often untraceable papers, journals and other publications. Special thanks are due to Mrs. E. Noel for the careful typing of this thesis.

As a recipient of a scholarship from the Atomic Energy Organisation of Iran for a period of three years, I would like to thank my sponsors. I am also grateful to the Imperial College Bursary for their financial support during the last stages of my work.

My last, but not least, thanks are due to my parents for their everlasting support and encouragement during the whole course of my life, and to my wife for her loving care and patience through the work.

LIST OF CONTENTS

	Page
ABSTRACT	2
ACKNOWLEDGEMENTS	4
NOMENCLATURE	9
CHAPTER 1. PREAMBLE	15
1.1 Introduction	16
1.2 The Importance of Fuel Pin Computer Codes	17
1.3 General Observations on Fuel Pin Behaviour	19
1.4 Present Status of Fuel Pin Computer Codes	28
1.5 The Integral Fuel Pin Computer Code "SAMURA"	30
CHAPTER 2. GENERAL CHARACTERISTICS AND BEHAVIOUR OF LIGHT WATER REACTOR FUEL PINS AND MATERIALS	34
2.1 Introduction	35
2.2 General Design Features of LWR Fuel Pins	39
2.3 Uranium Dioxide Fuel Properties and Behaviour	49
2.3.1 General Characteristics	49
2.3.2 Chemical and Physical Properties	53
2.3.3 Thermal Expansion and Cracking	60
2.3.4 Restructuring and Grain Growth	63
2.3.5 Fission Gas Release	65
2.3.6 Densification and Swelling	71
2.3.7 Mechanical Properties	78
2.4 Zircaloy Cladding Properties and Behaviour	85
2.4.1 General Characteristics	85

		Page
2.4.2	Irradiation-Induced Growth	91
2.4.3	Mechanical Properties	94
2.4.4	Internal and External Corrosion	109
CHAPTER 3.	MATHEMATICAL ANALYSIS AND MODELLING OF LIGHT WATER REACTOR FUEL PIN BEHAVIOUR	123
3.1	Introduction	124
3.2	Basic Assumptions and Method of Calculation in Computer Code "SAMURA"	139
3.3	Thermal Analysis	149
3.3.1	The Radial Heat Conduction Equation	152
3.3.2	Boundary Conditions	158
3.3.3	Method of Solution	161
3.3.4	Fuel/clad Gap Heat Transfer Coefficient	163
3.3.5	Gas Thermal Conductivity	170
3.3.6	Coolant Film Heat Transfer Coefficient	174
3.3.7	Power Distribution in Fuel	175
3.4	Mechanical Analysis	178
3.4.1	Mathematical Basis and Governing Equations	180
3.4.2	Finite Difference Method	189
3.4.3	The System of Equations in Finite Differences	192
3.4.4	Treatment of Fuel Cracking	206
3.4.5	Analysis of Plastic Yielding	210
3.5	Problem Parameterisation and Physical Models	215
3.5.1	Specific Heat Capacity	216
3.5.2	Thermal Conductivity	217
3.5.3	Emissivity	219

		Page
3.5.4	Thermal Expansion	220
3.5.5	Young's Modulus	224
3.5.6	Poisson's Ratio	225
3.5.7	Creep Rate models	226
3.5.8	Swelling Rates Model	231
3.5.9	Fracture Stress	232
3.5.10	Fission Gas Release and Pin Pressure	233
3.5.11	Pore Migration and Re-sturcturing in UO_2	238
3.5.12	Yield Stress Model	244
3.6	Error Analysis and the Control of Time-Step	248
3.7	Description and Mode of Operation of the Code	254
CHAPTER 4.	EVALUATION OF "SAMURA" MODELLING AND ANALYSIS CAPABILITIES	278
4.1	Introduction	279
4.2	Thermal Analysis Capabilities	280
4.2.1	Accuracy of the Finite Difference Scheme	281
4.2.2	Comparison of Fuel Centre-line Temperature with Experimental Data	291
4.3	Mechanical Analysis Capabilities	315
4.3.1	Comparison with Analytical Stress Analysis Solution	316
4.3.2	Primary Creep Behaviour of Thick Tubes	321
4.3.3	Effects of Grid Size on the Calculations	326
4.4	Modelling of a Typical Fuel Pin and Power History	337
4.5	Evaluation of "SAMURA" with Respect to EPRI Phase-III Studies	373

			Page
	4.5.1	Introduction	373
	4.5.2	Modelling of Main Yankee PWR Fuel Pin	375
CHAPTER 5. FINALE			409
	5.1	Conclusions on the Validity of Code Models	410
	5.2	Modelling of Fuel Pin under Normal Conditions	413
	5.3	Evaluation of "SAMURA" against Experimental Fuel Pin Data	414
	5.4	Recommendations for Further Work	419
APPENDIX A	A.1	SAMURA Input Organisation	424
	A.2	Definition of Major Arrays and Parameters in SAMURA	431
APPENDIX B	B.1	Partial Derivative of F_p in Eq.(3.119)	445
APPENDIX C	C.1	Derivation of Equations for the Anisotropic Case	449
	C.2	Typical Values of Anisotropic Parameters	453
APPENDIX D	D.1	Uranium-Dioxide Fuel Properties and Models	457
	D.2	Zircaloy Cladding Properties and Models	460
	D.3	Mixed-Oxide Fuel Properties and Models	463
APPENDIX E	E.1	Modelling of CC-7 Experiment (EPRI Phase-III Studies)	467
	E.2	Discussion of SAMURA Results	486
REFERENCES			490

NOMENCLATURE

Symbols

A_c	cladding surface area
A_f	fuel surface area
A_i	cross-sectional area at node i
a,b	empirical constants
B	creep bulk modulus
Bu	burn-up
C	empirical constant
C_p	constant pressure heat capacity
C_v	constant volume heat capacity
D	diameter
D_h	hydraulic diameter for a single fuel pin
e_r, e_θ, e_z	cylindrical polar components of the total elastic strain
E_r, E_θ, E_z	cylindrical polar components of the composite strain (sum of elastic and cracking strains)
E	calculation error
E	Young's modulus
E_f	rate of energy produced per fission
f_{dep}	flux depression factor
$f(\sigma_e)$	functional relationship between equivalent stress and equivalent plastic strain
F	fraction of pellet circumference in contact with the cladding
$F_p(\sigma_r, \sigma_\theta, \sigma_z)$	components of the creep rate functional in the r, θ and z directions (p $\equiv$ r,θ,z)
F_{GR}	fractional fission gas release
F_z	axial force acting on the fuel stack or the cladding

$\dot{g}(\sigma_e)$	functional relationship between equivalent stress and equivalent creep rate strain
G	fractional effect of burn-up on gap conductance
G	grain size
G	shear modulus
G	mass velocity
G_{fill}	number of initial fill gas moles
h_{cool}	coolant film heat transfer coefficient
h_{gap}	fuel/cladding gap conductance
h_c	closed fuel/cladding gap conductance component
h_o	open fuel/cladding gap conductance component
h_{rad}	radiative heat transfer component
H	Meyer's hardness
k	thermal conductivity
k_{mix}	pin gas mixture thermal conductivity
K	Boltzmann's constant
l_f	fuel stack length
M_i, M_j	molecular weight of components i and j in a gas mixture
N	number of rings in a region
NRF	number of rings in the fuel
P	porosity of the UO_2 pellets
P_{ext}	external pressure on the fuel pin
P_{int}	internal pressure of the fuel pin
P_i	linear power at radial node i
P_F	fuel pin internal pressure due to fission gases build-up and initial fill gas (= P_{int})
P_r, P_θ, P_z	cylindrical polar components of the swelling strain rate functional
P_{lin}	fuel pin linear power

P_w	coolant pressure
Pr	Prandtl's number
q	surface heat flux
Q_1, Q_2, Q_3	activation energy for different deformation processes
$Q_{L,i}$	linear power at node i
$\dot{Q}_v(r,t)$	volumetric rate of heat generation
r	radial distance
r	radius
r, θ, z	cylindrical polar coordinates
R	surface roughness
R	universal gas constant
$\dot{R}$	fuel power density (rating)
$\dot{R}_i$	fuel ring i power density (rating)
Re	Reynold's number
s_r, s_θ, s_z	cylindrical polar components of deviatoric stress
$\dot{S}$	rate of volume change due to swelling
t	time
T	temperature
T_{cv}	fuel central void average temperature
T_F	coolant film temperature
T_{GAP}	fuel/clad gap mean temperature
T_{GAS}	pin volumetric average gas temperature
T_{PL}	fuel pin plenum average hot temperature
u_r, u_θ, u_z	cylindrical polar components of displacement
v	volume
V_p	pore migration velocity
X_i, X_j	mole fractions of gas components i and j in a gas mixture

Y_s	yield stress
Z_k	axial strain in region k

Greek Letters

α_1, α_2	accommodation coefficients of surfaces 1 and 2
$\alpha_r, \alpha_\theta, \alpha_z$	cylindrical polar components of thermal expansion coefficients
$\gamma_r, \gamma_\theta, \gamma_z$	cylindrical polar components of total plastic strain (sum of all non-elastic strains)
δ	mean closed gap width (approximately equals the mean arithmetic roughness of fuel and cladding surfaces)
Δ	used to define finite differences
$\Delta L/L$	linear thermal expansion
$\Delta D/D$	diametral thermal expansion
Δt	time-step length
ε_f	fuel emissivity
ε_c	cladding emissivity
$\varepsilon_r, \varepsilon_\theta, \varepsilon_z$	cylindrical polar components of strain
$\dot{\varepsilon}_r, \dot{\varepsilon}_\theta, \dot{\varepsilon}_z$	cylindrical polar components of strain rate
ε_e	equivalent plastic strain
$\dot{\varepsilon}_e$	equivalent plastic strain rate
$\eta_r, \eta_\theta, \eta_z$	cylindrical polar components or cracking strain
λ	mean free path
μ	viscosity
ν	Poisson's ratio
ξ	characteristic dimension of fuel/cladding gap
π	3.14159 265
ρ	density

$\sigma_r, \sigma_\theta, \sigma_z$	cylindrical polar components of stress
σ_e	equivalent stress
σ_F	fracture stress
$\sigma_{y,i}$	yield stress at node i
σ_{SB}	Stefan-Boltzmann constant
σ_{trans}	transion stress
Σ_f	macroscopic fission cross-section
Φ_f	neutron flux

NOTATIONS

c	creep
C	subscript or superscript indicating cladding
e	elastic
f	subscript or superscript indicating fuel
i	subscript indicating nodal value
j	superscript indicating time-step number
p	plastic
p	r,θ,z
r	radial direction
s	swelling
t	thermal
w	collant
z	axial direction
θ	circumferential direction
O(x)	terms of order x
-	bar indicating average value or value at previous time-step

"Nothing in life to be feared, it has to be first understood ....."

Marie Curie

CHAPTER 1

PREAMBLE

CHAPTER 1

PREAMBLE

1.1 INTRODUCTION

The design of fuel elements for safe, efficient and economic operation in nuclear reactors requires the use of predictive methods and models which represent the main performance-limiting aspects of fuel pin behaviour. This in turn requires a thorough study of the different mechanisms which are responsible for the phenomena that occur inside or outside of a fuel pin during its course of life in a power reactor.

This subject has been an area for extensive research work during the past ten years. The fuel development engineers and scientists have tried to classify the fuel element behaviour data and to combine it with mathematical descriptions of the fundamental mechanisms in such a way that the behaviour of any fuel pin is accurately predictable.

The advent of large, fast digital computers and, the evolution of a large volume of data on fuel performance, basically from light water reactors, have stimulated a much increased level of effort that is directed toward the development of computer codes which will describe fuel pin behaviour. This activity, which is known as "computer modelling of reactor fuel element performance", has led to the generation of a number of computer codes. These codes would allow the prediction of fuel behaviour for existing or

proposed fuel element designs under normal operating and transient conditions such as load following, start-up, shut-down, refuelling and accident conditions like a loss-of-coolant accident (LOCA).

1.2 THE IMPORTANCE OF FUEL PIN COMPUTER CODES

The design and safe operation of nuclear power reactors is greatly influenced by the performance of their subassemblies throughout irradiation. Here the fuel pin being the smallest and perhaps the most vital member plays the main role. Thus, a realistic evaluation of its nuclear, physical, metallurgical and thermo-mechanical behaviour during irradiation is required. Such an evaluation involves the knowledge of a number of parameters, very intricate and generally interconnected, as for example, temperature, stress and strain distribution in the fuel pin, fuel swelling and fission gas release and, the complex fuel material behaviour.

In this context an experimental programme, carefully planned and performed, is an indispensable asset towards ascertaining the goals shared ultimately by the individual fuel pins. A detailed fuel pin experiment, particularly in-reactor, is however, a most expensive and time-consuming procedure. It is generally understood that a period of about six to eight years may elapse from the start to the final stages of performance and post-irradiation evaluation of an in-reactor experiment. Moreover not every organisation can afford setting-up their own adequately equipped test facilities, so there are very limited number of irradiation test facilities in operation. Consequently it can be realised

that apart from the data accumulated over the years from operating reactors, only a restricted amount of in-reactor experimental evidence will be available for the design of nuclear power plants.

The optimum means of reaping the maximum benefit from a limited amount of experimental data lies in a mathematical and physical computer model of the fuel pin behaviour. The overall performance of an actual fuel pin is the result of the interaction of a number of discrete processes taking place simultaneously in the pin. Fuel pin modelling routine proceeds accordingly. Where possible existing theories are used to describe the interacting processes occurring in an actual fuel pin; otherwise assumptions are made or new theories are established. These theories must, however, be compared with the results of relatively simple in-reactor or out-of-reactor experiments. Special purpose codes can also be written to check the validity of the assumptions made.

The integral fuel pin computer codes are then built up upon theoretical, physical and empirical models obtained in the manner described above. In this sound way they have many advantages to offer. First of all they provide a framework around which the theoretical models can be evaluated and further developed. Secondly, they can be used in a parameter study for interpolation and extrapolation of existing experimental data to provide a clear physical picture of the mechanisms responsible for the fuel pin behaviour. Computer models can identify areas of crucial importance or critical material properties and their effects on desired

parameters. Finally, the effects of up-ramps, down-ramps, power-cycling and fast transient may be studied in detail.

1.3 GENERAL OBSERVATIONS ON FUEL PIN BEHAVIOUR

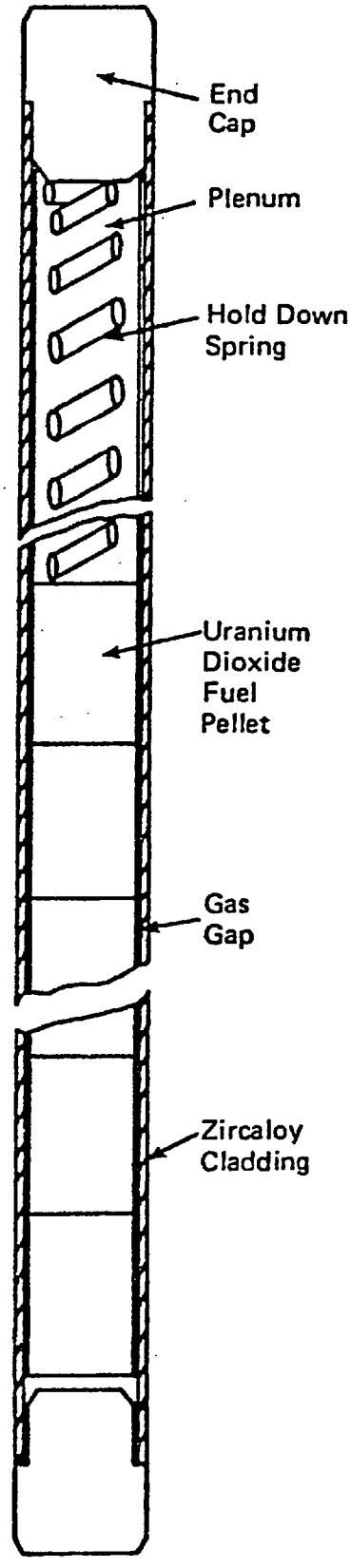
In spite of small differences in their performance characteristics, thermal and fast reactor fuels are similar in many respects; both having cylindrical configuration and oxide fuels with the same structure. In this regard, integral computer models are based on generally observed processes common to both types of reactor fuels.

The fuel pin in today's reactors consists of a stack of sintered uranium-dioxide or uranium/plutonium-dioxide pellets in a metal cladding. The pellets are small cylinders with or without a concentric central hole and have dished or flat end-faces. Their density is in the range 9.9-10.8 g/cm^3. Some allowance is made for the expansion of pellets by a radial gap between pellets and cladding of the order 50-300 μm. The stack of pellets is usually supported on a short sleeve or liner in the bottom of cladding; a soft helical spring in the upper part of the pin prevents any bulk movement of the stack during transportation, see Figure 1.1.

All observations have shown that ceramic fuels exhibit an extremely brittle behaviour at low temperatures. If the thermal expansion is not free to take place in every direction, a moderate temperature gradient is sufficient to cause thermal stresses in excess of the fuel fracture stress. This situation arises in ceramic fuel pellets during, for instance, the first reactor start-up. The pellets, while still at

Figure 1.1
CUTAWAY OF FUEL PIN USED FOR COMMERCIAL WATER COOLED NUCLEAR POWER REACTORS. TYPICAL FUEL DATA ARE AS FOLLOWS:

	PWR	BWR
OVERALL LENGH, mm	3802.4	4165.6
OUTSIDE DIAM., mm	10.72	14.30
CLADDING WALL THICKNESS, mm	0.62	0.94
PELLET DIAM., mm	9.30	12.12
PELLET LENGH, mm	15.24	12.70
PELLET STACK HEIGHT, mm	3657.6	3657.6
PLENUM LENGH, mm	109.22	406.40
FUEL PINS IN FUEL ASSEMBLY	204	49
FUEL PIN PITCH, mm	14.30	18.75
FUEL ASSEMBLIES IN CORE	193	764



relatively low temperatures, are subject to an increasing temperature gradient which on reaching to a certain amount is sufficient to cause the pellets to crack radially and axially into numerous wedge-shaped pieces. As a result, the radial displacement of pellets is further increased, eventually leading to pellet-cladding interaction (PCI) and radial gap closure, see Figures 1.2 through 1.5.

The performance of fuel pellets is also affected by their as-manufactured porosity. The pores originally present in the fuel migrate under the influence of the temperature gradients toward the centre of the fuel, decreasing the porosity. The porosity is further reduced by stress-directed (hydrostatic) diffusion of vacancies from the pores. In solid pellets a central void is created. Alternatively, the void in hollow pellets is enlarged. The fuel density increases accordingly, by an amount which varies with local fuel temperature. Pore migration under a given temperature is completed in the hotter fuel region within a very short time, while in the colder region the process may take a few days or even a few months (1,2).

Post-irradiation examinations on fuel pins have shown that, in general, three distinct regions can be identified with pore migration, namely (see Figure 1.6) :

(1) a high temperature region with columnar grain growth;

(2) a medium temperature region with equiaxed grains; and

(3) a low temperature region where the original microstructure of the fuel is essentially preserved (unrestructured grain region).

Figure 1.2
POST IRRADIATION SECTION OF A SOLID PELLET, 100 W/g MASS RATING
(AFTER REF. 183)

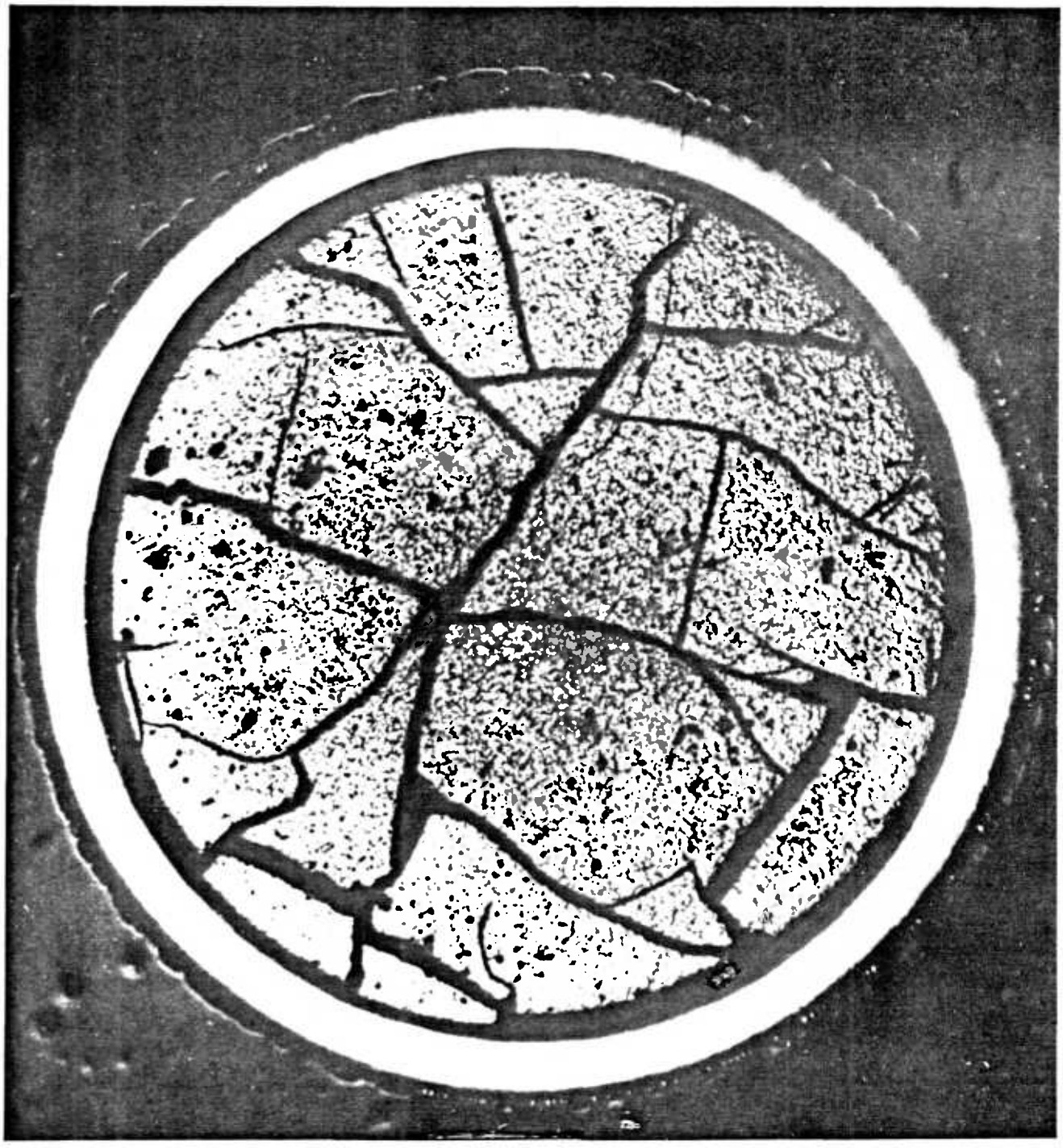


Figure 1.3
POST IRRADIATION SECTION OF A SOLID PELLET, 250 W/g MASS RATING
(AFTER REF. 183)

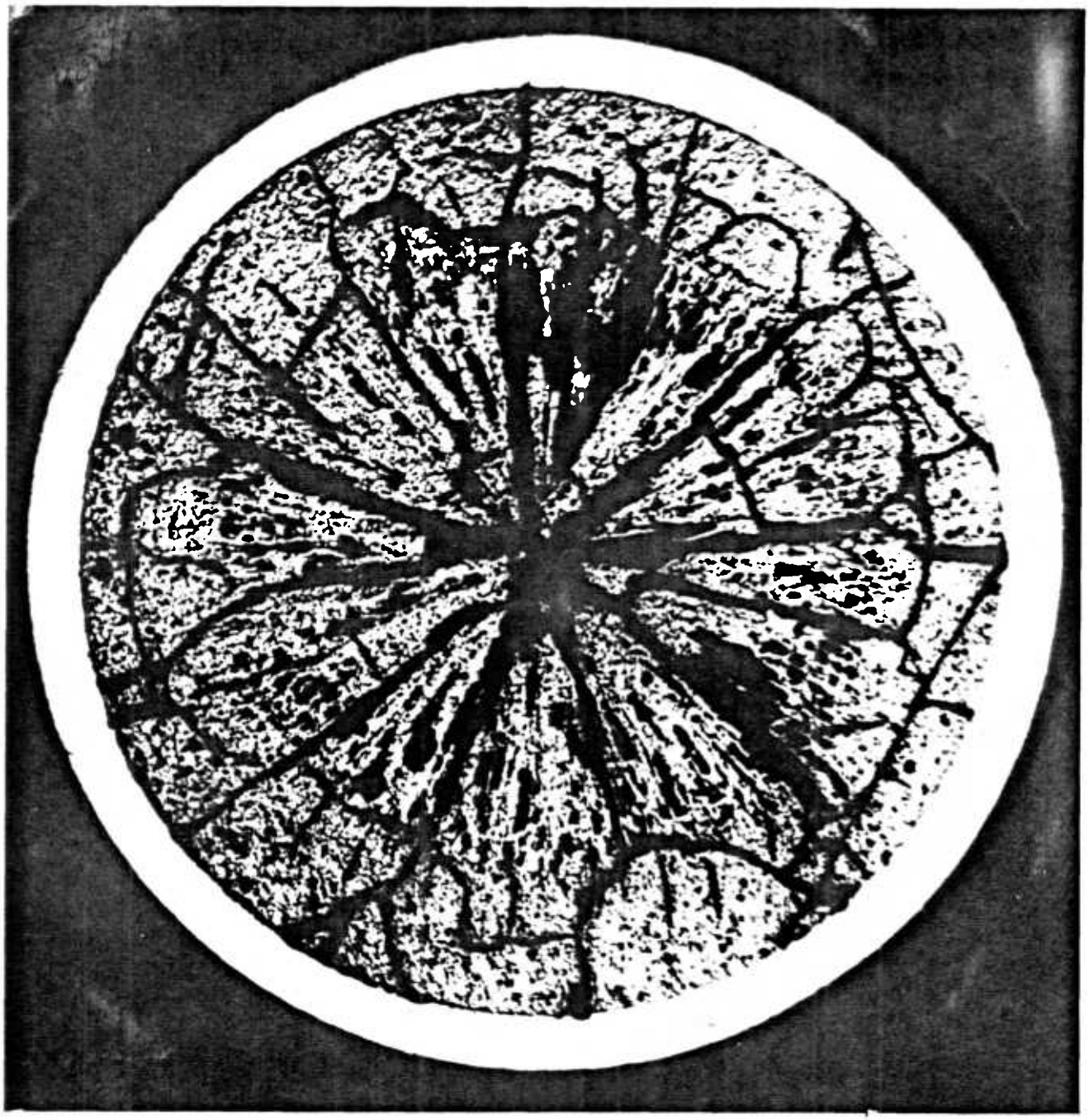


Figure 1.4
POST IRRADIATION SECTION OF A HOLLOW PELLET, 325 W/cm LINEAR POWER
(COURTESY AERE HARWELL , U.K.)

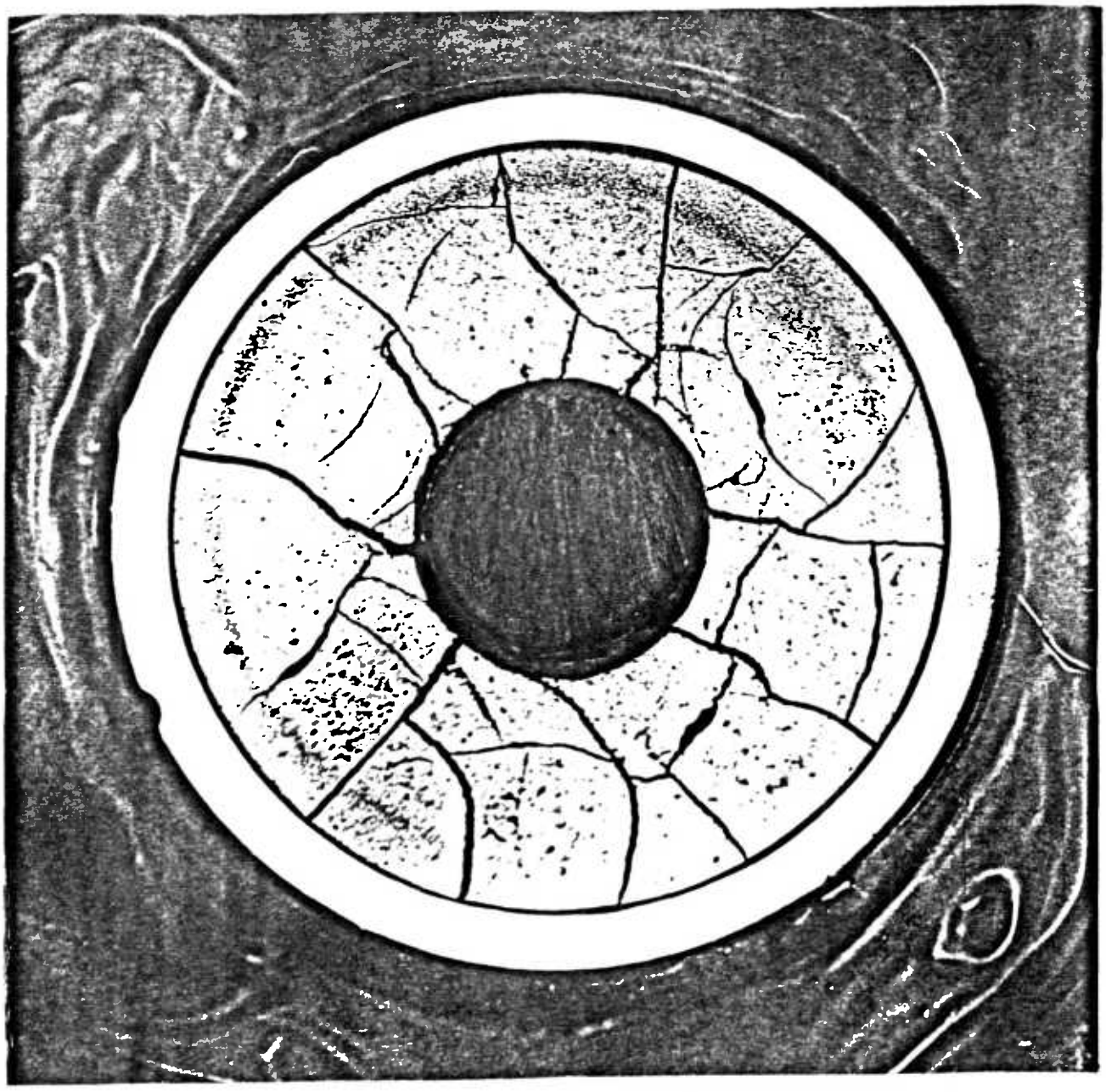


Figure 1.5
POST IRRADIATION SECTION OF A HOLLOW PELLET, 650 W/cm LINEAR POWER
(COURTESY AERE HARWELL, U.K.)

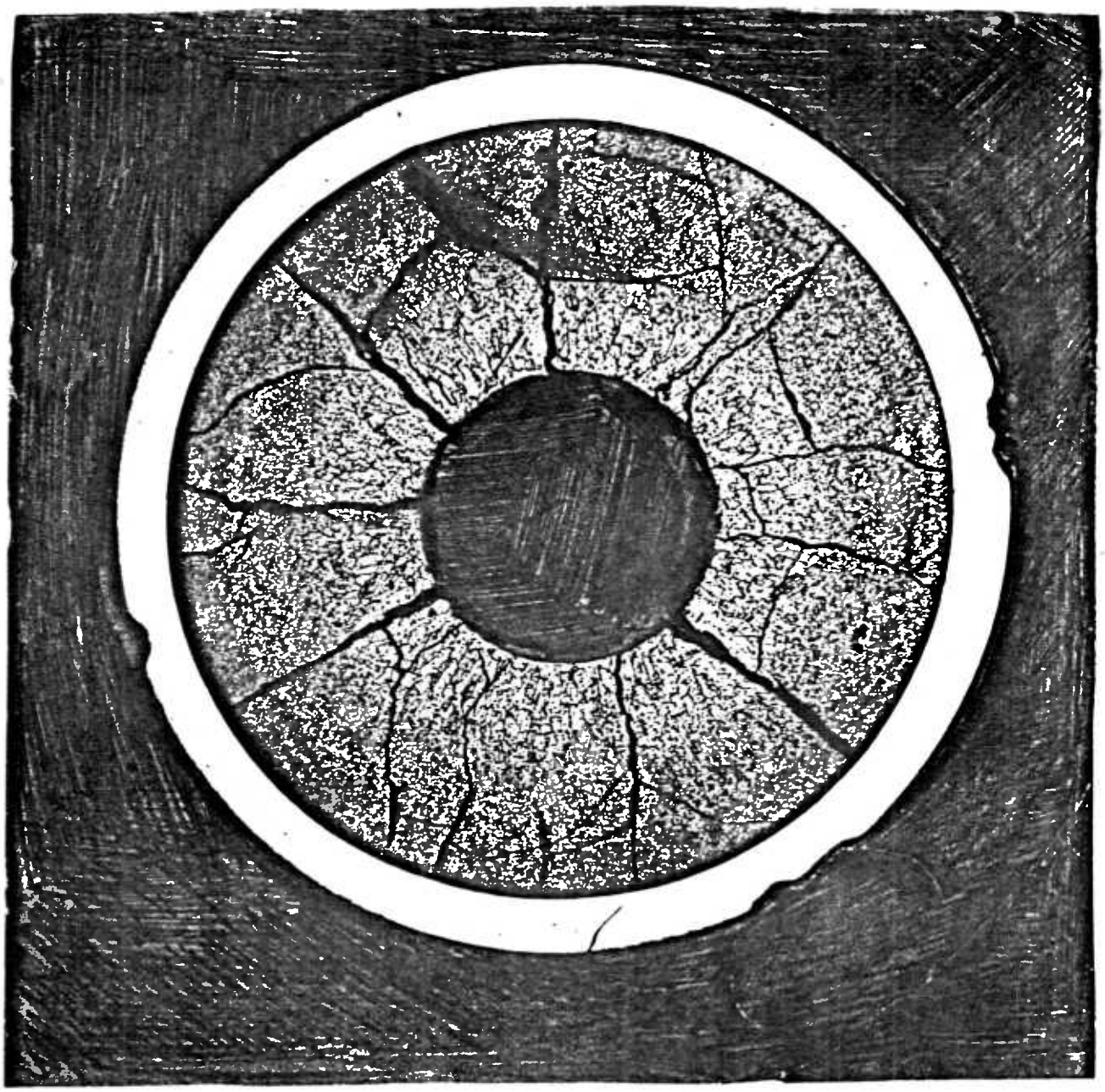
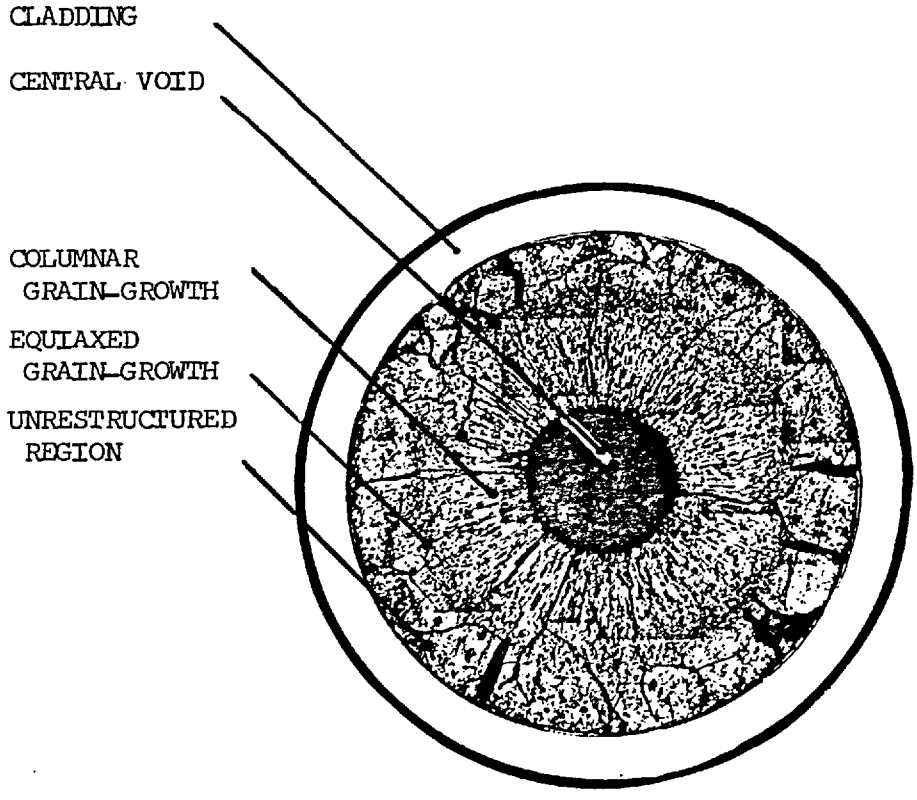


Figure 1.6

TRASVERSE SECTION OF A MIXED-OXIDE FUEL PIN
RUN AT 500 W/cm TO ABOUT 30,000 MWd/teU BURN-UP



The threshold temperature for the columnar grains is about 1700°C, and for the equiaxed grains around 1400°C. The observed densities in these regions, as moving towards the pellet centre, increase up to approximately 98% of the theoretical density of UO_2 (98% TD).

Swelling of the fuel pin materials at higher burn-ups is another contributory factor when dealing with overall deformations. The fuel pellets swell due to the retention of solid and gaseous fission products. The cladding swells, normally under fast dose, due to void nucleation and irradiation growth. The gas atoms produced by the fission process are partly released due to the inability of uranium dioxide to accommodate them within its structure. An internal gas pressure build-up follows and the thermal conductance of the fuel/cladding gap deteriorates due to contamination by the fission gases, leading indirectly to higher temperatures. Fuel and cladding may interact and develop a finite contact pressure between them. The overall behaviour of the fuel pin depends on this interaction, firstly, because of its effect on heat transfer between fuel and cladding, and secondly, because of the build-up of interfacial direct and friction forces which affect the stress distribution within the pellets and the cladding. The magnitude of these forces varies with burn-up and is a function of the relative mechanical strength of fuel and cladding. Both fuel and cladding suffer elastic, plastic and thermal and/or irradiation induced creep deformations, the fuel may flow into the cracks, the existing pores and the central void. The fuel cracks heal

and the central void gradually closes. These processes may be temporarily halted or even reversed by intermediate power changes. Eventually, the accumulative effect of these processes leads to fuel pin failure, most probably due to a cladding rupture or a perforation. The failure may be accelerated by irradiation induced embrittlement of the cladding, which leads to an increased yield strength but a serious loss of ductility, or by an excessive internal and external corrosion of the cladding material combined with stress and strain concentrations.

Chapter 2 describes the general characteristics and phenomenological water reactor fuel pins behaviour in detail.

1.4 PRESENT STATUS OF FUEL PIN COMPUTER CODES

It must now be clear that the complex problem of fuel pin analysis can only be properly handled by a computer program which analyses the fuel pin parameters at successive stages of its irradiation history. A number of computer codes for the prediction of the generally time-dependent fuel pin properties have been developed in the recent years (3-11). These computer codes can be utilized to facilitate the fuel element design and analysis for light-water reactors (LWR), as well as liquid-metal fast-breeder reactors (LMFBR). The physical and mathematical models in each code, however, differ more or less from one another. One objective of the present work was to study, as far as possible, these models and their differences in order to construct a sound basis for the development of an integral fuel pin computer code.

It became very soon clear that even with extensive use of modern high speed computing machinery, it was not feasible to conceive a computer code which would model all the phenomena, briefly described in Section 1.3, with a minute attention to detail in an economic amount of computer time. However, further study showed that this dilemma was not so incisive as appeared at the first place, because many kinds of fuel pins are found in reactor practice and it is highly unlikely that all of the discussed phenomena will simultaneously play a crucial part in the performance of any one particular fuel pin. A representative combination of these phenomena was found to have been chosen by most of the existing computer codes.

In general, therefore, an integral or scoping fuel pin computer model will not describe phenomena to that degree of complexity which present knowledge or insight would permit. This task is, however, reserved for sophisticated, special purpose codes, for instance, Levy and Wilkinson (12) have made a comprehensive finite element analysis of the fuel pin behaviour during start-up, and Poeppel (13) has written an advanced subroutine for gas release and swelling behaviour. Thus an integral fuel code will confine itself to a brief but comprehensive analysis of the most significant processes known to occur in a fuel pin, some attention to detail will be given to those areas where the specific code task finds it necessary.

The structural analysis of arbitrary fuel pins has been the subject of much endeavour during recent years. Accordingly,

structural models and computer programs are in abundance. These fuel pin performance models can be classified into two groups:

(a) spatially one or quasi-two-dimensional* models with highly complex material behaviour - integral fuel pin performance, and

(b) spatially truly two-dimensional models - local fuel pin performance.

A detailed comparison of all these codes was beyond the scope of the present work, however, since it has recently been realised that a quantitative comparison is desirable; and such a study has actually been performed by Electric Power Research Institute (14), it was decided to include such a comparison as far as possible. A qualitative comparison of all the codes found in the open literature is given in Chapter 3.

1.5 THE INTEGRAL FUEL PIN COMPUTER CODE "SAMURA"

The development, design, construction and commissioning of a nuclear power plant is primarily the concern of an industrial organisation. Clearly an indispensable asset in the fulfilment of these obligations is a reliable, efficient fuel pin performance computer code. Many such codes have been developed by the industry and research laboratories, but very few are non-proprietary. Bearing in mind the above facts and the growing importance of nuclear power the need for independent studies becomes obvious.

*This is also called 1½-dimensional and means the superposition of two one-dimensional solutions in different coordinates (r and z here).

The present work is the outcome of an independent study on the present status of the fuel pin computer models with the objective of developing an integral computer code to predict the behaviour of light water reactor (LWR) fuel pin as its first step. In a more general scope, a computer code was sought for performance studies on fuel pins in thermal or fast breeder reactor environments. The code had to be written in an organised and systematic way in order to make its development and use quite simple. However, it should incorporate within its models highly complex material behaviour; detailed description of radial (and axial) behaviour; be applicable to steady-state, quasi steady-state and transient problems; and finally be written in FORTRAN-IV programming language. The state of art at that time was exploited as far as seemed expedient, some new models and techniques were used where previous efforts were judged inadequate or even lacking. The fundamental models of the code are based on FRUMP (9), COMETHE (7) and LIFE (3).

The computer code system SAMURA, Stress Analysis Modelling with Unrestricted Reactor Applications, has evolved through these efforts. Here "unrestricted" refers to the type of variation of reactor power and to the parameterisation of the model.

SAMURA has been developed for the thermal and mechanical analysis, in-reactor performance prediction and parameter studies of arbitrary fuel pins. Of primary concern, however, have been the oxide fuelled, Zircaloy clad pins in light water reactors. For a given variation of the linear-power

of the fuel in time, the program has been designed to predict:
(a) the non-linear temperature distribution across the fuel and cladding, including the effects of pellet/cladding gap;
(b) the changes in the dimensions of the pellets and cladding (strains);
(c) the stress distribution in the three principal directions, including a partitioning into thermo-elastic, thermal and irradiation induced creep, plastic and, deformations by swelling in the fuel and cladding;
(d) the fission gas release across the fuel and the pore migration.

Further, SAMURA predicts the time(s) at which the pellet/cladding gap opens or closes and the temporal variation of such quantities as the contact pressure between the fuel and cladding and maximum cladding circumferential deformations. The cracking of the oxide fuel has also been modelled.

In the mechanical analysis a state of generalised plane strain has been assumed in the fuel and cladding. The set of coupled thermo-plastic equations, which involves non-linear terms related to important physical effects, has been solved numerically by finite differences and new algebraic methods. For the heat transfer calculation the general variable parameter form of transient heat conduction equation has been solved by a development of classical Crank-Nicholson method to include the effects of property variation. The heat conductance in fuel/cladding gap has been dealt with in detail. This is of crucial importance not only directly for fuel temperatures, but also indirectly for the mechanical loading of fuel and cladding (PCI).

SAMURA has been denoted as being a transient computer code in order to distinguish it from other approaches which consider only a steady state system (15). However, by use of the term transient it is also meant to denote only rapid power excursions from normal operating conditions such as may be caused by overpowering or loss-of-coolant accident (LOCA). The present code is capable of application to such problems with little or no modifications.

In Chapter 3 the basic equations used in SAMURA are given and the mathematical methods for their solution are discussed. Also the numerical techniques and the analysis of errors inherent in the solution method are presented in detail. Finally this chapter gives the programming features of SAMURA and serves as a Users' Guide too.

Chapter 4 deals with the results of some case studies performed by using SAMURA. Of great interest here, apart from accuracy and speed of computations, is a comparison of SAMURA output with the published results of four leading codes (3,5,7,16) and experimental data for a standard set of input data (14).

The final part, Chapter 5, discusses the results and draws conclusions from the present work and indicates the direction of future efforts in extending the capability of the computer code system SAMURA.

CHAPTER 2

GENERAL CHARACTERISTICS AND BEHAVIOUR OF LIGHT WATER REACTOR FUEL PINS AND MATERIALS

CHAPTER 2

GENERAL CHARACTERISTICS AND BEHAVIOUR OF LIGHT WATER REACTOR FUEL PINS AND MATERIALS

2.1 INTRODUCTION

The ideal fuel element should achieve its design performance without an excessive margin, which in practice would mean a small but finite failure rate, depending on the ease of discharge and local activity release criteria. Therefore it is the task of fuel analyst to recognise all possible performance-limiting processes and their relation to fuel material properties, then by modelling them provide a tool for the design of water reactor fuel pins.

The major changes that take place in uranium dioxide fuel during irradiation result in initial densification, then swelling as solid and gaseous fission products accumulate within the fuel, and release of a proportion of the fission product gases to create a pressure within the pin. Changes also take place in the cladding; some intrinsic to its own behaviour under irradiations, but others in response to the behaviour of the fuel. Once in contact with the cladding, the fuel, in turn, responds to the restraint that is thus imposed upon it. Heat flow from the fuel to coolant is also impeded by the thermal resistance between fuel and cladding, so that the fuel temperature is sensitive to the mechanical behaviour of fuel and cladding and mutual interactions. Important aspects of the fuel material behaviour such as creep, swelling and gas release are highly temperature-

sensitive, so that the overall performance of the fuel pin is determined by a complex set of thermal and mechanical interactions.

The above processes can greatly be influenced by operational factors. Power cycling and seasonal power variations are the two important operational factors which may have a bearing on fuel endurance. When a reactor is power-cycled on a regular daily basis, radial cracks form in an outer annulus of UO_2, then open and close as power is raised and lowered. If the cladding were prefectly bonded to the fuel it would rupture when a crack opened. In practice, this can lead to stress concentration which is not fully reversed during the power reduction phase. The result over a series of power cycles is a progressive thinning of the cladding wall over pellet cracks and also some reversed plastic strain cycling (17). A special case of power-cycling which can result in a large increment of damage in one cycle is reported to be "seasonal power variation". In this case, where a reactor may have been held at reduced power for several months, a similar situation of wall thinning and stress concentration results due to a returning to full power. Although it is unlikely in water reactor fuels generally that one event of this type will cause an overstrain failure, the high peak stress could be dangerous if there is a sensitivity to SCC (stress-corrosion-cracking) (17,18).

Many more life-limiting phenomena have been observed in water reactors. Since an integral fuel pin computer code should be able to consider most of them attention must be

given to their causes and effects. The principal such phenomena recognised today may be classified as follows:

(1) corrosion, due to hydriding, causes increased cladding surface temperature and wall thinning;

(2) cladding embrittlement, due to irradiation damage, hydriding and adverse texture;

(3) cladding overstrain, due to power cycling, UO_2 expansion and swelling; causes ridge and wrinkle formation;

(4) fission product attack, causes corrosion and stress-corrosion-cracking;

(5) dry-out, due to overpower operation, or standing coolant void; causes clad surface overheating and fuel pin bowing;

(6) crud deposition, causes flow obstruction and clad surface overheating;

(7) hydrodynamic instability, due to fuel pin vibrations, mechanical damage; causes fretting corrosion and fatigue;

(8) manufacturing defects in cladding, end caps, welds and spacers, cause early fuel failure.

It is in this context that the properties and performance of uranium dioxide fuel and Zircaloy, which have become the basic reference fuel pin materials for the water reactor industry, are of crucial importance. In fact without knowing the true behaviour of these materials under irradiation the task of developing computer models will not be successful.

The selection of UO_2 over other potential fuel materials is based on its excellent combination of chemical stability, especially to water reactor coolants; compatibility with

cladding materials such as Zircaloy and stainless steel; dimensional stability under irradiation; very high melting point; and straightforward and economical production from uranium hexafluoride in diffusion method. These desirable characteristics were recognised at a very early stage in the development of power reactors, and, as a result, the properties of UO_2 have been under intensive study for about 25 years. There has probably been more development work on UO_2 than all other fuel materials combined.

As for the cladding, from a review of published works, one has the impression that the majority of the fuel pins with Zirconium alloys cladding have performed satisfactorily in the reactors, and that only a small number have failed. The failures have generally been explained by some abnormality in the conditions of the exposure or in the material. Corrosion, mechanical rupture, or a combination of the two, i.e. stress-corrosion-cracking, are, however, the most likely causes. From the mechanical properties point of view, the most important limiting aspect of Zircaloy performance has undoubtedly been ductility under the multi-axial stress conditions which it experiences as a result of interaction with the UO_2 pellets.

This chapter discusses the phenomenological fuel pin behaviour through a study of characteristics and properties of UO_2 and Zircaloy fuel pin materials. Certain aspects of in-reactor behaviour of these materials which have a bearing on computer modelling of fuel pins have been discussed. The main objective here has been to recognise the mechanisms that are responsible for in-reactor fuel performance.

2.2 GENERAL DESIGN FEATURES OF LWR FUEL PINS

General design concepts for water reactors are based on optimisation involving reactor physics, thermal hydraulic performance, safety, cost, engineering aspects, fuel performance, reliability, system requirements and many others. The fuel designer is left with the task of translating the performance requirements (in other words fuel element power output capability and other constraints) into an economic and reliable design.

General design features of the better known fuel element types is as follows. Modern Boiling Water Reactor (BWR) and Pressurised Water Reactor (PWR) fuel elements differ little in concept as exemplified by Figures 2.1 and 2.2. They are clusters of long fuel pins arranged in a square array and spaced at intervals along their lengths by spring type spacer grids. The PWR element has empty pin positions containing thimbles into which slim control rods are inserted, the so-called control rod cluster design. In all cases cladding is Zirconium alloy and fuel is sintered UO_2 in pellet form. A fission gas plenum space is provided at one or both extremities of the UO_2 pellet stack (19).

Fuel elements for pressure tube reactors such as Steam Generating Heavy Water Reactor (SGHWR) and CANDU are round in geometry in order to economise on material in the pressure tube. Apart from this feature SGHWR fuel elements, Figure 2.3, are similar in concept to BWR elements, but employ a different type of spacer grid not having springs. An alternative spring type is also available. The CANDU/PHW

(Pressurised Heavy Water) concept, as used in Douglas Point and Pickering, is a substantial departure in that each fuel channel contains a number of separate short elements, Figure 2.4. Because of their short length the pins in these elements are attached at both ends to end plates and there are no intermediate spacer grids as such. Both wire-wrap and brazed-on spacers have been used to preserve intermediate spacing of pins, and wear pads are attached to outer pins to space the elements away from the horizontal pressure tube wall. In both these fuel elements the cladding is again Zirconium alloy and the fuel sintered UO_2 pellets. SGHWR fuel has a fission gas plenum at the top end of the pin and CANDU/PHW has no end plenum as such, but a void volume for fission gas storage is provided by the use of hollow end caps (20,21).

Fuel elements for Ågesta and MZFR, although these are pressure vessel reactors, have a round configuration because the elements are contained in flow tubes to separate the coolant flow from the rest of the moderator. Both otherwise follow the general pattern of full core length pins with spacer grids.

The main fuel design parameters for these reactor types and some others are given in Table 2.1.

Figure 2.1

SCHEMATIC VIEW OF BWR/6 FUEL ASSEMBLY AND ITS DETAILS.
(COURTESY GENERAL ELECTRIC COMPANY)

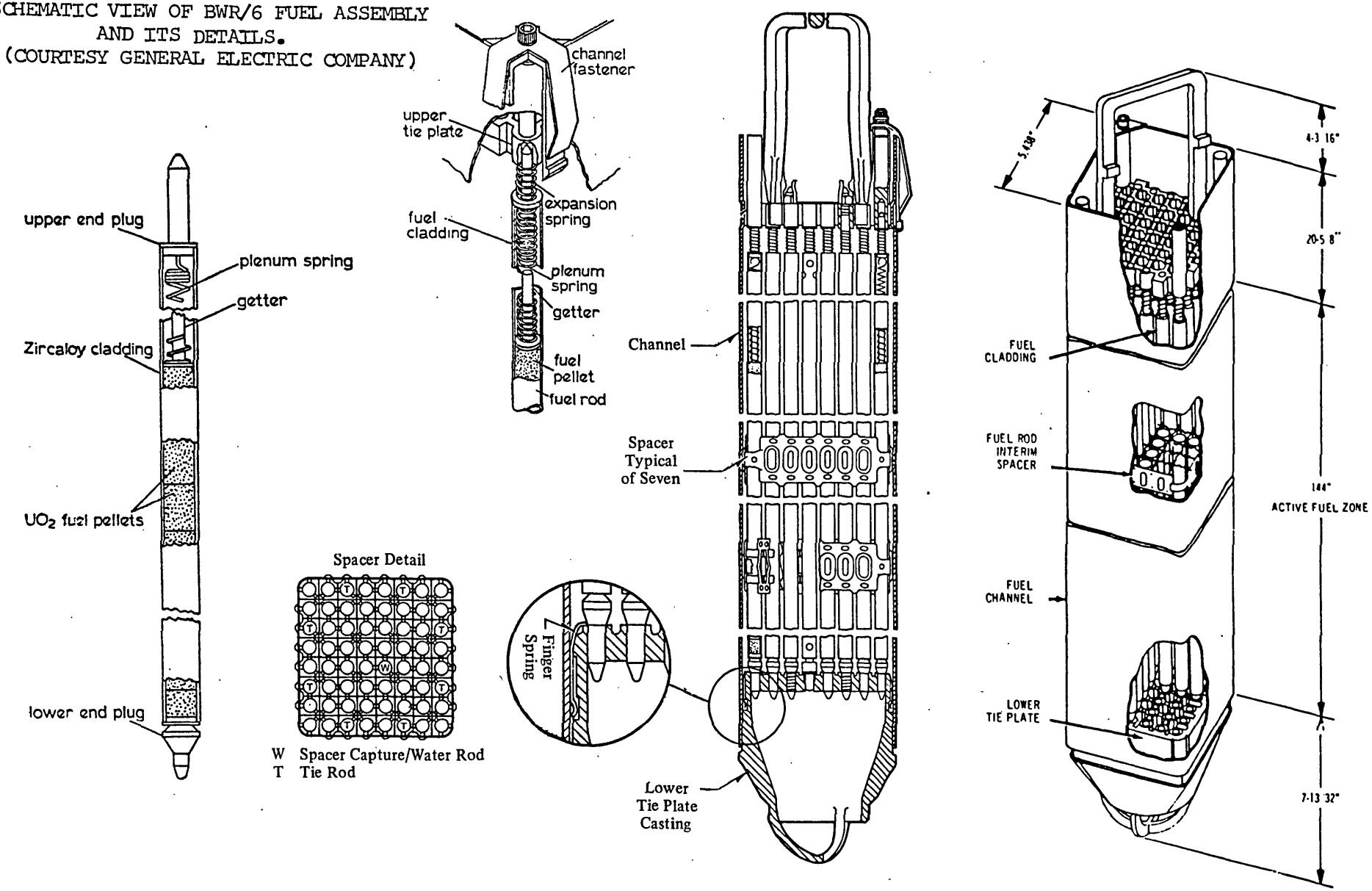
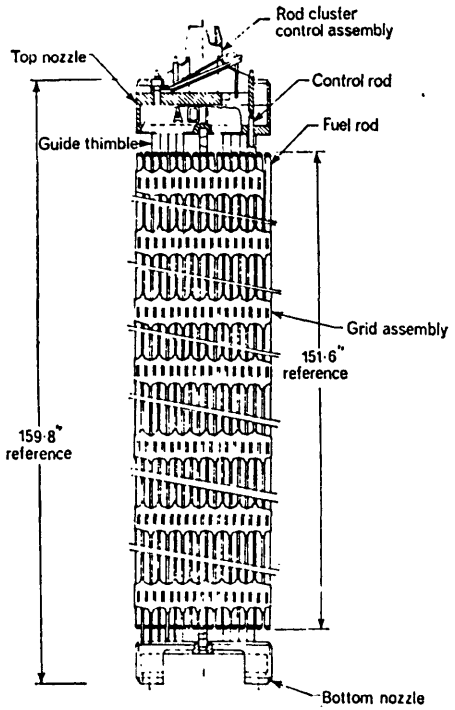


Figure 2.2

SCHEMATIC SHOWING CONSTRUCTION OF PWR FUEL ELEMENT.
(COURTESY WESTINGHOUSE CO.)



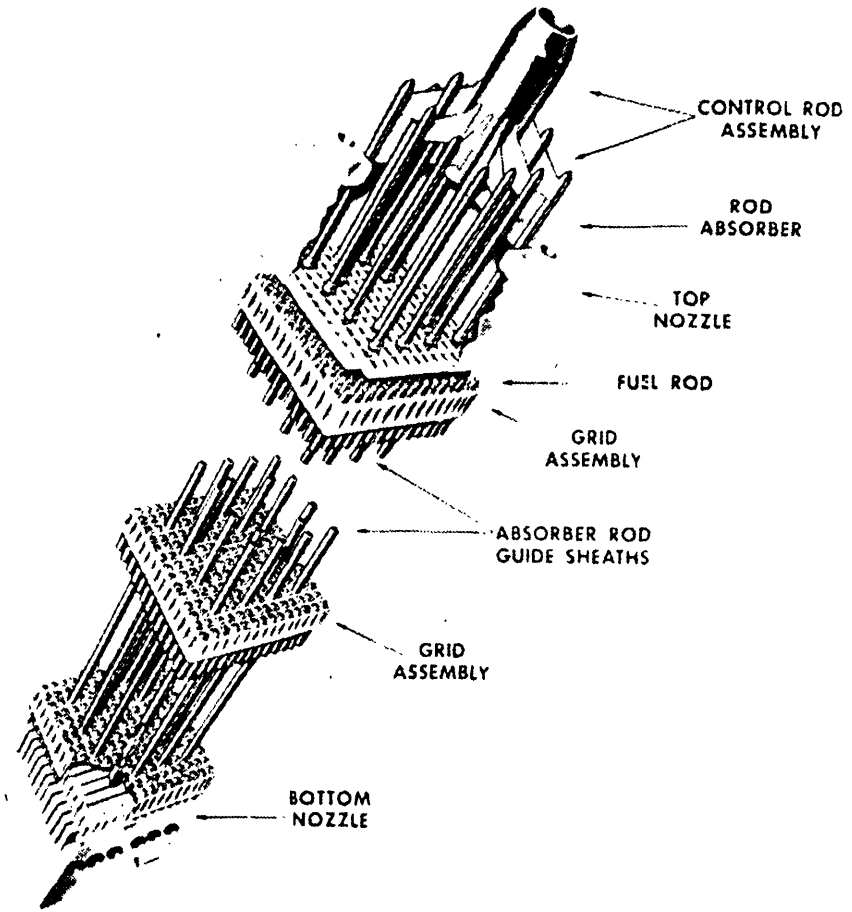
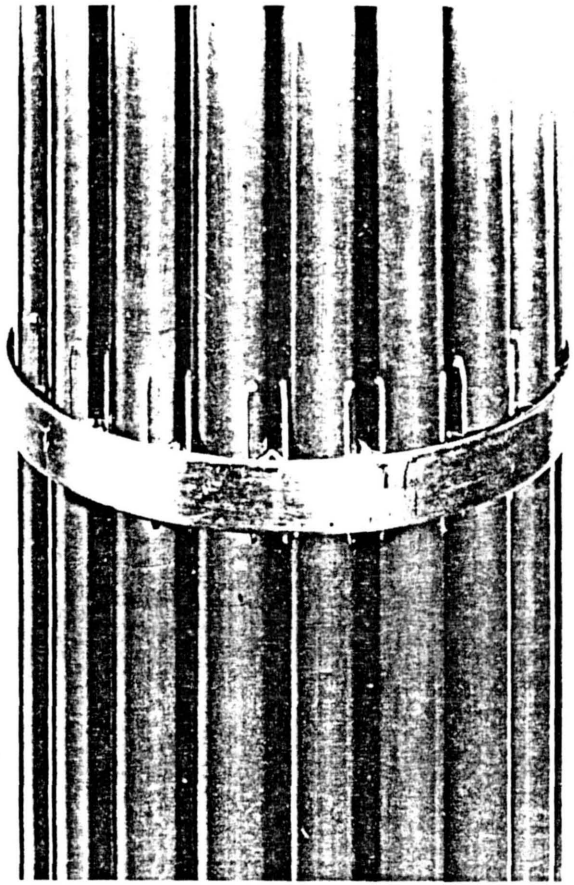


Figure 2.3

GENERAL VIEW OF PROTOTYPE SGHWR FUEL ELEMENT.
(AFTER REF.20)



DETAIL AT SPACER GRID

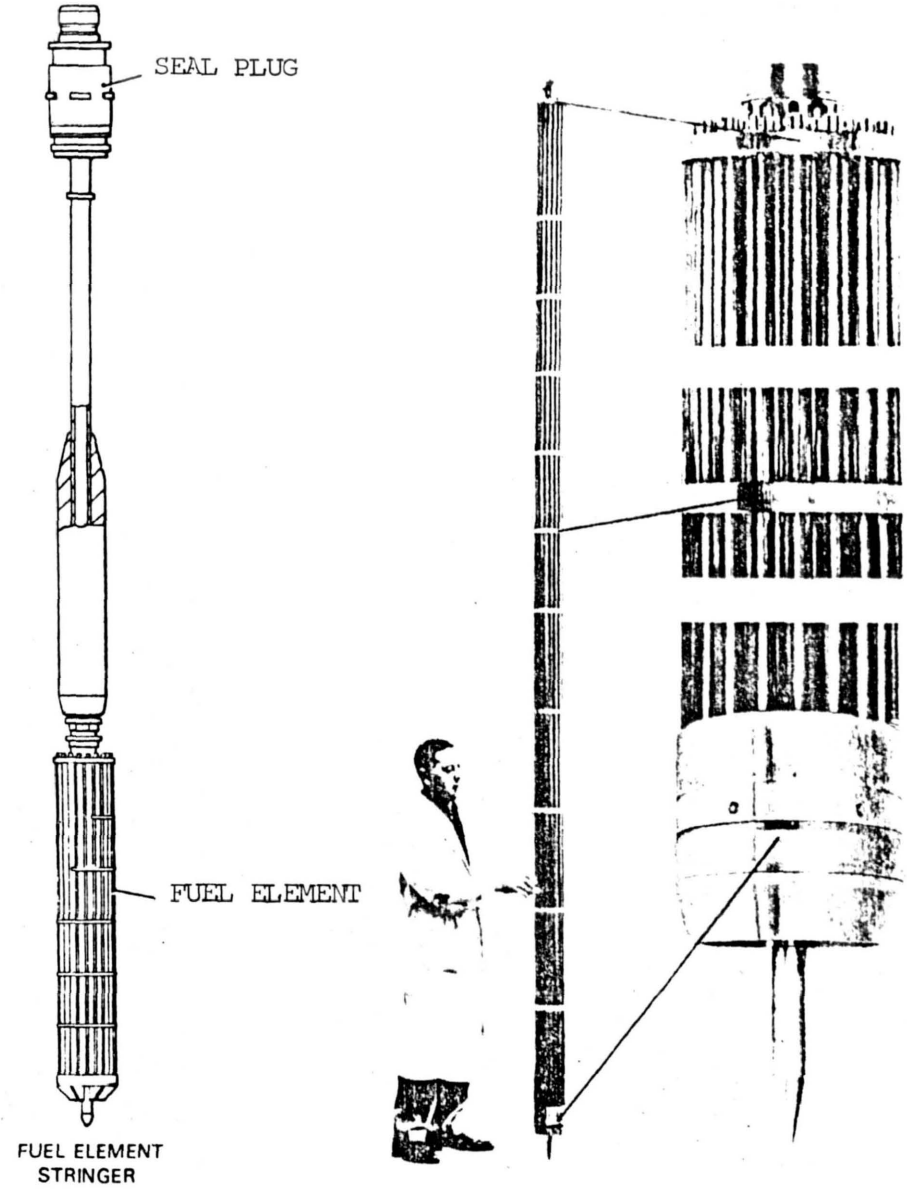
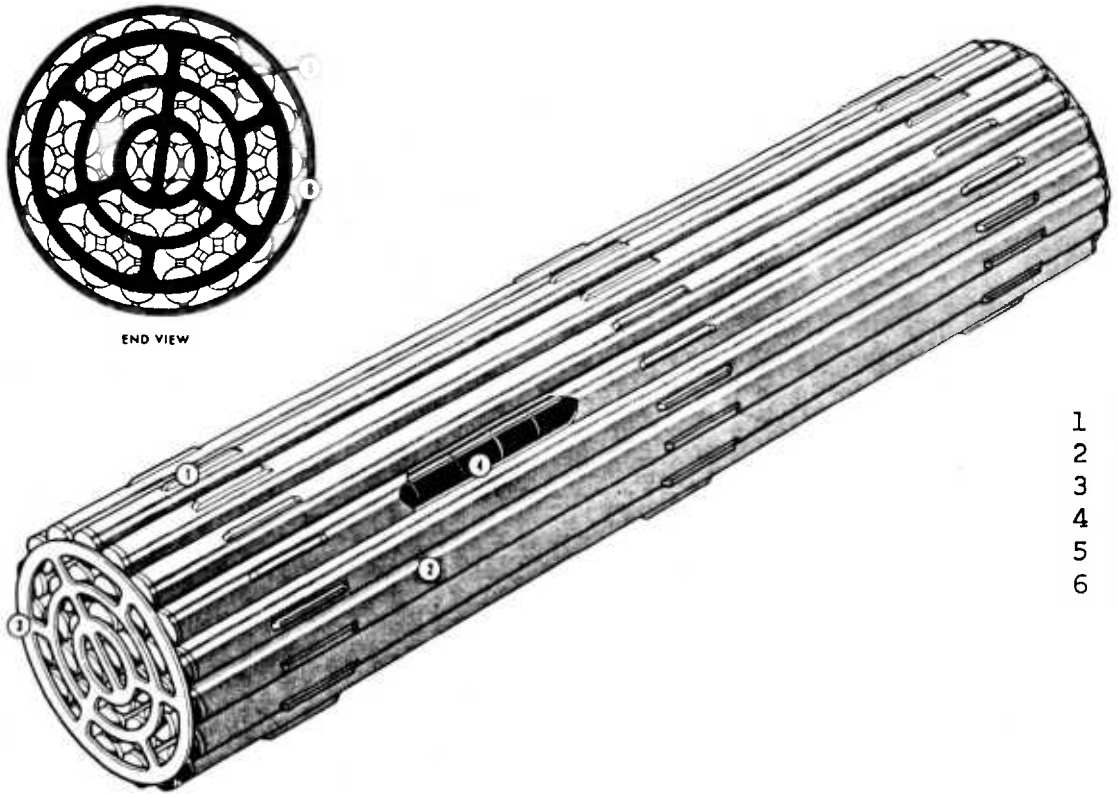


Figure 2.4

GENERAL VIEW OF CANDU PHWR 37 ELEMENT FUEL BUNDLE.
(AFTER REF. 21)



1 ZIRCALOY BEARING PADS
2 ZIRCALOY FUEL SHEATH
3 ZIRCALOY END SUPPORT PLATE
4 URANIUM DIOXIDE PELLETS
5 INTER ELEMENT SPACERS
6 PRESSURE TUBE

TABLE 2.1

GENERAL FUEL ELEMENT DATA FROM SOME TYPICAL NUCLEAR POWER REACTOR DESIGNS

General Data	PWR (W)	PWR (B & W)	PWR (CE)	BWR/6	HTGR	LMFBR	GCFR	CANDU PHW
Thermal output (MWt)	3411	3600	3800	3579	3000	2410	2530	1612
Electrical output (MWe)	1150	1200	1300	1200	1170	1000	1000	500
Efficiency (%)	33.7	33.3	34.2	33.5	39.0	39.0	39.5	31.00
Fuel type	UO_2	UO_2	UO_2	UO_2	UC,ThO_2	PuO_2,UO_2	PuO_2,UO_2	UO_2
Coolant	H_2O	H_2O	H_2O	H_2O	He	Na	He	D_2O
Structural material	Zircaloy	Zircaloy	Zircaloy	Zr-2	Graphite	316SS	316SS	Zr-4
Moderator	H_2O	H_2O	H_2O	H_2O	Graphite	-	-	D_2O
Core Data								
Active height (cm)	366	363	381	376	634	91	148	410
Equivalent active diameter (cm)	337	352	363	366	844	222	270	680
Height/diameter	1.09	1.03	1.05	1.03	0.75	0.41	0.55	0.60

TABLE 2.1 (cont.)

Core Data	PWR (W)	PWR (B & W)	PWR (CE)	BWR/6	HTGR	LMFBR	GCFR	CANDU PHW
Active core volume (ℓ)	32,800	37,600	40,000	63,910	354,000	6,300	8,510	130,000
Average core power density (kW/ℓ)	104	95.7	95	56.0	8.4	380	297	12.4
Fuel weight (kg)	90,200	94,900	103,000	138,000	39,000	19,000	28,000	80,000
Specific power (kW/kgU)	37.8	37.9	36.9	25.9	77	126	90	20.4
Burnup (MWd/teU)	33,000	33,000	33,000	27,500	98,000	100,000	100,000	10,000
C.R.	0.5	0.5	0.5	0.5	0.7	1.3	1.5	0.45
Fuel Assemblies								
Type	square bundles	square bundles	square bundles	canned-square bundles	hexagonal graphite prisms	hexagonal canned bundles	hexagonal canned bundles	pressure tube bundles
Number of assemblies	193	205	241	732	3944	394	347	473
Fuel element array	17 x 17	17 x 17	16 x 16	8 x 8	132 pins	hex	hex	pressure tube
Assembly dimension (cm)	21.4x21.4	21.7x21.7	29.3x20.3	14 x 14	35 x 79	12 x 12	17 x 17	8 x 50
Assembly pitch (cm)	21.5	21.8	20.7	30.5	36.1	12.4	17.5	27.9

TABLE 2.1 (cont.)

Fuel Assemblies (cont.)	PWR (W)	PWR (B & W)	PWR (CE)	BWR/6	HTGR	LMFBR	GCFR	CANDU PHW
Number of fuel elements/ assembly	264	264	236	63	132	217	225	28
Total number of fuel locations	50,952	54,120	56,876	46,116	35,496	85,464	77,031	13,244
Fuel Element Data								
Type	Clad rod	Clad rod	Clad rod	Clad rod	Graphite UC-ThO_2 rod[2]	Wire-wrap clad rod	Vented clad rod	Clad rod
Fuel element pitch (cm)	1.25	1.27	1.28	1.62		0.725	1.14	1.65
Fuel element OD(cm)	0.94	0.96	0.97	1.25	1.56	0.759	0.805	1.52
Pitch/diameter	1.32	1.32	1.33	1.30		1.25	1.41	1.08
Clad thickness (cm)	0.0572	0.0597	0.0635	0.0864		0.038	0.0295	0.038
Fuel pellet diameter (cm)	0.819	0.823	0.825	1.056	1.56	0.66	0.739	1.44
Pellete-clad gap (cm)	0.0082	0.010	0.0089	0.008		0.012	0.012	
Fuel enrichment	2.1/2.6/ 3.1	2.91	1.9/2.4/ 2.9	2.2-2.7	93.5	10 - 15	10 - 15	nat U

TABLE 2.1 (cont.)

Thermal Hydraulic Data	PWR (W)	PWR (B & W)	PWR (CE)	BWR/6	HTGR	LMFBR	GCFR	CANDU PHW
System pressure (bar)	155	155	155	72	50	14	86	89
Coolant flow (10^6kg/hr)	62	68	72	47	5	50	10	23.9
Avg.linear power (W/cm)	178	178	175	206	78.7	295	217	200
Max.linear power (W/cm)	426	483	410	440	229	492	390	528
Avg.heat flux (W/cm^2)	68.5	64	65	50.3	20.4	105	93	50
Max.heat flux (W/cm^2)	183	168	173	111.5	58.3	237	168	115
Minimum DNBR	1.3	1.4	1.3	1.9	-	-	-	-
Inlet temperature (^oC)	300^o	300^o	296^o	269^o	337^o	380^o	332^o	249^o
Outlet temperature (^oC)	332^o	333^o	328^o	286^o	755^o	552^o	642^o	293^o
Maximum fuel temperature (^oC)	1788^o	2021^o	1882^o	1829^o	1410^o	2000^o	2200^o	1500^o

2.3 URANIUM DIOXIDE FUEL PROPERTIES AND BEHAVIOUR

2.3.1 General Characteristics

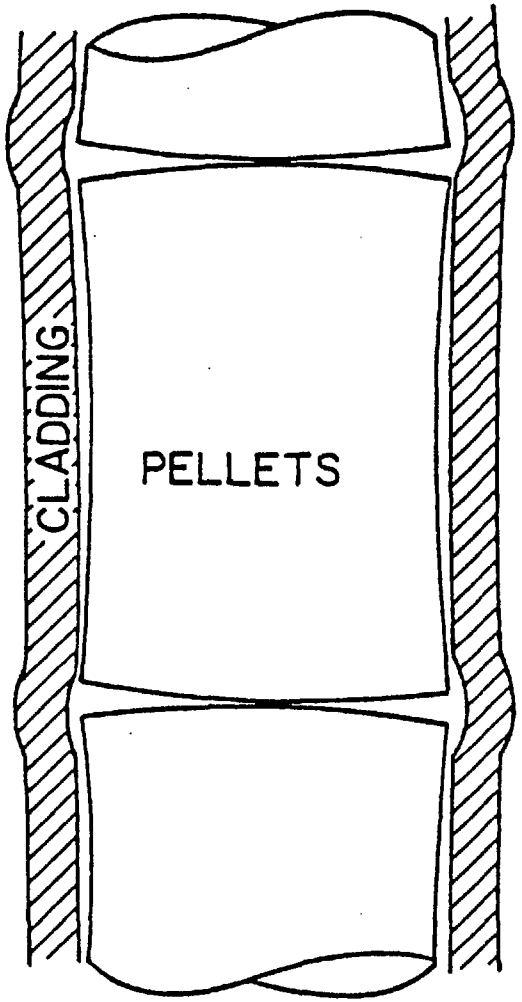
Conventional UO_2 pellet design for water reactor fuels incorporates double-end dishing which provides an allowance for thermal expansion of the hotter central regions, and in some designs there are allowances for UO_2 swelling. There is a small shoulder which should have a minimum width to mimimise the effective pellet temperature for axial expansion and is only there at all to improve robustness and avoid excessive chipping during loading. It is normal for pellet length/diameter ratios to lie in the range 1 to 1.5.

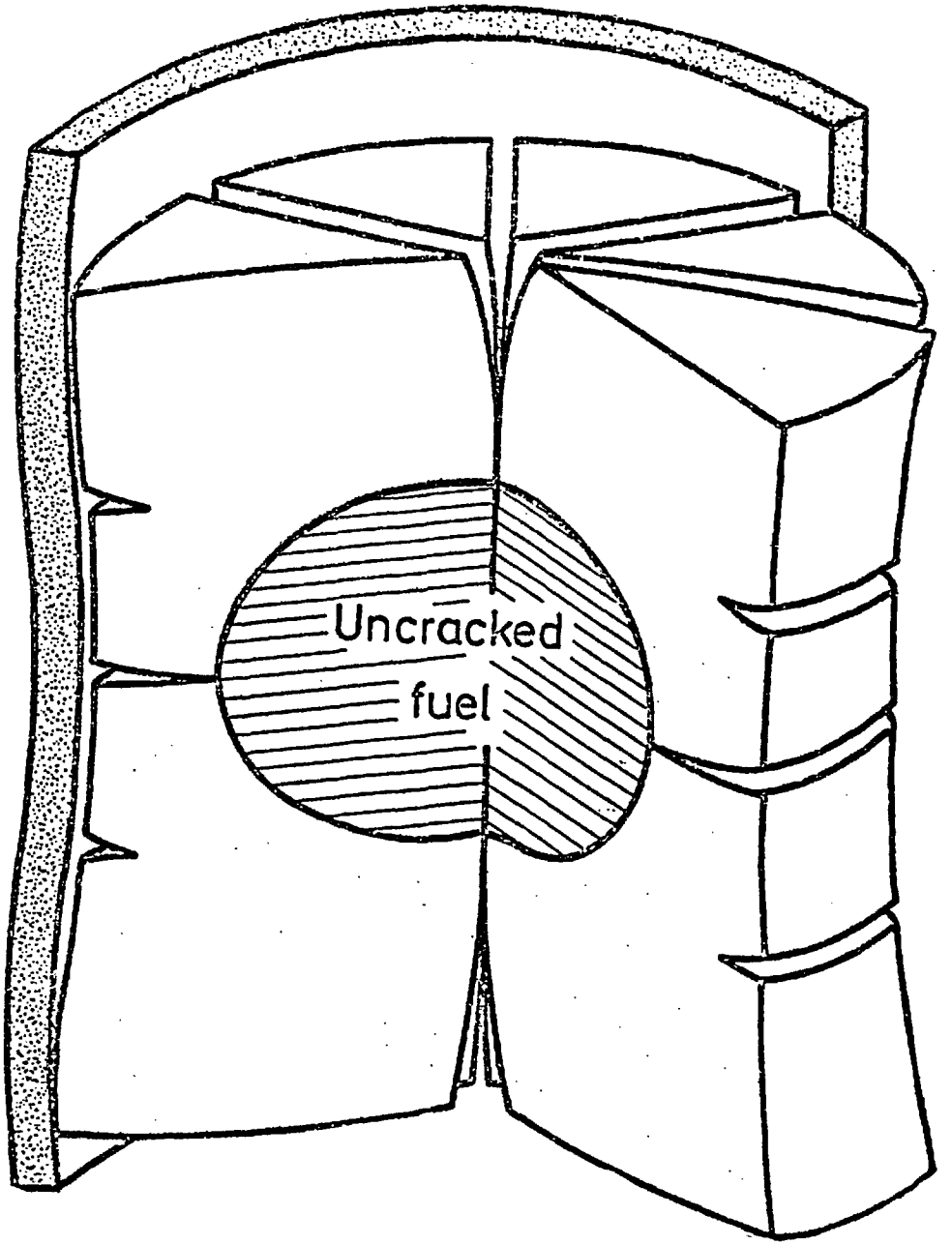
Pellets of this type undergo complex cracking and distortion under the influence of the temperature gradient. This results in the "wheat-sheaf" shape which is believed to cause the characteristic circumferential ridges in fuel cladding at inter-pellet locations. Ridge height is known to increase with pellet length and rating, and to decrease with increase in fuel/clad gap. It is reported to be relatively insensitive to clad thickness or strength (Fig. 2.5).

Many alternative pellet designs have been investigated from flat-ended and annular pellets to more complicated forms with end chamfers designed to minimise ridging. Flat ended pellets are attractive because they produce smaller ridges, but due to their higher expansion fuel/clad gap must be increased. The double end dished pellet with length/diameter ratio close to one has been reported to be the best choice available (22). Short chunky pellet of length/diameter ratios less than one have also attractions, but there are manufacturing problems associated with them.

Figure 2.5

PELLET CRACKING, HOUR-GLASSING AND RIDGE FORMATION IN A FUEL PIN UNDER IRRADIATION. (Courtesy Kernforschungszentrum Karlsruhe)





In practice, however, dimensional stability of fuel pins is of more importance. As discussed before some of the phenomena occurring in UO_2 influence the achievement of target burn-up levels by affecting the dimensional stability of fuel pellets. Among these processes swelling, densification, irradiation enhanced and thermally activated creep and fission gas release are most influential. In this context the mechanical properties of UO_2, especially those which are time and rate dependent, are quite important for the ramping and cycling behaviour of fuel pins.

A review of the published literature indicates that there has been much work on the above properties of UO_2. As a result of these investigations and fuel development programmes for water reactor systems a quantitative understanding has been built up of the general properties of UO_2 as well as its in-pile behaviour.

One of the major thermal characteristics of UO_2 is its very high melting point; exceeding 2800°C. On the other hand it falls in the category of thermal insulators. In fact, its thermal conductivity is quite low at room temperatures, and decreases at higher temperatures up to at least 1500°C. This low thermal conductivity has proven to be the most limiting feature of UO_2 pellets with respect to service as a nuclear fuel. Thus, the thermal conductivity and its relationship with temperature is a governing factor in UO_2 fuel pin performance.

UO_2 has a theoretical density of 10.96 g/cm^3. However, limitations in fabrication process technology and, occasionally, specific performance objectives have invariably dictated use of lower than theoretical density. So in practice UO_2 has densities ranging from 82% to 98% TD. The effect of UO_2 density on mechanical properties and on the thermal conductivity has been found to be very great and complex; therefore, influencing fuel performance strongly.

The uranium-oxygen system is considered to be one of the most complex metal oxide systems known with at least three oxidation states higher than UO_2. Deviations from stoichiometry about $UO_{2.00}$ have a pronounced effect on the mechanical properties, melting point and thermal conductivity.

The intrinsic nature of service as a nuclear reactor fuel, subjects the UO_2 structure to severe stresses from the kinetic energy of the fission fragments and the build-up of foreign fission product atoms within its lattice. Current fuel life requirements, however, demand the fuel pins to undergo 50,000 MWd/teU burn-up, leading to high fractions of impurities near the end of life. Due to the strength and stability of its lattice, UO_2 has shown remarkable resistance to fission and burn-up effects.

Finally, the mechanical properties of UO_2, especially creep which has been shown to enhance under irradiation, affect the performance. The level of thermal stresses in the fuel depend on these properties which in turn are related to all factors influencing the forces between the atoms in the crystal lattice, i.e. temperature, porosity, grain size, O/U ratio, and foreign atoms content.

2.3.2 Chemical and Physical Properties

Probably the single most important factor that has made UO_2 the preferred uranium compound for nuclear fuel service is its outstanding chemical stability and inertness. This advantage plus its dimensional stability is sufficiently compelling to outweigh distinct nuclear and thermal performance handicaps in using UO_2 related to its relatively low density and extremely low thermal conductivity respectively.

The usual quantitative measure of chemical stability for compounds is the free energy of formation. The more negative the free energy of formation, the less tendency there is for the compound to decompose into its constituent element or to react with other elements. From the reported data (23), the free energy of formation of UO_2 is substantially more negative than either the carbides or nitrides (- 218.2 kcal/mol against - 25.5 kcal/mol and - 47.0 kcal/mol respectively).

The tendency of UO_2 to decompose, even at temperatures approaching its extremely high melting point, is minimal. Stoichiometric UO_2 vaporises congruently with a vapour pressure of several atmospheres at the melting point (23). Hyperstoichiometric UO_2 vaporises as a mixture of UO_3 and oxygen with a substantially higher pressure at a given temperature (24). As for hypostoichiometric UO_2, the same composition, namely, UO and UO_2, exists at the end of vaporisation. At temperatures above 1800°C the formation of uranium metal precipitates in heated UO_2 has been taken to indicate the existence of single phase UO_{2+x} at high temperatures (23-24).

The compatibility of UO_2 with cladding and coolant has been reported to be satisfactory. In fact, the chemical reactions of UO_2 with Zirconium alloys have been studied experimentally in the laboratory and found to be slight for the practical cladding temperatures (24). The actual fuel element operating experience, with both Zirconium and stainless steel cladding, has verified such experiments. However, recent results have shown that at higher heat ratings or burn-ups incompatibility will appear and "fission-product/cladding" or "fuel/cladding" interactions coupled with high stresses are the most life-limiting factors. Regarding the coolant, the stability of UO_2 when exposed to high temperature water has also proved reasonable. Service experience with naturally and artificially defected fuel pins has demonstrated excellent stability regardless of the oxygen content of the coolant (19). It has also been shown that fuel loss, especially for sintered pellets, is usually negligible provided the cladding maintains its circumferential integrity. Again it must be mentioned that the excellent chemical stability of UO_2 exposed to water at current operating conditions may not persist at higher heat ratings or higher surface temperatures, thus one will have to consider the effects of corrosion and hydriding too.

Among the UO_2 physical properties, its melting point and thermal conductivity play the most crucial part in fuel behaviour, both influencing the maximum internal temperatures and the attainable power density. Current thermal reactor practice is to limit UO_2 operating temperature to below the melting point. Primary concerns regarding operation of

liquid UO_2 are; (a) excessive cladding deformations arising from the UO_2 phase change volume expansion; (b) clad-melting from contact with molten fuel; (c) possible nuclear instabilities from liquid movement; and (d) catastrophic pin deterioration and possible propagation to adjacent pins in the event of a cladding defect (26). These concerns make it vital to have an accurate knowledge of the UO_2 melting point, as well as the thermal conductivity in order to establish operating conditions that preclude melting, yet do not unnecessarily penalise pin performance.

Lately, surveys have been made regarding the problem of operation with fuel melting in commercial reactors. Some reports have indicated that experimental Zircaloy clad UO_2 fuel pins were successfully irradiated under extreme operating conditions with peak heat ratings of $\sim$ 1450 to 1800 W/cm and melting extending to 85% of the fuel radius or 70% of the cross-sectional area (29). As fuel designs become more advanced, the need for operation with fuel melting becomes better defined. The basic difficulties involved can be summarised in the following paragraphs (26,27,28):

(a) The basic limitation in operating UO_2 fuel with central melting is the pin swelling as a result of the volume expansion when UO_2 melts. However, tests have shown that the swelling can be accommodated for by providing a larger free volume within the fuel accessible to the molten UO_2.

(b) The fission product release, particularly the xenon, krypton and iodine release is large. The basic

difficulty is to accommodate these products inside the fuel cladding without endangering the integrity of the fuel element.

(c) Interaction between the UO_2 material and the cladding material occurs when the surface of the fuel reaches approximately 800°C (with large initial gaps). This interaction can result in cladding failure because of chemical reactions between the UO_2 and the cladding, with subsequent release of fission products in the reactor coolant and contamination of the primary cooling system.

(d) When melting occurs in the fuel pin, the cladding material must take over the support of the fuel assembly in the axial direction. This might result in buckling of the fuel pin, if not properly designed for support of the fuel. Buckling of the fuel pins results in a decrease in the distance between the neighbouring fuel pins and possibilities for burn-out arises.

From the above it can be concluded that it should be possible to design the fuel elements to withstand the problems resulting from molten UO_2. However, a comprehensive assessment of advantages versus risks associated with fuel melting is not possible considering presently available technology.

Regarding the thermal conductivity, its great importance has already been emphasised. Accurate knowledge of this property is vital because, among other things, it determines the maximum power that can be taken out of the fuel element per unit length of the material without exceeding the safety limits of the fuel element. It also determines the

temperature at every position within the fissioning UO_2 body and the temperature, in turn, is the principal independent variable governing all dynamic processes occurring in UO_2; like fission gas release, grain growth, diffusion, etc.

The thermal conductivity of UO_2 has been the subject of a great many investigations over the past ten years. In 1965 an IAEA panel comprehensively reviewed the existing data and considered that values of UO_2 thermal conductivity were reasonably well established in the range 500-1300°C, following the expected $k = (A + BT)^{-1}$ relationship for a dielectric in which thermal resistance results from temperature dependent phonon-phonon interactions and temperature independent phonon-impurity or structural defect interactions (30). However, at high temperatures, i.e. above 1700°C, there has been considerable difference of both the theoretical and experimental opinion as to whether there is an increase in conductivity. Any such increase has been variously ascribed to three different mechanisms: phonon (lattice) conductivity, photon (radiative) conductivity and electronic conductivity. Theoretically internal radiation will be important at high temperatures if the oxide is transparent to infrared and this is a function of photon absorption in the grains and scatter at the boundaries (30). It has been argued (31) that in the intrinsic range internal radiation could be reduced to a low level but a significant electronic component exists at high temperature. Theoretically therefore the picture is confused, partly due to the apparent inadequacy of the band theory to UO_2, but now there is a general opinion that there is some increase of thermal

conductivity at high temperature. The extent could be dependent upon grain size or stoichiometry, and is likely to be a function of porosity as pores act as scattering centres and reduce the radiation component (31). This emphasises the fact that the conductivity can vary according to a large number of variables, and this is further complicated under irradiation by changes in porosity, stoichiometry and by fuel cracking.

The thermal conductivity of UO_2 falls with increasing porosity. The relationship has been established for low porosity fuel, however, a lot of confusion still exists about the effect of porosity, particularly when the porosity is above 10%. Theoretically the effect is expected to be porosity and temperature dependent and will certainly be greatly affected by the size and the shape of pores and this could account for some apparent disagreements in published data. The morphology of low density material, with irregular and interconnected porosity, is very different from that of high density material, which contains largely isolated, near spherical pores, so that an accurate relationship must take account of pore shape (32). It follows that it is unlikely that a simple equation will give a good representation over a wide range of densities, although it may be adequate over a short range.

Experiments carried out at many laboratories have concluded that as a result of fuel cracking UO_2 conductivity will decrease. This effect varies according to the amount of fuel restraint. This is due to the fact that cracking

itself is restraint dependent. The whole question of how and when a fuel pellet cracks under irradiation is not fully understood, it is presumably very variable, and is dependent upon the rate of start-up and subsequent power changes. Cracks heal by sintering processes above the sintering temperature, especially in the hot central fuel regions. It has been established that fuel sintering begins at $\sim$ 1400°C (33). Therefore, it can be assumed that above $\sim$ 1400°C the effect of cracking is very small, even in low restraint fuel. Below 1400°C the effect increases with decreasing temperature.

As far as the fuel radial temperature is concerned the effects of cracking on thermal conductivity are negligible. This is because the pellet cracks mainly in the radial and axial directions and the gaps generated by cracking are thus parallel to radial heat flow. Nevertheless, since fission gases will fill up these gaps the effective conductivity of fuel will drop. On the other hand, circumferential cracks, if formed, may have a pronounced influence on the reduction of the effective thermal conductivity due to the formation of fission gas filled radial gaps.

Effects of stoichiometry have been studied more extensively. Howard and Culvin (34) have found the conductivity of UO_2 to decrease significantly as the O/U ratio increases, i.e. as the UO_2 becomes hyperstoichiometric. Other works, however, have indicated that in both hyper- and hypostoichiometric oxide fuels, the fuel centre becomes more non-stoichiometric under the influence of a temperature gradient,

with the fuel periphery tending towards stoichiometry. It follows that for oxide fuels operating at moderate ratings, i.e. well below melting, thermal conductivity will not be a sensitive function of initial stoichiometry.

2.3.3 Thermal Expansion and Cracking

At desirable fuel pin heat ratings UO_2 operating temperatures reach high levels; and even may approach melting point, so substantial differential thermal expansion can occur between the fuel and cladding as a result. If not properly accounted for in design, this differential expansion can easily exceed the clearance gap provided in fabrication and impose unacceptable strains on the cladding. The expansion characteristics of real fuel pellets and the deformation and cracking modes caused by them are much more complex than can be described by a simple differential thermal expansion calculation.

The fundamental driving force for fuel/cladding interaction is the UO_2 thermal expansion coefficient and the significance of such interactions to fuel pin performance has motivated measurement of the basic thermal expansion data up to the melting point and beyond. The scatter in data, as found in the literature, is minor compared to the uncertainties in temperature profile in the pellet.

The expansion of UO_2 pellets is very complicated and cannot be predicted from thermal expansion data alone. It seems that the general trend is to divide pellet expansion into two components - uniform expansion and local distortion.

The uniform expansion is influenced by temperature distribution within the pellet and by external restraints. For example, a large diametral gap between pellets and cladding results in poorer heat transfer with higher pellet temperature and greater expansion than would be the case with small gaps at the same fuel rating. External restraints (diametral interaction between cladding and pellets, and end-to-end interaction between adjacent pellets) reduce expansion by imposing counteracting compressive forces on the pellets.

Another aspect of thermal expansion to be considered here is the cracking modes of UO_2 pellets. This is partly because the ceramic fuels exhibit an extremely brittle behaviour at low temperatures and a moderate temperature gradient is sufficient to cause stresses in excess of the local fracture stress which leads to fuel cracking. Formation of wedge-shaped pieces of fuel is a generally accepted cracking pattern. A simple cracking model may assume a plastic core in the hot centre and an outer annulus of these blocks of the cracked pellet. Plastic flow depends on heating rate, as shown by Notley et al (35) in irradiation experiments where the pins reached their final power in different times. When thermal equilibrium was reached within about 1 min plasticity was effective only above 1600^{o}C. In slowly heated fuel pins plasticity was found even at 750^{o}C.

During constant operation of a fuel pin the initial cracks may become entirely closed by swelling and irradiation-enhanced creep, the cladding thereby acting as a confinement.

A new crack pattern develops during cooling with the larger cracks now in the inner plastic zone. This crack reversal effect corresponds to the well-known stress reversal effect in thermoplastic bodies.

Cracking of pellets increases the outer diameter compared to thermoelastic behaviour. But if enough space is available in a fuel pin the outer diameter of pellets expands by relocation effects even more than by the model previously discussed. The exact mechanism for relocation is not yet known. Experimental data are given in Refs.(36) and (37). Newer results can be found in Refs.(38-41). One of the important results of these investigations is that in fuel pins with large initial gap, with no limitation on pellet expansion by the cladding, pellet diameter increase due to relocation is about 0.5-2.5%. Brozoska and Wunderlich (42) have concluded from their direct measurements in instrumented fuel pins that 40 $\pm$ 20% of the initial gap is eliminated during the first start-up to full power (for diametral gap of 0.50-4.97% of pellet diameter and heat rating of 128-925 W/cm). After 500 hours of irradiation another 20% of the gap is closed. There is evidence that the fuel/cladding gap in most cases has almost completely closed due to the combined effects of relocation and cladding creep-down (particularly in PWRs).

Axial expansion of a stack of dished pellets can be calculated by assuming free expansion, and summing the individual elongations at the inner edge of the pellet shoulders, as long as mechanical interaction between fuel

and cladding does not become effective. If interaction occurs, prediction of axial length changes is more difficult.

Another deformation caused by thermal expansion, at least partly, is the so-called bamboo-ridging effect. This is due to the fact that UO_2 pellets are finite cylinders and therefore their ends expand more in diameter than their mid-section under the parabolic temperature profile. This effect is partly responsible for the bamboo-ridging of the cladding at the pellet/pellet interfaces. Additional axial forces acting particularly on the pellet shoulders in the case of dished pellets may slightly increase the ridging effect by pressing the UO_2 blocks outward. The results from LWR fuel pins have shown a small bamboo effect only, the diameter across the ridges being below the initial diameter.

2.3.4 Restructuring and Grain Growth

In the high temperature regions of a UO_2 pellet, characteristic microstructural changes occur by thermally activated processes. The pores originally present in the fuel migrate under the influence of the temperature gradient towards the centre of the fuel, the residual porosity is further reduced by hydrostatic stress-directed diffusion of vacancies from the pores (hot pressing). A central void is created within a very short time from start-up (43) or alternatively the one already present is enlarged if the fuel is composed of hollow pellets. The fuel density increases accordingly, by an amount dependent also on the local fuel temperature, see Figures 1.2 to 1.6 in Chapter 1.

Significant grain growth has been observed above about 1400°C. Up to about 1700°C the grain growth is isotropic. At higher temperatures radially aligned grains are formed. In general, three distinct regions have been identified with pore migration, namely:

(a) a low temperature region where the original microstructure of the fuel is essentially preserved;

(b) a medium temperature region with isotropic grain growth (equiaxed grains);

(c) a high temperature region with radially aligned grain growth (columnar grains).

Equiaxed grain growth is diffusion-controlled. The columnar grains are formed by an evaporation-condensation mechanism within pores or gas bubbles (43-45). Because of the temperature gradient, UO_2 is evaporated on the hot side of the pore and condensed on the cold side. Therefore the pores are moving up the temperature gradient leaving behind them columnar grains. The collected voidage forms a central channel or void, the free surface of which is an isotherm.

Equiaxed grain growth is hindered to some extent by the pores, which obviously pin up the grain boundaries, particularly at grain triple points. For instance, grain growth rates were found to be smaller for low density pellets than for high density pellets, whereas the activation energy was not affected (46).

Since grain growth is normally accompanied by a porosity decrease, particularly in the columnar grain region, for realistic temperature calculations these changes should

be taken into account. However this complex problem is not yet fully solved today because of the superposition of many different effects and the lack of sufficient experimental data.

2.3.5 Fission Gas Release

The behaviour of inert gases, mainly xenon and krypton, created during the irradiation of reactor fuel materials is of importance in the study of fuel swelling, of fission gas release and of the mechanical and thermal behaviour of reactor fuel elements. Many of the initial investigations and theories attempted to explain gas release and swelling (see Section 2.3.6) in terms of some controlling phenomena. The more recent models have combined phenomena and have either developed simulated stochastic models, Warner and Nichols (47), or dealt with distribution functions of bubbles, Li et al (48). Such models are then used in conjunction with fuel performance codes. An understanding of the competing processes and proposed mechanisms is necessary to evaluate performance prediction codes and to interrelate the observations made of irradiated fuel materials.

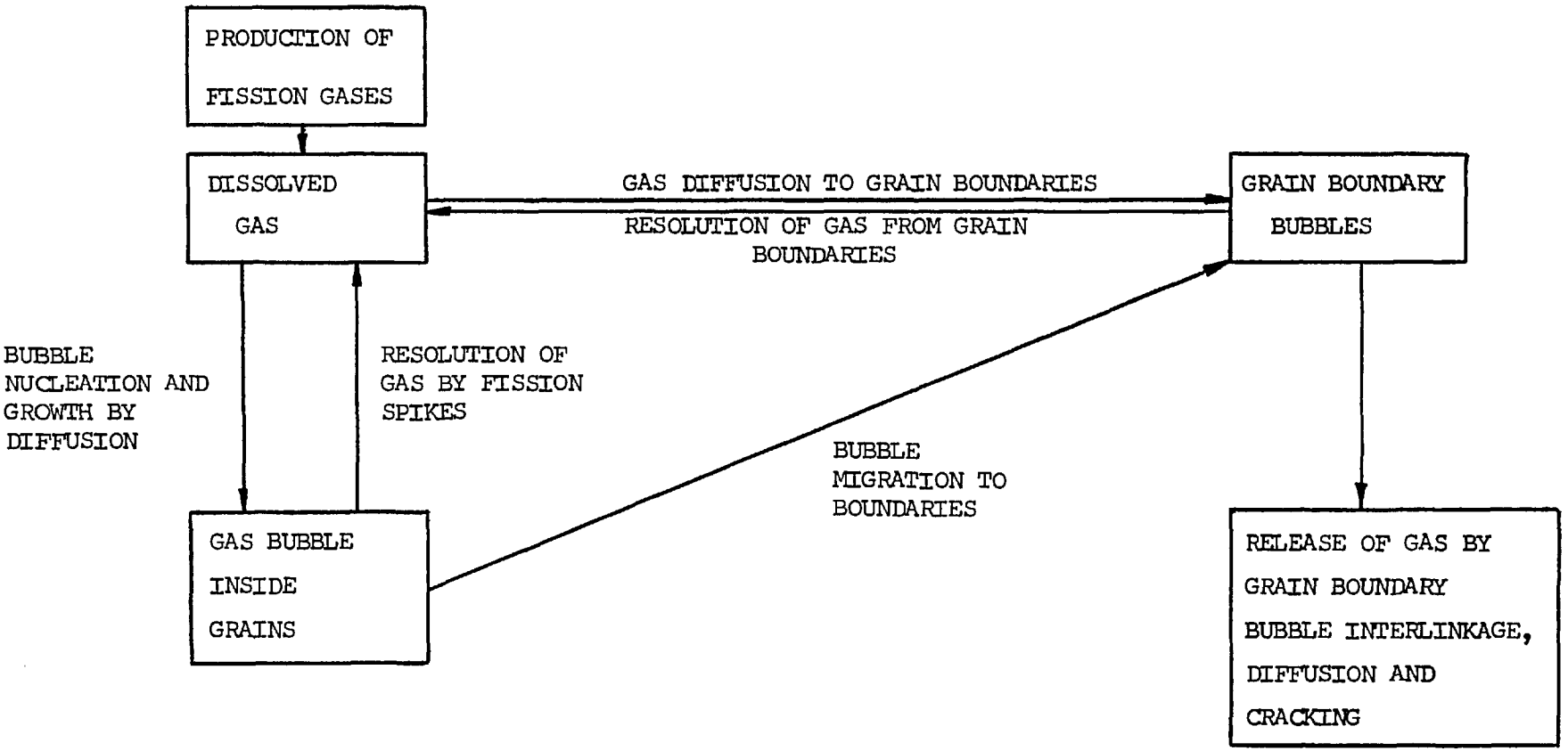
About 31 stable or long-lived inert gas atoms are produced per 100 fissions of uranium or plutonium in water reactors. Early in life the fission gas consists of about 86% xenon and 14% krypton. Later the composition shifts to a higher percentage of xenon due to an increasing amount of Pu^{239} fissions. The immediate effect of these gases, if released, will be on the fuel temperature. In fact the

thermal conductivity of the fission gas mixture is less than that of pure helium, the usual fuel pin filling gas, by a factor of about 22. The admixture of fission product gases strongly reduces the thermal conductivity of the gas in the fuel pin. The effect is more pronounced in fuel pins with helium under atmospheric pressure than in pressurised fuel pins. On the other hand, the release of fission gases will increase the internal pressure of the pin with time. This increasing gas pressure in the fuel pin must be limited by an appropriately designed plenum volume at one or both ends of the pins. In LWR fuel pins the expected internal pressure at the end of life must be below the external coolant pressure; this sets a design basis for plenum volume. Furthermore an accurate knowledge of the gas pressure as a function of time is necessary, mainly to be able to calculate the cladding creep-down, which is very important with respect to pellet/cladding interaction problems; and to know the starting conditions of a postulated LOCA (loss-of-coolant accident), because the cladding behaviour during the transient depends strongly on the initial gas pressure in the fuel pin.

The physical mechanisms which control fission gas release can be summarised in the following lines (49-52). Fission gas is found in three types of location within the fuel; dissolved in the fuel crystal lattice, in gas bubbles within the individual grains and in bubbles lying on the grain boundaries, on the face edges or nodes. The diagram in Fig.2.6 shows the relationship between the three types of site and how gas is transferred between them (53). When the gas is formed during the fission process it is first

Figure 2.6

GAS FORMATION AND MOVEMENT IN NUCLEAR FUEL
(AFTER REF. 53)



found as individual atoms lying interstitially in the fuel lattice. At temperatures high enough for gas atoms to diffuse through the lattice random encounters occur and gas bubbles nucleate, see Figure 2.7.

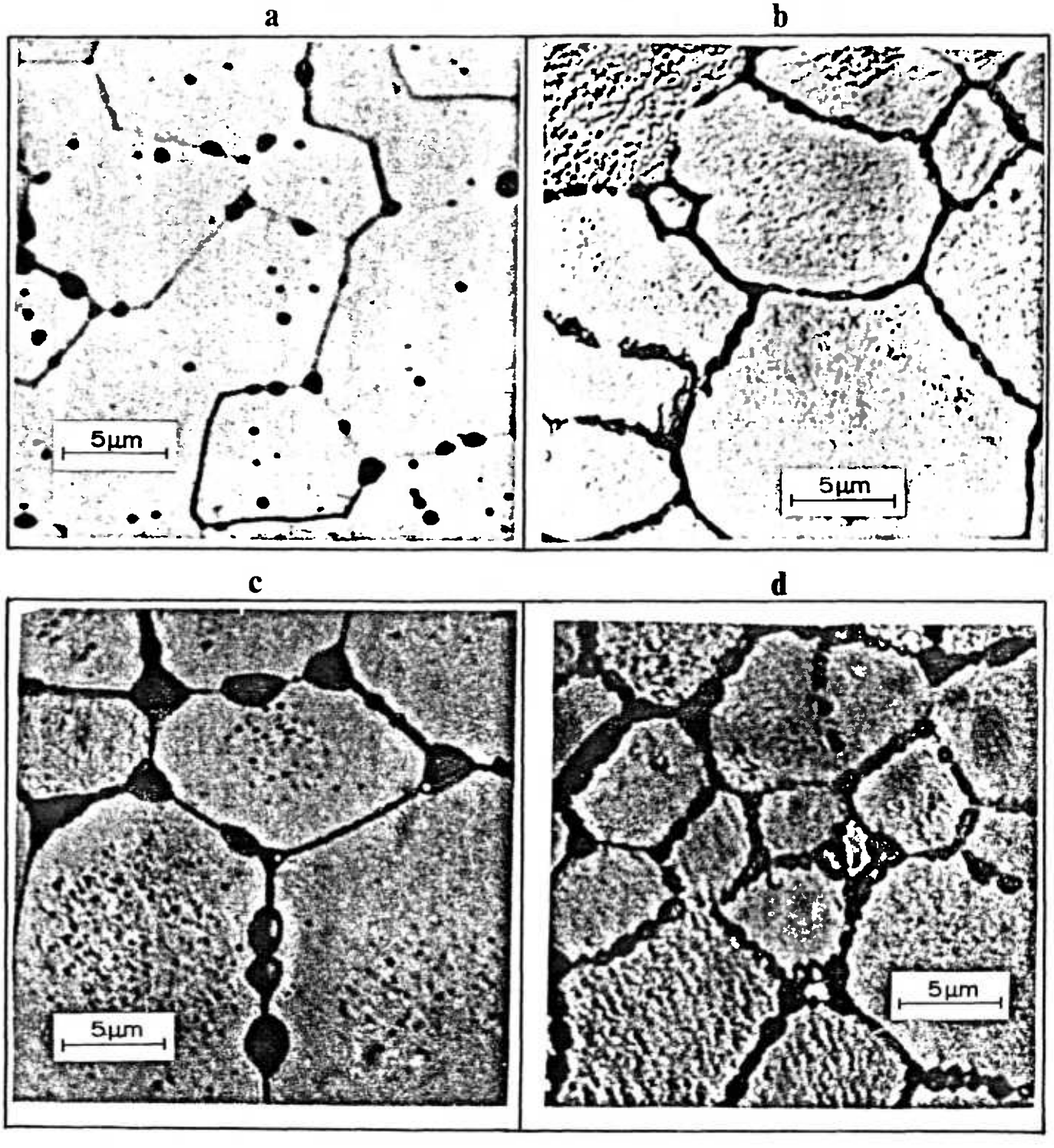
Below about 1000°C the inert gas atoms remain near the end points of their fission tracks. A few fission tracks end in the gas-filled space outside the UO_2, and fissions near the surface can sputter UO_2, together with trapped fission gas atoms, from the surface. Generally, less than 1% of the fission gas generated below 1000°C is released. At higher temperatures fission gas atoms are mobile and can reach grain boundaries by diffusion through the UO_2 matrix. A trapping and resolution process thereby plays an important role; diffusion is hindered by trapping of gas atoms at dislocations or in pores, fission-induced resolution of gas atoms from dislocation or pores accelerates the diffusion; Fig.2.7.

From the grain boundaries the gas can easily reach the free volume of the fuel pin. Either there are direct connections or such connections are formed during power changes because grain boundaries with accumulated fission gas bubbles are mechanically weakened so that thermal stresses can induce cracks more easily.

As was stated before, at very high temperatures bubble migration becomes important. Somewhat below 1700°C the thermally activated migration of intragranular bubbles to the grain boundaries becomes effective. Above about 1700°C almost 100% of the fission gas is released by bubbles moving

Figure 2.7

a TYPICAL UNIRRADIATED UO_2 FUEL STRUCTURE
b IRRADIATED UO_2 (NOTE THE ABSENCE OF INTRAGRANULAR POROSITY)
c DEVELOPMENT OF FISSION-GAS FILLED BUBBLES ON GRAIN BOUNDARIES
d INTERLINKAGE OF GRAIN-BOUNDARY FISSION-GAS FILLED BUBBLES
(AFTER REF. 54)



toward the central void by the evaporation-condensation mechanism. The initial porosity, as well as accumulated gas at grain boundaries and circumferential cracks caused by prior cooling down, have been considered as the origin of such bubbles. It is important to note that at these high temperatures no cracking of fuel is required as the gas forms its own escape route via the open grain edges. Fuel cracking is more important in the cold fuel regions where the gas has only time to move short distances and no grain boundary bubbles are interlinked (53).

The description given here shows that for fuel pin design purposes a good quantitative prediction of the temperature and time dependence of the fission gas release is mainly necessary for the temperature range 1000-1700°C. Above 1700°C, 100% release rate is good approximation whereas the contribution from that part of fuel below 1000°C is very small.

Many theoretical models and computer codes have been developed in recent years, mostly for fast breeder programmes. The GRASS-Code (13) is one example. A detailed fission gas release and swelling model has been developed at the UKAEA Reactor Development Laboratories (54). The movement of fission gas as single atoms in solution in the fuel matrix and their clustering in the form of bubbles, the resolution of bubbles into the matrix, and bubble migration and coalescence are phenomena that have been modelled in these codes. Work in this field is still going on, and adjustments to experimental results are very important.

For typical LWR conditions, i.e. relatively low fuel temperatures combined with long irradiation times, few data are available, because well-controlled in-reactor experiments at least three years long are needed. In using data for fission gas release from standard fuel pins in power reactors, two main problems arise: (a) in general the power history is not known in all details, and (b) the actual powers are lower in most cases than the powers desired for design calculations. Therefore simple fission gas release models are still applied in design calculations to determine the necessary plenum volume, and are conservative with respect to maximum admissible gas pressure (3,4,5,46,49). In such simple models the fuel is subdivided into temperature zones and each zone is given a release rate that is independent of time.

2.3.6 Densification and Swelling

Densification and swelling are defined as in-reactor volume changes of the UO_2 without stresses from external forces. Volume changes due to hot pressing, fracturing and relocation should be strictly separated from the densification and swelling effect. Thermal sintering in UO_2 occurs only to a measurable extent at temperatures in excess of 1200°C (55). A thermal component of the in-reactor densification has been observed by Ainscough (56). In-reactor densification has been found at temperatures as low as 400°C. In both cases, however, densification is caused by shrinkage and disappearance of pores, typical for the final stage sintering. Thermal sintering kinetics during the intermediate and final

stages have been first treated with vacancy diffusion models by Coble (57).

Early work on plate-type UO_2 fuel demonstrated that the generation of solid and gaseous fission products would cause the UO_2 matrix to expand and this expansion had to be accommodated in fuel designs to achieve high burn-ups. In fact it was found that since each fissioned atom yields two new atoms fission should induce a volume expansion. This unavoidable expansion was called swelling. It was also thought that the swelling was linearly proportional to burn-up; because one atomic volume was attributed to each fission product atom. However, later work showed that this was generally an under-estimate. These observations promoted a major concentration of resources on understanding the fuel swelling mechanisms in order to design fuel pins for breeder reactor service, both thermal and fast spectrum. The swelling phenomenon at elevated temperatures initiates at low enough burn-ups to be a potential end-of-life concern at current thermal reactor target burn-ups.

The densification effect did not become a subject of considerable interest before 1972. In that year there were reports of fuel problems in American PWR's. Clad collapsing along axial gaps (pellet-pellet gaps) in the fuel column was observed in several of these reactors (58). This was linked to the pellet pore structure and was found to be the consequence of high initial fuel densification. It was further understood that densification under irradiation gives both axial and radial dimensional shrinkage. Axial

shrinkage produces stack shortening and gaps between pellets which in turn can lead to clad collapse and flux peaking, due to the decreased neutron absorption in the vicinity of the pellet-pellet gap (58). Radial shrinkage initially increases the pellet/cladding gap which results in higher fuel operating temperatures and the possibility of centre fuel melting during normal and over-power operation, and high clad temperatures under LOCA conditions.

The inter-relation between swelling and densification thus becomes clear, they are closely linked to the pellet microstructure and pore distribution. Swelling of UO_2 is basically due to the accumulation of fission products. At low temperatures the effect is due to very fine fission gas bubbles ($\sim$ 50 Å) and other fission product atoms in solid solution. At intermediate temperatures the formation and growth of fission gas bubbles, which takes place particularly at grain boundaries, increase the swelling rate. When the grain boundaries are saturated, the bubbles become interconnected and the excess fission gas is released (59). The interlinked pores thus become unstable and sinter up again. Dynamic equilibrium of sintering and swelling is thereby established. At high temperatures the gas bubbles are swept out along the temperature gradient by the processes which are also responsible for the columnar grain growth (52,55). Therefore swelling is reduced in the high temperature range.

It has been assumed that densification through shrinkage and removal of initial porosity and the swelling of the

matrix operate simultaneously and, in a first order approximation, independently. Therefore a linear superposition of both effects is common practice. The relative volume change of UO_2 may be expressed by the addition of volume change due to the pore shrinkage and annihilation to the volume change due to matrix swelling. Since densification (decrease in porosity) is at least limited by the total initial porosity, the burn-up dependent volume change must run through a minimum; taking swelling as the positive volume change and densification as the negative volume change. The minimum is a function of pore characteristics and size. It is also dependent on the rate by which the pores are removed; it is large if the pores are rapidly removed and small if the pores are highly stable. Experiments by Freshley et al (64) have also shown that pore size distribution, fission rate, fuel temperature, and burn-up are the major factors that influence irradiation-induced densification of UO_2 pellets.

Now swelling and densification can be discussed in more detail. Some of the theories, relevant to swelling and densification, calculation methods and uncertainties in predicting them will be reviewed in the remainder of this section.

Swelling is induced by gaseous and solid fission products. The volume increase due to solid fission products is taken to be proportional to burn-up in a linear manner. Fission gas swelling is, however, more complicated. The common practice is to classify the swelling of UO_2 according to temperature range, i.e. low-temperature swelling, some

gaseous and some due to solid fission products and high-temperature swelling mainly due to gaseous fission products.

Some solid fission products have a very small solubility in fuels currently used such as oxides. They form precipitates which at high burn-ups are easily observed by optical micrography (55,61). Their composition depends on the local fuel temperature and thus varies radially. X-ray microprobe analysis in highly irradiated oxides shows that these precipitates generally belong to two families: those rich in molybdenum and those rich in barium (54,59). The swelling due to solid fission products either in solution or in precipitates is not easy to distinguish from the gaseous swelling, unless the range of temperatures is known. Thermodynamic estimates of the fate of gaseous and solid fission products and their affinity for the liberated oxygen (due to fission in UO_2) lead to estimates of fuel swelling. It has been reported (59) that, at temperatures below that at which the fission products are mobile ($\sim$ 1100°C) their accumulation creates relatively small volume changes in the fuel, but because of the low fuel temperature, the UO_2 has high strength so that these small volume changes may be instrumental in imposing strains on the fuel pin cladding through pellet/cladding interaction.

Contrary to solid fission products, gas atoms, mostly Xe and Kr, constitute a non-neglible proportion. Their solubility in fissile metals, alloys or ceramics being low, they should precipitate in the same way as solid atoms considered above. The difference is that the volume occupied

by a gaseous atoms is now much bigger than the atomic volume so that the linear proportionality of swelling to burn-up becomes a significant under-estimate (58,59). The precipitation of fission product gases has been reported to occur at fuel temperatures greater than 1100°C, since the mobility of gas atoms increases markedly at temperatures higher than this. The gas atoms thus precipitate into bubbles within the grains where they are generated but these bubbles are hit by highly energetic fission fragments. The result of this interaction is to create, within the grains, a population of very small bubbles, typically 5 μm (61). These bubbles are prevented from growing by the enforced re-solution of fission gas atoms and their contribution to fuel swelling is small but a proportion of the gas atoms so re-dissolved is able to diffuse to the grain boundaries. At the grain boundaries the ready supply of vacancies enables fission product gas bubbles to grow and lentigular bubbles with a maximum diameter in the plane of the grain boundary of several μm are typical (61). This is the process which, as was mentioned before, is responsible for the formation of the columnar grain growth.

Regarding the mechanisms of densification, many quantitative models describing its dependence on UO_2 properties and irradiation conditions are available today. Among these models two have received more attention. First the model developed by Marlowe (62) may be called an "irradiation-enhanced diffusion model". The model developed by Stehle and Assmann (55,60) is the second model and can be characterised by the assumption that the pores are atomized to

vacancies by the fission spikes traversing the pores. This process of vacancy generation is fission induced and thermally activated. On the other hand the migration of these vacancies to effective sinks is believed to be mainly thermally activated.

In general, Marlowe's derivation follows the Coble theory (63), which is based on the assumption that the driving force for pores shrinkage is their effort to lower their free energy by reducing their surface area. The thermal diffusion coefficient is replaced by and "enhanced diffusion coefficient". The model can be easily applied.

The model by Stehle and Assmann is based in principle on a two step mechanism: (1) generation of an excess vacancy concentration around the pores, and (2) migration of these vacancies along the concentration gradient from the sources to the sinks, e.g. grain boundaries. As stated earlier, vacancy generation is thermally activated as well as fission induced, but at low temperatures the fission induced generation exceeds the thermal generation. The vacancy migration is purely thermally activated except at very low temperatures, where an athermal irradiation component of migration exists (60). Based on these processes, four temperature regions have been identified which describe the dependence of irradiation induced fuel densification on temperature. These are:

Region I : Totally athermal densification below $\sim 450^{\circ}C$.

Region II : Densification depends on temperature in the region $\sim$ 450-750°C, where thermally

activated vacancy migration is rate controlling.

Region III : Densification is independent of temperature in the region ∿ 750-1300°C, where athermal excess vacancy generation by fission spike pore overlap mechanisms are rate controlling.

Region IV : Totally thermally activated densification above ∿ 1300°C.

According to this model the shrinkage rate of small pores strongly controls the initial densification. Coarser intergranular pores act as ineffective vacancy sinks during this initial stage as mentioned before. Grain size is of minor importance in the high temperature region especially if the pore concentration is low. At low temperatures and high pore concentration the fraction of excess vacancies which reach the grain boundaries decreases with increasing grain size. Therefore it has been concluded that in general large grain size material is more densification resistant (55,60). Finally most of the important features of the Stehle and Assmann densification model have been experimentally verified by recent work (64).

2.3.7 Mechanical Properties

The importance of UO_2 fuel mechanical properties, especially those which are time and rate dependent, has already been emphasised. Here, UO_2 properties most relevant to computer modelling, namely, elastic moduli, fracture strength and creep behaviour, are discussed.

The elastic behaviour of polycrystalline UO_2 can be adequately represented by isotropic elastic moduli. Of the four elastic moduli of an isotropic solid - shear modulus, Young's modulus, Poisson's ratio and bulk modulus - Young's modulus and Poisson's ratio are the most widely used properties. For UO_2 they depend on all factors which influence the forces between the atoms in the crystal lattice, i.e. temperature, porosity (sintering pores, fission gas bubbles), grain size, O/U ratio, and content of foreign atoms (impurities, fission products). The elastic moduli of UO_2 decrease with increasing temperature because the rigidity of the lattice decreases too. To a first approximation, Young's modulus is linear in temperature with a slope independent of porosity (65,66). There are very few results available on the dependence of Poisson's ratio on temperature. Normally a constant value or slightly temperature dependent values are used. The effect of porosity on elastic moduli is very complicated, because of the effects of pore shape. Theoretical expressions for the effect of spherical pores exist but they have been reported not to correlate well with measurements on sintered samples (67). However, some results have been obtained with simple linear fits. The elastic moduli have been corrected for the effect of porosity by multiplying the fully dense modulus by a linear function of fractional porosity. The effect of grain size on Young's modulus is very small. But an increase in O/U ratio decreases the Young's modulus (68). At higher burn-ups the influence of fission products on Young's modulus cannot be separated from the influence of the change of O/U. Few results are

published on the dependence of elastic moduli on the concentration of foreign atoms.

The variation of fracture strength has been studied by two groups of investigators, Evans and Davidge (69) and Cannon et al (70). Cannon et al have examined the effect of strain rate variations quite thoroughly but have used only the minimum number of temperature values thus missing some detail in the temperature dependence, particularly at low temperatures. Evans and Davidge have separated the fracture behaviour of UO_2 into three temperature regions. The low temperature region where fracture is initiated from fabrication pores. The fracture stress is constant with temperature up to about 600^{o}C (depending on grain size, porosity and strain rate) and then rises to a maximum. In this low temperature range the fracture stress is smaller than the yield stress leading to brittle fracture. The next region is characterised by a fall in the fracture stress with temperature, attributed to a change in mechanism of dislocation crack nucleation. Here the fracture stress exceeds the yield stress, so fracture is ductile. The third region, high temperature, is marked by the ductile-brittle transition and significant plastic flow can occur before failure. The fracture stress is seen to rise initially but will eventually fall again as the yield stress decreases. The results of Cannon et al are much simpler in their form. The fracture strength rises slowly with temperature until at 1400^{o}C or higher, depending on the strain rate, the strength falls off rapidly with increasing temperature. Past the ductile-brittle transition the material deforms in a steady manner

until failure. Because of the uncertain dependence of fracture stress on microstructural properties it is difficult to find values for use in spite of the above results. The best compromise so far has been a constant value and sometimes a linear dependency on temperature.

The creep behaviour of UO_2 has been studied theoretically and experimentally. Here the theoretical creep models for both out-of-reactor and in-reactor use are reviewed first, and then the out-of-reactor and in-reactor experimental results are discussed.

Theoretical models for UO_2 creep are generally based on the diffusion of vacancies at low stresses and on dislocation climb at high stresses. During irradiation the fission process introduces point defects that affect the creep rate. Theoretical models for out-of-reactor creep behaviour have received more attention than models for in-reactor creep behaviour. Two models have been proposed and applied to out-of-reactor creep: a viscous creep model based on dislocation climb (73). The theoretical model for viscous creep is based on diffusion of vacancies from grain boundaries in compression. This model results in a creep rate that is (a) proportional to the diffusion coefficient of the rate controlling species, (b) inversely proportional to the square of the grain size, and (c) proportional to stress. As usual the diffusion coefficient is represented by Arrhenius type equation*. This model is based on the assumption that the diffusion path is through the lattice

*Diffusion coefficient $\sim \exp(-Q/RT)$, where Q = activation energy, R = gas constant and T = temperature.

(volume diffusion). Therefore, this model results in a creep rate that is inversely proportional to the square of the grain size with an activation energy that corresponds to a value for volume diffusion. In addition to diffusion of vacancies, grain boundary sliding has also been observed to occur during viscous creep deformation of UO_2. However, both grain boundary sliding and diffusional creep have the characteristics of linear stress dependence and an activation energy nearly that of self-diffusion. So distinguishing between their mechanisms is impossible and regardless of which mechanism predominates, this model is still applicable. At high stresses, the movement of dislocations due to applied shear stresses within the crystal structure results in a macroscopic movement of material. And, at high temperatures, dislocation climb can occur and results in an increase in deformation rate by allowing dislocations to surmount barriers which normally would restrict movement (73). Weertman has proposed a power-law model based on dislocation climb which results in a creep rate proportional to stress raised to the 4.5 power. In this case, creep rate is not a function of grain size.

Regarding the theoretical models for in-reactor creep, Speight (74) has proposed a model for the irradiation enhancement of UO_2 creep. This model considers the effect of local dislocations and voids on the diffusion creep rate when large numbers of atomic displacements and the production of Frenkel defect pairs occur. Under these circumstances, dislocations show a preference for absorbing the irradiation produced interstitials, the excess vacacnies being absorbed

at voids. To establish equilibrium, the dislocations and voids behave as continuous thermal vacancy sinks and sources, and the resulting interchange of matter is the process that enhances the creep rate. The principal result from this model is that the diffusion creep rate is enhanced by irradiation although it has the same temperature dependence as unirradiated fuel. The defect concentration and the creep rate have been considered to depend upon the fission rate (75).

From the theoretical work the general form of the creep has been established. It has been concluded that the creep behaviour of UO_2 can be represented by the sum of viscous and dislocation climb creep rates. Several investigators have performed bending and compressive tests on UO_2 specimens to measure its creep rate and verify the results of previously discussed theoretical models. Scott et al (76), Armstrong et al (77), Bahaboy et al (80), Burton and Reynolds (81,82), Solomon et al (83) and Brucklacher et al (84) have performed creep tests on a wide range of UO_2 specimens. The overall conclusion from the review of experimental data is that the same two different thermal creep mechanisms have been observed. The viscous creep mechanism with some grain boundary sliding operates at low stresses and the creep rate at low stresses is linearly proportional to stress. The mechanism based upon dislocation climb operates at high stresses and the creep rate at high stresses is proportional to the stress raised to about the 4.5 power. There is a transition stress from viscous creep to dislocation creep, which is a function of grain size but

not temperature. The experimental data have confirmed that in the viscous creep regime, creep rate is inversely proportional to the square of grain size and is induced by lattice diffusion. The reported activation energy for this process varies between 90,000 and 100,000 cal/mole (0.377-0.419 MJ/mole). The only value for the activation energy for the high stress mechanism has been reported by Bohaboy to be 132,000 cal/mole (0.553 MJ/mole). It has generally been verified that the fission process enhances the thermal creep mechanism at high temperatures during irradiation, and even induces creep at low temperatures at which out-of-reactor thermal creep normally does not occur. Furthermore, in the viscous regime, the thermal creep rate is enhanced by a factor of four to five and the activation energy is near that of unirradiated fuel. No data are available for the creep enhancement in the dislocation-controlled regime. The same creep enhancement as in the viscous regime has been assumed by Solomon et al (83) in the dislocation-controlled regime but no data exist to substantiate this assumption. Finally, the fission-induced creep rate has been found to be linearly proportional to stress and fission rate. Early experiments reported the process to be athermal, but suggested that the temperature dependency could be masked by material variations. Later, Brucklacher et al (84) reported a slightly temperature-dependent process with an activation energy of 5200 cal/mole (0.022 MJ/mole). Available data are not sufficient to determine the effects of material properties such as grain size and density on the irradiation-induced creep of UO_2.

2.4 ZIRCALOY CLADDING PROPERTIES AND BEHAVIOUR

2.4.1 General Characteristics

A fuel cladding tube has two prime functions in a water-cooled power reactor: (a) it prevents radioactive fission products from spreading in the primary cooling system, and (b) it provides sufficient mechanical strength round the oxide fuel pellet stack. Successful irradiation to high burn-ups requires that the fuel pin be free of metallurgical, chemical and mechanical problems that could threaten the integrity of the cladding. But the trend in power reactors design is towards increased heat ratings, increased burn-ups and possibly higher operating temperatures. One consequence is that the cladding tube will be subjected to higher stresses in a state with higher hydrogen content and more irradiation damage. Thus a failure of cladding may occur through corrosion, mechanical rupture, or a combination of the two, i.e. stress-corrosion-cracking (SCC), sooner than expected. The question that arises is where the real limits of a cladding material are, and if Zircaloy will give satisfactory performance statistics. This has been partly answered today by extensive operating experience on water reactors. It has been shown that a sufficiently severe power increase can cause cladding failure at high burn-ups through pellet/cladding interaction (PCI). The cause of failure is thought to be stress concentration and formation of cracks in the caldding in the vicinity of pellet-pellet interfaces. There is now general agreement that most of the cladding failures are of the stress corrosion type, with the responsible chemical species being fission products iodine

and cadmium. Therefore a discussion on the importance of the various properties of the cladding in relation to the expected stress system affecting it is very useful. These stresses may be divided into two categories, namely: (1) stresses due to interaction forces between pellets and cladding, and (2) stresses due to external causes. Among the latter category one can mention local stresses due to spacer contact forces; bending stresses due to spacers and end fittings; axial stresses due to spacer friction forces and/or axial constraint of pin ends; and stresses due to pressure differential across cladding influenced by ovality. Stresses in this category, with some PWR exceptions, are relatively low and any resulting deformation will be due to creep. Very few failures have been attributed to these stresses, while the stresses in the first category have been responsible for the majority of cladding failures.

It is important for everyone concerned with Zircaloy core components to have a good understanding of the basic deformation mechanisms in Zircaloy. These will therefore be reviewed briefly here. Also some general effects of irradiation on Zircaloy characteristics will be discussed. The basic Zirconium alloys used in water reactors are Zircaloy-2 and Zircaloy-4. Their main difference is in their composition as to the amount of Fe and Ni. In practice their response to water environment, corrosion behaviour, and mechanical properties differ to some extent. There are a number of other Zirconium alloys under development and some of them have already been introduced in water reactors (85). Here, unless specified, Zircaloy will be used for both Zr-2 and Zr-4.

The α-Zirconium matrix, dominant in Zircaloy, has a hexagonal crystal structure. The metals Ti, Hf, Cd, Zn, Mg and Be also have this structure. All these hexagonal close-packed (HCP) metals have, unlike cubic metals, a unique direction, the basal plane normal of basal pole <0001> direction implying a pronounced "anisotropy" of the mechanical properties. However, very few other generalities can be made about the mechanisms of deformation of the HCP metals. With this anisotropy in Zircaloy the existence of preferred orientation (texture) in a tube will confer variations in strength and ductility. Due to this anisotropy the thermal expansion of Zircaloy is also different in the axial and radial directions. Thus the behaviour of Zirconium alloy cladding tube may be critically dependent on the manufacturing route. Many different textures can occur in a Zircaloy tube (86,87,88). A further important effect is related to the deformation occurring during manufacture of the tube, namely, hydride precipitation. It has been shown (88) that hydride precipitation follows the direction in which the metal flowed during the deformation, thus forming radially or circumferentially oriented hydride precipitates.

The effects of irradiation on the properties of Zircaloy must also be understood in order to design for the required endurance under reactor operational conditions. In common with other metals, Zirconium is strongly influenced by the lattice defects created by fast neutron irradiation. These effects must be reviewed and assessed in relation to clad temperature, metallurgical condition, hydrogen content and neutron dose. One of the difficulties is, however, that

few workers have tested irradiated fuel cladding under conditions which represent the stressing systems that are operative in a fuel pin. There is now greater realisation of the importance of doing so, but few results have been published.

Total fast neutron doses in water reactor fuel cladding are unlikely to exceed 10^{22} n/cm^2, but this is enough to cause pronounced changes mainly in Zircaloy strength, fracture behaviour and creep. The physical reason for these changes are thought to be the production of vacancies, interstitials, defect clusters and dislocation loops. No evidence has so far been found up to the above doses in thermal reactors for the formation of three-dimensional voids of the type reported in steels subjected to high neutron fluences at temperatures about 400°C. The size and distribution of the lattice defects has been found to depend on irradiation temperature, neutron fluence and chemical composition. By means of electron microscopy it has been observed that the total visible density of clusters ($\geq$ 30 Å) and loops increases initially with irradiation, eventually reaching a saturation value. The size spectrum does, however, continue to change; the size of the loops and clusters increasing with fluence far beyond the value observed when the above density saturation has occurred (89). The effect of a higher irradiation temperature is thought to be the appearance of larger and fewer loops. This is due to the enhanced mobility of defects causing the rate of defect cluster nucleation to decrease owing to the difficulty of achieving sufficient localised point-defect supersaturation.

The growth of loops will also be more rapid due to the enhanced mobility of the point defects. A steady state condition will, however, eventually appear during irradiation due to the recovery of irradiation damage which is associated with both a reduction of defect density and loop expansion (89).

Effects of the chemical composition on the influence of irradiation on Zirconium alloys have been observed. Oxygen atoms are thought to be responsible for the strain ageing peak in Zircaloy at about 350^{o}C (90). It has been observed that neutron irradiation suppresses the strain ageing response, due to the trapping of oxygen atoms by the irradiation-induced effects. Another effect of the chemical composition is the proved stabilising effect on small regions of radiation damage that is the result of a solute like niobium in Zirconium. Adding molybdenum is thought to stabilise the damage regions to an even higher temperature than does niobium provided molybdenum is in solution (91).

One further effect of neutron flux is the specificallly irradiation-induced growth of Zircaloy cladding. This is defined as a change in dimension during irradiation in the absence of any applied stress. The existence of irradiation growth was first reported by Buckley (92). He also proposed a mechanism to explain it. This phenomenon will be discussed later in this chapter.

Neutron irradiation has a pronounced effect on the tensile test properties of Zircaloy as was mentioned before. Tensile properties have been published in the literature covering different fluences, cold-work levels, irradiation

temperatures, test temperatures, post-irradiation annealing treatments and so forth. It has been shown that the principal effects of irradiation are an increase in yield strength and the occurrence of a drop in total elongation. Finally, in this section the effects of radiation on creep will be discussed. Much effort has been devoted to generating data, and in order to be able to extrapolate creep rates in time, temperature, flux and stress, considerable effort has also been extended on the development of mechanistic models. Most of the available information has been reported from the UK, Canada and the US.

Similar to UO_2 fuel pellets a knowledge of physical and chemical properties of Zircaloy cladding and their variation with temperature and neutron fluence is very important. Of course some of these cladding properties like its melting point or thermal conductivity may not be as crucial as they are in the fuel and so will not be discussed here. On the other hand, thermal expansion due to its anisotropy can be influential in cladding deformations. There are some published works which give expressions for diametral and axial thermal expansion of Zircaloy as a function of temperature. No other effects are thought to influence the thermal expansion. This is true for Zircaloy thermal conductivity and specific heat as well.

The final phenomenon to be discussed in this section is corrosion and hydrogen pick-up by Zircaloy in water and steam environment. Corrosion by the coolant has caused, or contributed to, failure by the following probable

mechanisms; (a) loss of wall thickness; (b) hydrogen pick-up and its influence on mechanical properties; and (c) crud deposition and the consequent rise in cladding temperature. A difficulty in defining the acceptance limits for corrosion and hydrogen pick-up from the coolant arises from the fact that the failure mechanisms for fuel elements are usually complex, ultimate failure being the result of joint action of a series of contributing chemical and mechanical phenomena. Thus, one will hardly find defects which are caused solely by corrosion or hydrogen pick-up from the coolant, under normal circumstances. There is also the internal corrosion (due to fission products, etc.) and can cause failures by the following mechanisms; (a) hydrogen pick-up from moisture or impurities in the fuel; (b) stress-corrosion-cracking with fission products as the corrodent. This was stated earlier in this sub-section.

2.4.2 Irradiation-Induced Growth

Irradiation growth in Zircaloy is defined as a shape change during irradiation in the absence of external stress. It has been shown to occur in all Zirconium alloys and has to be taken into account in the design of a fuel assembly. It is a part of the explanation to observed axial strains in fuel pin cladding. The growth phenomenon, however, has to be accounted for in all Zircaloy components in the core. One effect is for instance the bowing of fuel channels in a BWR that is predicted due to large flux gradients. Similarly, bowing of PWR fuel assemblies has been observed for the same reason.

The existence of irradiation growth was first reported by Buckely (92). He also proposed a mechanism to explain the phenomenon. The growth was thought to be due to the formation of vacancy loops on the basal planes and interstitial loops on the prism planes. The differential condensation of point defects was thought to be caused by the anisotropic thermal expansion coefficients setting up corresponding thermal stresses. Hesketh (93) adopted the model and found it consistent with his results for irradiation growth. Hesketh also found that the growth process was accompanied by no, or at least negligible, volume changes. Some results have been published recently that do not fully agree with the Buckley model (94,95). Ibrahim (94) has reported that the correlation with texture is less for cold-worked Zircaloy than fully annealed. He has suggested that there is a treatment contribution to the shape change due to stress-relieving and another component of growth due to cold-work. Fidleris (95) has also reported that cold-work changes the irradiation growth behaviour. During irradiation of cold-worked anisotropic materials there appear to be at least three components of dimensional change; crystallographic texture; stress-relief and cold-work dependent components. According to him the dimensional changes due to texture, i.e. those of annealed material, and stress relief can be of either sign and appear to saturate at low doses. Cold-work adds a component of positive length change in the direction of working, which does not appear to diminish up to higher doses. Kelly (96) has recently reviewed the available

data on irradiation growth in annealed Zircaloy. Based on the growth results and also on observations in electron microscopy he has proposed a slight modification of the original Buckley model. The modification involves differential drift of interstitials and vacancies to suitably oriented segments of grain boundaries.

Irradiation growth in Zircaloy is anisotropic and depends on the crystallographic texture and deformation substructure of the material. The deformation substructure relates to the amount and direction of cold-working. These two components of growth (crystallographic and deformation) would be present in both single crystals and polycrystalline material. In addition polycrystalline material could have a component of dimensional change, as stated earlier, due to irradiation-induced relieving of residual stresses (96). In textured polycrystalline, annealed materials the growth variation with the direction of testing is complex. There are only few irradiation growth results on cold-worked materials in directions perpendicular to the direction of working, not enough to evaluate the dependence of growth on dose or amount of cold work. In general, the available data on annealed and cold-worked Zircaloy have been found to be proportional to neutron dose, ϕt, to a power less than one.

The effect of flux intensity and spectrum on growth rate has not been investigated. From a comparison of some different results it has been concluded that growth is directly proportional to neutron dose under normal water

reactor flux ranges. The effect of temperature on growth has been investigated mostly with annealed materials and considered to be small up to 300°C (95). Finally, there has not been much work on the growth behaviour of other types of Zirconium alloys and the existing results seem to be contradictory.

2.4.3 Mechanical Properties

Similar to UO_2 pellets the mechanical properties of Zircaloy cladding are very influential factors in a computer modelling of fuel pin behaviour. These properties should satisfy certain requirements, based on a consideration of operational factors and the mechanical behaviour of fuel pin, to obtain maximum flexibility. Furthermore, the predicted mechanical deformation of the cladding is strongly dependent on the values used for the mechanical properties. From a designer's point of view, the strains induced in the cladding should not exceed the instantaneous fracture ductility for the strain pattern in question. So the cladding must meet the following requirements to start with; (a) good ductilities in the axial and circumferential direction; (b) a good value for the strain-hardening coefficient*, especially in the circumferential direction; and (c) a creep strength, also in the circumferential direction, high enough to prevent collapse during daily power excursions. In order to understand the reasons behind

*A theoretical study by Gittus (17) has shown that during pellet/cladding interaction, cladding fracture will occur if the cladding strain equals the strain-hardening coefficient and this is the maximum tolerable strain.

the choice of these requirements and to recognise the crucial properties, one has to study the in-reactor mechanical deformations of the cladding first.

When UO_2 pellets expand thermally, their interaction with the cladding is usually manifested through an increase in cladding length and diameter and in the formation of ridges at pellet-pellet interfaces. There is also the possibility of so-called ratchetting, which is progressive elongation under cyclic conditions. So it is clear that the overall deformation of the cladding depends on the mechanical interaction of the fuel and cladding with each other. In this context, the interfacial frictional forces set up between the cladding and the pellets, which affect the stress distribution within the cladding, are of major concern. This problem is generally referred to as pellet/cladding interaction (PCI). PCI problem has received far more discussion than any other problem in research on water reactor fuel elements. It has been demonstrated that the cladding tube can become plastically strained in the axial and circumferential directions because of PCI. In the axial direction high uniform permanent elongations have been recorded. This, of course, varies with heat load, cladding properties, pellet shape and dimensions and as-assembled gap between fuel and cladding. Axial deformation by ratchetting is conceivable, in particular with small as-assembled gaps. This elongation can occur under cyclic conditions of power and/or system pressure during PCI. If there is a decrease in power or pressure, the fuel stack would lose contact with the cladding and consolidate

(re-stack) by gravity. If the coefficient of friction between fuel and cladding is finite, the relative axial motion is not instantaneous but is nevertheless irreversible in the sense that a return to previous power or pressure conditions does not produce the previous fuel and cladding motion in reverse. In fact fuel and cladding will be once more brought into contact, but at a new relative position. This cyclic relative movement between fuel and cladding has been defined as a ratchetting process. This process depends on many factors like cladding properties, fuel cracking and displacement, gap friction between fuel and cladding, the magnitude of power or pressure cycle etc. It is not, however, clear whether all the axial deformation which has been measured and attributed to ratchetting is due to ratchetting. An extra source of cladding deformation during PCI is its circumferential (diametral) straining. This strain is basically due to thermal expansion of the fuel, opening of cracks in the fuel and, fuel swelling. The thermal expansion of the fuel has one uniform and one non-uniform component, the latter is caused because of the hour-glass shape that the pellets take up under parabolic temperature distribution, and commonly assumed to be the cause for the formation of ridges in the cladding near pellet ends. The height of these ridges is usually found to be in the range 0.01 mm to 0.1 mm, but higher ridges have also been observed. In general, the observations have shown that the ridge height is proportional to power and pellet geometry. Finally, the cladding is strained over pellet cracks and interfaces. Cracks in the cladding

have been found in the vicinity of ridges, suggesting that localised straining, even to failure, can occur over cracks in the UO_2. If there is a perfect bind between fuel and cladding, the cladding would fracture when the cracks open. However some sliding seems to occur in most cases, resulting in a stress gradient in the cladding with a maximum over the cracks. This stress concentration is not fully reversed when power is reduced, resulting in progressive thinning of the wall over a series of power cycles. At high burn-ups, a power ramp can cause the cladding to fracture under the above circumstances. There is still considerable discussion as to whether these cladding fractures are of the stress-corrosion-cracking type, with some fission products being the chemical species, or whether they arise from the mechanical overstraining of low ductility irradiated cladding (97).

The above brief examination of the cladding basic straining mechanisms shows why some cladding mechanical properties are so vital to the fuel pin overall performance. Also it provides a ground to fully understand the Zircaloy properties. Out-of-reactor, Zircaloy tubing for PWR and BWR fuel is a rather well-defined product. The common fabrication process is by hot extrusion of a tube hollow followed by cold reduction to final dimensions in several steps. According to what was said before, the material ends up with certain cold-work and a characteristic texture of its hexagonal crystals. Because of its anisotropy, Zircaloy cladding has different ductility and strength in different directions. The highest strength and best

ductility seem to be associated with a texture where the basal poles are radially oriented (98).

During irradiation in the core several material properties of Zircaloy, which are considered important to reactor design and performance, change. The most pronounced effects are the change in strength, fracture behaviour and creep.

Tensile properties of irradiated Zircaloy alloys have been investigated more fully than any others. This is understandable, since the exhaustion of ductility, under tensile stressing conditions is an important life-limiting phenomenon. Results on actual cladding are the most important, but some of the general effects are well illustrated by uniaxial tensile data. Neutron irradiation has similar effects to cold work, raising the yield and tensile strength and lowering the elongation. The reduction in area at fracture and associated non-uniform elongation is less affected than the unirform component of the total elongation. Necking starts early in the plastic range followed by ductile fracture with little further uniform elongation. This feature is common to other metals and alloys, and results from the fact that the irradiation hardening has exhausted the capacity for any further substantial work-hardening once plastic straining commences. This type of plastic instability is disadvantageous, particularly when associated with straining over very short gauge lengths associated with opening cracks in UO_2 fuel. The cause of the plastic instability in irradiated Zircaloy has been shown to be

the removal of defect clusters by dislocations moving in channels (99). The initial dislocation sweeps away some of the defects making the passage of subsequent dislocations in the channel easier. As the channel becomes cleared, the friction stress, associated with the channel, decays. During the subsequent deformation the material work hardens in the channel.

Workers in the US, Canada, Sweden and the UK have generally agreed on the principal effects of irradiation on tensile properties, but there are many differences of detail, and it is clear that materials from different manufacturers, or made by different routes, result in some modifications to the general picture. Some conclusions can, however, be made for tubing with a radial basal pole texture as follows: (a) the yield strength of annealed Zircaloy roughly doubles becoming virtually saturated, at an exposure of 5×10^{20} n/cm^2, at which time yield strength and ultimate tensile strength are effectively co-incident; (b) the yield strength of cold-worked Zircaloy shows a smaller increase, depending on the amount of cold work, and merges towards that for annealed material at high exposures; and (c) the total tensile elongation is reduced by a low fast neutron exposure, and saturation occurs probably at less than 5×10^{19} n/cm^2. The saturation ductility is reduced by cold work; highest residual ductility is found for annealed material.

The irradiation temperature has also a marked influence on the tensile properties. Bement (100) has found, contrary to expectation, a higher fluence exponent in the yield

strength - fluence relationship at 280°C than at 60°C. This means that after some irradiation (approximately 10^{20} n/cm^2), the specimens irradiated at the higher temperature have a higher yield strength. Some irradiation work in Sweden has demonstrated that the temperature dependence of the fluence exponent is strong in the range 240-325°C, however, at temperatures well above 400°C, neutron irradiation is expected to have a minor effect on the yield strength due to rapid self-diffusion healing of radiation damage (101).

Recently there has been much work on the high temperature tensile properties of Zircaloy under irradiation. These works have been performed in relation to the hypothetical loss-of-coolant accident (LOCA). The cladding temperature is expected to rise as high as 1200°C. The cladding deformation will be by a creep process until a certain uniform expansion is reached. This is set by the corresponding necking strain that is measured in temperature transient tests. The necking strain has been shown to be very high in the single phase regions. In the $\alpha + \beta$ region*, however, there is a reduction in ductility. It has been argued by Hobson et al (102) that the reason is a very low work-hardening rate implying also a very low uniform strain. Hardy (103) has, however, shown that the uniform strain is still considerable (> 10%) in the $\alpha + \beta$ region implying that considerable work-hardening still occurs in the two phase region. During the time when the cladding is exposed to

*Zircaloy similar to pure zirconium undergoes a phase transformation from α to β, beginning at 810°C and ending at 970°C.

steam at the above elevated temperatures, reaction of the Zircaloy outer surface causes the formation of an oxide film on the cladding surface and there will be an oxygen concentration gradient into the underlying metal. Due to this oxygen concentration at the outer surface some of the cladding material will not undergo $\alpha \rightarrow \beta$ transformation but is stabilised at the α phase. Emmerich et al (104) have concluded that in this situation the oxygen-saturated metal is only slightly less ductile than the rest of the material but has an increased strength. As a consequence of these results it has become clear that there does not exist a single burst stress; instead the burst stress is a function of heating rate and the creep law stress exponent. This has been confirmed by theoretical analysis too (105). Other factors such as heat treatment and texture are of course of minor importance for the cladding properties under LOCA conditions. The effects of high temperature Zircaloy creep law will be considered later.

The last property to be discussed here is creep. The creep behaviour of Zircaloys is of fundamental importance not only in the design and operation of fuel pins but also in pressure tube reactors (SGHWR and CANDU). Much effort has therefore been devoted to generating data, and also to developing mathematical model in order to be able to extrapolate creep rates in time, temperature, flux and stress. Most of the work has been performed on in-reactor creep of Zircaloy-2, Zr-2.5 wt % Nb, and Zircaloy-4. Some of the workers have included irradiation growth in their studies, assuming that irradiation growth cannot be separated from

creep. In fact it has been stated that in-reactor creep contains a strain component due to growth. This is the case in many reported data on creep and stress-free growth of Zircaloy cladding. This will, however, affect only the axial strain, because growth in the radial and circumferential directions is negligible.

Much of the in-reactor creep information on uniaxially stressed specimens has been reviewed by Gilbert (106). His review also covers some biaxial creep and irradiation growth tests. He has noted that differences in the methods of stressing do not affect the basic creep properties, only the magnitude of the measured strain is affected. So, here all uniaxial and biaxial creep and stress relaxation results are collectively described as "creep".

It is clear from the literature that in-reactor uses of Zirconium alloys are limited to temperatures between 20 and 500°C. For pressure tube reactors the range is from 260 to 400°C, while for experimental fuel element claddings the range is from 260° to 500°C. Therefore most of the experimental data are for temperatures around 300-400°C. With these temperature ranges, the various water reactor structural components that are made of Zirconium alloys will operate below one half the yield stress and under normal conditions are not expected to reach tertiary creep. The fuel claddings, on the other hand, are intermittently subjected to much higher stresses, sometimes exceeding the yield stress of the material. This may present complex problems in understanding the in-reactor creep of Zirconium

alloys. The normal procedure is a comparison with the known out-of-reactor deformations. Since the crystal structure of α-Zirconium is anisotropic, the creep behaviour will in general be a function of texture, i.e. will depend on the direction of the applied stress relative to the preferred orientation of the grains. The creep anisotropy is common to all Zirconium alloys and has been the subject of several investigations (107,108).

Out-of-reactor the dependence of the tensile and creep properties on temperature has been subdivided into three regions:

Region one is below about 200°C; the temperature is too low for recovery processes to take place and the creep rate decelerates with time at all stresses below the yield stress. The creep strain in this region has a linear relationship with the logarithm of time, the so-called logarithmic creep law. Below 200°C the temperature has been reported to have very little effect on creep rate or strain as most Zirconium alloys strain harden very rapidly in this temperature range. In the logarithmic creep range the total creep strains at stresses below the yield stress of most metals are less than 0.1% (109). In Zirconium alloys, however, the logarithmic creep strains have been observed to be quite high.

Region two is from 200°C to 550°C and nearly all in-reactor applications of Zirconium alloys fall in this temperature range as stated earlier. Here the yield stress is nearly independent of temperature and strain rate and creep rates at a given stress show a temperature dependence

only during early stages of creep. This temperature range is often described as "athermal". In this range some mechanical recovery becomes possible and offsets some of the strain hardening, especially during early stages of creep, with the result that creep rate declines less rapidly than in the logarithmic creep range, but still never reaches a steady state (109). The creep strain in region two has been shown to be a function of time to a power less than 1. This is not, however, a true representative of creep behaviour because of the occurrence of dynamic strain ageing as discussed by some authors (110).

Region three starts above about 550°C. In this range the deformation is strongly dependent on temperature and strain rate. Above 550°C recovery processes can proceed rapidly enough to cause complete recrystallisation of the cold-worked structures and keep pace with strain hardening during creep, resulting in steady state creep rates at a constant stress. Here in contrast to regions one and two, where the dislocation structures change continuously with strain, steady state creep in region three results in a dislocation structure that is constant for a given applied stress and changes only slightly with temperature (107). Grain boundary sliding can form a significant part of creep deformation in this temperature range.

Now that the out-of-reactor creep deformations under three temperature regions have been reviewed, one may proceed with the in-reactor creep behaviour. Nearly all the information on in-reactor creep of Zircaloys is confined to temperature region two, $\sim$ 200-550°C, corresponding to

practical in-reactor applications. As expected the available results on creep show a difference in longitudinal and transverse directions, emphasising the anisotropy of in-reactor creep of Zircaloy. This has been discussed in detail by Holicky and Schroeder (111) and Ross-Ross et al (112). Throughout the published literature one may find the results of investigations on the dependence of in-reactor creep rate on the flux intensity, dose, pre-irradiation, cold-work, temperature, stress, grain size, and alloying, the details of which cannot be given here. However, it may be useful to give overall observations.

Among the many authors that have dealt with the mechanisms of in-reactor creep there are those who consider the deformation to occur by one given mechanism and others who propose a multiple-mechanism approach with specific mechanisms controlling the deformation over a prescribed range of stress and temperature. There does not seem to be any general agreement on any integral model, and in fact only reasonable empirical choices for the ill-known parameters have been made to bring the experimental and theoretical works into agreement. This statement reflects the state in which the understanding of in-reactor creep behaviour of Zircaloy is today, i.e. even at best it is an educated guess. This situation is due, on the one hand, to the shortage of well documented in-reactor creep experiments and, on the other, to the fact that the understanding of out-of-reactor creep has not progressed much beyond dealing with semi-quantitative models in idealised situations.

A large number of in-reactor creep models are based on yielding creep or some modification of it originally introduced by Cottrell (113) to explain anisotropic growth and irradiation creep of uranium. Other explanations of the in-reactor creep behaviour are based on deformation models that have been developed for high-temperature and out-of-reactor creep with modifications to account for the effects due to radiation-induced point defects (vacancies, interstitials, displacement spikes, voids and loops). Recent models are based on three bascially different in-reactor mechanisms.

At high stress levels, the cutting by dislocations of neutron-produced depleted zones* as originally proposed by Seeger (114) is taken to be responsible for observed in-reactor hardening. The properties in this region are identical to those obtainable by post-irradiation testing at the same temperature and integrated exposure. Cold-worked material is stronger at low exposure but at large exposures becomes comparable with annealed material. At intermediate stress levels, it is thought that dislocations climb around the depleted zones at a rate set by radiation enhanced diffusion coefficient. Here, the in-reactor strength is less than that indicated by post-irradiation testing but no

*When fast neutrons collide with matrix atoms, regions depleted of matrix atoms are produced. These parts of the matrix are referred to as "depleted zones". At low temperatures ($T < 0.08\ T_{melt}$) the damage regions contain typically > 10 percent vacancies surrounded by interstitial atoms. At somewhat higher temperatures ($\sim 0.12\ T_{melt}$) clusters with a void-like contrast have been observed (114). It has therefore been assumed that at temperatures of interest ($\sim 300^{\circ}C$) for creep in Zircaloys the damage would consist of spherical voids and isolated interstitials with very few isolated vacancies (109-113).

less than the intrinsic strength of unirradiated annealed Zircaloy at a very low plastic strain level. This mechanism operates as an alternative or parallel mechanism to the normal thermal mechanism. The behaviour of annealed and cold-worked material is not greatly different, with the cold-worked material possibly showing a slightly higher creep rate (109). Of larger significance is the superior strength of annealed material tested in the transverse direction compared with annealed material tested in the longitudinal direction. No explanations for these differences are available. In the low-stress region, it is proposed that point defect loops are preferentially formed on particular planes to respond to the applied stress, thereby producing a "stress-directed growth" phenomenon (which in turn may cause yielding creep) at a deformation rate directly proportional to both stress and flux level (92,93). This mechanism which produces plastic strain even with no applied stress, and it is proposed that this mechanism operates independently of the thermal creep, is simply adding additional strain to that obtainable out-of-reactor at a rate essentially temperature-independent for the temperatures of interest in reactor design. This irradiation creep is assumed to operate at all stresses, independently of the other mechanisms discussed above. However, due to its weak stress dependence it dominates in the low-stress region and becomes completely negligible in the high-stress region. In the low-stress region, the in-reactor creep rate appears to increase with degree of cold-working, being about five times as great as annealed for 15% cold-work and about seven times

for 78% cold-work*. It is not yet clear whether this difference is maintained after large neutron exposures.

In order to make creep rate calculations it is necessary to know the depleted zone density (its number per unit volume), the vacancy and interstitial concentrations, the dislocation climb velocity, and the interaction between the dislocations and the zones. Then detailed mathematical analysis must be performed. Some quantitative formulations of the above mechanisms have been obtained by using the available creep data in the temperature range 300 to 350°C. The overall agreement between theory and experiment has been acceptable (11).

Regarding the high temperature in-reactor creep, it has been shown that at higher temperatures the thermal creep component is of sufficient magnitude and it overrides the irradiation creep components over most of the stress and strain rates of interest. Under these conditions in-reactor creep would rapidly approach out-of-reactor values making the in-reactor prescription less important. So isothermal creep laws have been developed for application to LOCA conditions. Under LOCA conditions, apart from tensile

*The cold-work effect on creep strength may be explained by the recovery creep theory. In the secondary creep stage, dislocation generation from work hardening and dislocation annihilation from recovery balance and result in a steady-state dislocation density. This implies a low creep rate. If the initial dislocation density is much higher or much lower than the steady-state density, there is a primary creep stage with a high creep rate. If the initial dislocation density is close to the steady-state density, the creep rate is low from the start and the secondary stage is soon reached. The implication of this is that less cold-work permits more recovery towards the steady-state dislocation density before grain recrystallisation becomes too plentiful. This structural refinement explains the lower creep strain at a lower degree of cold-work (99-102).

failure, the claddimg may fail due to creep rupture. Depending on the time/temperature response of the cladding, creep rupture has been stated to occur at circumferential stresses less than the ultimate tensile strength. There has not been enough published work on high temperature creep so no further comments can be made. However, the importance of appropriate creep models to cover a wider range of temperatures must not be forgotten, especially if transient behaviour of fuel pins is analysed.

2.4.4 Internal and External Corrosion

Zirconium is an almost unique metal in that it combines high strength and good corrosion resistance to high temperature water with low neutron capture cross-section. Although the out-of-reactor corrosion rate in water at 300°C is modest, and tolerable for long period exposures it is nevertheless accompanied by some pick-up by Zirconium of the corrosion hydrogen generated. Zirconium as might be expected from its position in the transition metal series shows a strong affinity for hydrogen, forming stable hydrides. Although Zirconium normally exhibits good ductility, material containing precipitated hydride may be embrittled particularly at lower temperatures under impact loading conditions. This is essentially because hydride precipitates, especially if suitably aligned, present low energy cleavage paths for fracture (115).

The position is the same for Zirconium alloys. Most of the early failures in water reactor fuel pins were attributed to the presence of Zirconium hydride formed as a

result of hydrogen absorption from the coolant and corrosion. Of course in those early days many of the processes known today to be influential in fuel pin performance had not yet been recognised. Today one will hardly find defects which are caused solely by corrosion or hydrogen pick-up under normal circumstances.

The corrosion behaviour of the Zircaloys out-of-reactor is well established. It has been shown that after a certain period a transition occurs in the mechanism of the attack, from a diminishing to a constant corrosion rate. Zirconium alloys, in general, absorb a substantial fraction of the hydrogen liberated by the corrosion after transition under out-of-reactor conditions. The hydrogen pick-up associated with corrosion can, in principle, be combatted by reducing the fractional hydrogen pick-up or the corrosion rate. Another possibility is to adjust the alloy so that the influence of hydrogen on the mechanical properties is minimised. Efforts to improve Zircaloy-2 with respect to fractional hydrogen pick-up led to the development of Zircaloy-4, which has nearly identical corrosion rate but an out-of-reactor hydrogen pick-up of only one third of that for Zircaloy-2. This was achieved by eliminating the 0.5% nickel in Zircaloy-2. It has been reported that Zircaloy-4 is more insensitive to the hydrogen content in the environment (116). Small amounts of oxygen in the environment reduce the hydrogen pick-up, especially for Zircaloy-2, so Zircaloy-2 and 4 become fairly similar under oxygenated conditions (117).

The position has been complicated by the growing realisation by workers in the field during the last few years that reactor irradiation can enhance the corrosion of Zircaloys in aqueous and steam environments more than that originally thought, particularly in the steam case the degree of enhancement observed is also sensitive to the water chemistry environment (117). Since the evidence suggests that the mechanism of oxidation of Zircaloy in water is changed under fast neutron flux in such a way that it becomes sensitive to the oxidation potential of the environment, whereas out-of-reactor no such sensitivity is observed, then it is evident that the mechanics and kinetics of hydrogen pick-up may also be significantly different in-reactor as it will be discussed later.

Zircaloy hydriding is not exclusive to the outer surface of cladding, internal hydriding has also been observed extensively. This severe localised internal hydriding occurs under two distinct and separate circumstances. In one instance the hydriding arises from hydrogenous impurities, e.g. moisture, oil, etc., introduced in the fuel pin during fabrication - these are internally generated failures. In the other case, the original breach occurs by some other mechanism which allows coolant entry into the pin. Again, the cladding hydrides locally. The two mechanism, usually designated primary and secondary hydriding, respectively, are indistinguishable in appearance and can only be differentiated unequivocally in the case of heavy water reactor irradiations where the secondary reaction product is deuterium rather than hydrogen (118,119).

Another consequence of corrosion is crud deposition. Although reactor materials are highly corrosion resistant, they corrode and form oxides under reactor conditions. Large amounts of corrosion products (oxides), called crud, are released to the water, carried by it, and deposited at various places in reactor system. The large heat-exchanger surfaces of nuclear reactors produce as much as several hundred grammes of corrosion products per day. Of major concern for reactor performance is crud deposition on the fuel elements, which can lead to increased cladding temperature and thus to a corresponding increase in external corrosion rate (120).

Apart from the hydriding mechanism mentioned above to cause failure by attacking the inside of the cladding, fission products are thought to be the major contributors to cladding failures. Attack from the fission products, notably iodine, was feared to be a problem when use of Zircaloy began. This problem has gained actuality as burn-up ratings increased. Iodine has been shown by many workers (121,122) to be capable of cracking stressed Zircaloy. Another fission product, caesium is volatile at UO_2 operating temperatures and is often found condensed on the inner surface of cladding, especially towards the cooler ends of a fuel pin, and adjacent to pellet ends.

The internal and external corrosion can now be discussed in more detail. The external corrosion by the coolant will be reviewed through the following mechanism:

(a) Loss of wall thickness;

(b) Hydrogen pick-up and its influence on mechanical properties;

(c) Crud deposition and the consequent rise in temperature;

and corrosion from the inside through the following mechanisms:

(d) Hydrogen pick-up from moisture or impurities in the fuel;

(e) Stress-corrosion-cracking (SCC) with fission products or contaminants as the corrodent.

Coolant water is decomposed in the strong radiation field of the core to H_2 and O_2 (or D_2 and O_2 in the case of heavy water reactors). Both neutrons and γ-rays contribute to the radiolytic decomposition and recombination. For the discussion of the effect of irradiation on corrosion, it is, however, essential to differentiate between BWR and PWR reactors. BWR's operate usually with purified water without additions. The water decomposes in the way described above. As a result the liquid phase will have an oxygen content of about 0.05-0.2 ppm, and the vapour phase about 5-20 ppm with about stoichiometric amounts of hydrogen. In PWR's, the radiolytic decomposition of the water is suppressed by adding about 1 ppm of hydrogen to the water, which leads to a very low oxygen content. The water in a PWR is further kept at pH about 10 by LiOH additions. As hydrogen chemically is a reducing agent, these water conditions are designated "reducing" in contrast to the BWR, which is called "oxidizing" due to the presence of oxygen (115).

The corrosion rate of Zircaloy-2 and 4 in BWR reactors is drastically increased (115-124). The effect is due to the combined action of oxygen and irradiation, and decreases with increasing temperature. The oxidising potential of the water in BWR reactors leads to a reduced hydrogen pick-up ratio. The hydrogen uptake of Zircaloy-2 does not normally exceed 20% of the stoichiometric equivalent of the corrosion, and may be as low as 5% (115-128). The low hydrogen pick-up ratio, attributed mainly to the oxygen in the environment, tends to compensate for the increased corrosion rate in BWR's (116). The difference in hydrogen pick-up for Zircaloy-2 and 4 is much reduced by irradiation under BWR conditions. A slightly lower pick-up for Zircaloy-4 than for Zircaloy-2 is expected (126). Since the effect of irradiation disappears at about 350-400^{o}C, it is expected that the difference between Zr-2 and 4 found out-of-reactor to be valid in-reactor at high temperatures (125). If this is true, the lower hydrogen pick-up of Zr-4 in the initial period should give this material an advantage over Zr-2 for attack by moisture on the inside of the cladding, during dry-out excursions and at increased temperatures due to crud.

The early reports from PWR's, on the other hand, indicated that the effect of irradiation on the corrosion rate was small. It is now generally agreed that a small, but well detectable, increase exists. The corrosion rate of Zr-4 has been reported to be slightly higher than out-of-reactor (115-118). The fractional hydrogen pick-up is

25-50%, depending mainly on the amount of hydrogen in the environment (115,116). If too high a hydrogen concentration is used, the hydrogen pick-up rises to much higher values, even above 100% (115,128).

The loss of wall thickness in both types of reactors has been found to be very small. The loss in wall thickness is due to the formation of Zirconium oxide and its gradual removal afterwards. In BWR's the highest corrosion rate after five years in-reactor at 325°C has led only to a uniform metal loss of about 35 µm. This has little consequences on strength and integrity. In temperature excursions due to dry-out, the amount of oxidised metal will be about the same in 10 minutes at 800-900°C as in five years at normal temperature (119-120). The internal oxidation and the embrittlement associated with it prevent any use of Zircaloy at these temperatures, even for short duration (125). With dry-out at 600-700°C, immediate failure by corrosion and hydrogen pick-up is not to be expected, but a nucleation of oxide nodules is possible which will initiate rapid corrosion rate under normal conditions (117,119).

The reasons for hydrogen pick-up and formation of hydrides in Zircaloys were discussed earlier. It was stated that hydrides could have drastic effects on the mechanical properties of Zircaloy cladding. A complicating phenomenon is that the effect of the hydride on mechanical properties is much dependent upon the orientation in the cladding tube and on the test conditions. According to the literature the hydride precipitates will have the smallest influence

when they are aligned parallel with the stress axis (98-101). The main stresses in cladding tubes are circumferential and axial, and this is also the preferred orientation for the hydride platelets. With this orientation the effect of relatively large amounts of hydrogen has been reported to be very small in a uniaxial tensile test at elevated temperatures (98). Some workers have obtained large reductions in dutility with increasing hydrogen content, which has been attributed to the characteristic of tube texture used (118-121).

Although the literature shows that there are still uncertain points with respect to the effect of hydrogen on Zircaloy subjected to a complex load under reactor conditions, a design limit of about 500 ppm hydrogen content has been universally accepted. In addition to the difficulty to defining limits for hydrogen pick-up, designers are faced with the problem that corrosion and hydrogen pick-up data are too uncertain to predict the in-reactor hydrogen pick-up of cladding tubes under conditions of interest. Available literature indicates that Zircaloy-2 and 4 cannot be pushed much further in temperature and exposure time than done in the present reactors before hydrogen pick-up becomes troublesome.

Practically all of the Zirconium oxide produced when Zirconium alloys corrode in water remains at the corroding metal itself. Stainless steel, and also carbon steels, are different in this respect, as a substantial part of the corrosion products are released to the water in ionic and

colloidal form. In the core this ionic and colloidal matter precipitates leading to crud deposition on fuel elements and other surfaces. The crud deposition on fuel elements has been shown to be influenced by: (a) water chemistry of the reactor system (in BWR alkaline water to reduce corrosion product transport and crud); (b) the type of materials and water clean-up in the primary circuit; (c) hydraulic parameters (at the site where the corrosion products are released, at the site where they plate out, and the complete coolant flow arrangement). The overall behaviour of the corrosion products will also be influenced by products present in minor amounts. Copper-base alloys in the feed water systems, situated after condensate clean-up system, have caused severe crudding of fuel elements in some BWR's.

The crud layer forms an extra barrier to heat transfer and form a potential danger for fuel pin behaviour. The mechanism of heat transfer in crud layers varies with the type of the layer and the surface heat flux. For a porous crud layer and low heat rating circulation of water and steam within the layer will occur, and the temperature rise will be small. With more closed type porosity, or a higher heat rating, the pores will be filled with steam and the temperature rise is much larger. Another mechanism for temperature rise and eventual cladding failure has been proposed by Pickman (120) to explain some SGHWR fuel pin failures. According to him, the crud has a tendency to crack and loosen from the cladding surface. Under such conditions the small gap between the cladding and the crud layer might be filled with a nearly stagnant steam which

acts as a barrier to heat transfer and causes a temperature increase of up to 50°C in the cladding.

It is unclear whether crud deposition will be a problem in reactors with high ratings and long fuel life time. With a temperature rise of 30-50°C due to crud, new cladding materials with improved corrosion and hydrogen pick-up have been considered, as it is doubtful whether Zr-2 and Zr-4 can tolerate higher temperatures than those in present BWR and PWR conditions (115-126).

Regarding the internal corrosion, two mechanisms can be held responsible as mentioned before; (a) moisture in fuel or water entering through a defect and causing internal hydriding; and (b) fission products.

The nature of defects arising from internal hydriding is well known. Externally they are characterised by bulges or blisters on the inner cladding surface. Large and small hydride defects are commonly known as "sunburst". They rise from the inside surface of the cladding and may ultimately lead to a blister on the outside cladding surface (118-119). According to some observations large sunbursts soon give rise to penetrating hydride needles and cracking can occur, probably triggered by power changes (127). This defect structure results in locally higher bore surface temperature, which in turn helps to spread the hydride regions outward from the site of the original sunburst, giving a circular or annular zone of hydride on the outer surface.

Recently it has been reported that internal hydriding may not take the form of the classical sunburst. Some early examples of defects in fuel pins containing hydrocarbon contaminated vibro-compacted UO_2 were found to have severe hydriding in the crevice between the clad and the cap. This has been explained by two entirely different mechanisms; (a) hydriding occurs because of an early depletion of oxygen as steam penetrates the crevice, leaving a hydrogen-rich atmosphere; (b) hydriding occurs at a hot spot near the centre of the face of the end cap and migrates by diffusion to the surface adjoining the crevice (126-128). Some of the reported hydriding failures have been associated with the above mechanisms.

Finally the attack of fission products from the inside must be considered. There are at least 20 stable or long life chemical elements produced in U^{235} fission with appreciable yields (greater than 1%). The possibility of a detrimental effect on clad performance by one or more of these elements has long been recognised. Logically, the possibility of such a mechanism occurring will increase with higher heat ratings and exposure where there is greater fission product release and higher concentrations, respectively. At the present time, the occurrence of fission product attack in stainless steel cladding, mixed-oxide fuel pins at high burn-ups seems to be firmly established but a similar mechanism with Zirconium alloy clad UO_2 remains speculative.

Originally, two fission products were regarded as potentially dangerous for Zirconium alloy cladding; namely, iodine and caesium. Recently, however, cadmium has also been suggested as another responsible species on the basis of some experimental results (129).

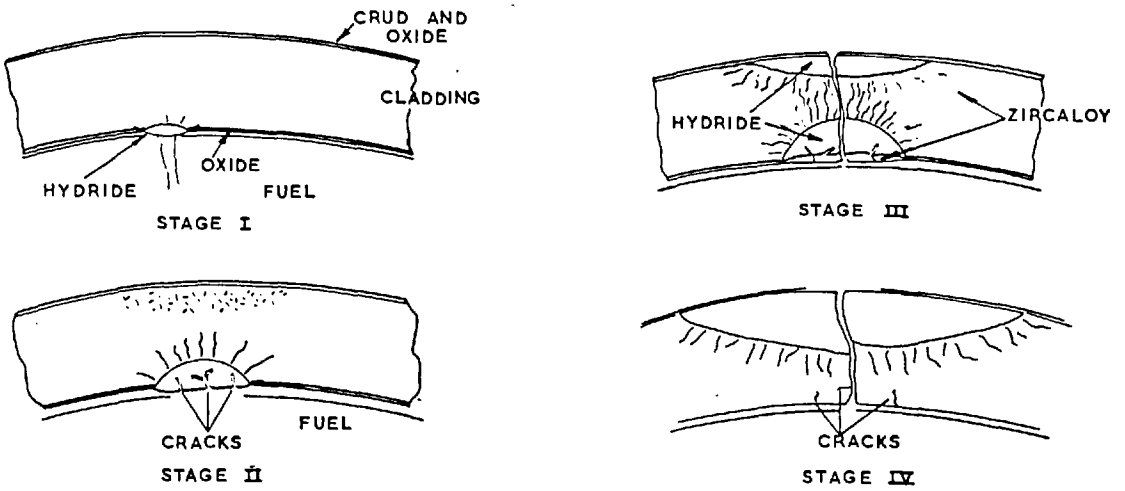
Iodine has been shown to be capable of cracking stressed Zirconium alloys (121,122,130). Caesium is volatile at UO_2 operating temperatures and is often found condensed on the inner surface of cladding, especially towards the cooler ends of a fuel pin, and adjacent to pellet ends (121,123). Furthermore, caesium and iodine have a strong affinity and are likely normally to be combined, but free iodine may be present too. Out-of-reactor experiments in the temperature range where the cladding tubes operate were published first by General Electric (121). Highly stressed samples were found to have fine cracks, while the unstressed samples did not crack. Since then this type of failure has been called iodine stress-corrosion-cracking (SCC). Attempts to induce cracking of stressed Zr by other fission products like Cs, F and Cd have not always been successful. However, the possibility of cracking cannot be ruled out especially with cadmium (129). Garlick's experiments (122) have been carried out in iodine vapour with Zircaloy. He has concluded that failure can occur in operating fuel pins by a process of SCC involving iodine and possibly other volatile fission products. Recent observations have confirmed that the cladding cracks formed as a consequence of a power increase and pellet cladding

interaction (PCI), are of the stress corrosion type, with the responsible chemical species arising from the fissioning of UO_2. Conditions most conductive to fission product SCC in fuel pins are envisaged as those arising from an up-rating of fuel which has previously been irradiated to a moderately high burn-up. In this way, circumferential tensile stresses are applied to the cladding as a result of the expansion of the fuel and, simultaneously, a burst of volatile fission products is released from the fuel. Under these conditions a SSC failure might occur before the concentration of available iodine was reduced by chemical combination; this may not be the case when slow straining of the cladding over a long period, e.g. by fuel swelling, is considered or if the burn-up is not high enough. Of course the type of surface treatment and fabrication processes have also a marked effect on the resistance of Zircaloy to fission product SCC. The different stages of corrosion described in this section are exemplified in Figure 2.8.

Figure 2.8

DIFFERENT STAGES OF CORROSION AND FAILURE DEVELOPMENT IN A TYPICAL ZIRCALOY CLAD UO_2 FUEL PIN

(AFTER REF.98)



CHAPTER 3

MATHEMATICAL ANALYSIS AND MODELLING OF LIGHT WATER REACTOR FUEL PIN BEHAVIOUR

CHAPTER 3

MATHEMATICAL ANALYSIS AND MODELLING OF LIGHT WATER REACTOR FUEL PIN BEHAVIOUR

3.1 INTRODUCTION

Fuel pins for power reactors consist of fuel in the form of a stack of sintered fuel pellets and a cylindrical cladding. The cladding is the first safety barrier against the release of radioactive fission products (as became clear in the previous chapter). The safety aspect of the cladding implies that proof of its integrity under normal and transient loading conditions is the most important criterion in fuel pin design work. Thermal and mechanical analyses appropriate to such design work must model, above all, the extremely complex mutual interaction between the pellets and the cladding. Here, in addition to the intricate physical phenomena, the non-linear material behaviour and the time-dependent operating characteristics must be considered.

Chapter 2 described the most significant phenomenological processes taking place and the thermal and mechanical properties of a typical fuel pin. Clearly, even with the advent of modern high speed computing machinery, it is not feasible to conceive a computer code which will model all these phenomena and property changes with a minute attention to detail in an economic amount of computer time. It is, however, unlikely that all of the phenomena simultaneously play a crucial part in the performance of any one particular fuel pin among so many kinds of fuel pins that are found in reactor practice. In general, therefore, an integral fuel

pin computer code will not model phenomena to that degree of complexity which present knowledge or insight would permit. This is reserved for sophisticated, special purpose codes (for instance see Refs.(12) and (13)). An integral fuel pin code will confine itself to a brief but comprehensive analysis of all the salient processes known to occur in a fuel pin, some attention to detail will be given in those areas where the specific code task deems this justified.

Many general purpose fuel pin computer codes have been written, in each code one or more phenomena were singled out for special treatment. A detailed comparison of all the codes found in the open literature is beyond the scope of the present work. A qualitative comparison can, however, be made. In Table 3.1 a summary of the computer codes currently used in the design and analysis of thermal and fast reactors is presented. And Table 3.2 presents a comparison in which the pertinent features and their degree of sophistication are listed for twelve popular codes (8,15).

Though the published codes differ widely in their specific tasks and methods of solution, many similarities exist among them as becomes clear from Tables 3.1 and 3.2. Most of the fuel pin codes have divided the fuel into two to four thermal and mechanical zones, the boundaries of the zones coinciding with the isotherms of restructured fuel as well as with the pellets and the cladding boundaries. Here, at most 4 zones can be obtained representing columnar grains, equiaxed grains, unrestructured grains, and the cladding. In the analysis average values for temperature, stresses, thermal and mechanical properties, etc. are used. However,

TABLE 3.1

LIST OF PRINCIPAL CODES USED FOR FUEL PIN BEHAVIOUR ANALYSIS

Name of Code	Organisation	Brief Description of Code
ACTIVE-II	PNC, Japan	1½-D fast reactor fuel pin code. Used for design studies in normal operation including restructuring mechanisms.
BEHAVE	GE, Sunnyvale U.S.A.	1½-D finite-element analysis, steady-state and transient. Developed for fast reactor pins but LWR version is available too. BEHAVE-2 is used for EBR-II experiments analysis, BEHAVE-3 is capable of transient analysis of TOP experiments. BEHAVE-4 is used for LWR pin analysis.
COMETHE	Belgonucleaire Belgium.	1½-D finite-difference steady-state analysis for design studies. Several fast and thermal reactor versions are available; COMETHE-IIIJ is the LWR version.
CYGRO	WARD, Madison & Bettis Atomic Power Laboratory	1-D finite element for steady-state fast and thermal reactor for design studies. Also used for the analysis of LWBR experiments. Several versions available after having been rejected by EPRI studies(170), its new version, CYGRO-4 was developed with major improvements.
DEFORM	Argonne National Laboratory, U.S.A.	Fuel analysis module of SAS-2A code used to analyse LOF experiments. Steady-state analytical solution.
FMODEL	Oak Ridge National Laboratory, U.S.A.	Steady-state 1-D code used for FBR analysis.

TABLE 3.1 (cont.)

Name of Code	Organisation	Brief Description of Code
FPIN	Argonne National Laboratory, U.S.A.	1-D code for analysis of accident conditions, includes simplified version of FRAS swelling and gas release code.
FRAP,FRAS		1½-D fast reactor analysis codes.
FRUMP	A.E.R.E., Harwell, U.K.	1½-D fast reactor analysis code. Used for both normal and transient calculation including a wide range of models with finite difference.
GAPCON		Fuel pin temperature and gas release anlaysis code 1-D and 1½-D versions plus fast and thermal reactor versions available. Only elastic deformations, swelling and densification considered.
IAMBUS	Interatom, Germany.	1½-D integral fuel pin analysis code. Used for design, in-pile performance prediction and post-irradiation analysis. Steady-state calculations.
LIFE	Argonne National Laboratory, U.S.A.	1½-D integral fuel pin analysis code. LIFE-III is a calibrated code for normal operation analysis, LIFE-IV is physically based and treats transients. LIFE-THERMAL-1 is the LWR version.
SATURN	GfK, Karlsruhe, Germany.	1½-D integral fuel pin analysis code. Used for analysis of steady-state and power-cycling experiments with special emphasis on fuel structure. LWR and FBR carbide versions also available.

TABLE 3.1 (cont.)

Name of Code	Organisation	Brief Description of Code
SLEUTH-SEER	RFL, Springfields, U.K.	1½-D integral fuel pin analysis code. Used for steady-state, cyclic and power-ramping analysis of normal operation. SLEUTH component calculates the radial distribution of temperature and of stresses and strains at each axial location. SEER component calculates circumferential variations and cladding failure.
SAFE-2D	General Electric Nuclear Energy Div., U.S.A.	2-D finite element model for thermo-mechanical analysis of fuel pins under transient power conditions. Elastic-plastic effects, creep, swelling, fuel cracking and hot pressing are included. Applied only to short experimental pins.
URANUS	IRT, Darmstadt, Germany.	1½-D computer code for thermal and mechanical analysis of fast or thermal reactor fuel pins. New analytical method is used for programming optimisation. Handles both steady-state and transient cases.
WAFER		LWR fuel pin analysis code. Several versions of 1-D, 1½-D and 3-D nature are available. Finite difference used in all versions.

TABLE 3.2

DETAILS OF SOME ADVANCED FUEL PIN PERFORMANCE COMPUTER CODES

CODE		URANUS	SIEX	SATURN-3	SATURN-1	LIFE	IAMBUS	FRUMP	FMODEL	DEFORM	CYGRO	COMETHE	BEHAVE
General Characteristics	Applicable to pin cross-section	X	X	X	X	X	X	X	X	X	X	X	X
	Applicable to total pin	X	O	X	O	X	X	X	O	X	X	X	X
	Applicable to steady state conditions	X	X	X	X	X	X	X	X	O	X	X	X
	Applicable to ramps and power cycling	X	X	X	X	X	X	X		O		X	
	Applicable to transient conditions	X	O	O	O	X	O	X		X			X
	Pin Type - LWR pins	X	O	X	X	X	X			O	X	X	
	Pin Type - FBR pins	X	X	X	X	X	X	X	X	X	X	X	X
	Pin Type - FBR carbide pins	X	O	X	X		O			O			
	Axial symmetry	X	O	X	O	X	X	X	O	X	O	X	X
	Stress-strain - plane strain	X	X	X	X	X	X	X	X	X	X	X	X
	Configuration - plane stress	O		X	X		X	O		O			X
	Axial coupling	X	O	X	X	X	X		O	X	O	X	X
	Radial modelling zones in fuel	20	3	1	3		X	20	2		1		3
	Radial mesh points (max.)	200	X	30	50		X	200				50	
	Axial zones in fuel	30	21	20	X	10	X				X		

(Legenda:

X = YES

O = NO

Blank = UNKNOWN)

TABLE 3.2 (cont.)

CODE		URANUS	SIEX	SATURN-3	SATURN-1	LIFE	IAMBUS	FRUMP	FMODEL	DEFORM	CYGRO	COMETHE	BEHAVE
Mathematical Methods	Numerical iteration	O	O*	O	X	X	X	O	O	O	O	X	O
	Analytical iteration	X	O	X	O	O	O	O	O	X	O	O	O
	Finite differences	O	O	O	O	O	O	X	X	O	O	O	O
	Finite elements	O	O	O	O	O	O	O	O	O	X	O	X
Fuel Mechanics Modelled	Thermal expansion	X	X	X	X	X	X	X	X	X	X	X	X
	Creep	X	O	X	X	X	X	X	X	X	O	X	X
	Plastic Flow	X	O	X	X	X	X	X	X	X		X	X
	Hot pressing and sintering	X	O	O	O	X	X	X	O	O	X	X	O
	Swelling	X	X	X	X	X	X	X	X	X	X	X	X
	Crack formation and healing	X	O	X	X	X	X	X		O	X	X	X
Migration and Segregation of Fuel Components	Pore migration	X	O	X	X	X	X	X		O	X	X	X
	Fission-gas release	X	X	X	X		X	X	O	X		X	X
	Oxygen redistribution	O	O	O	O	O		X	X	O	O	X	
	Pu migration	O	O	O	X	O	O	O	X	O	O		
	Fission product migration	O	O	O	O	O	O	O	O	O	O		
	Axial transport	O	O	O	O	O	O	O	O	O	O		
Fuel/Cladding Interaction	Radial interaction	X	X	X	X	X	X	X	X	X	X	X	X
	Axial interaction, friction	X	O	X	O	X	X		O	X			O
	Fission-gas pressure buildup	X	X	X	X	X	X	X	O	X	X	X	X
	Internal corrosion	X	O	O	O	O	X		O	O			O

*Analytical, no iteration.

TABLE 3.2 (cont.)

CODE		URANUS	SIEX	SATURN-3	SATURN-1	LIFE	IAMBUS	FRUMP	FMODEL	DEFORM	CYGRO	COMETHE	BEHAVE
Cladding Mechanics Modelled	Thermal expansion	X	X	X	X	X	X	X	X	X	X	X	X
	Primary creep	X	O					X		O		X	
	Secondary creep	X	O	X	X	X	X	X	X	O	X	X	X
	Plastic flow	X	O	X	X	O	X	X	X	X			X
	Void swelling growth	X	X	X	X	X	X	X	X	O	X	X	X
	Corrosion	X	O			O	X		O	O	O		
	Anisotropy	O	O	O	O	O	O	O	O	O	X		O
Thermal Analysis	Fuel thermal conductivity	X	X	X	X	X	X	X	X	X	X	X	X
	Gap conductance: open gap	X	X	X	X	X	X	X	X		X	X	X
	closed gap	X	X	X	X	X	X	X			X	X	X
	Cladding thermal conductivity	X	X	X	X	X	X	X	X	X	X	X	X
	Cladding/coolant heat transfer	X	X		O			O		O			
External and Internal Controlling Parameters for the Calculation	Time	X	X	X	X	X	X	X	X	X	X	X	X
	Linear power	X	X	X	X	X	X	X	X	X	X	X	X
	Temperature	X	X	X	X	X	X	X	X	X	X	X	X
	Neutron flux	X	X	X	X		X	X		X	X		X
	Fuel burn-up	X	X	X	X		X	X		X	X	X	X

TABLE 3.2 (cont.)

CODE		URANUS	SIEX	SATURN-3	SATURN-1	LIFE	IAMBUS	FRUMP	FMODEL	DEFORM	CYGRO	COMETHE	BEHAVE
Output	Temperature profiles	X	X	X	X	X	X	X	X	O	X	X	
	Cladding stresses	O	X	X	X	X	X	X	X	X	X	X	X
	Fuel/Cladding pressure	X	X	X	X	X	X	X	X	X	X	X	X
	Fission-gas pressure	X	X	X	X	X	X	X	O	X		X	
	Cladding strain - pin diameter	X	X	X	X	X	X	X	X	X	X	X	X
	Cladding strain - pin length	X	O	X	O		X					X	X
	Fuel/Cladding gap width	X	X	X	X	X	X	X	X	X	X	X	X
	Gas composition	X		X	X		X			O		X	
	Fuel structure - structure zones	X	X	X	X	X	X	X	X		X	X	
	Fuel structure - porosity distrib.	O	X	X	X	X	X	X		O	X	X	X
	Fuel structure - crack distribution	O	X	X	X		X	X	X	O		X	X
	Fuel structure - Pu distribution	O	O	O	X	O	O	O		O	O	O	O
	Fuel structure - O/M distribution	O	O	O	X	O	O			O	O	O	O
	Fuel structure - fission-prod.dist.	O	O	O		O	O			O	O	O	O
Failure Criteria/Damage Limits		O	O	O	O	X	X				X	X	

it has become increasingly apparent that this methodology is inadequate and most of the recent codes have been based on a multi-zone approach. The number of zones in the fuel and the cladding is dictated virtually only by the accuracy desired and the amount of computer time deemed economical.

For structural analysis, a state of generalised plane strain is widely assumed in the fuel and the cladding. While this can be accepted to give an overall view of the stress-strain pattern in a long fuel pin, it leaves much to be desired in an analysis of the individual pellets, where a stress-strain pattern intermediate to generalised plane strain and plane stress is known to prevail. Though some workers have used the plane stress analysis, it seems that the generalised plane strain assumption has more support, basically due to its easy formulation and adaptation to analytical or numerical solutions. Whichever assumption is used the fuel must be divided into a number of slices or sections because of axial variations in flux pattern and temperature. As a result of this idealisation of geometry a "quasi-two-dimensional" treatment has been obtained in the majority of codes. In this way the entire fuel pin has been analysed at reasonable computer cost. Localised phenomena, such as the typical bamboo contour or ridging formed by the fuel pellets in a light water reactor, have not therefore been modelled - a truly two-dimensional analysis is necessary in such cases. Fully two-dimensional analyses are of limited value, however, since integral fuel pin studies are no longer feasible; computer storage and running time limit this type of work to the analysis of a

fuel pin section covering just a relatively small number of pellets. Global and local analyses are thus inevitably complementary in exhaustive fuel pin design work.

The heat transfer in the fuel and the resulting temperature distribution is of crucial importance. Particularly the heat transfer in the fuel/cladding gap, not only directly for fuel temperatures, but also indirectly for the mechanical loading of the fuel and the cladding; since the deformations here are strongly temperature dependent and a mechanical interaction normally occurs. This is one area in particular where the state of the art has been combined favourably with new models and techniques. The mechanisms of heat transfer in fuel/cladding gap, open gap or closed gap, are quite well known and incorporated in codes. For temperature calculations, since axial and angular conduction of heat are relatively unimportant for the class of problems under consideration with integral fuel pin codes, a one-dimensional (radial direction) heat-flow model has been employed. The channel has been divided into axial segments, and the temperature calculations have been made for each section in succession following the direction of coolant flow. In this way again a large saving in computer time and storage has been obtained by not having to solve the heat-flow equations in a two-dimensional space.

Although the basic thermal and mechanical equations are the same in most of the codes, but the methods of solution are widely different. Matthews (15) has reviewed the literature and discussed the different methods. Analytical solutions are not very popular because of the very

non-linear nature of the problem and the sometimes very complicated boundary conditions which imply great simplifications and idealisations if an exact solution is sought. The importance of exact solutions, however, has not been ruled out, since they can be used in design parameter studies and sometimes as a benchmark to check the accuracy of the approximate numerical techniques. The alternative to analytical solutions are numerical methods. The most widely used numerical methods are iterative techniques, finite differences and finite elements.

In the codes with iterative techniques the fuel pin geometry has been assumed to be that described earlier, namely, a four zone geometry. The cladding has been loaded externally by the coolant pressure, and provision has normally been made for an additional axial load. As in other codes, an initial gap between the fuel and cladding has been considered, and this gap can open or close any number of times depending on the fuel element operating history. For the gross mechanical analysis, the fuel has always been divided into three radial zones, corresponding physically to the columnar grain region, the equiaxed grain region, and the unrestructured region. The cladding then has formed the fourth zone. For each of these zones, the integral averages for the stresses, strains and displacements have been determined using normally a generalised plane strain analysis with material properties evaluated at the average temperature of each zone. This has been combined with an iteration procedure (guessing the increment in total strain or non-elastic strain and solving the equations

for new stresses, and then checking the accuracy by comparing calculated and assumed values of the strain increments) that allows these codes to follow changing boundary conditions resulting from reactor power fluctuations. Here, the mechanical analysis is limited to four regions because the resultant equations may be readily solved algebraically, which requires less computer time (3).

In the finite difference method the geometry is again similar to what was explained before. The fuel pin has been divided into a number of slices axially. Theses slices containing fuel, gas-filled gap and cladding are again divided into concentric rings. The division of fuel pin into slices and rings is completely arbitrary although the division of a zone into slices of equal thickness and rings of equal cross-sectional area undoubtedly has practical advantages. It seems that whilst the number of slices and rings chosen in different codes is also arbitrary, the decision will nevertheless depend on the main topic of interest in the pin being studied as well as on the accuracy desired and the computer time justified in obtaining a solution. Programming demands that the maximum possible number of rings in the fuel, blanket and cladding be defined. The rest of the basic assumptions are not much different than those used in other methods. Some codes have combined iterative and finite difference techniques by following the same procedure described for iterative codes but employing a multi-zone geometry (4,6). Others have solved the finite difference equations with algebraic methods and without any iterations by linearisation of the

non-elastic part of the total strain increment and its combination with stress-strain relationships and equilibrium equations. The advantages of this method, namely, the stability of solution and the speed and accuracy of computation have already been demonstrated by the computer code FRUMP (9). This technique is chosen for use in the present work in the development of computer code SAMURA.

Finally, in the finite element method, the structure is idealised by being cut into a finite number of smaller geometrical shapes. For instance, a good example of a 3-dimensional idealisation of fuel pin can be found in the work by Levy and Wilkinson (12). A two-dimensional geometrical idealisation (plane or axisymmetrical) is, however, generally preferred, considering its lower computational cost. There are actually very few finite element integral computer codes in service. One reason may be the high computing cost associated with this technique. It has, nevertheless, been extensively employed for studies concerning localised effects in fuel pins and other reactor parts. In these studies, generally two-dimensional, two types of elements have been considered. the first type, usually used to represent the body of fuel or cladding, is a triangular element (sometimes a rectangular element with certain characteristics). The second type is a uniaxial element which simulates the fuel/cladding gap and the contact between individual pellets (in some codes the same triangular elements with different properties have been used to represent the gap). These uniaxial elements have been characterised to be highly non-linear in their response

and they are capable of simulating gap closure, gap re-opening, friction, and pellet separation (11,15,131). The uniaxial elements may also be used to model other boundary conditions. The same techniques of thermal and mechanical analysis have been applied to the fuel pin idealised in the above manner by finite elements. Here, however, one may have the advantage of being able to include all the phenomenological changes of the fuel pin during its life, i.e. the restructuring of UO_2, variable density and other mechanical and physical properties which differ from zone to zone in fuel, without having to alter the basic structure of the code. In this respect finite elements are very similar to finite differences, the final decision being a matter of personal choice and specific task required from fuel modelling.

The computer code SAMURA is developed through an extensive study of the above techniques. The thermal and mechanical analyses used in most of the codes given in Table 3.1 were considered in great detail. Since the basic task was to develop an integral computer code for the study of LWR fuel pins at Imperial College using its computer facilities, certain restrictions on computing time and storage had to be taken into account as well. After careful consideration of all the factors involved and also future developments of the desired code, a combination of the most suitable geometrical models, physical models and calculation techniques was chosen from about twelve published codes to represent the mathematical basis for the computer program SAMURA.

In the following sections the basic equations incorporated in the SAMURA code for the analysis of fuel pins will be given. Then algebraic and numerical techniques used to tackle them will be presented. Finally problem parameterisation, as regards the temperature distribution, fuel/cladding heat transfer, creep rates, swelling rates and other physical and mechanical properties in SAMURA, will be discussed.

3.2 BASIC ASSUMPTIONS AND METHOD OF CALCULATION IN COMPUTER CODE "SAMURA"

The computer code "SAMURA" has been designed to determine temperature, stresses and strains during steady state and transient power operation of an oxide-fueled, metal clad cylindrical-type fuel pin in a pressurised environment. The name which has been given to the program stands for Stress Analaysis Modelling with Unrestricted Reactor Applications (SAMURA). Here "Unrestricted" refers to the type of reactor fuel element (fast or thermal), to the type of variation of power and to the parameterisation of the model. At the moment the programme has been developed to analyse the behaviour of Zircaloy tubes containing bulk oxide fuel, but the calculational techniques may be used for other materials by using appropriate parameterisation of quantities.

The basic geometry of the fuel pins shown in Figs.3.1 and 3.2 consists of a long metal tube (cladding), closed at each end, containing cylindrical pellets of porous fuel. The pellets may be in radial contact with the cladding

initially, or a gap may be present between them which can close or open any number of times, depending on the fuel pin operating history. The fuel pellets may be solid or annular and the centre hole may vary its radius in accordance with fuel restructuring. Axial symmetry is assumed to exist in the system of Fig.3.2 at all times, and plane cross sections perpendicular to the axis remain plane, so that all variables change only with radius and time. The fuel pores, assumed to be spherical and initially distributed homogeneously, change in size as a result of fission gas accumulation and hot pressing effects. The fuel porosity is therefore a function of temperature and thermal migration of the pores through the fuel.

The fuel pin is subjected to the following time-dependent loading functions: coolant temperature, coolant pressure, pressure in the gap between pellets and cladding, fission gas pressure in the fuel pores and voidage, and power level. The power level is input to the program, as well as the fast neutron flux. The fission rate, which produces fission gas and solid products in the pin, and generates heat in the fuel and cladding, can then be determined. Axial heat transfer has been neglected, however, axial variations of coolant temperature and neutron flux have been included. Specific heat and thermal storage effects have also been considered so the temperature distribution at any time is the solution of the transient equation of radial heat conduction. Film coefficients have been used at the outer surfaces of both fuel and cladding. The film heat transfer coefficient between the fuel and

Figure 3.1

IDEALISATION OF A FUEL PIN
FOR ANALYSIS PURPOSES

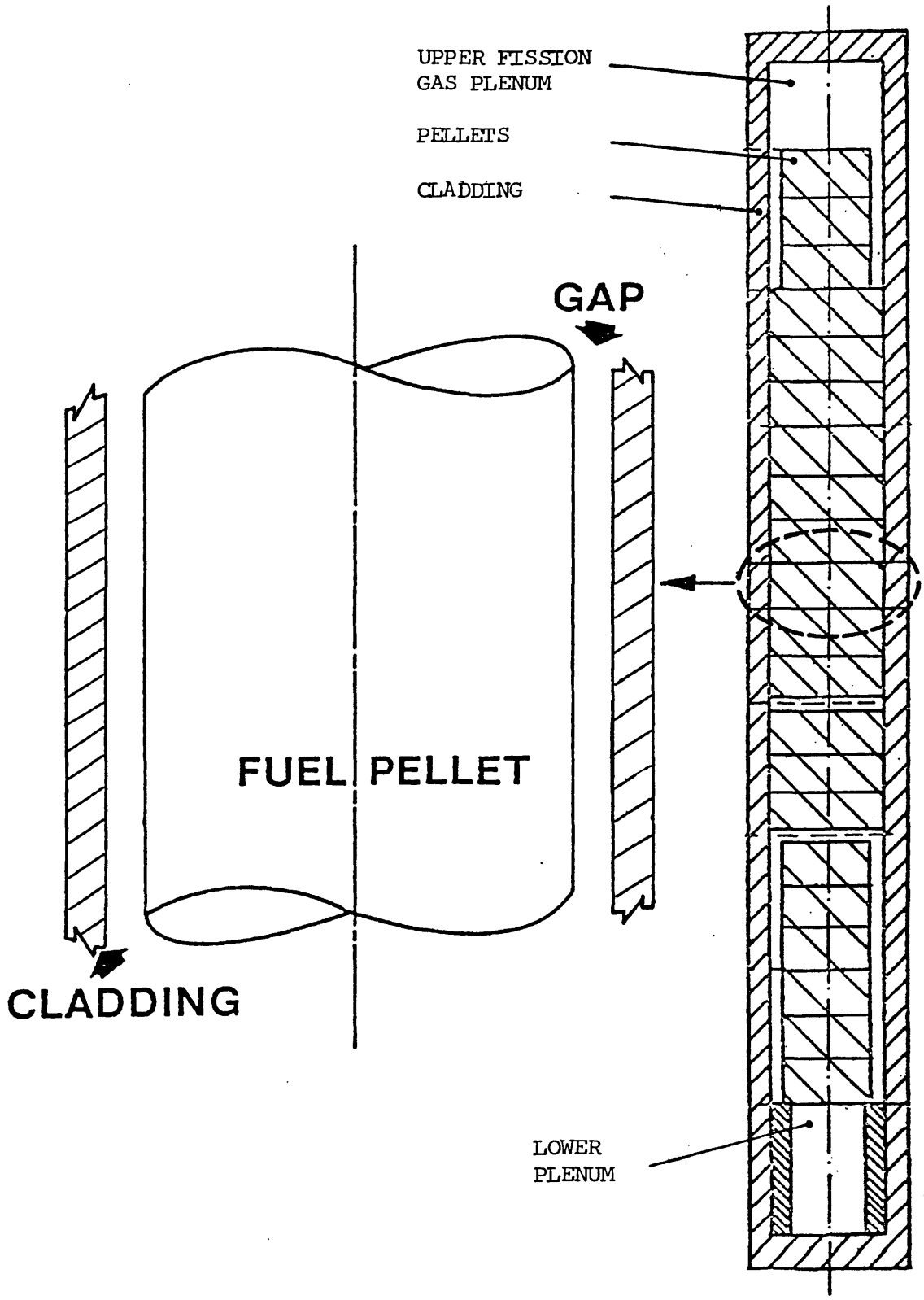
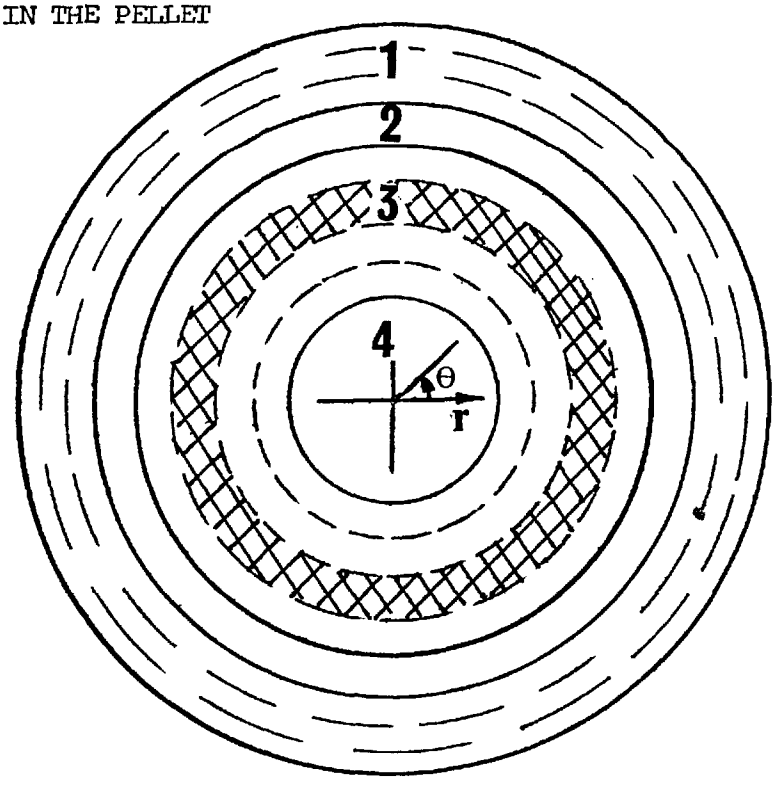


Figure 3.2

SUBDIVISION OF FUEL PIN CROSS-SECTION INTO RADIAL RINGS

1 CLADDING
2 GAP
3 RADIAL RINGS IN THE PELLET
4 CENTRAL VOID



cladding has been dealt with in great detail, however. Thermal conductivity and specific heat of the fuel are functions of temperature and porosity, and the conductivity and specific heat of the cladding depend only on temperature.

During a change in time the change in fuel volume is derived from thermal expansion, solid and gaseous fission products swelling as affected by local temperatures and stresses. The change in clad volume and free shape is derived from thermal expansion and neutron irradiation as affected by local temperatures and stresses. Deformation of both fuel and cladding is affected by the elastic and creep properties of the fuel and cladding materials. These properties are functions of temperature and fission rate or fast neutron flux and its integral with respect to time. Further deformations are caused in the fuel by cracking and porosity closure (in general, restructuring of the fuel). These effects have been modelled too. If there is a radial gap between fuel and cladding, the fuel and cladding act as mechanically independent bodies related only through fission gas pressure in the gap and their coupled temperature distributions. Otherwise, when the fuel is in contact with the cladding, radial and axial contact forces exist between the fuel and the cladding, in addition to the external pressure loads.

It is clear that a quantitative description of the complex time dependent mechanical interactions in a fuel element operating under thermal reactor conditions requires the solution of a set of coupled thermo-plastic equations which involves non-linear terms related to thermal and

irradiation creep and probably other physical effects. The solution of these equations can be divided into two distinct, but related parts. Firstly there is the problem of choosing a suitable physical model which involves the parameterisation of quantities which are not easily measurable experimentally, since one is concerned with the in-reactor behaviour of the materials of the fuel pins, and at the same time are not amenable to simple theoretical treatments. Secondly, one has the purely mathematical task of solving the set of coupled differential equations obtained from the model assumptions. In developing SAMURA the main emphasis has been on the second of these problems and a new method has been used which solves the equations numerically by finite differences. This technique, already incorporated in FRUMP (9), has proven to be very efficient in terms of computing demands and test calculations have shown that it is stable under all conditions investigated and the accuracy of the method may be determined quite simply.
For a given variation of the linear power density of the fuel in time, the method has been designed to calculate the following quantities: the non-linear temperature distribution across the pellets and the cladding, including the effects of the fuel/cladding gap and the coolant film at the surface of cladding; the changes in the dimensions of the fuel and cladding; the stress distribution in the three principal directions which due to axial and circumferential symmetry coincide with the cylindrical coordinates; and thermo-plastic, thermal and irradiation creep and swelling deformations in the fuel and cladding. Porosity distribution and cracking behaviour of the fuel are calculated too.

Further, the programme predicts the time (s) at which the fuel/cladding gap will open or close and the temporal variation of such quantities as the interaction pressure between the fuel and cladding, percentage of fission gas release and other useful information as desired.

For computation reasons, the pin height is assumed divided in "slices"; averaged values of the thermal and mechanical characteristics over the height of these slices are used in the calculations. It is necessary to account for axial variations in the flux, power, coolant temperature, coolant pressure, and fuel pin geometry. However, in the first version of SAMURA only one axial slice has been considered. Inclusion of several slices can be implemented with little modifications.

The slices containing the fuel and cladding are, in turn, divided in the radial direction into several coaxial "regions" (Fig.3.2), each divided again into a number of concentric "rings". The rings are characterised by values of the fuel properties averaged over the width of each of them. The regions can have completely different properties and radial gaps may exist between them. These radial gaps may close or open in time. Especially in the case of circumferential cracks, one can allow gaps to appear between already established regions for modelling purposes. Up to 10 such regions can be used, but in all of the work presented here, only 2 regions have been used, one describing the fuel and the other the cladding. The regions can also be extended to cover the different states of the fuel, e.g. the inner columnar grain growth region, the equiaxed region

and the outer unrestructured region. The maximum number of radial mesh points is 200, which is distributed among the regions according to width. So a maximum of 199 rings can be accommodated across the fuel pin. The radii of these rings are determined in such a way that their fuel inventory remains constant during all the life of the pin. The radii vary thus with time. Consequently, the fuel and cladding regions are composed of elementary cells to which models of heat transfer, expansion, swelling, creep, cracking and gas release are applied. This enables the code to predict diffusion effects and local thermal and mechanical transients in great detail.

Since axial and angular conduction of heat are relatively unimportant for the class of problems under consideration with SAMURA, a one-dimensional (radial) transient heat-flow model is used. The channel is divided into axial segments, coinciding with the fuel slices, and the temperature calculations are made for each section in succession following the direction of coolant flow. Calculations made thus far show that the neglect of axial conduction is quite reasonable. The advantage gained thereby, namely, of not having to solve the heat-flow equations in a two-dimensional space, represents a large saving in computing time. The model used in SAMURA for heat transfer is similar to those usually employed in calculation of reactor fuel temperature (3-9). The transient heat-conduction equations are discretised in space (radial) and time by means of an extrapolated generalised Crank-Nicholson scheme. That is to assume that the temperature gradients over the space can

be represented as a combination of their values at the beginning and at the end of the specified time increment. In this way the method can vary from a totally implicit to a totally explicit calculation. Somewhere in between the usual Crank-Nicholson scheme can be obtained. This method was chosen because it is numerically stable for very small to reasonably large increments of time (the latter quite important in steady-state calculations), and also because it is efficient in handling the non-linearities in the diffusion equation resulting from the wide variation of fuel thermal conductivity with temperature. In addition to the use of the new differencing scheme, the numerical model of heat transfer also takes into account the radial flux depression effects; the variable heat transfer coefficient at the fuel/cladding interface; temperature dependence of all properties; and dimensional changes due to elastic and non-elastic deformations.

The computational scheme used for the mechanical analysis of the fuel, is based upon an extremely efficient finite difference scheme developed by Wilmore (9). The constitutive equations are, in general, non-linear due to the thermal creep terms in both the fuel and the cladding. By using a Taylor series expansion technique coupled with a very sophisticated accuracy checking algorithm it is possible to linearise the equations and hence solve the elastic-plastic equations quickly and accurately. These equations are solved numerically by a matrix method which solves for all variables simultaneously without the necessity of iterating the results. The time dependence

of the problem entrers through the use of transient heat conduction equation and indirectly through the equations describing the creep and swelling rates. In this way, although quite complicated, the code is very economical in computing demands and is very stable.

The mechanical analysis is also one-dimensional with the assumption of axisymmetry and plane strain. Strains in the radial and circumferential directions are assumed independent of the tangential and axial coordinates, and axial strains are also independent of the radial position. The strains are assumed to be made up of the elastic, thermal, plastic/creep, swelling from solid and gaseous fission products, and cracks on planes normal to the tangential and axial directions. Each contribution is modelled using either theoretically derived equation or empirically derived data. Instantaneous plastic deformation is not very important in ceramic fuels due to the low fracture stress in the outer tensile region and the domination of creep at high temperatures which ensures stresses are always low. However, temperature dependent yield stress models are included for both fuel and cladding. The cladding plastic deformation becomes significant during fuel/cladding mechanical interaction. Also the analysis of fast transients, to which the code is equally applicable, required the yield and further mechanisms i.e. the effects of thermal inertia and fuel and cladding melting to be modelled.

In the following sections the basic equations of thermal and mechanical analysis will be given and the methods used in their solution enumerated. An account of

the errors arising from the method of mechanical analysis will be given too. This will include the procedure used to allow the automatic (computer generated) choice of time-steps by reference to accuracy criteria built into the code. Finally the particular parameterisation employed for the first version of SAMURA will be presented which will describe the equations used to model properties or phenomena like thermal conductivity, specific heat, thermal expansion, yield stress, fracture stress, elastic moduli, swelling, gas release, creep, etc.

3.3 THERMAL ANALYSIS

Thermal analysis is an essential prerequisite for structural analysis, not only because of thermal strains and stresses, but also because of the temperature dependence of the fuel pin materials properties. It is therefore necessary to predict, with reasonable accuracy, the temperature distribution throughout the pin during its entire life. This requires, basically, a global heat transfer analysis of the core and the fuel elements.

Generally, the main factors affecting fuel element heat transfer are geometrical configuration, neutron flux distribution, types of fuel and cladding used and coolant flow conditions. In a fuel pin inevitably the heat transfer coefficient will vary around the pin periphery, reaching minimum values at positions of closest pin proximity. In an individually cooled pin the heat transfer coefficient varies peripherally if, due to poor tolerances or bowing, the fuel pin is not concentric with respect to the channel

wall. Furthermore, in the heterogeneous reactors referred to here the neutrons are thermalised in the moderator outside the fuel pin and absorbed in the fuel. As a consequence the neutron flux varies in the fuel reaching its maximum value at the fuel pin periphery. This is the so-called flux-depression effect in thermal reactors. Heat generation in fuel, being proportional to the neutron flux, varies in approximately the same manner. It is normally assumed that the heat generation is symmetrical with respect to the fuel pin axis. However, this is not the case for pins situated away from the core centre or even from a fuel element centre. Here an asymmetric heat source distribution prevails. In addition, factors inherent to the fuel pin also may have an important effect on heat transfer. Fuel and cladding are separated by a gas gap. The presence of this gap and the variation of its width during operation introduces a considerable change, and sometimes resistance, against the heat transfer. In case the fuel pellet is not entirely concentric with respect to the cladding the thermal resistance may vary significantly around the pin and thus the temperature distribution in the fuel pin will not be symmetrical any more.

The non-uniform heat transfer conditions referred to above have an effect on the temperature and flux distribution in fuel and cladding which may be evaluated by solving the Poisson's heat conduction equation in its general form,

$$\text{div}\,\{k\ \text{grad}(T)\} + \dot{Q}_v(r,\theta,z,t) = \rho C_p \frac{dT}{dt} \qquad (3.1)$$

where k = thermal conductivity, ρ = density, C_p = heat capacity, T = temperature, t = time and r,θ,z are cylindrical

coordinates. $\dot{Q}_v$ is the volumetric heat generation rate and is a function of r,θ and z directions. Thermal conductivity, heat capacity and density are also general functions of temperature and direction.

The solution of heat conduction equation in the general time and space-dependent form is neither practical nor economical for an integral fuel pin code. Many simplifications should be made to bring it into a desirable form amenable to analytical or numerical solutions. A study of the literature shows that many authors believe that it is often adequate to make a heat transfer analysis of the fuel pin using simplified one-dimensional steady-state form of the heat conduction equation. Although this has been used extensively in LWR performance codes, it is recognised that they cannot give sufficiently accurate results in transient fuel temperature calculations.

The model used here is similar to those usually employed in calculation of reactor fuel temperature. However a major difference exists between SAMURA's heat transfer model and those of other codes; it has the capability to model both equilibrium and transient conditions a facility that has proved to be very useful. The differencing scheme developed to solve the one-dimensional (radial) transient heat-conduction equation is based on a method formulated by Lees (132) for parabolic partial differential equations. In addition to the use of new differencing scheme, the numerical model also takes the following into account:

(a) Dimensional changes due to thermal expansion, swelling, creep, cracking and phase change (fuel melting).

(b) Variable fuel/clad gap size and its associated variable thermal resistance based on a modified Ross and Stoute model.

(c) The desirability of being able to use widely varying time increments for different portions of a transient.

(d) Temperature dependence of fuel and cladding thermal conductivity and heat capacity, as well as those of the filling gas and fission gas in the fuel/cladding gap and fuel plenum.

(e) Radial variation in fuel thermal conductivity, heat capacity, and density due to fuel restructing (porosity change).

(f) Inclusion of the neutron flux depression effects on heat generation rate.

(g) The facility to alter the outer fuel pin boundary condition. Either the cladding outer surface temperature or the coolant bulk temperature can be input as a boundary condition. In the latter case a coolant film heat transfer coefficient is used to calculate the cladding surface temperature.

3.3.1 The Radial Heat Conduction Equation

Figure 3.1 shows the cross section of a typical fuel pin under consideration. The bond gap may be filled with helium or other inert gases and the coolant in the case of PWR's and BWR's is light water. The time-dependent radial temperature profile is obtained by solving the diffusion equation (3.1) in cylindrical geometry:

$$\rho(r,T)\ C_p(r,T)\frac{dT}{dr} = \frac{d}{rdr}\left[k(r,T)\,r\,\frac{dT}{dr}\right] + \dot{Q}_v(r,t) \qquad (3.2)$$

where

T = temperature

C_p = heat capacity

ρ = density

k = thermal conductivity

$\dot{Q}_v$ = volumetric rate of heat generation

t = time

and r = radius of the cylinder.

Figure 3.3 shows the manner in which the radius of the fuel pin is discretised for performing the numerical solution. The various discretised forms of equation (3.2) obtained when the differencing scheme is used will be described here.

The approximation to equation (3.2) can be obtained by first multiplying both sides by r.dr and then integrating between r_i to r_{i+1} (see Figure 3.3):

$$\int_{r_i}^{r_{i+1}} \rho(r.T).C_p(r,T)\ \frac{dT}{dt}\ rdr = \int_{r_i}^{r_{i+1}} \frac{d}{dr}\left[k(r,T).r\frac{dT}{dr}\right] dr$$

$$\int_{r_i}^{r_{i+1}} \dot{Q}_v(r,T)\,rdr \qquad (3.3)$$

Now, if the ring between r_i and r_{i+1} represents one ring in the discretised fuel or cladding the radial dependence of ρ, C_p and $\dot{Q}_v$ can be ignored over this small distance. Thus

$$\tfrac{1}{2}(r_{i+1}^2 - r_i^2).\rho(T_i).C_p(T_i)\frac{\partial T_i}{\partial t} = k(\bar{T}_{i+1}).r_{i+1}\left(\frac{\partial T}{\partial r}\right)_{r=r_{i+1}}$$

$$- k(\bar{T}_i).r_i\left(\frac{\partial T}{\partial r}\right)_{r=r_i} + \tfrac{1}{2}(r_{i+1}^2 - r_i^2)\dot{Q}_{v,i} \qquad (3.4)$$

where $\bar{T}$ = linear average temperature at the location shown, and ρ, C_p, k and $\dot{Q}_v$ have the same definitions as before only localised here. The subscript i denotes radial space nodes. Furthermore, ∂ is used instead of d to define the local temperature partials.

To write equation (3.4) in first order difference form in time and space the Taylor expansions of T in space and time are taken as below (temperatures are calculated from known values at time t - Δt), in time:

$$T_i^j = T_i^{j-1} + \left(\frac{\partial T}{\partial t}\right)_i \Delta t + \left(\frac{\partial^2 T}{\partial t^2}\right)_i \frac{(\Delta t)^2}{2!} + O[\Delta t]^3 \qquad (3.5)$$

in space:

$$T_{i+1}^j = T_i^j + \left(\frac{\partial T}{\partial r}\right)_i \Delta r + \left(\frac{\partial^2 T}{\partial r^2}\right)_i \frac{(\Delta r)^2}{2!} + O[\Delta r]^3 \qquad (3.6)$$

$$T_{i-1}^j = T_i^j - \left(\frac{\partial T}{\partial r}\right)_i \Delta r + \left(\frac{\partial^2 T}{\partial r^2}\right)_i \frac{(\Delta r)^2}{2!} - O[\Delta r]^3 \qquad (3.7)$$

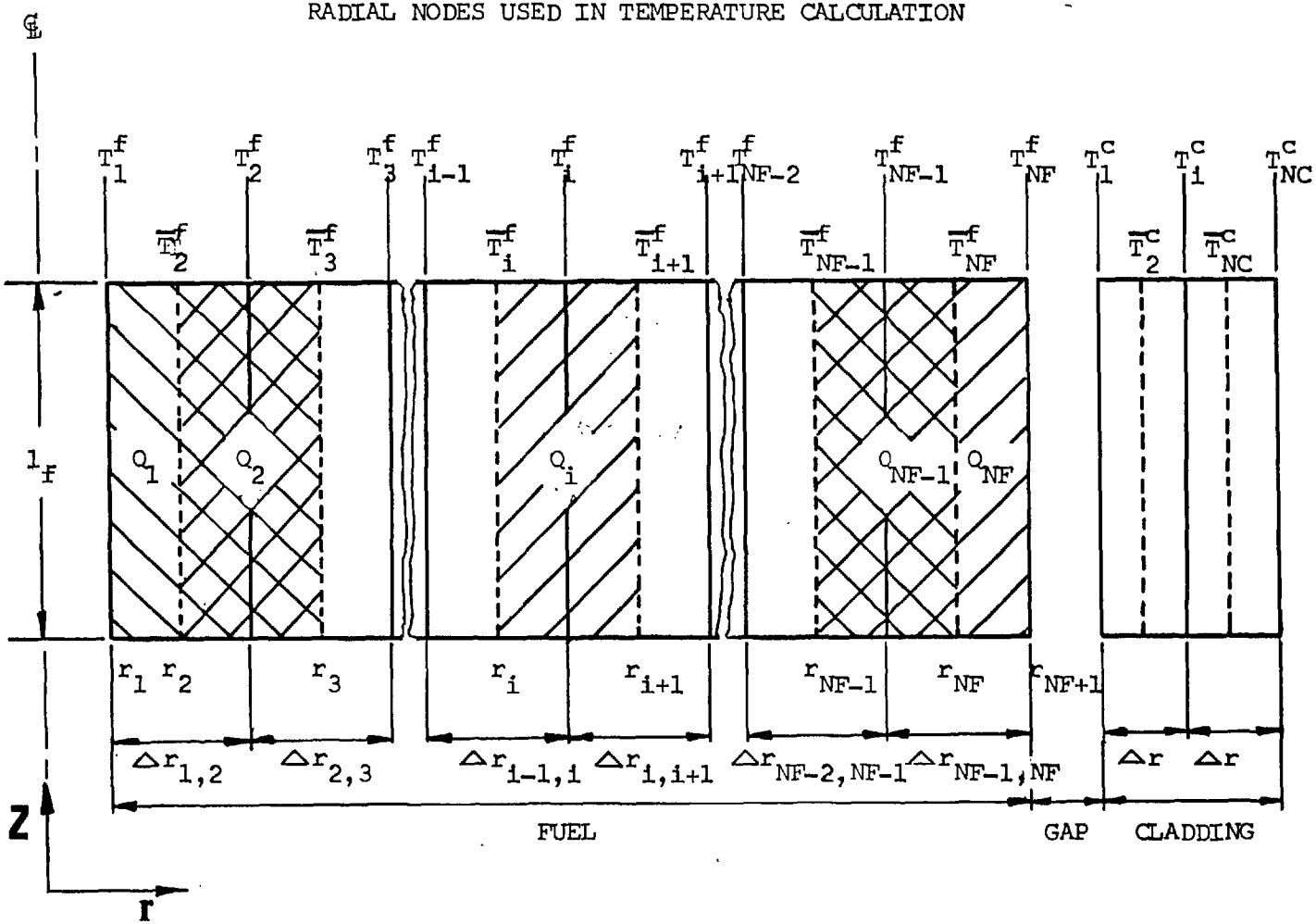
where the superscript j denotes time nodes. Further, it is assumed that since the temperature gradients on the right-hand side of equation (3.4) vary continuously with time the nature of the solution will depend on the value taken for these gradients. If $\partial T/\partial r$ is calculated at the beginning of a time-increment an "explicit" differencing scheme is obtained, while if it is calculated at the end of the time-increment the scheme becomes totally "implicit". It was decided, therefore, to vary the implicity of the method by representing the space gradients by a combination of their value at time j and time j-1, i.e.

$$\left(\frac{\partial T}{\partial r}\right)_i = \theta \left(\frac{\partial T}{\partial r}\right)_i^j + (1-\theta) \left(\frac{\partial T}{\partial r}\right)_i^{j-1} \qquad (3.8)$$

$$(0 \leq \theta \leq 1)$$

Figure 3.3

RADIAL NODES USED IN TEMPERATURE CALCULATION



It is obvious that $\Theta = 0$ gives the explicit solution and $\Theta = 1$ the implicit one. For $\Theta = \frac{1}{2}$ the usual Crank-Nicholson scheme is obtained. Now using Eqs.(3.4), (3.6) and (3.7) we have:

$$
\begin{aligned}
(r_{i+1}^2 - r_i^2)\rho(T_i)C_p(T_i)\,\frac{T_i^j - T_i^{j-1}}{\Delta t}
&= 2k(\bar{T}_{i+1})r_{i+1}\,\frac{(T_{i+1}^j - T_i^j)\Theta + (T_{i+1}^{j-1} - T_i^{j-1})(1-\Theta)}{\Delta t_{i+1,i}} \\
&- 2k(\bar{T}_i)r_i\,\frac{(T_i^j - T_{i-1}^j)\Theta + (T_i^{j-1} - T_{i-1}^{j-1})(1-\Theta)}{\Delta r_{i,i-1}} \\
&+ \dot{Q}_{v,i}^j\,(r_{i+1}^2 - r_i^2)
\end{aligned}
\qquad (3.9)
$$

Equation (3.9) can be applied to a region with N nodes as shown in Fig.3.3. As it is seen the first and last nodes in both fuel and cladding regions have half the width of the other nodes (rings). This is to ensure a correct representation of space gradients at boundaries. ρ, C_p and k are functions of temperatures as mentioned before. k values are taken at the linear average temperature between two adjacent nodes ($\bar{T}$), while ρ and C_p values are taken at nodal temperature.

Having applied Eq.(3.9) to a region with N nodes provides N coupled algebraic equations, which have to be solved simultaneously to obtain T_i^{j+1} for all i at each axial node. The differencing scheme is implicit ($1 \geq \Theta \geq 0$), and since k, ρ and C_p are non-linear functions of temperature, the equation is non-linear too. Consequently, an exact solution

of the coupled finite-difference equations is not easily possible. A method suggested by Lees (132) can be used to treat the non-linearity. The same Θ parameter can be used to obtain temperatures at the point of time where the space gradients are calculated, i.e. (j-1) + Θ. In other words, since temperatures at time (j-1) + Θ are needed to calculate k, ρ and C_p, a linear extrapolation of temperature to (j-1) + Θ from j-1 and j-2 gives the desired temperature:

$$T_i^{(j-1)+\Theta} = T_i^{j-1} + \frac{\Delta t^j}{\Delta t^{j-1}} \Theta (T_i^{j-1} - T_i^{j-2}) \qquad (3.10)$$

where

Δt^j = time-increment between j-1 and j;

Δt^{j-1} = time-increment between j-2 and j-1;

in general,

$$\Delta t^j \neq \Delta t^{j-1}$$

By the use of values thus obtained for $T_i^{(j-1)+\Theta}$ (i = 1,N) the values of k, ρ and C_p are computed and used to calculate the coefficients of finite difference equation (3.9) for all the nodes. It must be noted that the values of $\dot{Q}_v$ are always known a priori, either as input or calculated for every time-increment before temperature calculations.

Equation (3.9) has the following general form after application to an annular region:

$$\begin{aligned} &- \alpha_i.\Theta\ .T_{i-1}^j + (1 + \alpha_i.\Theta + \beta_i\ \Theta)\ T_i^j - \beta_i\Theta\ T_{i+1}^j \\ &= \alpha_i(1 - \Theta).T_{i-1}^{j-1} + (1 - \alpha_i(1 - \Theta) - \beta_i(1 - \Theta))T_i^{j-1} \\ &+ \beta_i(1 - \Theta).T_{i+1}^{j-1} + \dot{Q}_{v,i}^j(\Delta t^j/\rho_i C_{p,i}) \end{aligned} \qquad (3.11)$$

where α_i and β_i are general functions of T, k, ρ, C_p, t and r as defined below

$$\alpha_i = \frac{4\,k(\bar{T}_i)\,r_i\,\Delta t^j}{\rho(T_i)C_p(T_i)(r_{i+1}^2 - r_i^2)(r_{i+1} - r_{i-1})} \qquad (3.12)$$

$$\beta_i = \frac{4\,k(\bar{T}_{i+1})\,r_{i+1}\,\Delta t^j}{\rho(T_i)C_p(T_i)(r_{i+1}^2 - r_i^2)(r_{i+2} - r_i)} \qquad (3.13)$$

$$\dot{Q}_{v,i}^j = \dot{Q}_{v,i}^j(r,T) \qquad (3.14)$$

Equation (3.11) forms the basic finite difference equation and its application to all the nodes provides a set of N coupled algebraic equations. One has then to apply the appropriate boundary conditions to completely solve the problem.

3.3.2 Boundary Conditions

There are N unknown temperatures T_i^j in a region with N nodes. However from Eq .(3.11) it is obvious that it can only be applied to nodes 2 to N-1, because for i=1 and i=N it produces two fictitious temperatures T_o and T_{N+1} respectively. Thus Eq.(3.11) provides only N-2 equations and two more equations must be obtained or the two fictitious temperatures eliminated. Application of the boundary conditions at the inner and outer region surfaces does this. Furthermore, when fuel and cladding regions are considered together a common boundary condition - gap heat transfer coefficient - exists between them.

At fuel centre the temperature is maximum and thus the gradient of temperature is zero;

$$- k_1 \left(\frac{\partial T}{\partial r}\right)_{r=r_1} = 0 \qquad (3.15)$$

This automatically omits the negative term on the right-hand-side of Eq.(3.9) and therefore leads to (see Eq.(3.11)):

$$\alpha_{1,f} = 0 \qquad (3.16)$$

$$\beta_{2,f} = \frac{4k_f(\bar{T}_2)\, r_{2,f}\, \Delta t^j}{\rho(T_1)C_{p,f}(T_1)(r_{2,f}^2 - r_{1,f}^2)(r_{2,f}+r_{3,f}-2r_{1,f})} \qquad (3.17)$$

The subscript f denotes fuel region. Note that $\Delta r_{1,2} = \frac{1}{2}(r_2+r_3) - r_1$ (see Fig.3.3).

At the common boundary of the fuel and cladding (fuel/clad gap) it can be assumed that all the heat flux from fuel surface is transferred through the gap medium, which has a heat transfer coefficient h_{gap}, to the cladding inner surface. Thus it can be written:

$$- k_{N,f}\left(\frac{\partial T}{\partial r}\right)_{r=r_{N,f}} = h_{gap}\cdot(T_{N,f} - T_{1,C}) \qquad (3.18)$$

where

T_N = fuel outer surface temperature

T_1 = cladding inner surface temperature

Also

$$- k_{1,c}\left(\frac{\partial T}{\partial r}\right)_{r=r_{1,c}} = h_{gap}\cdot(T_{N,f} - T_{1,C}) \qquad (3.19)$$

Assuming that h_g is known for time j, as will be explained later, then Eqs.(3.18) and (3.19) can be incorporated into (3.9) and (3.11) for node N of the fuel and node 1 of the cladding. This will again omit the ficitious temperatures and give the appropriate values of α and β for these nodes:

$$\alpha_{N,f} = \frac{4k_f(\bar{T}_N)\, r_{N,f}\, \Delta t^j}{\rho_f(T_N)\; C_{p,f}(T_N)\,(r^2_{N+1,f}-r^2_{N,f})\,(2r_{N+1,f}-r_{N,f}-r_{N-1,f})} \tag{3.20}$$

$$\beta_{N,f} = \frac{2r_{N+1,f}\, h_{gap}\, \Delta t^j}{\rho_f(T_N)\, C_{p,f}(T_N)\,(r^2_{N+1,f}-r^2_{N,f})} \tag{3.21}$$

$$\alpha_{1,c} = \frac{2r_{N+1,c}\, h_{gap}\, \Delta t^j}{\rho_c(T_1) C_{p,c}(T_1)\,(r^2_{2,c} - r^2_{1,c})} \tag{3.22}$$

$$\beta_{1,c} = \frac{4\, k_c(\bar{T}_1) r_{2,c}\, \Delta t^j}{\rho_c(T_1) C_{p,c}(T_1)\,(r^2_{2,c}-r^2_{1,c})\,(r_{3,c}+r_{2,c}-2r_{1,c})} \tag{3.23}$$

Finally at the outer cladding surface two different boundary conditions can be used. First, it can be assumed that $T_{N,c}$ at time j is known for all the axial nodes. This omits the N^{th} equation when Eq.(3.11) is applied to the caldding for i=N, and the number of equations and unknowns in the cladding becomes N-1. The second method is to assume that the coolant temperature is known at time j. Here again the heat flux at cladding outer surface must be equal to the heat removed by the coolant with a film heat transfer coefficient of h_{cool}:

$$-k_{N,c}\left(\frac{\partial T}{\partial r}\right)_{r=r_{N,c}} = h_{cool}\cdot(T_{N,c} - T_F) \tag{3.24}$$

The temperature gradient from Eq.(3.24) is used in Eqs.(3.9) and (3.11) to obtain $\alpha_{N,c}$ and $\beta_{N,c}$:

$$\alpha_{N,c} = \frac{2\, r_{N+1,c}\, h_{cool}\, \Delta t^j}{\rho_c(T_N) C_{p,c}(T_N)\,(r^2_{N+1,c}-r^2_{N,c})\,(2r_{N+1,c}-r_{N,c}-r_{N-1,c})} \tag{3.25}$$

$$\beta_{N,c} = \frac{2\, r_{N+1,c}\, h_{cool}\, \Delta t^{j}}{\rho_c(T_N) C_{p,c}(T_N) (r^2_{N+1,c} - r^2_{N,c})} \tag{3.26}$$

It should be noted that when the second boundary condition is used h_{cool} must be calculated first from coolant information or be input data.

3.3.3 Method of Solution

Considering Eq.(3.11) and making the following substitutions:

$$\begin{aligned} A(i) &= 1 + \alpha_1.\theta + \beta_i\theta \\ B(i) &= -\alpha_i.\theta \\ C(i) &= -\beta_i.\theta \\ A'(i) &= 1 - \alpha_i(1-\theta) - \beta_i(1-\theta) \\ B'(i) &= \alpha_i(1-\theta) \\ C'(i) &= \beta_i(1-\theta) \end{aligned} \tag{3.27}$$

we obtain

$$A(i).T^{j}_{i-1} + B(i).T^{j}_{i} + C(i).T^{j}_{i+1} = A'(i).T^{j-1}_{i-1} + B'(i).T^{j-1}_{i} + C'(i).T^{j-1}_{i+1} + Q(i) \tag{3.28}$$

where

$$Q(i) = \dot{Q}^{j}_{v,i}(\Delta t^{j}/\rho_i C_{p,i}) \tag{3.29}$$

When (3.28) is applied to fuel and cladding regions it provides a system of N equations . This system can be written in matrix form which yields a "tridiagonal matrix":

$$[D]\{T\} = [X] \tag{3.30}$$

where

$$[D] = \begin{bmatrix} B(1) & C(1) & & & & O \\ A(2) & B(2) & C(2) & & & \\ O & A(3) & B(3) & C(3) & & \\ \vdots & \ddots & \ddots & \ddots & & \vdots \\ O & A(N-2) & B(N-2) & C(N-2) & O & \\ & & A(N-1) & B(N-1) & C(N-1) & \\ O & \text{----------} & & A(N) & B(N) & \end{bmatrix} \quad (3.31)$$

and

$$X_i = A'(i).T_{i-1}^{j-1} + B'(i).T_i^{j-1} + C'(i).T_{i+1}^{j-1} + Q(i) \quad (3.32)$$

It is obvious that

$$A(1) = A'(1) = C(N) = O$$

This matrix equation is solved by the Gauss elimination procedure. The procedure starts from the second row and replaces the B(i) and X(i) factors by

$$\begin{aligned} \text{New } B(i) &= B(i) - A(i).C(i-1)/B(i-1) \\ \text{New } X(i) &= X(i) - A(i).X(i-1)/B(i-1) \qquad (3.33) \\ i &= 2,N \end{aligned}$$

Thus the final will remain with T(N) as the only unknown, so

$$T(N) = \text{New } X(N)/\text{New } B(N) \quad (3.34)$$

and the recurrence equation to calculate the rest of temperatures is

$$\begin{aligned} T(i) &= (\text{New } X(i) - C(i).T(i+1))/\text{New } B(i) \\ i &= N - 1,1 \qquad (3.35) \end{aligned}$$

3.3.4 Fuel/Clad Gap Heat Transfer Coefficient

As mentioned earlier, in order to solve the temperature matrix equation it is necessary to calculate the fuel/clad gap heat transfer coefficient. The model developed here encompasses geometries ranging from an open gap with partial fuel-to-cladding contact to a closed gap with hard contact.

Fuel pellets crack extensively upon irradiation both because of thermal stresses induced by power changes, fuel low fracture stress and, at high burn-ups, the accumulation of gaseous fission products at grain boundaries. Therefore, the distance between the fuel and cladding will be circumferentially non-uniform, varying between that calculated for an annular gap in an intact fuel pin and essentially zero (fuel segments lying against the cladding wall). Since uranium dioxide pellets tend to crack in the radial direction, the pellet thermal conductivity will be only slightly influenced by this phenomenon. However, the fuel/cladding gap thermal conductance will be strongly increased and will generally correspond to a value reflecting both contact and open gas gap conductance.

Efforts to calculate fuel temperatures for pins with large hot gaps based on conductance across an annular gap between the cladding and the fuel using Ross and Stoute (133) or similar models have given poor agreement with available inpile high burn-up temperature measurements. Calculated fuel temperatures are much higher than observed, and the calculated effect of filling-gas conductivity is greater than that measured. This disagreement between predictions and measurements is not surprising, because pellet cracking

in effect moves the gap thermal resistance towards the centre of the pellet and replaces, to a certain extent, gap gas conduction with contact conduction. Calculated fuel temperatures using the cracked pellet gap conductance model developed for SAMURA compare well with available data. The analytical basis of the model is described here.

If a nominal hot gap is calculated in the mechanical analysis, a fraction of the fuel pellet is assumed to be in contact with the cladding at zero contact pressure and an effective fuel/cladding gap conductance is calculated as follows:

$$h_{gap} = (1-F)h_o + F.h_c + h_{rad} \qquad (3.36)$$

where

h_{gap} = net gap conductance

h_o = nominal open gap conductance

h_c = contact gap conductance (zero pressure)

h_{rad} = radiation heat transfer

F = fraction of pellet circumference in contact with the cladding

The nominal open gap conductance is determined from

$$h_o = \frac{k_{mix}}{GAP + \delta} \qquad (3.37)$$

where

k_{mix} = thermal conductivity of gas mixture in the gap determined as will be described later

GAP = nominal hot radial gap width

δ = the arithmetic mean of the fuel and the cladding surfaces roughness

The nominal hot radial gap width, GAP, is a gap width calculated assuming radial fuel cracking and fuel/cladding symmetry but no movement of the fuel segments. The zero pressure contact gap conductance, h_c, is determined from the equation for contact gap conductance discussed subsequently.

Recent post-irradiation examinations on LWR fuel elements have verified the assumption of partially-closed partially-open gap. It is assumed that after the first start-up always at least 30% of the pellet circumference is in light contact with the cladding. This fraction, F, is further assumed to be an inverse power law function of the ratio of the nominal hot radial gap and the hot pellet radius as follows (134):

$$F = \frac{1}{a\left(\frac{100.GAP}{r_f}\right)^b + 1.429} + 0.30 \qquad (3.38)$$

where

r_f = hot radius of the fuel pellet surface

a and b = empirical constants determined from data

The relationships for a and b as a function of burn-up, when the burn-up is greater than 600 MWd/teU, are described by Eqs.(3.39) and (3.40), respectively:

$$a = 100 - 98\ G \qquad (3.39)$$

$$b = 4 - 0.5\ G \qquad (3.40)$$

where

$$G = 1 - \frac{1}{\left(\frac{Bu - 600}{1000}\right)^4 + 1} \qquad (3.41)$$

Bu = Burn-up (MWd/teU)

when the burn-up is less than or equal to 600 MWd/tu, then

$a = 100$ and $b = 4$

The fraction of pellet/cladding contact, Eq.(3.38), is plotted in Fig.3.4 for both beginning and end of life. The burn-up relationship, G, is plotted in Fig.3.5. Eqs .(3.39) and (3.40) combined with Eq.(3.38) yield a family of curves between the two curves shown in Fig.3.4. Thus the fraction of the pellet circumference in contact with the cladding is calculated to increase with both decreasing nominal hot radial gap and burn-up. The asymptotic value of pellet/cladding contact for large gaps, F = 0.30, and the empirical constants a and b, were determined empirically by comparison of predictions with the fuel centreline temperature data (134-138).

Now, the second contributor to gap conductance in Eq.(3.36), namely h_c, is discussed. When the fuel and cladding are in contact, the classic Ross and Stoute (133) analysis of the heat transfer coefficient between two surfaces in contact is incorporated into SAMURA. Following their analysis the heat transferred across the interface between UO_2 and Zircaloy surfaces in contact may consist of two components:

(i) that by thermal conduction through solid/solid contact spots;

and (ii) that by conduction, convection and radiation through the medium which is trapped in the voids between these spots.

The convection term is not very significant compared to other terms and radiation can be treated separately as

Figure 3.4

FRACTION OF PELLET CIRCUMFERENCE IN CONTACT WITH THE CLADDING
AS A FUNCTION OF THE RATIO OF THE HOT RADIAL GAP TO THE HOT PELLET RADIUS

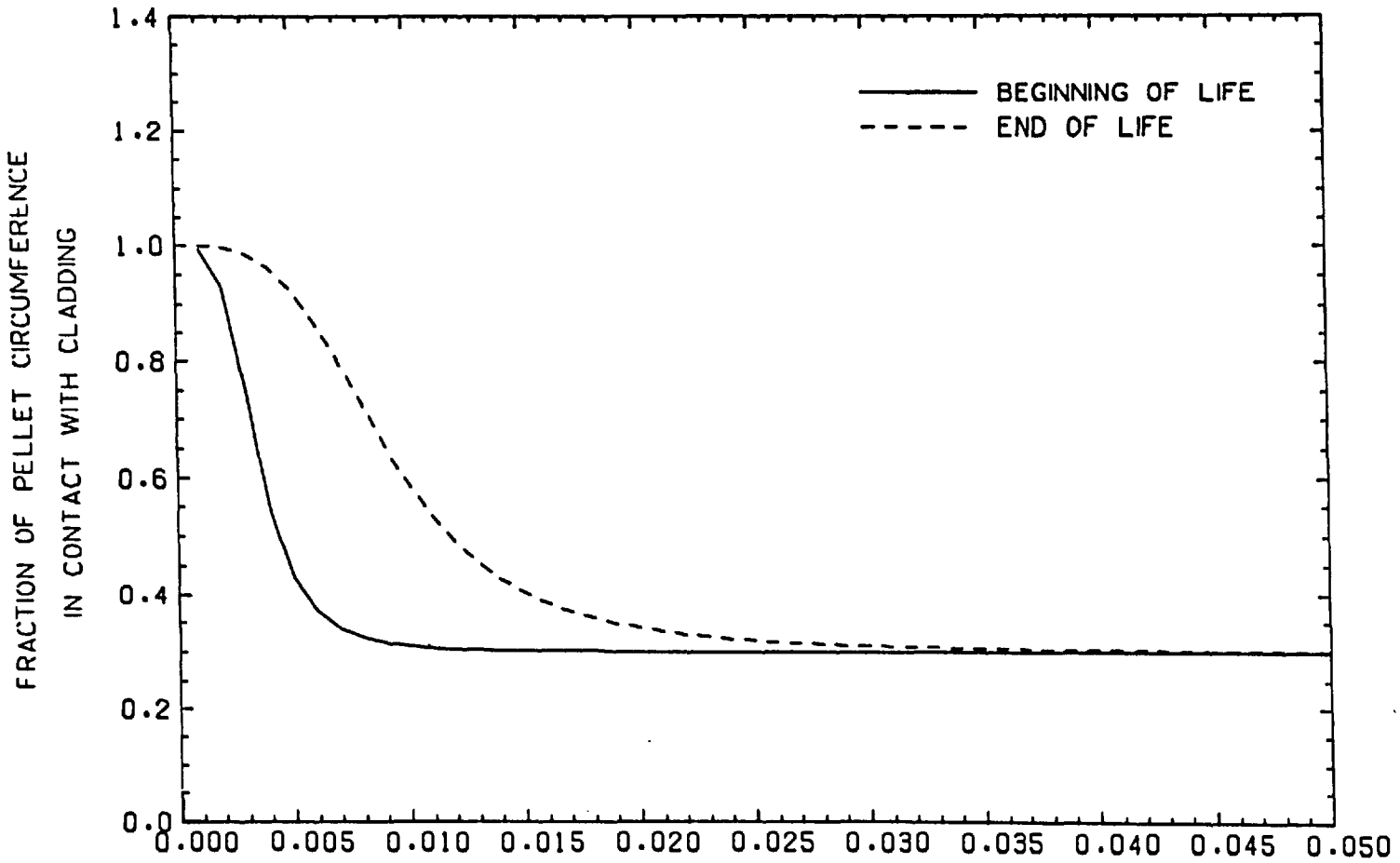
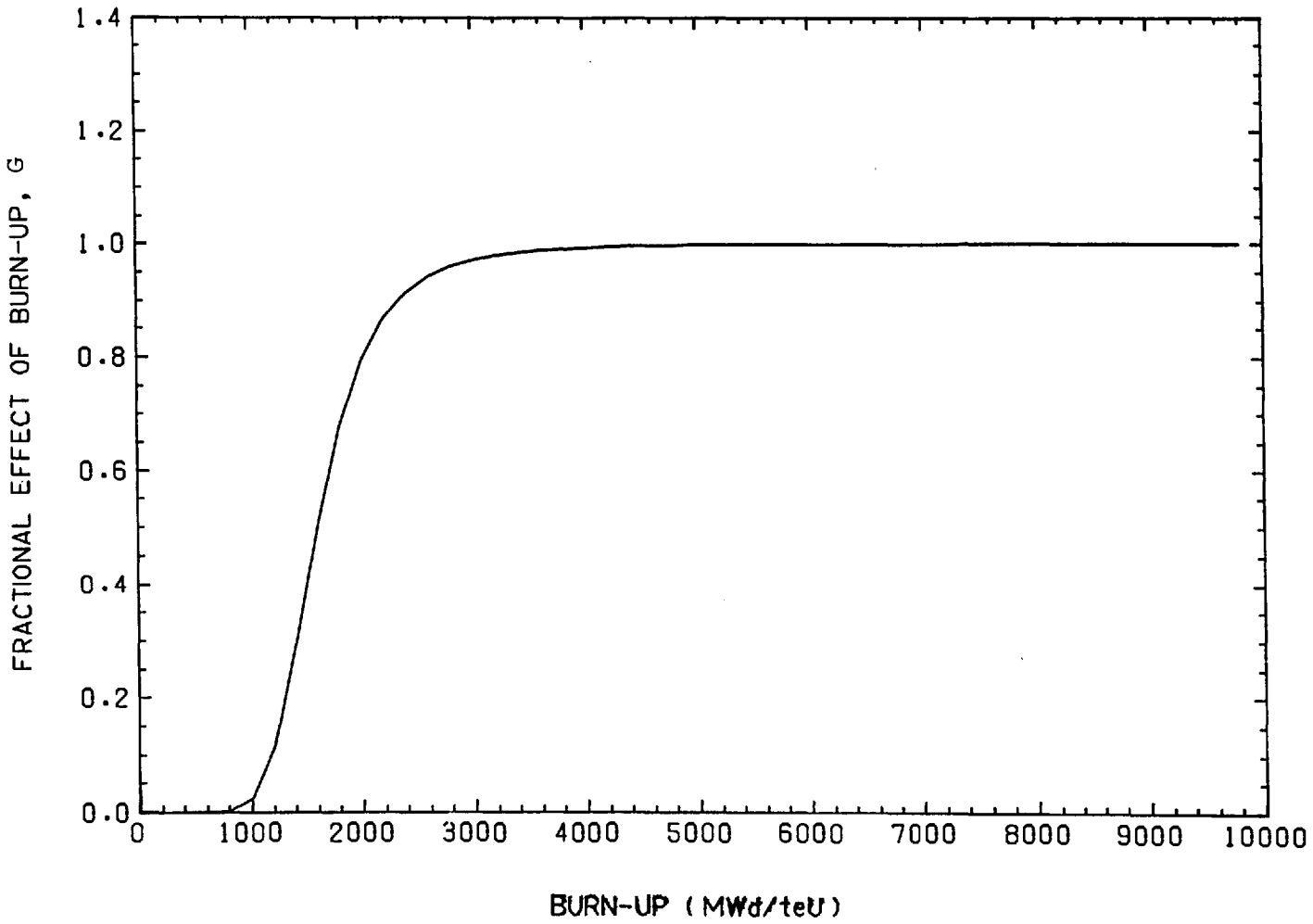


Figure 3.5

EFFECT OF FUEL BURN-UP ON FRACTION OF

PELLET CIRCUMFERENCE IN CONTACT WITH THE CLADDING



shown in Eq.(3.36). Thus the governing equation for contact conductance is

$$h_c = \frac{k_{mix}}{\delta} + C \left(\frac{P}{H}\right)^n \qquad (W/m^2\,{}^oK) \qquad (3.42)$$

where

k_{mix} = gas mixture thermal conductivity, (W/m^oK), (see Sub-Section 3.3.5);

δ = the arithmetic mean roughness height between the fuel and the cladding, (m);

$C = \frac{2\,k_f k_c}{k_f + k_c} \left(\frac{1}{a_o R^{\frac{1}{2}}}\right)$; where k_f = fuel thermal conductivity, $a_o = 0.05$, $m^{\frac{1}{2}}$; and R = the root mean square roughness between the fuel and cladding, (m);

P = contact pressure between the surfaces, (MPa);

H = Meyer hardness of the cladding, where H ≃ 3.35 x (yield stress of Zircaloy), (MPa);

and n = 1, assuming that one of the materials is flowing plastically*.

*Recently this assumption has been challenged by a number of workers in the field (see SMiRT 4 proceedings). Based on the theory proposed by Mikic (139,140) and the modifications suggested by Jacob and Tadreas (141) it is now thought that the value of the exponent, n, is governed by the behaviour of the fuel and cladding at the interface of the contact points. An exponent of 1.0 is valid only if the surface peaks of one of the materials are flowing plastically. This type of behaviour is consistent with Ross and Stoute (133) theory of contact conductance. If the contact points of both materials are behaving elastically, the correct value for the exponent, n, is approximately 0.5 (134). The experimental results of Fenech and Rohsenow (140) support this value and also indicate that for metal-ceramic pairs, the transition pressure from elastic to plastic flow is about 6.8947 MPa (1000 psi). It is further concluded that n=0.5 is applicable to contact pressures ≤ 6.8947 MPa, and n=1.0 is applicable to higher contact pressure interfaces. Unfortunately, it was not possible to incorporate these new assumptions into SAMURA to access their validity. This was basically due to the fact that parameter C in Eq.(3.42) has another definition in Mikic theory which could not be easily defined in terms of the available data.

Finally, the radiation term in Eq.(3.34) is described. The heat flux through the gap by radiation is

$$q_{rad} = \bar{\varepsilon}_{fc} \cdot \sigma_{SB} (T_f^4 - T_c^4) \tag{3.43}$$

where

q_{rad} = radiation heat flux

$\bar{\varepsilon}_{fc}$ = average fuel/cladding emissivity

σ_{SB} = Stefan Boltzmann constant ($\sim 5.775 \times 10^{-4}$ $W/cm^2 . {}^{o}K^4$)

T_f = fuel surface temperature

T_c = cladding inner surface temperature

$\bar{\varepsilon}_{fc}$ is defined as

$$\bar{\varepsilon}_{fc} = \frac{1}{\frac{1}{\varepsilon_f} + \frac{A_f}{A_c} (\frac{1}{\varepsilon_c} - 1)} \tag{3.44}$$

where

ε_f = fuel emissivity

ε_c = cladding emissivity

A_f = fuel outer surface area

A_c = cladding inner surface area

By assuming $q_{rad} = h_{rad}(T_f - T_c)$, h_c can be determined:

$$h_{rad} = \frac{\sigma_{SB} (T_f^2 + T_c^2) (T_f + T_c)}{\frac{1}{\varepsilon_f} + \frac{A_f}{A_c} (\frac{1}{\varepsilon_c} - 1)} \tag{3.45}$$

3.3.5 Gas Thermal Conductivity

The fuel/cladding gap conductance is, in part, dependent on the thermal conductivity of the gap gas mixture (see Eqs.(3.37) and (3.42)). Thermal conductivity relations for seven gases have been taken from literature as has a method

for calculating the thermal conductivity of mixtures of those gases. The thermal conductivities of the light gases, hydrogen and helium, have been adjusted to allow for imperfect energy transfer between solids and gas in the Knudsen regime.

The relationship used in SAMURA for calculating the thermal conductivity of a monatomic gas mixture is based on the work of Brokaw (142); which approximately holds for other gas mixtures too:

$$k_{mix} = \sum_{i=1}^{n} \left(\frac{k_i}{1 + \sum_{\substack{j=1 \\ j \neq i}}^{n} \phi_{ij} \frac{X_j}{X_i}} \right) \tag{3.46}$$

where

$$\phi_{ij} = \frac{\left[1 + \left(\frac{k_i}{k_j} \right)^{\frac{1}{2}} \left(\frac{M_i}{M_j} \right)^{\frac{1}{4}} \right]^2}{2^{3/2} \left(1 + \frac{M_i}{M_j} \right)^{\frac{1}{2}}} \times \left[1 + \frac{2.41 (M_i - M_j)(M_i - 0.142\, M_j)}{(M_i + M_j)^2} \right] \tag{3.47}$$

and

n = number of components in mixture

M = molecular weight of gas

X = mole fraction of gas in the mixture

k = gas thermal conductivity

The mixture of gases in the gap is assumed to contain the following gases at most at any time:

1. Helium
2. Argon
3. Xenon
4. Krypton
5. Nitrogen
6. Hydrogen
7. Steam (water)

Helium, argon and nitrogen may be used as filling gas and therefore their mole fraction and initial pressure is known prior to calculations. Xenon and krypton are the products of fission process and are released during irradiation of fuel pin. Their quantity and pressure is estimated before the temperature calculation as will be described later. The thermal conductivity equations of the rare gases (He, Ar, Xe and Kr) are based on the correlative work of Gandhi and Saxena (143). The conductivity of other gases are taken from other sources (144). It must be noted that steam or water exists in very small quantities in the interior of pin, however, it can be increased through internal and external corrosion of cladding (see Chapter 2).

It was stated before that the thermal conductivity of the gas mixture plays an important role in determining so-called "contact" gap conductance as well as "open" gap conductance in a fuel pin. In calculating the gas mixture conductivity one important effect known as Knudsen effect must be considered. When the ratio of the mean free path of the gas molecules to the characteristic dimension (gap) of the body exceeds about 0.01, normal heat flow formulas become inaccurate. Heat transfer from a solid to a gas in this Knudsen domain is then dependent on an accommodation coefficient which is defined as the ratio of the actual energy interchange to the maximum possible energy interchange between a surface and a gas. Generally, the

accommodation coefficient of a heavy gas such as argon or xenon is near unity and this effect can be neglected. But the effect cannot be neglected when the gap is filled with a light gas such as helium. Dean (145) has presented the following factor by which the bulk thermal conductivity of the light gases, helium and hydrogen, should be divided when temperature drops are calculated in the Knudsen domain:

$$f = 1 + \frac{\alpha_1 + \alpha_2 - \alpha_1 \alpha_2}{\alpha_1 \alpha_2} \cdot \frac{4}{C_p + C_v} \frac{k}{\mu} \frac{\lambda}{\xi} \qquad (3.48)$$

where

α_1 = accommodation coefficient of the fuel

α_2 = accommodation coefficient of the cladding

C_p = constant pressure heat capacity

C_v = constant volume heat capacity

k = gas thermal conductivity

μ = gas viscosity

λ = mean free path of gas molecules

ξ = characteristic dimension (gap)

The mean free path (λ) can be written as

$$\lambda = \frac{3\mu}{\rho} \sqrt{\frac{M}{8KT}} \qquad (3.49)$$

where

μ = gas viscosity

T = gas temperature

M = mass of molecule

K = Boltzman constant

ρ = density of gas

If λ and ρ are substituted in Eq.(3.48) and C_p and C_v are assumed to be temperature independent, then Eq.(3.48) can be written as

$$f = 1 + C \frac{k\sqrt{T}}{P\xi} \tag{3.50}$$

where

k = thermal conductivity

T = temperature

P = pressure

ξ = characteristic dimension

C = empirical constant

The characteristic dimension, ξ, is essentially equal to the gap dimension and during fuel/cladding contact should be equal to the root mean square of the surface roughness (δ in Eq.(3.42)), taken as 4.389×10^{-6} metres for most commercail fuel pins. If metric systems is used, a value for C of approximately 2.4944 $N^{o}K^{\frac{1}{2}}/W$ (8.5×10^{-4} psi ft^2 hr $^{o}F^{\frac{1}{2}}$/Btu) was determined in conjunction with the development of the cracked pellet gap conductance model discussed earlier.

3.3.6 Coolant Film Heat Transfer Coefficient

There are two sets of boundary condition that can be specified for temperature calculations. One is to specify cladding temperatures at all axial nodes and times. The time variation is slight under equilibrium conditions and varies linearly in start-up or shut-down cases. During transients the changes with time of the cladding temperature are more pronounced and non-linear relationships can be obtained from separate analyses and used as input. The other form of boundary condition is to specify coolant temperatures along the channel at all times. It is in this second case that the calculation of film heat transfer coefficient as used in Eq.(3.24) becomes necessary.

The following expression is incorporated in SAMURA to calculate h_{cool}; film heat transfer coefficient under equilibrium conditions:

$$h_{cool} = 0.03\ (k_W/D_h)\ Pr^{1/3}.Re^{4/5} \qquad (3.51)$$

where

k_W = thermal conductivity of coolant (water) at bulk temperature

D_h = hydraulic diameter of the channel

Pr = Prandtl number defined by

$$Pr = \frac{C_{p,W}.M_W}{k_W}$$

Re = Reynold's number defined by

$$Re = \frac{G_W.D_h}{\mu_W}$$

$C_{p,W}$ = specific heat of coolant

μ_W = viscosity of coolant

G_W = coolant mass velocity

If sufficient data is available Eq.(3.51) is used to determine h_{cool} for every time-increment, otherwise an input overall value for h_{cool} must be specified (especially in transient cases).

3.3.7 Power Distribution in Fuel

The thermal analysis of a fuel pin, particularly in a thermal flux, implies a knowledge of the radial power distribution in the fuel itself. According to literature, the best possible analytical description of the flux depression in the fuel is, at the present time,

$$\phi_f = a + br_f + Cr_f^2 \qquad (3.52)$$

where

ϕ_f = neutron flux in the fuel

r_f = fuel radius

a,b,c = constants

The boundary conditions on Eq.(3.52) are

$$\text{for } r_f = r_{1,f} \qquad d\phi_f/dr_f = 0$$

$$\text{for } r_f = r_{1,f} \qquad \phi_f = \phi_{1,f} \tag{3.53}$$

and

$$\text{for } r_f = r_{N,f} \qquad \phi_f = \phi_{N,f}$$

where

$r_{1,f}$ = fuel inner radius

$r_{N,f}$ = fuel outer radius

$\phi_{1,f}$ = flux at inner fuel surface

$\phi_{N,f}$ = flux at outer fuel surface

and the so-called flux depression factor is

$$f_{dep} = \phi_{1,f}/\phi_{N,f} \tag{3.54}$$

Now if Eqs.(3.53) and (3.54) are substituted into Eq.(3.52), a, b and c can be determined. The final result for radius $r_{i,f}$ is

$$\phi_{i,f} = \phi_{N,f} \left[f_{dep} + (1 - f_{dep}) \frac{r_{i,f} - r_{1,f}}{r_{N,f} - r_{1,f}} \right]^2 \tag{3.55}$$

The linear power distribution is defined as below for any ring i (see Fig.3.3):

$$P_i = 2\pi \Sigma_f E_f \int_{r_{i,f}}^{r_{i+1,f}} \phi_{i,f} r dr \tag{3.56}$$

where

Σ_f = macroscopic fission cross-section

E_f = rate of energy produced per fission

Combining Eqs.(3.55) and (3.56) and performing the integration, we have

$$P_i = 2\pi \sum_f E_f \phi_{f,N} \left[\tfrac{1}{2} f_{dep} r_f^2 \right]_{r_{i,f}}^{r_{i+1,f}} + \left[\frac{\tfrac{1}{4}(r_{i,f} - r_{i,1})^4 + 1/3\, r_{1,f}(r_{i,f} - r_{1,f})^3}{(r_{N,f} - r_{1,f})^2} (1-f_{dep}) \right]_{r_{i,f}}^{r_{i+1,f}}$$

or

$$P_i = 2\pi \sum_f E_f \phi_{N,f} I(i) \qquad (3.57)$$

where

$$I(i) = \tfrac{1}{2} f_{dep}(r_{i+1,f}^2 - r_{i,f}^2) + (1 - f_{dep}) \frac{\tfrac{1}{4}(r_{i+1,f} - r_{1,f})^4 + 1/3\, r_{1,f}(r_{i+1,f} - r_{1,f})^3}{(r_{N,f} - r_{1,f})^2} \qquad (3.58)$$

The linear power of the (i)th ring in terms of the linear power of the fuel is

$$P_i = \left\{ I(i) / \sum_{i=1}^{NRF} I(i) \right\} \cdot P_{lin} \qquad (3.59)$$

where

NRF = number of rings in the fuel

P_{lin} = fuel linear power (input to the programme)

and the mean power density (rating) in the (i)th ring is

$$\dot{R}_i = P_i / A_i \cdot \rho_{i,f} \qquad (3.60)$$

where

A_i = fuel ring cross-sectional area

$\rho_{i,f}$ = fuel ring density

Volumetric rate of heat generation as used in Sub-Section (3.3.1) is given by

$$\dot{Q}_{v,i} = P_i / A_i \qquad (3.61)$$

3.4 MECHANICAL ANALYSIS

The mechanical analysis is performed to model the state of stress and strain with time in a cylindrical ceramic fuel subjected to internal and external axial and radial loadings. The treatment is one dimensional with the assumption of axi-symmetry and plane strain in the fuel pin. In a cylindrical system of coordinates, strains in the radial and circumferential directions are assumed to be independent of the θ and z coordinates and axial strains are also independent of the radial position, though they can vary with time (see Fig.3.6). The strains are assumed to be made up of the following contributions:

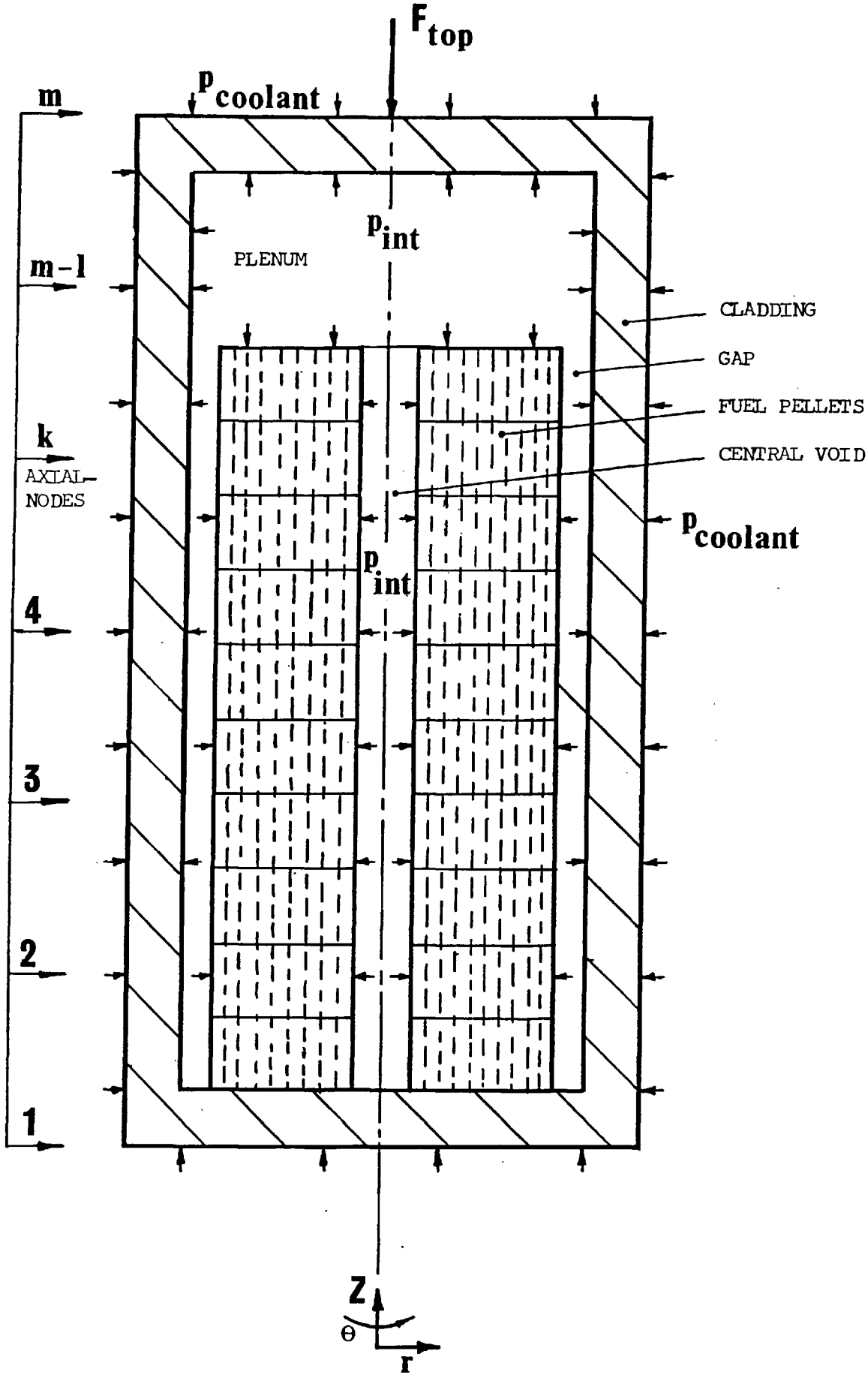
1. elastic
2. thermal
3. creep (thermal and irradiation induced)
4. plastic
5. swelling from solid and gaseous fission products
6. cracks on planes normal to the θ and z directions.

Each contribution is modelled using analytically derived relationships or empirically derived data.

The usual equations of state, equilibrium and flow laws from the mechanics of continua are employed to arrive at the differential equations which describe the mechanical behaviour of the system in Fig.3.6. Then a special method is used which solves the equations numerically by finite differences. The fuel pin cross-section is divided into radial zones or regions which their number can be varied up to 10 with different input data being provided for each region. The first version of SAMURA, however, uses only

Figure 3.6

GEOMETRICAL MODEL OF A FUEL PIN FOR ANALYSIS PUPOSES



2 regions to describe the fuel pin, an inner fuel region consisting of uranium dioxide surrounded by a second region of Zircaloy or stainless steel cladding material. The regions are divided into a total of N radial nodes with one node in the initial gas gap between the fuel and the cladding regions. The finite difference equations are so arranged that at each node there are only three unknowns u, the node radial displacements, γ_r the radial irreversible strain (the sum of non-elastic strains, see Eqs. (3.68)-(3.70) and γ_θ the circumferential irreversible strain. Since the analysis assumes a state of plane strain there is a further single unknown, the axial strain in each region, Z. When the gap between the regions is open, there are obviously different constant values Z_k which refer to the various regions. In the case where the gap between the regions is closing during the course of a calculation the values of Z appropriate to the different regions may be unequal. It is assumed that no axial slipping occurs while the gap is closed.

It is clear from the above that there are 3N + 1 unknowns for a total of N nodes in all the regions. The following sub-sections show the derivation of the equations that are used in the code to solve for these unknowns.

3.4.1 Mathematical Basis and Governing Equations

Considering a cylindrical body along with the cylindrical coordinates, the field equations for deformation analysis with axial and circumferential symmetry are:

(a) Constitutive equations

In a fuel pin all sources of strain are present and the final strain will be a combination of all sources. Thus:

$$\varepsilon_r = \varepsilon_r^e + \varepsilon_r^t + \varepsilon_r^c + \varepsilon_r^p + \varepsilon_r^s + \eta_r \quad (3.62)$$

$$\varepsilon_\theta = \varepsilon_\theta^e + \varepsilon_\theta^t + \varepsilon_\theta^c + \varepsilon_\theta^p + \varepsilon_\theta^s + \eta_\theta \quad (3.63)$$

$$\varepsilon_z = \varepsilon_z^e + \varepsilon_z^t + \varepsilon_z^c + \varepsilon_z^p + \varepsilon_z^s + \eta_z \quad (3.64)$$

where

$\varepsilon_{r,\theta,z}$ = components of total strain at time t,

$\eta_{r,\theta,z}$ = components of cracking strain at time t,

and superscripts e, t, c, p and s denote elastic, thermal, creep, plastic and swelling strains respectively.

To simplify the analysis the following definitions are made; ignoring the cracking strains momentarily:

$$e_r = \varepsilon_r^e + \varepsilon_r^t \quad (3.65)$$

$$e_\theta = \varepsilon_\theta^e + \varepsilon_\theta^t \quad (3.66)$$

$$e_z = \varepsilon_z^e + \varepsilon_z^t \quad (3.67)$$

$$\gamma_r = \varepsilon_r^c + \varepsilon_r^p + \varepsilon_r^s \quad (3.68)$$

$$\gamma_\theta = \varepsilon_\theta^c + \varepsilon_\theta^p + \varepsilon_\theta^s \quad (3.69)$$

$$\gamma_z = \varepsilon_z^c + \varepsilon_z^p + \varepsilon_z^s \quad (3.70)$$

Hence

$$\varepsilon_r = e_r + \gamma_r \quad (3.71)$$

$$\varepsilon_\theta = e_\theta + \gamma_\theta \quad (3.72)$$

$$\varepsilon_z = e_z + \gamma_z \quad (3.73)$$

For the moment the cracking strains have been ignored and e_p ($p \equiv r,\theta,z$) taken as the elastic strains (see Sub-Section 3.4.4). Using Hooke's law in the three directions r, θ and z these strains are given by

$$e_r = \frac{1}{E}\sigma_r - \frac{\nu}{E}\sigma_\theta - \frac{\nu}{E}\sigma_z + \alpha_r T \tag{3.74}$$

$$e_\theta = -\frac{\nu}{E}\sigma_r + \frac{1}{E}\sigma_\theta - \frac{\nu}{E}\sigma_z + \alpha_\theta T \tag{3.75}$$

$$e_z = -\frac{\nu}{E}\sigma_r - \frac{\nu}{E}\sigma_\theta + \frac{1}{E}\sigma_z + \alpha_z T \tag{3.76}$$

where

E = Young's modulus

ν = Poisson's ratio

$\sigma_{r,\theta,z}$ = components of stress at time t

$\alpha_{r,\theta,z}$ = coefficients of thermal expansion

T = temperature

By using the shear modulus relationship with E and ν, $G = E/2(1+\nu)$, Eqs.(3.74) to (3.76) can be solved for stresses σ_r, σ_θ and σ_z. The easiest way to do this is to eliminate σ_z from Eqs.(3.74) and (3.75) by its value from Eq.(3.76). This gives two equations in terms of σ_r and σ_θ which are readily solved. The final result provides the relation between stresses and elastic strains:

$$\frac{\sigma_r}{2G} = e_r + \frac{\nu(e_r + e_\theta + e_z)}{1 - 2\nu} - \frac{1 + \nu}{1 - 2\nu}\alpha_r T \tag{3.77}$$

$$\frac{\sigma_\theta}{2G} = e_\theta + \frac{\nu(e_r + e_\theta + e_z)}{1 - 2\nu} - \frac{1 + \nu}{1 - 2\nu}\alpha_\theta T \tag{3.78}$$

$$\frac{\sigma_z}{2G} = e_z + \frac{\nu(e_r + e_\theta + e_z)}{1 - 2\nu} - \frac{1 + \nu}{1 - 2\nu}\alpha_z T \tag{3.79}$$

(b) Prandtl-Reuss flow laws

The contributions of creep or plastic flow to strain are derived for a three dimensional state of stress from uniaxial creep or plasticity tests. In an isotropic medium the general equations for plastic deformation or creep are:

$$\varepsilon_e^p = f(\sigma_e) \tag{3.80}$$

$$\dot{\varepsilon}_e^c = \dot{g}(\sigma_e) \tag{3.81}$$

where f and $\dot{g}$ coincide with the relations obtained in uniaxial tests. ε_e^p is the effective (or equivalent) plastic strain, $\dot{\varepsilon}_e^c$ is the effective creep strain rate and σ_e the effective stress. The effective strain ε_e and the effective stress σ_e are defined in the theory of von Mises as follows:

$$\varepsilon_e = \sqrt{2}/3 \left[(\varepsilon_r - \varepsilon_\theta)^2 + (\varepsilon_\theta - \varepsilon_z)^2 + (\varepsilon_z - \varepsilon_r)^2 \right]^{\frac{1}{2}} \tag{3.82}$$

$$\sigma_e = \sqrt{1/2} \left[(\sigma_r - \sigma_\theta)^2 + (\sigma_\theta - \sigma_z)^2 + (\sigma_z - \sigma_r)^2 \right]^{\frac{1}{2}} \tag{3.83}$$

According to Prandtl-Reuss flow laws we have

$$\frac{\varepsilon_r^p - \varepsilon_\theta^p}{\sigma_r - \sigma_\theta} = \frac{\varepsilon_r^p - \varepsilon_z^p}{\sigma_r - \sigma_z} = \frac{\varepsilon_\theta^p - \varepsilon_z^p}{\sigma_\theta - \sigma_z} = \text{const.} \tag{3.84}$$

$$\frac{\dot{\varepsilon}_r^c - \dot{\varepsilon}_\theta^c}{\sigma_r - \sigma_\theta} = \frac{\dot{\varepsilon}_r^c - \dot{\varepsilon}_z^c}{\sigma_r - \sigma_z} = \frac{\dot{\varepsilon}_\theta^c - \dot{\varepsilon}_z^c}{\sigma_\theta - \sigma_z} = \text{const.} \tag{3.85}$$

Furthermore, the condition of constant volume states,

$$\varepsilon_r^p + \varepsilon_\theta^p + \varepsilon_z^p = 0 \tag{3.86}$$

$$\dot{\varepsilon}_r^c + \dot{\varepsilon}_\theta^c + \dot{\varepsilon}_z^c = 0 \tag{3.87}$$

By a combination of Eqs.(3.80) to (3.87) Prandtl-Reuss plastic deformation equations can be deduced:

$$\varepsilon_r^p = \frac{f(\sigma_e)}{2\,\sigma_e} \left[3\,\sigma_r - (\sigma_r + \sigma_\theta + \sigma_z) \right] \tag{3.88}$$

$$\varepsilon_\theta^p = \frac{f(\sigma_e)}{2\,\sigma_e} \left[3\,\sigma_\theta - (\sigma_r + \sigma_\theta + \sigma_z) \right] \tag{3.89}$$

$$\varepsilon_z^p = \frac{f(\sigma_e)}{2\,\sigma_e} \left[3\,\sigma_z - (\sigma_r + \sigma_\theta + \sigma_z) \right] \tag{3.90}$$

Similarly for creep:

$$\dot{\varepsilon}_r^c = \frac{\dot{g}(\sigma_e)}{2\,\sigma_e}\left[3\,\sigma_r - (\sigma_r + \sigma_\theta + \sigma_z)\right] \tag{3.91}$$

$$\dot{\varepsilon}_\theta^c = \frac{\dot{g}(\sigma_e)}{2\,\sigma_e}\left[3\,\sigma_\theta - (\sigma_r + \sigma_\theta + \sigma_z)\right] \tag{3.92}$$

$$\dot{\varepsilon}_z^c = \frac{\dot{g}(\sigma_e)}{2\,\sigma_e}\left[3\,\sigma_z - (\sigma_r + \sigma_\theta + \sigma_z)\right] \tag{3.93}$$

The plastic strains and creep rates can be given in the more conventional form by using the deviatoric stresses as defined by:

$$s_p = \sigma_p - \frac{1}{3}\sum \sigma_p, \qquad p \equiv r,\theta,z \tag{3.94}$$

where s_i is the deviatoric stress component in direction i. Thus from Eqs.(3.88) to (3.94):

$$\varepsilon_p^p = \frac{3}{2}\frac{f(\sigma_e)}{\sigma_e}\,s_p, \qquad p \equiv r,\theta,z \tag{3.96}$$

$$\dot{\varepsilon}_p^c = \frac{3}{2}\frac{\dot{g}(\sigma_e)}{\sigma_e}\,s_p, \qquad p \equiv r,\theta,z \tag{3.96}$$

(c) Swelling strains

The swelling term in the strain ε_p^s, Eqs.(3.62) to (3.64), is obtained from the rate of volume change, $\dot{S}$, derived from experimental data. The available data, in the form of empirical expressions, give the variation of irradiation induced volume changes due to fission products with time, temperature, and hydrostatic stress level.

Swelling is assumed to be isotropic so in the principal directions we have:

$$\dot{\varepsilon}_p^s = \frac{1}{3}\dot{S} \qquad p \equiv r,\theta,z \tag{3.97}$$

(d) The irreversible strain rate equation

The creep (or plastic) equations are in general non-linear. In order to avoid unnecessary restrictions the creep (plastic) strain rate equation will be written quite generally as

$$\dot{\gamma}_p = P_p + F_p(\sigma_r,\sigma_\theta,\sigma_z), \quad p \equiv r,\theta,z \tag{3.98}$$

where

$\dot{\gamma}_p$ = plastic strain rate in direction p

P_p = swelling strain rate

$F_p(\sigma_r,\sigma_\theta,\sigma_z)$ = the creep rate functional (non-linear).

From Eqs.(3.96) and (3.97) it is obvious that:

$$P_p = \frac{1}{3}\dot{S}, \qquad p \equiv r,\theta,z \tag{3.99}$$

$$F_p = \frac{3}{2}\frac{\dot{g}(\sigma_e)}{\sigma_e} s_p, \quad p \equiv r,\theta,z \tag{3.100}$$

(e) Cracking strains

The cracking strains η_i ($i \equiv r,\theta,z$) are the contribution to total strain from the width of cracks lying normal to the direction i. Two possibilities are considered, axial cracks ($i \equiv z$) and circumferential cracks ($i \equiv \theta$). The effects of these cracks are included in an approximate way by assuming that there are a very large number of very narrow cracks distributed homogenously throughout the material. That is to say the strain is made up of a uniform distribution of infinitesimal cracks, which when summed over a path give a finite value for η. This approximation corresponds to the observation of a large number of small cracks in most of the irradiated fuel pins.

(f) Equilibrium conditions

The stress in the system must satisfy the condition of equilibrium. In cylindrical coordinates with the assumptions of axial symmetry, zero shear stresses and no torsion, the equilibrium equations reduce to a single equation in the radial direction:

$$\frac{\partial \sigma_r}{\partial r} = \frac{\sigma_\theta - \sigma_r}{r} \tag{3.101}$$

Two boundary conditions must be satisfied; on the exterior pellet or cladding surface:

$$\sigma_r \big|_{r=r_{ext}} = - P_{ext} \tag{3.102}$$

where P_{ext} for the pellet with no contact with the cladding is equal to the fission gas pressure in the pin; in the case of a fuel/cladding gap closing P_{ext} takes the value of the contact pressure between the two surfaces. P_{ext} may vary with time and power history. On the exterior of the cladding P_{ext} is equal to the coolant pressure and can again be variable.

The boundary condition at the interior of the fuel depends on the type of the pellets. In the case of a solid pellet the condition at the origin is:

$$\frac{\partial \sigma_r}{\partial r} \Big| _{r=0} = 0 \tag{3.103a}$$

and in the case of a hollow pellet:

$$\sigma_r \Big| _{r=r_{int}} = - P_{int} \tag{3.103b}$$

where P_{int} is the internal pin pressure.

In the axial direction it is assumed that the axial stresses are balanced by a force F_z:

$$2\pi \int_{r_{int}}^{r_{ext}} \sigma_z \, r dr = - F_z \qquad (3.104)$$

The axial force, F_z, acting on the cross-section of pellets or cladding is made up of the fission gas pressure acting on the cross-section, the weight of the fuel column and friction forces* between the pellets and the cladding after contact. In the case of the cladding, coolant pressure and other external forces acting on its cross-section are included.

(g) Compatibility equations

With plane strain and axial symmetry, the circumferential displacement is zero and the variation of axial displacement with z is constant. Thus the relation between the radial displacement, u, and the total strains is:

$$\varepsilon_r = \frac{\partial u}{\partial r} \qquad (3.105)$$

$$\varepsilon_\theta = \frac{u}{r} \qquad (3.106)$$

$$\varepsilon_z = Z \qquad (3.107)$$

where Z is the constant axial strain. By comparison with Eqs .(3.71)-(3.73) the final form of compatibility equations are:

$$\frac{\partial u}{\partial r} = e_r + \gamma_r \qquad (3.108)$$

$$\frac{u}{r} = e_\theta + \gamma_\theta \qquad (3.109)$$

$$Z = e_z + \gamma_z \qquad (3.110)$$

(h) Summary of equations

Now that all the basic governing equations have been discussed we can proceed with finding an appropriate system

*Friction forces currently not included in SAMURA calculations.

of equations. Ignoring the cracking strains η_r, η_θ and η_z, it can be easily seen that the expressions (3.77), (3.78), (3.79), (3.98), (3.101), (3.108), (3.109) and (3.110) form a system of ten differential and algebraic equations. The unknowns are σ_r, σ_θ, σ_z, e_r, e_θ, e_z, γ_r, γ_θ, γ_z, u and Z, all dependent on the radial position and time. This system together with boundary conditions given by Eqs.(3.102) to (3.104), and the initial conditions that must be fixed provides the basis for mechanical analysis:

$$
\begin{aligned}
\sigma_r/2G &= e_r + \nu(e_r + e_\theta + e_z)/(1 - 2\nu) - \alpha(1 + \nu)T/(1 - 2\nu) \\
\sigma_\theta/2G &= e_\theta + \nu(e_r + e_\theta + e_z)/(1 - 2\nu) - \alpha(1 + \nu)T/(1 - 2\nu) \\
\sigma_z/2G &= e_z + \nu(e_r + e_\theta + e_z)/(1 - 2\nu) - \alpha(1 + \nu)T/(1 - 2\nu) \\
\partial\sigma_r/\partial r &= (\sigma_\theta - \sigma_r)/r \\
\dot{\gamma}_p &= P_p + F_p(\sigma_r,\sigma_\theta,\sigma_z) \quad , \quad p \equiv r,\theta,z \\
\partial u/\partial r &= e_r + \gamma_r \\
u/r &= e_\theta + \gamma_\theta \\
z &= e_z + \gamma_z
\end{aligned}
\tag{3.111}
$$

From the definition of $\dot{\gamma}_p (p \equiv r,\theta,z)$ and the Eqs.(3.98) to (3.100) it can be seen that $\dot{\gamma}_p$ is a function of $\sigma_p (p \equiv r,\theta,z)$ thus providing three extra differential equations which can be used to eliminate the stresses σ_r, σ_θ and σ_z from the system of Eqs.(3.111). Then we are left with only eight unknowns ($\gamma_r,\gamma_\theta,\gamma_z,e_r,e_\theta,e_z$,u and Z) and eight equations - seven from the system (3.111) plus Eq.(3.104). By introducing new assumptions and algebraic re-arrangements this system of differential equations may be reduced to have less unknowns and then integrated to give stress-strain state of the fuel and the cladding.

3.4.2 Finite Difference Method

Many different schemes were examined, numerical and analytical, to solve the system of Eqs.(3.111). The finite difference method was finally chosen for the present work because of the following advantages compared to other solutions:

(i) the possibility of including the variation of materials properties with temperature even if they are non-linear;

(ii) to be able to formulate the time dependence of the problem with explicit and implicit components, increasing the stability of the solution particularly in the high temperature region of the fuel;

(iii) the possibility of a simple treatment of cracks, the strain contribution from these being calculated explicitly;

(iv) the possibility of extending the calculation to include the interaction between any two regions using one overall calculation for all the regions;

(v) the possibility of straightforward adaptation to computer programming.

This is not, of course, to say that for example finite element method does not have the above possibilities, rather from an integral computer code point of view the finite difference scheme adopted here provides the best overall accuracy and economy in terms of computation. The general rules of the method are as follows.

The fuel pin is divided into a total number of N rings; see Fig.3.7. The variables are defined on these mesh in space and the difference equations are solved by relating

quantities at time j to the appropriate known quantities at time j-1; similar to what was done for the temperature calculation. The temperature T^j is calculated prior to the mechanical analysis. The various equations are replaced by difference equations using only first order differences in space and time. The spatial and temporal variations will be described separately. The derivative of a function f at the ring radius r_i is given by:

$$\left.\frac{\partial f}{\partial r}\right|_{r=r_i} = \frac{f_{i+1} - f_i}{r_{i+1} - r_i} \tag{3.112}$$

where f_i is the value of f at r_i. In the expression (3.112) it is not assumed that the rings are equally spaced. In order to integrate the system of equations in the time variable, the time dependence is also expressed in finite differences. Given an increment of Δt, the change in a variable V is:

$$\Delta V = V(t) - V(t - \Delta t) \tag{3.113}$$

In the case of creep and swelling, Eqs.(3.98)-(3.100), we expand the variation in a Taylor's series which we limit to the first order:

$$V = \langle \dot{V} \rangle \Delta t \tag{3.114}$$

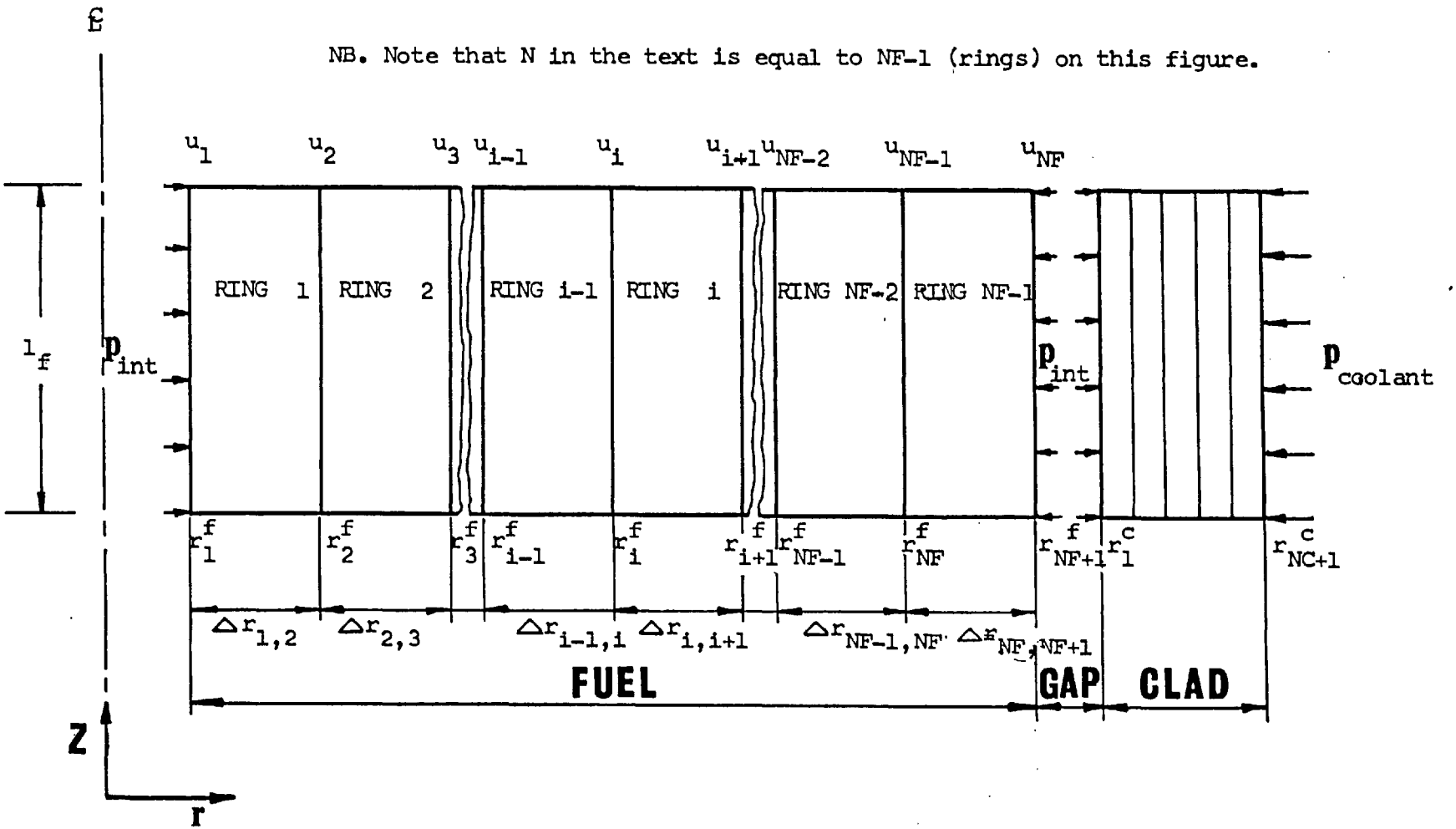
In order to assure convergence, the value of $\langle \dot{V} \rangle$ is taken to be some average between the value at the start and end of the time increment:

$$\langle \dot{V} \rangle = \theta . \dot{V}(t) + (1 - \theta) . \dot{V}(t - \Delta t) \tag{3.115}$$

where θ is a parameter fixed between 0 to 1, as described in the section about the thermal analysis Eq.(3.8).

Figure 3.7

RADIAL NODES USED FOR MECHANICAL ANALYSIS



3.4.3 The System of Equations in Finite Differences

Using the approximations in Sub- ection 3.4.2, one may express the differential equations in (3.111) in finite differences for the i^{th} ring (i = 1,N):

(a) The creep equation

Eq .(3.98) can be written in its finite difference form; see Eqs.(3.113)-(3.115)

$$\frac{\gamma_{r,i}^{j} - \gamma_{r,i}^{j-1}}{\Delta t} = \theta\{P_r^j + F_r(\sigma_r^j,\sigma_\theta^j,\sigma_z^j)\} + (1 - \theta)\{P_1^{j-1} + F_r(\sigma_r^{j-1},\sigma_\theta^{j-1},\sigma_z^{j-1})\} \tag{3.116}$$

$$\frac{\gamma_{\theta,i}^{j} - \gamma_{\theta,i}^{i-1}}{\Delta t} = \theta\{P_\theta^j + F_\theta(\sigma_r^j,\sigma_\theta^j,\sigma_z^j)\} + (1 - \theta)\{P_\theta^{j-1} + F_\theta(\sigma_r^{j-1},\sigma_\theta^{j-1},\sigma_z^{j-1})\} \tag{3.117}$$

$$\frac{\gamma_{z,i}^{j} - \gamma_{z,i}^{j-1}}{\Delta t} = \theta\{P_z^j + F_z(\sigma_r^j,\sigma_\theta^j,\sigma_z^j)\} + (1 - \theta)\{P_z^{j-1} + F_z(\sigma_r^{j-1},\sigma_\theta^{j-1},\sigma_z^{j-1}) \tag{3.118}$$

The quantities with superscript j-1 are at time t-Δt and therefore known.

Eqs.(3.116)-(3.118) will in general be of known, but non-linear form. A linearised version can be obtained by expanding the creep rate F_p (p $\equiv$ r,θ,z) in a Taylor series about the point $(\sigma_r^{j-1},\sigma_\theta^{j-1},\sigma_z^{j-1})$ and truncating it at the first order term,

$$F_p(\sigma_r^j,\sigma_\theta^j,\sigma_z^j) = F_p(\sigma_r^{j-1},\sigma_\theta^{j-1},\sigma_z^{j-1}) + (\sigma_r^j - \sigma_r^{j-1})\left(\frac{\partial F_p}{\partial \sigma_r}\right)_{\sigma_r=\sigma_r^{j-1}}$$

$$+ (\sigma_\theta^j - \sigma_\theta^{j-1})\left(\frac{\partial F_p}{\partial \sigma_\theta}\right)_{\sigma_\theta=\sigma_\theta^{j-1}} \qquad (3.119)$$

$$+ (\sigma_z^j - \sigma_z^{j-1})\left(\frac{\partial F_p}{\partial \sigma_z}\right)_{\sigma_z=\sigma_z^{j-1}}$$

There are nine partial derivatives in the form of $(\partial F_p/\partial \sigma_p)$ in (3.119) which can be determined through the definition of F_p, Eq.(3.100), and substituted into the above equation (see Appendix B). Then the substitution of Eq.(3.119) into Eqs.(3.117)-(3.118) gives rise to a linear expression

$$\gamma_p^j = \Bigg\{ \gamma_p^{j-1} + \Delta t(\theta\, P_p^j + (1-\theta)P_p^{j-1}) + \Delta t\Big(\theta\, F_p(\sigma_r^j,\sigma_\theta^j,\sigma_z^j) + (1-\theta)\, F_p(\sigma_r^{j-1},\sigma_\theta^{j-1},\sigma_z^{j-1})\Big)$$

$$- \theta\cdot\Delta t\left(\left(\frac{\partial F_p}{\partial \sigma_r}\right)_{\sigma_r=\sigma_r^{j-1}}\cdot\sigma_r^{j-1} + \left(\frac{\partial F_p}{\partial \sigma_\theta}\right)_{\sigma_\theta=\sigma_\theta^{j-1}}\cdot\sigma_\theta^{j-1} + \left(\frac{\partial F_p}{\partial \sigma_z}\right)_{\sigma_z=\sigma_z^{j-1}}\cdot\sigma_z^{j-1}\right)\Bigg\}$$

$$+ \theta\cdot\Delta t\left(\frac{\partial F_p}{\partial \sigma_r}\right)_{\sigma_r=\sigma_r^{j-1}}\cdot\sigma_r^j + \theta\cdot\Delta t\left(\frac{\partial F_p}{\partial \sigma_\theta}\right)_{\sigma_\theta=\sigma_\theta^{j-1}}\cdot\sigma_\theta^j$$

$$+ \theta\cdot\Delta t\left(\frac{\partial F_p}{\partial \sigma_r}\right)_{\sigma_z=\sigma_z^{j-1}}\cdot\sigma_z^j \qquad (3.120)$$

or in general

$$\gamma^j_{p,i} = Q_{p,i} + P^{(p)}_{r,i} \cdot \sigma^j_{r,i} + P^{(p)}_{\theta,i} \cdot \sigma^j_{\theta,i} + P^{(p)}_{z,i} \cdot \sigma^j_{z,i}$$

$$p \equiv r,\theta,z \qquad (3.121)$$

where

$Q_{p,i} \equiv$ the terms in { } on the RHS of (3.120),

$P^{(p)}_{p,i} \equiv$ the coefficients of σ^j_p in (3.120)

$i = 1,N$ (P not to be confused with P for swelling)

To completely determine the divisions between the swelling, P, and the creep rate F it is assumed that creep introduces no volume change

$$\sum_p F_p = 0 \qquad (3.122)$$

Using (3.122) introduces a restraint on the sum of the three equations (3.116)-(3.118). They can be added to obtain

$$\gamma^j_r + \gamma^j_\theta + \gamma^j_z - \sum_p \gamma^{j-1}_p = \theta.\Delta t(\sum_p P^j_p + \sum F^j_p) + (1 - \theta).\Delta t(\sum_p P^{j-1}_p + \sum_p F^{j-1}_p)$$

thus

$$\gamma^j_z = \theta.\Delta t \sum_p P^j_p + (1 - \theta)\Delta t \sum_p P^{j-1}_p - \gamma^j_r - \gamma^j_\theta + \sum_p \gamma^{j-1}_p \qquad (3.123)$$

Since swelling was assumed to be isotropic

$$\sum_p P^j_p = 3P^j$$

$$\sum_p P^{j-1}_p = 3\,P^{j-1} \text{ (assuming } P_r = P_\theta = P_z = P).$$

By substitution into (3.123)

$$\gamma^j_{z,i} = 3\Delta t\{\theta\, P^j_i + (1-\theta)P^{j-1}_i\} - \gamma^j_{r,i} - \gamma^j_{\theta,i} + \sum_p \gamma^{j-1}_{p,i} \tag{3.124}$$

The Eq.(3.121) for γ_z is accordingly dropped and this equation is used in the reduction to three unknowns at any ring i.

(b) The radial stress equilibrium equation

Eq.(3.101) is written in difference form as

$$\sigma^j_{r,i+1} = \sigma^j_{r,i} + \left(\frac{r_{i+1} - r_i}{r_i}\right)(\sigma^j_{\theta,i} - \sigma^j_{r,i}) \tag{3.125}$$

(c) The axial loading condition

In order to obtain the difference form of Eq.(3.104) we use the trapezoidal rule for integration:

$$\sigma^j_{z,1}(r_2 - r_1)r_1/2 + \sum_{i=2}^{N-1} \sigma^j_{z,i}(r_{i+1} - r_{i-1})r_i/2 + \sigma^j_{z,N}(r_N - r_{N-1})r_{N/2} = -F_z/2\pi \tag{3.126}$$

(d) Relation between total strain and displacement

Eq.(3.108) becomes

$$u^j_{i+1} = u^j_i + (r_{i+1} - r_i).(e^j_{r,i} + \gamma^j_{r,i}) \tag{3.127}$$

and Eqs.(3.109)-(3.110)

$$u^j_i = r_i(e^j_{\theta,i} + \gamma^j_{\theta,i}) \tag{3.128}$$

$$z^j = e^j_{z,i} + \gamma^j_{z,i} \tag{3.129}$$

In all the equations written in difference form so far the value of r_i is variable with time; so r_i is the value of ring radius at time j.

(e) Method of solution

The system of equations in (3.111) is now completely defined and is solved by the following method. The composite strains $e^j_{p,i}$ are obtained from (3.127) to (3.129):

$$e^j_{r,i} = \frac{u^j_{i+1} - u^j_i}{r_{i+1} - r_i} - \gamma^j_{r,i}$$

$$e^j_{\theta,i} = \frac{u^j_i}{r_i} - \gamma^j_{\theta,i}$$

$$e^j_{z,i} = Z^j - \gamma^j_{z,i} = Z^j - 3\Delta t[\theta . p^j_i + (1-\theta) . p^{j-1}_i] - \gamma^j_{r,i} - \gamma^j_{\theta,i} + \sum_p \gamma^{j-1}_{p,i}$$

These are now substituted into the first three equations of (3.111) to obtain stresses in terms of u, γ_r, γ_θ and Z:

$$\sigma^j_{r,i} = a_{1,j}\, u^j_{i+1} + a_{2,i}\, u^j_i + a_{3,i}\gamma^j_{r,i} + a_{4,i}\gamma^j_{\theta,i} + a_{5,i}\, Z^j + a_{6,i}$$

$$\sigma^j_{\theta,i} = a_{7,i}\, u^i_{i+1} + a_{8,i}\, u^j_i + a_{9,i}\gamma^j_{r,i} + a_{10,i}\gamma^j_{\theta,i} + a_{11,i}\, Z^j + a_{12,i}$$

$$\sigma^j_{z,i} = a_{13,i}\, u^j_{i+1} + a_{14,i}\, u^j_i + a_{15,i}\gamma^j_{r,i} + a_{16,i}\gamma^j_{\theta,i} + a_{17,i}\, Z^j + a_{18,i} \qquad (3.130)$$

Where the coefficients a_k, k = 1,18 are defined as below

$$a_{1,i} = \frac{2\, G_i}{r_{i+1} - r_i} \cdot \frac{1 - \nu_i}{1 - 2\nu_i}$$

$$a_{2,i} = \frac{2\, G_i}{1 - 2\nu_i} \left(\frac{\nu_i}{r_i} - \frac{1 - \nu_i}{r_{i+1} - r_i} \right)$$

$$a_{3,i} = -\, 2\, G_i$$

$$a_{4,i} = 0 \qquad (3.131)$$

$$a_{6,i} = -\frac{2\,G_i}{1-2\nu_i}\{\nu_i[3\Delta t(\theta\,P_i^j + (1-\theta)P_i^{j-1}) + \sum_p \gamma_p^{j-1}] + \alpha_i(1+\nu_i)T_i^j\} \quad \text{(3.131 cont.)}$$

$$a_{7,i} = \frac{2\,G_i\,\nu_i}{(1-2\nu_i)(r_{i+1}-r_i)}$$

$$a_{8,i} = \frac{2\,G_i}{1-2\nu_i}\left(\frac{1-\nu_i}{r_i} - \frac{\nu_i}{r_{i+1}-r_i}\right)$$

$$a_{9,i} = 0$$

$$a_{10,i} = -2\,G_i$$

$$a_{11,i} = \frac{2\nu_i\,G_i}{1-2\nu_i}$$

$$a_{12,i} = -\frac{2\,G_i}{1-2\nu_i}\{\nu_i[3\Delta t(\theta.P_i^j + (1-\theta)P_i^{j-1}) + \sum_p \gamma_p^{j-1}] + \nu_i(1+\nu_i)T_i^j\}$$

$$a_{13,i} = \frac{2\,G_i\,\nu_i}{(1-2\nu_i)(r_{i+1}-r_i)}$$

$$a_{14,i} = \frac{2\,G_i\,\nu_i}{1-2\nu_i}\left(\frac{1}{r_i} - \frac{1}{r_{i+1}-r_i}\right)$$

$$a_{15,i} = 2\,G_i$$

$$a_{16,i} = 2\,G_i$$

$$a_{17,i} = \frac{2\,G_i(1-\nu_i)}{1-2\,\nu_i}$$

$$a_{18,i} = -\frac{2\,G_i}{1-2\nu_i}\{(1-\nu_i)[3\Delta t(\theta.P_i^j + (1-\theta)P_i^{j-1}) + \sum_p \gamma_p^{j-1}] + \alpha_i\,(1+\nu_i)T_i^j\} \quad (3.131)$$

The substitution of stresses from (3.130) into the first two equations of (3.121) gives rise to two linear equations;

$$A^{(r)}_{1,i}.u^j_{i+1} + A^{(r)}_{2,i}.u^j_i + A^{(r)}_{3,i}.\gamma^j_{r,i} + A^{(r)}_{4,i}.\gamma^j_{\theta,i} + A^{(r)}_{5,i}.z^j + A^{(r)}_{6,i} = 0$$

$$A^{(\theta)}_{1,i}.u^i_{i+1} + A^{(\theta)}_{2,k}.u^j_i + A^{(\theta)}_{3,i}.\gamma^j_{r,i} + A^{(\theta)}_{4,i}.\gamma^j_{\theta,i} + A^{(\theta)}_{5,i}.z^j + A^{(\theta)}_{6,i} = 0 \qquad (3.132)$$

where

$$A^{(p)}_{1,i} = a_{1,i}.P^{(p)}_{r,i} + a_{7,i}.P^{(p)}_{\theta,i} + a_{13,i}.P^{(p)}_{z,i}$$

$$A^{(p)}_{2,i} = a_{2,i}.P^{(p)}_{r,i} + a_{8,i}.P^{(p)}_{\theta,i} + a_{14,i}.P^{(p)}_{z,i}$$

$$A^{(p)}_{3,i} = a_{3,i}.P^{(p)}_{r,i} + a_{9,i}.P^{(p)}_{\theta,i} + a_{15,i}.P^{(p)}_{z,i} - 1$$

$$A^{(p)}_{4,i} = a_{4,i}.P^{(p)}_{r,i} + a_{10,i}.P^{(p)}_{\theta,i} + a_{16,i}.P^{(p)}_{z,i}$$

$$A^{(p)}_{5,i} = a_{5,i}.P^{(p)}_{r,i} + a_{11,i}.P^{(p)}_{\theta,i} + a_{17,i}.P^{(p)}_{z,i}$$

$$A^{(p)}_{6,i} = a_{6,i}.P^{(p)}_{r,i} + a_{12,i}.P^{(p)}_{\theta,i} + a_{18,i}.P^{(p)}_{z,i} + Q_{p,i}$$

$$p \equiv r,\theta \qquad (3.133)$$

Using radial equilibrium Eq.(3.125) and Eqs.(3.130) a third equation is obtained but with a term in u^j_{i+2}. This term is only non-existent for the last 2 nodes, N-1 and N, and can be eliminated by using the first euqation in (3.132) written for the next mesh point:

$$B_{1,i}.u^j_{i+2} + B_{2,i}.u^j_{i+1} + B_{3,i}.u^j_i + B_{4,i}.\gamma^j_{r,i+1}$$

$$+ B_{5,i}.\gamma^j_{r,i} + B_{6,i}.\gamma^j_{\theta,i+1} + B_{7,i}.\gamma^j_{\theta,i} + B_{8,i}.Z^i + B_{9,i} = 0$$

(3.134)

where

$$B_{1,i} = a_{1,i+1}$$
$$B_{2,i} = a_{2,i+1} - a_{1,i} - \frac{r_{i+1} - r_i}{r_i}(a_{7,i} - a_{1,i})$$
$$B_{3,i} = -a_{2,i} + \frac{r_{i+1} - r_i}{r_i}(-a_{8,i} - a_{2,i})$$
$$B_{4,i} = a_{3,i+1}$$
$$B_{5,i} = -a_{3,i} - \frac{r_{i+1} - r_i}{r_i}(a_{9,i} - a_{3,i})$$
$$B_{6,i} = a_{4,i+1}$$
$$B_{7,i} = -a_{4,i} - \frac{r_{i+1} - r_i}{r_i}(a_{10,i} - a_{4,i})$$
$$B_{8,i} = a_{5,i+1} - a_{5,i} - \frac{r_{i+1} - r_i}{r_i}(a_{11,i} - a_{5,i})$$
$$B_{9,i} = a_{6,i+1} - a_{6,i} - \frac{r_{i+1} - r_i}{r_i}(a_{12,i} - a_{6,i})$$

(3.135)

The two Eqs.(3.132) together with (3.134) provide 3N equations when i is varied from 1 to N. But there are 3N+1 unknowns (3N for γ_r, γ_θ and u and one single Z). The final equation is found by substituting σ_z from (3.130) into the axial equilibrium Eq.(3.126); we have

$$\sum_{i=1}^{N} (F_{1,i}.u^j_i + F_{2,i}.\gamma^j_{r,i} + F_{3,i}.\gamma^j_{\theta,i}) + D.Z^j = E \quad (3.136)$$

where

$$\sum_i F_{1,i}\, u_i^j = r_1(r_2 - r_1)a_{14,1}\, u_1^j + r_1(r_2 - r_1)a_{13,1}\, u_2^j$$
$$+ \sum_{i=2}^{N-1} r_i(r_{i+1} - r_{i-1})a_{14,i}\, u_i^j$$
$$+ \sum_{i=2}^{N-1} r_i(r_{i+1} - r_{i-1})a_{13,i}\, u_{i+1}^j$$
$$+ r_N(r_N - r_{N-1})a_{14,N} u_N^j + r_N(r_N - r_{N-1})a_{13,N}\, u_{N+1}^j$$

$$\sum_i F_{2,i}\, \gamma_{r,i} = - r_1(r_2 - r_1)a_{15,1}\gamma_{r,1}^j - \sum_{i=2}^{N-1} r_i(r_{i+1} - r_{i-1})a_{15,i}\gamma_{r,i}^j$$
$$- r_N(r_N - r_{N-1})a_{15,N}\, \gamma_{r,N}^j$$

$$\sum_i F_{3,i}\gamma_{\theta,i}^j = r_1(r_2 - r_1)a_{16,1}\gamma_{\theta,1}^j + \sum_{i=2}^{N-1} r_i(r_{i+1} - r_{i-1})a_{16,i}\gamma_{\theta,i}^j$$
$$+ r_N(r_N - r_{N-1})a_{16,N}\, \gamma_{\theta,N}^j$$

$$D = r_1(r_2 - r_1)a_{17,1} + \sum_{i=2}^{N-1} r_i(r_{i+1} - r_{i-1})a_{17,i}$$
$$+ r_N(r_N - r_{N-1})a_{17,N}$$

$$E = - F_z/\pi - r_1(r_2 - r_1)a_{18,1} - \sum_{i=2}^{N-2} r_i(r_{i+1} - r_{i-1})a_{18,i}$$
$$- r_N(r_N - r_{N-1})a_{18,1} \qquad (3.137)$$

The application of Eqs.(3.132) and (3.134) to nodes 1 to N-1 provides 3N-3 equations. But for the N^{th} node we have to use other equations since $\gamma_{r,N+1}^j$, $\gamma_{\theta,N+1}^j$ and u_{N+1}^j are outside the physical boundary of the system. The boundary condition (3.102) is used instead:

$$\sigma^{j}_{r,N} = - P_w \text{ (the coolant pressure)} \tag{3.138}$$

Combining this equation with the first equation of (3.130) for node N we have

$$u^{j}_{N+1} = \frac{- P_w}{a_{1,N}} - \frac{a_{2,N}\, u^{j}_{N}}{a_{1,N}} - \frac{a_{3,N}\, \gamma^{j}_{r,N}}{a_{1,N}} - \frac{a_{4,N}\, \gamma^{j}_{\theta,N}}{a_{1,N}} - \frac{a_{5,N}\, z^{j}}{a_{1,N}} - \frac{a_{6,N}}{a_{1,N}}$$

This can now be substituted into (3.132) for i = N,

$$\left(A^{(r)}_{2,N} - \frac{A^{(r)}_{1,N}\, a_{2,N}}{a_{1,N}}\right) u^{j}_{N} + \left(A^{(r)}_{3,N} - \frac{A^{(r)}_{1,N}\, a_{3,N}}{a_{1,N}}\right) \gamma^{j}_{r,N}$$

$$+ \left(A^{(r)}_{4,N} - \frac{A^{(r)}_{1,N}\, a_{4,N}}{a_{1,N}}\right) \gamma^{j}_{\theta,N} + \left(A^{(r)}_{5,N} - \frac{A^{(r)}_{1,N}\, a_{5,N}}{a_{1,N}}\right) z^{j}$$

$$+ A^{(r)}_{6,N} - \frac{A^{(r)}_{1,N}}{a_{1,N}} (P_w + a_{6,N}) = 0 \tag{3.139}$$

A similar equation can be obtained in the θ direction for node N:

$$+ \left(A^{(\theta)}_{2,N} - \frac{A^{(\theta)}_{1,N}\, a_{2,N}}{a_{1,N}}\right) u^{j}_{N} + \left(A^{(\theta)}_{3,N} - \frac{A^{(\theta)}_{1,N}\, a_{3,N}}{a_{1,N}}\right) \gamma^{j}_{r,N}$$

$$+ \left(A^{(\theta)}_{4,N} - \frac{A^{(\theta)}_{1,N}\, a_{4,N}}{a_{1,N}}\right) \gamma^{j}_{\theta,N} + \left(A^{(\theta)}_{5,N} - \frac{A^{(\theta)}_{1,N}\, a_{5,N}}{a_{1,N}}\right) z^{j}$$

$$A^{(\theta)}_{6,N} - \frac{A^{(\theta)}_{1,N}}{a_{1,N}} (P_w + a_{6,N}) = 0 \tag{3.140}$$

These two equations plus Eq.(3.136) and the 3N-3 equations obtained earlier make a total of 3N equations. The last single equation to complete the system (3N+1 unknowns, 3N+1 equations) comes from the boundary condition at fuel centre Eq .(3.103).

If the central hole is open, then

$$\sigma^j_{r,1} = - P_F \text{ (the pin internal pressure)}$$

This combined with (3.130) gives

$$a_{1,1}\, u^j_2 + a_{2,1}\, u^j_1 + a_{3,1}\, \gamma^j_{r,1} + a_{4,1}\, \gamma^j_{\theta,1} + a_{5,1}\, z^j + a_{6,1} + P_F = 0 \qquad (3.141)$$

If the central hole approaches zero during the calculation, a small radius is defined in the following manner

$$r^j_1 + u^j_1 = 10^{-7} \qquad (3.142)$$

In the case of a solid pellet the condition (3.103a) is used which gives

$$\sigma_{r,1} = \sigma_{\theta,1}$$

Or from (3.130)

$$(a_{1,1} - a_{7,1})\, u^j_2 + (a_{2,1} - a_{8,1})\, u^j_1 + (a_{3,1} - a_{9,1})\gamma^j_{r,1} + (a_{4,1} - a_{10,1})\gamma^j_{\theta,1} + (a_{5,1} - a_{11,1})z^j + a_{6,1} - a_{12,1} = 0 \qquad (3.143)$$

Thus according to the conditions one of the Eqs.(3.141), (3.142) or (3.143) is used for node 1. We will then have a complete set of equations for solving all the unknowns. These equations are written in a matrix form as shown in the following page. This matrix equation is solved in SAMURA by a method of pivotal condensation which chooses the pivots in an economical way.

$$
\begin{bmatrix}
a_{2,1} & a_{3,1} & a_{4,1} & a_{1,1} & & & & & & & & a_{5,1} \\
A^{(r)}_{2,1} & A^{(r)}_{3,1} & A^{(r)}_{4,1} & A^{(r)}_{1,1} & & & & & & & & A^{(r)}_{5,1} \\
A^{(\theta)}_{2,1} & A^{(\theta)}_{3,1} & A^{(\theta)}_{4,1} & A^{(\theta)}_{1,1} & & & & & & & & A^{(\theta)}_{5,1} \\
B_{2,1} & B_{4,1} & B_{6,1} & B_{1,1} & B_{3,1} & B_{S,1} & & & & & & B_{7,1} \\
 & & & A^{(r)}_{2,2} & A^{(r)}_{3,2} & A^{(r)}_{4,2} & A^{(r)}_{1,2} & & & & & A^{(r)}_{5,2} \\
 & & & A^{(\theta)}_{2,2} & A^{(\theta)}_{3,2} & A^{(\theta)}_{4,2} & A^{(\theta)}_{1,2} & & & & & A^{(\theta)}_{5,2} \\
 & & & B_{2,2} & B_{4,2} & B_{6,2} & B_{1,2} & B_{3,2} & B_{5,2} & & & B_{7,2} \\
 & & & & & & & & & & & \\
 & & & & & & A_{2,N-1} & A_{3,N-1} & A_{4,N-1} & A_{1,N-1} & O & O & A^{(r)}_{5,N-1} \\
 & & & & & & A_{2,N-1} & A_{3,N-1} & A_{4,N-1} & A_{1,N-1} & O & O & A^{(\theta)}_{5,N-1} \\
 & & & & & & B_{2,N-1} & B_{4,N-1} & B_{6,N-1} & B_{1,N-1} & B_{3,N-1} & B_{5,N-1} & B_{7,N-1} \\
 & & & & & & O & O & O & C^{(r)}_1 & C^{(r)}_2 & A^{(r)}_{4,N} & C^{(r)}_3 \\
 & & & & & & O & O & O & C^{(\theta)}_1 & C^{(\theta)}_2 & A^{(\theta)}_{4,N} & C^{(\theta)}_3 \\
F_{1,1} & F_{2,1} & F_{3,1} & F_{1,2} & F_{2,2} & \cdots & F_{1,N-1} & F_{2,N-1} & F_{3,N-1} & F_{1,N} & F_{2,N} & F_{3,N} & D
\end{bmatrix}
\begin{Bmatrix}
u_1 \\ \gamma_{r,1} \\ \gamma_{\theta,1} \\ u_2 \\ \gamma_{r,2} \\ \gamma_{\theta,2} \\ u_3 \\ \\ \gamma_{r,N-1} \\ \gamma_{\theta,N-1} \\ u_N \\ \gamma_{r,N} \\ \gamma_{\theta,N} \\ Z
\end{Bmatrix}
=
\begin{Bmatrix}
a_{6,1} - P_F \\ -A^{(r)}_{6,1} \\ -A^{(\theta)}_{6,1} \\ -B_{8,1} \\ -A^{(r)}_{6,2} \\ -A^{(\theta)}_{6,2} \\ B_{8,2} \\ \\ -A^{(r)}_{6,N-1} \\ -A^{(\theta)}_{6,N-1} \\ -B_{8,N-1} \\ C^{(r)}_4 \\ C^{(\theta)}_5 \\ E
\end{Bmatrix}
$$

Matrix Equation (3.144)

where $C^{(p)}_j$, $P \equiv r,\theta$, $j = 1,4$ are the coefficients of Eqs. (3.139) and (3.140)

(f) Application to multi-region problems

The system of equations thus obtained can be easily adapted to suit a multi-region boundary with different material properties. The gap between such regions may be open or closed. In order to represent this gap as one of the node points, a spurious radial point is introduced which lies between the end of one region and the beginning of the next. Since this node must possess similar number of equations as other nodes (so that the form of the matrix in (3.144) does not change) three variables are specified at this spurious point; u_s^j, $\sigma_{r,s}^i$ and a third which is not used. The radial displacement u_s^j at the spurious point s is an extension of u outside the region. The stress $\sigma_{r,s}^j$ is the radial stress at the boundary, and this must be continuous across the gap between the regions. In order to describe the two boundaries on either side of the spurious point the subscripts s-1 and s+1 are used. The Eqn.(3.134) for the node s-1 refers to the values u_s^j, $^j_{r,s}$ and $\gamma_{\theta,s}^j$ (if i=s-1 then i+1=s) where only u_s^j is used. Eq .(3.134) is, therefore, replaced by Eq .(3.130) for σ_r:

$$\sigma_{r,s}^j = a_{1,s-1}\, u_s^j + a_{2,s-1}\, u_{s-1}^j + a_{3,s-1}\, \gamma_{r,s-1}^j + a_{4,s-1}\, \gamma_{\theta,s-1}^j + a_{5,s-1}\, z_1^j + a_{6,s-1} \qquad (3.145)$$

where in z_1^j the subscript 1 refers to region 1. Eq .(3.145) may be taken as the definition of u_s^j. The value of $\sigma_{r,s}^j$ is determined from node s+1:

$$\sigma_{r,s}^j = a_{1,s+1}\, u_{s+2}^j + a_{2,s+1}\, u_{s+1}^j + a_{3,s+1}\, \gamma_{r,s+1}^j + a_{4,s+1}\, \gamma_{\theta,s+1}^j + a_{5,s+1}\, z_2^j + a_{6,s+1} \qquad (3.146)$$

where z_2^j here is the axial strain in region 2.

The one further equation required to define the boundary differs according to whether the gap is open or closed.

For an open gap,

$$\sigma^j_{r,s} = - P_F \text{ (the gap pressure)} \tag{3.147}$$

and for a closed gap,

$$u^j_{s+1} = u^j_{s-1} \tag{3.148}$$

In the actual programming of SAMURA since $\gamma^j_{r,s}$ or $\gamma^j_{\theta,s}$ are not used, $\gamma^j_{r,s}$ is used to represent the value of gap pressure $\sigma^j_{r,s}$. At the same time appropriate modifications are made in Eqs.(3.132) and (3.134) when applied to nodes s-1 and s+1 to correctly model the closing or opening of the gap.

Another connection between the regions is through the axial strain. When a gap between the regions is open, we have different constant values Z^j_k (k = 1, number of regions). The axial loading equation also applies to each region separately. On the other hand, when the gap between the two regions closes during a calculation the values of Z^j_k for every region cannot vary independently. In one extreme, they must be equal if very high frictional forces develop between the contact surfaces of the two regions. In the other, they may be unequal provided the total length changes in the regions remain equal or have a constant ratio until the gap re-opens. The second condition is used in SAMURA plus the assumption that no axial slipping occurs while the gap is closed. Thus we have

$$\frac{1 + Z^j_k}{1 + Z^j_{k+1}} = \text{constant} \tag{3.149}$$

where z_k^j and z_{k+1}^j are the respective axial strains of regions k and k+1.

3.4.4 Treatment of Fuel Cracking

In SAMURA it is supposed that when the circumferential stress, σ_θ, or the axial stress, σ_z, in any given ring exceeds the fracture stress of the material, σ_F, this ring is cracked radially or axially in the sense discussed in Sub-Section 3.4.1(e). The corresponding principle stress in the ring is considered to reduce to a constant lower than that assigned to the unknown in the system of equations. The new unknown is treated as the resulting crack width η_p of the cracks in the direction p. At the moment of the crack opening, the residual stress in the ring, the other principle stresses, the creep and swelling in the ring plus the state of stress and in the rest of the pellet may lead to an increase or decrease in the strain of the given ring. In the case where we meet open cracks the combined system in a given time interval determines the variation of the principle stress in the rings and the directions in which there is no cracking and the variation in crack width in those rings where cracking is encountered.

In order to keep the form of the matrix (3.144) and not to introduce any new unknowns Eqs.(3.77-3.79) are re-written using new definitions for the composite strains e_p from (3.65-3.67) as

$$E_p = e_p + \eta_p \quad , \quad p \equiv r,\theta,z \tag{3.150}$$

This leaves unchanged all the equations, except the Hooke's Law expressions (3.77-3.79), with e_p replaced by Ep

everywhere. Eqs. (3.77 - 3.79) become

$$\frac{\sigma_p}{2G} = E_p + \frac{\nu(E_r + E_\theta + E_z)}{1 - 2\nu} - \frac{1 + \nu}{1 - 2\nu}\alpha_p T$$

$$- \eta_p - \frac{\nu}{1 - 2\nu}(\eta_r + \eta_\theta + \eta_z) \qquad (3.151)$$

The cracking strain in r direction is assumed to be zero at all times thus we are left with only two unknowns η_θ and η_z. However, as stated earlier a residual stress, σ_p^R, must be assigned in the cracked direction and since σ_p^R has a known value (at least equal to the internal gas pressure) the number of unknowns remains unchanged. As an example, Eqs .(3.130) for fuel cracked in θ direction become

$$\sigma_{r,i}^j = a_{1,i}\, u_{i+1}^j + a_{2,i}\, u_i^j + a_{3,i}\gamma_{r,i}^j + a_{4,i}\gamma_{\theta,i}^j$$

$$+ a_{5,i} z^j + a_{6,i} - \frac{2\nu_i G_i}{1 - 2\nu_i}\eta_{\theta,i}^j$$

$$\sigma_{\theta,i}^j = \sigma_\theta^R = a_{7,i}\, u_{i+1}^j + a_{8,i}\, u_i^j + a_{9,i}\gamma_{r,i}^j + a_{10,i}\gamma_{\theta,i}^j$$

$$+ a_{11,i}\, z^j + a_{12,i} - 2G_i\eta_\theta^j - \frac{2\nu_i G_i}{1 - 2\nu_i}\eta_{\theta,i}^j$$

$$\sigma_{z,i}^j = a_{13,i}\, u_{i+1}^j + a_{14,i}\, u_i^j + a_{15,i}\gamma_{r,i}^j + a_{16,i}\gamma_{\theta,i}^j$$

$$+ a_{17,i}\, z^j + a_{18,i} - \frac{2\nu_i G_i}{1 - 2\nu_i}\eta_{\theta,i}^j$$

$\eta_{\theta,i}$ can be calculated from the second equation and substituted into the other two equations to obtain $\sigma_{r,i}$ and $\sigma_{z,i}$:

$$\sigma^j_{r,i} = (a_{1,i} - \frac{\nu_i}{1-\nu_i} a_{7,i}) u^j_{i+1} + (a_{2,i} - \frac{\nu_i}{1-\nu_i} a_{8,i})\ u^j_i$$

$$+ (a_{3,i} - \frac{\nu_i}{1-\nu_i}) \gamma^j_{r,i} + (a_{4,i} - \frac{\nu_i}{1-\nu_i} a_{10,i}) \gamma^j_{\theta,i}$$

$$+ (a_{5,i} - \frac{\nu_i}{1-\nu_i} a_{11,i}) z^j + a_{6,i} - \frac{\nu_i}{1-\nu_i} a_{12,i}$$

$$+ \frac{\nu_i}{1-\nu_i}\ \sigma^R_\theta \qquad (3.152)$$

$$\sigma^j_{z,i} = (a_{13,i} - \frac{\nu_i}{1-\nu_i} a_{7,i}) u^j_{i+1} + (a_{14,i} - \frac{\nu_i}{1-\nu_i} a_{8,i}) u^j_i$$

$$+ (a_{15,i} - \frac{\nu_i}{1-\nu_i} a_{9,i}) \gamma^j_{r,i} + (a_{16,i} - \frac{\nu_i}{1-\nu_i} a_{10,i}) \gamma^j_{\theta,i}$$

$$+ (a_{17,i} - \frac{\nu_i}{1-\nu_i} a_{11,i}) z^j + a_{18,i} - \frac{\nu_i}{1-\nu_i} a_{12,i}$$

$$+ \frac{\nu_i}{1-\nu_i}\ \sigma^R_\theta \qquad (3.153)$$

These equations compared with the Eqs (3.130) show that after cracking in θ direction only a repeat of the calculations with $a_{k,i}$, k = 1,18 and i = 1,N, see (3.131), corrected in the following form will suffice to adjust the other principle stresses:

$$\begin{cases} \text{New } a_{k,i} = a_{k,i} - \dfrac{\nu_i}{1-\nu_i} a_{k+6,i} & \text{for } k = 1,6 \\ \text{New } a_{k,i} = 0 \quad \text{for } k = 7,11 \quad \text{and} \quad a_{12,i} = \sigma^R_\theta & \\ \text{New } a_{k,i} = a_{k,i} - \dfrac{\nu_i}{1-\nu_i} a_{k-6,i} & \text{for } k = 13,18 \end{cases} \qquad (3.154)$$

(Note that a further correction is made to $a_{6,i}$ and $a_{18,i}$ by adding to them the term $\nu_i \sigma^R_\theta/(1-\nu_i)$, see Eqs.(3.152-3.153). Similar corrections are made when the calculation shows there

is a cracking in z direction or both θ and z directions. In the latter case only $\sigma_{r,i}$ exists and the other two stresses are equal to σ_θ^R and σ_z^R, respectively. The corrections are:

$$\begin{cases} \text{New } a_{k,i} = a_{k,i} - \nu_i\, a_{k+6,i} - \nu_i\, a_{k+12,i}, \text{ for } k = 1,5 \\ \text{New } a_{6,i} = a_{6,i} - \nu_i\, a_{12,i} - \nu_i\, a_{18,i} + \nu_i\, \sigma_\theta^R + \nu_i \sigma_z^R \\ \text{New } a_{k,i} = 0 \quad \text{for } \begin{cases} k = 7,11 \\ k = 13,17 \end{cases} \quad \text{and} \quad \begin{cases} a_{12,i} = \sigma_\theta^R \\ a_{18,i} = \sigma_z^R \end{cases} \end{cases} \tag{3.155}$$

In the above manner the variation of the crack width at each interval of time is calculated by the program and is accumulated. When the accumulated value changes sign the crack is assumed to have closed and the corresponding unknown at this ring passes once again to the respective principle direction.

Another cause by which the cracks may close is a power reduction by which the temperature of the elements changes the sign of the thermal stresses. One factor which determines the program's ability to model fuel behaviour in complicated power cycles is the possibility that a crack may have healed or simply closed. The difference depends on the local temperature and is important for the behaviour on a new power rise. It is assumed that cracks which have simply closed, open again when the stress in the corresponding principle direction becomes positive (zero fracture stress), whilst healed cracks require the stress to reach the original fracture stress (∿ 150 MPa) before they may open again. This is accomplished by assuming that crack healing occurs only at temperatures higher than 1400°C.

3.4.5 Analysis of Plastic Yielding

Calculation of plastic strains is similar to that described for the cracking strains in the sense that the level of stresses must be known beforehand. So the calculation can proceed using the matrix equation (3.144) and then checks be made on plastic deformation. A method will be described here which determines the plastic strains by only replacing some of the matrix coefficients, but without changing its shape.

First a word about the plastic yielding in the fuel and cladding. Instantaneous plastic deformation is not important in ceramic fuel because of the low fracture stress in the outer tensile region (see Sub-Section 3.4.4) and the domination of creep at high temperatures which ensures stresses are always low. However, since the yield stress of UO_2 at temperatures greater than 1400^{o}C is very low, a plastic region can be defined in the fuel to have constant stress level (hydrostatic). In the cladding, on the other hand, the plastic yielding is very important for the reasons already discussed in Chapter 2. In this sense it is necessary to provide the program with a reliable yield stress model for the cladding.

In order to determine the onset of plastic deformation and calculate the plastic strains two conditions must be met as explained in 3.4.1(b):

(a) Von Mises yield criterion must be satisfied, i.e.

$$\sigma_{e,i} = \sigma_{y,i} \tag{3.156}$$

where

$\sigma_{e,i}$ = equivalent stress at node i

$\sigma_{y,i}$ = material yield stress for node i.

(b) The yield process should obey the Prandtl- Reuss flow law (3.84) which with some manipulation becomes:

$$\frac{\Delta\varepsilon_r^P}{s_r} = \frac{\Delta\varepsilon_\theta^P}{s_\theta} = \frac{\Delta\varepsilon_z^P}{s_z} \tag{3.157}$$

where

$\Delta\varepsilon_p^P$ = the changes in the plastic deformation in the direction p ($p \equiv r,\theta,z$)

$s_p = \sigma_p - \frac{1}{3}\sum_m \sigma_m$, deviatoric stress ($m = r,\theta,z$)

Equations (3.156) and (3.157) can be adapted in a way to conform with the general Equations (3.132) and thus replace them. The third equation for the node undergoing plastic deformation will be the same as the one used for the rest of the nodes, i.e. Eqn.(3.134).

In order to linearize Eqs.(3.156) and (3.157) we assume that $\bar{\sigma}_{e,i}$ is an estimate of the effective stress and $\bar{\sigma}_{p,i}$ and $\bar{s}_{p,i}$ the corresponding principle and deviatoric stress components, respectively. The true stress should differ from the estimated value by a small value $\Delta\bar{\sigma}_{p,i}$ hence

$$\sigma_{p,i} - \bar{\sigma}_{p,i} = \Delta\bar{\sigma}_{p,i}\ , \qquad p = r,\theta,z \tag{3.158}$$

The effective stress given by Eq.(3.83) can be re-written using (3.158) as

$$\sigma_{e,i} = \Big\{ \tfrac{1}{2}\Big[(\bar{\sigma}_{r,i} - \bar{\sigma}_{\theta,i}) + (\Delta\bar{\sigma}_{r,i} - \Delta\bar{\sigma}_{\theta,i})\Big]^2 + \tfrac{1}{2}\Big[(\bar{\sigma}_{\theta,i} - \bar{\sigma}_{z,i}) + (\Delta\bar{\sigma}_{\theta,i} - \Delta\bar{\sigma}_{z,i})\Big]^2 + \tfrac{1}{2}\Big[(\bar{\sigma}_{z,i} - \bar{\sigma}_{r,i}) + (\Delta\bar{\sigma}_{z,i} - \Delta\bar{\sigma}_{r,i})\Big]^2 \Big\}^{\frac{1}{2}}$$

$$= \left\{ \tfrac{1}{2}\left[(\bar{\sigma}_{r,i} - \bar{\sigma}_{\theta,i})^2 + (\bar{\sigma}_{\theta,i} - \bar{\sigma}_{z,i})^2 + (\bar{\sigma}_{z,i} - \bar{\sigma}_{r,i})^2\right]\right.$$

$$+ (\bar{\sigma}_{r,i} - \bar{\sigma}_{\theta,i})\ (\Delta\bar{\sigma}_{r,i} - \Delta\bar{\sigma}_{\theta,i})$$

$$+ (\bar{\sigma}_{\theta,i} - \bar{\sigma}_{z,i})\ (\Delta\bar{\sigma}_{\theta,i} - \Delta\bar{\sigma}_{z,i})$$

$$\left. + (\bar{\sigma}_{z,i} - \bar{\sigma}_{r,i})\ (\Delta\bar{\sigma}_{z,i} - \Delta\bar{\sigma}_{r,i})\right\}^{\frac{1}{2}}$$

Note that the higher orders of $\Delta\bar{\sigma}_{p,i}$ have been ignored. The first term of the above equation is $\bar{\sigma}^2_{e,i}$ and the other terms after multiplication and then factorisation are in the form of $(2\bar{\sigma}_{r,i} - \bar{\sigma}_{\theta,i} - \bar{\sigma}_{z,i})$. $\Delta\bar{\sigma}_{r,i}$, etc., which are equal to $3\ \bar{s}_{r,i}\ \Delta\bar{\sigma}_{r,i}$, etc. So we have

$$\sigma_{e,i} = \{\bar{\sigma}^2_{e,i} + 3(\bar{s}_{r,i}\cdot\Delta\bar{\sigma}_{r,i} + \bar{s}_{\theta,i}\cdot\Delta\bar{\sigma}_{\theta,i} + \bar{s}_{z,i}\cdot\Delta\bar{\sigma}_{z,i})\}^{\frac{1}{2}}$$

The LHS of this equation according to Eq.(3.156) must be equal to $\sigma_{y,i}$ and the RHS is re-written as

$$\sigma_{y,i} = \bar{\sigma}_{e,i}\left\{1 + \frac{3(\bar{s}_{r,i}\ \Delta\bar{\sigma}_{r,i} + \bar{s}_{\theta,i}\Delta\bar{\sigma}_{\theta,i} + \bar{s}_{z,i}\Delta\bar{\sigma}_{z,i})}{\sigma^2_{e,i}}\right\}^{\frac{1}{2}}$$

Expand the RHS in a Taylor series and multiply both sides by $\frac{2}{3}\ \bar{\sigma}_{e,i}$

$$\sigma_{y,i} = \bar{\sigma}_{e,i} + \frac{3}{2\ \bar{\sigma}_{e,i}}\ (\bar{s}_{r,i}\cdot\Delta\bar{\sigma}_{r,i} + \bar{s}_{\theta,i}\cdot\Delta\bar{\sigma}_{\theta,i} + \bar{s}_{z,i}\cdot\Delta\bar{\sigma}_{z,i})$$

$$\frac{2}{3}\ \bar{\sigma}_{e,i}\cdot\sigma_{y,i} = \frac{2}{3}\ \bar{\sigma}^2_{e,i} + (\bar{s}_{r,i}\cdot\Delta\bar{\sigma}_{r,i} + \bar{s}_{\theta,i}\cdot\Delta\bar{\sigma}_{\theta,i} + \bar{s}_{z,i}\cdot\Delta\bar{\sigma}_{z,i})$$

Using the definitions of $\Delta\bar{\sigma}_{p,i}$ and $\bar{\sigma}_{e,i}$, once more, we finally obtain

$$\frac{2}{3}\ \bar{\sigma}_{e,i}\cdot\sigma_{y,i} = \bar{s}_{r,i}\cdot\sigma_{r,i} + \bar{s}_{\theta,i}\cdot\sigma_{\theta,i} + \bar{s}_{z,i}\cdot\sigma_{z,i} \qquad (3.159)$$

Equation (3.159) can then replace the first of (3.132) equations after σ_r, σ_θ and σ_z are substituted for from Eqs .(3.130) resulting in

$$(\bar{s}_r.a_{1,i} + \bar{s}_\theta.a_{7,i} + \bar{s}_z.a_{13,i}).u^j_{i+1}$$

$$+ (\bar{s}_r.a_{2,i} + \bar{s}_\theta.a_{8,i} + \bar{s}_z.a_{14,i}).u^j_i$$

$$+ (\bar{s}_r.a_{3,i} + \bar{s}_\theta.a_{9,i} + \bar{s}_z.a_{15,i}).\gamma^j_{r,i}$$

$$+ (\bar{s}_r.a_{4,i} + \bar{s}_\theta.a_{10,i} + \bar{s}_z.a_{16,i}).\gamma^j_{\theta,i}$$

$$+ (\bar{s}_r.a_{5,i} + \bar{s}_\theta.a_{11,i} + \bar{s}_z.a_{17,i}).Z^j - \frac{2}{3}\bar{\sigma}_e.\sigma_y$$

$$+ (\bar{s}_r.a_{6,i} + \bar{s}_\theta.a_{12,i} + \bar{s}_z.a_{18,i}) = 0 \qquad (3.160)$$

By comparing Eq.(3.160) with the first equation in (3.132) the new values for $A^{(r)}_{k,i}$ (k = 1,6, i = 1,N) coefficients to be used in the case of plastic yielding may be determined.

Now for the second equation we consider Eq .(3.157). Using the difference equations (3.113) to (3.115) and the definition of $\dot{\gamma}_p$, the first equality in (3.157) can be re-written as:

$$\frac{(\gamma^j_{r,i} - \gamma^{j-1}_{r,i}) - (\theta P^j + (1-\theta)P^{j-1}).\Delta t}{\theta\, s^j_{r,i} + (1-\theta)\, s^{j-1}_{r,i}}$$

$$= \frac{(\gamma^j_{\theta,i} - \gamma^{j-1}_{\theta,i}) - (\theta\, P^j + (1-\theta)P^{j-1}).\Delta t}{\theta\, s^j_{\theta,i} + (1-\theta)\, s^{j-1}_{\theta,i}} \qquad (3.161)$$

Using Eq.(3.158) once more, we have

$$\sigma_{p,i} = \bar{\sigma}_{p,i} + \Delta\bar{\sigma}_{p,i}$$

$$s_{p,i} = \sigma_{p,i} - \frac{1}{3}\sum_m \sigma_{m,i} = \bar{\sigma}_{p,i} + \Delta\bar{\sigma}_{p,i} - \frac{1}{3}\sum_m (\bar{\sigma}_{m,i} + \Delta\bar{\sigma}_{m,i})$$

or

$$s_{p,i} = \bar{s}_{p,i} + (\Delta\bar{\sigma}_{p,i} - \frac{1}{3}\sum_m \Delta\bar{\sigma}_{m,i}) \qquad (3.162)$$

When this definition is used in Eq.(3.161) and re-arrangements made while second order terms such as

$$(\gamma_p^j - \gamma_p^{j-1})(\Delta\bar{\sigma}_p - \tfrac{1}{3}\sum_m \Delta\bar{\sigma}_m)$$

are ignored we obtain

$$\gamma_{r,i}^j(\theta\,\bar{s}_{\theta,i}^j + (1-\theta)\bar{s}_{\theta,i}^{j-1}) - \gamma_{r,i}^{j-1}(\theta\,\bar{s}_{\theta,i}^j + (1-\theta)\bar{s}_{\theta,i}^{j-1})$$

$$- \gamma_{\theta,i}^j(\theta\,\bar{s}_{r,i}^j + (1-\theta)\,\bar{s}_{r,i}^{j-1}) + \gamma_{\theta,i}^{j-1}(\theta\,\bar{s}_{r,i}^j + (1-\theta)\bar{s}_{r,i}^{j-1})$$

$$+ (\theta\,p^j + (1-\theta)p^{j-1})\Delta t[\theta(s_{r,i}^j - s_{\theta,i}^j)$$

$$+ (1-\theta)(s_{r,i}^{j-1} - s_{\theta,i}^{j-1})] = 0$$

Note that in the above equation terms like

$$\bar{s}_{p,i} + (\Delta\bar{\sigma}_{p,i} - \tfrac{1}{3}\sum_m \Delta\bar{\sigma}_{m,i})$$

have again been replaced by $s_{p,i}$ according to (3.162). Now $s_{r,i}^j - s_{\theta,i}^j$ can be replaced by $s_{r,i}^j - \sigma_{\theta,i}^j$ and then Eqs.(3.130) used to arrive at the following equation:

$$[\theta\,\Delta t(\theta\,p^j + (1-\theta)p^{j-1}).(a_{1,i} - a_{7,i})]\cdot u_{i+1}^j$$

$$+ [\theta\,\Delta t(\theta\,p^j + (1-\theta)p^{j-1}).(a_{2,i} - a_{8,i})]\cdot u_i^j$$

$$+ [\theta\,\Delta t(\theta\,p^j + (1-\theta)p^{j-1}).(a_{3,i} - a_{9,i}) + \theta\,\bar{s}_{\theta,i}^j$$

$$+ (1-\theta)\bar{s}_\theta^j]\cdot\gamma_{r,i}^j$$

$$+ [\theta\,\Delta t(\theta\,p^j + (1-\theta)p^{j-1}).(a_{4,i} - a_{10,i})$$

$$- \theta\,\bar{s}_{r,i}^j - (1-\theta)\bar{s}_{r,i}^{j-1}]\cdot\gamma_{\theta,i}^j$$

$$+ [\theta\,\Delta t(\theta\,p^j + (1-\theta)p^{j-1}).(a_{5,i} - a_{11,i})]\cdot z^j \qquad (3.163)$$

$$+\left\{\Delta t(\theta\ p^{j} + (1-\theta)p^{j-1})\left[(1-\theta)\ (s_{r,i}^{j-1} - s_{\theta,i}^{j-1}) \right.\right. \qquad \text{(3.163 cont.)}$$

$$\left. + \theta\ (a_{6,i} - a_{12,i})\right] - \gamma_r^{j-1}(\theta\ \bar{s}_{\theta,i}^{j} + (1-\theta)\ \bar{s}_{\theta,i}^{j-1})$$

$$\left. + \gamma_\theta^{j-1}(\theta\ \bar{s}_{r,i}^{j} + (1-\theta)\bar{s}_{r,i}^{j-1})\right\} = 0 \qquad (3.163)$$

This equation replaces the second equation in (3.132) and as before the new $A_{k,i}^{(\theta)}$ ($k = 1,6$, $i = 1,N$) coefficients can be easily recognised.

In practice, since the scheme used in the mechanical analysis is non-iterative, without any significant error instead of the quantities with a "bar" their values at the end of previous time interval are used, i.e. $\bar{s}_{r,i}$ replaced by $s_{r,i}^{j-1}$, etc.

As it is implied by Eq.(3.160) the value of σ_y must be known for every node. Appropriate yield models have been incorporated in SAMURA and will be described later.

3.5 PROBLEM PARAMETERISATION AND PHYSICAL MODELS

So far the numerical methods used to solve the thermal and mechanical equations of the system have been discussed. In this section the parameterisation used to define the quantities which were left as general functions in the previous sections are described. These are in the form of explicit empirical relations for each of the physical phenomena that contribute to the fuel and cladding behaviour. It must be emphasised that the equations and physical models given here should be considered as the best

available examples rather than the latest assessed and accurate data. They are written into SAMURA in a way to enable the future users to replace them easily and supply their own models for further studies (see also Appendix D).

3.5.1 Specific Heat Capacity

The specific heat capacity of fuel and cladding is needed for temperature calculations in time-dependent fuel behaviour problems.

FUEL: For UO_2 fuel the following expression which is based on enthalpy data is used (146):

$$C_p^f(T) = 15.496 \left[\frac{A_1 A_2^2 . \exp(A_2/T)}{T^2 (\exp(A_2/T) - 1)^2} + 2A_3 . T \right.$$

$$\left. + \frac{A_4 . A_5}{R . T^2} \exp(-A_5/RT) \right], \ (J/kg.^\circ K) \qquad (3.164)$$

where $A_1 = 19.145$ (cal/mole $^\circ K$)

$A_2 = 535.285$ ($^\circ K$)

$A_3 = 7.8473 \times 10^{-4}$ (cal/mole$^\circ K^2$)

$A_4 = 5.6437 \times 10^6$ (cal/mole)

$A_5 = 3.7695 \times 10^4$ (cal/mole)

T = temperature, 298 to $3113^\circ K$

and $R = 1.987$ (cal/mole$^\circ K$)

Note that $C_p^f(T)$ has the units of J/kg.$^\circ K$ although the quantities used in (3.164) are not in metric units. This expression is used up to the UO_2 solidus temperature ($3113^\circ K$). For temperatures greater than $3113^\circ K$ and less than the liquidus temperature ($3113 + \varepsilon\ ^\circ K$, $\varepsilon \leq 2^\circ K$) the following expression is used:

$$C_p^f(T) = (1 - F_m)\ C_p^f(T_m) + 502.95\ F_m, \quad (J/kg.^oK) \qquad (3.165)$$

where

$C_p^f(T_m)$ = fuel specific heat from (3.164) for $T = T_m$, where $T_m = 3113^oK$

F_m = fraction of molten fuel (ratio of the molten fuel cross-section area to the total fuel surface area, $0 < F_m \leq 1$).

For a completely molten fuel, $F_m = 1$, we use

$$C_p^f(T) = 502.95 \quad (J/kg.^oK) \qquad (3.166)$$

CLAD: The specific heat of Zircaloy cladding has not been reported in the form of an expression. There are some existing data up to 1323^oK (147), where the effects of α-β transformation region are included. Although the variation of $C_p^c(T)$ below the α-β transus ($\sim 1100^oK$) is almost linear with temperature, after the transformation and up to $\sim 1248^oK$ there is a sudden peak which cannot be correlated. So in SAMURA the data are provided in a tabular form up to 1248^oK. Linear interpolation is performed by a special routine in the program to return the heat capacity at the required temperature. Above 1248^oK, a constant value of 355.7 J/kg.^oK is used.

3.5.2 Thermal Conductivity

FUEL: The thermal conductivity of UO_2 has been the subject of numerous publications with fair agreement being exhibited for temperatures up to about 1673^oK. For temperatures above 1673^oK considerable uncertainty exists in the thermal conductivity of irradiated fuel. The effects

of irradiation and fuel cracking on thermal conductivity are not clearly established as discussed in Chapter 2; however, corrections for porosity variation have been established. In SAMURA the following correlation for 95% TD UO_2 along with the temperature dependent porosity correction factor is employed.

For temperatures between 0 and 1923°K:

$$k^f(T) = 100 \left[\frac{1 - P.B}{1 - 0.05B}\right] \cdot \left[\frac{40.4}{464 + T} + 5.86 \times 10^{-5} \exp(2.14 \times 10^{-3} T)\right]$$

For temperatures between 1923°K and fuel melting:

$$k^f(T) = 100 \left[\frac{1 - P.B}{1 - 0.05B}\right] \cdot \left[0.02 + 5.86 \times 10^{-5} \exp(2.14 \times 10^{-3} T)\right] \quad (3.167)$$

where

$k^f(T)$ = thermal conductivity of UO_2 (W/m°K)

P = fuel porosity

B = porosity correction factor (B = 2.58 - 2.58 x 10^{-3}T)

T = temperature in °C

CLAD: The model used for the thermal conductivity of Zircaloy covers all temperatures from room temperature to the melting point and is based on the data of Chirigos et al (148), Feith (149) and Scott (150). A least square fit of the data to a third order polynomial combines the results of all the above sources in the following correlation:

$$k^C(T) = 7.848 + 2.200 \times 10^{-2}T - 1.676 \times 10^{-5}T^2 + 8.712 \times 10^{-9}T^3 \quad (3.168)$$

where

$k^C(T)$ = cladding thermal conductivity (W/m^oK)

T = temperature (^oK)

It must be stated that these data are considered reliable up to about 1123^oK. Between this temperature and 1733^oK, the correlation is less accurate because fewer data were available. Above 1723^oK, data were not available, and the correlation is an extrapolation of the lower temperature data.

3.5.3 Emissivity

The transfer of heat from a fuel pin during an off-normal transient may be dependent upon convection and radiation. The rate of radiation heat transfer is directly proportional to the emissivity of the pin surface (see Eq.3.4.3).

FUEL: Fuel emissivity is a highly variable property because of its strong dependence on the roughness and reflective properties of the surface. Belle (151) has reported tabulated values for spectral emissivity of UO_2 for the temperature range 900 to 2673^oK. A regression analysis of these data was performed to obtain a fifth order polynomial to be used in SAMURA;

$$\varepsilon_f = 19.324 - 6.68 \times 10^{-2}T + 9.396 \times 10^{-5}T^2 - 6.397 \times 10^{-8}T^3 + 2.100 \times 10^{-11}T^4 - 2.667 \times 10^{-15}T^5 \quad (T \text{ in } ^oK) \quad (3.169)$$

The emissivity is assumed to take on constant values outside the range 900-2400°K; below 900°K, the emissivity is assumed to be 0.83, and above 2400°K the emissivity is taken as equal to 0.40.

CLAD: Cladding emissivity has not been reported in detail. A constant value at all temperatures is used:

$$\varepsilon_c = 0.74 \qquad (3.170)$$

It must be, however, mentioned that shortly after fuel pin irradiation (few months) an oxide layer forms on Zircaloy cladding due to exposure to oxygen in the environment or in reactor coolant. This layer thicknes with time and its emissivity is the value which should be used instead of Zircaloy emissivity. This may be particularly important to loss-of-coolant accident (LOCA) analyses. The only available data have been reported by Juenke and Sjodahl (152). If such data are used then the thermal conductivity of this zirconium oxide must be also accounted for.

3.5.4 Thermal Expansion

Fuel and cladding thermal expansion models are required to predict changes in fuel pin geometry due to changes in temperature (see Eqs.(3.74-3.76)). For calculational continuity in accident analyses, the thermal expansion correlations must span the range from room temperature to the melting temperature of the material. Linear thermal expansion models have been developed for both UO_2 and Zircaloy. The models used in SAMURA include three regimes: expansion in the solid phase, expansion due to the phase change at the melting point, and expansion in the liquid phase.

FUEL: Linear thermal expansion data for unirradiated UO_2 have been published by many workers. They are generally consistent although some give slightly lower values at temperatures lower than 2273°K. The effect of irradiation on UO_2 thermal expansion is usually assumed to be negligible. However, no experimental data are available to support this assumption. In-reactor fuel thermal expansion is uncertain because accurate descriptions of fuel cracking (resulting from thermal stresses) and healing are not available.

UO_2 SOLID PHASE: The available data presented by several sources for the solid phase were fit by regression analysis to a third order polynomial (151, 153-156):

$$\left(\frac{\Delta L}{L}\right)_f = -4.972 \times 10^{-4} + 7.107 \times 10^{-6} T + 2.581 \times 10^{-9} T^2 + 1.140 \times 10^{-13} T^3 \qquad (3.171)$$

where

$\left(\frac{\Delta L}{L}\right)_f$ = linear thermal expansion of the fuel (m/m°C)

T = temperature (°C)

UO_2 PHASE CHANGE AT MELTING POINT: The data of Christensen (154) are used for the thermal expansion due to the phase change at the melting point. Uniform expansion is assumed. The resulting correlation is:

$$\left(\frac{\Delta L}{L}\right)_f = \left(\frac{\Delta L}{L}\right)_f^{T_m} + 3.096 \times 10^{-2} F_m \qquad (3.172)$$

where

$\left(\frac{\Delta L}{L}\right)_f^{T_m}$ = the thermal expansion given by Eq.(3.171) with $T = T_m$, the melting temperature (m/m°C)

F_m = fraction of molten fuel

UO_2 LIQUID PHASE: The coefficient of expansion presented by Christensen (154) is used for the liquid phase (above the temperature at which all the fuel is molten). The result is

$$\left(\frac{\Delta L}{L}\right)_f = \left(\frac{\Delta L}{L}\right)_f^{T_m} + 3.096 \times 10^{-2} + 3.5 \times 10^{-5}(T-T_m) \tag{3.173}$$

where

T = liquid fuel temperature (^oC)

CLAD: Due to the strong texture (preferred crystallographic orientation) of cold-worked Zircaloy, the thermal expansion is different in the axial and diametral directions. Diametral thermal expansion in tubing is a combination of circumferential and radial thermal expansion.

AXIAL: Mehan and Cutler (157) have reported data for the axial thermal expansion of Zircaloy-2 plate. The thermal expansion of Zircaloy tubing has not been measured and reported. The following second degree polynomial least squares fit has been generated from the above data to be used in SAMURA up to 1073^oK:

$$\left(\frac{\Delta L}{L}\right)_c^a = 1.708 \times 10^{-3} + 5.224 \times 10^{-6}T + 1.204 \times 10^{-9}T^2 \tag{3.174}$$

where

$\left(\frac{\Delta L}{L}\right)_c^a$ = cladding axial thermal expansion (m/m^oK)

T = cladding mesh point temperature (^oK)

The assumption is made that this equation will adequately describe both Zircaloy-2 and Zircaloy-4 cladding since these materials are quite similar.

Additional data is taken from Refs.(109,157) to generate a table of data describing the thermal expansion over the temperature range where alpha Zircaloy is transforming to beta Zircaloy ($\sim$ 1073 to 1290^{o}K). In this data set interpolations are made by a special routine in SAMURA to return the requried value at a given temperature. Above about 1290^{o}K, assumption is made that Zircaloy completely transform to the beta phase and that the thermal expansion of Zirconium will adequately describe the thermal expansion of Zircaloy. A constant value of the coefficient of thermal expansion of Zirconium of 9.7×10^{-6} $^{o}K^{-1}$ is used to generate the following linear equation describing the thermal expansion of Zircaloy from 1290^{o}K to the end of liquid phase (2148^{o}K).

$$\left(\frac{\Delta L}{L}\right)_c^a = -8.208 \times 10^{-3} + 9.683 \times 10^{-6} T \qquad (3.175)$$

The large contraction during α-β transition prevents the use of a single analytical function to describe the thermal expansion of Zircaloy over the entire temperature range.

DIAMETRAL: Again the data of Mehan and Cutler (157) are used to generate the following third degree polynomial least squares fit up to a temperature of 1073^{o}K:

$$\left(\frac{\Delta D}{D}\right)_c = 8.208 \times 10^{-4} - 7.856 \times 10^{-6} T + 1.924 \times 10^{-8} T^2 - 6.141 \times 10^{-12} T^3 \qquad (3.175)$$

where

$\left(\frac{\Delta D}{D}\right)_c$ = the thermal expansion in diametral direction, (m/m^{o}K)

T = cladding mesh point temperature (^{o}K)

The assumption is made that the diametral thermal expansion in parallel to the axial thermal expansion curve from 1073°K to the completion of beta phase, i.e. 1290°K. This again provides a data table to describe the diametral thermal expansion in the same manner as described before. From 1290°K to the liquid phase, a similar approach as in the case of axial expansion is made. The result is

$$\left(\frac{\Delta D}{D}\right)_c = -6.514 \times 10^{-3} + 9.701 \times 10^{-6} T \qquad (3.176)$$

3.5.5 Young's Modulus

The Young's modulus is required to calculate mechanical properties of UO_2 and Zircaloy at stresses less than the yield stress. The Young's modulus is defined by Hooke's law as the ratio of stress to strain for stresses below the yield point. The data available are for unirradiated material and span the range from room temperature to about 2000°K for UO_2 and to about 1100°K for Zircaloy.

FUEL: The data reported by Vollatah (158) is used in SAMURA because they describe the elastic modulus as a function of both temperature and porosity. The data can be represented by the following correlation:

$$E_f = (188627.4372 - 90.6275T) \cdot PC; \text{ (MPa)} \qquad (3.177)$$

where

E_f = fuel Young's modulus (MPa)

T = temperature (°K)

PC = porosity correction factor defined as below:

If P (porosity) $\leq$ 0.1: PC = 1 - 2.28P

If $0.1 < P \leq 0.8$: $PC = (1 - P)/(1 + 1.66P)$

If $P > 0.8$: $PC = 0.086$

The porosity correction factor is taken from a Harwell experimental work (159). Eq .(3.177) is used up to a temperature of 1973°K and since there are no available data above this temperature a constant value of

$$E_f = 9805.8823 \text{ (MPa)} \tag{3.178}$$

is used without any porosity dependence.

CLAD: The correlation used to calculate the Zircaloy Young's modulus is a linear function of temperature and represents a combination of the available correlated data (109,150,160):

$$E_c = 114800.0 - 59.90T \text{ (MPa)} \tag{3.179}$$

where

E_c = Zircaloy Young's modulus (MPa)

T = cladding temperature (°K)

This relation is only accurate up to about 1135°K (end of α-phase). Since there were no reliable reported data, for higher temperatures a constant value is chosen:

$$E_c = 46813.5 \text{ (MPa)} \tag{3.180}$$

3.5.6 Poisson's Ratio

Poisson's ratio is defined as the ratio of transverse to axial strain and is dimensionless. The theoretical value of Poisson's ratio for isotropic or ideal metals is about 0.33.

FUEL: In SAMURA the following equation is used to calculate the Poisson's ratio of UO_2:

$$\nu_F = 0.325339867 - 1.791 \times 10^{-5} T \qquad (3.181)$$

where

ν_F = fuel Poisson's ratio

T = fuel temperature (^oK)

For temperatures greater than 1973^oK a constant value is chosen:

$$\nu_F = 0.29 \qquad (3.182)$$

CLAD: Scott (150) has reported experimental data for the Poisson's ratio of Zircaloy. There are other reports too, however, his data are more extensive and thus are used in SAMURA:

$$\nu_c = 0.333314800 - 0.12654 \times 10^{-3} T \qquad (3.183)$$

where

ν_c = Zircaloy Poisson's ratio

T = cladding temperature (^oK)

Eq .(3.183) is only valid up to 672^oK. For higher temperatures a constant value is used as below:

$$\nu_c = 0.248275 \qquad (3.184)$$

3.5.7 Creep Rate Models

Creep rates are required to calculate F_p ($p \equiv r,\theta,z$) values as defined by Eq.(3.100). Creep rates are presented by a general function $\dot{g}(\sigma_e)$; see Sub-Section 3.4.1(b). The creep rate, $\dot{g}(\sigma_e)$, is a function of several factors i.e. stress, time, temperature, grain size, density, fission rate, and flux level. The $\dot{g}(\sigma_e)$ functions should reflect these parameters so that fuel pin deformation during operation can be predicted realistically. As discussed in Chapter 2, a theoretically based model is required to

provide guidance in the selection of the most appropriate relationships between variables because the data are limited and exhibit much scatter.

FUEL: The model incorporated in SAMURA to determine fuel creep rate is based on the UO_2 creep theories and models explained in Sub-Section 2.3.7 as proposed by Bohaboy et al (80) with the modifications suggested by Solomon et al (83) for fission-enhanced and fission-induced creep and the corrections made by Andres et al (14) for time- dependent UO_2 creep rate. The fission-induced creep constant proposed by Solomon et al (83) has been changed slightly by Olsen (161) to reflect the slight temperature dependence of fission-induced creep. The steady-state creep rate equation for UO_2 is, therefore, represented by the following expression:

$$\dot{g}_f^{ss}(\sigma_e) = C_1\sigma_e \exp(-Q_1/RT) + C_2.\sigma_e^{4.5} \exp(-Q_2/RT) + C_3\,\sigma_e\,\dot{F}\exp(-Q_3/RT),\ (m/m.day) \qquad (3.185)$$

where

$\dot{g}_f^{ss}(\sigma_e)$ = steady-state fuel creep rate (m/m.day)

C_1 = $(3.3862252 \times 10^{10} + 1.1278134 \times 10^{-8}\dot{F})/(D-87.7)G^2$

$\dot{F}$ = fission-rate (fissions/m^3.s)

D = fuel density in %TD (if less than 92% then 92% is used)

G = fuel grain size (microns)

σ_e = equivalent uniaxial compressive stress (MPa)

Q_1 = 0.37659331 (MJ/mole)

R = 8.3143435×10^{-6} (MJ/mole^oK)

C_2 = $1.759925 \times 10^7/(D-90.5)$

Q_2 = 0.55233686 (MJ/mole)

C_3 = $3.2163570 \times 10^{-24}$

Q_3 = 0.021758724 (MJ/mole)

T = fuel temperature (^{o}K)

The first two terms of this equation reflect high-temperature thermal creep mechanisms. The first term, according to Olsen (161), represents a viscous creep mechanism with some grain boundary sliding occurring at low stresses. The viscous creep is linearly proportional to stress; inversely proportional to the square of grain size; and enhanced by a factor that is proportional to the fission rate. A dislocation-climb mechanism, expressed in the second term of Eq.(3.185), operate at stresses greater than a transition stress that is governed by the grain size as described in Chapter 2. The dislocation-climb creep rate is proportional to the stress to approximately the 4.5 power. The mechanism of irradiation enhanced dislocation-climb-controlled has not been modelled in the above equation due to lack of sufficient data.

Wolfe and Kaufman (79) have stated that the stress necessary for transition from viscous creep to dislocation creep is independent of temperature because of the apparently small difference in measured activation energies for the two mechanisms. The transition stress, σ_{trans}, is given by the following expression:

$$\sigma_{trans} = 165.474160\ G^{-0.5714}\ (MPa) \qquad (3.186)$$

where G is the grain size of UO_2 in μm. When the stress in the fuel is less than σ_{trans}, the actual stresses are

used in the first term of Eq.(3.185); for stresses greater than σ_{trans}, the transition stress calculated from the above equation is used in the first term of Eq.(3.185).

To include some effects of the primary creep Andrews et al (14) have corrected Eq.(3.185) through comparison with experimental results. Using their definitions the total creep rate of UO_2 in SAMURA is given by the following expressions:

For T (fuel temperature) $\leq 1473^{o}K$;

$$\dot{g}_f(\sigma_e) = (1 + 20.38\ t^{-0.37})\ \dot{g}_f^{ss}(\sigma_e);\ (m/m.day) \qquad (3.187)$$

For T $> 1473^{o}K$;

$$\dot{g}_f(\sigma_e) = (1 + 7.80\ t^{-0.26})\ \dot{g}_f^{ss}(\sigma_e);\ (m/m.day)$$

where

$\dot{g}_f^{ss}(\sigma_e)$ = total fuel creep rate (m/m.day)

t = irradiation time from beginning of life (hours)

$\dot{g}_f^{ss}(\sigma_e)$ = steady-state creep rate from (3.184)

CLAD: Unfortunately there is very little data in the open literature for quantifying the deformation behaviour of Zircaloy cladding, especially in the regimes of high stress, high temperature and primary thermal creep. Owing to the lack of sufficient data, uncertainties as experienced in many modelling programs (7,14,17,86,91) are faced in predicting the deformation of fuel pin cladding.

In the first version of SAMURA the anisotropy of Zircaloy cladding creep rate has been ignored. This was

only due to the lack of appropriate data for the anisotropic constants as well as creep rate equations. Its inclusion, however, will not pose any difficulties and will need little modifications in the matrix (3.144) coefficients (see Appendices B and C).

As in the case of the fuel we have thermal and irradiation creep rates. However, due to the nature of the measured data in which thermal or irradiation creep rates could not be separated (14), two separate expressions for thermal and irradiation creep rates are provided, but the greater of either of them at any time is used in accumulating creep strain with time*. These equations apply at temperatures up to 673°K and effective stresses up to the cladding yield stress;

$$\dot{g}_c^{th}(\sigma_e) = 0.962 \{(3.264 \times 10^{11} \exp(-0.192t) + 2.4 \times 10^{9}) \times \sinh(0.011545\ \sigma_e) + (16547.42/Y_s) \times \sinh(0.071649\ \sigma_e)\} .\exp(-0.167/RT);(m/m.day) \quad (3.189)$$

$$\dot{g}_c^{irr}(\sigma_e) = 0.793 \{(2.9518 \times 10^{-19}\exp(-0.096t) + 3.968 \times 10^{-18}) \cdot \Phi\ \sigma_e\} .\exp(0.03347/RT); \quad (m/m.day) \quad (3.190)$$

where

$\dot{g}_c^{th}(\sigma_e)$ = cladding isotropic thermal creep rate (m/m.day)

t = irradiation time (days)

σ_e = effective stress (MPa)

*Note that this is done only for the particular creep data used here. If other models are used the necessary modifications must be made.

Y_s = cladding mesh point yield stress (MPa)

R = 8.3143435×10^{-6} (MJ/mole ^{o}K)

T = cladding mesh point temperature (^{o}K)

$\dot{g}_c^{irr}(\sigma_e)$ = cladding isotropic irradiation creep rate (m/m•day)

Φ = fast neutron flux ($n/cm^2.s$)

So at any instant we have

$$\dot{g}_c(\sigma_e) = MAX(\dot{g}_c^{th}, \dot{g}_c^{irr}), \text{ (m/m•day)} \qquad (3.191)$$

where $\dot{g}_c(\sigma_e)$ is the total isotropic cladding creep rate.

3.5.8 Swelling Rates Model

As discussed in Chapter 2, swelling in LWR fuel pins is only significant for pellets. Thus SAMURA only considers UO_2 fuel swelling.

FUEL: The model used to calculate swelling rates, $\dot{S}_f$, is the form of empirical expression recommended by Hayns and Wilmore (9) adjusted to the experimental data presented by Gittus (162):

$$\dot{S}_f = \dot{R} \cdot \left[1.2 \times 10^{-7} + \frac{1.08 \times 10^{-6} + 0.73\ S.Bu^{-1}}{1 + \exp(40S - 4.8)} \right] (day^{-1}) \qquad (3.192)$$

where

$S = 3.24 \times 10^{-8}\ Bu^{0.75} T^{1.5} \exp(-0.0628/RT)$

$\dot{R}$ = fuel pin rating (W/g)

Bu = burn-up (MWd/teU)

T = fuel mesh point temperature (^{o}K)

$R = 8.3143435 \times 10^{-6}$ (MJ/mole^{o}K)

CLAD: Zircaloy swelling rate has been assumed to be insignificant:

$$\dot{S}_c = 0.0 \qquad (3.193)$$

3.5.9 Fracture Stress

The magnitude of the fracture stress in UO_2 is required to determine the onset of cracking. However, as discussed in Chapter 2, the fracture stress is very sensitive to fabrication conditions and the available experimental results are sometimes contradictory. Because of this two models are used in SAMURA:

(1) Constant value fracture stress, i.e.

$$\sigma_F = 150 \text{ (MPa)} \tag{3.194}$$

This is an average value in the experimental range.

(2) Variable fracture stress;

$$\sigma_F = 108.15 + 0.021864T \text{ (MPa)} \tag{3.195}$$

where

T = fuel mesh point temperature (^oK).

This expression is used for the cracking analysis of all uncracked parts of the fuel, e.g. during the first start-up. For those parts of the fuel where the cracks have closed or healed a condition must first be met before the application of (3.194) or (3.195). That is, as mentioned in 3.4.4, the difference between simple crack closure and cracks healing. In SAMURA it is assumed that at temperatures lower than 1673^oK no crack healing can occur, in other words, at these temperatures there is no possibility to restore the fuel strength to the uncracked value (159). So in the fuel areas with temperatures lower than 1673 after the first cracking has occurred the value of fracture stress is simply set to zero, i.e. $\sigma_F = 0$.

In this version of SAMURA, since there is no cladding failure mechanism, the Zircaloy fracture stress is set to a

very large number to automatically halt any possibility of fracture.

3.5.10 Fission Gas Release and Pin Pressure

As the generated fission gases are released to the interior of pin, the internal pressure builds up and becomes an important contributor to pin deformation. The internal pin pressure is expected to be lower than the coolant pressure at all times.

The space available to the released gases consists of

(a) plenum volume

(b) central void

(c) pellet dishing

(d) pellet cracked volume

and (e) fuel/clad gap.

It is generally assumed that the gas molecules have access to all the available space, and thus the overall volume of the above cavities and voids is used to calculate the internal pin pressure at any time.

FISSION GAS RELEASE: The amount of gas release is required in the calculation of fission gas pressure. It was stated in Chapter 2 that gas release is a very complicated phenomenon and cannot easily be dealt with through simple models. However, in the first version of SAMURA two simple models are employed (basically for equilibrium cases) to enable the code to concentrate on more important phenomena:

(1) First model of fission gas release.

This model is based on the work by Jankus and Weeks (3) and assumes that the fraction of fission gas release is

simply a function of time and temperature, i.e.

$$F_{GR,i} = 24 \cdot \Delta t \cdot \exp(-4.71 - 4444.44/T_i) \qquad (3.196)$$

where

$F_{GR,i}$ = fraction of gas release in ring i

Δt = time-step length (days)

T_i = fuel mesh point temperature (^oK)

(2) Second model of fission gas release

The second model is based partly on analytical work and partly on experimental data. This model is in the tabular form and incorporates fuel temperature and burn-up:

$F_{GR,i}$	Burn-up (MWd/teU)	Temperature
Bu/160,000	Bu $\leq$ 80,000	T $\leq$ 1573^oK
1 - 40,000/Bu	Bu > 80,000	T $\leq$ 1573^oK
Bu/40,000	Bu $\leq$ 20,000	1573^oK<T$\leq$1973^oK
1 - 10,000/Bu	Bu > 20,000	1573^oK<T$\leq$1973^oK
0.7394	Bu > 0	T = 2073^oK
0.8975	"	T = 2273^oK
0.9710	"	T = 2473^oK
1.0	"	T $\geq$ 2873^oK

The calculations made so far with SAMURA have shown that the second fission gas release model predicts 50 to 100% higher values than the first model.

INTERNAL GAS PRESSURE: Thirty-one gas atoms are produced in a thermal flux for every 100 atoms fissioned (this is actually an upper limit; values as low as 20 atoms per 100 atoms fissioned have been used). With a fission energy

equivalent (excluding capture) of about 200 MeV/fission, 1 WATT $\equiv 3.128 \times 10^{10}$ fissions/s. So we can write

$$1 \text{ WATT} \equiv 3.128 \times 10^{10} \left[\frac{\text{fissions}}{\text{s}}\right] \times 0.31 \left[\frac{\text{atoms}}{\text{fissions}}\right]$$

$$\times 86400 \left[\frac{\text{s}}{\text{day}}\right] \times \frac{1}{6.023 \times 10^{23}} \left[\frac{\text{moles}}{\text{atoms}}\right]$$

$$\equiv 1.391 \times 10^{-9} \left[\frac{\text{moles}}{\text{day}}\right] \qquad (3.197)$$

Therefore the increment of fission gas moles produced in an elementary fuel ring is

$$\Delta G^{j}_{p,i} = 1.391 \times 10^{-9} . Q_{L,i} . \ell_f . \Delta t \quad \text{(moles)} \qquad (3.198)$$

where

$\Delta G^{j}_{p,i}$ = increment of gas produced in ring i, at time j,

$Q_{L,i}$ = linear power in ring i, (W/m)

ℓ_f = fuel stack length, (m)

Δt = time-step length, (day)

Eq .(3.198) together with one of the fractional fission gas release models is applied to each ring separately and the amount of gas release from that ring during any time-interval is estimated and added to the accumulated gas release from the rest of the rings:

$$\Delta G^{j}_{REL,i} = \Delta G^{j}_{p,i} . F^{j}_{GR,i} \quad \text{(moles)} \qquad (3.199)$$

$$\Delta G^{j}_{REM,i} = \Delta G^{j}_{p,i} . (1 - F^{j}_{GR,i}) \quad \text{(moles)} \qquad (3.200)$$

where

$\Delta G^{j}_{REL,i}$ = number of moles released in ring i, at time j

$\Delta G^{j}_{REM,i}$ = number of moles remaining in ring i, at time j.

It is usually assumed that the fission gas previously produced in a fuel ring but still retained in the ring is not released with the same fractional release rate as the youngest fission gas moles just produced*. In SAMURA, it is assumed that the gas moles retained within the fuel grains can only be released if the fraction of gas released during the current time-step is greater than the mean fraction of gas released over all previous time-steps (due, for instance, to an increase in power). Then the fission gas previously produced in any ring i, but still retained, is partially released by an amount such that the fraction of the total fission gas released to date is equal to the fraction of fission gas released as calculated for the current time-step. If the former fraction is called $F^{j}_{O,i}$, then the total gas released from ring i at time j will be

$$G^{TOT,j}_{REL,i} = G^{j}_{REL,i} + G^{j-1}_{REM,i} F^{j}_{O,i} \qquad \text{(moles)}$$

Thus the total number of gas moles released over N fuel rings up to time j and the total number of gas moles produced are, respectively :

$$G^{TOT,j}_{REL} = \sum_{i=1}^{N} \sum_{jj=1}^{j} G^{TOT,jj}_{REL,i} \qquad \text{(moles)} \qquad (3.201)$$

$$G^{TOT,j}_{p} = \sum_{i=1}^{N} \sum_{jj=1}^{j} \Delta G^{jj}_{p,i} \qquad \text{(moles)} \qquad (3.202)$$

The percentage of total gas release is finally

$$C_{GAS} = 100 \left(G^{TOT,j}_{REL} / G^{TOT,j}_{p} \right) \qquad (3.203)$$

Now, if the number of filling gas moles is given by G_{FILL}, the pin internal gas pressure can be determined from the ideal gas law, i.e.,

$$P_F = \left(G^{TOT,j}_{REL} + G_{FILL} \right) R \, T_{GAS} / V \qquad \text{(MPa)} \qquad (3.204)$$

where

*This is because fission gas moles are produced equally distributed over a fuel grain, they collect in pores and migrate to the grain boundary. The assumption is that only those gas moles reaching the boundary are released.

P_F = internal gas pressure (MPa)

R = gas constant, 8.3143435×10^{-6} (MJ/mole^{o}K)

V = total available volume to the gas moles defined as

$$V = V_{PL} + V_{CV} + V_{GAP} + V_{DISH} \qquad (3.205)$$

V_{PL} = plenum volume (m^3)

V_{CV} = central void volume (m^3)

V_{GAP} = fuel/clad gap volume (m^3)

V_{DISH} = pellets dishing volume (m^3)

and T_{GAS} = volumetric average gas temperature (^{o}K) defined as

$$T_{GAS} = \left[\frac{V_{PL}}{T_{PL}} + \frac{V_{CV}}{T_{CV}} + \frac{V_{GAP}}{T_{GAP}} + \frac{V_{DISH}}{T_{CV}} \right]^{-1} . V \qquad (3.206)$$

T_{PL} = hot plenum temperature (^{o}K)

T_{CV} = central void temperature (^{o}K)

T_{GAP} = gap average temperature (^{o}K)

AXIAL VARIATION OF POWER: Since axial flux varies along the fuel pin height, the power distribution as well as the temperature of any radial node i is not constant along the pin. Thus the contribution to gas release from different axial positions is also variable. In a multi-axial zone treatment of the fuel pin such differences are automatically accounted for; but, in the present version of SAMURA with only one axial zone there is no such possibility. The simplest solution to this problem as incorporated in SAMURA, is to use the axially-averaged linear power and temperatures for any ring i in all the equations. If the axial flux is not available a cosine distribution is used. The average

linear power, knowing that the power is proportional to the flux, will be

$$Q_{L,avg,i} = Q_{L,max,i} \left(\frac{2}{\pi}\right) \qquad (3.207)$$

where

$Q_{L,avg,i}$ = average linear power at i along the pin

$Q_{L,max,i}$ = maximum linear power at i along the pin

This value of linear power has been used in Eq.(3.198) instead of $Q_{L,i}$; which is the local value. The code is then run using the axially averaged input power history (in the above manner) with the axially averaged cladding surface or coolant temperature. Output pin-pressures from this run are input to the code for further calculations at any desired axial position. If, however, the actual axial shape factors are known they are used instead of the $2/\pi$ factor (see Chapter 4).

3.5.11 Pore Migration and Re-structuring in UO_2

In oxide fuel pins large radial temperature gradients are generated during irradiation. They produce among other effects porosity re-distribution owing to the migration of the as-fabricated pores. The most conspicuous result is the formation of a central channel through the accumulation of pores in the central position and the generation of columnar grains with radial orientation in the fuel. The latter are generally linked to the appearance of lenticular voids which are assumed to migrate by the evaporation condensation mechanism (43).

Pore migration at the beginning of irradiation can be explained qualitatively. Observations show that the following structural zones can be recognised, from the outside to the centre of the pellet; a zone of as-fabricated

porosity followed by a zone of equiaxed grain growth with a smaller number of statistically distributed spherical pores and, finally, a zone of columnar grains in the process of formation with planoconvex lenticular voids. It is assumed that the relatively small number of spherical voids are formed by diffusion of vacancies from the relatively large number of sinter pores which, however, have smaller dimensions. Under the influence of the temperature gradient, the latter migrate to the nearest grain boundary and then preferably along these boundaries towards the thermal centre. The planoconvex lenticular voids formed by agglomeration on the hot grain boundaries lead to the actual densification of the fuel; they form the central void and cause the columnar grain structure (43-51).

A critical review of literature by Clement (163) has confirmed the assumption that the major contribution to the total migration rate of pores larger than 10 μm is made by the evaporation-condensation mechanism. The following velocity relationship obtained by Nichols (43) for the migration of sinter pores has been rejected by Clement (163) as having poor agreement with experimental data:

$$V_p = A\, T^{-3/2} \cdot \frac{dT}{dr} \cdot \exp(-Q/RT) \qquad (3.209)$$

where

V_p = pore velocity

A = constant; function of fuel properties

T = temperature

$\frac{dT}{dr}$ = temperature gradient across the fuel

Q = activation energy $\sim$ 0.590 (MJ/mole)

R = 8.3143435×10^{6} (MJ/mole^{o}K)

Clement has proposed that instead of the $T^{-3/2}$ temperature-dependent factor in Eq.(3.209) a factor of $T^{-5/2}$ which is indicated by the experimental results, to be used. This factor favours the hypothesis that the total gas pressure in the pore is proportional to T according to the gas law. If, however, the pressure were connected to external pressures or were dependent on geometry a $T^{-3/2}$ factor would appear, as in Nichol's model. The velocity, as obtained by Clement (163) is a function of O/U ratio too, i.e.

For $\frac{O}{U} = 2.00$

$$V_p = 1.607 \times 10^{14} T^{-5/2} \frac{dT}{dr} \exp\left(-\frac{73400}{T}\right) \quad (m/day) \tag{3.210}$$

and for $\frac{O}{U} = 2.01$

$$V_p = 2.255 \times 10^{10} T^{-5/2} \frac{dT}{dr} \exp\left(-\frac{46240}{T}\right) \quad (m/day) \tag{3.211}$$

where $\frac{dT}{dr}$ is in $^{o}Km^{-1}$ and T in ^{o}K. He has also given an approximate representation of the available experimental results (164) as

$$V_p = 5.5296 \times 10^{11} T^{-5/2} \frac{dT}{dr} \exp\left(-\frac{53000}{T}\right) \quad (m/day) \tag{3.212}$$

A comparison of the above equations shows that the second equation agrees well with the experiments, provided that the O/U ratio was greater than 2.00 in the central lenticular pore region of the pellets used in the experiments. Since there is a possibility of considerable, though not complete, re-distribution of oxygen to higher temperature regions of the pellets and thus an increase in O/U ratio, it is likely that Eq.(3.211) presents the actual situation.

The migration model in Eq.(3.211) is used in SAMURA. For each annular ring i which is defined by the radii r_i and r_{i+1}, the mean temperature and the porosity are specified. The pores within an annular ring are taken as porosity without being defined more closely. They migrate at the same rate which is determined by the average annular temperature. The mechanics of pore migration between the annular rings is as follows:

1. At the end of each time-step a pore transfer takes place from each ring into its neighbouring ring, which would be the one closest to the centre in the case of normal temperature gradients.
2. The total original solid fuel volume in each ring is held constant, which means the radii of the boundaries follow the fuel. Thus the following balance equation always exists:

$$(1 - P_i)(r_{i+1}^2 - r_i^2) = (1 - \bar{P}_i)(\bar{r}_{i+1}^2 - \bar{r}_i^2) \qquad (3.213)$$

where

P_i = fuel porosity in ring i at the end of time-step

$\bar{P}_i$ = fuel porosity in ring i at the beginning of time-step

r_i = fuel radius at the end of time-step

$\bar{r}_i$ = fuel radius at the beginning of time-step

However, the heat generation rate in each ring is the same fraction of total heat generation rate throughout the power history of the fuel pin.

3. The movement of pores is not assumed to change the stress equilibrium equations directly, but only indirectly to the extent that the ring dimensions and temperature change.

4. When a void crosses a ring boundary it is assumed to take on the pore characteristics corresponding to the ring it enters.

The fraction of porosity which according to the above assumptions migrates from one ring to the next is defined by

$$\Delta P_i = P_i \frac{\Delta t}{r_{i+1} - r_i} V_{p,i} \qquad (3.214)$$

where

P_i = fraction of porosity change

P_i = porosity in ring i

Δt = time-step length

$V_{p,i}$ = pore migration velocity in ring i

The calculation starts from the outer pellet radius (which is assumed to remain constant during pore migration) by establishing the movement of the rings' boundaries through their pore velocities. Then the changes in porosities are determined. Having calculated the porosity for each ring, the new rings radii can be obtained by using Eq.(3.213) starting again from the outer pellet ring.

In order to account for porosity closure due to hot-pressing, it has been assumed that the total change in porosity of any ring is the sum of porosity change due to migration and porosity change due to hot pressing. The latter being calculated by using the bulk creep properties of the fuel according to Small (165). If the creep rate of the bulk material is linearly proportional to stress the volume change rate can be written as

$$\dot{\gamma} = \frac{3}{4} \frac{B.P.\sigma}{1 - P} \qquad (3.215)$$

where

$\dot{\gamma}$ = volume change rate

B = creep bulk modulus

P = porosity

σ = average hydrostatic stress $(= \frac{1}{3} \sum_{p} \sigma_{p})$

The volume change of material is equivalent to the volume change of the pores it is surrounding, thus if $\dot{\gamma}$ from (3.215) is multiplied by the time-step, Δt, the change in porosity due to hot-pressing will be obtained. This is because hot pressing can be looked upon as creep of a porous body in a restrained condition.

An approximate value for the creep bulk modulus, B in Eq.(3.215), can be obtained by using the fuel creep rates given by Eq.(3.185).

Finally, during calculation a minimum porosity which must be observed is fed into the program. The value is 0.02 and was taken from experimental data. As the pores migrate towards the pellet centre, the porosity in that region increases and can reach values as high as 0.80 (164, 169). The maximum porosity for the calculation is, however, a function of migration rate, pellet geometry and the number of radial nodes in the pellet. This is in accordance with the assumption of constant mass in the rings and the movement of ring boundaries towards the centre. The maximum porosity that the code can tolerate is, therefore, the porosity which prevents the second node of the fuel reaching the first node (calculated radius of the second node at the end of a time-step during which some pore migration has

occurred does not become equal to the radius of the first node; especially in the case of solid pellets where the first node is stationary). This can easily be calculated for any particular fuel geometry by running the code once and finding out the point in time where the second node's radius starts decreasing too fast. The porosity in the first ring at that time is the maximum value that can safely be used to avoid any problems. In the present work a maximum porosity of 0.25 was used throughout the calculations. In practice only the central region of the fuel pellet developes very high porosities shortly after the start of irradiation. This eventually leads to the formation of a central hole in solid pellets or the widening of the one already present in hollow pellets. In SAMURA, it is assumed that in the case of solid pellets a central hole can only form after some time of irradiation and during the first reactor shut-down. The radius of this central hole is estimated from the second node's radius and the overall reduction in pellet porosity up to that particular time. If, however, the fuel has been operating at low temperatures (which means no significant pore migration and irradiation induced densification is responsible for porosity loss) only a small radius is assigned to the first node to allow it to crack during the shut-down.

3.5.12 Yield Stress Model

For the reasons stated before (see 3.4.5), there is no yield stress model for UO_2 in SAMURA. Only a very large value is assigned to $\sigma_{y,f}$, fuel yield stress, in most of

of the calculations. There is, however, the option of taking $\sigma_{y,f} = 0$, or a small number at temperatures greater than 1673^{o}K in accordance with the cracking model.

The yield stress model for the cladding, on the other hand, is very important, and accurate models must be used in order to predict the onset of cladding yield.

There are very few available data on the Zircaloy yield stress, specially on irradiated material. Baroch et al (166) and Baroch (167) have conducted a series of tests to determine the effects of irradiation and thermal ageing on the tensile properties of Zircaloy-2 and 4. Both cold-worked and annealed specimens were irradiated to fluences up to 9×10^{20} neutrons/cm^2. The data indicate that, at test temperatures above about 850^{o}K, the unirradiated and irradiated properties are essentially identical for both the cold-worked and annealed Zircaloy. Below 850^{o}K there are significant differences. Furthermore, the properties of irradiated material differ from those of unirradiated material, and these differences in properties increase with decreasing temperature. Irradiation at these temperatures results in an increase in strength and a decrease in ductility of all materials.

Baroch (167) has indicated that the following equation is suitable for predicting the change in yield stress as a function of fluence:

$$\Delta\sigma_{y,c} = A(1 - e^{-B\phi t})^{\frac{1}{2}} \qquad (3.216)$$

where

$\Delta\sigma_{y,c}$ = change in cladding yield stress (MPa)

A = constant, for cold-worked Zr, A_{CW} = 248.21(MPa); and for annealed Zr, A_{AN} = 406.80 (MPa)

B = constant, function of temperature, etc. The following equations have been fitted to the available data (166-167):

For cold-worked and annealed Zr, respectively,

$$B_{CW} = -2.1568 \times 10^{-21} + 1.1750 \times 10^{-23} T_c - 1.1676 \times 10^{-26} T_c^2$$

$$B_{AN} = 3.2044 \times 10^{-21} - 1.1700 \times 10^{-23} T_c + 1.1416 \times 10^{-26} T_c^2$$

where T_c is the cladding temperature,

ϕ = neutron flux, ($n/cm^2 s$), and

t = time (s)

The value of $\Delta\sigma_{y,c}$ calculated from (3.216) must be added to the yield stress value obtained from unirradiated test results.

The variation of yield stress with temperature are given in tabulated form in SAMURA. Two sets of data, one for cold-worked, $\sigma_{y,c}$(CW), and the other for annealed, $\sigma_{y,c}$(AN), Zircaloy are provided as follows:

Temp. ^{o}K	$\sigma_{y,c}$(CW), MPa	$\sigma_{y,c}$(AN), MPa
588	399.61	181.34
644	393.99	181.34
700	371.47	181.34
755	315.19	164.34
810	213.88	138.83
866	129.45	107.67
922	92.87	88.17
977	67.54	59.50
1033	50.65	50.65
1088	33.77	33.77
1144	19.70	28.33

The appropriate value of unirradiated Zircaloy yield stress at any desired temperature is returned by a special interpolation routine in SAMURA, using the above table. Then the increase in yield stress is calculated from Eq.(3.216) and added to the unirradiated value of yield stress.

It is felt that the model used here may not be always accurate, specially there is some doubt about the validity of the methods used to establish "A" in Eq.(3.216) of irradiation work-hardening (167). Also, the Zircaloy clad anisotropy has not been included in the first version of SAMURA.

3.6 ERROR ANALYSIS AND THE CONTROL OF TIME-STEP

In a complicated program as SAMURA, the establishment of the time-steps used for integration can be critical. This must influence the balance between convergence of the results and the computer running time. This implies that the time-steps must be controlled by means of reference to error checks and an accuracy criterion.

There are three principal sources of error in the solution methods employed in SAMURA. The first error is due to the finite difference representation of the spatial derivatives, the second source of error lies in the numerical approximation of time derivatives and the third error arises from the truncation of the Taylor series expansion of the creep equations. The spatial grid must be chosen to adequately represent the variables, but for reasons of convenience, no attempt is made to vary the grid as a function of time. The other sources of error are, however, very crucial and must be checked. The Taylor series error is checked for, by comparing the creep rates obtained from the full creep law as given in Eqs .(3.116-3.118), with the creep rates calculated from Taylor series expansion in Eq.(3.121). The error introduced by the time dependence of the equations and its numerical approximation is dealt with in more detail since this is the factor that controls the time-steps.

This error arises from the time-differences we defined in Eqs.(3.114) and (3.115). In fact, if they are combined we have

$$\frac{\Delta \dot{V}}{\Delta t} = \theta . \dot{V}(t) + (1 - \theta) . \dot{V}(t - \Delta t) \qquad (3.127)$$

This is the equation that was used to approximate the time dependence of creep equations (see Eqs.(3.116-3.118), i.e.

$$\frac{\gamma^{j} - \gamma^{i-1}}{\Delta t} = \theta(P^{j} + F^{j}(\sigma)) + (1 - \theta)\ (P^{j-1} + F^{j-1}(\sigma)) \qquad (3.218)$$

represents

$$\frac{\partial \gamma}{\partial t} = P + F(\sigma) \qquad (3.219)$$

Note that here only a single dimensional equation has been used to describe the plastic strain rate. This is only to simplify the analysis. Now if we look at the behaviour of Eq.(3.219) the error caused by the numerical method can be obtained according to the Hayns and Wilmor analysis (9).

Since all the elastic equations relating the stresses, σ, to the strains and displacements are linear, the approximation may be made that σ is a linear function of γ so Eq.(3.219) becomes:

$$\frac{\partial \gamma}{\partial t} = a + b\gamma \qquad (3.220)$$

If a and b in Eq.(3.220) are taken to be constant over the time-step, then this equation gives a good description of the behaviour of γ. The solution of Eq.(3.220) is

$$\gamma = A \exp(bt) - \frac{a}{b} \qquad (3.221)$$

where A is an integration constant.

Now, to estimate the errors in the numerical method it is necessary to determine the difference between the correct values of γ at time j and those calculated numerically. Using the approximation (3.218) by reference to (3.219) gives

$$\frac{\gamma^j - \gamma^{i-1}}{\Delta t} = \theta . \frac{\partial \gamma^j}{\partial t} + (1-\theta) . \frac{\partial \gamma^{j-1}}{\partial t} \qquad (3.222)$$

which will provide an exact solution for some value of between 0 and 1. If the approximation of (3.222) is used to solve (3.220) we obtain

$$\frac{\gamma^j - \gamma^{j-1}}{\Delta t} = \theta(a + b\gamma^j) + (1 - \theta)(a + b\gamma^{j-1})$$

or when solved for γ^j

$$\gamma^j = \gamma^{j-1} + \Delta t(a + b\gamma^{j-1})/(1 - \theta b\Delta t)$$

The second term may be expanded to give

$$\gamma^j = \gamma^{j-1} + \Delta t(a + b\gamma^{j-1})(1 + \theta b\Delta t + (\theta b\Delta t)^2 ..) \qquad (3.223)$$

And the expansion of the exact solution (3.221) is

$$\gamma^j = \gamma^{j-1} + \Delta t(a + b\gamma^{j-1})(1 + \frac{b\Delta t}{2!} + \frac{(b\Delta t)^2}{3!} + ...) \qquad (3.224)$$

Comparison of (3.223) and (3.224) gives the error E

$$E = \Delta t(a + b\gamma^{j-1})[(\theta - \tfrac{1}{2})b\Delta t + (\theta^2 - \tfrac{1}{6})(b\Delta t)^2 + ..] \qquad (3.225)$$

In order to use this equation, the parameters, a and b must be related to real quantities that can be evaluated in the program. Since $\frac{\partial \gamma}{\partial t} = \dot{\gamma}$, from (3.22o) we have

$$\dot{\gamma}^j - \dot{\gamma}^{j-1} = b(\gamma^j - \gamma^{j-1})$$

For small Δt, $\dot{\gamma}^{j-1} \simeq \frac{\gamma^j - \gamma^{j-1}}{\Delta t}$ and from (3.220) $\dot{\gamma}^{j-1} = a + b\gamma^{j-1}$, hence

$$b\Delta t(a + b\gamma^{j-1}) = \dot{\gamma}^j - \dot{\gamma}^{j-1} \qquad (3.226)$$

It can also be assumed that $(a + b\gamma^{j-1}) \simeq \frac{\dot{\gamma}^j + \dot{\gamma}^{j-1}}{2}$; so from (3.226) we obtain

$$(b\Delta t)^2(a + b\dot{\gamma}^{j-1}) = \frac{2(\dot{\gamma}^j - \dot{\gamma}^{j-1})^2}{\dot{\gamma}^j + \dot{\gamma}^{j-1}} \tag{3.227}$$

When (3.226) and (3.227) are substituted into (3.225) E can be written as

$$E = (\theta - \tfrac{1}{2})(\dot{\gamma}^j - \dot{\gamma}^{j-1})\Delta t + (\theta^2 - \frac{1}{6})\frac{2(\dot{\gamma}^j - \dot{\gamma}^{j-1})^2}{\dot{\gamma}^j + \dot{\gamma}^{j-1}}\Delta t \tag{3.228}$$

Here $\dot{\gamma}^j$ is the effective creep rate during the present time-step and $\dot{\gamma}^{j-1}$ the effective creep rate from the previous step. It can be seen that for $\theta = \frac{1}{2}$ the first order terms vanish and this is the value of θ that is used in SAMURA. E is the error term evaluated in SAMURA. It must be noted that Eq.(3.228) is evaluated for all the nodes in the radial grid and the maximum value is chosen to be used in the estimation of a new time-step.

It is difficult to assess the time-steps required for a particular calculation since a small step is required in times of rapid variations of the stresses and temperatures, but much larger steps may be taken when the variations are slow. Consequently a method has been incorporated into the program whereby the time-steps are fixed by means of reference to error checks and an "accuracy criterion". In this way the user merely controls the overall "accuracy, the program then fixes the time-steps automatically. The default value of the error criterion is ½%, but it can be varied if more accurate or less accurate calculations are needed. The errors are then divided by the error criterion. The peak relative error is calculated for each region separately. If any of them is greater than 5, i.e. 2½%

the step is then repeated with a shorter time-step which ensures the peak error to have an acceptable value. This is explained below.

When the calculation in the present time-step produces unacceptable error in any region, then this peak error is used together with the error from the previous time interval to estimate a new time-step where the error will be 1, i.e. ½%.

As in FRUMP (9), the error E and the time-step t are assumed to be related through an expression of the form

$$E = A.(\Delta t)^n \tag{3.229}$$

The unknowns A and n can be determined by using the values of Δt^j, Δt^{j-1}, E^j and E^{j-1}; which are known:

$$n = \frac{\ell n(E^j/E^{j-1})}{\ell n(\Delta t^j/\Delta t^{j-1})} \quad , \quad A = E^j/(\Delta t^j)^n \tag{3.230}$$

Then we can calculate a new time-step, Δt , which ensures an error of 1, by putting E = 1 in (3.229) and taking the logarithm of each side

$$0 = \ell n\ A + n\ \ell n(\Delta t\ )$$

$$\therefore \Delta t\ = \exp\ (-\frac{1}{n}\ \ell n\ A)$$

and from (3.230)

$$\Delta t\ = \frac{\ell n(\Delta t^j/\Delta t^{j-1}).\ell n\ E^j}{\ell n(E^j/E^{j-1})} - \ell n\ \Delta t^j \tag{3.231}$$

This will be the new time-step. However, if Δt from Eq.(3.231) is higher than Δt^j and E^j less than one or if

Δt is less than Δt^j but E^j greater than one, the above method is not used. Instead, a simple approach is made by assuming the error of the next step to be

$$E = (E^j)^{0.1} \tag{3.232}$$

and

$$\Delta t = \frac{\Delta t^j}{E} \tag{3.233}$$

The variation of E is furthermore restricted by the following conditions;

if $E < 0.1$ then $E = 0.1$

and if $E > 1.0$ then $E = 10.$

Therefore it is always ensured that neither a step can be lengthened by more than ten times in one step, nor it can be shortened to less than a tenth.

The time-step thus calculated is further checked by two other controls. The first check is on the fuel centre temperature rise during the time-step, which is restricted to $50^{\circ}K$. If T_1 is the fuel centre temperature, the time-step length that satisfies the above condition is

$$\Delta t_1 = \frac{50.\Delta t^j}{(T_1^j - T_1^{j-1})} \tag{3.234}$$

The second check is on the rate of gap closure. To avoid any "overshooting" and obtain a smooth closure, we assume the rate of gap closure to be linear thus

$$\Delta t_2 = \frac{\Delta t^j . GAP^j}{(GAP^j - GAP^{j-1})} \tag{3.235}$$

where GAP^j and GAP^{j-1} are the new and old gap widths. The program then uses the minimum of the three time-steps Δt, Δt_1, and Δt_2.

3.7 DESCRIPTION AND MODE OF OPERATION OF THE CODE

The code is written in FORTRAN-IV, and developed on CDC-6500, 6600 machines at Imperial College and the University of London Computer Centre. Great care is taken to use the simplest and most straightforward standard FORTRAN statements. The only optimisation employed in the code is to allocate the same computer location to all those dimensional variables which are used only once during a time-step. This reduced the size of the program to a great extent and made it possible to run SAMURA with only about 40K bytes of storage (compare this, for instance, with FRUMP (9), LIFE (3), and BEHAVE (5)). Of course, any future additions may increase the storage requirements of the code. However, it is not expected that the program should use more than 60K bytes (which is the maximum available storage at Imperial College under normal circumstances) in any future development.

The flow-diagram of the code is shown in Fig.3.8. It can be seen that apart from the main central routine, also called SAMURA, there are 34 other subroutines. In this section we describe these subroutines and the operation of the program. Details of the actual manipulation of the program in terms of input and output and the definition of all the variables used are given in Appendix A.

The code can be divided into 5 groups of subroutines. The first group consists of the main central routine SAMURA, input data subroutine, PROBLM, and PRINTX, results output subroutine. The second group of subroutines starts

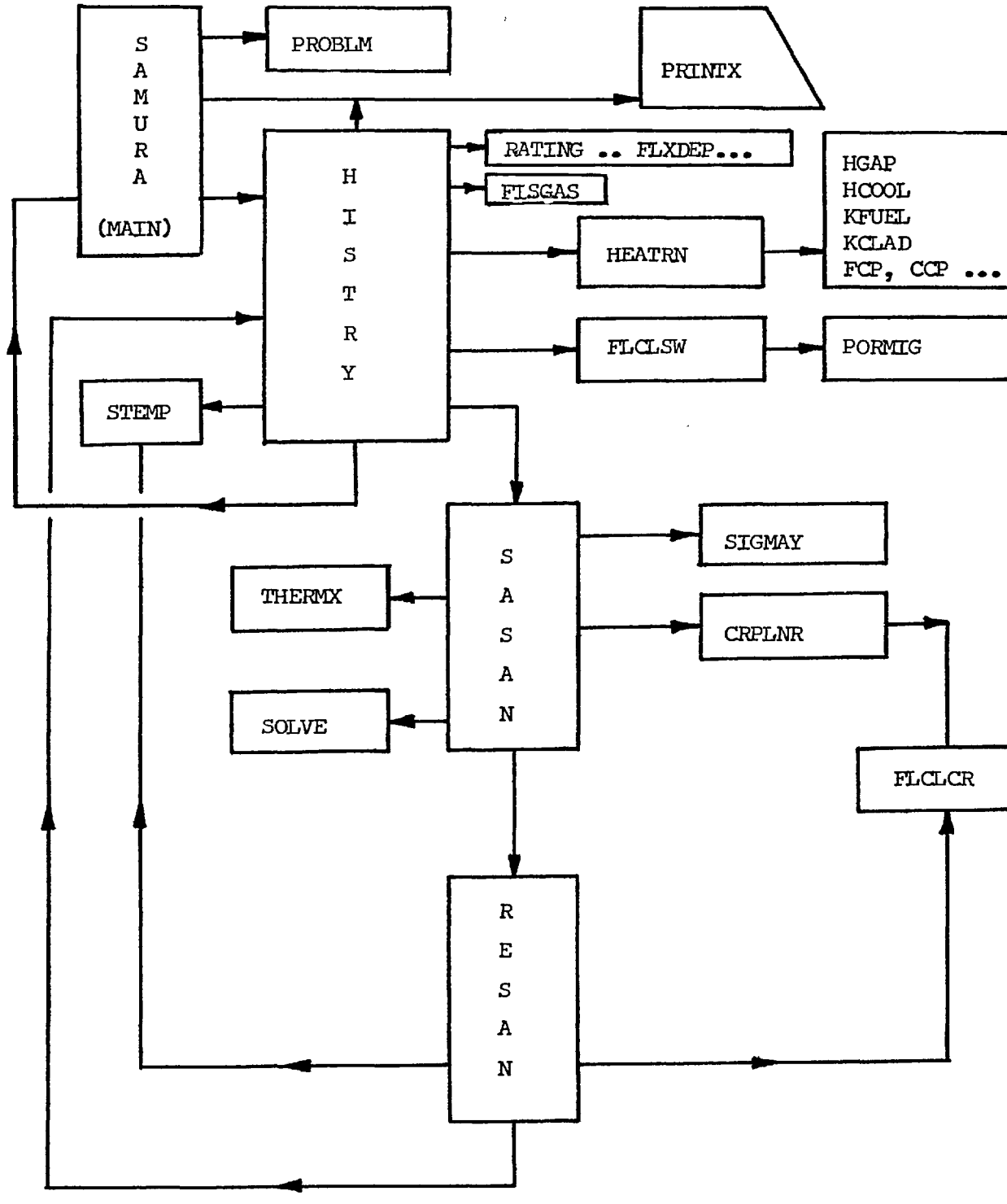
with HISTRY, which controls the power history and all the calculations. The rest of subroutines in this group, i.e. PHYPRO, RATING, FLXDEP, COOLAN and FISGAS, prepare the necessary information for the thermal analysis. The third group deals with all the thermal calculations, like thermal expansions, specific heats, conductivities, gap heat transfer, swelling, porosity migration and temperature distribution. These subroutines are HEATRN, FTXP, FCP, KFUEL, GCP, CCP, KCLAD, CATXP, CDTXP, HGAP, GCON, HCOOL, STEMP, THERMX, FLCLSW and PORMIG. The fourth group of subroutines are connected with the assembly of the mechanical analysis matrix, linearisation of creep equations and error analysis. They are SASAN, SIGMAF, ELMOD, SIGMAY, CRPLNR, FLCLCR, and RESAN. The final group are the interpolation routine POLATE, matrix inversion and solution routine SOLVEX, and BLOCK DATA which initialises some of the variables. In what follows we describe each of the above subroutines in more detail.

SAMURA: This is the main control program. All the main variables, stresses, strains, temperatures, creep rates, swelling rates, displacements, matrix coefficients, etc., which are transferred to the rest of the program through BLANK COMMON are initialised here. Then PROBLM is called to define the input data and the problem to be solved. The radial mesh is set up and the input for each "period" is defined. Periods are obtained by partitioning of the power history into certain parts, as desired by the user, that cover a time during which the linear power is changing in a similar way, i.e. up-ramp, down-ramp or steady-state.

Figure 3.8

FLOW DIAGRAM OF COMPUTER PROGRAMME "SAMURA"

(Note that only the main calculation SUBOUTINES are shown here.)



Then the HISTRY subroutine is called which controls the rest of the program. If need be the PRINTX subroutine can also be called after each call to HISTRY to print out the results.

PROBLM: Through special "keywords", as explained in Appendix A, this subroutine reads in the necessary input data*. The fuel and cladding radii and their initial physical properties are read here. The data on periods is read too. At present the program can handle up to 50 periods, but extension to a larger number is trivial. Each period has its own set of data, i.e. starting time-step, which is obtained by multiplying the length of the period by 10^{-5}, type of power variation, etc. Currently three types of power change, linear increase or decrease and steady-state, can be allowed. However, the inclusion of non-linear power ramps is again very simply implemented. Periods can be steady-state or transient from the viewpoing of thermal analysis. The time variations are always in days, but when a transient period is being used the period duration and time-steps are changed to seconds by the use of a code-word.

The spatial variations are handled by means of "regions". Each region is defined by a particular set of data in PROBLM. The material properties of regions are given by

*Contrary to most of the other codes, SAMURA has a relatively simple and small input data. This is because all the fuel and cladding material properties for water reactors are written into the code as separate subroutines. In this way the user who studies water reactors does not have to supply any material data to start with, and further reduces the chances of making any mistakes in input material data; which could be disastrous. Nevertheless, these data sub-routines may easily be replaced by other data if desired.

independent subroutines throughout the code. Up to 10 such regions can be used, but in all of the early calculations only 2 have been used, one describing the fuel and the other the clad. In future developments these regions may be extended to cover the different states of the fuel at varying radii, e.g. the inner columnar grain growth region, the equiaxed grain region and the outer unrestructured region. Further use of the regions can be made by defining cracked and uncracked regions, for cracks in the r and z directions whilst cracks in the θ direction may be defined as gaps between already established regions. PROBLM also reads in the number of mesh-points in each region. The maximum total number of points in all regions has been set at 200. The experience with the program has indicated that 200 points is more than sufficient for most applications.

Finally, PROBLM prints out all the data it has read, to enable the user to make all the necessary references or modifications to it.

PRINTX: This subroutine has the function of printing out the calculated values of up to 24 variables at every mesh-point plus a number of other important quantities. The variables desired to be printed out can be decided upon by some input code-words. These variables include radii of mesh-points, temperatures, stresses, elastic, creep, plastic, cracking and swelling strains, porosity, displacements, etc.

The call to PRINTX can be monitored by the user. It may be called at certain specified times or after every

certain number of steps. However, after significant changes like gap closure, gap opening or central void opening have occurred a call to PRINTX is made through HISTRY automatically.

HISTRY: As its name implies, HISTRY deals with pin power history and periods. All the program is controlled from here; control returns to SAMURA only when enough time-steps have been taken to end a pin period. So the call to a whole set of subroutines is repeated by HISTRY every time a new time-step is started.

HISTRY starts with calculating the total time and period time elapsed and ensuring that the chosen time-step will not cause overshoot of the calculation to the next period. Then it makes an estimate of the temperature, using Eq.(3.10), and calls some preliminary subroutines which provide physical properties (initial values), fuel linear power, flux distribution, coolant or cladding outer temperature (whichever is desired, see Sub-Section 3.3.2) and fission gas release. This is preparatory information for the thermal analysis subroutines; which are called by HISTRY through calls to HEATRN, STEMP and FLCLSW. Finally SASAN, the stress and strain analysis subroutine is called.

Return of control from SASAN will give an indication of whether the calculation during the present time-step has been acceptable (low errors) or unacceptable where the calculation has to be repeated. This is done by returning the parameter NWSTEP = 1, which means a repetition of the step. After a successful calculation, HISTRY investigates the

behaviour of the gap in order to predict the time at which it will close or open. It also modifies the new time-step to ensure a fuel centre temperature rise of not more than $50^{o}K$ and a smooth gap closing. Calls to PRINTX are made if any major changes occur.

PHYPRO: This subroutine provides some of the basic initial physical properties of the fuel and clad. These include solidus temperature, liquidus temperature, latent heats, cladding phase transformation temperatures, solid and liquid material densities.

RATING: Here we calculate the present fuel rating in the form of linear power density. The rating is estimated by linear relationship between the ratings at the beginning and the end of period.

RATING also calculates the fuel burn-up by multiplying the average power density rating (Watts/gramme) by Δt (in days).

FLXDEP: The equations given in Sub-Section 3.3.7 for flux depression are evaluated here. The radial flux at fuel surface is also calculated.

COOLAN: The changes in coolant temperature are calculated here by using a linear relationship between the coolant temperature at the beginning and the end of any period.

The coolant temperatures are automatically re-named as cladding temperatures, through a code-word, if the input data indicates so.

FISGAS: Fission gas production, release and internal pressure are calculated by FISGAS using the equations in Sub-Section 3.5.10.

Since the filling gas pressure is known at the beginning of fuel pin life, FISGAS determines the number of filling gas moles at the start of first time-step. In the calculations after that these moles are added to the number of released fission gas moles to estimate the total pressure.

It must be noted that because the fission gas moles are accumulating during the power history, at the beginning of every step these values are saved, only to be referred to in the case of step repetition with a new length.

There is an optional form of FISGAS which only calculates the fission gas pressure by using an input empirical pressure relationship.

HEATRN: This subroutine calculates the temperature distribution in fuel and cladding according to Sub-Sections 3.3.1 to 3.3.3.

HEATRN can be divided into four parts. The first part sets up the radial mesh; see Fig.3.3. A comparison of the mesh used for mechanical analysis, Fig.3.7, with the mesh in Fig.3.3 for thermal analysis shows that the nodes in the latter matches the mid-point nodes of the former. However, the variables like temperature, stress, etc. are calculated for the same common nodes of the two grids. The number of mesh-points is, therefore, the same, but there is one more ring in the thermal analysis mesh as can be seen in Fig.3.3.

This is why a new parameter (RT) is used to define the radii.

In the second part of HEATRN, the average temperatures are estimated and then the thermal conductivities, densities and heat capacities are calculated for every mesh-point; through calls to appropriate material property subroutines. In this part the fraction of molten fuel is estimated too. This affects the values of fuel heat capacity.

The third part deals with the setting up of all the matrix equation coefficients; Eq.(3.30). It starts with calculating α_i and β_i (see Sub-Section 3.3.1) and then forms the A(i), B(i) and C(i) coefficients. During these computations two code-words are used which decide on transient or steady-state form of the solution as well as on the boundary conditions to be used, i.e. cladding outer surface temperature or coolant temperature.

Finally, in the fourth part, the Gauss elimination method is used to solve the matrix equation. The control is then returned to HISTRY.

A point must be noted here. Since the temperature and stress-strains calculations are performed separately in SAMURA, small errors can arise during steady-state calculations. These errors may propagate from step to step and lead to instability. This is specially true when the gap is small and approaches closure. Instead of using an iterative method to deal with this problem a simple method developed for FRUMP (9) is adopted and presented by the subroutine called STEMP. This will be explained later.

FTXP: This function-subroutine estimates the linear thermal expansion of UO_2, as given by Eqs.(3.171) to (3.173). FTXP is a function of fuel temperature, fraction of molten fuel, burn-up and melting temperature.

FCP: Here Eqs.(3.164-3.166) are used to calculate the heat capacity of UO_2. The input parameters are, fuel temperature, fraction of molten fuel and fuel melting temperature.

KFUEL: KFUEL is a function-subroutine for the calculation of fuel conductivity as a function of fuel mesh-point temperature and porosity. Eqs.(3.167) and (3.168) are used here.

GCP: This function-subroutine calculates the gap gas heat capacity as a function of gap temperature. This facilitates the inclusion of gap properties in the temperature calculations.

CATXP,CDTXP: These two function-subroutines estimate the cladding linear thermal expansion in the axial and diametral directions respectively. Since some of the data is in the form of a table, $(\Delta\ell/\ell,T)$, a call to POLATE, the subroutine for linear interpolations, is made in both subroutines. The equations given in Sub-Section 3.5.4 for Zircaloy are used here.

CCP: Here we calculate the heat capacity of Zircaloy cladding according to the data discussed in Sub-Section 3.5.1. Again the data is in tabular form, (Cp,T), and POLATE must be called.

KCLAD: This function-subroutine calculates the thermal conductivity of Zircaloy cladding using Eq.(3.168).

HGAP: The function-subroutine HGAP calculates the fuel/clad gap conductance. The input variables are gap width and gap average temperature.

HGAP has two preliminary sections which deal with the calculation of volume fraction of the gases present in the gap (estimated from their partial pressures), and the estimation of radiation heat transfer term as given by Eq .(3.44). Then the control is transferred to either of the two sections which calculate the closed-gap or open-gap conductance. At the end the radiation term is added to either of the closed-gap or open-gap conductance terms.

During HGAP calculations calls are made to a gas conductivity subroutine, GCON, which is described below.

GCON: This function-subroutine calculates the gas conductivity of gap gas mixture with a correction made for Knudsen effect, if necessary. The details of equations are given in Sub-Section 3.3.5. The input parameters are volume fraction of gases (calculated in HGAP), mixture temperature and pressure, and gap width. Seven gases are considered and the order of their appearance in the calculation (as indicated by an index I which varies from 1 to 7) is He, Ar, Kr, Xe, H_2, N_2 and H_2O.

HCOOL: This function-subroutine is called by HEATRN whenever the coolant film heat transfer coefficient is needed in temperature calculations.

There are two options of HCOOL: one uses an input constant value for h_{cool}, see Eq.(3.5.1), and the other tries to estimate h_{cool} from coolant input data according to Eq.(3.51).

STEMP: This is the subroutine that was mentioned in HEATRN to connect temperature-strain calculations. As discussed, since temperature and strain-stress calculations are performed separately in SAMURA, during steady-state periods errors may arise. This is basically because the temperatures are calculated first and then these new temperatures are used to estimate strains and stresses. Obviously, the new temperatures might affect the gap width, thus changing the gap conductance and temperatures again. An approximate method is used in STEMP in order to make a small correction to all strains and temperatures at the end of every temperature or strain calculation to balance the system and avoid the propagation of errors.

In STEMP, we assume there is a small uniform temperature change Δt that can be made across the fuel in order to couple the stresses and temperatures without major errors. This will change the gap conductance. Since the heat fluxes remain constant after this change, the new gap conductance is

$$h_{gap}^{(1)} = \bar{h}_{gap} \cdot \overline{\Delta T} / (\Delta T + \overline{\Delta T}) \qquad (3.236)$$

where $\bar{h}_{gap}$ is the old conductance and $\overline{\Delta T}$ the old temperature difference across the gap.

The gap conductance as calculated from HGAP is a function of T_{gap}, the gap temperature and W_{gap} the gap width. So h_{gap} can also be estimated this way, by first introducing the effect of T on gap width. This is done by using the fuel thermal expansion:

$$W_{gap} = \bar{W}_{gap} - r_{N,f}\, \alpha_f \cdot T \qquad (3.237)$$

where

$\bar{W}_{gap} = r_{1,c} + u_{1,c} - (r_{N,f} + u_{N,f})$, the old gap width

$r_{1,c}$ = cladding inner radius

$u_{1,c}$ = cladding inner radial displacement

$u_{N,f}$ = fuel outer radial displacement

α_f = fuel thermal expansion coefficient

The new gap temperature from the inner clad temperature, $T_{1,c}$;

$$T_{gap} = T_{1,c} + \tfrac{1}{2}\,(\Delta T + \overline{\Delta T}) \qquad (3.238)$$

Eqs.(3.237) and(3.238) are then used to call HGAP, i.e.

$$h_{gap}^{(2)} = \text{HGAP}\,(W_{gap},\, T_{gap}) \qquad (3.239)$$

The difference between the conductances from (3.236) and (3.239), s, is the error

$$s = h_{gap}^{(1)} - h_{gap}^{(2)} \qquad (3.240)$$

To ensure a quick convergence the real value of ΔT must make $s = 0$, thus if s_1 and ΔT_1, and s_2 and ΔT_2 are two consecutive trials, a new estimate of ΔT is made from

$$\Delta T = \frac{\Delta T_2 \cdot s_1 - \Delta T_1 \cdot s_2}{s_1 - s_2} \qquad (3.241)$$

When this procedure leads to sufficient convergence, the final ΔT and $\alpha_f . \Delta T$ are used to correct the temperatures

and strains in STEMP. It must be noted that STEMP is only called when the gap is open and a steady-state calculation is being performed. There is sufficient damping in transient cases and no significant errors will occur.

THERMX: This subroutine calculates the fuel and cladding linear thermal expansion $\alpha_i \Delta T_i$.

The fuel and cladding volumetric thermal expansions are first calculated for a reference input temperature (normally $T_{ref} = 293^{o}K$). Then the volumetric expansions are estimated for the current temperature of every fuel and cladding node.

The volumetric expansion from a volume $V_{ref,i}$ to V_i can be written as follows

$$V_i = V_{ref,i}(1 + \alpha T)^3$$

From here αT can be determined for any node i,

$$(\alpha T)_i = \left[\frac{V_i}{V_{ref,i}}\right]^{1/3} - 1 \qquad (3.242)$$

This is the equation used in THERMX for αT.

FLCLSW : Here we calculate the swelling rates of fuel and cladding. UO_2 swelling is equal to the algebraic sum of densification and volume changes calculated from Eq.(3.192). At the moment the lower rate of densification is estimated by using Eq.(3.215). As more accurate models become available the function DP(I), which represents densification in FLCLSW, can be modified or changed.

Since there has been no report on Zircaloy swelling, this is taken as zero in FLCLSW.

Before FLCLSW starts its calculations, it makes a call to PORMIG, pore migration subroutine, if a code-word and the value of fuel outer ring porosity indicate so.

PORMIG: If the porosity in the fuel outer ring is greater than 0.02 and pore migration calculation is required, a call to PORMIG is made from FLCLSW.

Here the pore migration velocity, Eq.(3.211) is incorporated into PORMIG. Using the fuel rings temperatures and temperature gradients, this velocity is calculated. Note that rings rather than mesh-points are used here; i.e. if there are N radii in the fuel we have N-1 rings.

The velocities are then used to estimate the movement in boundaries and porosity changes. Hot-pressing effects are also calculated. Then the mean fuel ring porosity is the algebraic sum of the porosity calculated from pore migration and hot-pressing rate multiplied by time-step length. The mean ring porosities obtained in this way are later put into mass balance equation (Eq.(3.213)) to determine the new radius of each ring. A minimum radius for the first node must be observed ($r_1 = 10^{-5}$) if we are dealing with hollow pellets. This is true for solid pellet too, once a central void is formed the central hole cannot close to a radius smaller than 10^{-5}. The innermost radius of solid pellets, however, is kept stationary (10^{-60}) until the time when a central hole opened. At the moment this can occur only during reactor shut downs where the stresses are tensile in the centre.

Finally, the mesh-point porosities are calculated from the mean ring porosities. A minimum porosity of 0.02 is assumed at all times.

SASAN: This is the main subroutine in the thermal mechanical analysis group of subroutines. SASAN is called from HISTRY at the beginning of every time-step. Its main purpose is to set up the matrix equation (3.144) coefficients. When the matrix is assembled the matrix inversion routine SOLVEX is called. SASAN then makes a series of tests of the situation in the fuel and cladding to find out if a major change has occurred on the present time-step. If any changes are predicted, like fuel cracking, gap closure, etc., the whole SASAN calculations are repeated until an equilibrium state is obtained. Finally a call to RESAN is made which is the subroutine for error analysis. More detailed description of SASAN follows.

At the start of calculation in SASAN, most of the arrays which store matrix coefficient are zeroed in order to avoid any unwanted values appearing in the matrix. This is because these arrays are used in other subroutines for the storage of other variables to save computer space. The boundary conditions are then set. These are fuel inner and outer radial stress, cladding inner and outer radial stress (= - pressure) fuel and cladding axial forces and residual stresses. Then CRPLNR is called. This is the creep linearisation subroutine and provides the coefficients needed for Eq.(3.121).

After a call to THERMX for $(\alpha T)_i$ values, a DO loop calculates all the $a_{k,i}$ coefficients as given in (3.131). During this calculation tests are made to find out if the fuel is cracked; if so, $a_{k,i}$ coefficients are corrected in the manner described in Sub-Section 3.4.4 and an appropriate cracking control parameter (an integer) is set equal to 1 for cracked rings and to 0 for uncracked rings. There are some more code-words (again integers) which by their values define a certain ring or radial position (see Appendix A for detailed definitions). Thus while the DO loop index varies from 1 to NL (last node) the control is transferred to the appropriate ring or part of the subroutine by the help of these code-words. This is specially important in the next DO loop which calculates matrix coefficients. The coefficients are those given by (3.133) and (3.135) as well as those used in Eqs.(3.136), (3.139), (3.140), and (3.141) or (3.142). The coefficients of u_{i+1}, u_i, $\gamma_{r,i}$, $\gamma_{r,i+1}$, $\gamma_{\theta,i}$ and $\gamma_{\theta,i+1}$ are all stored in the array called A(i,j,k), where i = 1,3, j = 1,7 and k = 1,NL. The coefficient of Z are stored by B(i,k) array; i = 1,3, k = 1,NL, and the constant values in the matrix by C(i,k); i = 1,3 and k = 1,NL. The relations of A, B and C arrays with the original coefficients are (see Eqs.(3.133 and 3.135)):

$$
\begin{aligned}
A(1,j,k) &= A^{(r)}_{j,k} \quad , \quad j = 1,4,\ k = 1,NL \\
A(2,j,k) &= A^{(\theta)}_{j,k} \quad , \quad j = 1,4,\ k = 1,NL \\
A(3,j,k) &= B_{j,k} \quad , \quad j = 1,7,\ k = 1,NL \\
B(1,k) &= A^{(r)}_{5,k} \quad , \quad k = 1,NL \\
B(2,k) &= A^{(\theta)}_{5,k} \quad , \quad k = 1,NL \\
B(3,k) &= B_{8,k} \quad , \quad k = 1,NL \\
C(1,k) &= A^{(r)}_{6,k} \quad , \quad k = 1,NL \\
C(2,k) &= A^{(\theta)}_{6,k} \quad , \quad k = 1,NL \\
C(3,k) &= B_{9,k} \quad , \quad k = 1,NL
\end{aligned}
\tag{3.243}
$$

The coefficients of Eq.(3.136) are stored in F,D and E arrays in the following manner:

$$
\begin{aligned}
F(1,k) &= F_{1,k} \quad k = 1,NL \\
F(2,k) &= F_{2,k} \quad k = 1,NL \\
F(3,k) &= F_{3,k} \quad k = 1,NL \\
D(j) &= D_j \quad j = 1,NREG \\
E(j) &= E_j \quad j = 1,NREG
\end{aligned}
\tag{3,244}
$$

where NREG is the number of regions considered.

These coefficients are then modified or replaced if plastic deformation occurs in the fuel or cladding. Here the coefficients of Eqs.(3.160) and (3.163) are used.

The SOLVEX subroutine is then called to solve the matrix equation. On return from SOLVEX all stresses, irreversible strains and displacements are known. Small corrections are made here for the boundary conditions. Now these results are used to calculate the composite strains defined by Eq.(3.150). Some tests are made in order to estimate the value of cracking strains and separate the

elastic from cracking strains. Then more checks are made to see if other major changes have occurred, i.e. plastic deformation, opening or closing of the central void, and opening or closing of the fuel/clad gap. If this is the case, a code word will send the control back to the beginning of the first DO loop and the calculation is repeated until the same state is obtained twice. This is the only major iteration in the program apart from the case where the whole calculation as started from HISTRY is repeated due to un-acceptable level of errors.

SASAN calls the subroutine RESAN at the end of a successful calculation for the analysis of errors.

SIGMAF: This subroutine sets the values of fuel and cladding fracture stresses according to Sub-Section 3.5.9.

ELMOD: Here we calculate the elastic moduli, Young's modulus and Poisson's ratio for fuel and cladding. These are used to determine their shear modulus as required in SASAN calculations. The data is taken from Sub-Sections 3.5.5 and 3.5.6.

SIGMAY: This subroutine is called at the start of SASAN and is required to calculate the fuel and cladding yield stress at every mesh-point. These are stored in YS(i) array.

Two sets of tabular data in the form of (YS(i),T) are provided for cold-worked and annealed Zircaloy respectively. Irradiation work-hardening for Zircaloy is estimated as described in Sub-Section 3.5.12 and stored in DELYS. This value is then added to the unirradiated Zircaloy yield stress to obtain the final YS(i).

Here calls are made to POLATE to interpolate the data for desired temperature.

CRPLNR: This is the subroutine used to calculate the coefficients of Eq.(3.121) by differentiating the creep equations. Appendix B gives the form of differentiation performed within CRPLNR.

In order to expand the creep equations about a point which gives the minimum errors, the stresses are extrapolated from the previous two steps in the following manner:

$$\sigma^{o}_{p,i} = \sigma^{j-1}_{p,i} + \frac{\Delta t^{j}}{\Delta t^{j-1}} (\sigma^{j-1}_{p,i} - \sigma^{j-2}_{p,i}); \quad (p \equiv r,\theta,z) \tag{3.245}$$

where

$\sigma^{o}_{p,i}$ = the estimated stress at time j about which the the Taylor expansion is made

$\sigma^{j-1}_{p,i}$ = stress in p direction at time j-1

Δt = time-step

These stresses are then used to calculate an effective stress which is used to estimate creep rates (by a call to FLCLCR). Another call is made to FLCLCR with a new effective stress which differs with the previous value only slightly ($10^{-4}\ \sigma_e$) to obtain a new creep rate. The difference between these two creep rates divided by the difference between their corresponding effective stresses (i.e. $10^{-4}\ \sigma_e$) provides $\partial\dot{g}/\partial\sigma_e$, which is needed in the calculation of P and Q coefficients of Eq.(3.121); see Appendix B.

This procedure is repeated until all the nodal points have their P and Q coefficient calculated.

FLCLCR: As mentioned already FLCLCR is used to determin the fuel and cladding creep rates according to Sub-Section 3.5.7. Each call to FLCLCR calculates the creep rate in only one mesh-point.

The values of fuel and cladding creep equation coefficients are all stored in an array called CC(i). In order to have the calculated creep rates under control two numbers are used, one a very small number (10^{-60}) and the other a large number (10^{30}) with which the creep rates are compared. Always the maximum of 10^{-60} and creep rate or the minimum of 10^{30} and creep rate are used. (Note that these comparisons are written in exponential form.) Also, if the final creep rate is less than 10^{-30} it is taken as equal to zero.

RESAN: RESAN is concerned with evaluating the errors in the solution arising from the Taylor series solution, truncation and the numerical method adopted in SAMURA. These errors are evaluated in Section 3.6 which deals with error analysis.

AT the start of RESAN the errors (which are supposed to be the maximum errors in any region) for the fuel and clad regions are set to zero. Then in the first DO loop using the new stresses obtained in SASAN we calculate $\sigma_{e,i}$ for every mesh-point and call FLCLCR to get the actual creep rates. If yielding has occurred in any ring of the fuel or clad, the first source of error is estimated as

$$E_c = \left| \frac{\sigma_{e,i} - \sigma_{y,i}}{0.0001 + \sigma_{y,i}} \right| \qquad (3.246)$$

The maximum value of E_c over fuel or clad is chosen to be compared with other errors later.

Eq.(3.228) is used then to estimate the major source of error; as described in 3.6. Also the creep rates as estimated by Taylor expansion and those obtained from the actual stresses are compared and the errors calculated in both fuel and cladding. The outcome of this DO loop is the maximum errors in fuel and cladding.

If the errors are within acceptable bounds a new time-step is evaluated so that a certain error should result from that time-step, i.e. ½%. If errors are too high the whole step is repeated using a smaller Δt as given by RESAN.

Before the control is returned to SASAN and HISTRY, a call is made to STEMP once more (the first call is from HISTRY after temperature calculation) if the gap is open and the period is a steady-state one. This again makes the small corrections to the temperatures and strains as explained earlier.

If the calculation is acceptable, the new value of parameters are stored as "old values" to be used in the next step and the control returned to SASAN. Otherwise, the new time-step is used to correct the current step with NWSTEP put equal to 1 and the variables replaced by their old values. On return to SASAN and then HISTRY, the keyword NWSTEP will give

an indication of the situation to HISTRY, i.e. a repeat of the whole of the calculation with the new shorter step.

POLATE: This is a linear interpolation subroutine. It is written because a number of SAMURA subroutines contain tables of data for a property rather than analytical expressions. Examples are cladding axial and radial thermal expansion in the region of ∿ 1000 to 1300°K and cladding specific heat capacity (see Section 3.5). In these cases discontinuities exist in the temperature range of the Zircaloy α and β phase transformation. Theory-based analytical expressions are not available, and interpolation of reported data was found simpler than use of an empirical equation.

POLATE uses the usual linear interpolation rule for any value situated between two pairs of variables. There are four input parameters as below

XY = table of Y(1),X(1), Y(2),X(2) ,...Y(NN),X(NN),

XX = the given value for X(i)

NN = the number of pairs of entries in XY

KK = the position guess

Since POLATE is a function-subroutine, on return the value obtained for Y(i) (corresponding to X(i)) is stored in POLATE.

SOLVEX: As stated in SASAN, once the matrix is assembled the matrix incersion subroutine SOLVEX is called. This is a special routine developed at Harwell (168). Bascially it uses a pivotal condensation method and yields the values of all plastic strains, stresses and displacements at every

mesh-point at the end of each time-step.

The whole cycle of calculation described in the above manner continues until the end of a reactor period is reached. Full print-outs of temperatures, stresses, strains, etc. are produced for desired times throughout the calculation by appropriate calls to PRINTX. In this way the code treats the reactor periods provided by the user as input. SAMURA can deal with quite complicated power cycles as will be seen in the next two chapters, which present the preliminary results obtained from the code calculations.

CHAPTER 4

EVALUATION OF 'SAMURA' MODELLING AND ANALYSIS CAPABILITIES

CHAPTER 4

EVALUATION OF 'SAMURA' MODELLING AND ANALYSIS CAPABILITIES

4.1 INTRODUCTION

In this chapter some examples of SAMURA analysis and modelling capabilities are presented. Naturally, the amount of data emanating from such a code is formidable, consequently it was decided to present most of the results mainly in graphical form. In this way, it is hoped to provide a wide range of possible calculations, that can be performed, without having to go through very detailed explanations.

In order to make the evaluations of the code more complete three areas of investigation were considered:

1. To check the overall accuracy of calculations and to benchmark the results against available analytical solutions.
2. To model an LWR fuel pin under normal conditions to show the usefulness of the program and to illustrate its capabilities.
3. To compare SAMURA output with available experimental results particularly along the lines of the Electric Power Research Institute (EPRI) Phase-III studies (14, 170).

In the following sections these efforts have been described in detail.

4.2 THERMAL ANALYSIS CAPABILITIES

Thermal analysis is an essential prerequisite for structural analysis, not only because of thermal strains and stresses, but also because of the temperature dependence of the fuel pin materials properties. It was stated in Section 3.3 that the solution of heat conduction equations in the general time and space-dependent form is neither practical nor economical for an integral fuel pin code. This has not, however, prevented SAMURA from using a sophisticated one-dimensional finite difference solution. SAMURA's differencing scheme is capable of modelling both equilibrium and transient conditions, a facility that can be very useful. The accuracy and reliability of this method has been verified and will be described here.

The crucial part in the thermal analysis of a fuel pin is the calculation of the fuel/cladding gap heat transfer coefficient. This determines not only the stability of the numerical solution but also the level of temperatures. SAMURA has used a new approach which is based on post-irradiation observations and available experimental results employing the concept of "cracked pellet model" (see Sub-Section 3.3.4).

Thus, the evaluation of thermal analysis models in SAMURA was performed with two particular aims in mind: firstly to verify the accuracy of the differencing scheme, especially in determining transient fuel pin temperature fields, and secondly to compare the gap conductance model predictions with available fuel centreline temperature data.

4.2.1 Accuracy of the Finite Difference Scheme

The analytical work of Lewis (171) was chosen for accuracy checks. The thermal analysis subroutines were taken out of the code and used separately with the data in Table 4.1. It must not be forgotten that the cases described here are highly idealised problems customarily used for accuracy checks.

TABLE 4.1

FUEL PIN DATA (171)

Diameter (mm):		
inner fuel		0.0
outer fuel		12.4968
inner cladding		12.4968
outer cladding		14.0208
Thermal conductivity ($W/m^{o}K$):		
fuel		2.0
cladding (no thermal resistance)		1000.0
Specific heat ($J/kg^{o}K$):		
fuel		330
cladding		340
Density (kg/m^{3}):		
fuel		10000
cladding		6500
Thermal expansion coefficient ($^{o}K^{-1}$):		
fuel		0.0
cladding		0.0
Initial conditions:		
linear power	450	W/cm
fuel/cladding heat transfer coefficient	5678.3	$W/m^{2o}K$
coolant heat transfer coefficient	13627.8	$W/m^{2o}K$
coolant temperature	273	^{o}K

It is important to establish how sensitive the accuracy of calculation is to the number of nodes in the fuel and cladding. For this purpose calculations were carried out which consider a situation in which a fuel pin and surrounding coolant are initially at a uniform temperature of 1773^{o}K. At time t = 0 the coolant temperature is reduced to 273^{o}K in a step. For different values of the fuel and cladding nodal points, transient histories of bulk fuel temperature (volume average) and inner cladding temperature were determined. The results obtained for this severe transient are compared with those of Ref.(171) in Table 4.2. The results show that SAMURA's differencing scheme is very stable even with small numbers of nodal points; and it is accurate with as few as 20 rings across the fuel and 4 rings across the clad.

TABLE 4.2

TEMPERATURE CALCULATION FOR DIFFERENT VALUES OF FUEL AND CLADDING RADIAL RINGS

Time (s)	Bulk Fuel Temperature* (^{o}K)					Inner Cladding Temperature (^{o}K)				
	Ref. (171)	SAMURA				Ref. (171)	SAMURA			
		NF = 5 NC = 2	NF = 20 NC = 4	NF=50 NC=10	NF=160 NC= 30		NF = 5 NC = 2	NF=20 NC= 4	NF=50 NC=10	NF=160 NC= 30
0.0	1773.0	1773.0	1773.0	1773.0	1773.0	1773.0	1773.0	1773.0	1773.0	1773.0
0.6	1650.7	1608.8	1647.5	1650.3	1650.7	567.1	601.1	568.6	567.3	567.1
1.2	1529.5	1476.9	1526.3	1529.0	1529.5	420.1	426.7	419.8	420.0	420.1
3.0	1289.9	1249.1	1287.5	1289.5	1289.9	348.6	343.5	348.2	348.5	348.6
6.0	1042.5	1013.8	1040.8	1042.3	1042.5	320.0	317.7	319.8	320.0	320.0
12.0	744.7	729.1	743.8	744.6	744.7	299.6	298.3	299.3	299.6	299.6
15.0	645.5	634.2	644.8	645.4	645.5	294.0	292.8	293.7	294.0	294.0
18.0	567.6	559.5	567.1	567.5	567.6	289.7	288.7	289.5	289.7	289.7
30.0	388.3	386.6	388.1	388.2	388.3	280.0	279.3	279.7	280.0	280.0

NF = number of radial rings in the fuel NC = number of radial rings in the cladding

*By bulk fuel temperature it is meant a volume average temperature.

To examine the coupled behaviour of the fuel and cladding regions, SAMURA's thermal analysis module is next applied to the following transient problems:

(1) The fuel pin is initially at steady-state conditions for constant power production using the data of Table 4.1. At time zero the heat source vanishes while the coolant remains at a constant temperature.

(2) The fuel pin is initially at steady-state conditions for constant power production as before. At time zero the heat source vanishes, and the fuel pin also loses its heat transfer capability ($h_{cool} = 0.0$).

(3) The fuel element is initially at a uniform temperature with zero heat generation. At time zero the coolant temperature is reduced to a lower value (i.e. from $1773^{o}K$ to $273^{o}K$ as in Table 4.2) with heat generation maintained at zero.

For these idealised situations, analytical solutions are available and are given by Lewis (171). The results of these cases are given graphically in Figures 4.1 through 4.5 . The first two problems, Figures 4.1 and 4.2 , may be viewed, as Lewis (171) has pointed out, respectively as an idealised reactor coast-down and an idealised, instantaneous loss-of-coolant transient, where decay heat is neglected in both cases. The non-dimensional fuel and cladding temperature, T(t)/T(o), is plotted against time. For 50 nodes in the fuel and 10 in the cladding the accuracy is quite remarkable (note that bulk fuel and cladding temperatures (volume averages) are used and T(o) is the fuel bulk temperature at time zero). In order to

Figure 4.1

COMPARISON WITH ANALYTICAL SOLUTIONS

FUEL PIN TEMPERATURE RESPONSE TO AN INSTANTANEOUS LOSS OF HEAT SOURCE

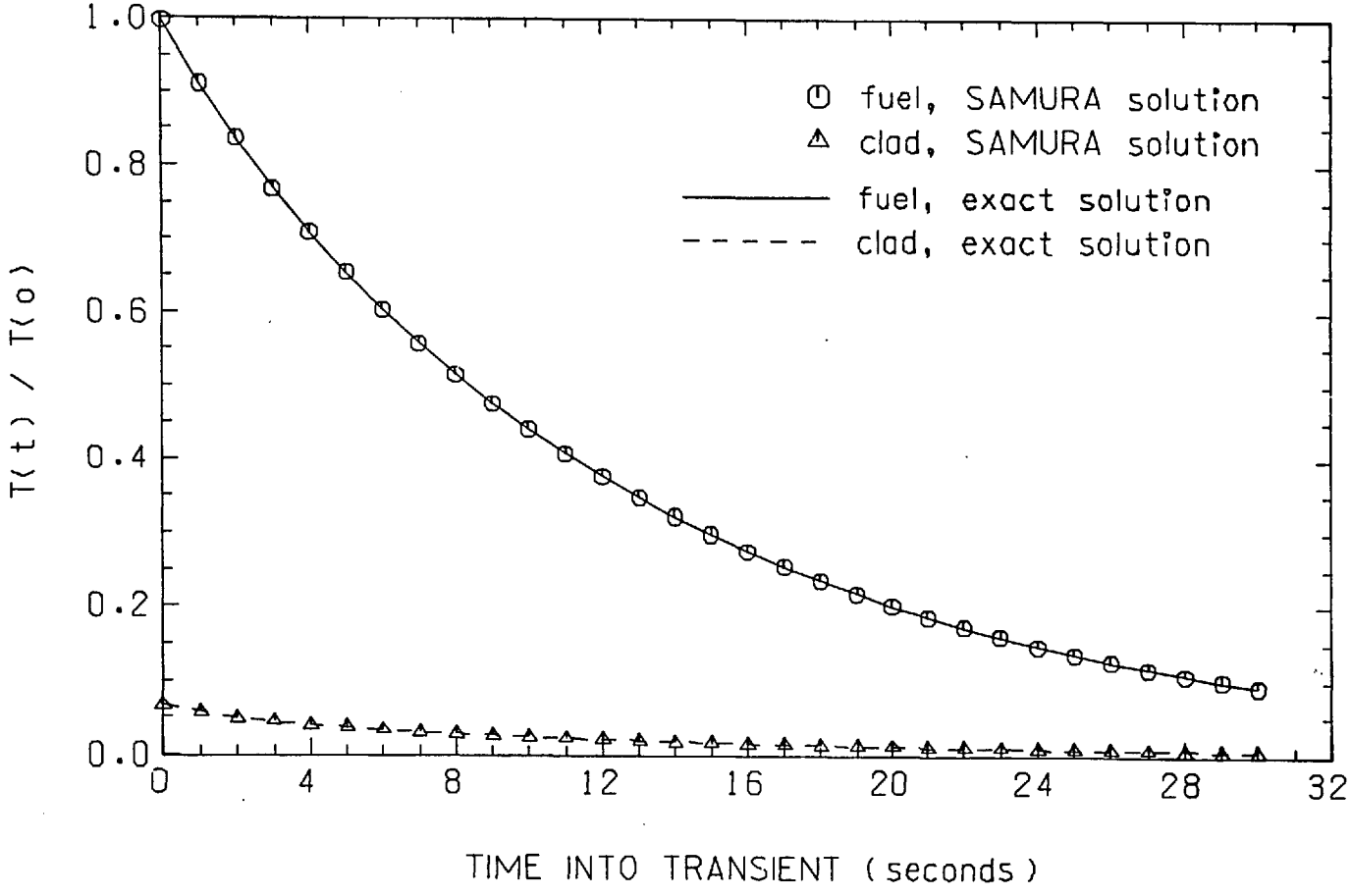
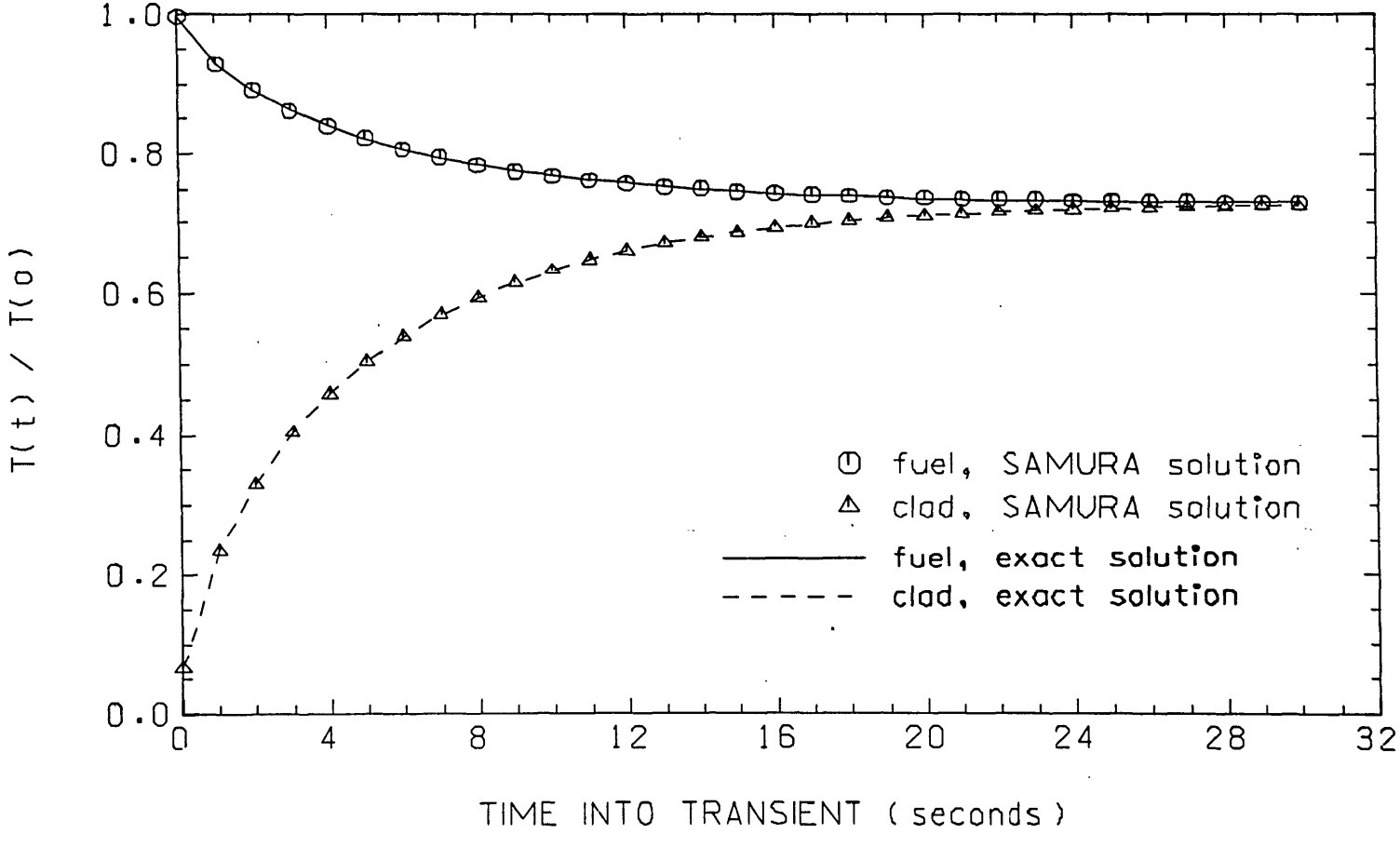


Figure 4.2

COMPARISON WITH ANALYTICAL SOLUTIONS

FUEL PIN TEMPERATURE RESPONSE TO AN INSTANTANEOUS

LOSS OF HEAT SOURCE AND COOLING CAPACITY



have a better idea of how the fuel temperature varies during these transients, in Figures 4.3 and 4.4 fuel pin radial temperature distribution is given for different times after the start of the respective transients. The reason for no temperature gradient in the cladding is the high conductivity used for it in accordance with the analytical solution of Lewis (171). This has only simplified his numerical example of the solution. It can be seen, Fig.4.4, that re-distribution of stored heat within the fuel leads to a uniform temperature across the fuel after about 30 seconds, with very high percentage of the heat being re-distributed during the first 10 seconds.

Comparison of the SAMURA solution for the third problem with the exact solution is presented in Fig.4.5. Again very good agreement is achieved but with the expense of smaller time-steps, particularly during the first few seconds into the transient, as compared with previous cases. This was basically due to severity of the transient. The numerical scheme would remain stable only with smaller time-steps (0.6 sec as opposed to 1.0 sec for Cases 1 and 2). One may argue, however, that the two first transients are of primary significance. For example, thermal transients following both large sudden changes in power level, e.g. during a reactor scram, and thermal insulation of the fuel pin, e.g. during flow blockage or loss-of-coolant, are among major transients. According to Lewis (171), transients of the type illustrated in Fig.4.5 are of less interest; for either the temperature drop across the clad is not very large, or burn-out will result. If burn-out

Figure 4.3
FUEL PIN TEMPERATURE RESPONSE TO AN INSTANTANEOUS LOSS OF HEAT SOURCE

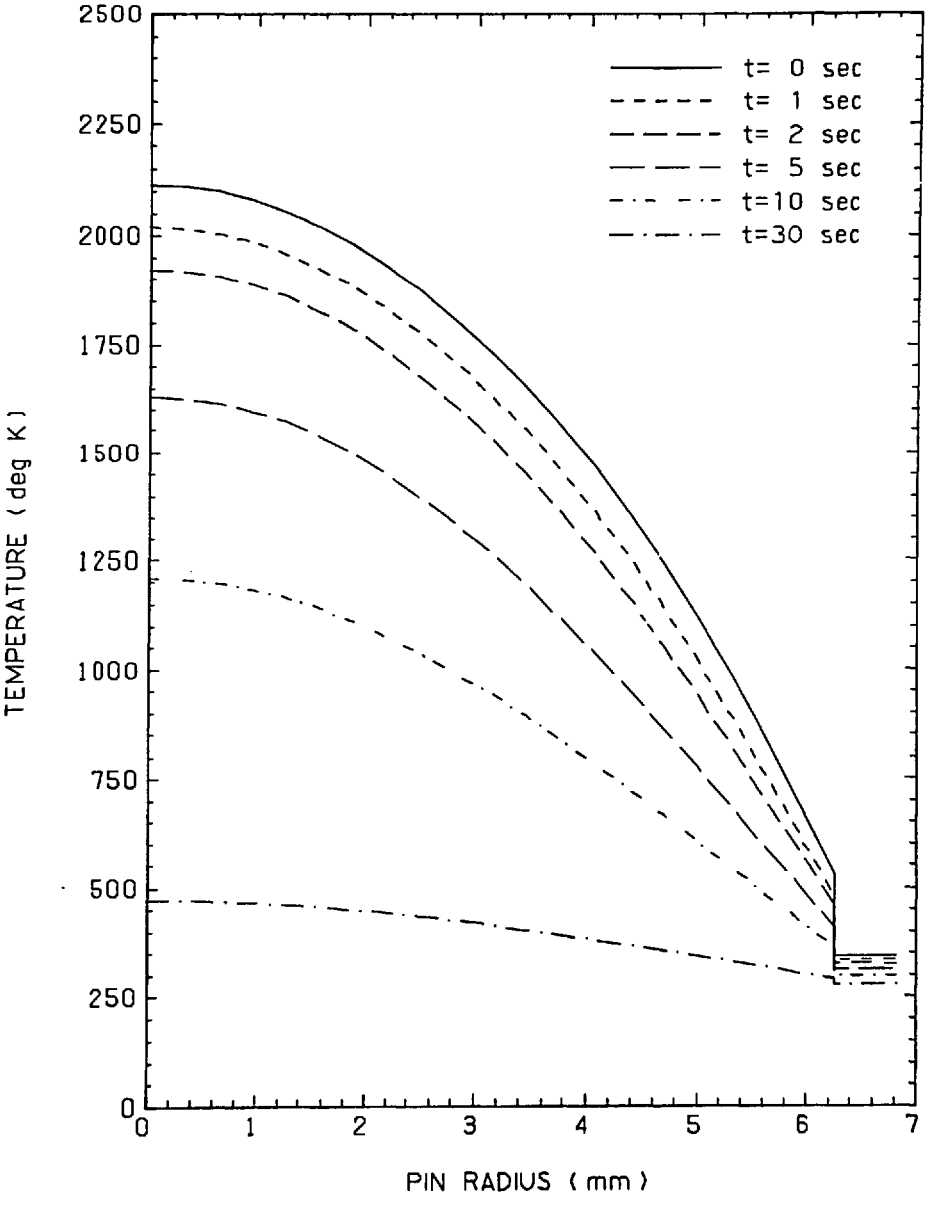


Figure 4.4

FUEL PIN TEMPERATURE RESPONSE TO AN INSTANTANEOUS LOSS OF HEAT SOURCE AND COOLING CAPACITY

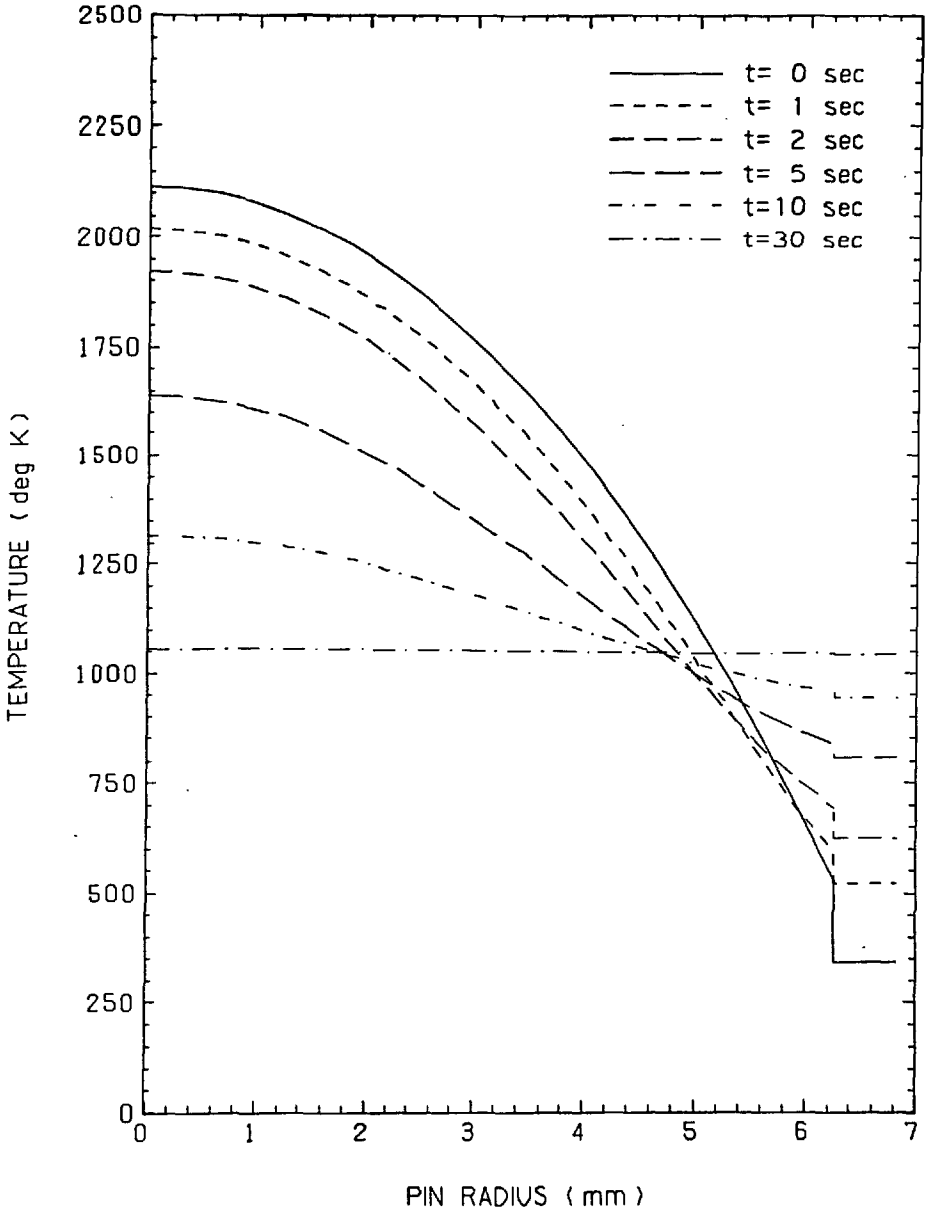
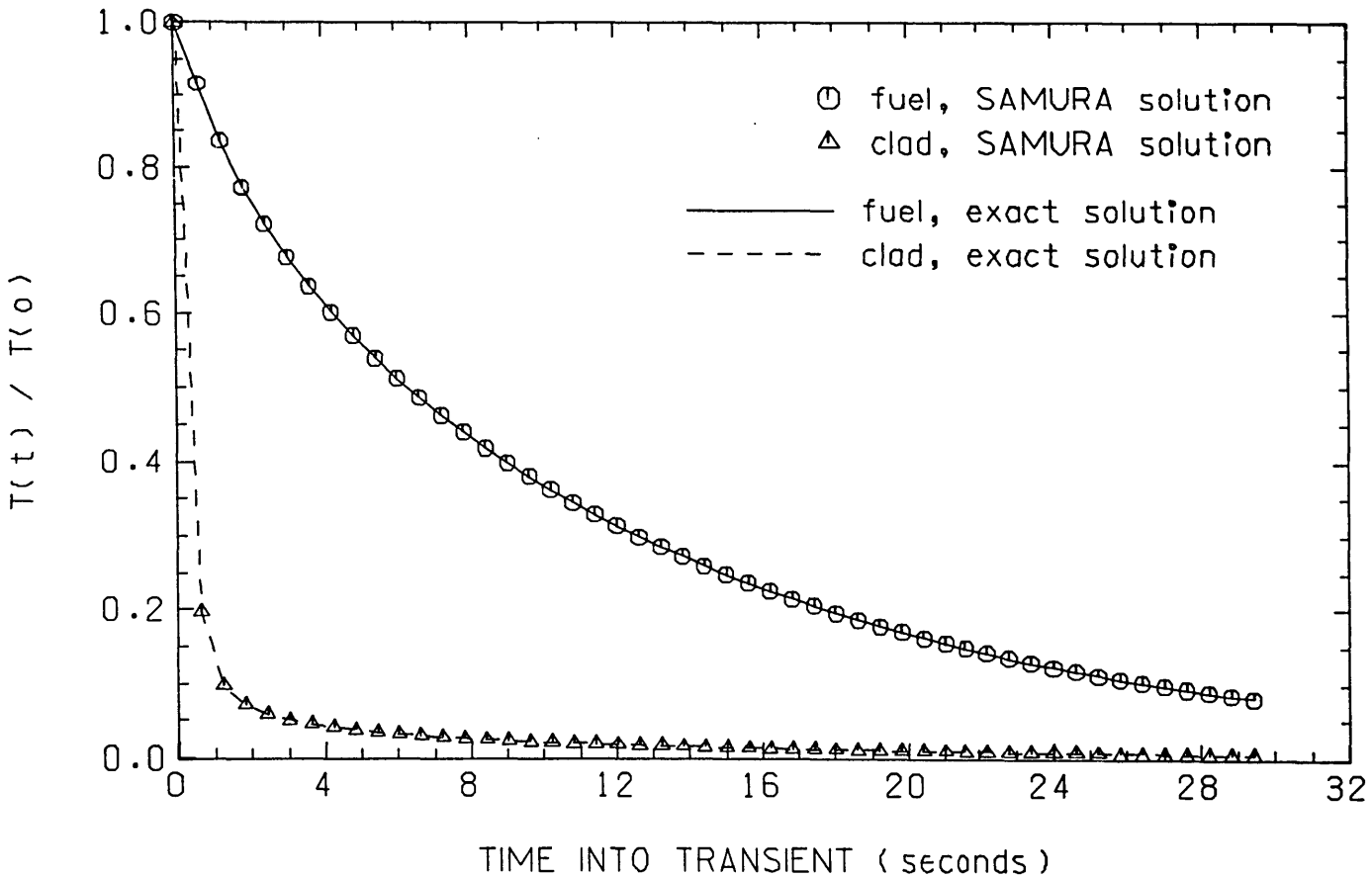


Figure 4.5

COMPARISON WITH ANALYTICAL SOLUTIONS

FUEL PIN TEMPERATURE RESPONSE TO AN INSTANTANEOUS

DECREASE IN THE COOLANT TEMPERATURE



occurs, the situation becomes more analogous to the instantaneous loss-of-coolant than to the step change in coolant temperature.

Finally, in Figures 4.6 and 4.7 SAMURA results are compared with exact solutions for a series of idealised LOCA's. It is assumed that full power heat transfer capability is maintained for some period of time, θ, after the reactor scram. For times greater than θ, the fuel pin is assumed to lose all cooling capacity. The decay heat is given by (171):

$$q(t)/q(o) = 0.056e^{-0.004t} + 0.20e^{-0.1t}, \quad t \leq 60 \text{ sec.}$$

where $q(o)$ is the constant power linear heat at $t = o$.

4.2.2 Comparison of Fuel Centreline Temperatures with Experimental Data

In this test the actual code in its entirety rather than its simplified* thermal analysis routines has been used. This is to ensure that the evaluation of gap conductance model is based on real situations.

Measured fuel centreline temperature data are available in the literature. For the sake of accuracy only well characterised fuel pins with known power levels and measured coolant conditions or cladding temperatures were considered. Three major groups of data could be distinguished, namely:

(a) helium-filled pins with very short burn-ups;

(b) fission -gas-filled pins with very short burn-ups; and

(c) helium-filled pins at longer burn-ups. The fuel pin

*This means constant thermal properties as used in the previous sub-section.

Figure 4.6

COMPARISON WITH ANALYTICAL SOLUTIONS

FUEL PELLETS TEMPERATURE BEHAVIOUR DURING AN

IDEALISED LOSS OF COOLANT ACCIDENT

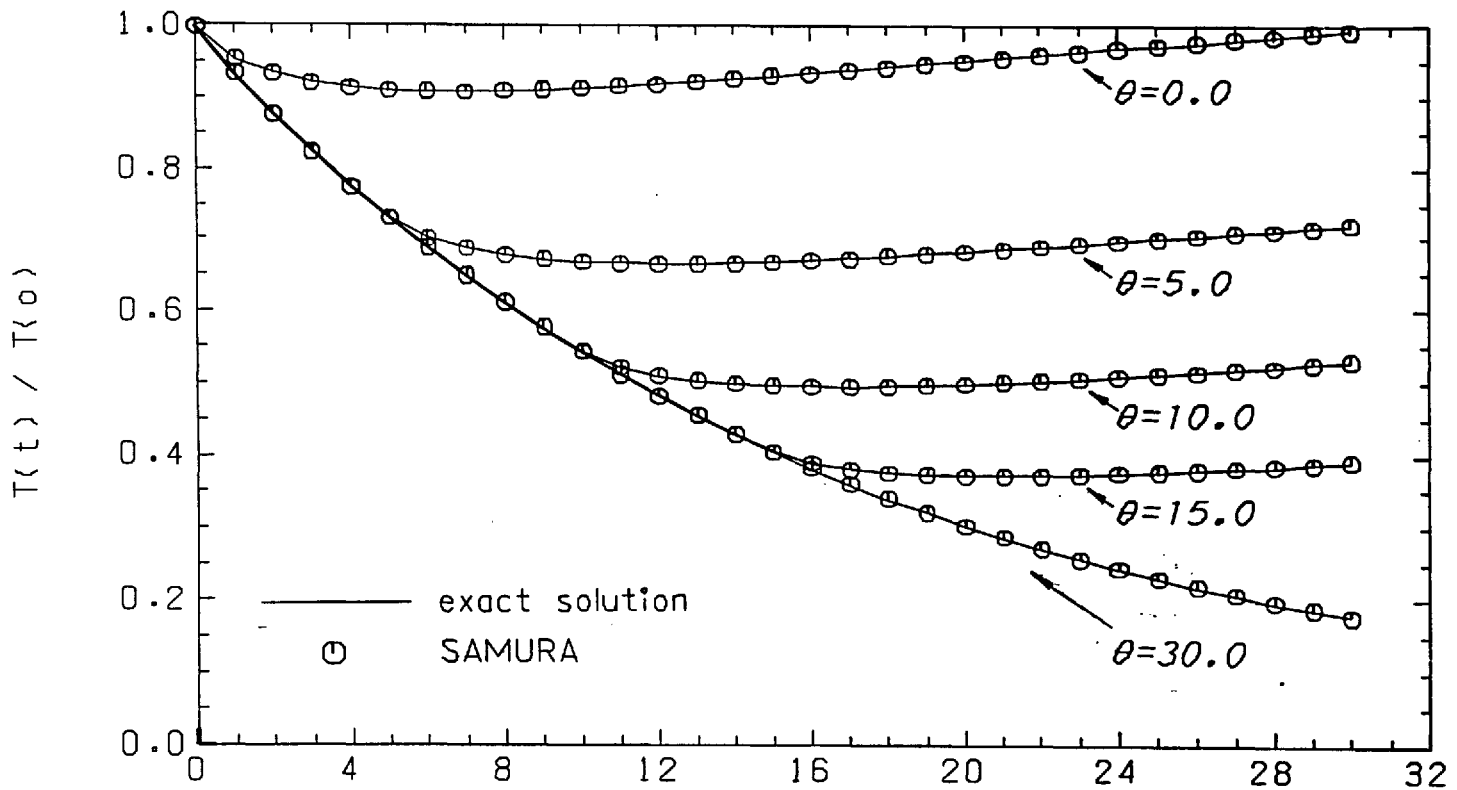


Figure 4.7

COMPARISON WITH ANALYTICAL SOLUTIONS

CLADDING TEMPERATURE BEHAVIOUR DURING AN

IDEALISED LOSS-OF-COOLANT ACCIDENT

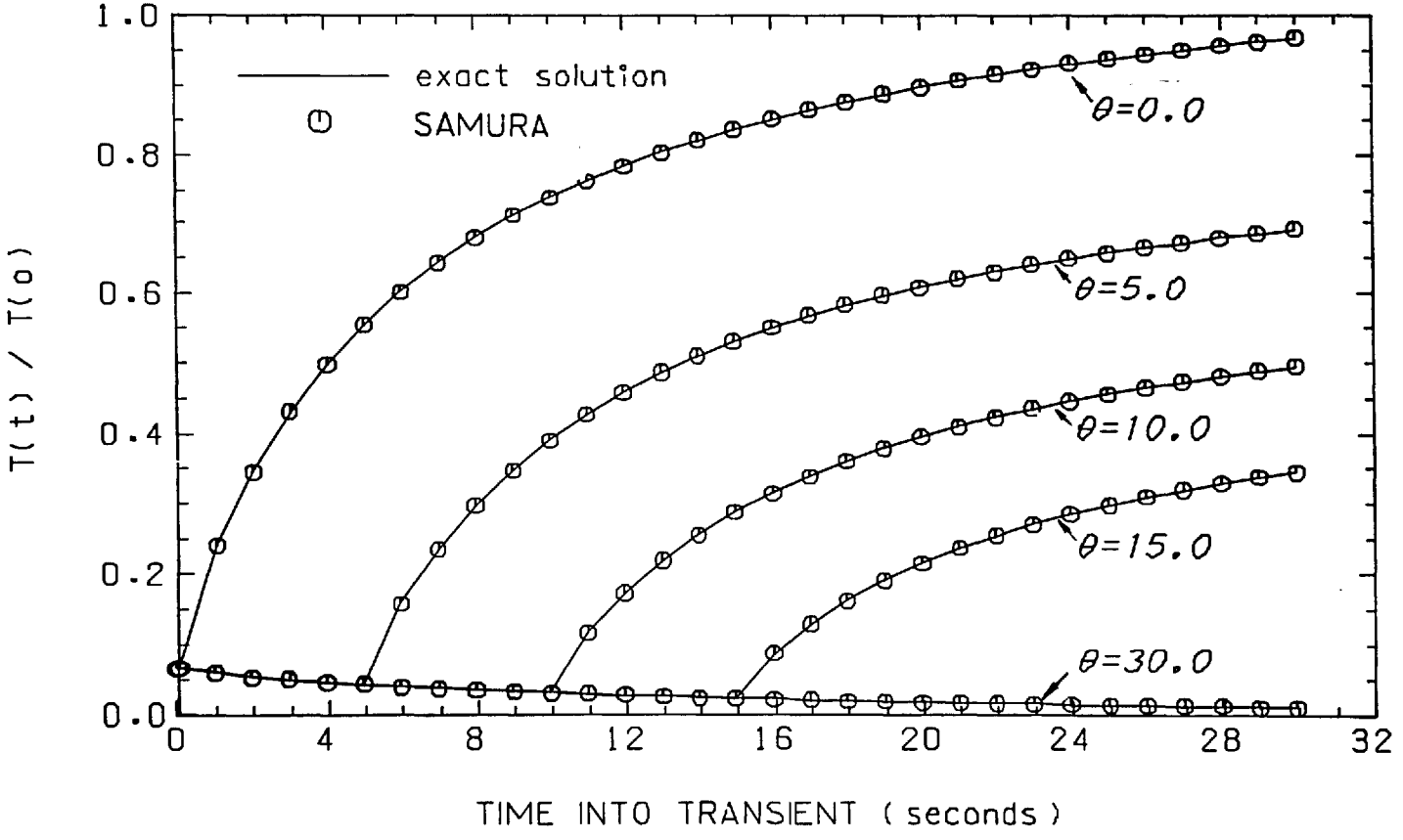
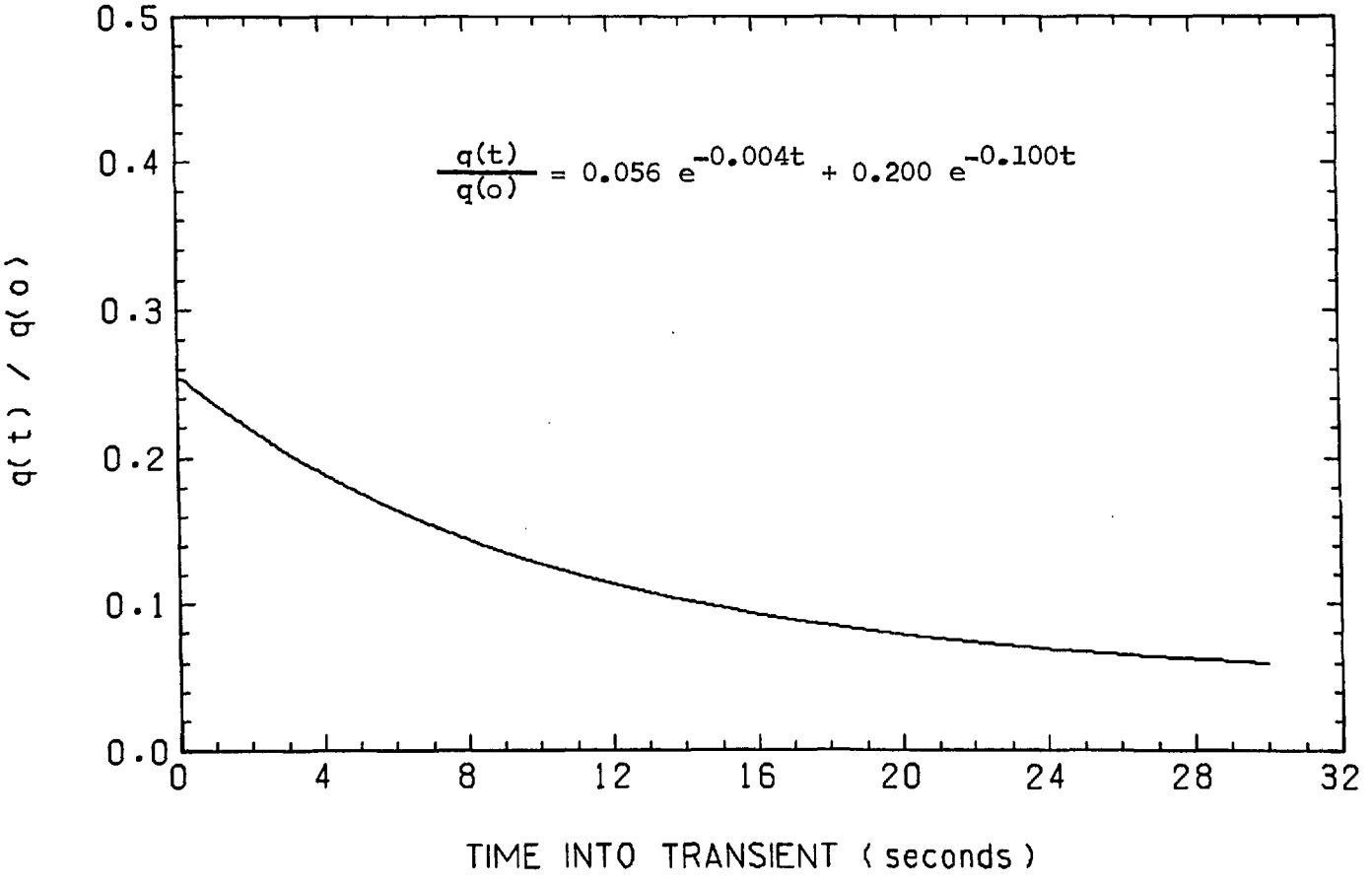


Figure 4.8

FUEL DIMENSIONLESS DECAY HEAT MODEL USED IN THE IDEALISED LOSS-OF-COOLANT ACCIDENT



conditions were in the following range: pellet density, 92-96% TD; cold radial gap, 25-160 μm; and initial internal gas composition, helium or fission gas. The burn-up range of these fuel elements was from 0 to about 15300 MWd/teU. SAMURA was run with appropriate fuel data and a simple power history (up-ramp, steady-state and down-ramp) for each individual fuel pin. For comparison purposes all cases were also run with F = 0 in the gap conductance equation (see Eq.(3.36), Sub-Section 3.3.4) to simulate the Ross and Stoute classical gap conductance model (133). The results of this study are presented graphically in Figures 4.9 to 4.23 . Note that SAMURA predictions refer to the beginning of life (BOL) unless specified otherwise on the graphs.

Cohen et al (135) carried out a series of in-pile experiments which were designed to measure the effective thermal conductivity of UO_2 as a function of the fuel/cladding gap, fill-gas and the centreline fuel temperature. The temperature data from these experiments are plotted in Figures 4.9 to 4.14 along with the results of SAMURA modelling for the six representative fuel capsules.* The main fuel parameters are given in Table 4.3. The overall view, as it appears from these graphs, is that the cracked pellet model ($F \geq 0.3$†) results are in much better agreement with the experimental data. This lends support to

*The cladding of these capsules was made of stainless steel. So the creep law incorporated into SAMURA was changed to the following thermal creep law:

$$\dot{\varepsilon}_{ss} = 2.0 \times 10^{8}\, \sigma_e^{4} \exp(-\, 80 \times 10^{3}/RT)$$

The cladding deformation is not however significant here because of its high thickness and low pressures involved.

†From this point onwards $F \geq 0.3$ will indicate that the value of F is the one obtained from Eq.(3.37) during program calculations.

Figure 4.9

EVALUATION OF SAMURA GAP CONDUCTANCE MODEL

MEASURED AND PREDICTED CENTRELINE TEMPERATURE VS.POWER

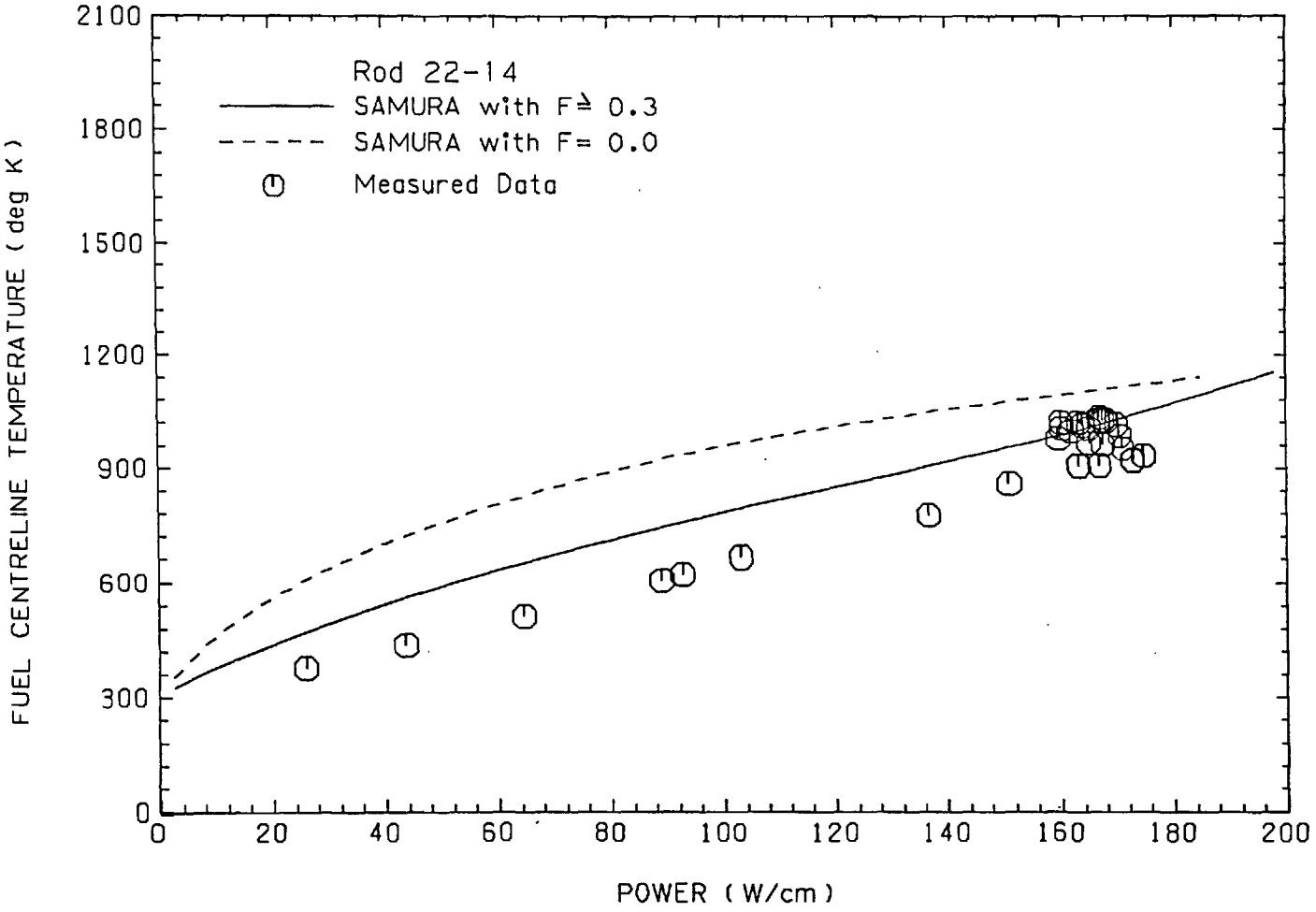


Figure 4.10

EVALUATION OF SAMURA GAP CONDUCTANCE MODEL

MEASURED AND PREDICTED CENTRELINE TEMPERATURE VS. POWER

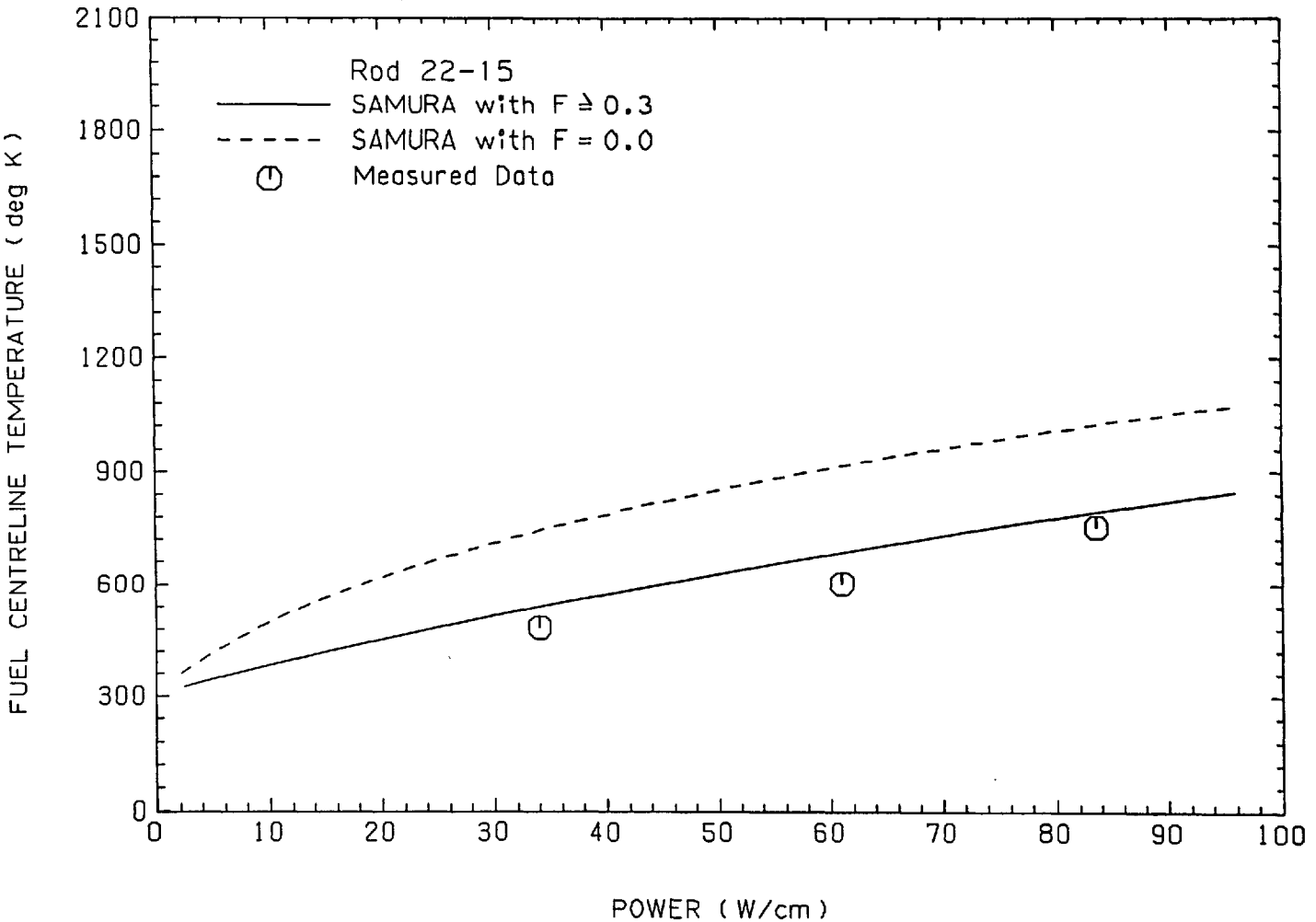


Figure 4.11

EVALUATION OF SAMURA GAP CONDUCTANCE MODEL

MEASURED AND PREDICTED CENTRELINE TEMPERATURE VS. POWER

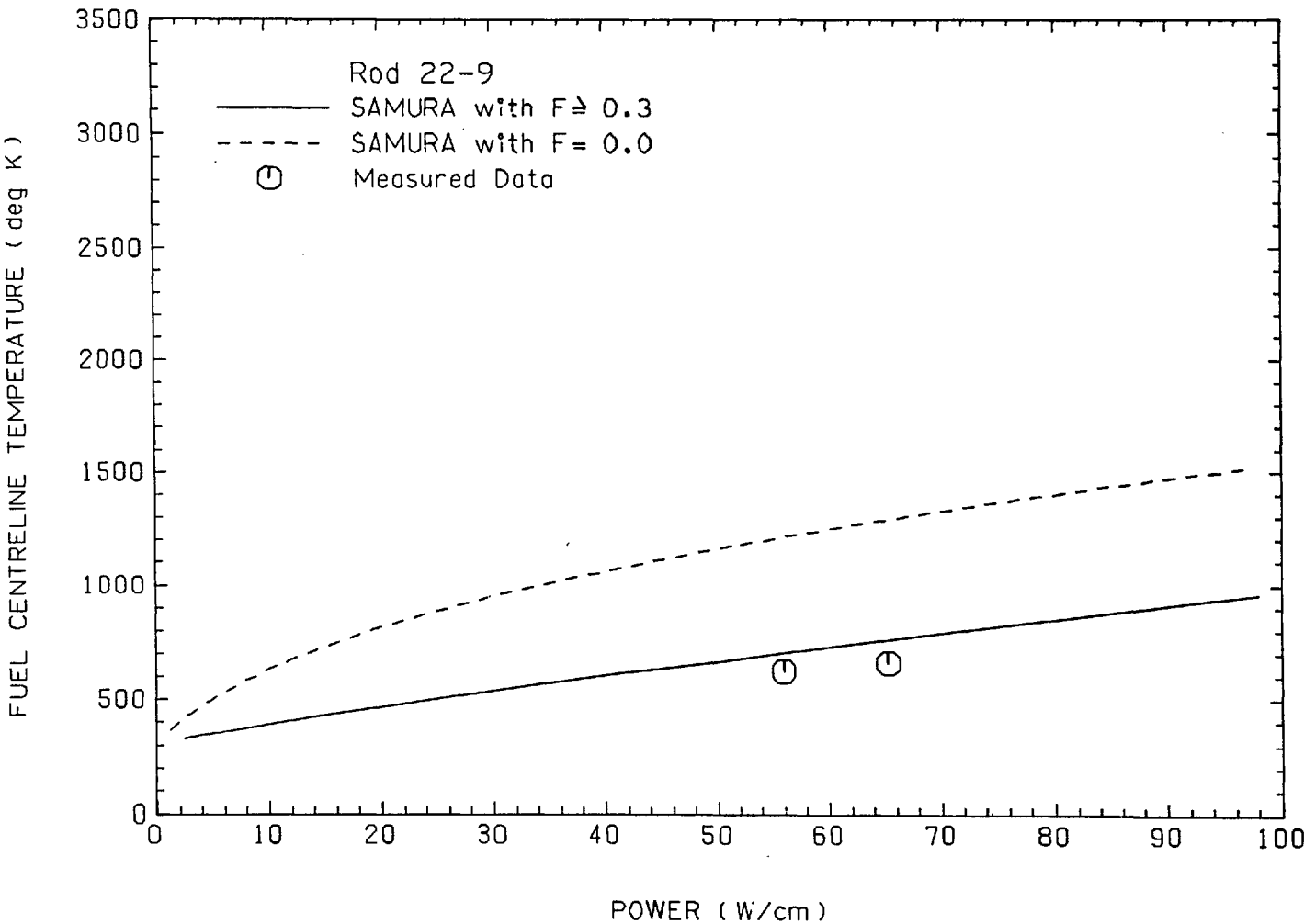


Figure 4.12

EVALUATION OF SAMURA GAP CONDUCTANCE MODEL

MEASURED AND PREDICTED CENTRELINE TEMPERATURE VS. POWER

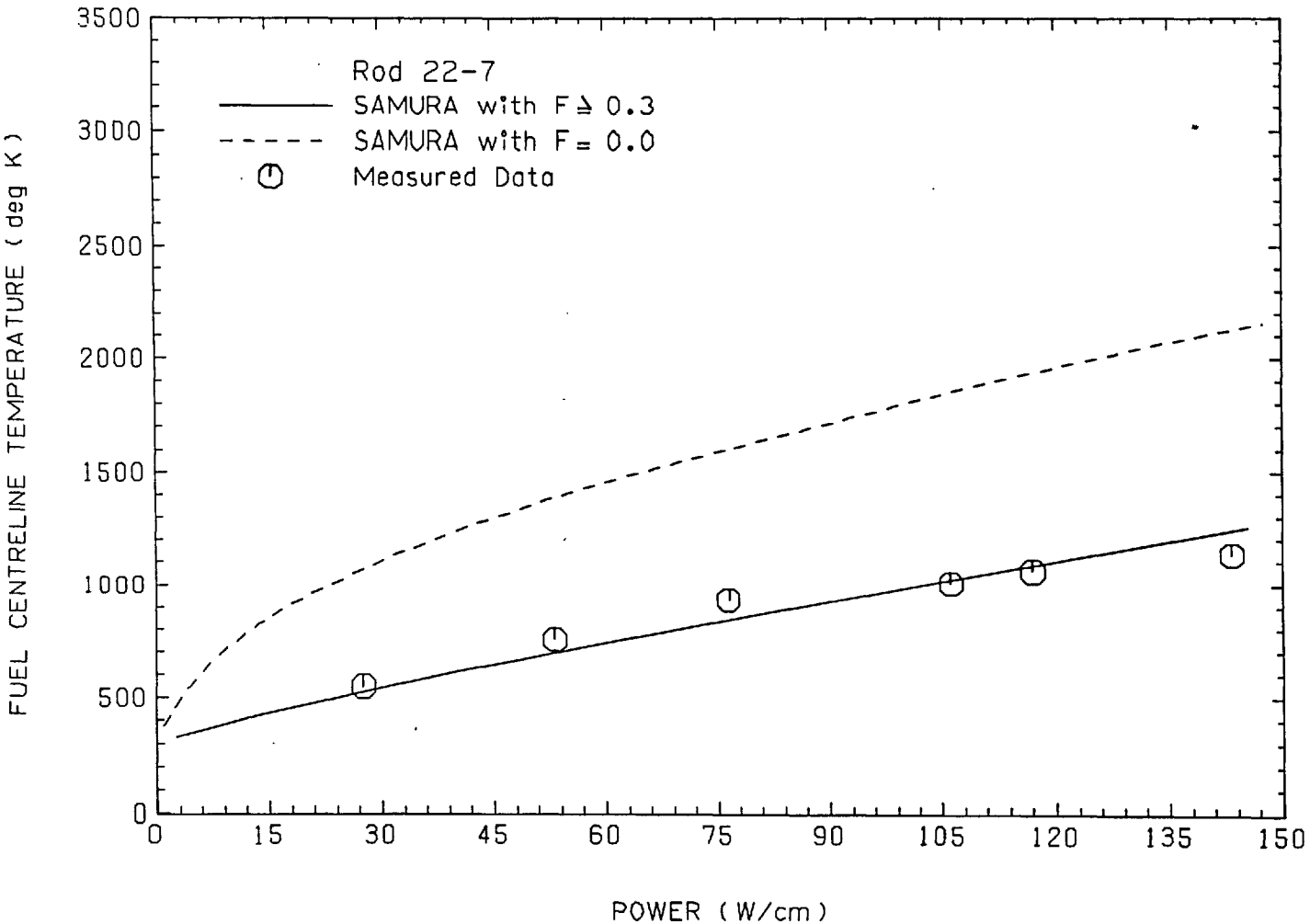


Figure 4.13

EVALUATION OF SAMURA GAP CONDUCTANCE MODEL

MEASURED AND PREDICTED CENTRELINE TEMPERATURE VS.POWER

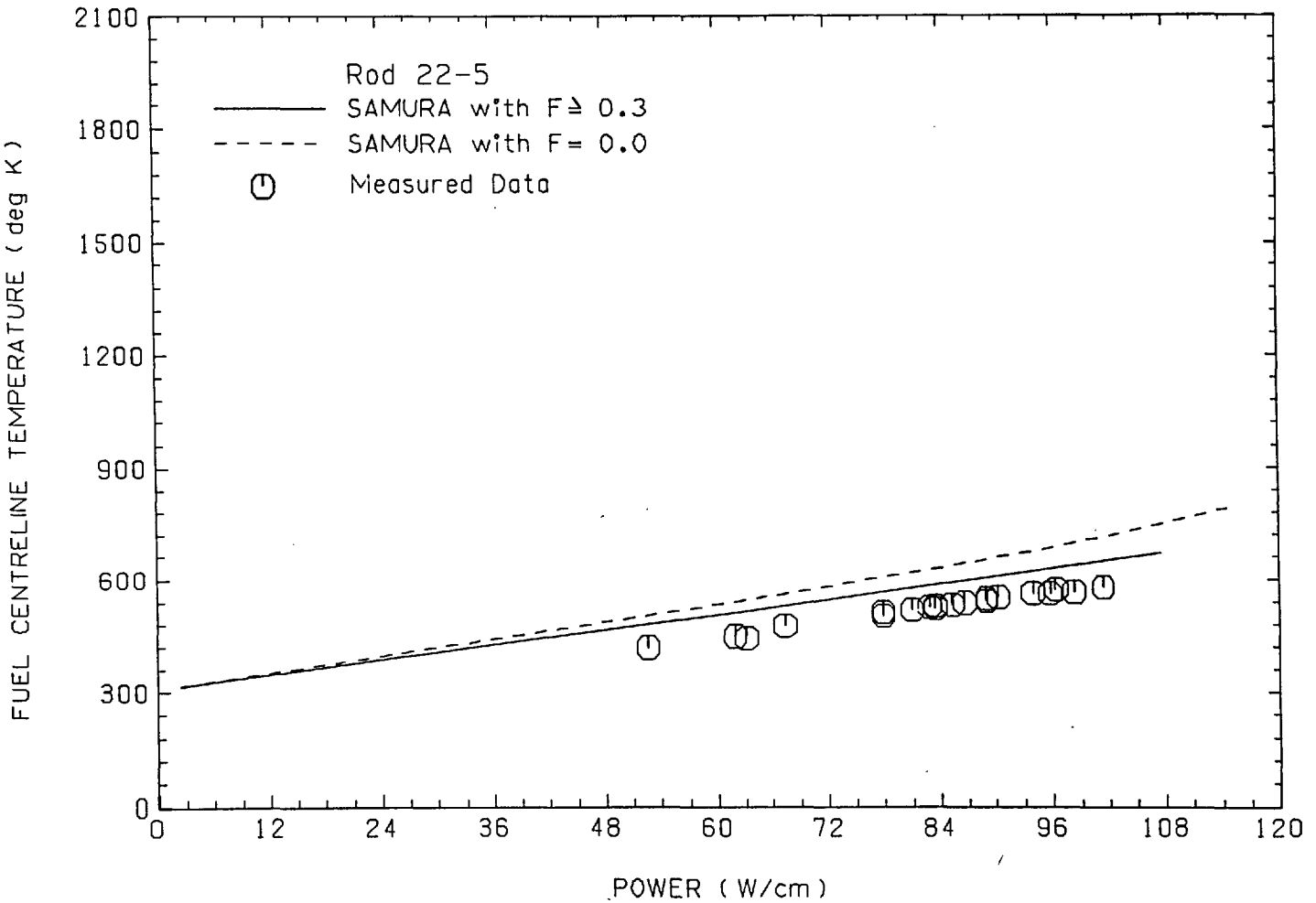


Figure 4.14

EVALUATION OF SAMURA GAP CONDUCTANCE MODEL

MEASURED AND PREDICTED CENTRELINE TEMPERATURE VS.POWER

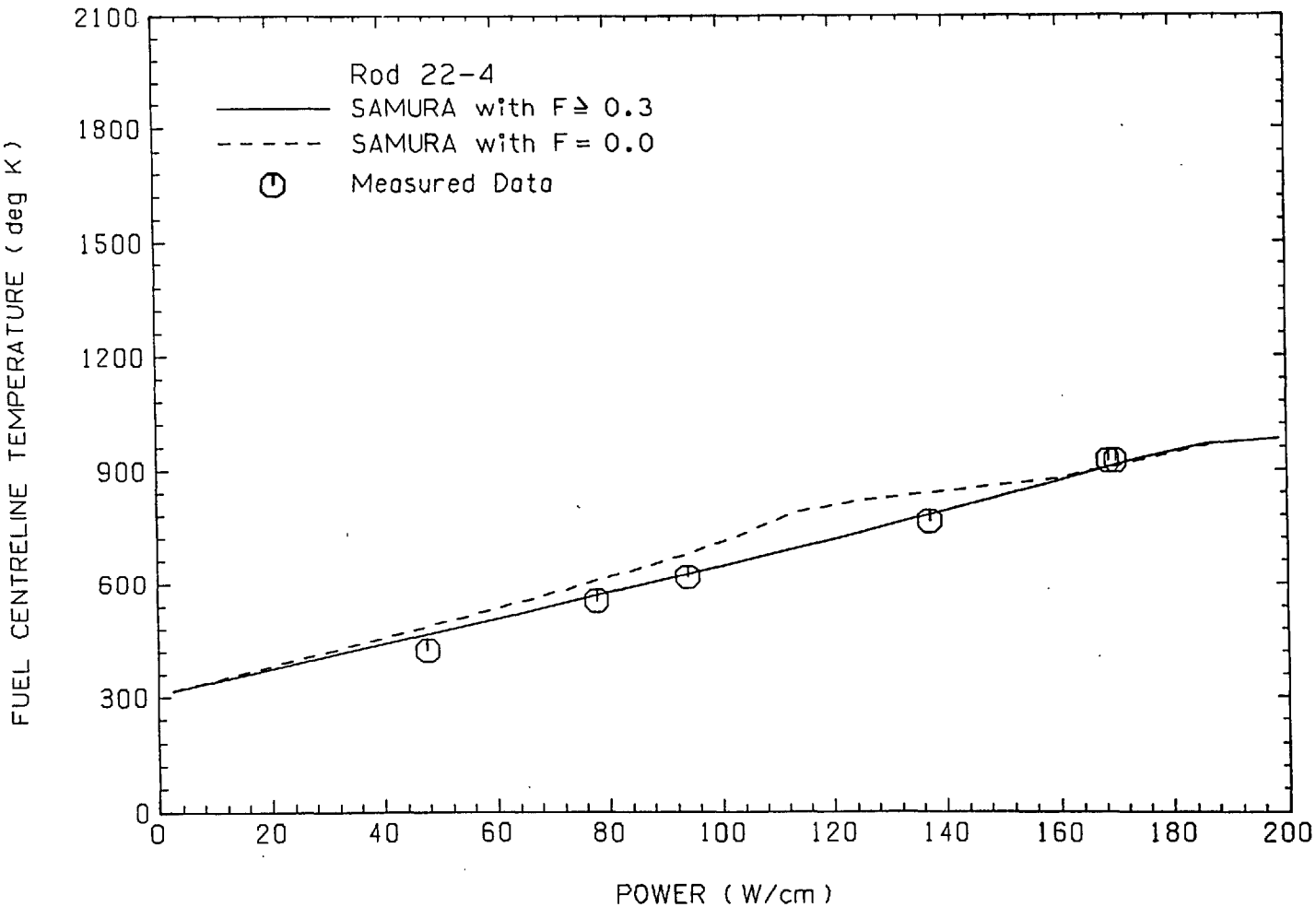


TABLE 4.3

FUEL CAPSULE COLD INITIAL DATA (135)

Fuel Pin	Pellet[1] Radius (mm)	Inner Clad Radius (mm)	Outer Clad[2] Radius (mm)	Pellet Porosity (%)	Radial Gap (μm)	Fill Gas[3] % vol	No. of Irrad. Days
22-4	4.51485	4.53390	14.2875	6.3	19.05	He	1
22-5	4.51485	4.53390	14.2875	5.9	19.05	He	38
22-14	4.50214	4.53390	14.2875	5.9	31.75	1Kr+3Xe	30
22-15	4.48945	4.53390	14.2875	3.7	44.50	1Kr+3Xe	15
22-9	4.50850	4.61010	14.2875	6.2	101.60	1Kr+3Xe	1
22-7	4.4450	4.61010	14.2875	5.0	165.00	1Kr+3Xe	15

(1) All pellets have a central hole of 0.8507 mm.

(2) Note that a very thick cladding is used.

(3) Fill gas is at 1 atm pressure.

the concept that pellet cracking and relocation effectively increase the gap conductance and that a significant proportion of the heat is transferred through the contact of material asperity points rather than by gas gap conduction.

Next the work of Devold (137) was modelled. He measured the centreline fuel temperatures of some Halden Reactor (Norway) fuel pins, code named IFA-3, IFA-4 and IFA-10 (IFA stands for Instrumented Fuel Assembly). These measurements were carried out during a period of about 18 months of reactor operation. The fuel pins all contained UO_2 pellets, were made of Zr-2 and filled with helium gas. The Halden reactor is of the boiling water type (BWR) with a coolant temperature of 503^{o}K and a pressure of 30 bar. Other relevant parameters are given in Table 4.4.

TABLE 4.4

HALDEN TEST FUEL PIN COLD INITIAL DATA (137)

Parameters	IFA-3	IFA-4	IFA-10
Pellet Inner Radius (mm)	0.865	0.865	0.865
Pellet Outer Radius (mm)	6.290	6.290	6.235
Cladding Inner Radius (mm)	6.380	6.380	6.300
Cladding Outer Radius (mm)	7.140	7.140	6.900
Pellet Porosity	0.04	0.04	0.04
Pellet Enrichment	0.015	0.06	0.028
Linear Power (W/cm)	299.0	564.0	401.0
No. of Irrad.Days	120	38 & 220	1

Figures 4.15 to 4.17 compare predictions obtained using both models ($F \geq 0.3$ and $F = 0.0$) with measured fuel centreline data obtained from these experiments. The main feature

of these results is that both models have predicted similar temperatures. This is because the initial fuel/cladding gaps are relatively small so the effect of F is small too. As soon as the gap approaches closure the difference between the two models vanishes. SAMURA predictions for IFA-3 pin are in very good agreement with the measured data. Note that the measured data are divided in two categories, firstly those collected early in life (BOL) and secondly those recorded after about 18 months of irradiation (EOL). It is apparent that in the case of IFA-4 and IFA-10 SAMURA has generally underpredicted the temperatures, with the Ross and Stoute having predicted much closer temperatures. It is thought that this is due to low fission gas release prediction by SAMURA for these pins, thus overpredicting the gap conductance by using higher gap gas conductivity values. Also there is the influence of the gap width and its higher rate of closure - due to probably higher cladding creep-down. The cladding is Zr-2 and the following creep law, as given by Gittus et al (17), was used:

$$\dot{\varepsilon} = 1.14 \times 10^{-19} t^{-0.915} \sigma_e^{2.76} \exp\left[1.19(T-573)/T\right]$$

$$+ 1.22 \times 10^{-10} \phi^{0.85} \sigma_e^{2.3} \exp\left[12.2(T-573)/T\right]$$

ε = creep strain rate (day^{-1})

t = time (days)

σ_e = equivalent stress (MPa)

T = temperature (^{o}K)

ϕ = neutron flux ($n/cm^2.s$)

Figure 4.15

EVALUATION OF SAMURA GAP CONDUCTANCE MODEL

MEASURED AND PREDICTED FUEL CENTRELINE TEMPERATURE VS. POWER

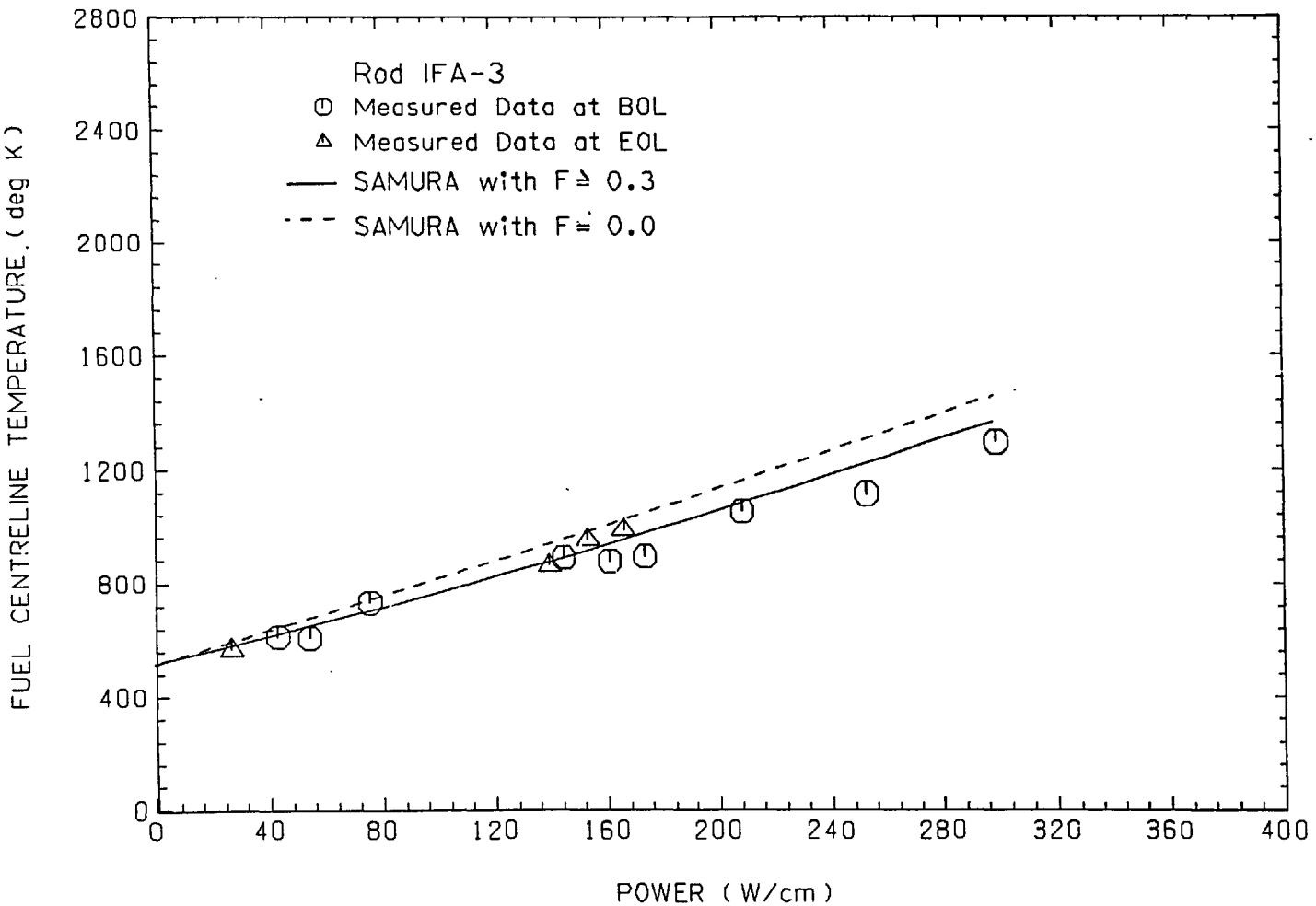


Figure 4.16

EVALUATION OF SAMURA GAP CONDUCTANCE MODEL

MEASURED AND PREDICTED FUEL CENTRELINE TEMPERATURE VS. POWER

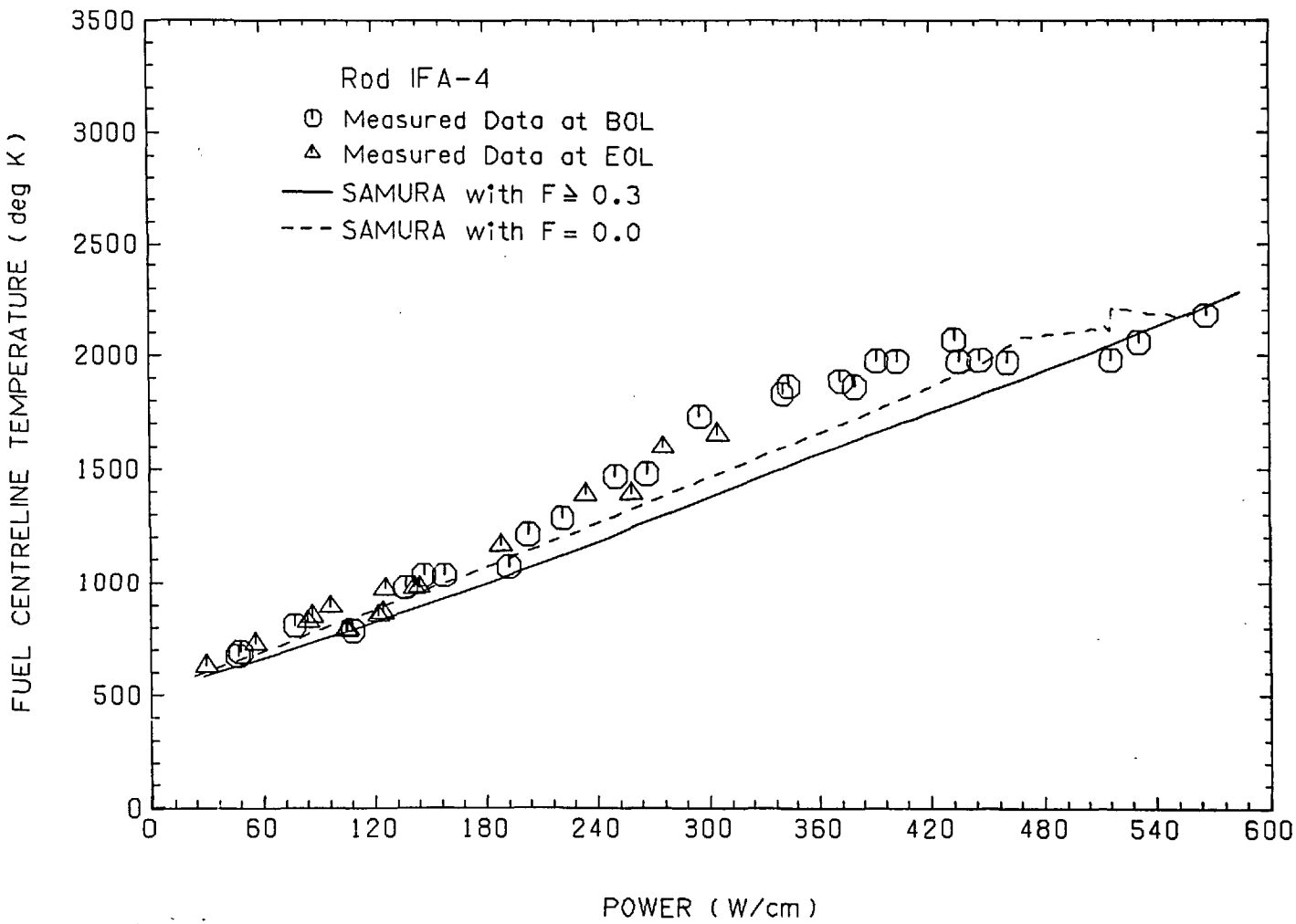
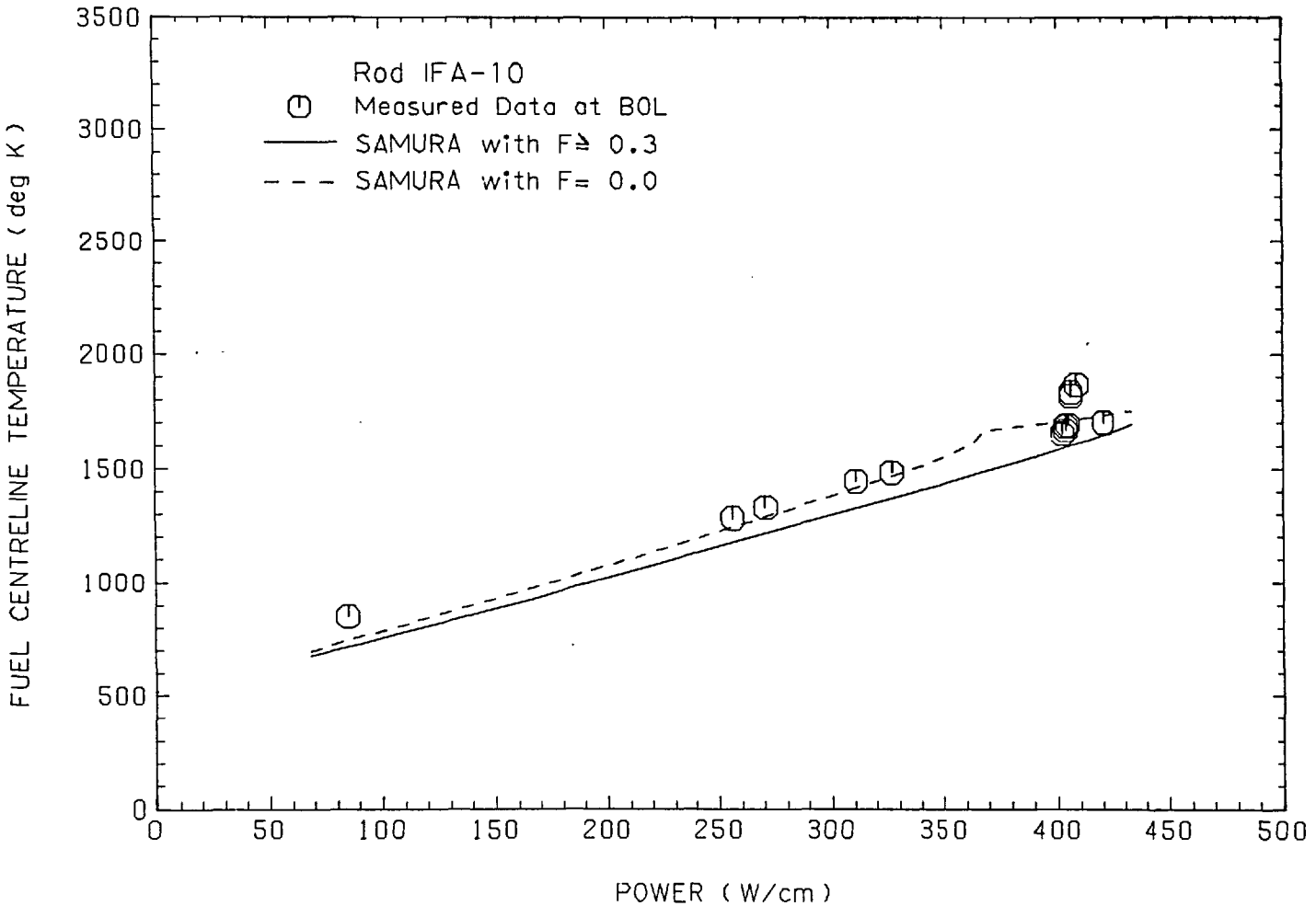


Figure 4.17

EVALUATION OF SAMURA GAP CONDUCTANCE MODEL

MEASURED AND PREDICTED FUEL CENTRELINE TEMPERATURE VS. POWER



Finally, the IFA-226 fuel pins were modelled. Experimental data have been obtained in the Halden BWR from several types of IFA-226 fuel assembly (138). Pin AA of this assembly has been irradiated up to a burn-up of 15,300 MWd/teU and was chosen for SAMURA calculations. The important pin parameters are outlined in Table 4.5.

TABLE 4.5

IFA-226 FUEL PIN COLD INITIAL DATA (138)

Parameters	Pin AA of IFA-226 Assembly
Pellet I.D. (mm)	1.73
Pellet O.D. (mm)	9.30
Cladding I.D. (mm)	9.51
Cladding O.D. (mm)	10.69
Fuel Stack Length (mm)	630.0
Cladding Length (mm)	868.1
Fuel Porosity	0.0794
Fill-gas	He at 0.101 MPa
Coolant Pressure (MPa)	3.45
Coolant Temperature (^{o}K)	513.0
Linear Power (W/cm)	400.0

Comparisons of SAMURA predictions with the experimental data at various burn-ups are shown in Figs. 4.18 through 4.23 . The overall impression from the graphs is that the effects of burn-up are not noticeable in the experimental data until about 1000 MWd/teU of burn-up. Above this value, according to Laads et al(138), burn-up

Figure 4.18

EVALUATION OF SAMURA GAP CONDUCTANCE MODEL

MEASURED AND PREDICTED FUEL CENTRELINE TEMPERATURE VS. POWER

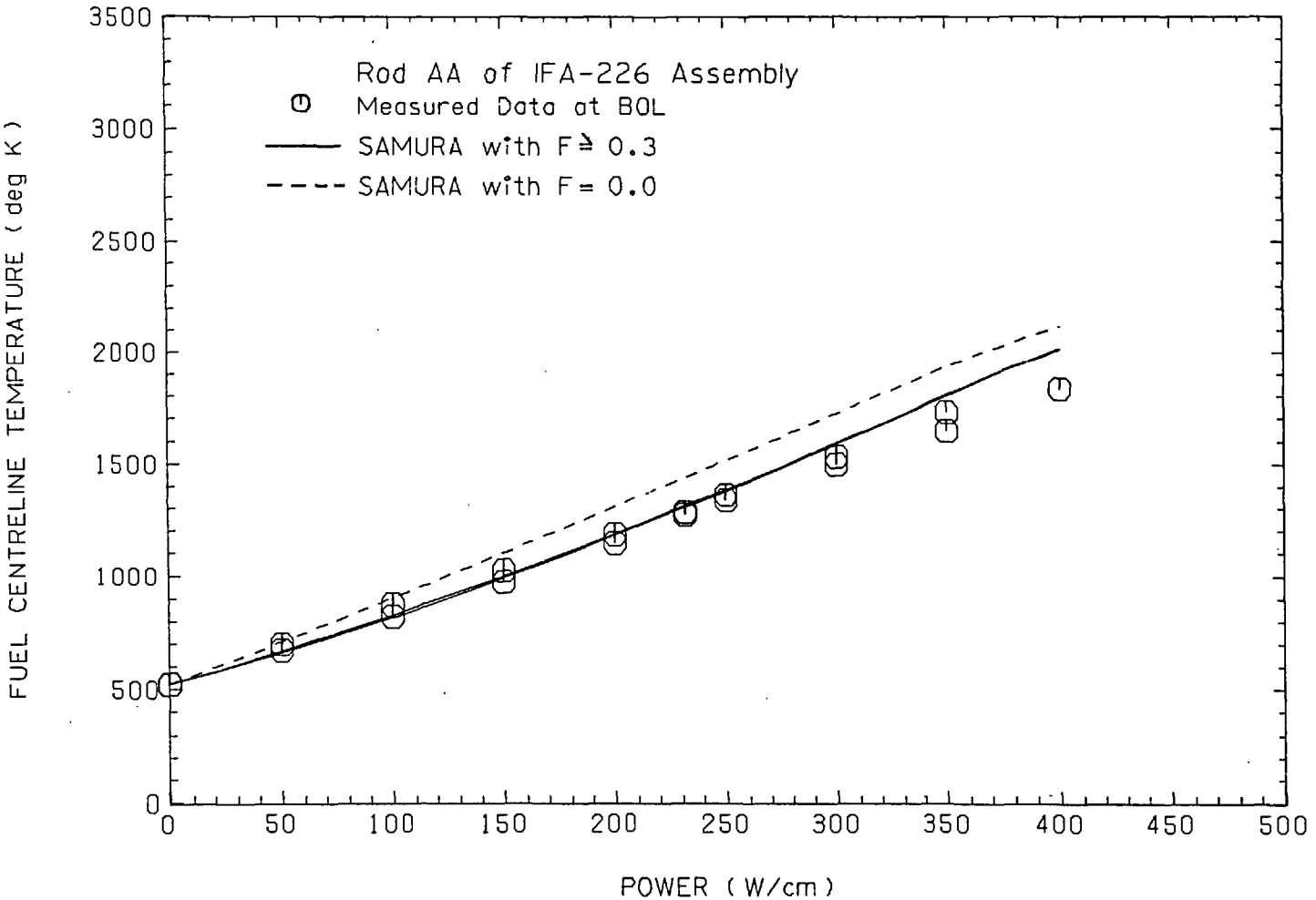


Figure 4.19

EVALUATION OF SAMURA GAP CONDUCTANCE MODEL

MEASURED AND PREDICTED FUEL CENTRELINE TEMPERATURE VS. POWER

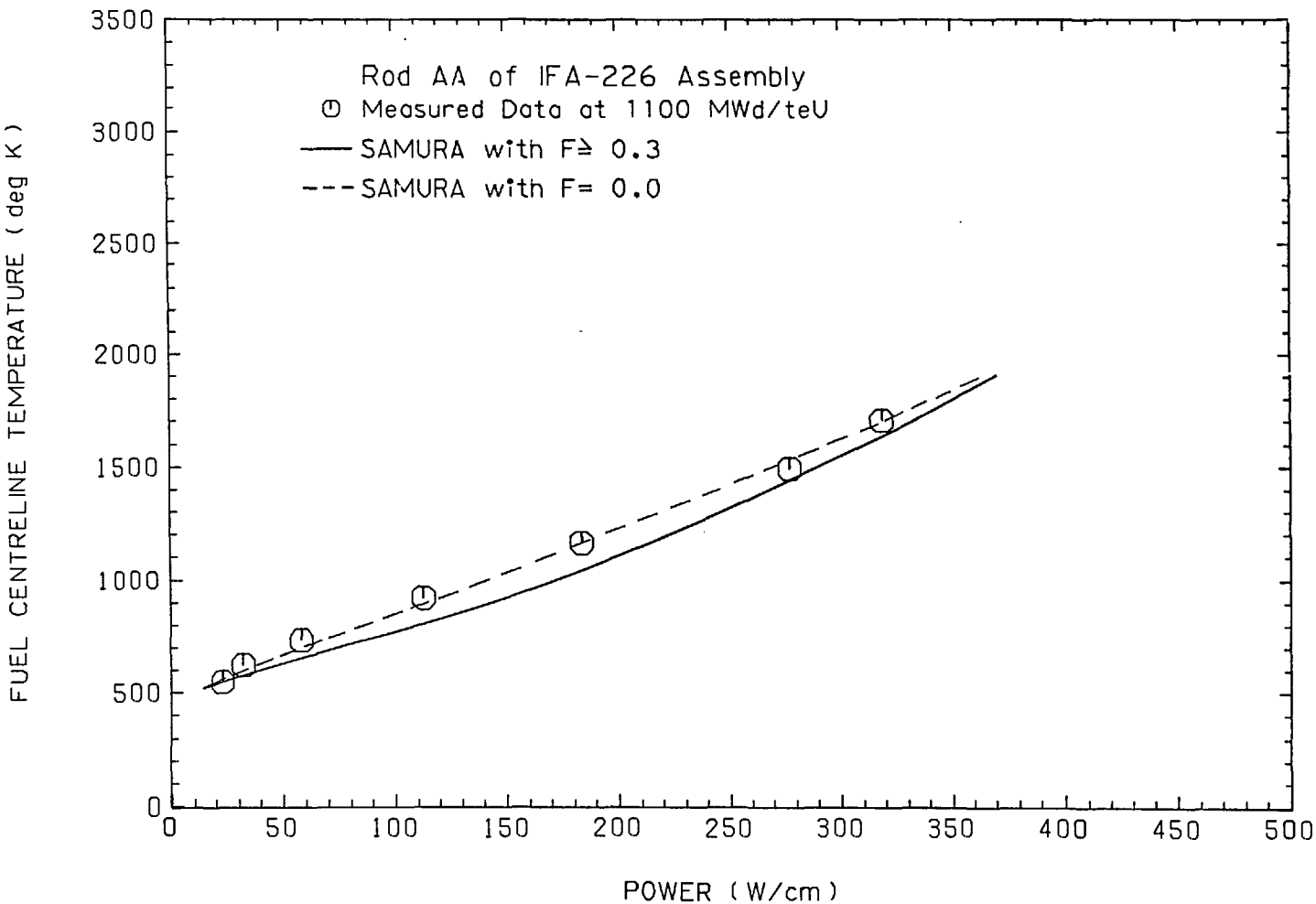


Figure 4.20

EVALUATION OF SAMURA GAP CONDUCTANCE MODEL

MEASURED AND PREDICTED FUEL CENTRELINE TEMPERATURE VS. POWER

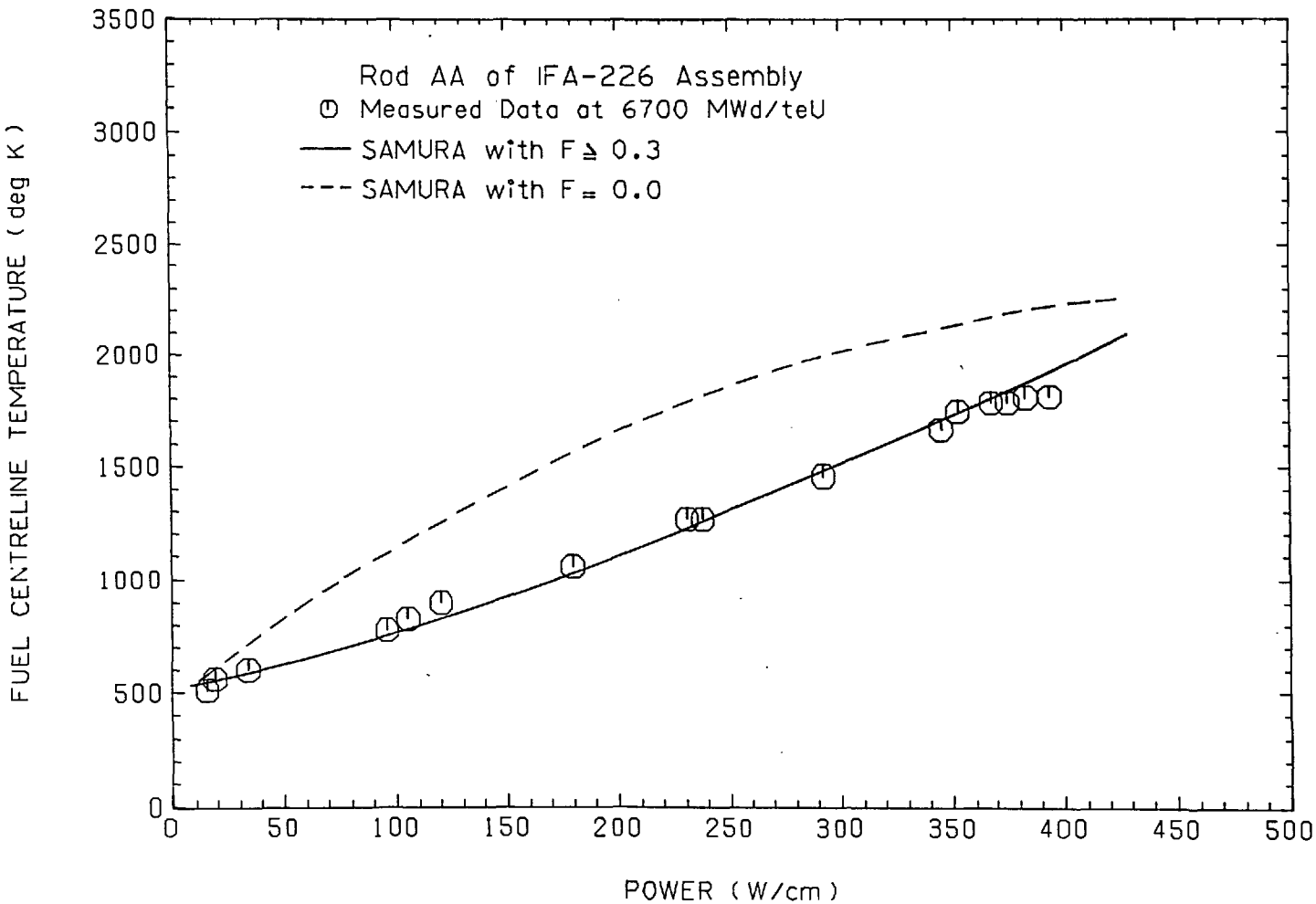


Figure 4.21

EVALUATION OF SAMURA GAP CONDUCTANCE MODEL

MEASURED AND PREDICTED FUEL CENTRELINE TEMPERATURE VS. POWER

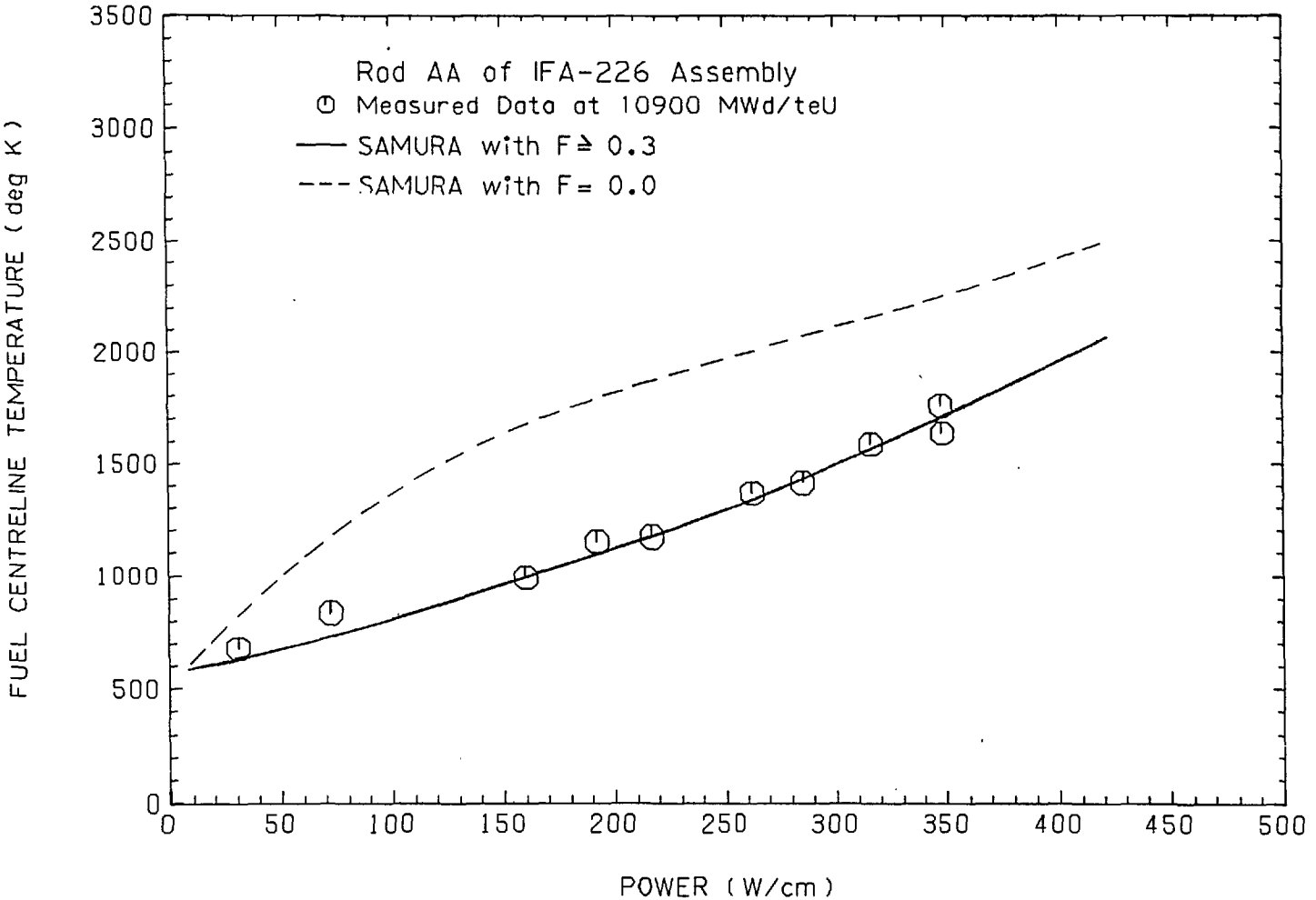


Figure 4.22

EVALUATION OF SAMURA GAP CONDUCTANCE MODEL

MEASURED AND PREDICTED FUEL CENTRELINE TEMPERATURE VS. POWER

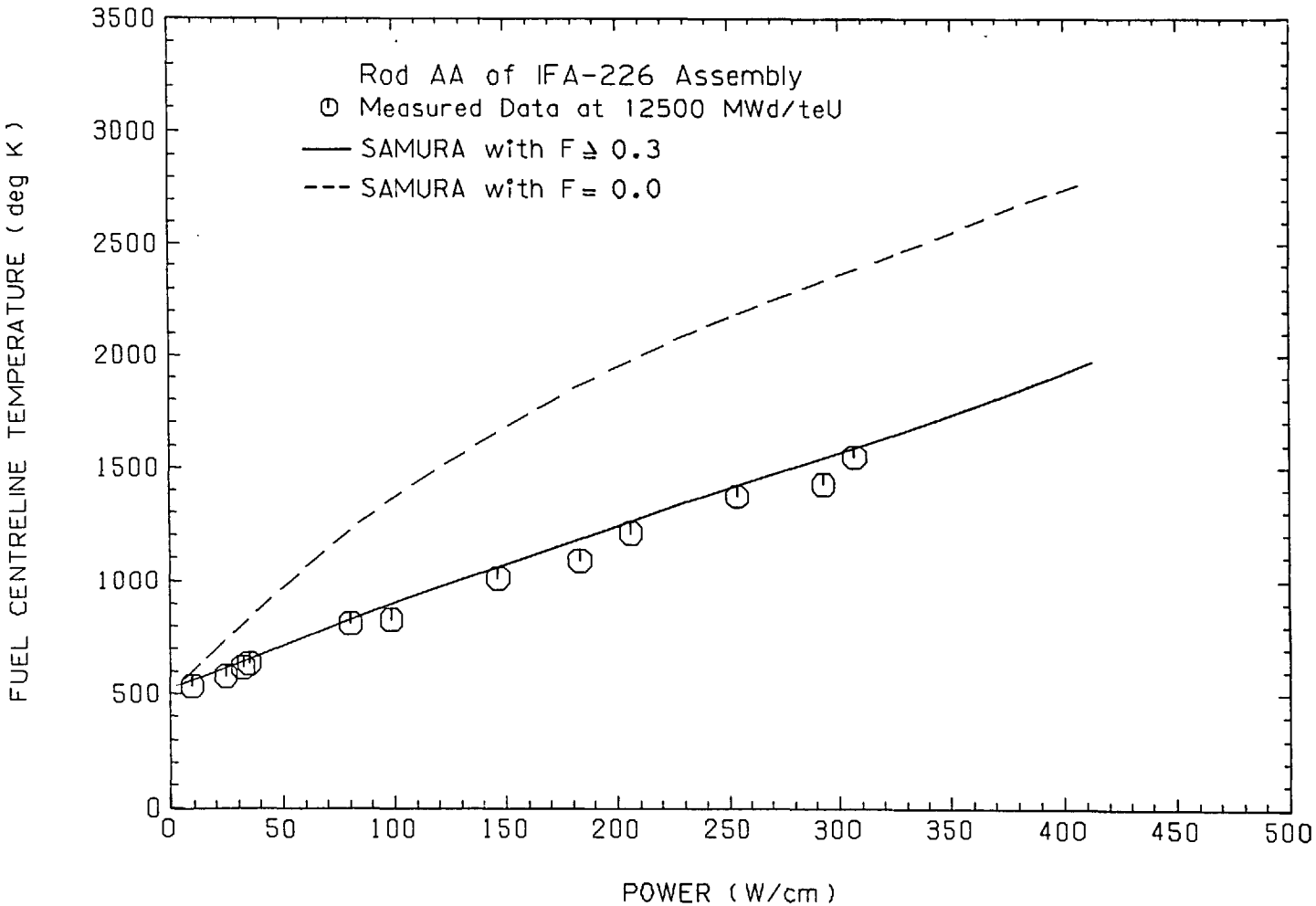
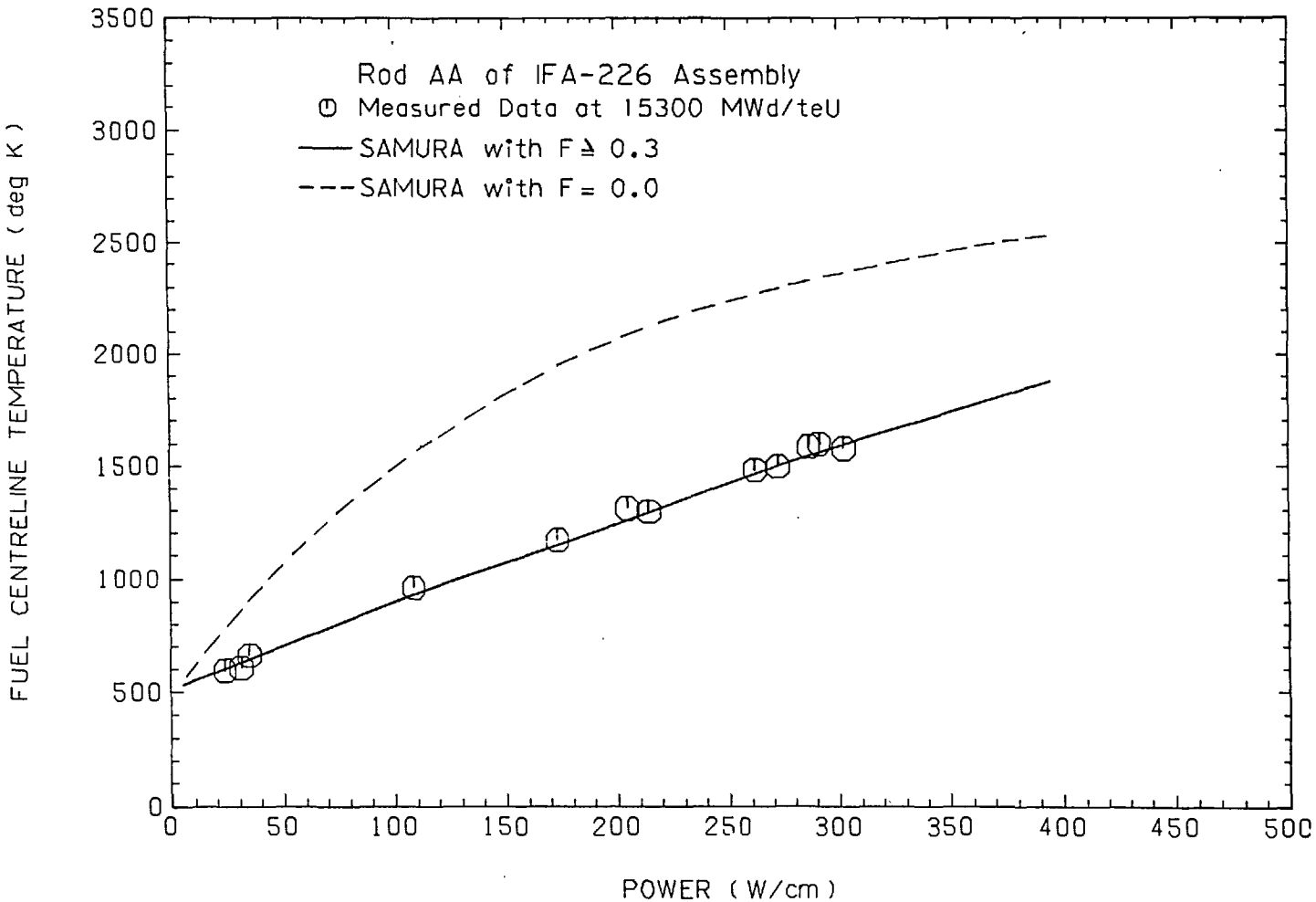


Figure 4.23

EVALUATION OF SAMURA GAP CONDUCTANCE MODEL

MEASURED AND PREDICTED FUEL CENTRELINE TEMPERATURE VS. POWER



reduces the temperature at a given power in a non-linear manner possibly due to its effect on pellet cracking and relocation. It is obvious from these graphs (Figs. 4.18 to 4.23) that the Ross and Stoute model (F = o) is very conservative at high burn-ups and predicts much smaller gap conductance values than those of the cracked pellet model ($F \geq 0.3$). They also indicate that in this particular case the predictions obtained by cracked gap model compare well with the experimental data and that the increased pellet cracking and relocation/gap closure with burn-up generally compensats for the deterioration of gap gas thermal conductivity. This, however, may not happen in all cases; thus leading to a gap conductance overprediction by SAMURA. It must also be remembered that the cracked pellet model used in SAMURA is a semi-empirical model and, as described in Sub-Section 3.3.4, is developed on the basis of somewhat limited available experimental data. Thus it should still be validated further or modified as more data become available.

4.3 MECHANICAL ANALYSIS CAPABILITIES

The main objective in this section is to evaluate the accuracy of SAMURA's stress calculation routines against some simple analytical solutions.

Here again a finite difference scheme is developed and incorporated into appropriate subroutines to solve the set of non-linear field equations described in Sub-Section 3.4.1. In order to check the accuracy of SAMURA's calculations it was decided to perform three tests:

(1) a general test of accuracy by using constant material properties and a simple temperature-independent linear creep law for, which an analytical solution exists, to predict the stresses in the cladding wall of a fuel pin (172);

(2) a test on the accuracy of creep approximations used in the code by referring to Bailey's (174) classical work on the utilization of creep test data for engineering design of thick tubes;

(3) a test on the effects of grid size (number of rings in the fuel and cladding) on the calculated results, its relation to the accuracy achieved and the computer time used.

The results of these studies are described below.

4.3.1 Comparison with Analytical Stress Analysis Solution

An exact closed-form solution for the stresses and strains in an idealised fast breeder reactor fuel pin under operational conditions has been given by D.E. Lamkin (172). This solution was used to benchmark SAMURA's numerical analysis and provide the essential assurance that the numerical techniques employed are actually giving a reasonably accurate solution.

In the analytical solutions, the fuel is considered as a single region, either solid or annular, which may or may not interact with the surrounding cladding, depending on initial fuel/cladding gap subsequent reactor operating conditions. Temperature-dependent thermal conductivity,

irradiation swelling and temperature-independent linear creep in both fuel and cladding are allowed. Although the model is considerably simplified from those used in the more detailed codes like SAMURA, design parameters of interest can be easily and readily studied, and the important mechanisms contributing to cladding deformation can be identified (172).

This stress analysis solution is applied to a specific hypothetical LMFBR fuel element operating at a constant linear heat rate of 492 W/cm. The final burn-up is assumed to be 100,000 MWd/teU. A summary of other parameters are given in Table 4.4.

TABLE 4.4

SUMMARY OF LMFBR FUEL PIN DATA (172)

Parameter	Fuel Value	Cladding Value
Geometry		
inner diameter (mm)	1.8204	5.5880
outer diameter (mm)	5.4610	6.3500
Elastic mechanical constants		
Young's modulus (MPa)	275790.3	161337.3
Poisson's ratio	0.325	0.348
Creep law (day^{-1})	$2.8 \times 10^{-8} (\frac{W}{g}) . \sigma_e$	$7.89 \times 10^{-24} . \phi . \sigma_e$ (ϕ in $n/cm^2 s$)
Power density (W/g)	265	-
Linear power (W/cm)	492	-
Coolant pressure (MPa)	-	0.5171
Fission gas pressure (MPa)	$5.171 \times 10^{-5} . Bu$ (Burn-up in MWd/teU)	-
Outer cladding temperature (^oK)	-	873

Figure 4.24

CLADDING HOOP STRESS DISTRIBUTION

AS A FUNCTION OF POSITION AND BURN-UP

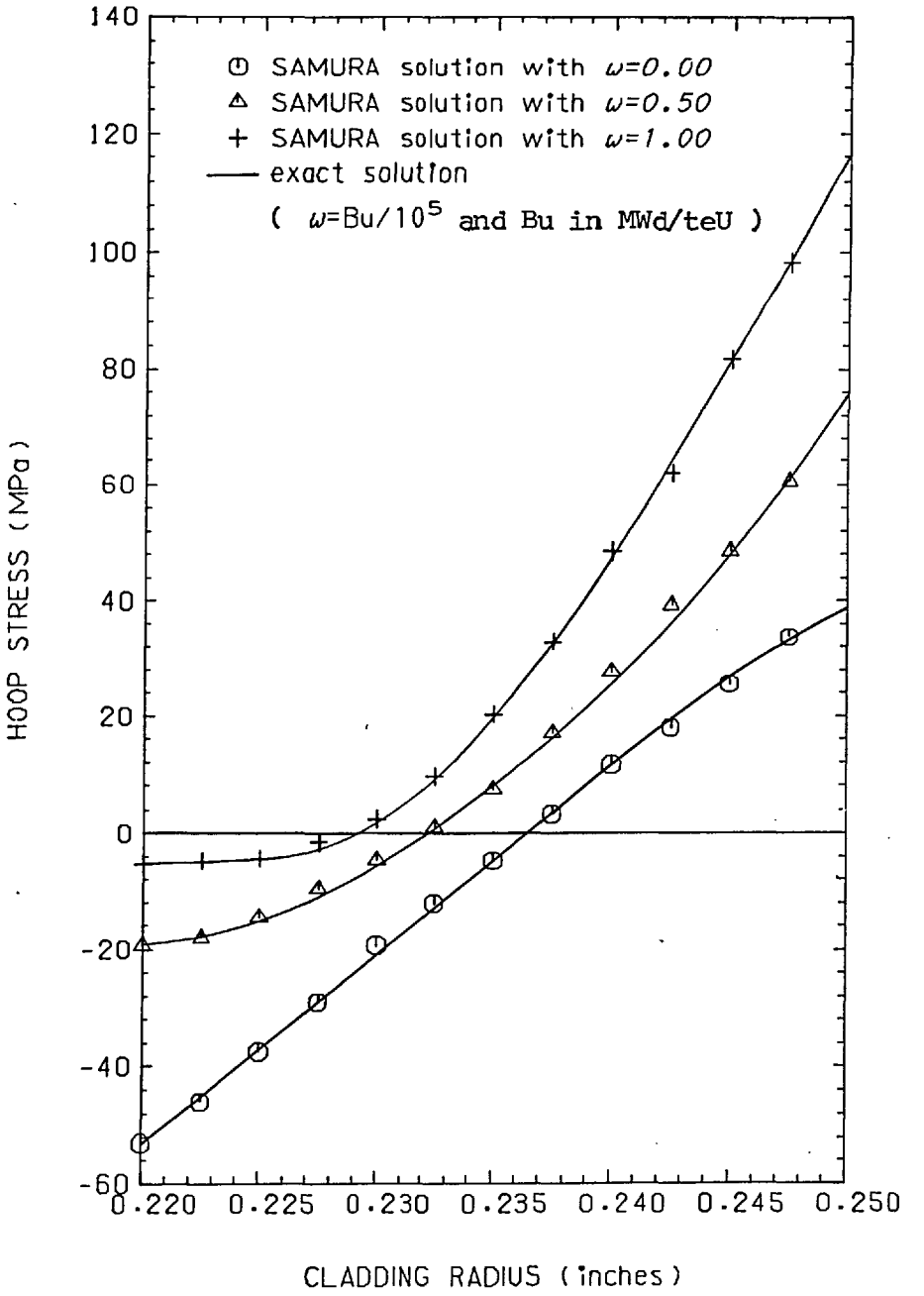


Figure 4.25

CLADDING AXIAL STRESS DISTRIBUTION

AS A FUNCTION OF POSITION AND BURN-UP

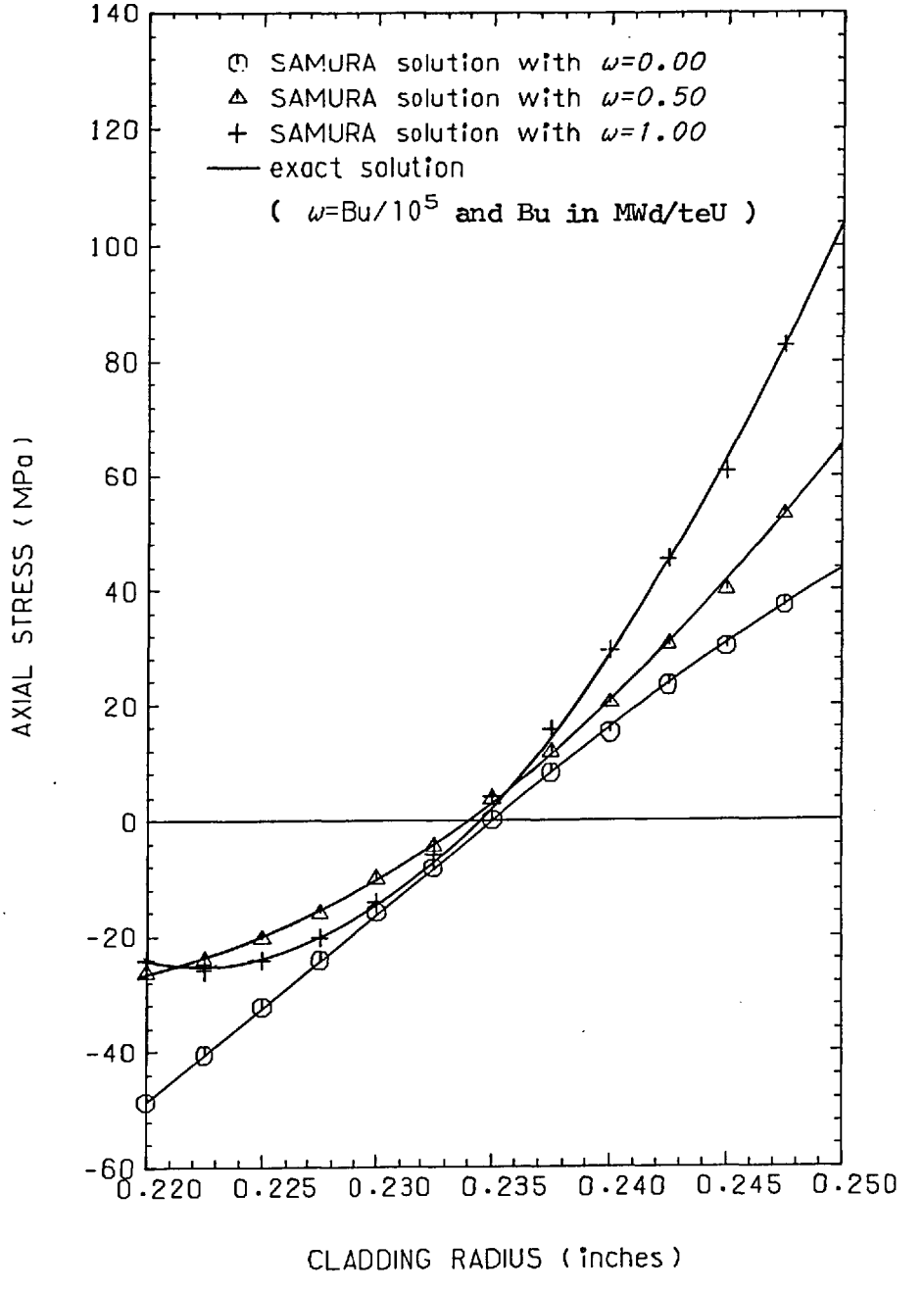
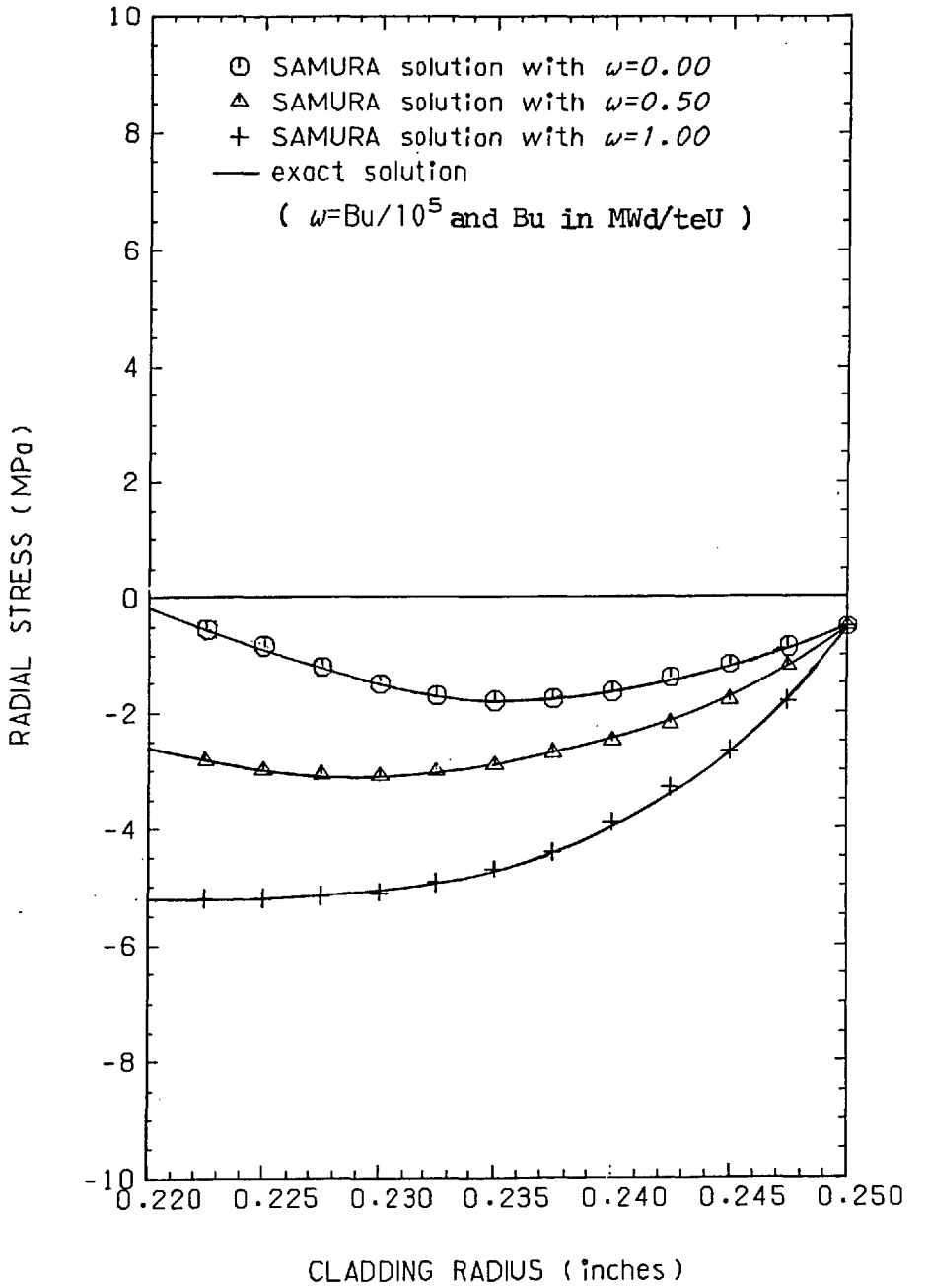


Figure 4.26

CLADDING RADIAL STRESS DISTRIBUTION

AS A FUNCTION OF POSITION AND BURN-UP



Since the stresses in the cladding are of primary interest, they have been computed for the above parameters as a function of burn-up using Lamkin's solution and that of SAMURA. Figures 4.24 through 4.26 present the results. It can clearly be seen that SAMURA's solution, which is obtained with 40 nodes in the fuel and 10 nodes in the cladding, compares well with that of the exact solution at all burn-up levels.

4.3.2 Primary Creep Behaviour of Thick Tubes

For thick tubes subjected to internal and external pressure and constant heat flux (no temperature gradient) through the wall, estimation of the creep life requires knowledge of the time variation of stress and strain in the tube wall throughout deformation. An analytical solution was first forwarded by Bailey (174) for the case of steady-state creep. Among those who have considered primary creep too, but used a numerical solution, the work of Smith (173) was found appropriate for the purpose of this test. In this work, Smith carried out his analysis for the case of a 0.2% carbon steel pressure vessel at 450^{o}C with internal and external radii of 1 and 2 inches (2.54 and 5.08 cm), respectively, subject to an internal pressure of 10 ton/in^{2} ($\sim$ 155 MPa). Assuming that creep strain for isothermal tensile data may be represented by $\varepsilon = A\sigma_e^n t^p$, then for an isotropic material subjected to complex stress, a time-hardening law for creep rate would be

$$\dot{\varepsilon} = A.p.\sigma_e^n.t^{p-1} \quad (day^{-1});$$

where the following parameterisation has been given by

Figure 4.27

SAMURA ANALYSIS OF PRIMARY CREEP BEHAVIOUR OF THICK TUBES

HOOP STRESS AT DIFFERENT RADIAL NODES VS. TIME

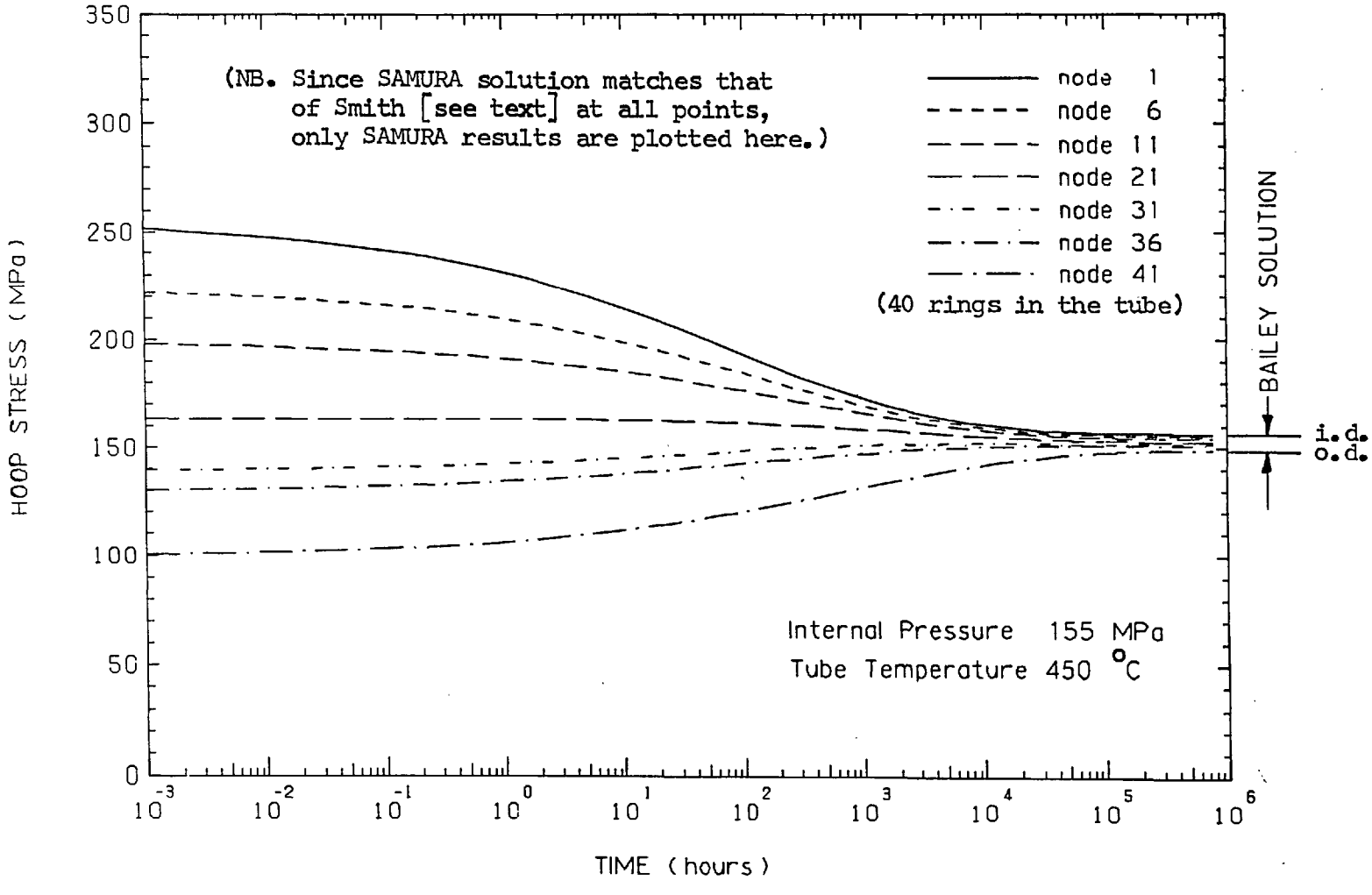


Figure 4.28

SAMURA ANALYSIS OF PRIMARY CREEP BEHAVIOUR OF THICK TUBES

AXIAL STRESS AT DIFFENET RADIAL NODES VS. TIME

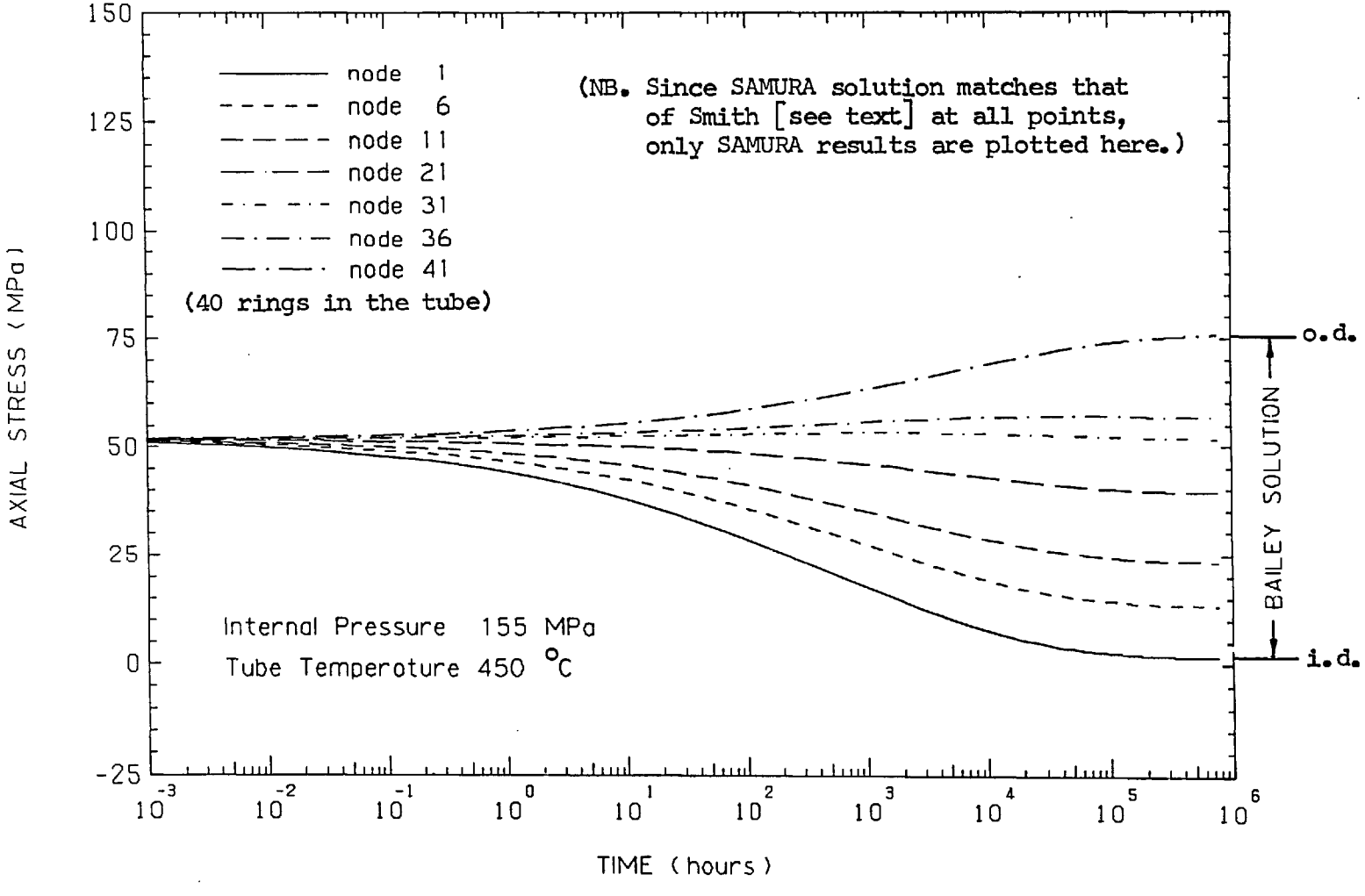


Figure 4.29

SAMURA ANALYSIS OF PRIMARY CREEP BEHAVIOUR OF THICK TUBES

INNER AND OUTER RADIUS TANGENTIAL STRAIN IN THE TUBE VS. TIME

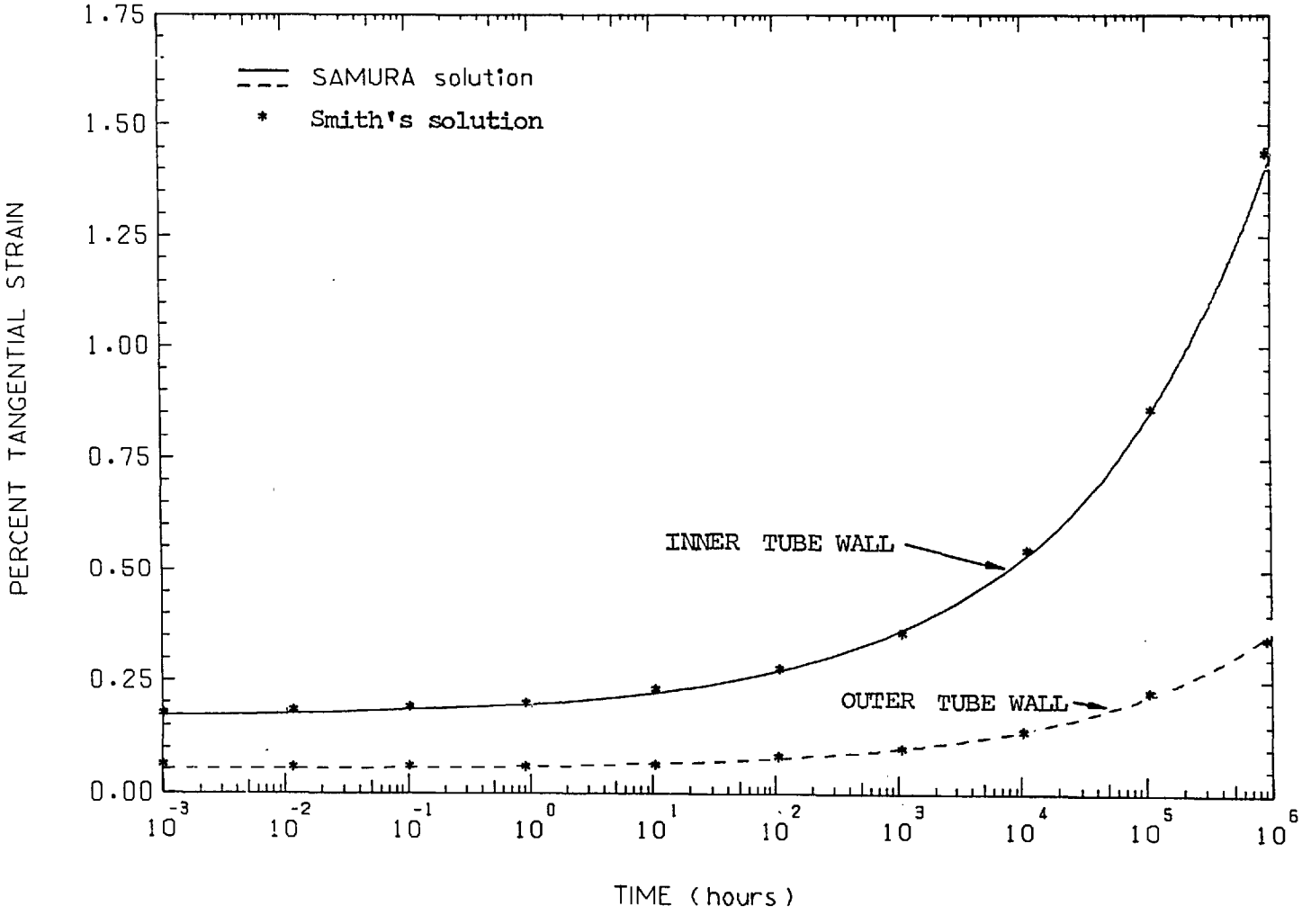
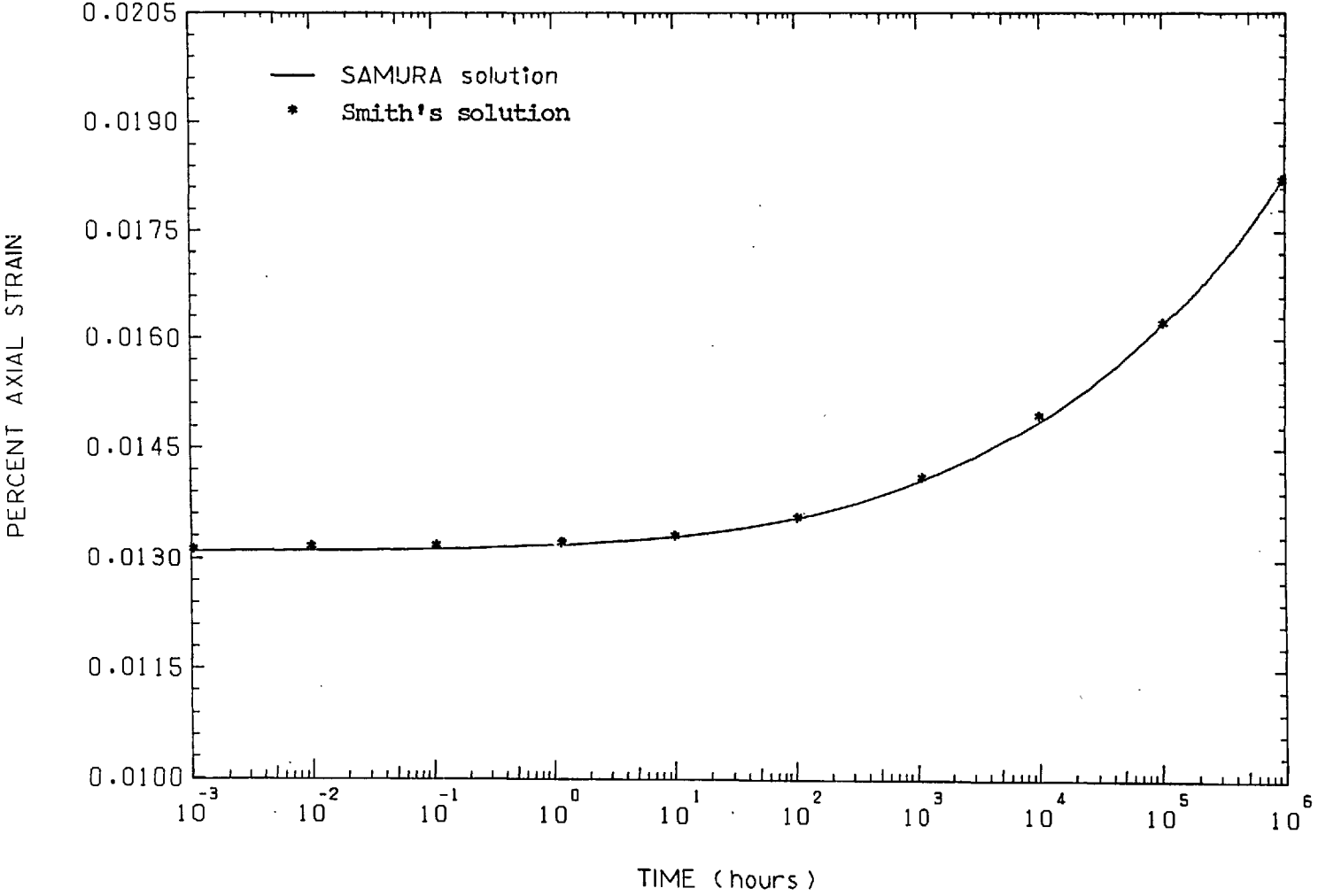


Figure 4.30

SAMURA ANALYSIS OF PRIMARY CREEP BEHAVIOUR OF THICK TUBES

AXIAL STRAIN IN THE TUBE VS. TIME



Smith (173) (with σ_e in MPa and t in days):

$$A = 5.48 \times 10^{-9},\ p = 0.27,\ n = 1.9$$

A value of 10700 ton/in^2 (165255.5 MPa) for material's Young's modulus and 0.3 for Poisson's ratio were also given.

A simple version of SAMURA (constant properties) incorporating the above information with only one region was used to obtain the stress distribution in the tube wall and the variation of these stresses with time. The results are shown in Figures 4.27 through 4.30 alongside those of Bailey (174) and Smith (173). The agreement is very good and it is seen that the stress distribution at about 10^5 hours is tending to that given by Bailey for steady-state creep law, which is indicated on the graphs.

4.3.3 Effects of Grid Size on the Calculations

In order to ascertain the effects of varying the grid size some calculations were performed with 10, 20, 40, 60 and 120 radial rings in the fuel, with the number in the cladding held constant at 10 since it was felt that the results would be more sensitive to the number of nodes in the fuel. For this study a pre-pressurised pin of UO_2 fuel with Zircaloy cladding, which is a typical fuel pin in the Argentine Atucha PWR (175), was used. No central fabrication hole nor dishing is reported to exist in the fuel pellet which has an external radius of 5.31 mm at room temperature. The cladding external radius is 5.95 mm and its internal radius is 5.40 mm, leaving an initial cold

gap of 90 μm. The pin has an initial internal He pressure of 17 atm (1.72 MPa) at room temperature and the coolant pressure is 120 atm (12.16 MPa) with an axially average cladding surface temperature of 578^{o}K. For the sake of clarity a simple power history was considered in which the pin linear heat rating was raised from zero to 550 W/cm in 0.5 days and then a constant rating of 550 W/cm was maintained for 110 days. This two-period power history was simulated for the Atucha pin using the full version of SAMURA with the different grid sizes mentioned earlier. Several variables were chosen as the optimal parameters, and are plotted against number of rings in the fuel in Figures 4.31 through 4.33 . Also, the variation of gap width, contact pressure and stress distribution are presented for different numbers of nodes in Figures 4.34 to 4.39 .

Figure 4.31 gives the variation of time of gap closure against the number of rings in the fuel. Here the gap closure time varies quite markedly with the number of rings; the variation being from $\sim$ 1.05 days with 10 rings to 1.78 with 120 rings. There is, however, an apparent threshold above which the approach to a limiting value of gap closure time is very close. This starts at about 50 rings, above which gap closure time varies by less than 5% from the estimated asymptotic value of 1.78 days. Next graph, Fig. 4.32 , presents the variation of program execution time/time-step against the number of rings for this case. The dependence is almost linear suggesting that the higher the number of rings the higher the total program

Figure 4.31

SENSITIVITY OF SAMURA TO RADIAL GRID SIZE

TIME OF GAP CLOSURE VS. NUMBER OF RINGS IN THE FUEL

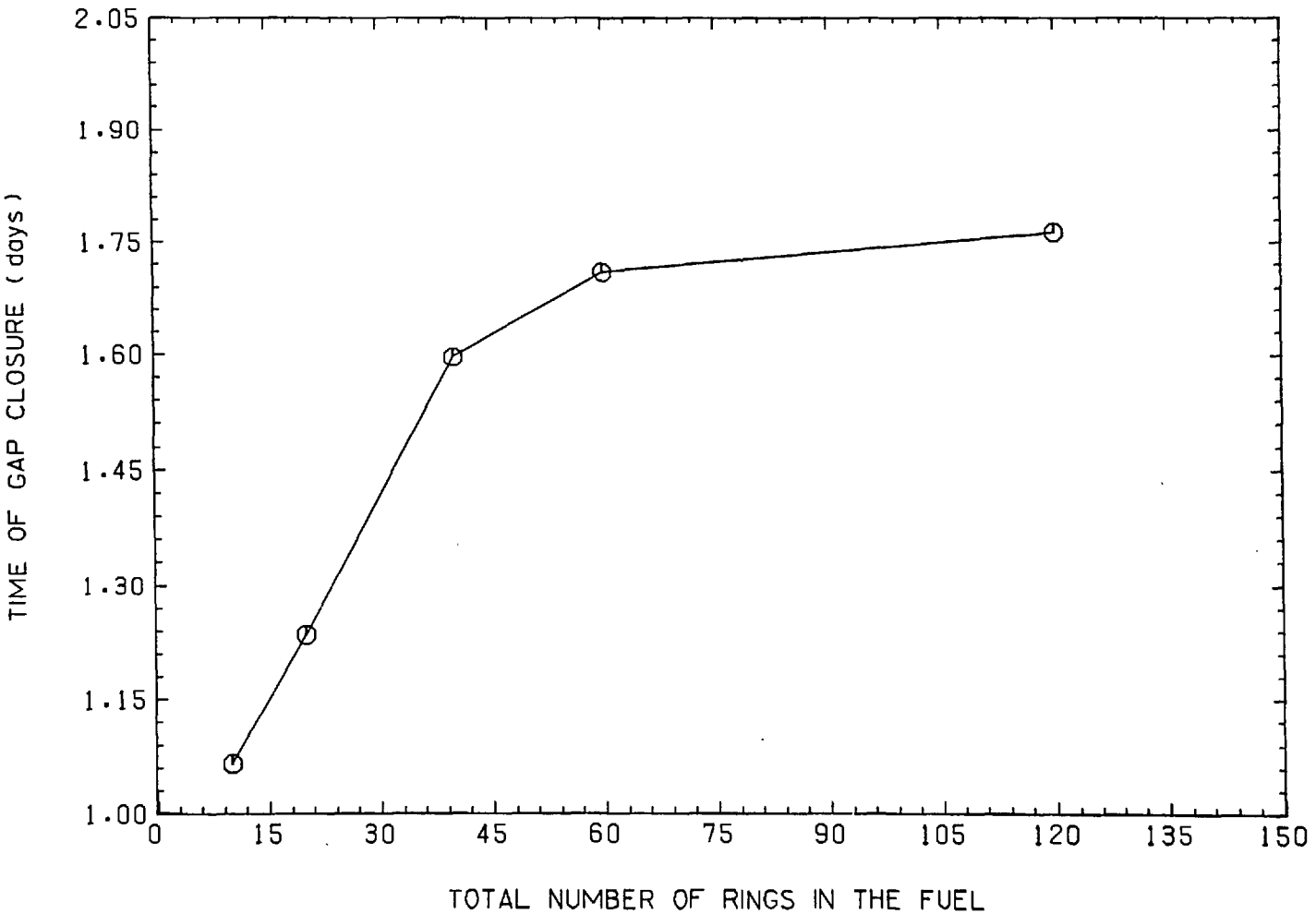


Figure 4.32

SENSITIVITY OF SAMURA TO RADIAL GRID SIZE

EXECUTION TIME/TIME-STEP VS. NUMBER OF RINGS IN THE FUEL

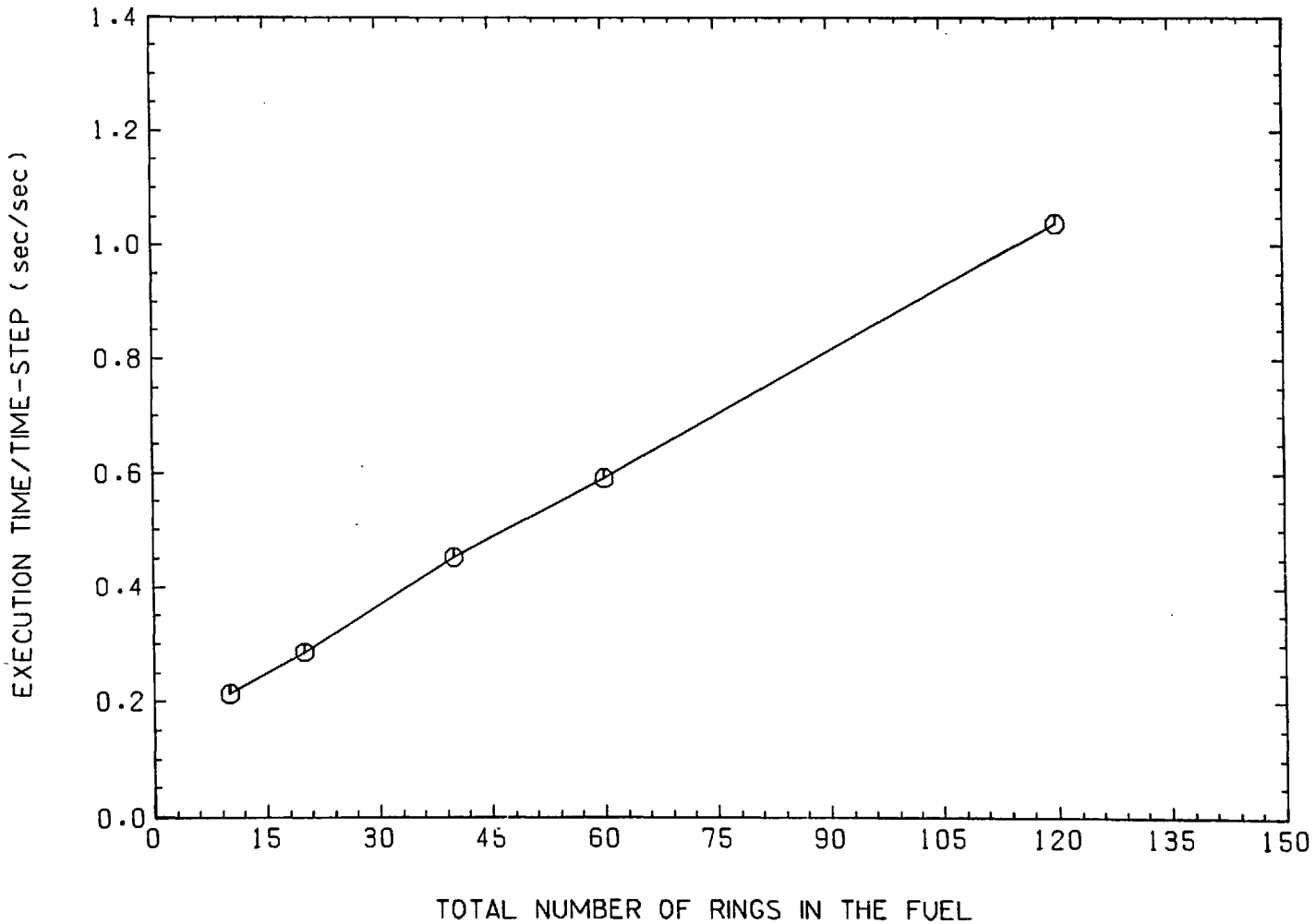
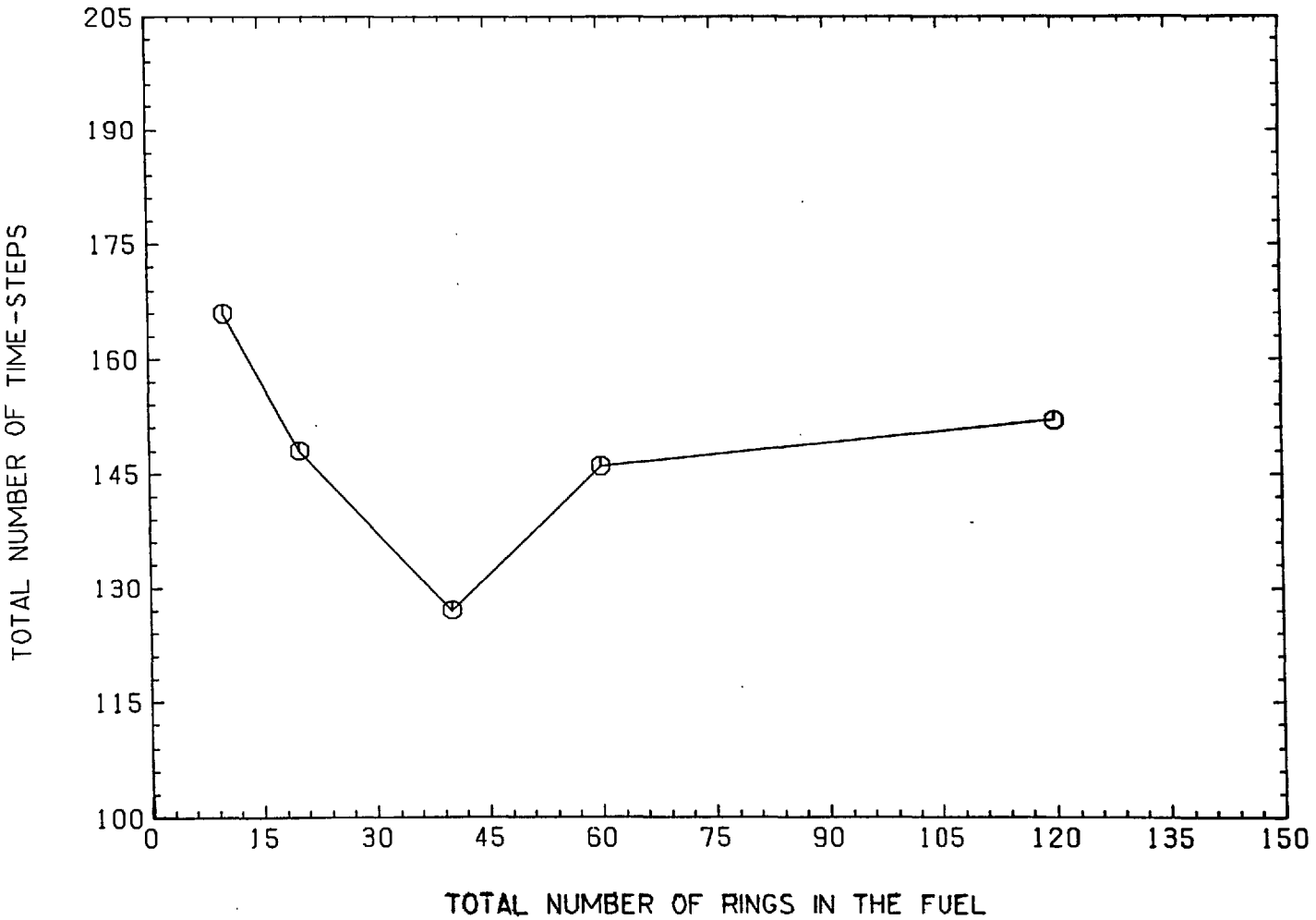


Figure 4.33

SENSITIVITY OF SAMURA TO RADIAL GRID SIZE

NUMBER OF TIME-STEPS FOR EXECUTION VS. NUMBER OF RINGS IN THE FUEL



execution time/time-step. However, it must be remembered that the actual time used "per time-step per radial node" is decreasing with increasing number of nodes. For instance, with 120 rings this value is 8.65 msec per time-step per node and with 40 nodes it is 14.3 msec per time-step per node. For comparison purposes, in Fig. 4.33 the variation of the number of time-steps used for each case is plotted against the number of rings.

In Figures 4.34 and 4.35 the gap width as a function of time for various values of the radial grid size is shown. It is seen that the gap width calculated at the end of up-ramp with 10 rings is approximately half that calculated with 120 rings, while the difference between the 60 ring grap and that of 120 is very little. This explains the differences predicted in gap closure time by different grid sizes. (For clarity, in Fig. 4.35 part of Fig. 4.34 has been enlarged.) Another parameter of interest is the contact pressure. This is shown in Fig. 4.36 for various grid sizes. The difference between the maximum value of contract pressure for this parameter is small.

In order to demonstrate the distribution of stresses in the fuel as a function of the radial mesh size the values of σ_r, σ_θ and σ_z are shown in Figures 4.37 - 4.39 , respectively, at the end of up-ramp. Convergence towards an asymptotic value for larger numbers of rings is rapid, with the exception of the 10 ring grid all the values are very close over the whole range of pellet radius. The interesting phenomenon, which is more apparent on the σ_z

Figure 4.34

SENSITIVITY OF SAMURA TO RADIAL GRID SIZE

FUEL/CLAD GAP WIDTH VS. GAP CLOSURE TIME FOR VARIOUS GRID SIZES

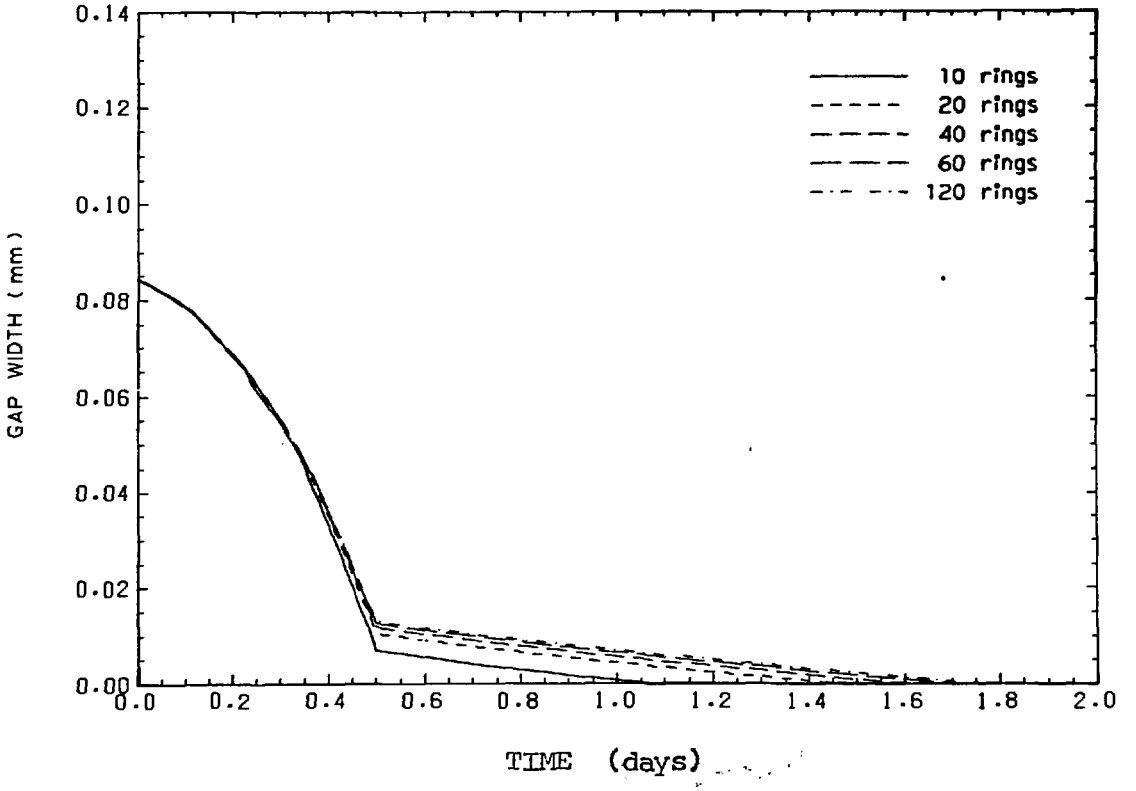


Figure 4.35

SENSITIVITY OF SAMURA TO RADIAL GRID SIZE

FUEL/CLAD GAP WIDTH VS. GAP CLOSURE TIME FOR VARIOUS GRID SIZES

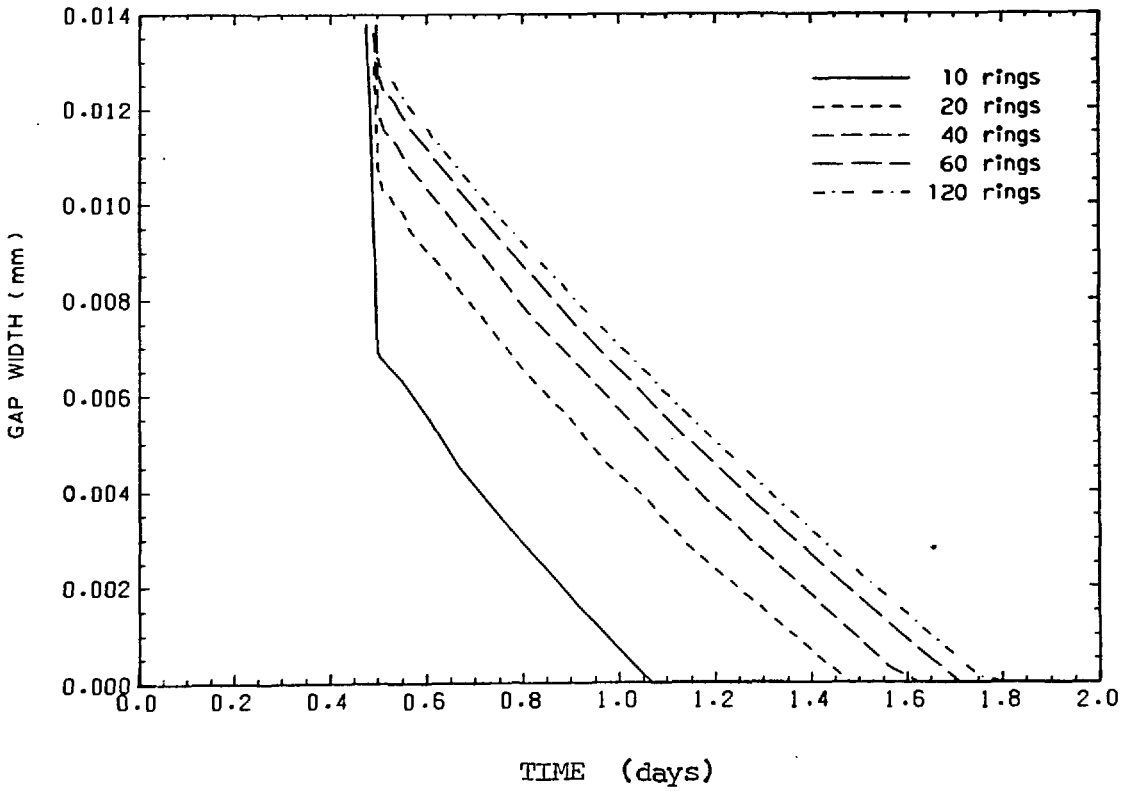


Figure 4.36

SENSITIVITY OF SAMURA TO RADIAL GRID SIZE

GAP CONTACT PRESSURE VS. IRRADIATION TIME FOR VARIOUS GRID SIZES

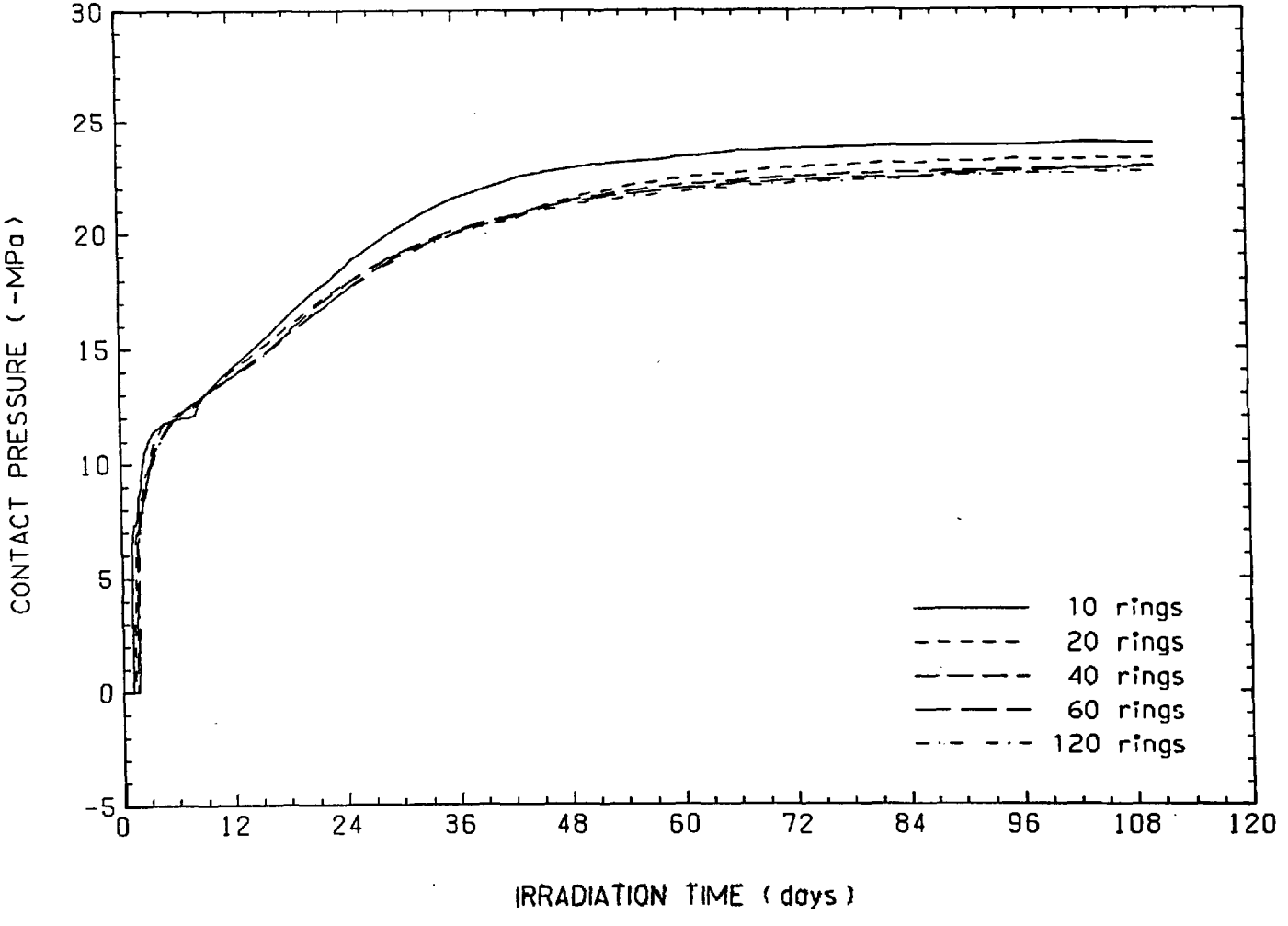


Figure 4.37

SENSITIVITY OF SAMURA TO RADIAL GRID SIZE

RADIAL STRESS DISTRIBUTION VS. PELLET RADIUS FOR VARIOUS GRID SIZES

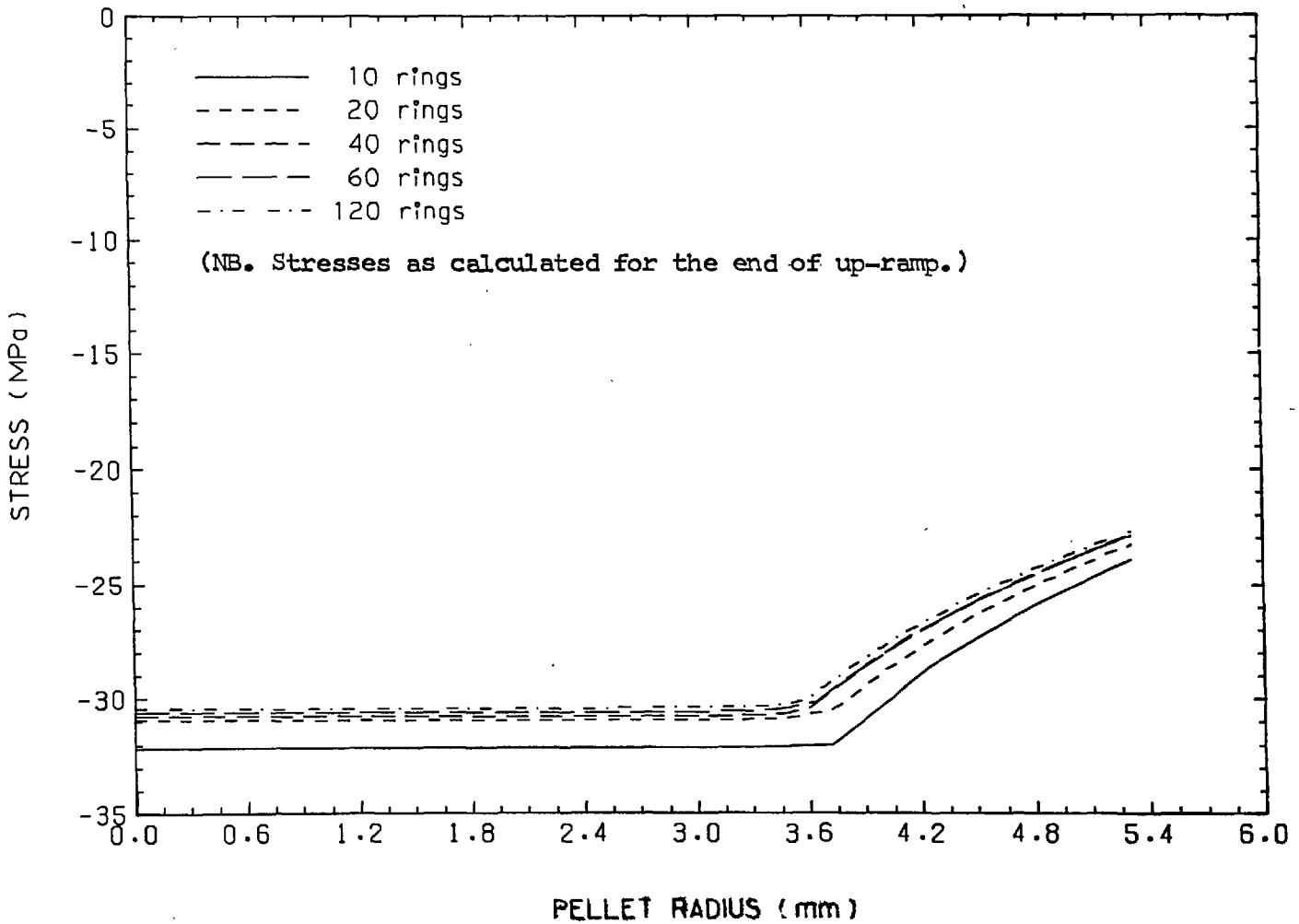


Figure 4.38

SENSITIVITY OF SAMURA TO RADIAL GRID SIZE

RADIAL STRESS DISTRIBUTION VS. PELLET RADIUS FOR VARIOUS GRID SIZES

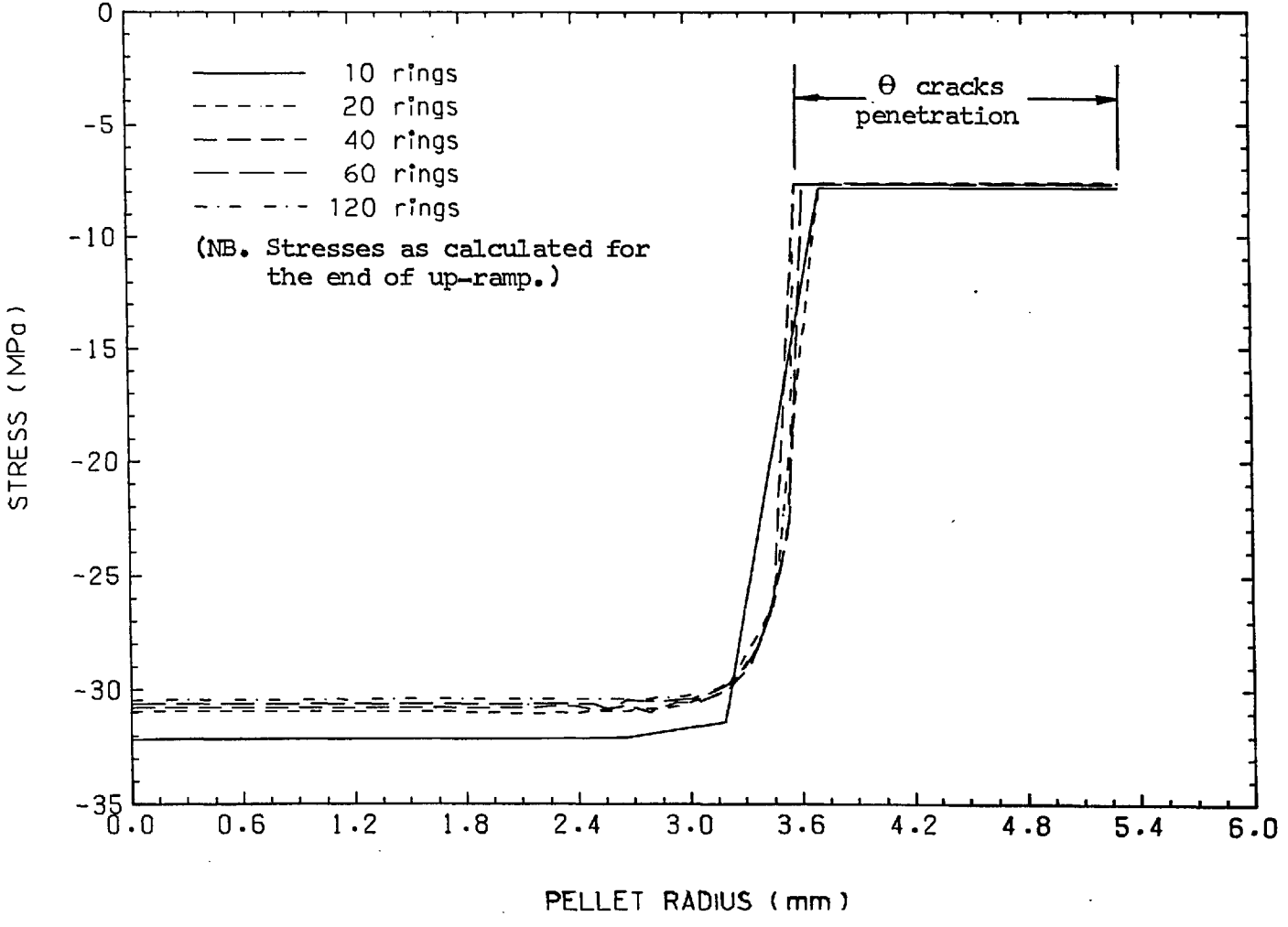
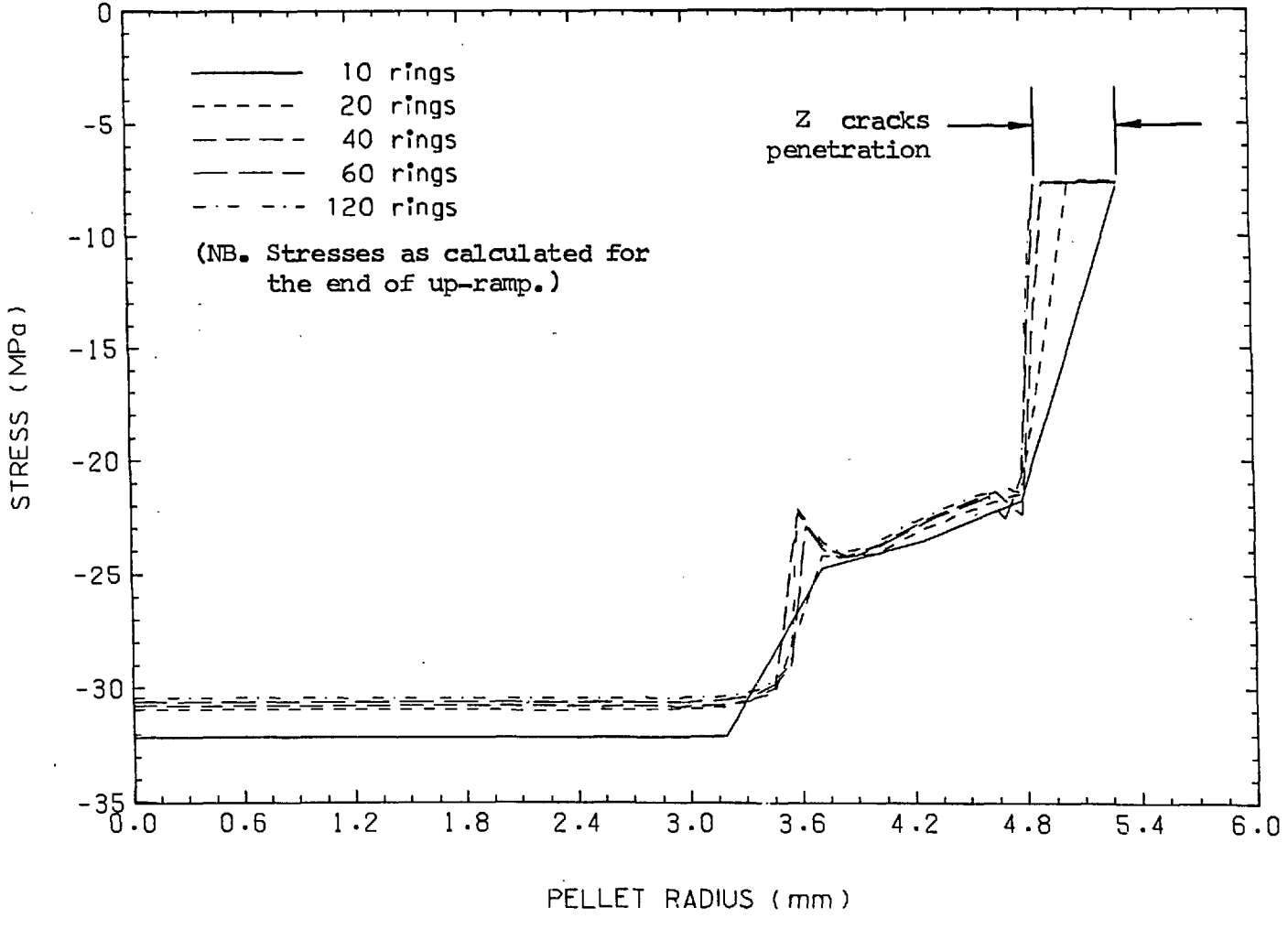


Figure 4.39

SENSITIVITY OF SAMURA TO RADIAL GRID SIZE

AXIAL STRESS DISTRIBUTION VS. PELLET RADIUS FOR VARIOUS GRID SIZES



graph, is that of the 10 ring calculation where it is seen that the stresses have actually averaged themselves over the radius without causing any failure of the numerical solution. This is attributed to the stability of the differencing shceme and the automatic choice of time-steps by reference to accuracy criteria built into the program.

It may finally be concluded that accurate calculations can be performed with moderate grid sizes and considerable saving in computer time. The above results show that for this particular case any grid size of between 40 to 60 rings in the fuel would give quite satisfactory results. The author's own experience with the program, so far, has provided him with a rule of thumb to estimate the grid size and that is about 10 rings for every millimetre of fuel radius (i.e. for r_f = 5.31 mm, NF = 50).

4.4 MODELLING OF A TYPICAL FUEL PIN AND POWER HISTORY

In this section SAMURA is used to model a PWR fuel pin irradiated under the Atucha reactor (175). The simulated power cycle, shown in Figure 4.40 , resembles the one suffered by the fuel pin at the Atucha reactor when the fuel is replaced from one channel to another during operation. The fuel residence time for the first part of the cycle is 80 days attaining a burn-up of 2500 MWd/teU under a constant linear heat rating of 250 W/cm. After the second up-ramping the linear heat rating is increased to 550 W/cm and maintained for 110 days to achieve a total burn-up of about 10,000 MWd/teU for the whole of the cycle.

TABLE 4.5

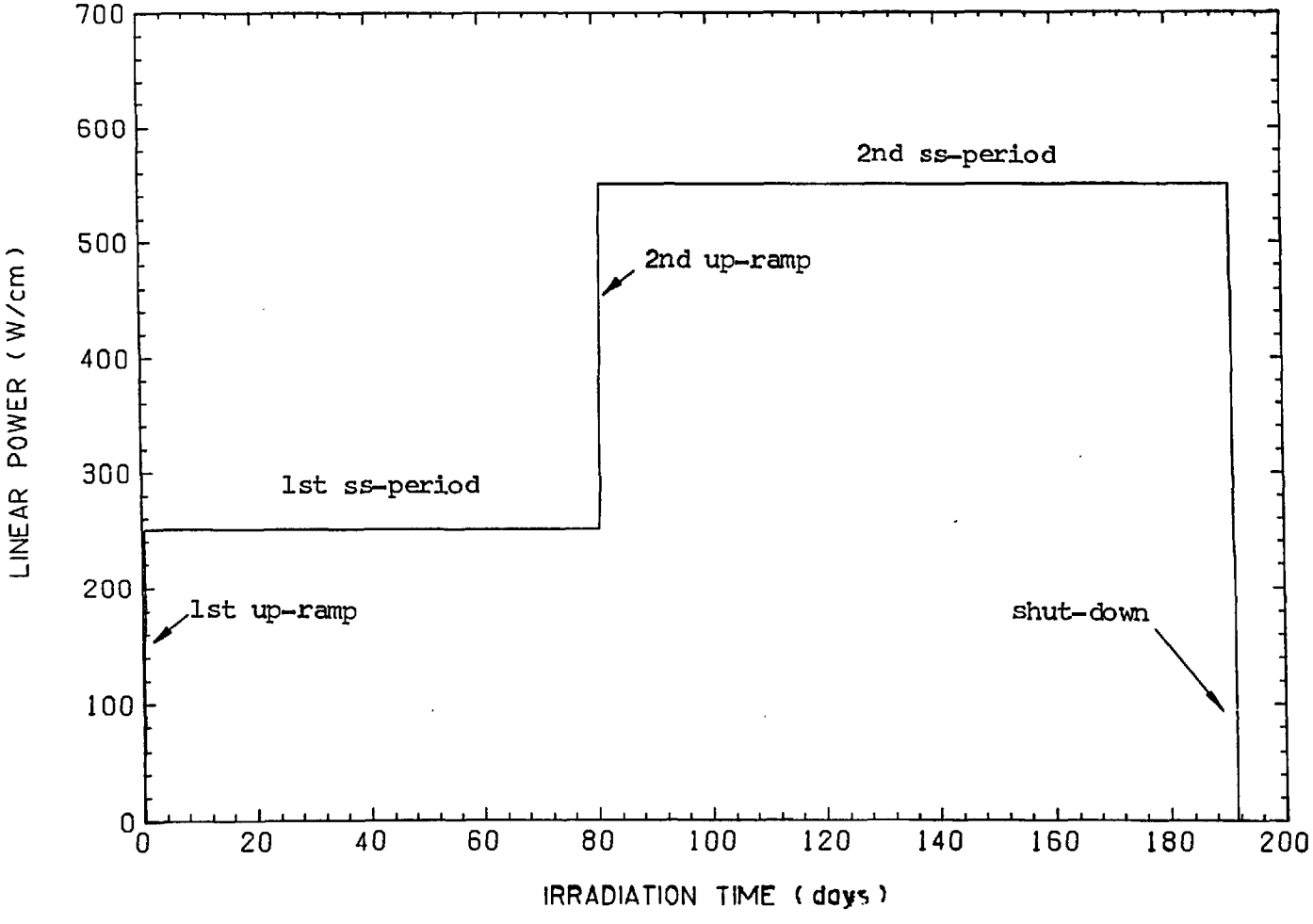
FUEL PIN DATA FOR ATUCHA PWR (179)

General Input Requirements	Value	Units
Fuel Pellet ID	0.0	mm
Fuel Pellet OD	10.62	mm
Active Fuel Length	3.4722	m
Effective Pin Length	3.7338	m
Fuel Density	95.0	% TD
Fuel Enrichment	4	%
Fuel Grain Size	7	μm
Total Fuel Column Dish Volume	0.0	m^3
In-pile Fuel Densification by 4000 MWd/teU	0.0	% TD
Fuel Surface Roughness	4.38×10^{-6}	m
Cladding ID	10.80	mm
Cladding OD	11.90	mm
Initial Fill Gas	100% He	by volume
Initial Fill Pressure STP	1.72	MPa
Plenum Gas Temperature	600	^oK
Plenum Void Volume	2.3965×10^{-5}	m
Average Coolant Temperature	578	^oK
Coolant Pressure	12.16	MPa

Figure 4.40

MODELLING OF ATUCHA PWR ROD UNDER A TYPICAL POWER CYCLE

ROD LINEAR HEAT RATING VS. IRRADIATION TIME FOR THE GIVEN POWER CYCLE



The fuel pin is the same as the one described in the previous section (Sub-Section 4.3.3). Table 4.5 contains a complete set of parameters relevant to the pin. Some characteristic results for this case are presented graphically in Figures 4.40 through 4.70 and discussed below. Note that two calculations were performed, one ignoring pellet cracking (to emphasise the importance to the code predictions of including a pellet fracture model) and another with pellet cracking. The power history and the rest of the data were identical for these calculations. Furthermore, the particular parameterisation used in SAMURA as described in Section 3.5 was applied to this analysis.

Figures 4.41 and 4.42 give the variation of fission gas release and fuel centreline temperature versus irradiation time with and without cracking. Fission gas release remains less than 2% during the first steady-state period (80 days) and there is no significant difference between the two cases (cracking and no cracking). This is basically because the temperature behaviour is the same. Fuel centreline temperature during this period is quite low and stays around 1200^{o}K. That explains the low release of fission gases. However, after the second up-ramp (in 0.5 days the power is raised from 250 W/cm to 550 W/cm) the fuel centreline temperature is suddenly raised to 2120^{o}K with cracking and to 2220^{o}K without cracking. The differences have become quite apparent due to the fact that with cracking pellet radial displacement is much larger during the up-ramping and the gap closure occurs earlier so there

Figure 4.41

MODELLING OF ATUCHA PWR ROD UNDER A TYPICAL POWER CYCLE

FISSION GAS RELEASE VS. IRRADIATION TIME

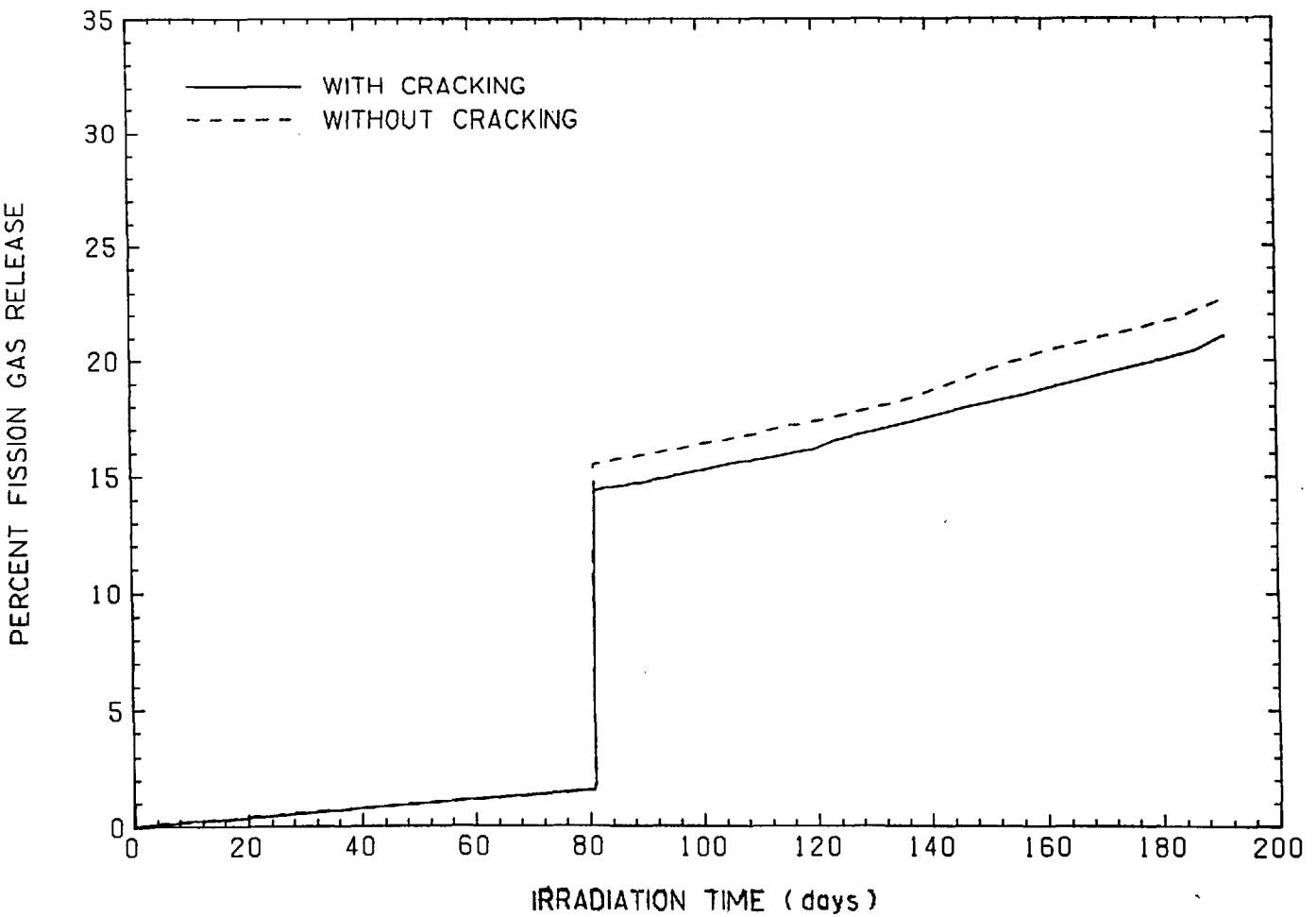
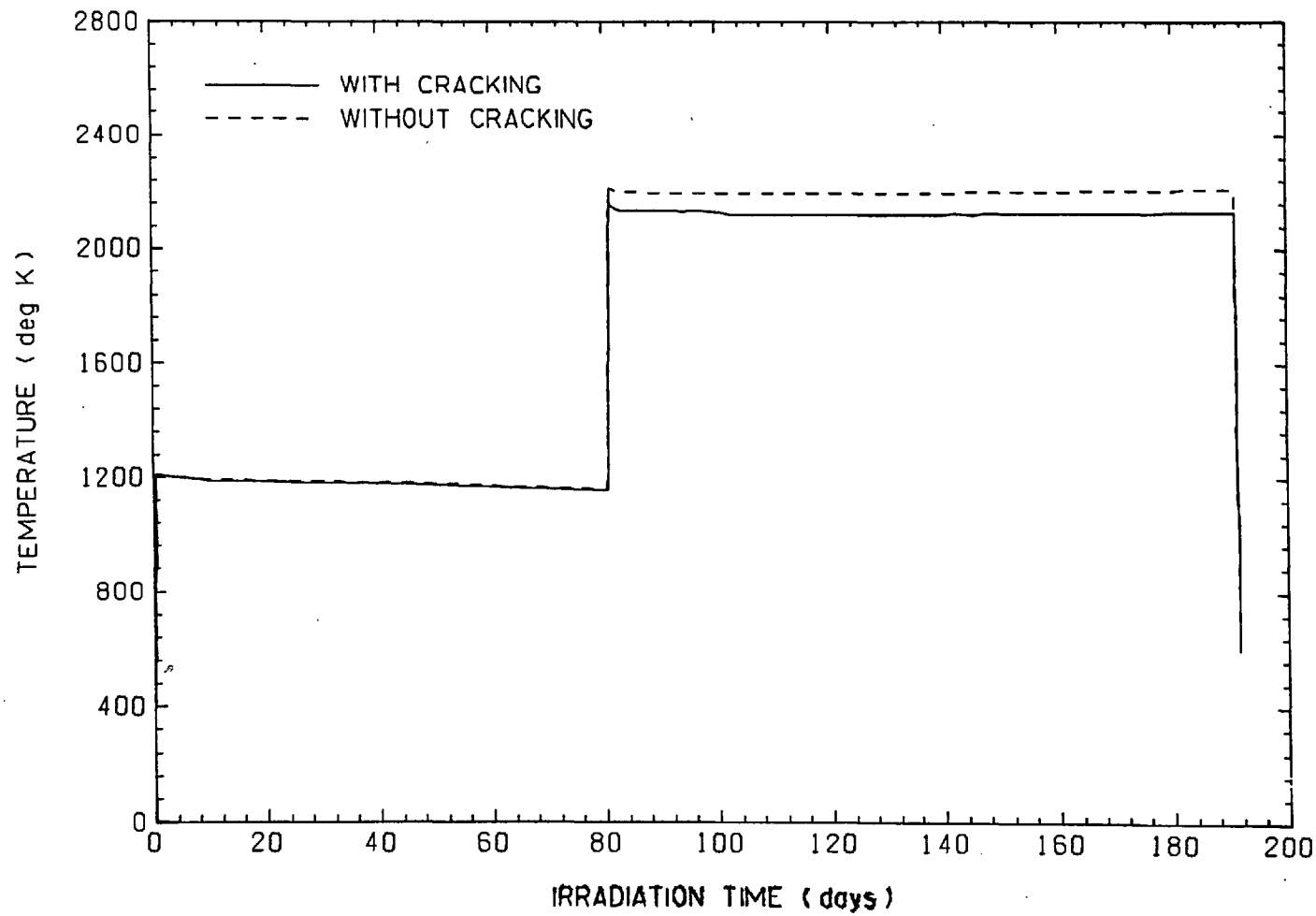


Figure 4.42

MODELLING OF ATUCHA PWR ROD UNDER A TYPICAL POWER CYCLE

FUEL CENTRELINE TEMPERATURE VS. IRRADIATION TIME



is more heat transferred via the cladding. Obviously due to high fuel temperatures fission gas release increases too; without cracking it is 23% at the end of life and with cracking 21%.

Figure 4.43 shows the radial temperature distribution in the fuel at several times during irradiation with pellet cracking. The highest temperature is achieved at 81 days (end of up-ramping). The temperatures in the central region of the fuel fall by about 60^{o}K during the second steady-state period that follows. While the temperatures in the colder region have slightly increased. The temperature fall in the central region is due to pore migration effects; and the rise in pellet surface temperature due to a fall in gap conductance. In fact, if one looks at how the gap conductance and gap width (shown in Figures 4.44 and 4.45) vary during this period one may be able to explain the temperature behaviour more clearly. It is seen that gap conductance is decreasing during the second steady-state period due to the relaxation of contact pressure. This means that fuel temperature must actually rise. However, due to high temperatures (above 2000^{o}K) in the central fuel region after the up-ramp , high rates of pore migration occurs towards the centre causing the movement of fuel radii outwards, the formation of a small central void, and the temperature fall in the centre.

It is interesting to note the differences between the cracked and uncracked pellet solutions in Figures 4.44 and 4.45 . The gap closure occurs during the second

Figure 4.43
MODELLING OF ATUCHA PWR ROD
FUEL TEMPERATURES WITH CRACKING
VS. PELLET RADIUS AT DIFFERENT TIMES

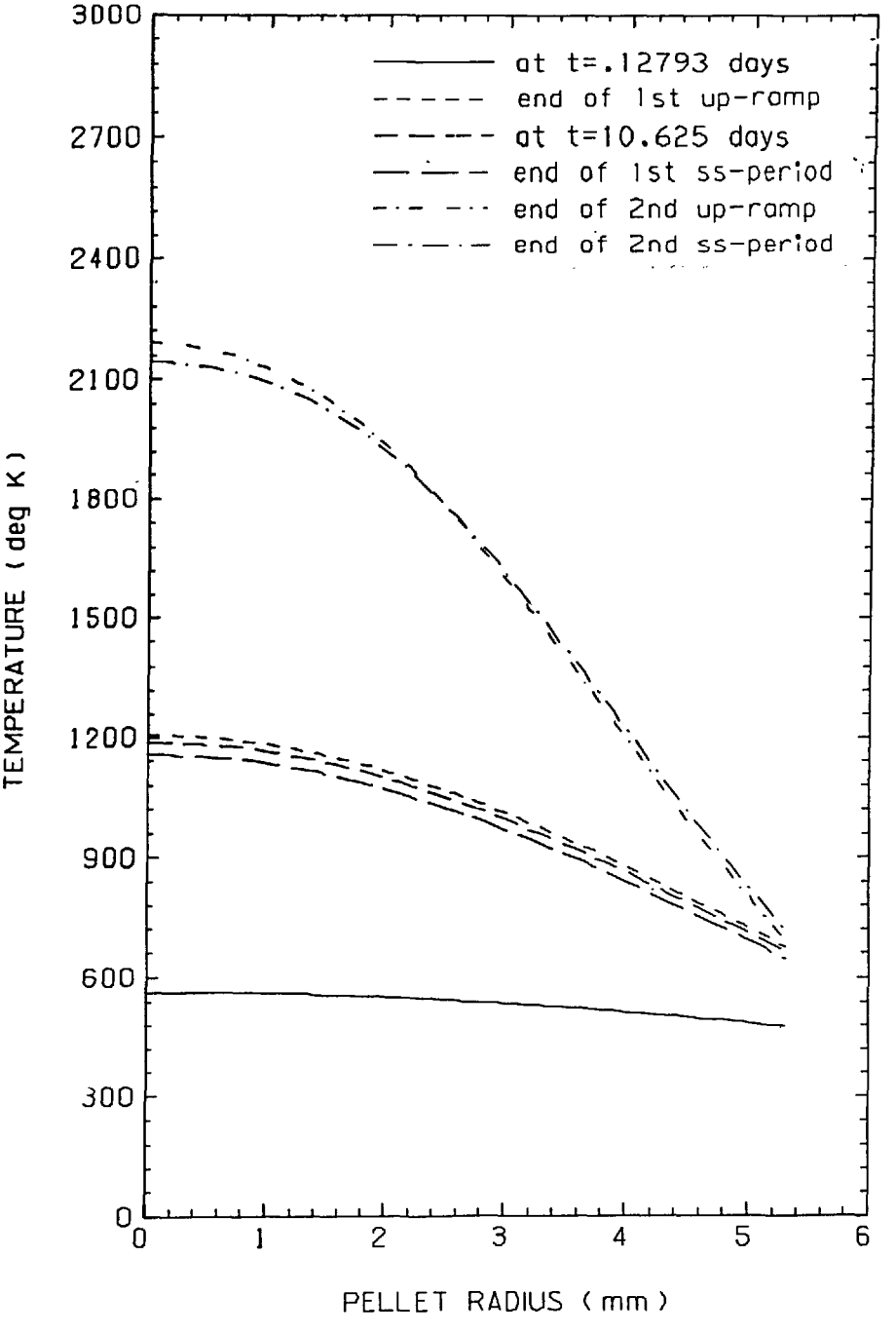


Figure 4.44

MODELLING OF ATUCHA PWR ROD UNDER A TYPICAL POWER CYCLE

FUEL/CLAD GAP CONDUCTANCE VS. IRRADIATION TIME

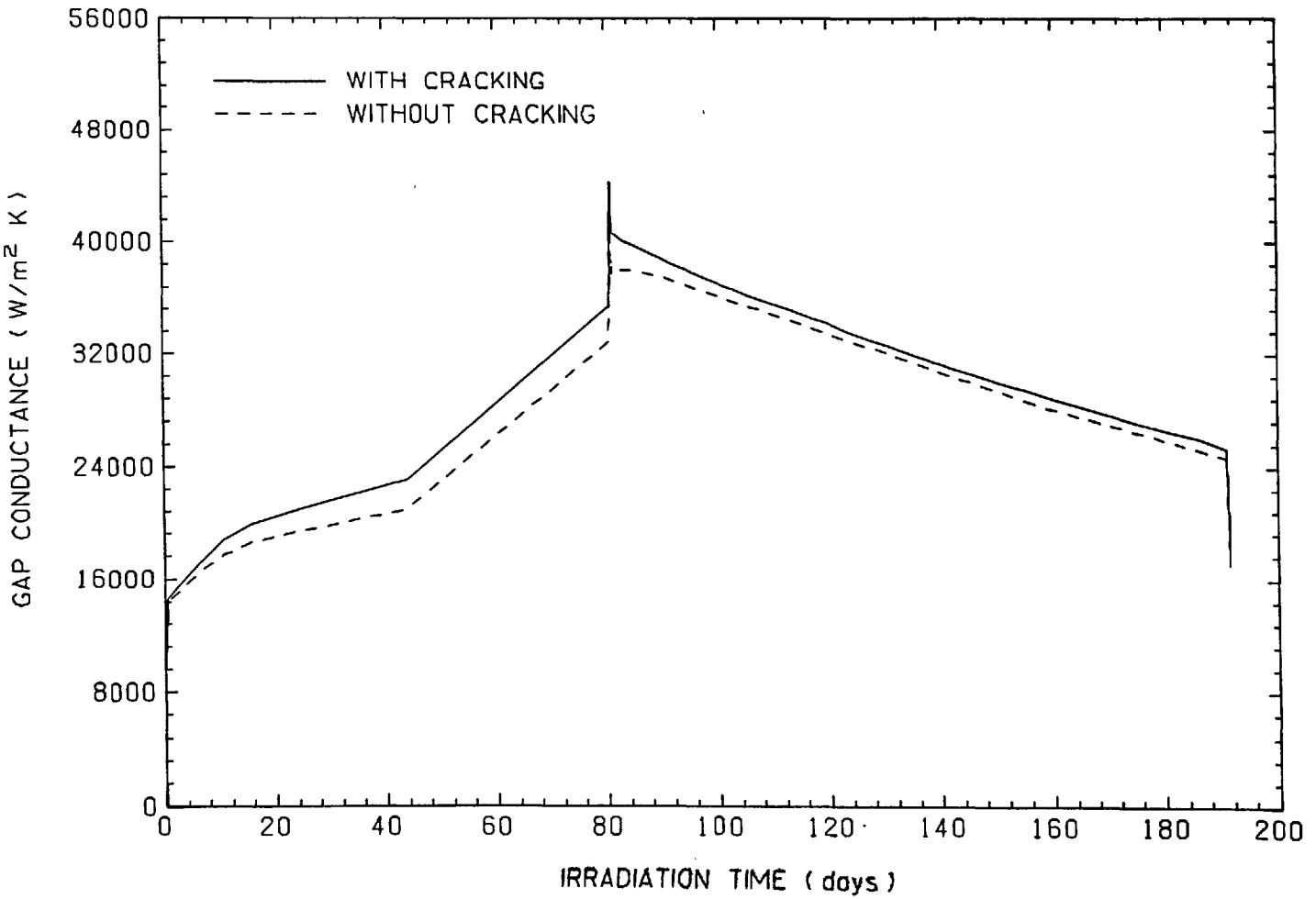
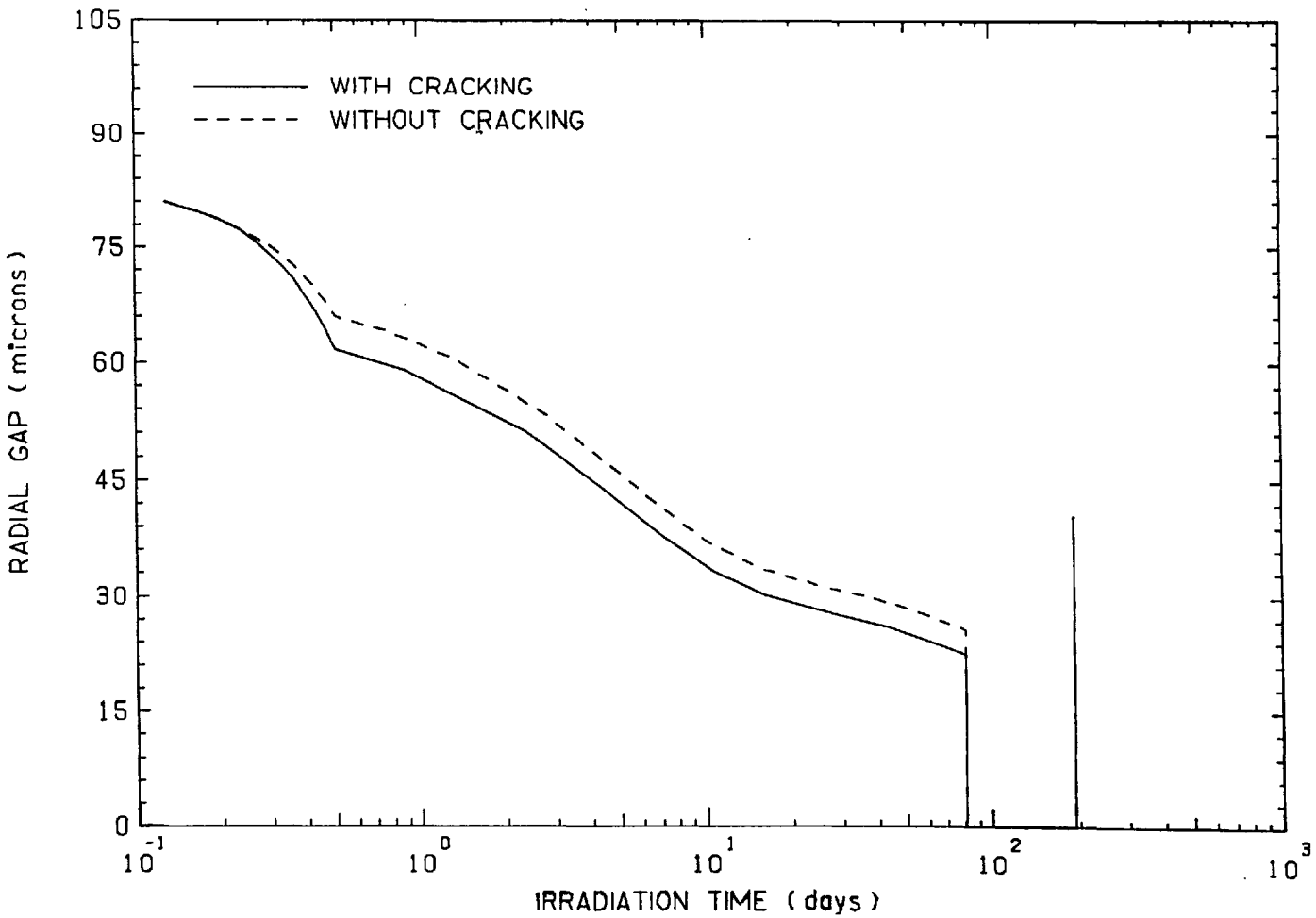


Figure 4.45

MODELLING OF ATUCHA PWR ROD UNDER A TYPICAL POWER CYCLE

FUEL/CLAD RADIAL GAP VS. IRRADIATION TIME



up-ramp for both cases, with that of cracked pellet occurring earlier, at 80.2 days, and that of uncracked pellet at 80.8 days. The gap opens again during shut-down (at 191.2 days). Figures 4.46 and 4.47 illustrate the behaviour of fuel/cladding contact pressure. In the first graph it is seen that the contact pressure for cracked pellet rises abruptly after the gap closure, reaching a value of about - 38 MPa. However, immediately after the end of up-ramp the contact pressure has started to decrease sharply during approximately the first 40 days of the second steady-state period and then stayed at a constant value of about - 28 MPa. The decrease is because the cladding follows the deformation of the fuel after contact. The temperature reached in the fuel is sufficient for fuel creep to be important and at the same time cladding creep is still significant. Thus the combination of the two reduces the contact pressure very sharply. However, the fuel swelling and expansion soon take over and balance out the effects of creep. Thus an equilibrium state is reached while the fuel and cladding keep expanding further. The variation of contact pressure with uncracked pellet is quite different in this particular example. As seen on Figure 4.47 it reaches a value of about - 8 MPa and then after a very small fall almost immediately starts rising. By the end of the steady-state period the contact pressure has attained a value of - 30 MPa. This, as will be shown later, is because of much lower fuel axial and tangential expansion thus making the combination of cladding and fuel creep more significant and causing this gradual rise of the contact pressure. It is, however, clear that with or without cracking after the gap has

Figure 4.46

MODELLING OF ATUCHA PWR ROD UNDER A TYPICAL POWER CYCLE

FUEL/CLAD CONTACT PRESSURE VS. IRRADIATION TIME

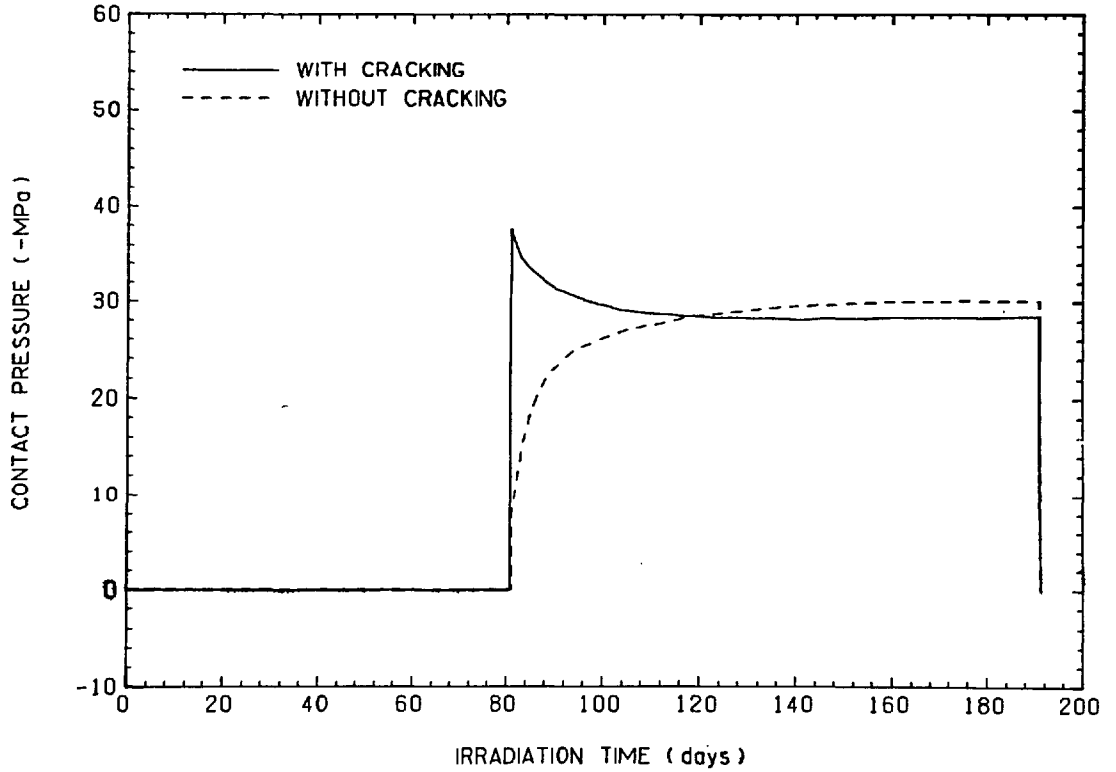
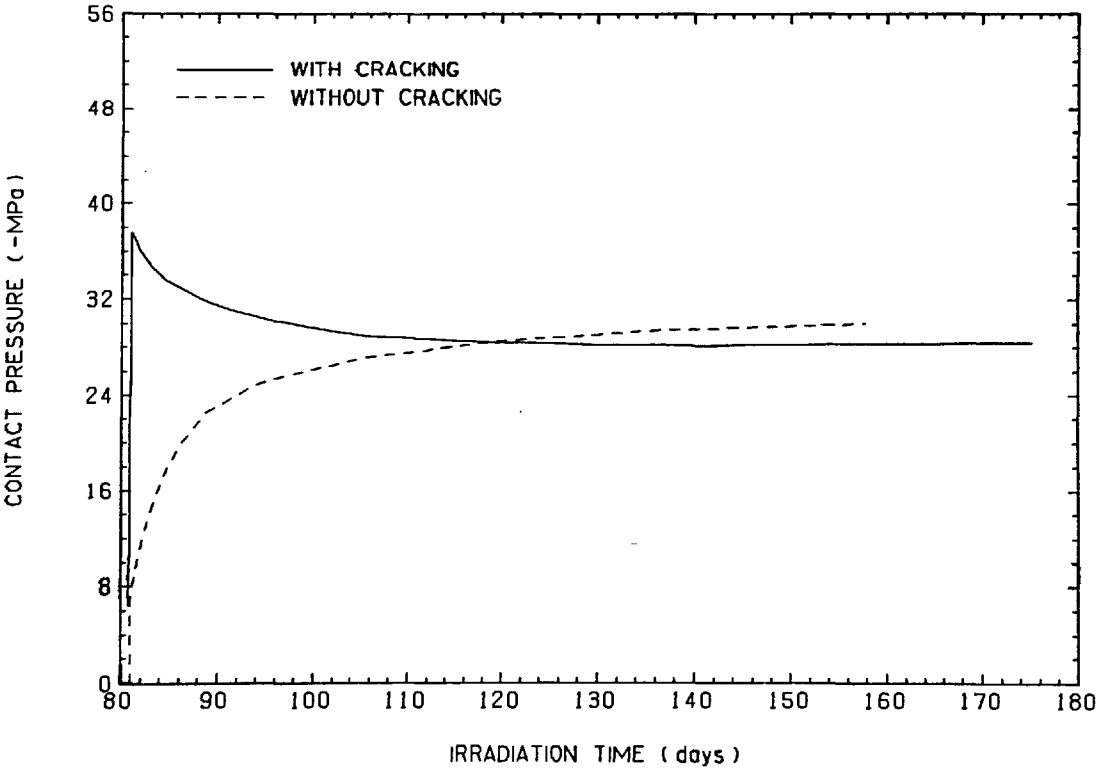


Figure 4.47

MODELLING OF ATUCHA PWR ROD UNDER A TYPICAL POWER CYCLE

FUEL/CLAD CONTACT PRESSURE VS. IRRADIATION TIME



closed fuel expansion is the dominant deformation and soon takes over. Figures 4.48 and 4.49 demonstrate this point by showing the variation of fuel radial displacement. As expected the cracked pellet has much higher deformation. One may compare the two cases at the end of first up-ramp. A difference of 0.006 mm is apparent between the displacement calculated with cracking and that without cracking which is maintained thereafter during the steady-state period. During the second up-ramp where the cracking is more extensive this difference is much larger reaching around 0.02 mm. These figures can be put into some meaningful relations when fuel axial deformation given in Figure 4.50 is also considered. At the end of first up-ramp:

$$u_N^f(\text{with cracking}) = 1.21\ u_N^f(\text{without cracking})$$

$$Z^f(\text{with cracking}) = 1.33\ Z^f(\text{without cracking})$$

At the end of second up-ramp:

$$u_N^f(\text{with cracking}) = 1.45\ u_N^f(\text{without cracking})$$

$$Z^f(\text{with cracking}) = 1.50\ Z^f(\text{without cracking})$$

The axial strain with cracking, Figure 4.50 , during the second steady-state period seems to relax while that of uncracked pellet rises continuously. This is in line with the explanation given earlier for contact pressure behaviour.

Next the internal stresses generated in the pellets are considered. These are plotted in Figures 4.51 to 4.54 for uncracked pellet and in Figures 4.55 to 4.58 for cracked pellet. The stresses are given for several times during the irradiation cycle. If one considers the hoop and axial stresses (Figures 4.52-4.53 and 4.56-4.57)

Figure 4.48

MODELLING OF ATUCHA PWR ROD UNDER A TYPICAL POWER CYCLE

PELLET RADIAL DISPLACEMENT VS. IRRADIATION TIME

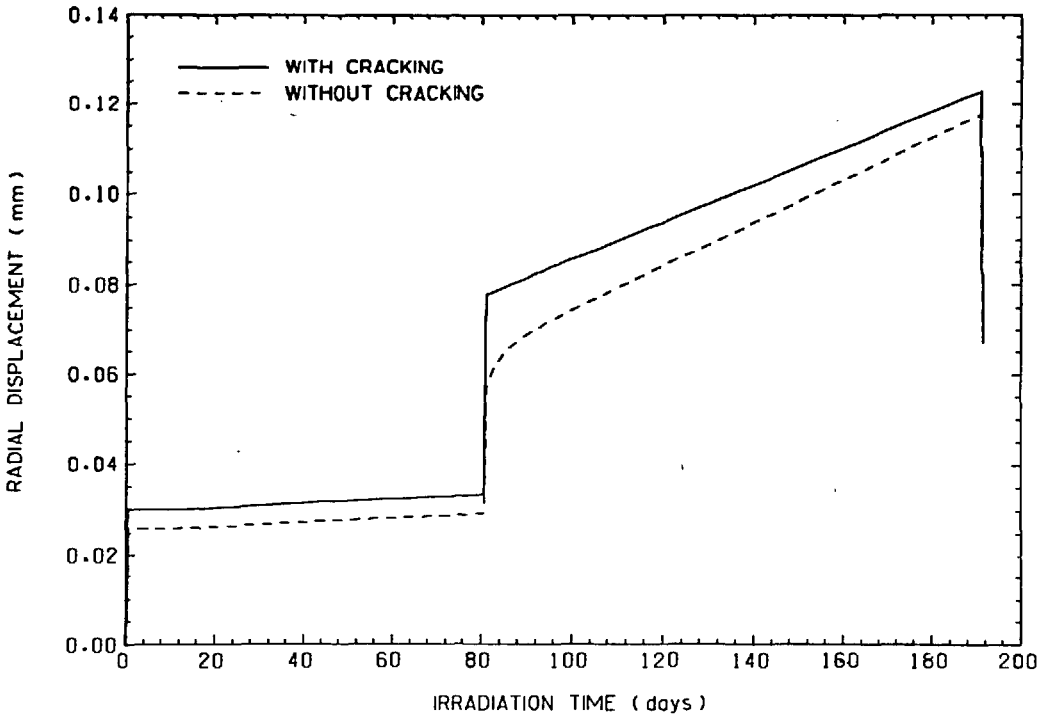


Figure 4.49

MODELLING OF ATUCHA PWR ROD UNDER A TYPICAL POWER CYCLE

PELLET RADIAL DISPLACEMENT VS. IRRADIATION TIME DURING START-UP

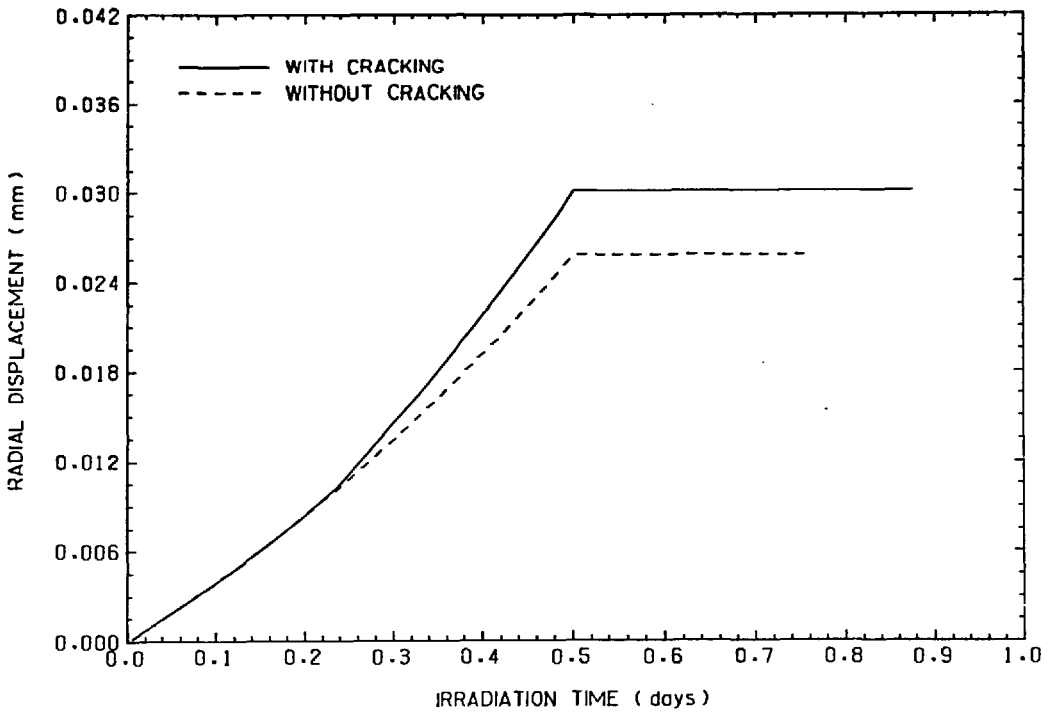
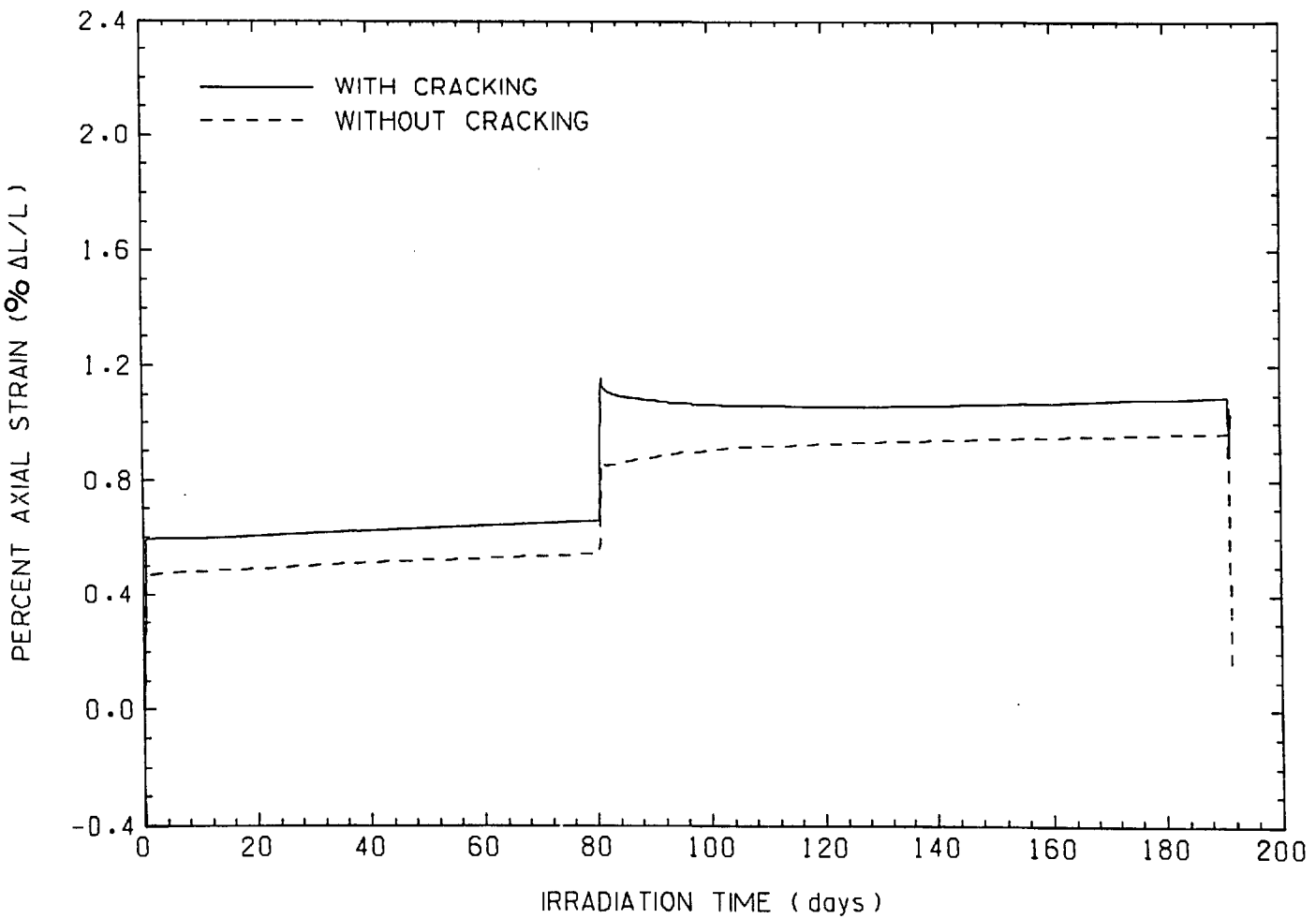


Figure 4.50

MODELLING OF ATUCHA PWR ROD UNDER A TYPICAL POWER CYCLE

FUEL AXIAL DEFORMATION VS. IRRADIATION TIME



at low fuel rating (end of first up-ramp without cracking and at 0.12793* days with cracking) one may find that they approximate satisfactorily to analytical solution of a heat generating cylinder obtained with constant thermal conductivity, e.g. the radius at which the hoop stress changes sign is $r/r_{pellet} = 1/\sqrt{3}$ and for the axial stress $r/r_{pellet} = 1/\sqrt{2}$. Using these graphs one finds the following figures:

$$\text{Hoop stress} \begin{cases} \text{without cracking} & r/r_{pellet} = 0.550 \\ \text{with cracking} & r/r_{pellet} = 0.570 \end{cases}$$

$$\text{Axial stress} \begin{cases} \text{without cracking} & r/r_{pellet} = 0.680 \\ \text{with cracking} & r/r_{pellet} = 0.695 \end{cases}$$

which are close enough to $1/\sqrt{3} = 0.577$ for hoop stress and $1/\sqrt{2} = 0.707$ for axial stress, respectively. This is basically because of low fuel temperature at these particular points and insignificant creep. It can be seen, however, that by the end of first steady-state period the magnitudes of the three principle stresses have decreased very significantly in both cases due to creep. One may also observe the fact that stresses have become more equal, i.e. the deviatoric stresses have diminished. This effect is quite noticeable during the second up-ramp (81.0 days) where the value of hydrostatic stress reached in the uncracked pellet is about - 160 MPa, this value has a greater magnitude than that of the cracked pellet (- 75 MPa). The axial stress in Figure 4.57 is particularly affected, where the competition between creep relaxation of stress

*This particular time was chosen just because it was one of the computer generated time-steps prior to fuel cracking.

and the increasing thermal strain alters the position of the axial stress minimum from the fuel centre to a radius of about 3.2 mm. In the case of uncracked pellet, the large amount of creep relaxation in the fuel centre also reduces the highly tensile exterior stresses. At the end of the second up-ramp the tangential stress is about 640 MPa at the pellet surface and the axial stress about 480 MPa; both far higher than the UO_2 fracture stress. However, these stresses decrease so rapidly, after steady-state has been reached that at the end of the period they are all about - 35 MPa.

The effects discussed earlier for the case when cracks are permitted, which produce much higher strains, are reflected in stress distributions presented in Figures 4.55 through 4.58 . One may see the effectiveness of cracking, together with thermal creep, in relaxing the stresses initially produced by the temperature gradient. The variation of tangential and axial stresses at the end of first up-ramp (see Figures 4.56 and 4.57) shows how the penetration of cracking has changed the pattern of stresses as compared with the uncracked pellet. This can also be seen by comparing the equivalent stresses between the two cases; Figures 4.54 and 4.58 . For example, at the end of first up-ramp the equivalent stress reaches a value of 360 MPa at the fuel surface decreasing to about 160 MPa at a radius of 4 mm and remaining at this value all the way to the centre. While, in the cracked pellet the equivalent stress is almost zero (0.1 MPa) from the surface down to the 4 mm radius. From this radius towards the centre its

value is determined by the values of the principle stresses.

The effect of gap closure on stress distribution can also be studied here. After contact, the stresses which have completely relaxed during the first steady-state period, start becoming more compressive. It is also seen that after contact the stresses which tended to open the cracks now cause closure due to this reversal effect. For example, the axial stress at 81.0 days (end of second up-ramp) shows the effect of creep at the centre of the pellet. This stress has relaxed to a constant value of - 65 MPa (Fig.4.57), but has become more compressive in the vicinity of the crack root. It is obvious that these effects are caused by the external constraint, i.e. contact with the cladding. The new boundary loading due to contact not only influences the magnitude of the internal stresses but also their re-distribution. This demonstrates the inter-relation found in the whole system.

One may now look at the stress reversal at the fuel centre during shut-down which is clearly demonstrated in Figures 4.51 to 4.53 . The axial stress of the centre attains the highest value ($\sim$ 1640 MPa) while the radial and tangential stresses reach just about half that ($\sim$ 960 MPa). This effect occurs in the cracked pellet too and cracking in the fuel central region.

In Figures 4.59 and 4.60 the distribution of cracking strains are shown at different times. The transient value of stress in the whole pellet determines these

Figure 4.51

MODELLING OF ATUCHA PWR ROD

PELLET RADIAL STRESS WITHOUT CRACKING

VS. RADIUS AT DIFFERENT TIMES

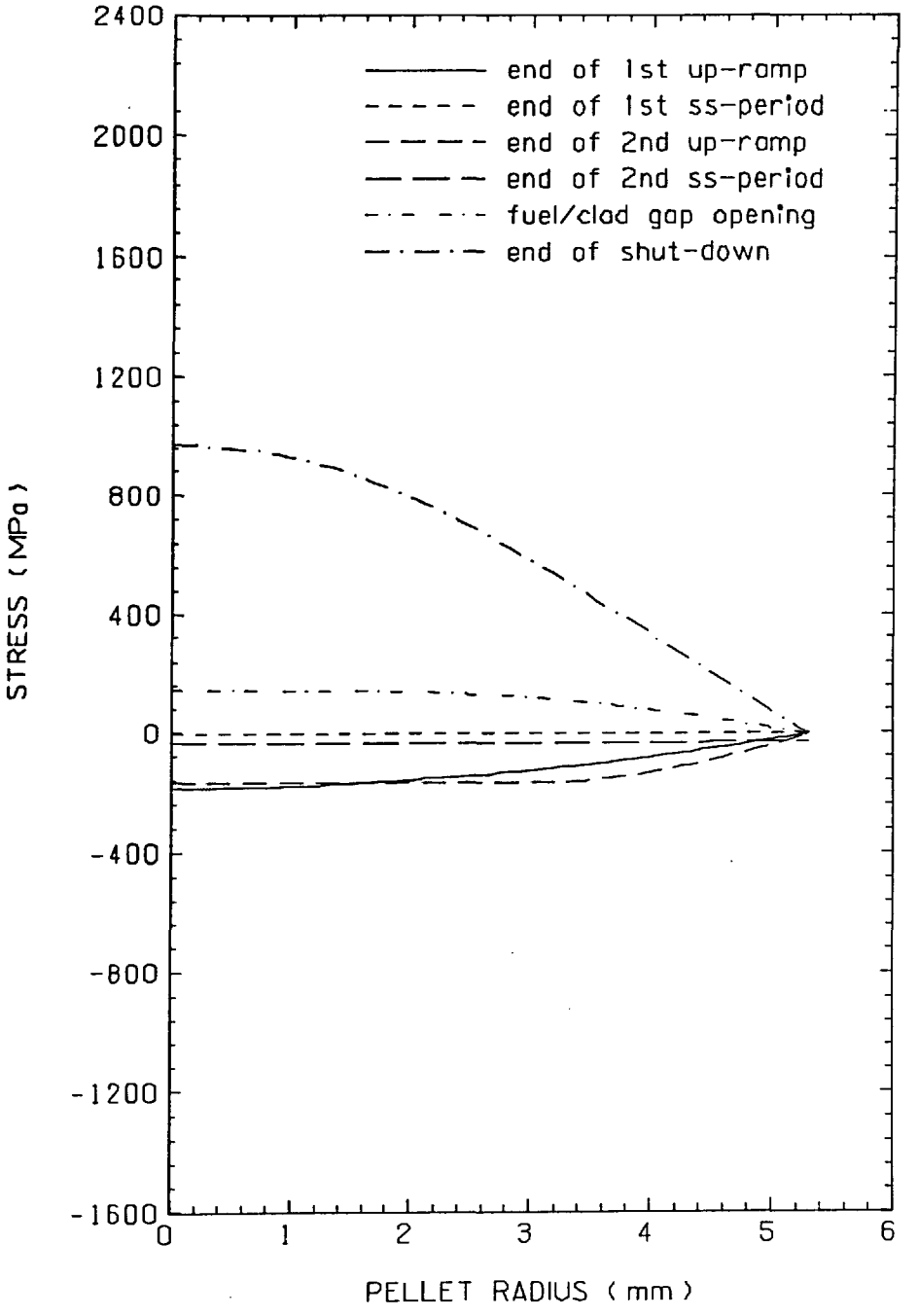


Figure 4.52

MODELLING OF ATUCHA PWR ROD

PELLET TANGENTIAL STRESS WITHOUT CRACKING

VS. RADIUS AT DIFFERENT TIMES

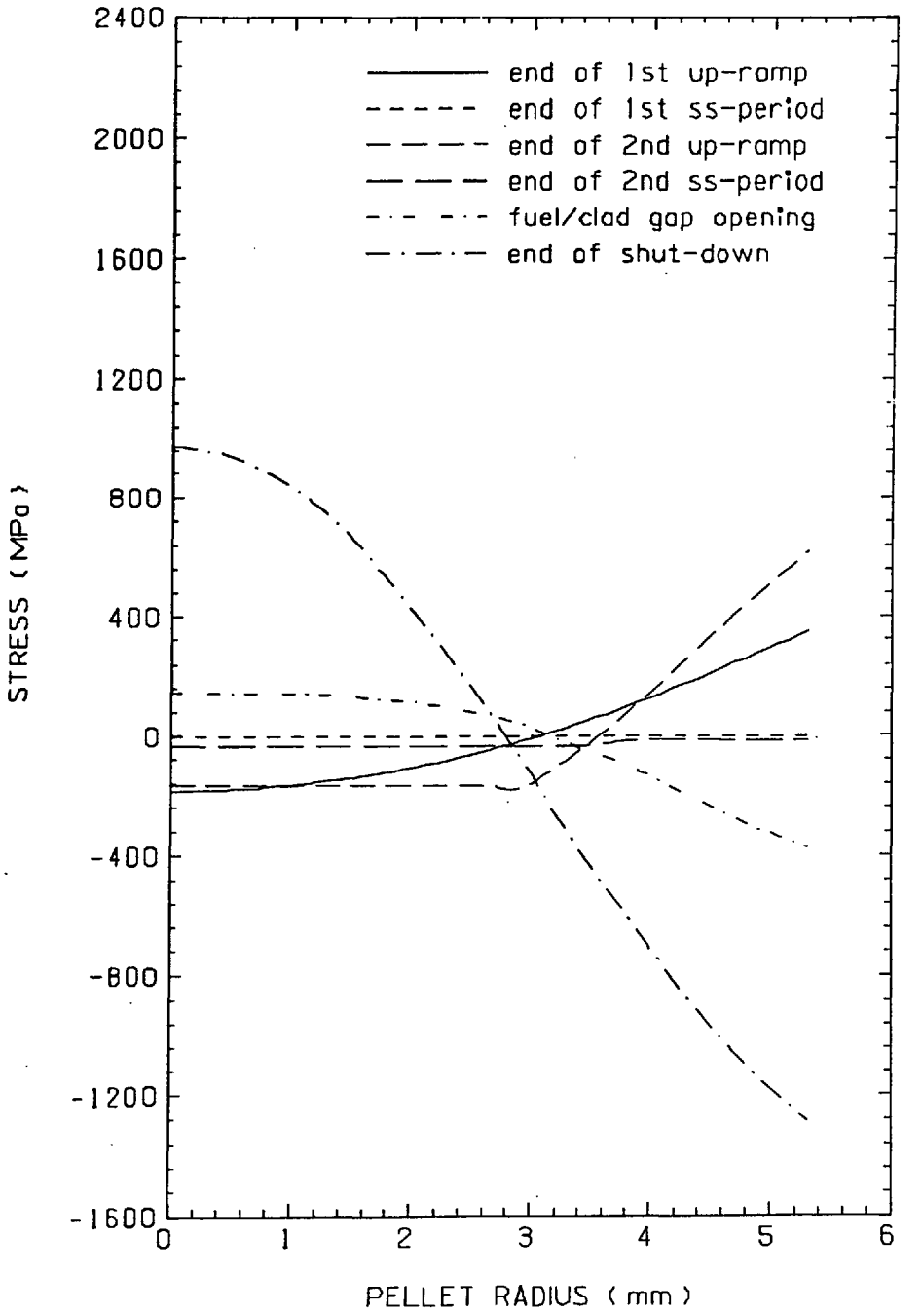


Figure 4.53
MODELLING OF ATUCHA PWR ROD
PELLET AXIAL STRESS WITHOUT CRACKING
VS. RADIUS AT DIFFERENT TIMES

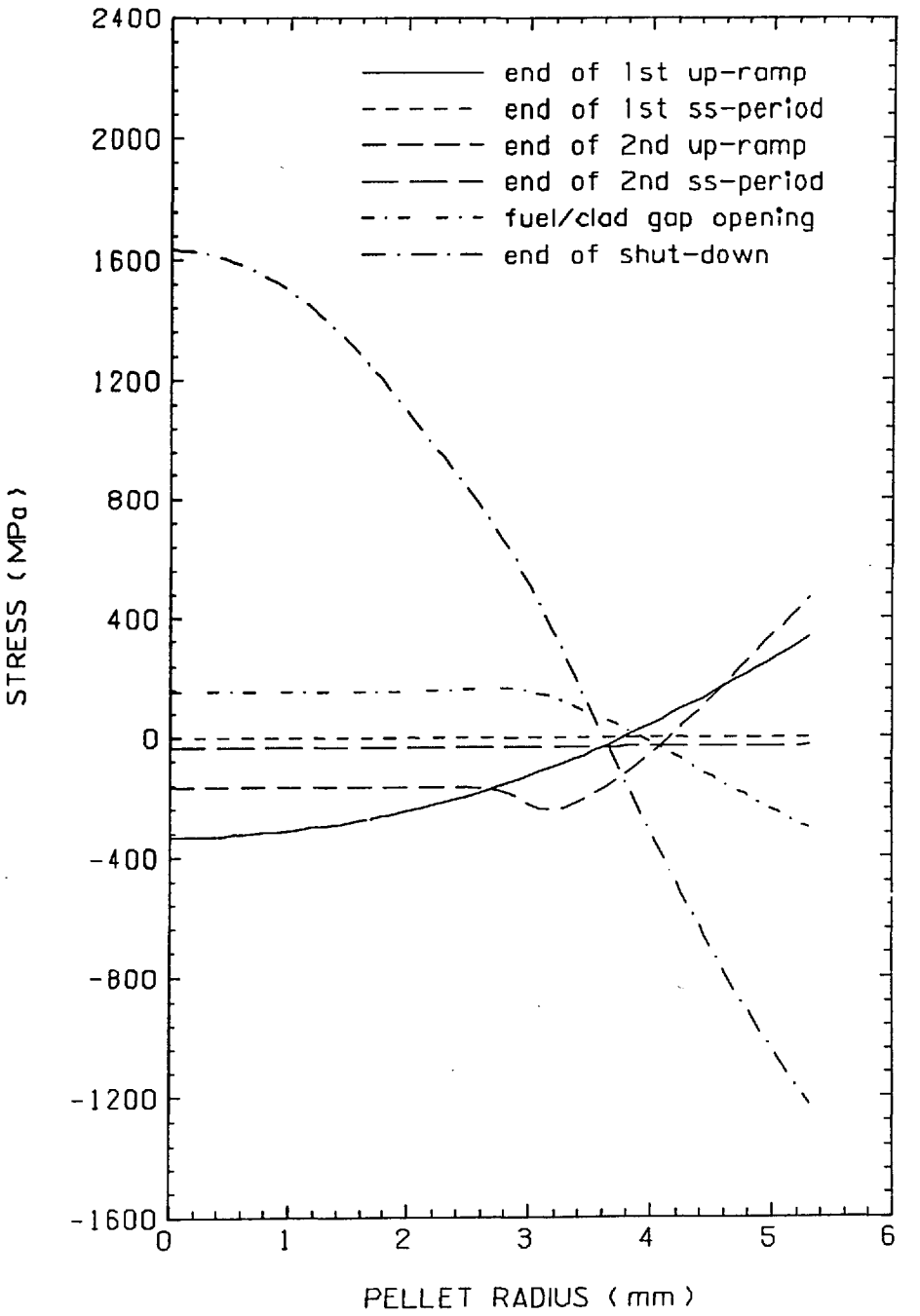


Figure 4.54

MODELLING OF ATUCHA PWR ROD

PELLET EQUIVALENT STRESS WITHOUT CRACKING

VS. RADIUS AT DIFFERENT TIMES

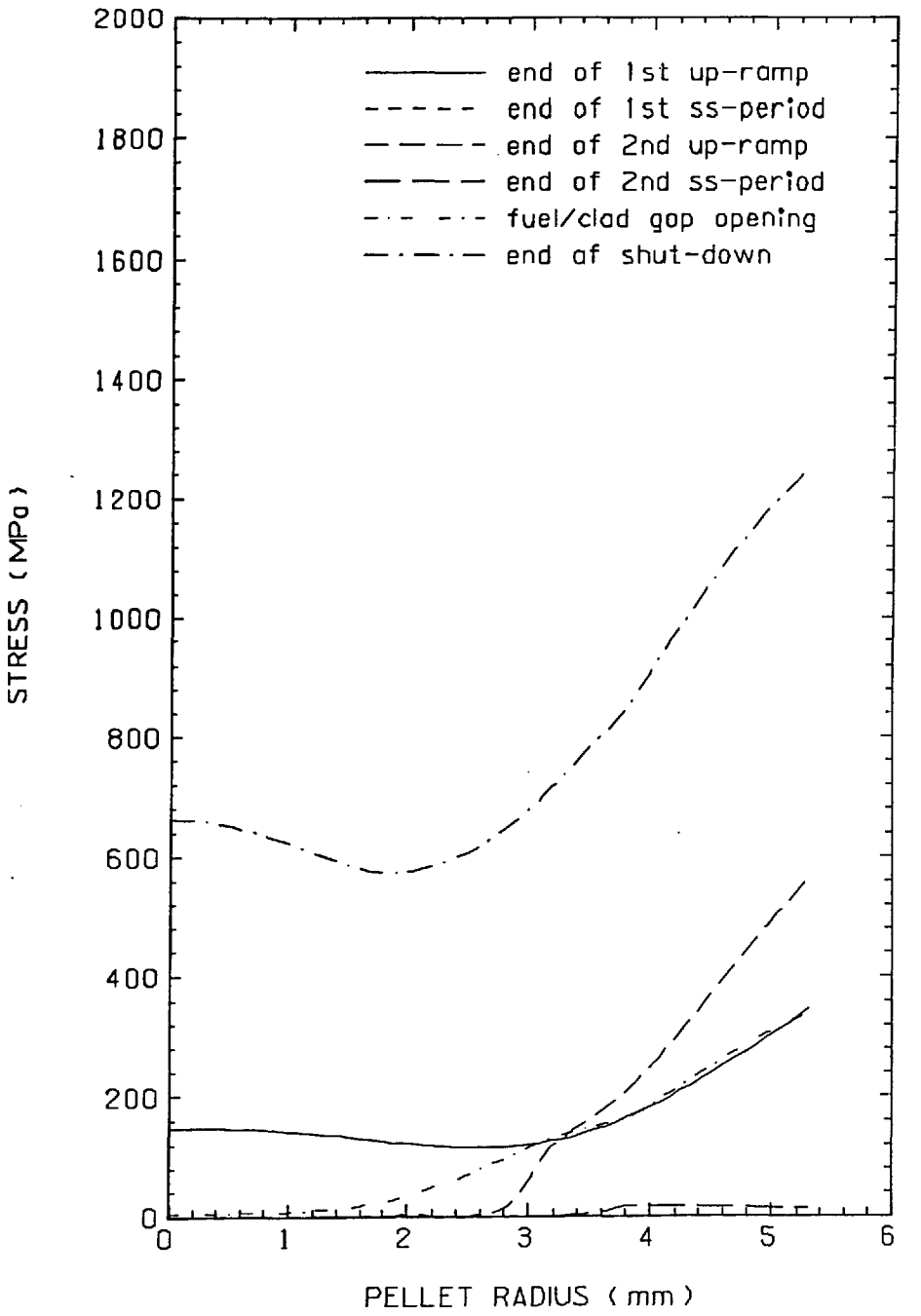


Figure 4.55
MODELLING OF ATUCHA PWR ROD
PELLET RADIAL STRESS DITRIBUTION WITH CRACKING
VS. PELLET RADIUS AT DIFFERENT TIMES

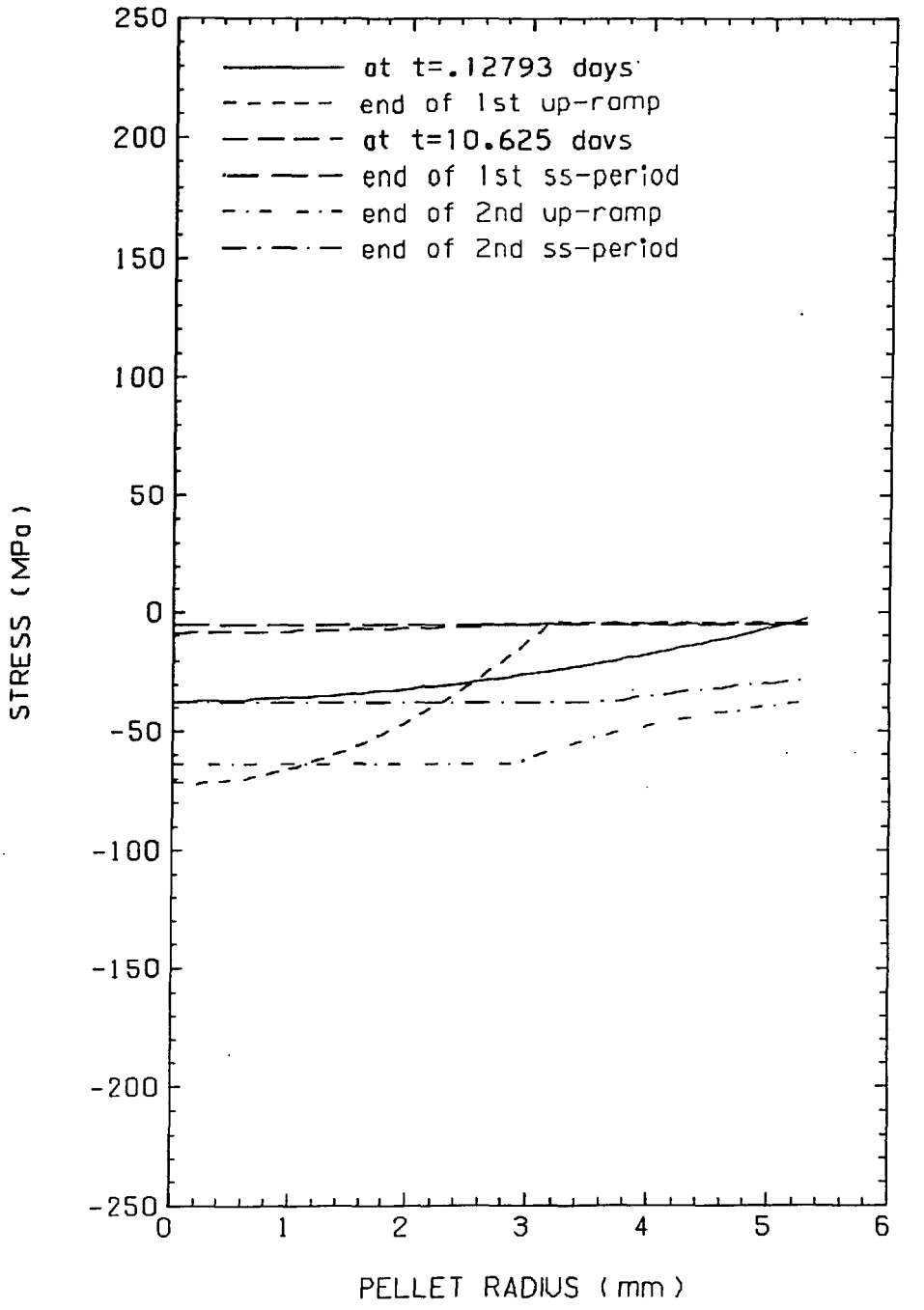


Figure 4.56
MODELLING OF ATUCHA PWR ROD
PELLET HOOP STRESS DISTRIBUTION WITH CRACKING
VS. PELLET RADIUS AT DIFFERENT TIMES

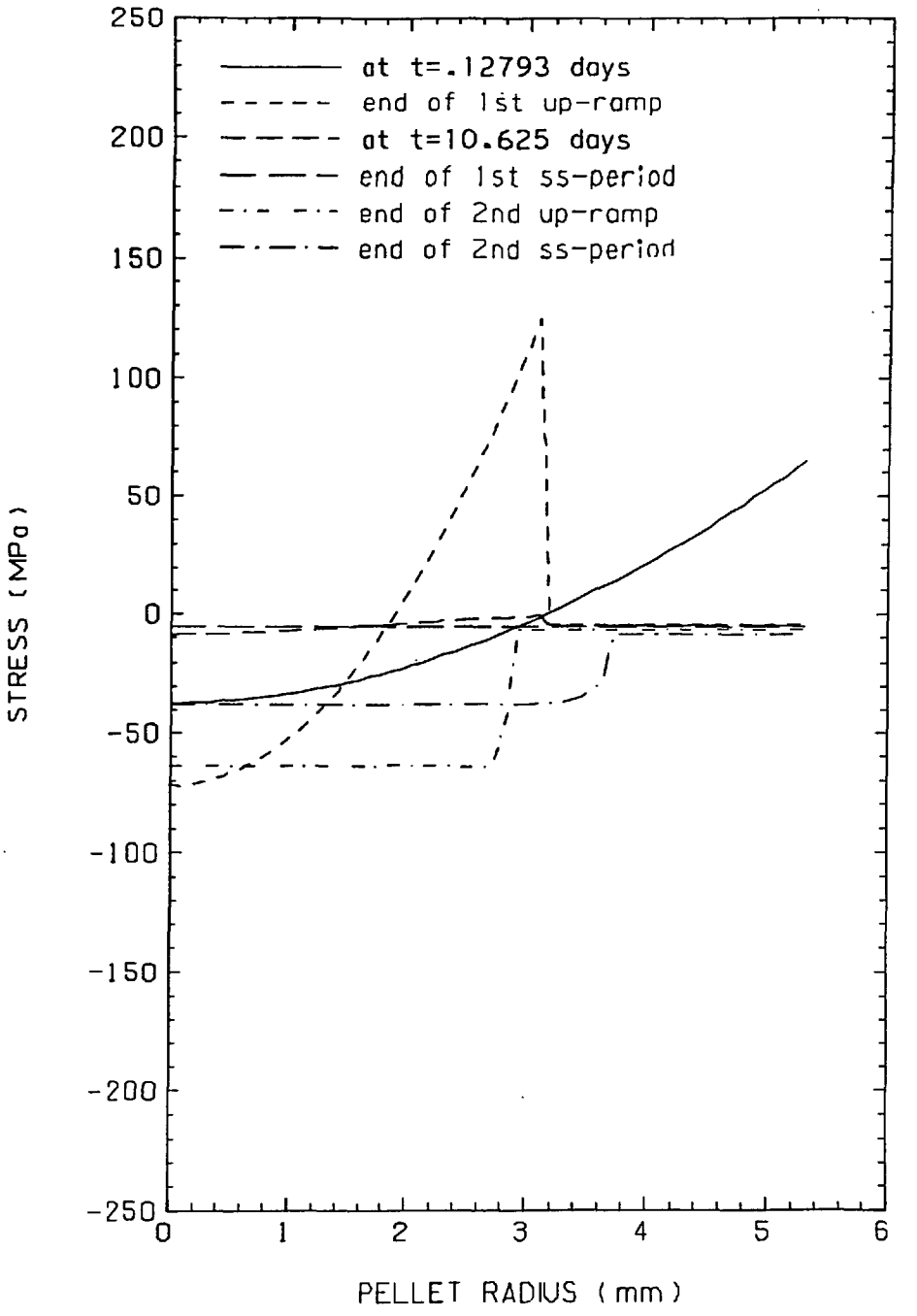


Figure 4.57
MODELLING OF ATUCHA PWR ROD
PELLET AXIAL STRESS DISTRIBUTION WITH CRACKING
VS. PELLET RADIUS AT DIFFERENT TIMES

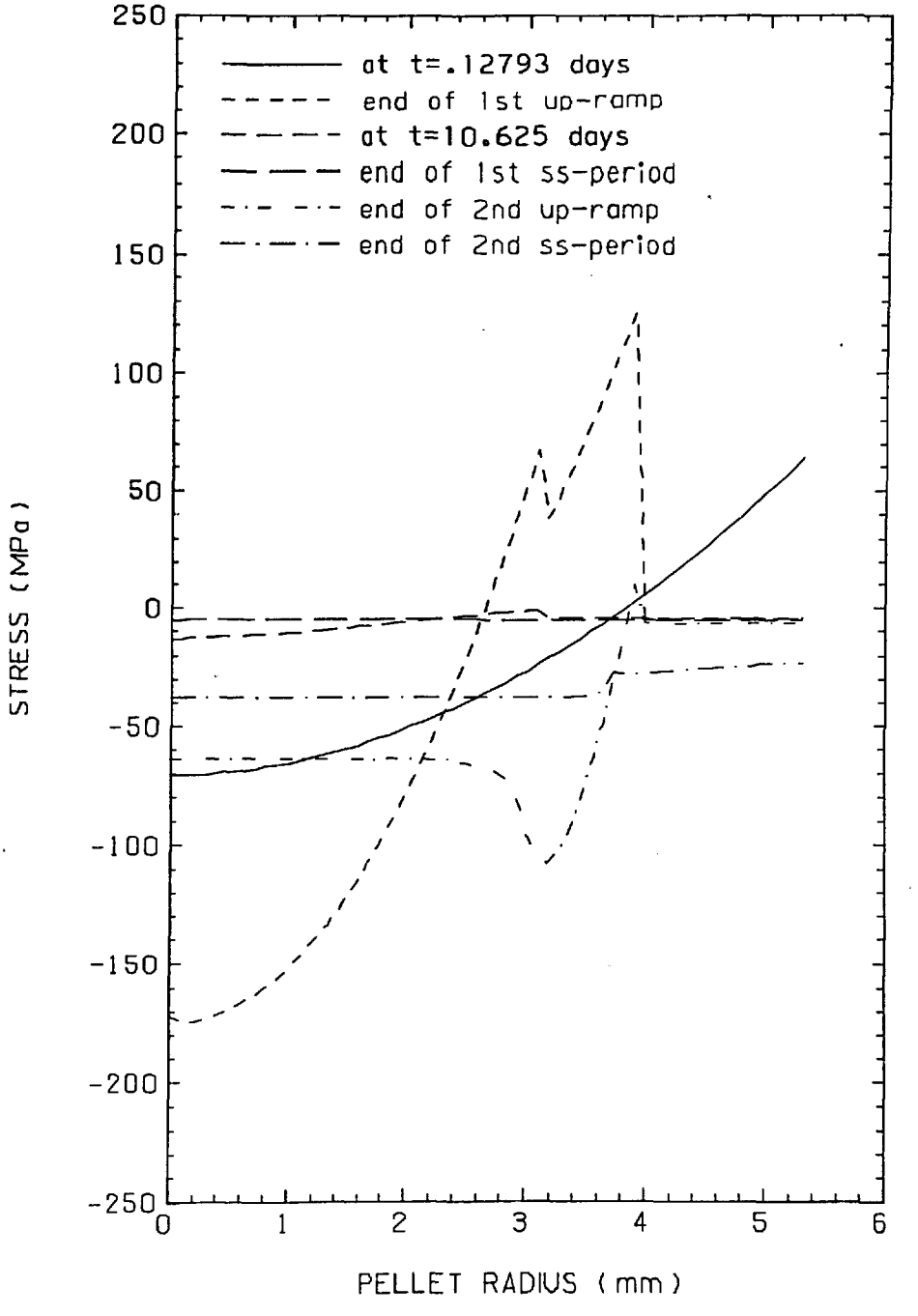
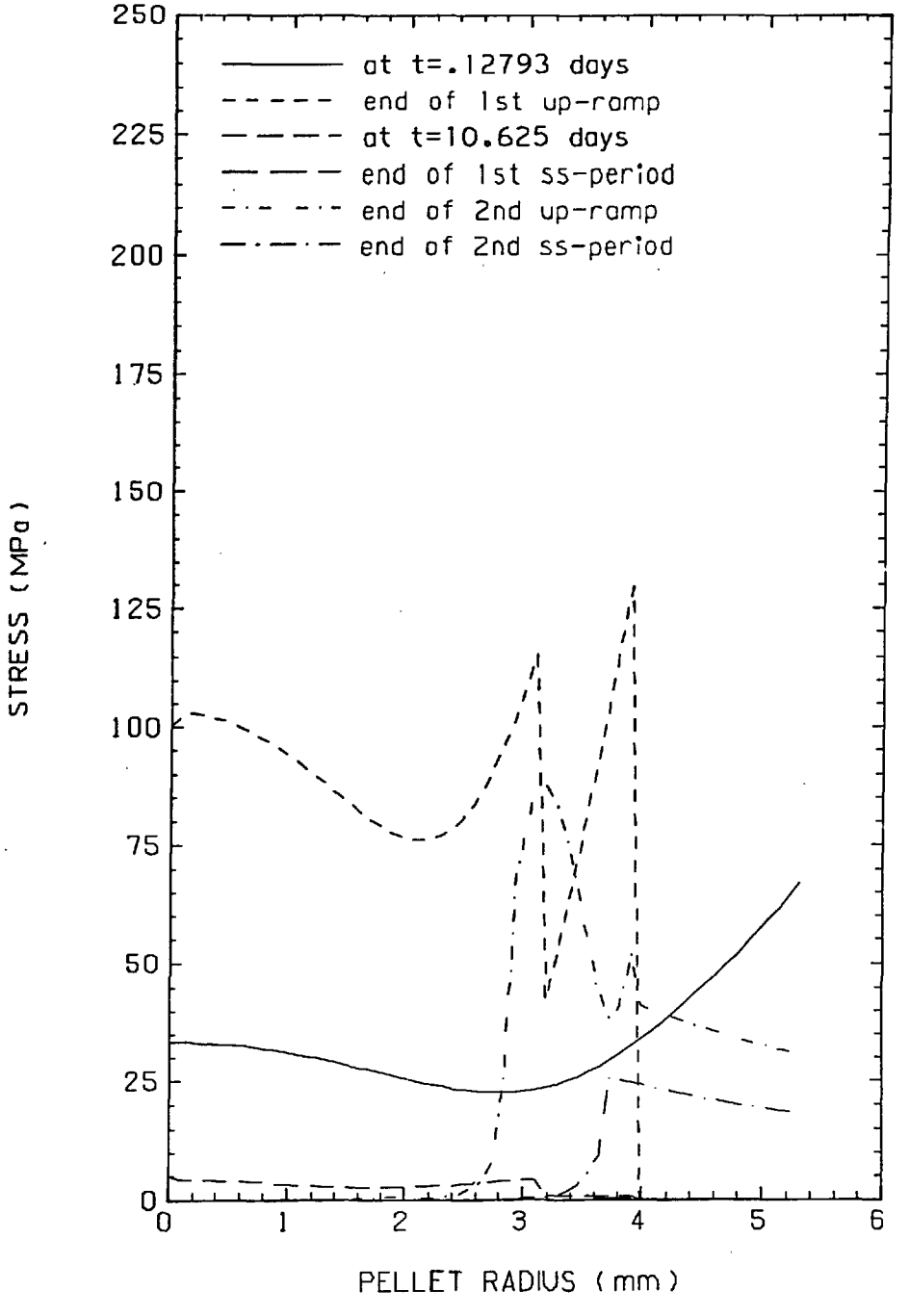


Figure 4.58

MODELLING OF ATUCHA PWR ROD

PELLET EQUIVALENT STRESS DISTRIBUTION WITH CRACKING VS. PELLET RADIUS AT DIFFERENT TIMES



crack patterns. As long as the gap is open there is no limit to the radial crack penetration during up-ramp, until the stress at the crack tip is relaxed by creep. This limits the crack penetration but apparently does not restrict greatly the crack width in the outer fuel region during the up-ramp. The axial cracks, however, behave differently, i.e. any limit to crack penetration reduces the crack width along the whole of its length. In these figures η_z is the total axial crack strain and $2\pi r\eta_\theta$ is the total tangential crack width at any radius r. The effects described above are illustrated in these graphs. For example it may be seen that although the radial crack width has more than trebled after the second up-ramp its penetration has not changed much. While the axial crack has only about doubled in value and stayed at the same radius of penetration. In Figures 4.61 and 4.62 the crack penetration is shown as a function of irradiation time (the graphs are identical except for the time scale, where one uses a log-time scale for more clarity). It is seen that after fuel/cladding contact the radial cracks first penetrate more into the pellet but soon begin to heal. The axial cracks on the other hand stay at the same penetration until 12 days into the steady-state period and then are drastically reduced. It is also apparent that the shut-down has sent the axial crack penetration to the limit (60 rings i.e. all across the pellet) and that of the radial crack to 40 rings with radial cracks partly closing in the outer pellet region.

So far the behaviour of fuel and its interaction with the cladding has been dealt with in some detail. Next the

Figure 4.59
MODELLING OF ATUCHA PWR ROD
PELLET θ CRACK STRAIN DISTRIBUTION
VS. PELLET RADIUS AT DIFFERENT TIMES

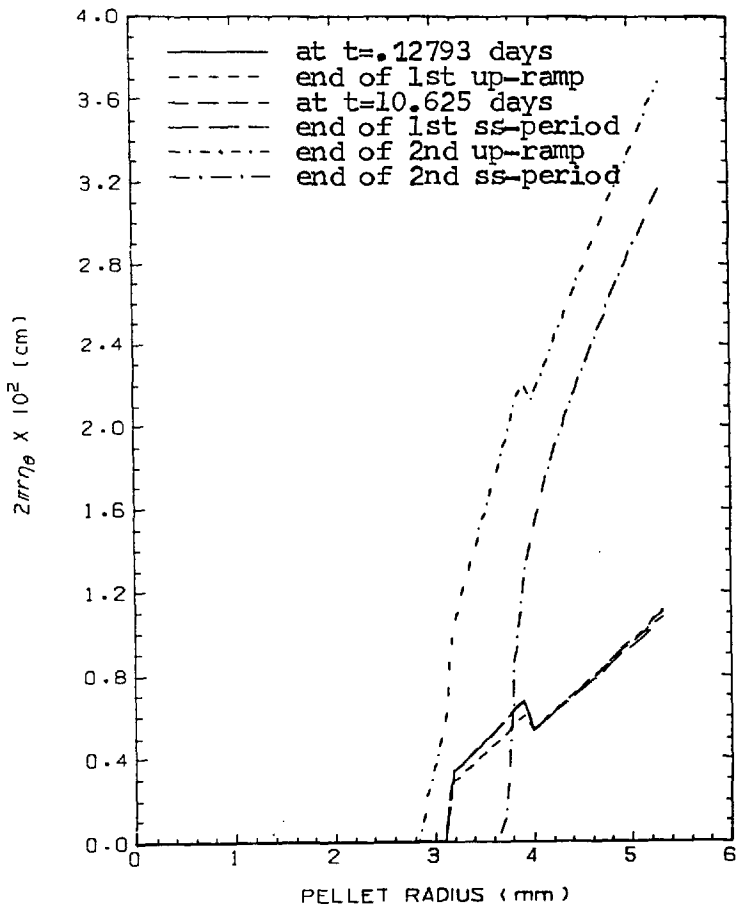


Figure 4.60
MODELLING OF ATUCHA PWR ROD
PELLET Z CRACK STRAIN DISTRIBUTION
VS. PELLET RADIUS AT DIFFERENT TIMES

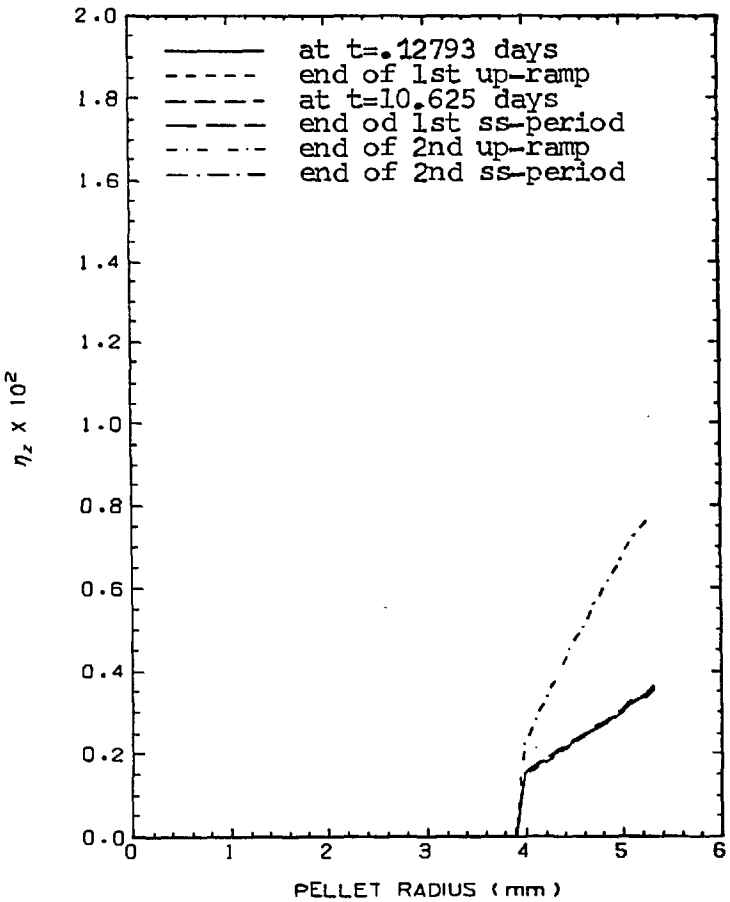


Figure 4.61

MODELLING OF ATUCHA PWR ROD UNDER A TYPICAL POWER CYCLE

RADIAL AND AXIAL CRACK PENETRATION IN THE PELLET VS. IRRADIATION TIME

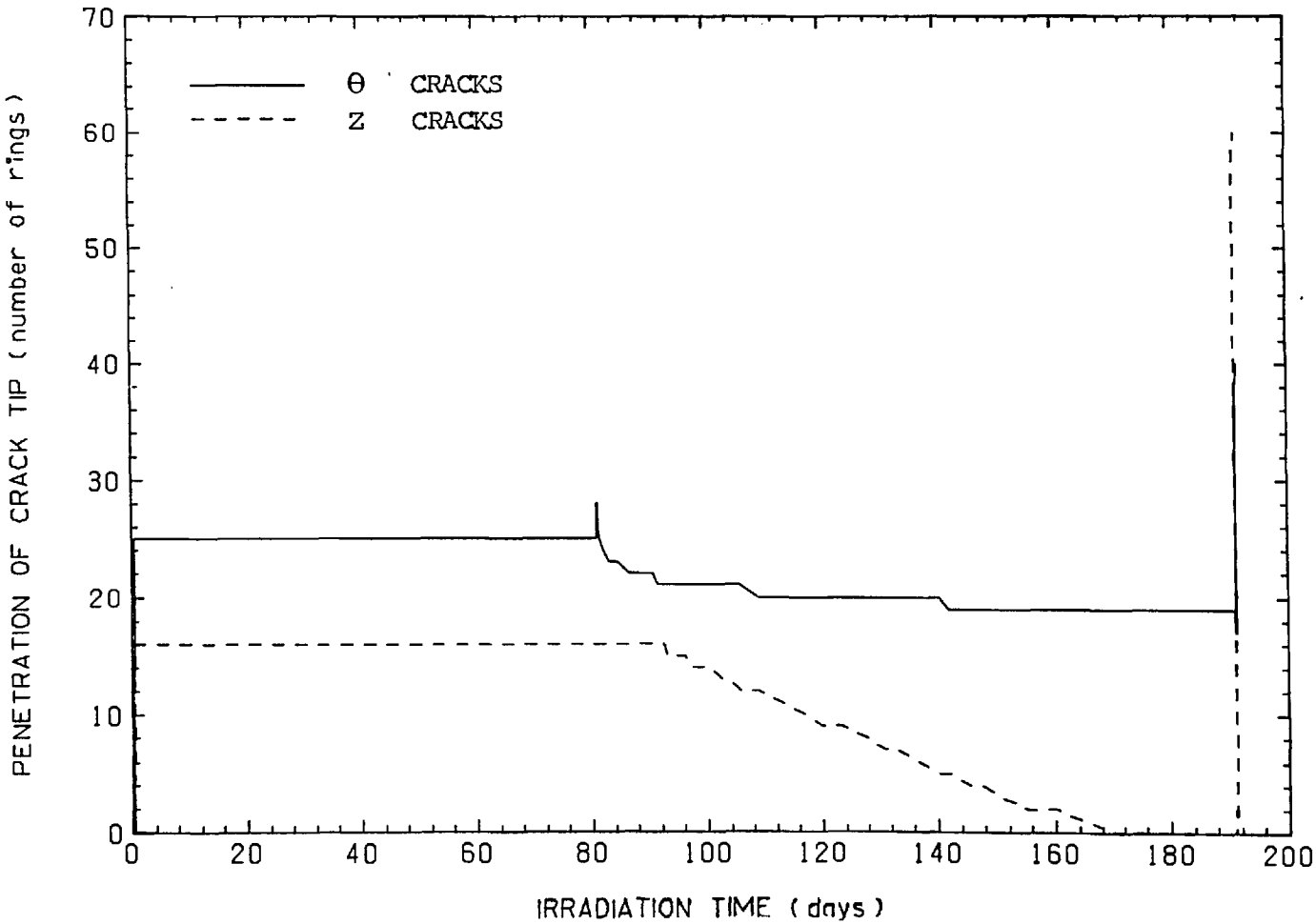
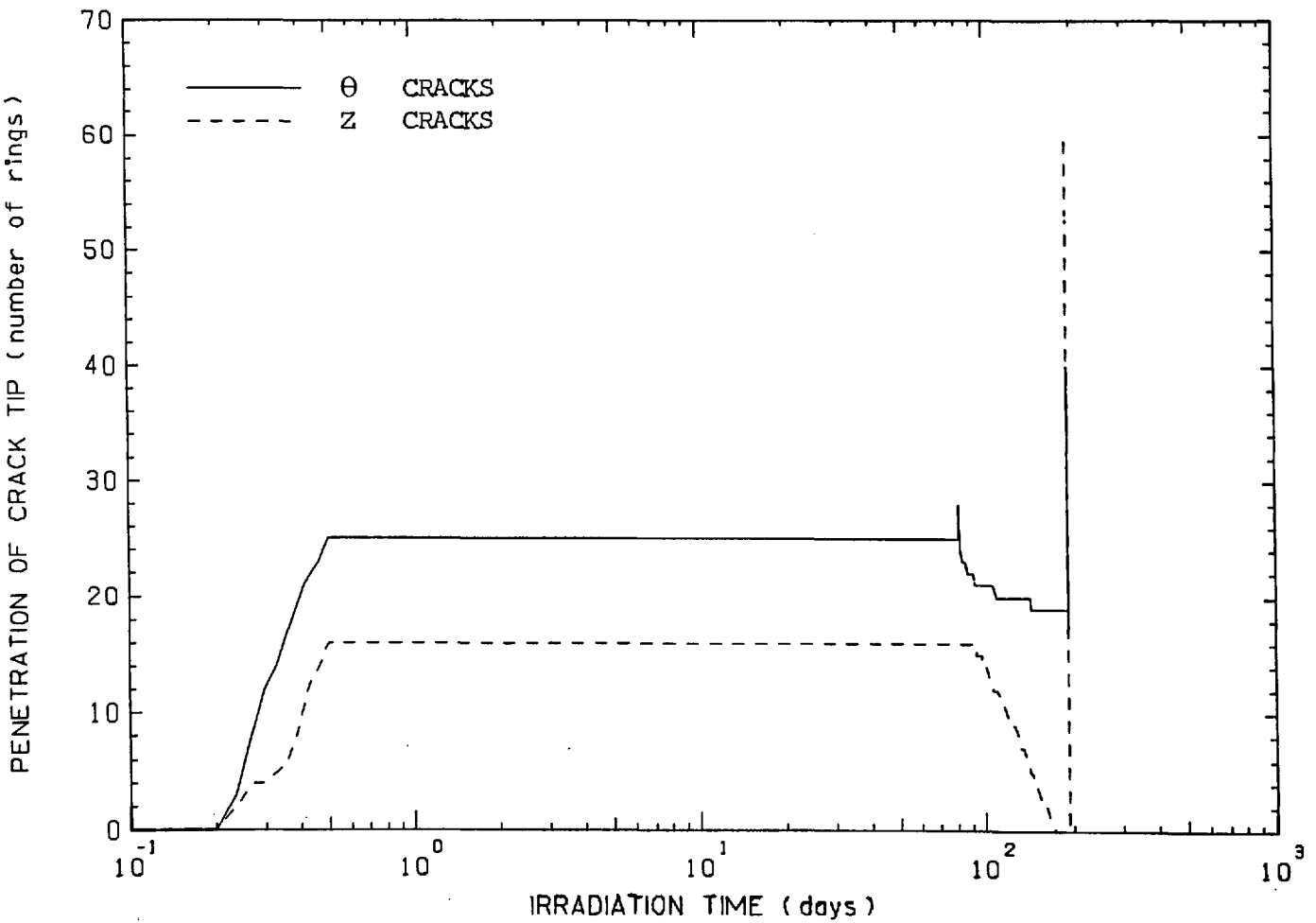


Figure 4.62

MODELLING OF ATUCHA PWR ROD UNDER A TYPICAL POWER CYCLE

RADIAL AND AXIAL CRACK PENETRATION IN THE PELLET VS. IRRADIATION TIME



variation of some important parameters in the cladding are considered, although in somewhat less detail. It is important to note that the material of the cladding is of a very different nature to that of the fuel, the effects of power cycling are expected to be less dramatic; generally because in normal operation one would not expect the cladding to crack or such effects as porosity change to occur. From an engineering point of view, nevertheless, the stresses and strains to which the material of the cladding is subjected are of great importance.

In Figures 4.63 and 4.64 the cladding tangential strains, in its inner and outer wall, are plotted versus irradiation time. The phenomenon of cladding creep-down is clearly demonstrated during the first up-ramp and steady-state periods. The innder wall creeps down to about - 0.6%, and the outer wall to - 0.5%. There is not any significant difference between the "with cracking" and "without cracking" cases up to gap closure. After contact the cladding creep has a sudden change of direction, as it has to follow the fuel expansion. The tangential strain is seen to actually change sign and become positive after some time into the second steady-state period.

Figure 4.65 presents the variation of cladding axial deformation during irradiation. The previous differences between the two cases are also apparent here.

As it has already been discussed the level of tangential stresses in the cladding wall is of great interest at any time during irradiation, especially that of the inner wall

Figure 4.63

MODELLING OF ATUCHA PWR ROD UNDER A TYPICAL POWER CYCLE
INNER CLAD PERMANENT TANGENTIAL STRAIN VS. IRRADIATION TIME

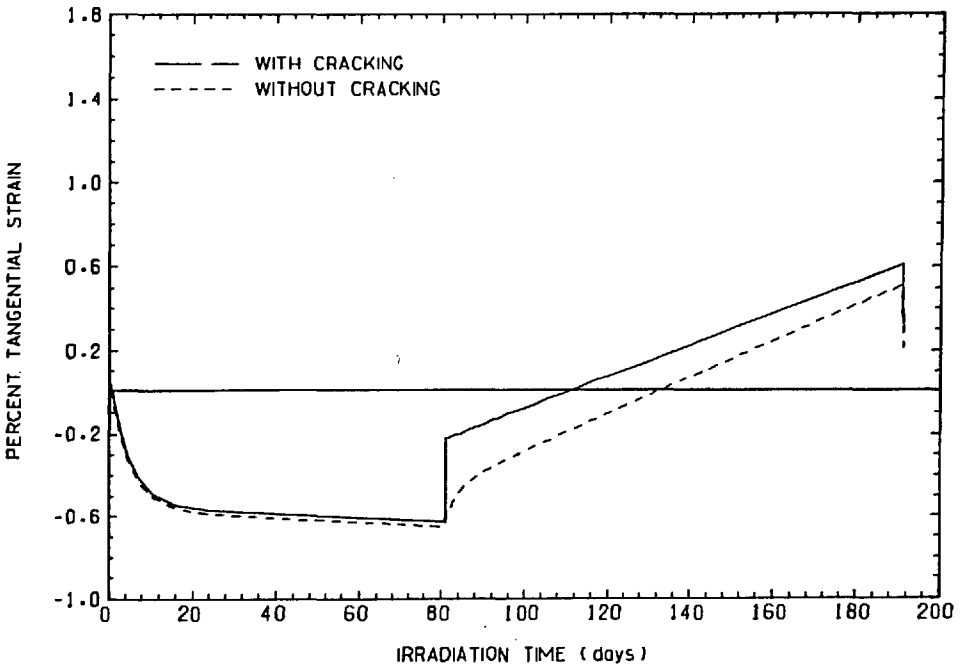


Figure 4.64

MODELLING OF ATUCHA PWR ROD UNDER A TYPICAL POWER CYCLE
INNER CLAD PERMANENT TANGANTIAL STRAIN VS. IRRADIATION TIME

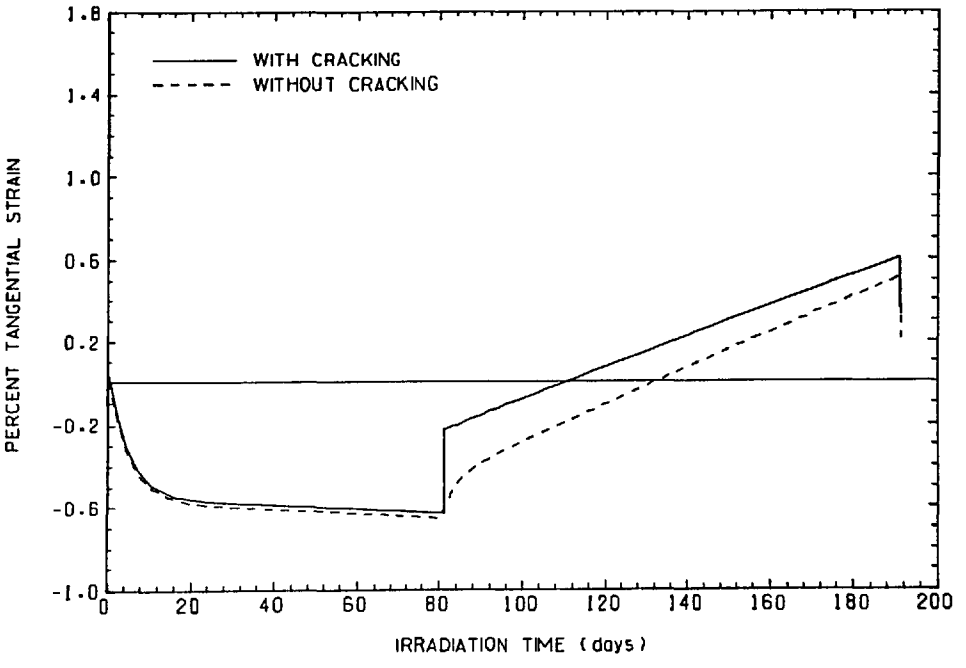
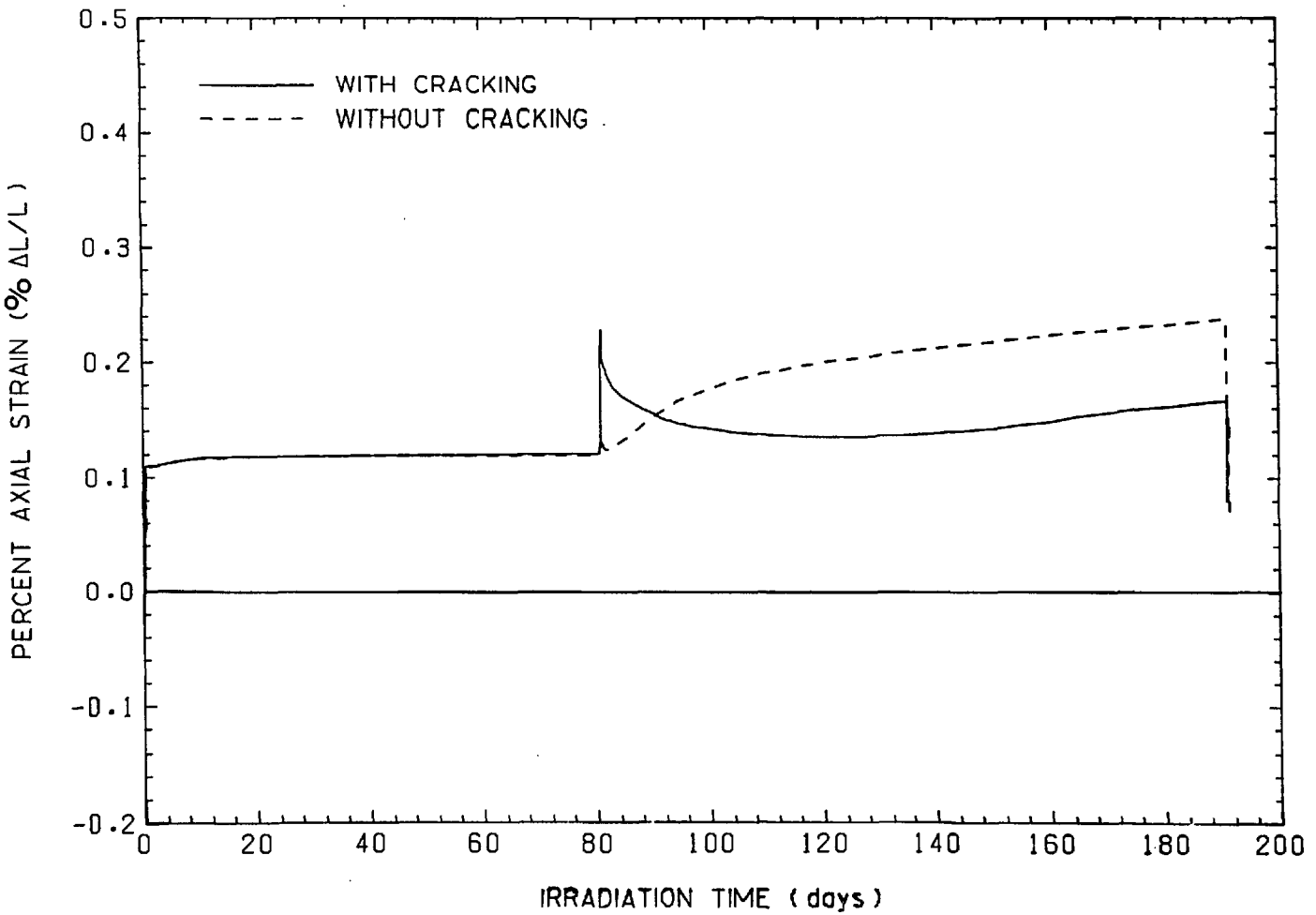


Figure 4.65

MODELLING OF ATUCHA PWR ROD UNDER A TYPICAL POWER CYCLE

CALDDING AXIAL DEFORMATION VS. IRRADIATION TIME



because later in the life the cladding is susceptible to stress-corrosion-cracking (SCC) type of failures. In Figures 4.66 and 4.67 the inner and outer cladding hoop stresses are plotted against time (the graphs are identical except for the time scale). The first interesting point is the cross-over of the stresses very early in life. This is basically believed to be a characteristic of the creep law used (otherwise one expected to see results like those shown earlier in Figure 4.27 for the classical Bailey (147) analysis). It is also thought that when a radial thermal gradient exists in addition to the internal and external pressure, the creep behaviour of a thick wall tubes can change dramatically. An analysis carried out by Johnson and Khan (178) for the same thick tube conditions as the one used in Sub-Section 4.3.2, but with a radial thermal gradient of either + 25 or - 25^{o}C across the wall, concluded that the disposition of the stress distribution with radius would be virtually reversed with heat flow. Thus it is conceivable that, under the influence of both external pressure and a thermal gradient which is higher at the inner cladding wall than at the outer wall, the inner wall hoop stress could initially be more compressive than the outer wall value, but this situation would be soon reversed by the cross-over, and then the stresses vary almost in parallel until a change in power (see Figure 4.67).

It is important to note that the stress levels are quite high at the end of the second up-ramp, particularly the inner wall hoop stress has reached a value of $\sim$ 256 MPa. This stress has, however, soon relaxed sharply, while the

Figure 4.66

MODELLING OF ATUCHA PWR ROD UNDER A TYPICAL POWER CYCLE

CLADDING TANGENTIAL STRESS VS. IRRADIATION TIME

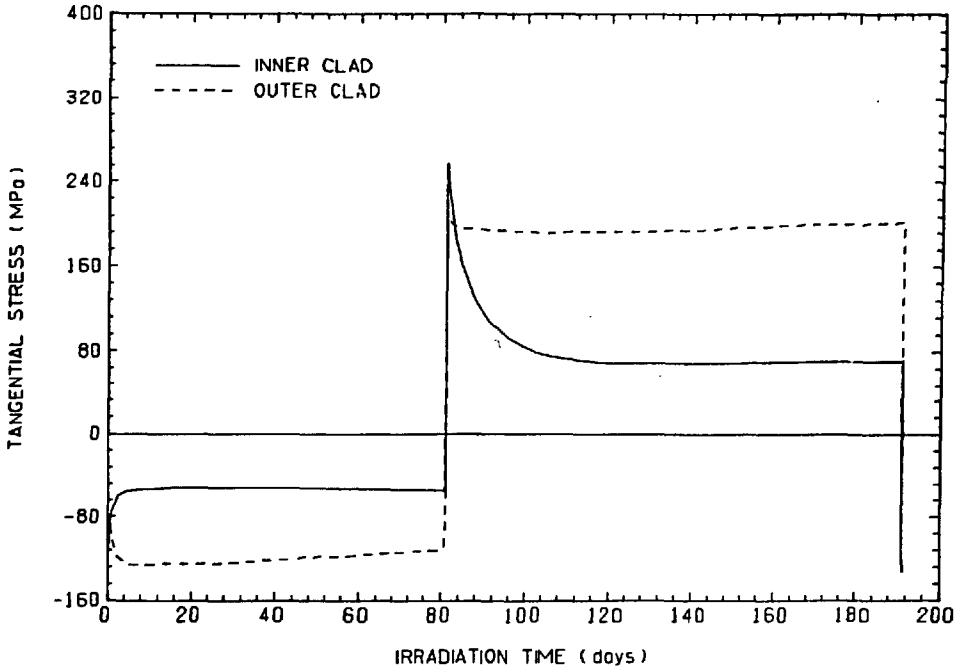


Figure 4.67

MODELLING OF ATUCHA PWR ROD UNDER A TYPICAL POWER CYCLE

CLADDING TANGENTIAL STRESS VS. IRRADIATION TIME

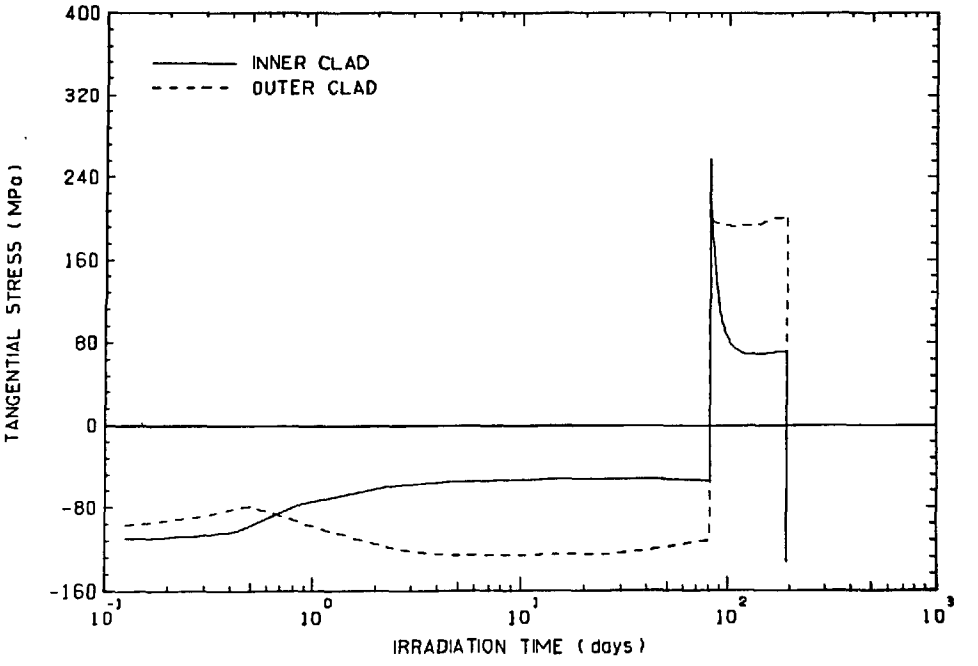


Figure 4.68

CLADDING HOOP STRESS DISTRIBUTION
VS. RADIUS FOR DIFFERENT TIMES

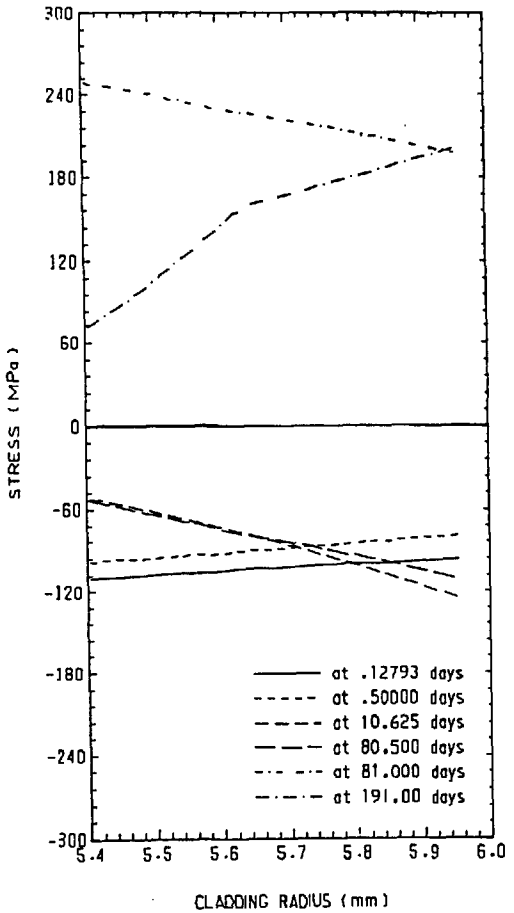


Figure 4.69

CLADDING RADIAL STRESS DISTRIBUTION
VS. RADIUS FOR DIFFERENT TIMES

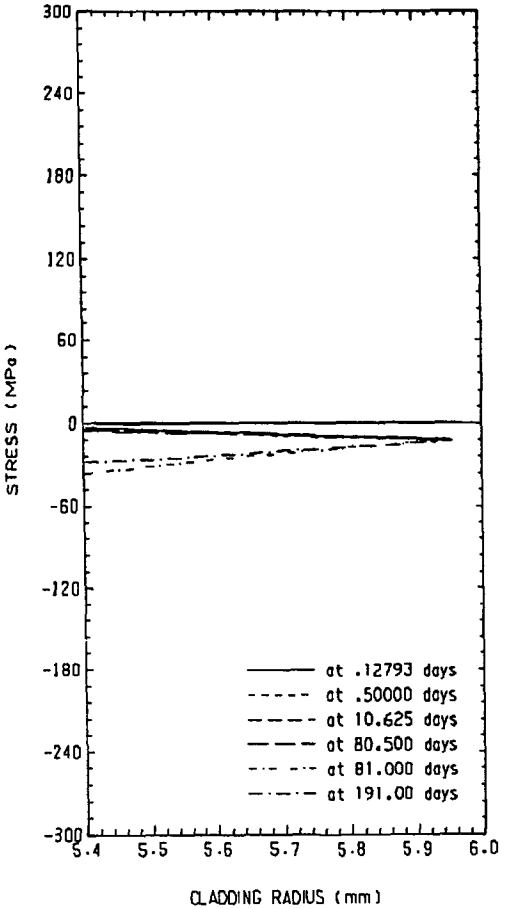
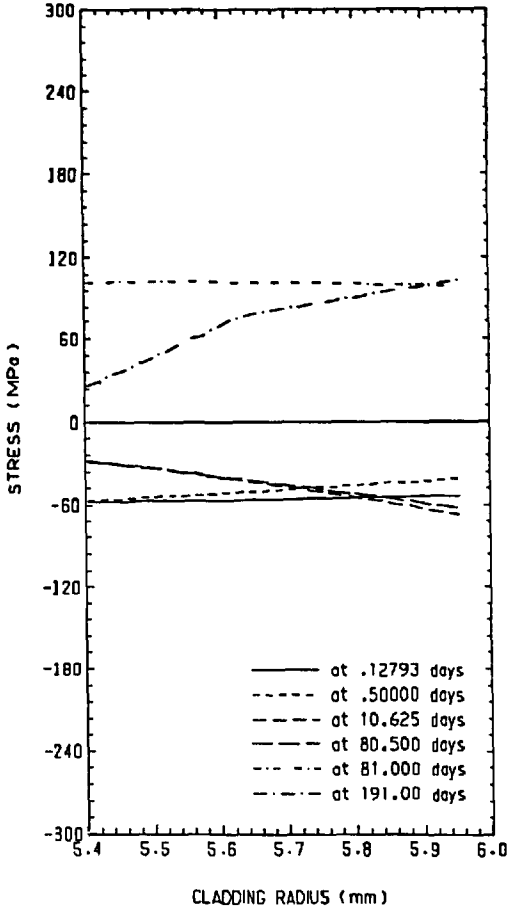


Figure 4.70

CLADDING AXIAL STRESS DISTRIBUTION
VS. RADIUS FOR DIFFERENT TIMES



outer wall stress has remained almost constant for the next 110 days, moving once again in parallel to the inner wall stress.

Finally in this section, the distribution of stresses in the cladding wall as a function of its radius are presented in Figures 4.68 to 4.70 . One may observe that the stresses remain low and compressive for the duration of the first steady-state period. While at the end of second up-ramp the hoop and axial stresses have risen to very high tensile values. These stresses relax very rapidly during the equilibrium period that follows, but only in the inner wall. The values of the outer wall axial and hoop stress remain almost the same. This is because the fuel/cladding interaction keeps the outer fibres of the cladding wall in constant tension during this period and the fuel creep is just enough to let the inner wall stress to relax.

4.5 EVALUATION OF SAMURA WITH RESPECT TO EPRI PHASE-III STUDIES

4.5.1 Introduction

The Electric Power Research Institute (EPRI) has sponsored an evaluation of six fuel pin modelling codes, and performed the task in three phases, as a step toward a more effective utilisation of these codes by the electric utility industry (14,170). The evaluation consists of a summary and qualitative comparison of relative code attributes and weaknesses, and a ranking of the codes according to objective and subjective criteria. Accordingly, the

evaluated codes have been ranked as follows: 1. COMETHE-IIIJ (7); 2. BEHAVE-4 (5) and LIFE-THERMAL-1 (3); 3. GAPCON-THERMAL-2 (16); 4. CYGRO-3 (11) and FMODEL (4). COMETHE-IIIJ has been judged to be the most versatile code for applications to both thermal and structural analyses of Zircaloy-cald UO_2 fuel pins, and also can provide considerable savings in computer running times relative to the next two best codes. BEHAVE-4 has, according to EPRI report, an excellent potential for structural analysis while LIFE-THERMAL-1 has an excellent potential for thermal analysis. Only CYGRO-3 and FMODEL have been judged to be unsuitable in their present state (December 1977) for application by the utility industry, considering the alternatives offered by the higher-ranked codes. Thus in Phase-III evaluation (170) only four codes have been included. These are: BEHAVE-4, COMETHE-IIIJ, GAPCON-THERMAL-2 and LIFE-THERMAL-1.

In order to standardise the calculations, a set of material properties and behavioural models for Zircaloy-clad UO_2 fuel pins has also been compiled by EPRI for use in the codes. These properties and models have been incorporated into all the modelling codes and are presented here for reference in Appendix D.

Finally, the objective ranking of the codes has been based largely on code predictability of thermal and structural performance variables, particularly fuel central temperature; fission gas release; end-of-life gap; fuel central void and cladding strains. Twelve well-characterised experimental and commercial fuel pins have been used for this

purpose. The relative abilities of the codes in predicting these experimental data have been the basis for their ranking.

In order to evaluate SAMURA abilities in this context, it was decided to consider one of the cases studied in the EPRI Phase III studies and model it*. It was thought that this could serve as the first step toward full evaluation of SAMURA models and their improvement. Thus Maine Yankee Core 1 pins were chosen, because of their somewhat unique power history, but specifically because they were typical commercial PWR fuel pins; designed by Combustion Engineering (U.S.A.). The main objective, however, was firstly to find out how well SAMURA predictions compare with the measured data; and secondly to establish SAMURA's preliminary standing among the four major codes evaluated by EPRI.

4.5.2 Modelling of Maine Yankee PWR Fuel Pin

The fuel pin for this case study was selected from a commercial PWR. The pin contained UO_2 pellet fuel and was unpressurised. The cladding was cold-worked Zircaloy-4. The pin was 147 inches (373.4 cm) long and had an active fuel column length of 136.7 inches (347.2 cm). Table 4.6 provides other general code input data for this case. The pin was irradiated for one refuelling cycle to a pin-averaged burn-up of 13,350 MWd/teU. The total time at power was 492 days. Table 4.7 provides values for burn-up, linear heat rating, fast neutron flux and coolant pressure for each of 15 separate burn-up periods. Following

*See Appendix E for modelling of two more EPRI cases.

TABLE 4.6

MAINE YANKEE PWR - GENERAL CODE INPUT (170)

General Input Requirements	Value	Units
Fuel Pellet O.D.	9.63930	mm
Fuel Pellet I.D.	0.0	mm
Fuel Pellet Length	16.51	mm
Active Fuel Length	3472.18	mm
Effective Rod Length	3733.80	mm
Fuel Density	92.8	% TD
Fuel Enrichment	2.01	% U-235
Fuel Grain Size	4	microns
Fuel Open Porosity	2.2	%
Dish Diameter (both ends)	7.4170	mm
Dish Depth (spherical)	0.3810	mm
Total Column Dish Volume	3.47×10^{-6}	m^3
In-Pile Fuel Densification by 4000 MWd/teU	4.0	% TD
Fuel Surface Roughness	2.49×10^{-6}	m
Cladding Surface Roughness	2.54×10^{-7}	m
Cladding I.D.	9.86790	mm
Cladding Thickness	0.6604	mm

TABLE 4.6 (cont.)

General Input Requirements	Value	Units
Initial Fill Gas	88% He/12% N	by volume
Initial Fill Gas Pressure STP	0.101	MPa
Plenum Gas Temperature	600	^{o}K
Plenum Void Volume	1.8452×10^{-5}	m^3
Total Cold Void Volume (Annular, Dish and Plenum)	3.41×10^{-5}	m^3
Inverse Diffusion Length for Neutrons in the Fuel	1.3	cm^{-1}
Energy Deposition Assumed:		
Fuel	95	%
Cladding	1	%
Coolant	4	%
Hydraulic Data*:		
Inlet Water Temperature	555	^{o}K
Mass Flow Rate	18600.0	kg/s
Cladding Surface Coefficient	33000.0	$W/m^2.^{o}K$
Power Change Rate	630	W/cm.day

*Alternatively, the cladding OD temperature may be calculated for input based on the following assumptions given by EPRI (170):

a. A linear rise of water temperature up the channel from T_{in} at inlet to T_{in} + (0.102°C x Pin Peak Power for given cycle) at the outlet; and
b. A local cladding temperature rise above the local water temperature, based on 0.088°C per W/cm local power.

TABLE 4.7

MAINE YANKEE PWR - IRRADIATION HISTORY

Burn-up Period	Pin Averaged Burn-up (MWd/teU)		Pin Peak Linear Heat (W/cm)		Pin Peak Fast Neutron Flux (n/cm^2s)	Coolant Pressure (MPa)	Inlet Coolant Temperature (^oK)
	Period	Cumulative	Total*	Fuel Only			
1	345	345	214.60	203.74	5.95×10^{13}	13.79	553
2	100	445	213.25	202.76	5.91×10^{13}	13.79	553
3	2955	3400	226.71	215.22	5.28×10^{13}	13.79	553
4	670	4070	208.66	198.16	5.78×10^{13}	13.79	553
5	640	4710	175.85	166.99	4.87×10^{13}	13.79	553
6	470	5180	90.55	85.96	2.51×10^{13}	12.41	537
7	720	5900	249.34	236.88	6.91×10^{13}	12.41	537
8	325	6225	238.19	226.38	6.60×10^{13}	12.41	537
9	1840	8065	246.39	233.92	6.83×10^{13}	12.41	537
10	160	8225	253.94	241.14	7.04×10^{13}	12.41	537
11	495	8720	260.50	247.38	7.22×10^{13}	12.41	537
12	1305	10025	245.08	232.94	6.79×10^{13}	12.41	537
13	635	10660	269.03	255.58	7.45×10^{13}	12.41	537
14	250	10910	291.01	276.6	8.06×10^{13}	12.41	537
15	2440	13350	244.75	232.61	6.75×10^{13}	12.41	537

*Fuel, cladding and coolant power deposition.

irradiation, a detailed post-irradiation examination was performed as part of a joint EPRI/CE program (180). A total of thirty pins were shipped for hot cell examination as part of this effort. The fuel pin selected for this case has been identified as the JBY097 pin (180). The hot cell examination included measurements of cladding strain and fission gas release. Metallographic examinations were made at several axial positions for characterisation of fuel grain-growth and residual gaps. A summary of the experimental data available on the JBY097 pin for code benchmarking is given in Table 4.8. The data include fuel grain-growth radii, fission gas release, residual cold gaps and cladding strains. Applicable data uncertainties are also provided (170).

According to examiners (180), the overall hot-cell results showed two populations of fission gas release among the pins: less than 1% and 11.3 to 15.3%. Pins with low gas release showed no fuel restructuring, whereas pins with high gas release showed equiaxed grain-growth in the fuel, up to a fractional radius of approximately 0.6, along the entire fuel column, except for a short length at each end. One does not expect, theoretically at least, that fuel pins of a given design, and operating at similar power levels, to exhibit either high or low gas release. This can be attributed to strong dependencies of gap conductance, fuel temperatures and gas release on the fuel/cladding hot gap during power operation. It has already been discussed how the hot gap is, in turn, related to many parameters but particularly to differences in as-manufactured gaps and

in-pile densification properties. EPRI (180) have reported that pins with initial fuel/cladding radial gaps of 4 mils (∿ 100 μm) and above showed higher gas release, and those with gaps of less than 4 mils showed low gas release. The initial gap of the JPBY097 pin was 4.5 mils (∿ 115 μm) and the gas release measured for this pin was 13.4%.

TABLE 4.8

MAINE YANKEE PWR - EXPERIMENTAL DATA SUMMARY

1. Fuel Peak Central Temperature:			
T_{gg} (Equiaxed) (^{o}K)			
Best Estimate		1622	
Uncertainty		± 50	
Axial Location (inches)	6.5	36	129.5
Ratio of Equiaxed Grain Growth Radius to Pellet Radius:			
Best Estimate	0.30	0.50	0.60
Uncertainty	±0.05	±0.05	±0.05
Applicable Linear Heat Rating (W/cm)			
Best Estimate	see Table 4.9		
Uncertainty	± 0.3 (on lifetime pin-average rating)		
Inferred Peak Central Fuel Temperature (^{o}K)			
Best Estimate	see Table 4.9		
Uncertainty	+67 at 150 W/cm	+106 at 253 W/cm	+100 at 160 W/cm
2. Fission Gas Release		13.4%	
3. Cold Radial Gap (μm):			
BOL	115	115	115
EOL	66.1	58.4	55.9
EOL uncertainty	± 6.3	± 6.3	± 6.3
4. Cladding Strains:			
EOL % ΔD/D	-0.23	-0.55	-0.34
Uncertainty	±0.5%	±0.5%	± 0.5%

In Table 4.8, fuel peak centreline temperatures have been inferred from the measured equiaxed grain-growth radii in the fuel, however, they are not listed as part of the data. Since each code calculates peak centreline fuel temperatures at different times in life and slightly different powers, the corresponding experimental temperatures have been inferred separately for each code. The local linear power used in the calculation depends upon the time in life that each code predicts the peak temperature to occur. These results are presented in Table 4.9. The method used to calculate the experimental peak temperatures may be found in Reference 170.

Before describing the code results and comparing them with experimental data, a few points should be made about the SAMURA modelling of the case. The main difference between the first version of SAMURA (as used in the present work) and the four major codes studied by EPRI is that they are all quasi-two-dimensional (or the so-called 1½ dimensional) and perform the calculation at several axial locations along the pin while SAMURA has only one axial node. Thus it was necessary to calculate pin-averaged axial relative powers for each burn-up period from time-dependent axial power shapes given in Reference 180. With these data an average power run was performed for the whole pin history and the internal pin pressures, as a function of irradiation time, were thus obtained*. Then it was possible to run the

*This procedure is not expected to provide the same results as would the alternative of making runs at several axial positions and averaging the gas release rates (due to non-linearities in fission gas release models). In fact for the present 1-D version of SAMURA this is the simplest procedure and the most economic one too. The desirable and more accurate method would obviously be a quasi-two-dimensional one.

program for the three desired axial positions along the pin (6.5, 36.0 and 128.5 inches) using the above pin pressures and the appropriate axial power shapes at each axial location. The input data were compiled from Tables 4.6 and 4.7. Some material behavioural models in SAMURA had to be changed to bring it into accord with the other codes. For simplicity the parameterisation provided by EPRI (170), and given in Appendix D *, was incorporated into SAMURA. So that one had three options of fission gas release models (two already described in Chapter 3 and the third given in Appendix D); two options of UO_2 thermal expansion and thermal conductivity; and two options of Zr thermal expansion. These options, plus the two options of gap conductance ($F \geq 0.3$ and $F = 0.0$, see Sub-Section 4.2.2) provide numerous possibilities. However, the only options the choice of which can cause significant differences in the final results, are fission gas and gap conductance models. It was then decided to have only three main SAMURA runs to show representative results, namely;

---

* UO_2 swelling model was not, however, changed and the same model given in Sub-Section 3.5.8 was utilised with a modification made to account for densification. This is because SAMURA presently does not have a separate densification model. The following procedure was therefore adopted: Since according to the pin data it densifies by 4% TD by 4000 MWd/teU (or after $\sim$ 160 days), the densification rate is 0.04/160 per day. The volume change cause by this is

$$\left(\frac{\Delta V}{V}\right)_{dens} = - \frac{\Delta P}{1-P}$$

So the rate of volume change can be calculated for each time-step by up-dating the porosity at every step, starting from an initial value of 7.2%. Then the swelling rates can be corrected by simply adding $\left(\frac{\Delta V}{V}\right)_{dens}$ to $\left(\frac{\Delta V}{V}\right)_{SW}$.

(A) Cracked pellet model (Eq.(3.37)) for gap conductance, gas release model option 2, given in Sub-Section 3.5.10; and the rest of models as given in Appendix D;

(B) Cracked pellet model (Eq.(3.37)) for gap conductance; gas release model given in the EPRI Phase III studies (170), and the rest of models as given in Appendix D;

(C) Ross and Stoute model (F = 0.0 in Eq.(3.37)) for gap conductance; gas release model option 2, given in Sub-Section 3.5.10; and the rest of models as given in Appendix D.

The results of these runs are given in Tables 4.9 through 4.12 along those of BEHAVE-4, COMETHE-IIIJ, GAPCON-THERMAL-2 and LIFE-THERMAL-1. Only the results of SAMURA's run (A) are presented graphically, for comparison with results of the other codes, in Figures 4.71 through 4.80 . The following is a discussion of codes results and comparison with experimental data. It must be pointed out that all the comments made about other codes are taken from EPRI reports (14, 170, 180).

In Table 4.9 peak fuel centreline temperatures predicted by each code are presented together with the associated time in life and the local heat rating in the fuel. Experimentally inferred peak centreline temperature, as given by EPRI, are also presented, and the differences between the predicted and the experiments are listed in the last column of the table.

BEHAVE-4 with the EPRI Phase III gas release model has encompassed the experimental temperatures at all the three axial locations, i.e. its temperature predictions fall within the acceptable range of experimental data considering the measurement uncertainties. Other codes predictions have much higher deviations from the experimental temperatures. BEHAVE-4 with the EPRI Phase II gas release model (14) underpredicts the temperature by 278°K at the 6.5 inch location and by 327°K at the 128.5 inch location. Use of the Phase III gas release model, however, leads to temperature overpredictions of about 11°K at the 128.5 inch location and 162°K at the 36 inch location. The above differences are consistent with a higher gas release prediction by the Phase III model than by the Phase II model (14).

COMETHE-IIIJ has been said to show significant sensitivity to the cladding creep model in its prediction of peak fuel centreline temperature. As will be discussed later on, it has been observed that the Phase III cladding creep model (the same as used in SAMURA for all cases studied here - see Sub-Section 3.5.7 or Appendix D) somewhat overpredicts cladding creep rates. To evaluate the sensitivity of this parameter, COMETHE-IIIJ has used both the Phase III and a reduced Phase III cladding creep model*. It is apparent that the predictions of fuel temperature and gas release (Tables 4.9 and 4.10) by COMETHE-IIIJ vary from significant underpredictions to significant overpredictions depending on the cladding creep model used. As is naturally

*Phase III creep rate model was arbitrary reduced by 60%.

expected, predicted temperatures decrease with increasing creep-down. It has also been observed that in addition to the sensitivity to cladding creep, COMETHE-IIIJ shows a large sensitivity in its temperature prediction to the local heat rating. For example, using the Phase III cladding creep model, it underpredicts the temperature at the 36 inch elevation by only 15°K; in contrast, at the 6.5 and 128.5 inch locations, underpredictions are 177° and 371°K, respectively. According to EPRI, this occurs in COMETHE-IIIJ due to a strong dependence of gap closure kinetics to local power (170).

LIFE-THERMAL-1 underpredicts fuel temperatures by at least 142°K with use of the Phase III creep model. At other power locations the underpredictions are by as much as 356°K. LIFE-THERMAL-1 has also been found to be sensitive to cladding creep. Application of the Phase II cladding creep model (14) to this case in Phase III has reduced the temperature underpredictions by a maximum of 47°K at the 128.5 inch location. Underpredictions of fuel temperatures by LIFE-THERMAL-1 are caused principally by large gap closure rates. Predicted hot radial gaps plotted in Figures 4.74 and 4.78 show that LIFE-THERMAL-1 provides the largest gap closure of all codes, and it is the only code which predicts a gap closure at the 36 inch power location.

GAPCON-THERMAL-2, which does not perform any creep calculations, overpredicts fuel temperatures by 367°K at the lower power location and by 647°K at the higher

power location. With an input correction for cladding creep, equivalent to a 0.5% diametral shrinkage, overpredictions are reduced by between 60^{o} to 90^{o}K. This is not a large sensitivity compared to the magnitude of the overpredictions. Figures 4.74 and 4.78 show that the gaps predicted by GAPCON-THERMAL-2 as compared to those by BEHAVE-4 are much less sensitive to burn-up (time). This has resulted in a larger hot gap prediction by GAPCON-THERMAL-2 compared to that of BEHAVE-4 at the time of peak power and has reflected accordingly on the calculation of peak temperature. GAPCON-THERMAL-2 also provided fuel densification of 5.2% rather than the 4.0% specified for this case. This must have artificially increased the gap throughout life.

SAMURA with cracked gap model underpredicts the centre-line temperatures by large amounts; irrespective of the fission gas release model used. Run (A) which uses SAMURA's own gas release model (option 2, see Sub-Section 3.5.10) underpredicts the temperature by 539^{o}K at the 6.5 inch location and by 302^{o}K at the 36 inch location. The use of EPRI Phase III gas release model, which improved the BEHAVE-4 prediction of temperatures, does not, however, improve SAMURA's run (B). In fact the underprediction increases by up to 50^{o}K. SAMURA, nevertheless, overpredicts the fuel centreline temperature when using the Ross and Stoute gap model. Here SAMURA's overprediction of the temperature at the 6.5 inch location is 266^{o}K, at the 36 inch is 145^{o}K, and at the 128.5 inch is 138^{o}K. This overprediction is expected and is in line with the previously discussed results in Sub-Section 4.2.2.

Figures 4.75 and 4.79 , comparing SAMURA's gap conductance (calculated with cracked pellet model) with that of the other codes, show its large difference with their values (as expected the cracked pellet model calculates values at least 30% higher than the Ross and Stoute simulation). That explains the low temperatures in runs (A) and (B). As for why the cracked pellet model has provided such large gap conductance values, one may recall that the cracked gap model has a tendency to underpredict temperatures in low-powered helium filled pins (see Sub-Section 4.2.2). This is because the closed-cap thermal conductance term in Eqs.(3.36), (3.37) and (3.42), i.e. $(k_{mix}/\delta)F$, has a minimum value of about 1000 $W/m^{2o}K$ (with He fill gas and low gas release) throughout the calculation which is superimposed on the open-gap thermal conductance term. Thus owing to low linear power operation the value of k_{mix} does not deteriorate much and the contribution from the first term of Eq.(3.36) is always significant, especially at higher burn-ups when F sharply approaches unity (see Figure 3.4). It must be remembered that in this particular case the Zr creep rate model used has also contributed to fuel temperature underprediction through its prediction of smaller hot gaps early in life*. It is then possible that the same high rates of

*Nevertheless, since SAMURA's creep-down predictions, as given in Table 4.12, are not much different from those of the others, it is believed that the gap conductance model has played the main role throughout these calculations. In fact if one takes the hot radial gap predicted by the codes, Figs.4.74 and 4.78, one may observe a clear distinction between the high-temperature codes (BEHAVE-4 and GAPCON-THERMAL-2) and the low temperature ones (SAMURA, COMETHE-IIIJ and LIFE-THERMAL-1) during the first 6 periods. The former codes predict a sharp increase in gap value just after 12 days (end of period 2), while the latter codes lag behind. SAMURA in fact predicts an increasing gap value (due to its modified swelling model for densification) and moves in parallel with BEHAVE-4, especially

cladding creep-down are responsible for increasing the usually low values of Ross and Stoute gap conductance (see Sub-Section 4.2.2) to reasonable values; so much that SAMURA's run (C) has provided one of the good temperature predictions, fortuitously of course.

The temperature calculations are also presented graphically for some particular runs of the codes, namely, for BEHAVE-4 with Phase III gas release; for COMETHE-IIIJ with Phase III Zr creep; for GAPCON-THERMAL-2 without - 0.5% $\Delta D/D$ input; for LIFE-THERMAL-1 with Phase III creep; and for SAMURA with cracked pellet model, run (A). The specified linear power histories at the three axial locations for this case and the average linear power are plotted in Figure 4.71 . Figures 4.73 and 4.77 show the code predictions of the fuel centreline temperature histories at the 6.5 inch and 36 inch locations, respectively. At the lower power positions (6.5 and 128.5 inch) all of the codes predict peak temperatures to occur at the time of the fuel lifetime peak power at these locations (see Table 4.9 and Figures 4.71 and 4.73 . At the 36 inch location, however, BEHAVE-4 and LIFE-THERMAL-1 predict peak temperatures to occur during

---

*at the 6.5 inch location, but with a smaller gap (by 30 μm). At the 36 inch location, though this difference is maintained initially, SAMURA eventually approaches nearer to BEHAVE-4 gap values reducing the difference to about 10 μm. In the same graph (Fig.4.78), it can be seen that the hot gap predicted by SAMURA runs almost parallel with that given by COMETHE-IIIJ with a small difference of about 10 μm. This means that SAMURA's other physical and behavioural models provide similar predictions as those of the COMETHE-IIIJ code in particular. It is therefore the high conductance value provided by the cracked pellet model which is responsible for SAMURA's low temperature prediction; and this in turn, as discussed in the text, is partly due to the low gas release prediction.

burn-up period 7, which is about 200 days ahead of the life-time peak power position at this elevation (see Table 4.9 and Figures 4.71 and 4.77 . These trends are consistent with the time-dependent gap conductance and hot radial gaps calculated by the codes, which are plotted versus time in Figures 4.73 , 4.74 , 4.78 and 4.79 . At the6.5 inch location, all codes show a gradual decrease in gap conductance (Figure 4.75, notice SAMURA's values which are continuously above all) as well as in hot radial gap (after the termination of densification at about 260 days, Fig. 4.74 with time. It seems, therefore, that the temperature history follows the input power history. In Figure 4.78 , however, one may see that BEHAVE-4 and LIFE-THERMAL-1 predict marked decreases of hot radial gap at the beginning of period 7. This causes the subsequent increased gap conductance which dominates the effect of power peaking leading to a prediction of lower temperatures later in life, as discussed earlier. One interesting point to note aboute BEHAVE-4 (Figs.4.78 and 4.79) is an instability in its gap conductance and gap closure kinetics calculations. According to EPRI, this was fixed in a subsequent run by using very small time-steps during the affected irradiation period.

The predicted and measured end-of-life (EOL) cold gaps are given in Table 4.11. LIFE-THERMAL-1 calculates the largest gap closure, as is evident from an EOL cold gap comparison. Thus it underpredicts the EOL cold gaps at all power locations, with the largest underprediction occurring at the 36 inch location. BEHAVE-4 slightly underpredicts the EOL gap at the 36 inch elevation using the Phase III gas

release model. All other codes overpredict the measured EOL cold gaps at all locations with SAMURA's run (C) giving the closest prediction after BEHAVE-4. As expected the differences between run (A) and (B) of SAMURA are very small due to their also small temperature differences.

Table 4.10 and Figure 4.72 compare the calculated and measured fission gas release data. The closest agreement with the experimental data is provided by BEHAVE-4 with use of the Phase III gas release model. Consistent with their temperature predictions, BEHAVE-4 and COMETHE-IIIJ bracket the measured gas release by using variations in gas release and cladding creep model, respectively. GAPCON-THERMAL-2 shows a large overprediction, and LIFE-THERMAL-1 shows a large underprediction in conformity with their temperature calculations. SAMURA largely underpredicts gas release in runs (A) and (B), while in run (C) it overpredicts the release. Runs (A) and (C) use SAMURA's own gas release model which is basically a function of burn-up, and only distinguishes three temperature regions. Thus, for example, at low fuel temperatures ($\leq 1573^{o}K$) it always gives the same gas release rate at the same burn-up, i.e. no other parameters apart from temperature and burn-up affect SAMURA's option 2 gas release model. Use of the EPRI Phase III gas release model has not affected run (B) due to low temperature prediction in the first place.

From the time dependent gas release predictions plotted in Figure 4.72, it is apparent that only BEHAVE-4 and GAPCON-THERMAL-2 show a sharp increase in gas release at

the onset of burn-up period 7 (where a sharp rise in linear power from 85 to 240 W/cm occurs). Qualitatively, the predicted behaviour is in line with the observed fuel pin behaviour in general. BEHAVE-4 and GAPCON-THERMAL-2 predict gas release values of 14.4% and 49.5% at EOL, respectively, compared to a measured release of 13.4%. One may see from Figures 4.73 and 4.77 that all of the codes show a temperature increase with an increase in power during period 7. The calculated release fractions, however, indicate that the fuel temperatures calculated by all codes except BEHAVE-4 and GAPCON-THERMAL-2 do not exceed the threshold required for appreciable gas release.

Finally, predicted and measured tangential creep strains are compared in Table 4.12 and Figures 4.76 and 4.80. At the 6.5 inch location, COMETHE-IIIJ calculates the values of - 0.44% and - 0.17% using the Phase III and reduced Phase III cladding creep models, respectively. GAPCON-THERMAL-2 does not calculate cladding creep, and a value of - 0.5% $\Delta D/D$ has been used as an input for the entire pin to account for the axial average effect on gap closure. BEHAVE-4 does not use the Phase III cladding creep model, but utilises its own built-in constitutive equations for Zircaloy. It is apparent that except for the results provided by the reduced Phase III cladding creep model used by COMETHE-IIIJ, all of the codes overpredict the creep strains at this location.

Much closer agreement is obtained between the predicted and measured creep strains at the 36 inch elevation, except

for the - 1.05% ΔD/D value calculated by COMETHE-IIIJ using the Phase III creep model. Using the same cladding creep model, LIFE-THERMAL-1 predicts only - 0.65% ΔD/D because of its gap closure prediction at burn-ups above 8000 MWd/teU. According to EPRI's experimental evidence, pellet/cladding contact is inferred at the pellet interfaces of high-gas-release Maine Yankee pins. But there is no suggestion that pellet/cladding contact was sufficient to reduce cladding creep-down as calculated by LIFE-THERMAL-1. With the Phase III creep model all the 3 runs of SAMURA overpredict the cladding tangential strain; with run (A) giving the smallest overprediction. BEHAVE-4 does not predict gap closure, but by using its own constitutive equations for Zircaloy, gives the closest agreement with the experimentally measured strain.

At the 128.5 inch location, BEHAVE-4 slightly under-predicts the strain. LIFE-THERMAL-1 and COMETHE-IIIJ bracket the measured creep strain using variations of the cladding creep model. SAMURA overpredicts the creep strain in all its runs by up to 20% with respect to the data.

It is obvious from the above comparison that BEHAVE-4 provides the closest agreement with the measured cladding creep data. LIFE-THERMAL-1, COMETHE-IIIJ and SAMURA, with use of the Phase III cladding creep model have all over predicted strains. SAMURA predictions are, however, more in line with the experimental strains as far as the location is concerned. The arbitrarily reduced Phase III cladding creep (by 60%) and its use in COMETHE-IIIJ has led to some underpredictions of the strains (by about 20% with respect to the experimental data).

TABLE 4.9

MAINE YANKEE PWR - PREDICTED vs EXPERIMENTAL PEAK CENTRELINE TEMPERATURE

Fuel Axial Location From Inlet (inches)	Code	Irradiation Period	Local Linear Heat Rating (W/cm)	Peak Centreline Temperature (^{o}K)		Temperature Difference (^{o}K)(6)
				Code Prediction	Experiment	
6.5	BEHAVE-4(1)	14	150.92	1383	1666	- 278
		11	141.08	1721	1661	+ 60
	COMETHE-IIIJ(2)	14	154.20	1489	1666	- 177
		14	154.20	1969	1666	+ 303
	GAPCON-THERMAL-2(3)	14	150.92	2033	1666	+ 367
		14	150.92	1964	1666	+ 298
	LIFE-THERMAL-1(4)	14	150.92	1391	1666	- 275
		14	150.92	1416	1666	- 250
	SAMURA-1(5)	14	148.0	1125	1664	- 539
		14	148.00	1088	1664	- 576
		14	148.00	1930	1664	+ 266

TABLE 4.9 (cont.)

Fuel Axial Location From Inlet (inches)	Code	Irradiation Period	Local Linear Heat Rating (W/cm)	Peak Centreline Temperature (^{o}K)		Temperature Difference (^{o}K)(6)
				Code Prediction	Experiment	
36	BEHAVE-4	7	226.38	1669	1800	- 131
		10	239.50	1967	1805	+ 162
	COMETHE-IIIJ	14	255.90	1807	1822	- 15
		13	236.22	2025	1805	+ 220
	GAPCON-THERMAL-2	14	252.62	2463	1816	+ 647
		14	252.62	2366	1816	+ 550
	LIFE-THERMAL-1	7	226.38	1628	1800	- 172
		7	226.38	1658	1800	- 142
	SAMURA-1	14	256.00	1520	1822	- 302
		14	256.00	1470(7)	1822	- 352
		11	240.00	1950(7)	1805	+ 145

TABLE 4.9 (cont.)

Fuel Axial Location From Inlet (inches)	Code	Irradiation Period	Local Linear Heat Rating (W/cm)	Peak Centreline Temperature (^{o}K)		Temperature Difference (^{o}K)(6)
				Code Prediction	Experiment	
128.5	BEHAVE-4(1)	14	160.76	1473	1800	- 327
		14	160.76	1811	1800	+ 11
	COMETHE-IIIJ(2)	14	150.92	1418	1789	- 371
		14	150.92	1944	1789	+ 155
	GAPCON-THERMAL-2(3)	14	160.76	2090	1800	+ 290
		14	160.76	2023	1800	+ 223
	LIFE-THERMAL-1(4)	14	160.76	1444	1800	- 356
		14	160.76	1491	1800	- 309
	SAMURA-1(5)	14	151.00	1205	1789	- 584
		14	151.00	1166	1789	- 623
		14	151.00	1927	1789	+ 138

(1) With Phase II (14) and Phase iII (170) gas release models, respectively.
(2) With Phase III and reduced Phase III cladding creep models, respectively.
(3) With zero and - 0.5% $\Delta D/D$ input for cladding creepdown, respectively.
(4) With Phase III and Phase II cladding creep models, respectively.
(5) Runs (A), (B) and (C) as described in the text, respectively.
(6) Predicted minus experimental.
(7) Note that this temperature is predicted for period 11 at 36 inches; SAMURA prediction for period 14 at the same location is $1889^{o}K$.

TABLE 4.10

MAINE YANKEE PWR -

PREDICTED vs EXPERIMENTAL FISSION GAS RELEASE

Experimental Fission Gas Release at EOL (%)	13.4
Predicted Fission Gas Release at EOL (%):	
BEHAVE-4 (1)	1.6, 14.4
COMETHE-IIIJ (2)	2.2, 22.6
GAPCON-THERMAL-2 (3)	60.2, 49.5
LIFE-THERMAL-1 (4)	5.1, 5.9
SAMURA-1 (5)	8.1, 1.4, 21.9

(1) With Phase II (14) and Phase III (170) gas release models, respectively.

(2) With Phase III and reduced Phase III cladding creep models, respectively.

(3) With zero and - 0.5% $\Delta D/D$ inputs for cladding EOL creepdown, respectively.

(4) With Phase III and Phase II cladding creep models, respectively.

(5) Runs (A), (B) and (C) as described in the text, respectively.

TABLE 4.11

MAINE YANKEE PWR -

PREDICTED vs EXPERIMENTAL EOL COLD GAPS

Axial Location from Inlet (inches)	6.5	36	128.5
Experimental EOL Cold Radial Gaps[6] (μm)	66.0	58.4	55.9
Predicted EOL Cold Radial Gaps(μm):			
BEHAVE-4[1]	147.3 97.8	85.1 50.8	148.6 95.3
COMETHE-IIIJ[2]	139.7 121.9	97.8 76.2	118.1 114.3
GAPCON-THERMAL-2[3]	148.6 120.7	144.8 116.8	149.9 121.9
LIFE-THERMAL-1[4]	54.6 53.3	25.4 25.4	44.5 47.0
SAMURA-1[5]	137.7 136.2 115.3	92.3 91.9 64.2	122.5 121.1 100.5

(1) With Phase II and Phase III gas release models, respectively.

(2) With Phase III and reduced Phase III cladding creep models, respectively.

(3) With zero and - 0.5 $\Delta D/D$ inputs for cladding creep, respectively.

(4) With Phase III and Phase II cladding creep models, respectively.

(5) Runs (A), (B) and (C) as described in the text, respectively.

(6) Uncertainty is $\pm$ 12.5 μm.

TABLE 4.12

MAINE YANKEE PWR-PREDICTED vs EXPERIMENTAL CLADDING

PERMANENT TANGENTIAL STRAINS

Axial Location from Inlet (inches)	6.5	36	128.5
Experimental EOL Permanent Tangential strain (% $\Delta D/D$)(6)	- 0.23	- 0.55	- 0.34
Predicted EOL Permanent Tangential Strain (% $\Delta D/D$) :			
BEHAVE-4(1)	- 0.31 - 0.38	- 0.56 - 0.59	- 0.29 - 0.28
COMETHE-IIIJ(2)	- 0.44 - 0.17	- 1.05 - 0.41	- 0.85 - 0.32
GAPCON-THERMAL-2(3)	0.00 - 0.50	0.00 - 0.50	0.00 - 0.50
LIFE-THERMAL-1(4)	- 0.39 - 0.35	- 0.65 - 0.58	- 0.57 - 0.42
SAMURA-1(5)	- 0.29 - 0.31 - 0.33	- 0.68 - 0.70 - 0.82	- 0.44 - 0.45 - 0.56

(1) With Phase II and Phase III gas release, respectively.

(2) With Phase III and reduced Phase III cladding creep models, respectively.

(3) With zero and - 0.5% $\Delta D/D$ inputs for cladding creep, respectively.

(4) With Phase III and Phase II cladding creep models, respectively.

(5) Runs (A), (B) and (C) as described in the text, respectively.

(6) Uncertainty is $\pm$ 0.5% $\Delta D/D$.

Figure 4.71
EVALUATION OF MAINE YANKEE PWR CORE 1 RODS
FUEL LINEAR HEAT RATING VS. IRRADIATION TIME

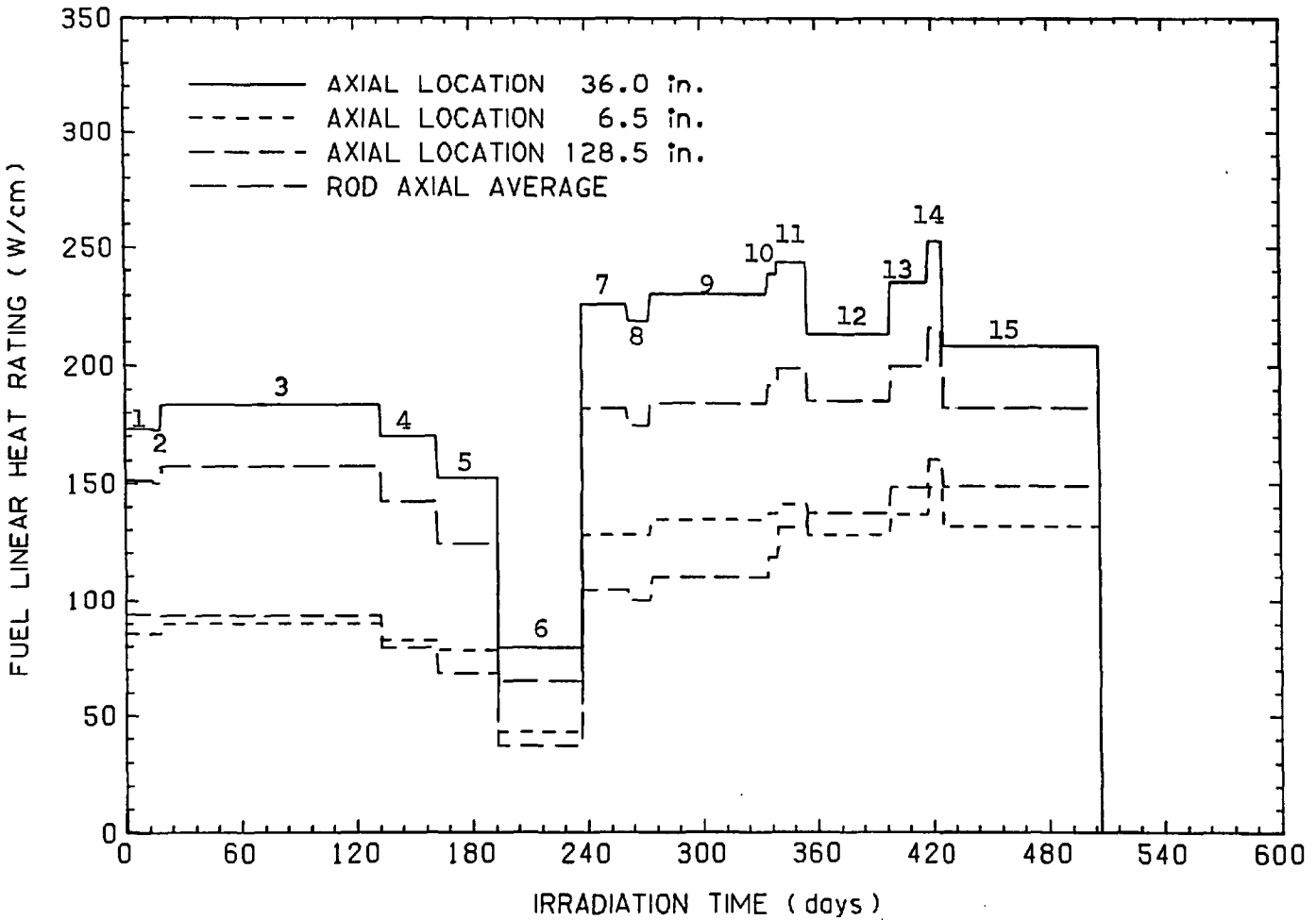


Figure 4.72
EVALUATION OF MAINE YANKEE PWR CORE 1 RODS
FISSION GAS RELEASE VS. IRRADIATION TIME

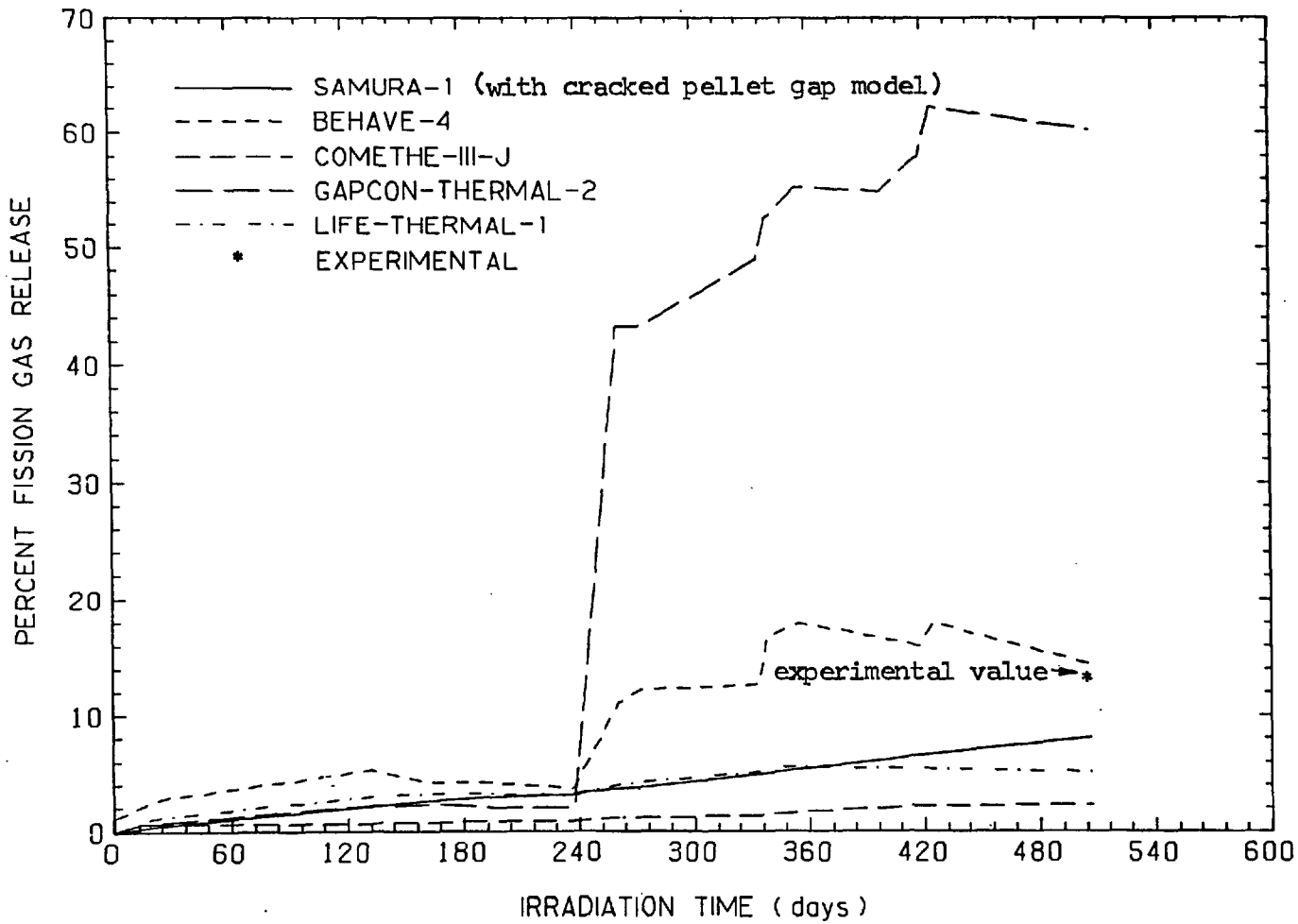


Figure 4.73

EVALUATION OF MAINE YANKEE PWR CORE 1 RODS

FUEL CENTRELINE TEMPERATURE VS. IRRADIATION TIME AT 6.5 INCHES

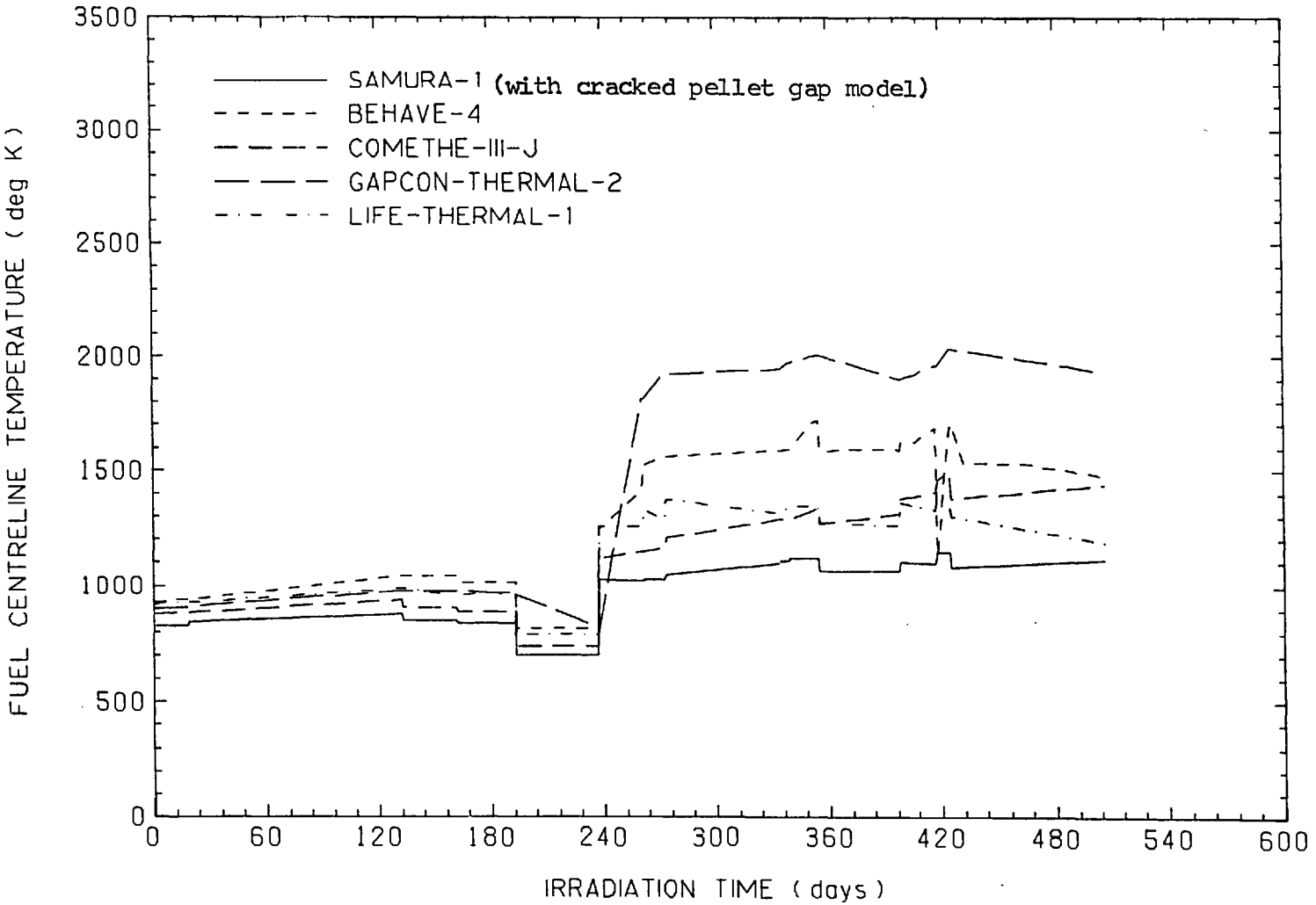


Figure 4.74

EVALUATION OF MAINE YANKEE PWR CORE 1 RODS

HOT RADIAL GAP VS. IRRADIATION TIME AT 6.5 INCHES

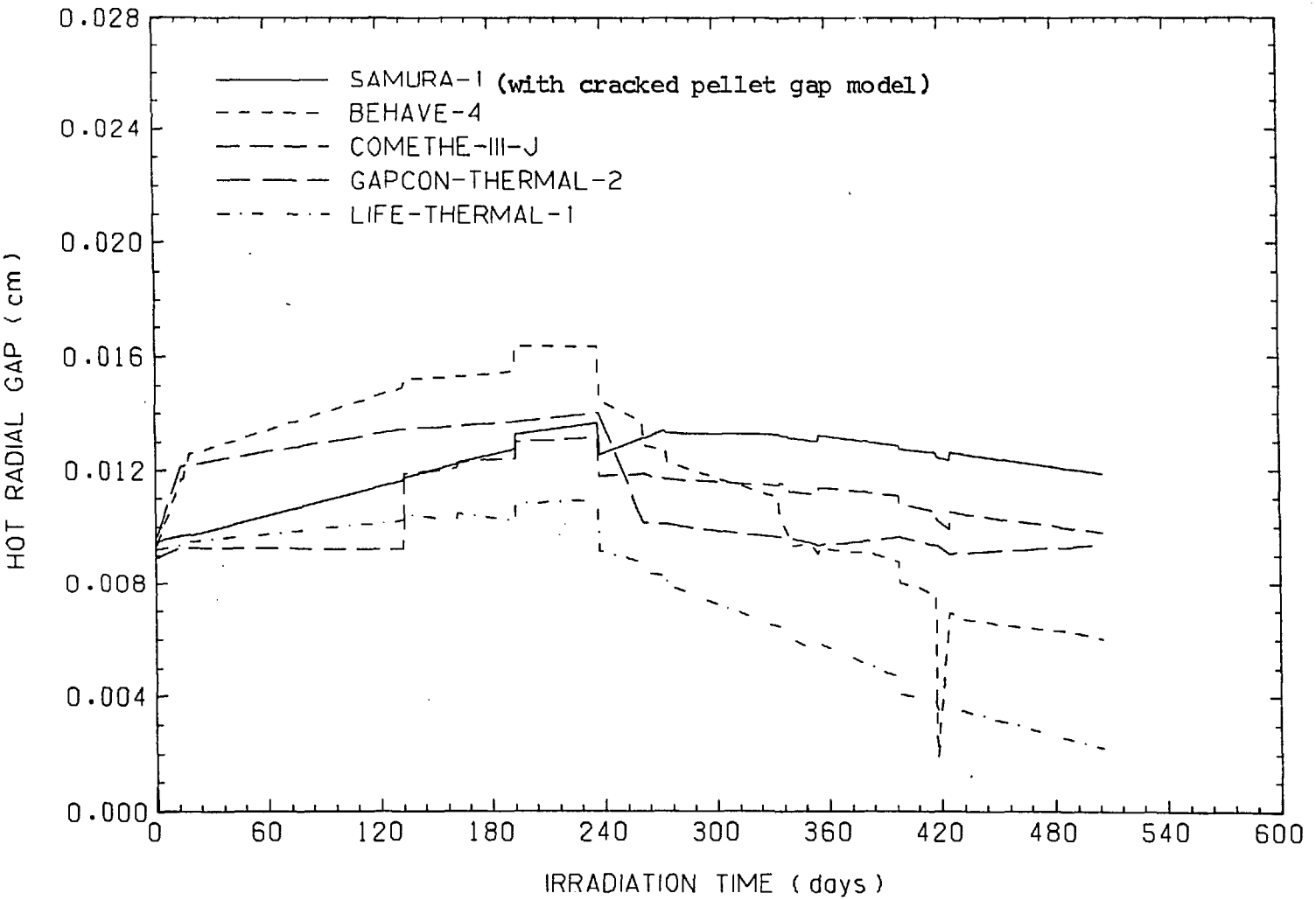


Figure 4.75
EVALUATION OF MAINE YANKEE PWR CORE 1 RODS
GAP CONDUCTANCE VS. IRRADIATION TIME AT 6.5 INCHES

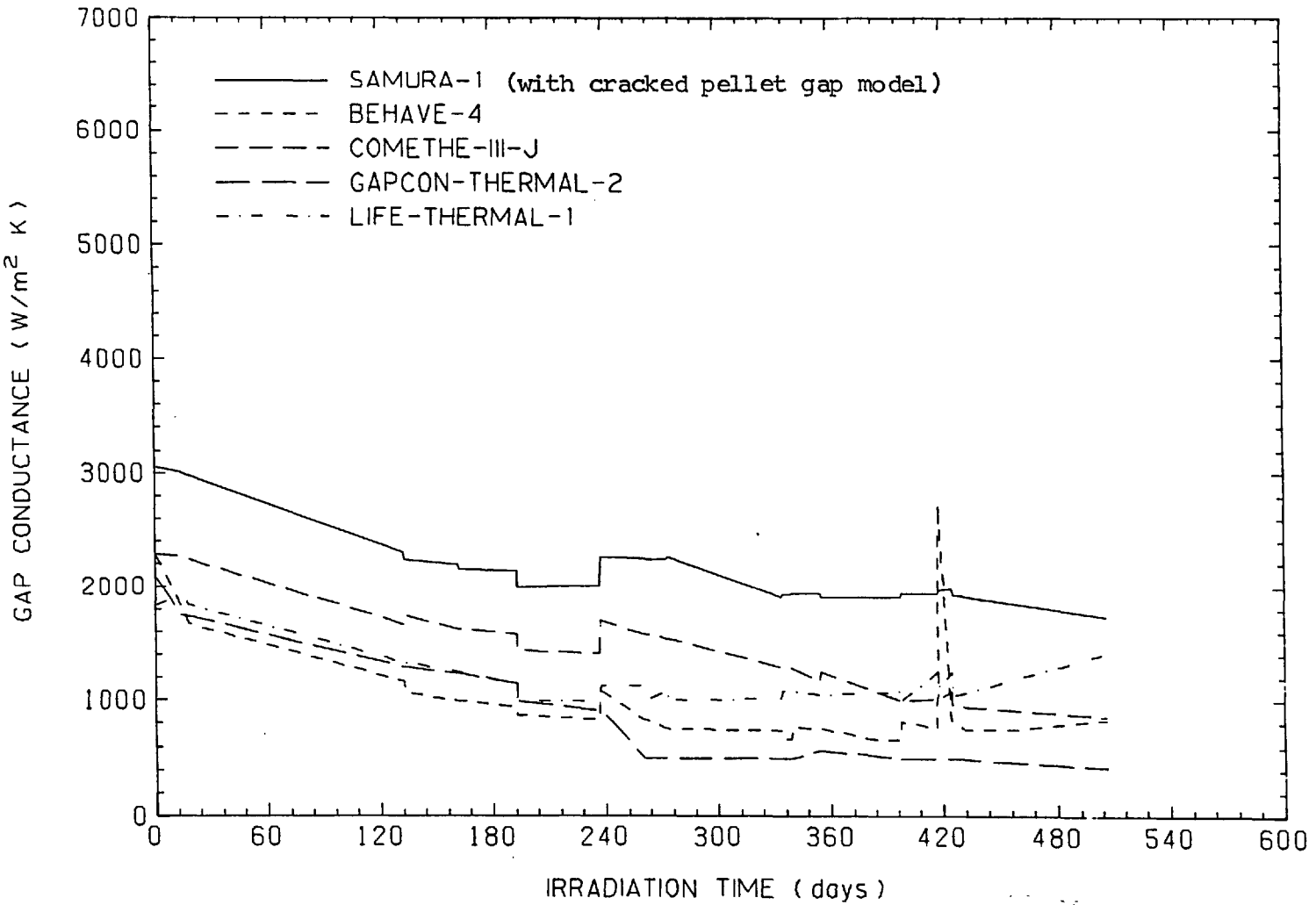


Figure 4.76

EVALUATION OF MAINE YANKEE PWR CORE 1 RODS

CLADDING PERMANENT TANGENTIAL STRAIN VS. IRRADIATION TIME AT 6.5 INCHES

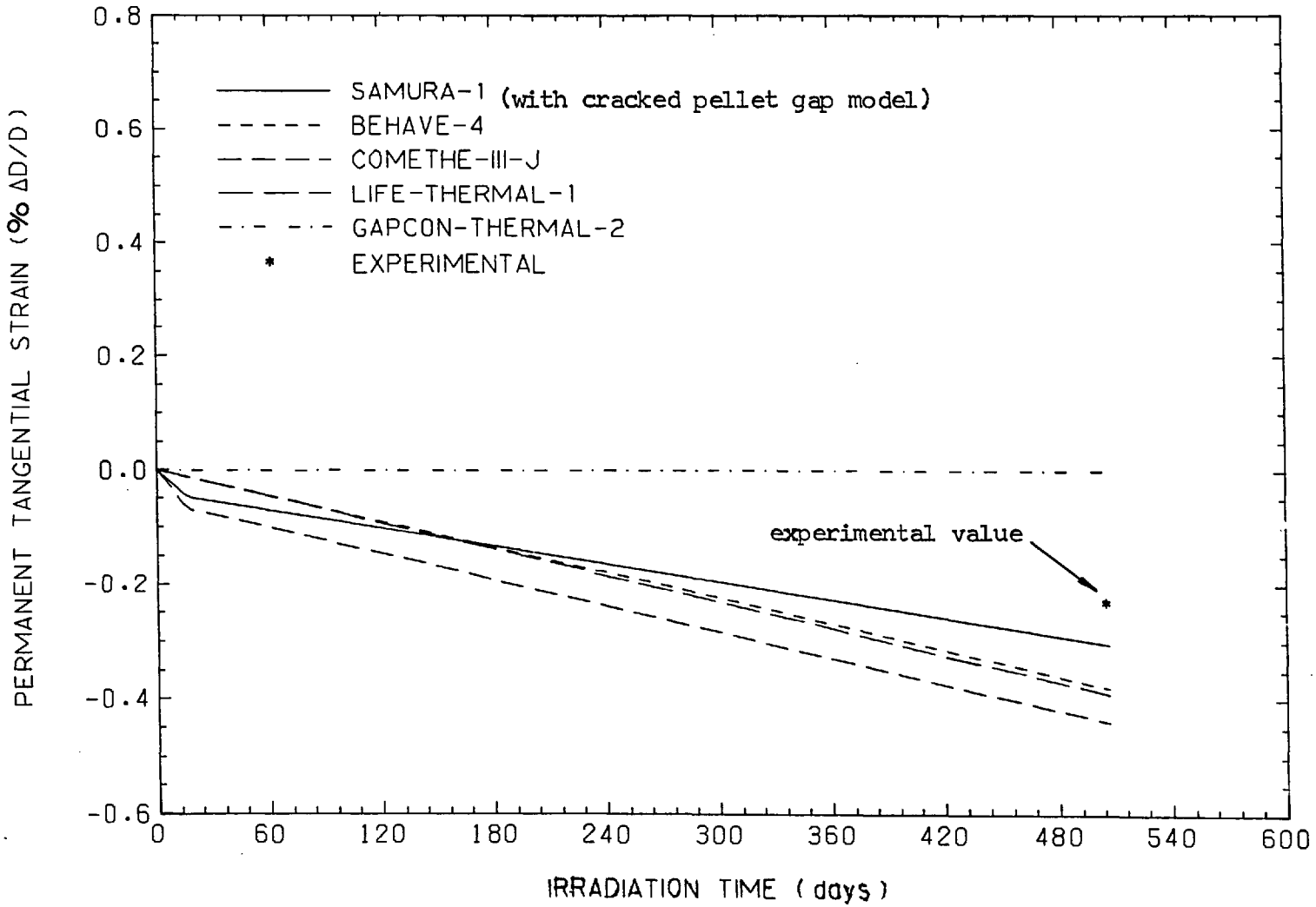


Figure 4.77

EVALUATION OF MAINE YANKEE PWR CORE 1 RODS

FUEL CENTRELINE TEMPERATURE VS. IRRADIATION TIME AT 36 INCHES

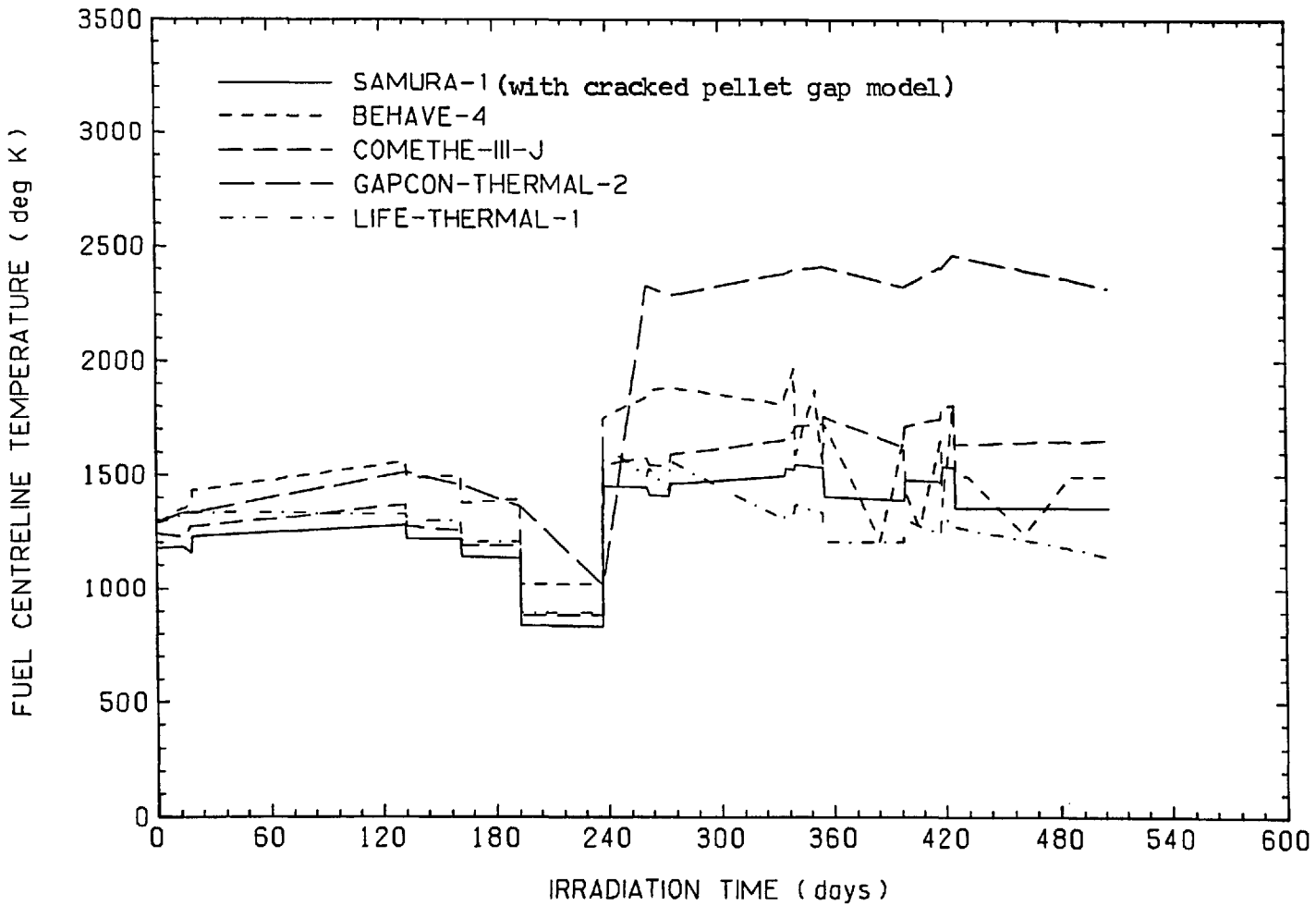


Figure 4.78

EVALUATION OF MAINE YANKEE PWR CORE 1 RODS

HOT RADIAL GAP VS. IRRADIATION TIME AT 36 INCHES

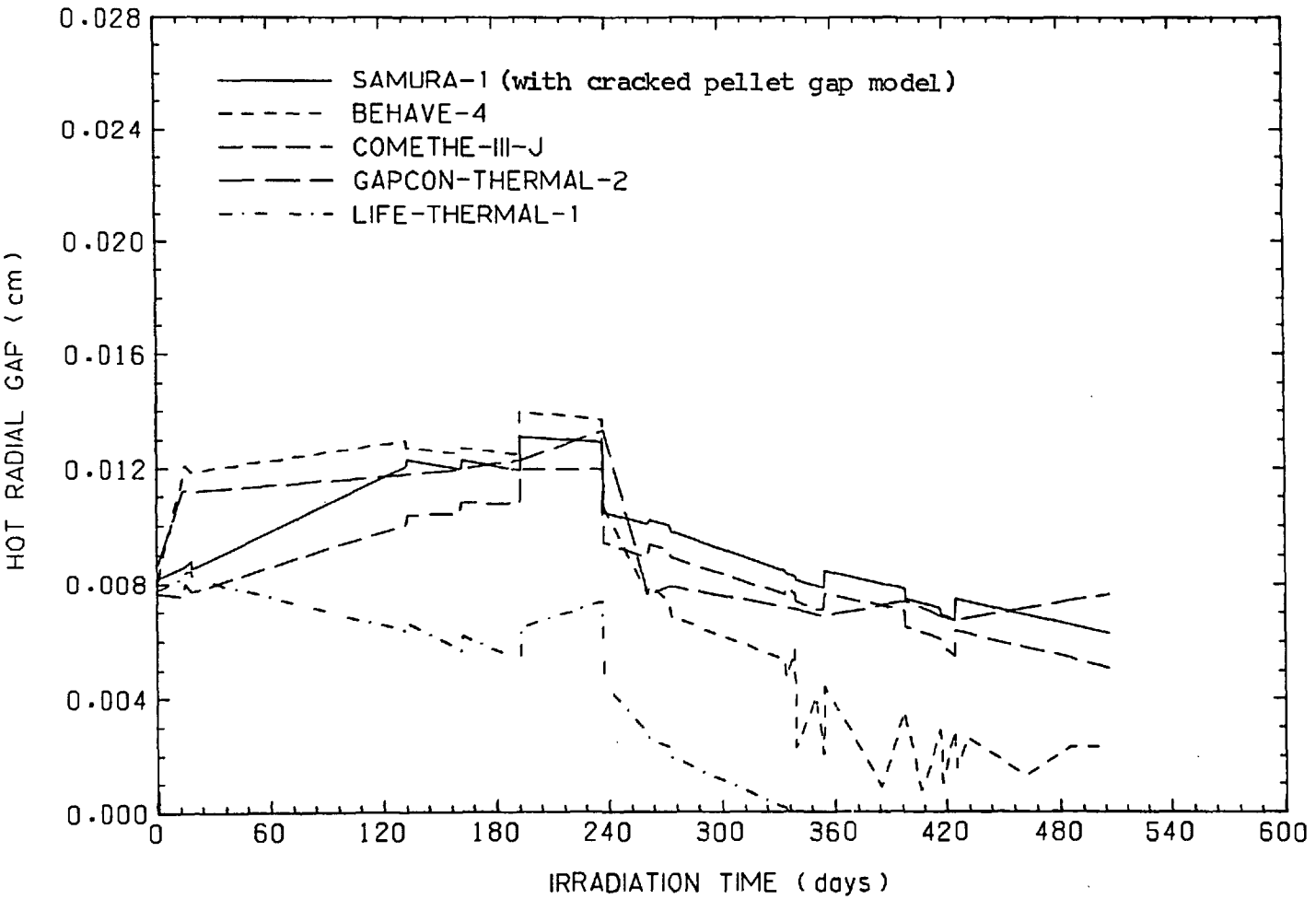


Figure 4.79
EVALUATION OF MAINE YANKEE PWR CORE 1 RODS
GAP CONDUCTANCE VS. IRRADIATION TIME AT 36 INCHES

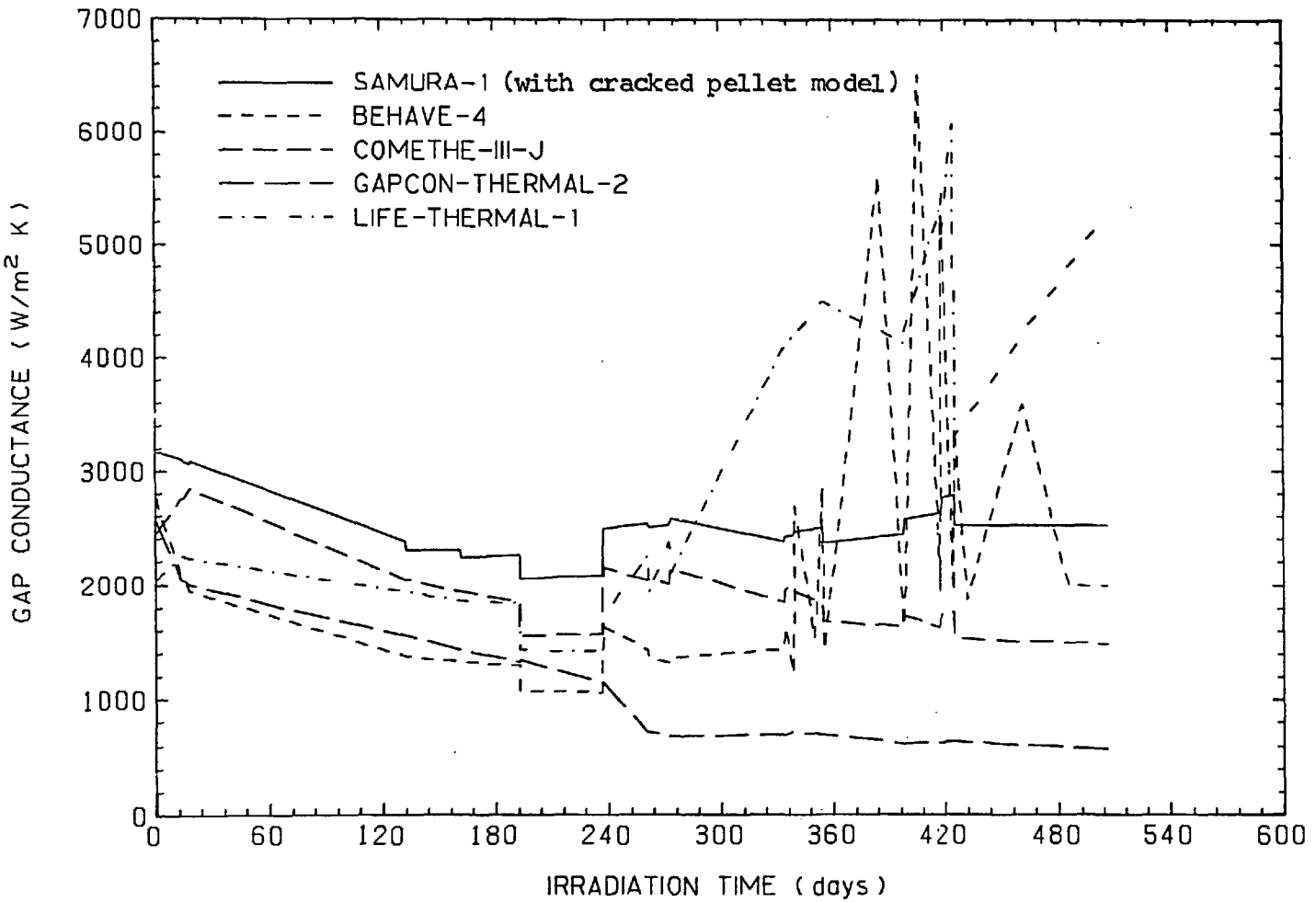
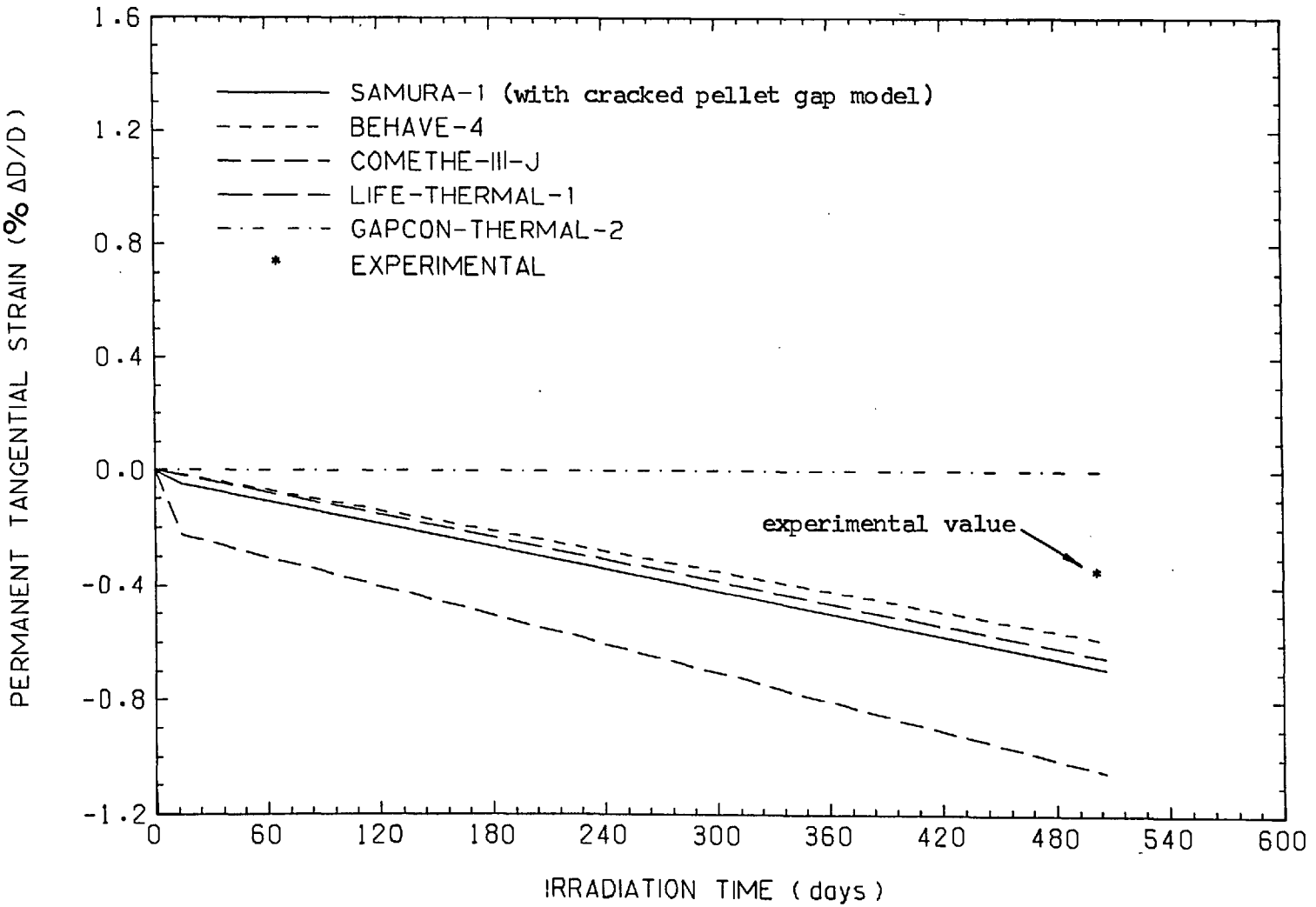


Figure 4.80

EVALUATION OF MAINE YANKEE PWR CORE 1 RODS

CLADDING PERMANENT TANGENTIAL STRAIN VS. IRRADIATION TIME AT 36 INCHES



CHAPTER 5

FINALE

CHAPTER 5

FINALE

5.1 CONCLUSIONS ON THE VALIDITY OF CODE MODELS

It has been demonstrated that, within the limits of the physical model adopted, the method described in this work and implemented in the code SAMURA is capable of giving reliable quantitative results for the parameters involved in the interactions within and between the fuel and cladding in a fuel pin operating under water reactor conditions. From the numerical point of view SAMURA is exceptionally stable and rapidly converges*, providing accurate results. The accuracy of these results, nevertheless, may be decided by the user to suit the specific needs of the problem in hand, and can be made very high with moderate demands in computing time. Less accurate results can of course be obtained with much less time consuming calculations. This confirms the soundness of the choice of the finite difference method, which approximates derivatives at a particular fuel or cladding ring by forward-differences in terms related to its inner and outer boundaries. The advantage of this numerical scheme when compared with a closed-form solution, apart from its rapid convergence with respect to other numerical methods, is the possibility of including complete empirical models of the relevant material properties or physical phnomena.

*This refers to the accuracy and stability of the numerical solution with respect to the analytical solutions presented in Secs.4.2 and 4.3. Numerical stability naturally is not an absolute property of a computer code, but it is a function of the case or the application involved.

Although the assumptions of one-dimensionality and plane strain facilitate the mechanical analysis, in certain cases its use may become limited and especially modelling of some axial effects become impossible. It has, however, been shown that in spite of its limitations, SAMURA's assumptions are well justified, not only because of the large thermal gradients that operate radially, but because of soaring computer requirements of a quasi-two-dimensional model. An axial version of SAMURA would, nevertheless, be very useful, particularly if a more appropriate treatment of fission gas release is required. Fission gas release and swelling is presently dealt with in an almost totally empirical way. It has been shown that SAMURA prediction of swelling and fission gas release is not very accurate. The fuel swelling model apparently overemphasises swelling in the columnar region when the peak swelling rates have already moved to the equiaxed region. This should certainly affect the cracking pattern, the gap closure rate (and times) and probably other variables such as the fuel/cladding contact pressure. In this context, one must also include fuel densification, the proper treatment of which would greatly improve the values of hot radial gap predictions.

As far as the temperature calculations are concerned, the numerical method developed for use in SAMURA has proved to be very accurate and fast indeed. It is capable of handling both transient and equilibrium temperature calculations. The combined thermal analysis routines in SAMURA, however, show great sensitivity to the value of gap conductance. The gap conductance model adopted here is

a semi-empirical model in the sense that it is based on somewhat limited measured full centreline temperature data, mostly derived from Halden BWR and some experimental fuel capsules. Though it does generally predict fuel temperatures accurately, it has a tendency to largely underpredict fuel temperatures in some particular cases. This is atributed to the fact that the cracked pellet model is very sensitive to the values of hot pellet radius and gap gas thermal conductivity (see Eq. (3.38)). It actually relies on the assumption that the increased pellet cracking and relocation/gap closure with burn-up compensate for the deterioration of gap gas thermal conductivity. This demands an accurate gas release prediction in the first place. It is also implied that the cracked pellet model will generally predict much more accurate temperatures in high-rated fuel pins; probably with high gas release rates too (see Appendix E).

A further cause of temperature underpredictions could be initiated by the pore migration model used in SAMURA. Though, as discussed in Chapter 3 a recent porosity migration expression was adopted, it is thought that pore velocities are overpredicted and therefore the central void grows larger than expected. This results in the fuel centreline temperature being too low. Presently this has been remedied by not allowing the central void to form unless a centreline temperature of 1973^{o}K is reached, and then only during shut-down where the central fuel region stresses have completely relaxed.

It may finally be concluded that, apart from the gap conductance model which needs further validation, SAMURA

is capable of resolving most fuel pin problems. Although its benchmarking has so far been limited, SAMURA provides very reasonable predictions and has the potential to stand among the high-ranked codes discussed in this work.

5.2 MODELLING OF FUEL PIN UNDER NORMAL CONDITIONS

A typical application of the code has been presented in Section 4.4. Details of the calculations show that SAMURA is capable of resolving fine structure in the quantities involved. The particular examples of the variation in gap width and the time of gap closure provide confidence that, if required, such quantities may be investigated with accuracy*. This simple example has also reflected the effectiveness of cracking, together with thermal creep, in relaxing the fuel stresses initially produced by the thermal gradient. It has been shown that the transient value of stress in the whole pellet determines the resulting crack structure. The penetration of cracks is, thus, restricted by the value of the stress at the tip of cracks. When the point, to which the cracks have penetrated, has singificant creep the stress becomes compressive and the cracks cease to penetrate. It must not, however, be forgotten that the cracks are not related with the current internal stresses in the system. This means that the results of the uncracked pellet may not be extrapolated to give the behaviour of the cracked pellet.

*Provided the input physical models are reasonably reliable.

The modelling of this fuel pin under the simulated power cycle has also emphasised the importance of tangential stresses and strains in the cladding. As discussed before, from the cladding failure point of view, it is desirable to have a clear indication as to how the cladding stress varies with time for a wide range of power ramp conditions. It has clearly been shown that overall behaviour of the fuel pin depends on the mechanical interaction of the fuel and cladding with each other after contact, i.e. the value of contact pressure and its variation with time. SAMURA assumes isotorpic mechanical behaviour for the cladding, but according to some recent works this may cause an over-prediction of the cladding stress levels. So eventually it will be necessary to incorporate anisotropy into SAMURA. This should include the thermal expansion, the elastic distortion, the creep and plasticity laws and also an irradiation growth law for the cladding (see Appendix C for details).

As far as the pellet/cladding interaction is concerned, it is essential to develop a failure criterion for the cladding, so that an indication of whether failure is likely to occur during a power-ramping similar to the one modelled here can be obtained.

5.3 EVALUATION OF SAMURA AGAINST EXPERIMENTAL FUEL PIN DATA

Experimental data on fuel centreline temperatures were available and these experiments were modelled to validate the gap conductance model used in SAMURA (Section 4.2). Overall the results obtained were very satisfactory indeed.

It was shown that the classical Ross and Stoute model (F = 0.0 in Eq.(3.37)) generally overpredicted the fuel centreline temperatures by large amounts, especially where the pins had high burn-ups and had undergone a relatively high-powered cycle. On the other hand the cracked pellet model (F as calculated from Eq.(3.38)) predicted results which were in much better agreement with the experimental data. The latter model, however, tended to underpredict temperatures in certain cases as discussed before.

It is believed that the cracked pellet model in spite of the above weakness, has very good potentials for further use in SAMURA provided some improvements were made in the values of the parameters implemented in it. For instance, if the minimum value of F which is equal to 0.30 (and is based on somewhat limited experimental data) were to be reduced to 0.25 or even 0.20, the calculated gap conductance value would greatly improve (this will obviously effect the empirical Equation (3.38)).

SAMURA was further evaluated with respect to the EPRI fuel modelling code evaluation studies (Section 4.5 and Appendix E). The main objective was to shed light on some SAMURA attributes and weaknesses relative to the codes studied by EPRI. This does not, however, mean that objective ranking of SAMURA could be performed with only few case studies as against twelve cases that have been modelled by the other codes through only the Phase III EPRI programme.

In evaluating the overall fuel temperature predictability of the codes, EPRI have divided the individual case

runs into two categories. The first category contains pins with least influence of gap size and/or fission gas release on fuel temperature calculations. These pins could have small as-manufactured gap and low EOL gas release; or contain low-conductivity fill gas such as argon; or be pre-pressurised helium-filled with expected low EOL gas release. The second category contains pins with a strong inter-dependence of gap conductance, fission gas release and fuel temperature. These pins have generally large hot gaps and are helium filled. Obviously the interdependence of gap conductance, fission gas release and fuel temperature is extremely difficult to model accurately. The Maine Yankee PWR pin which has been modelled is, according to EPRI studies, among the second category of pins. In this pin, a strong divergence effect is present between low and high gas-release, and fuel-temperature conditions. Small changes in design or operating parameters can set off the divergence. This effect can be elaborated by use of code sensitivity studies.

For the Maine Yankee PWR pin, BEHAVE-4 has provided good agreement on gas release and fuel temperature with use of the EPRI Phase III gas release model. COMETHE-IIIJ and LIFE-THERMAL-1 (both with use of the EPRI Phase III Zircaloy creep model) have significantly underpredicted both gas release and temperature. COMETHE-IIIJ, re-run with Zircaloy creep reduced by about 60 percent, and GAPCON-THERMAL-2 have significantly overpredicted the gas release and the fuel temperature. As for SAMURA, it has largely under-predicted both gas release and temperature with use of the

EPRI Phase III parameterisation (but using its own UO_2 swelling rate) and the cracked pellet model gap conductance (run (B)). The underprediction can be improved by replacing the EPRI Phase III gas release model with SAMURA option 2 gas release model (run (A)); but not very significantly. Use of the Ross and Stoute gap conductance has, however, significantly changed the SAMURA results, i.e. ∿ 50% overprediction of the gas release (as opposed to 50% and 90% underprediction in (A) and (B)), and 16% overprediction of the temperatures. Although the Ross and Stoute gap conductance has fortuitously provided one of the good results in this particular case (due to a combination of several factors as discussed before), it has been judged not to be suitable for permanent use in SAMURA due to its disregard for burn-up and pellet cracking effects. It is interesting to note that at the time of EPRI code evaluation all of the other codes also used a somewhat modified Ross and Stoute gap conductance model*.

Additional comments, as regards the temperature calculation, may be made on the modelling of gas release in SAMURA. The fission gas release models contained within SAMURA (2 options) are very simplistic and are basically temperature dependent. No such effects as initial grain size, open porosity, bubble migration, and the growth of equiaxed and columnar fuel grains are considered. The diversity of results obtained for this particular case has emphasised the need for a more reliable gas release model.

---

*Comparisons on this basis, however, cannot be made since the codes did not use similar parameterisation in their gap conductance model and some took account of relocation by other means.

This cannot be achieved unless the assumption of single axial node in SAMURA is altered. An axial version of SAMURA, naturally with much greater computer requirements, will then provide an accurate integration of axial effects on the total gas release and fuel temperature.

Gap closure predictions (or EOL cold radial gaps) have also been compared with the experimental data. Due to inherently large measurement uncertainties, gap closure comparisons are considered of secondary importance relative to the fuel temperature and gas release comparisons. For the Maine Yankee PWR, overall agreement of cold gap closure at low and high power regions has not been obtained with any code. GAPCON-THERMAL-2 has provided little gap closure at any axial location. LIFE-THERMAL-1 has significantly overpredicted the gap closure at all axial locations. COMETHE-IIIJ has significantly underpredicted the gap closure at all axial locations. BEHAVE-4 has provided a good prediction of gap closure at the high power location, but greatly underpredicted gap closure at the low power location. Runs (A) and (B) of SAMURA have underpredicted gap closure to a large extent. Run (C) has, however, provided a very close agreement at the high power location, but somewhat underpredicted the gap closure at the low power locations. As pointed out before, it is believed that SAMURA's generally large gap predictions in this case are due to its large temperature underprediction and probably due to its unsuitable swelling and densification models too.

Another phenomenon which has been used for code evaluation purposes is cladding creep. In the PWR pin studied, significant cladding creep-down occurred at low and high regions of power without evidence of significant fuel/cladding contact. For this pin, the primary creep component in the EPRI Phase III Zircaloy creep equation has tended to overpredict the measured creep when used in the COMETHE-IIIJ, LIFE-THERMAL-1 and SAMURA codes. BEHAVE-4 cladding creep-down predictions have been in reasonable agreement with experimental strains. The important conclusion that can be drawn here is that, of the three codes which have used the EPRI Phase III Zircaloy creep, SAMURA has provided the best results (least overprediction). This is true even when it has actually overpredicted the temperatures (run (C)).

It may finally be concluded that within the limitations associated with a one-dimensional code such as SAMURA, its overall predictions have bracketted the experimental fuel data modelled in this study in a reasonable manner*. SAMURA should, nevertheless, be further validated against the rest of the cases studied by EPRI, probably with improved swelling and densification models; and perhaps using a modified gap conductance model if required.

5.4 RECOMMENDATIONS FOR FURTHER WORK

It is not presently felt that the first step towards an improvement of SAMURA should be its conversion into a quasi-two-dimensional code. The calculations performed so far, using its present version, have clearly demonstrated its

*See also Appendix E.

versatility for application to both thermal and structural analyses of Zircaloy-clad UO_2 fuel pins. Furthermore, it has been shown to provide considerable savings in computer storage and running times relative to quasi-two-dimensional codes*. It is, therefore, recommended that the one-dimensional version of SAMURA be used on its own merits, but with some improved material behavioural models as required by the nature of the particular problem at hand.

As far as the EPRI evaluation studies are concerned, they remain the only well compiled and comprehensive study ever made on the subject. So it will be very beneficial to continue the modelling of the rest of the cases studied by EPRI. Since SAMURA's fission gas release model has been judged to be inadequate, as regards the evaluation studies, one may use the measured gas release data as input (or use the best gas release prediction provided by the rest of the codes) in SAMURA, to make sure that the right amount of fill gas dilution is provided for the gap conductance model. In this way, it should be possible to evaluate the code predicatability of thermal and structural performance variables in a more objective manner. (It is important to note that the magnitude of the quantities of interest and the times at which they occur are governed largely by fuel/cladding gap conductance, the thermal conductivity assumed for the gap

*This does not, however, mean that an axial version (1½-D or quasi-2D, as it is known alternatively) of SAMURA should be abandoned. In fact, as a recent review by Lassmann (8) has also suggested, the influence of axial effects, especially of friction forces, on the mechanics of the fuel pin must not be neglected. This is really meaningful when a quasi-2D calculation is performed.

gas, and its width. Slight variations in these parameters can cause relatively large changes in rate of gap closure and fuel temperature. Thus, if with the correct amount of fission gas release as input one does not get the other quantities right, one may concentrate on improving other code weaknesses.)

As far as the material properties are concerned, it is felt that the set of data compiled for Zircaloy-clad UO_2 fuel pins by EPRI (Appendix D) and currently incorporated into SAMURA, provide very reasonable results. The Zircaloy cladding creep model may, however, be changed if more accurage creep models become available. The UO_2 swelling model should also be replaced with a more accurate model linked with gas release. Since there is no appropriate treatment of fuel densification in SAMURA, it is thought that some work in this area would greatly improve the code predictions (especially for PWR pin analysis).

No serious transient studies have so far been performed with SAMURA. Since it is basically designed to be a transient code, some modelling of transient over-powers or loss-of-coolant accident may be tried and the code potentials in this context evaluated. Naturally, some modifications, particularly to cladding models, must be made if such transients are envisaged. This is because most of the available property models are only valid for normal reactor operation. Some provisions have been made in SAMURA, as far as possible, to include fuel and cladding material properties for higher temperatures; and up to the melting point.

Finally, as far as the code's basic assumptions are concerned, one main modification is highly recommended and that is the inclusion of anisotropic mechanical analysis of the cladding. This has recently been proved to be very important if one is hoping to have a realistic prediction of the cladding failure (175). The modifications needed to include anisotropy will only affect some of the subroutines in the code and should not cause great difficulty (see Appendices B and C).

APPENDIX A

APPENDIX A

A.1 SAMURA INPUT ORGANISATION

In order to set up a suitable input data deck for the present version of SAMURA the following parameters must be known:

1. Fuel Pin Geometry:

   Pellet inner radius, RIN(1), (m)

   Pellet outer radius, ROUT(1), (m)

   Cladding inner radius, RIN(2), (m)

   Cladding outer radius, ROUT(2), (m)

   Fuel stack length, FLEN, (m)

   Cladding length, CLEN, (m)

   Plenum initial volume, PLVL, (m^3)

   Fuel/clad initial radial gap, GAP (m)

   Fuel stack total dishing volume, DISHVL, (m^3)

2. Physical Properties:

   Pellet porosity, POROSF, (% TD)

   Fuel fracture stress (this is used when a value different than the one calculated internally is required), SF, (MPa)

   Fuel pellet grain size, FGS, (μm)

   Fuel enrichment, PC235, (%)

   Type of Zircaloy texture, i.e. cold-worked or annealed; specified through parameter ICWZR; if ICWZR = 1 cold-worked Zr
   if ICWZR = 0 annealed Zr

   Fuel cladding arithmetic mean roughness, RRG,(m)

   Fuel cladding root mean square roughness, RMS,(m)

3. General Initial or Boundary Conditions:

Inventory of filling-gas, this includes He, Ar, N_2, H_2, steam, Kr and Xe; represented by the following parameters: HEPCNT, ARPCNT, N2PCNT, H2PCNT, STEAM, KRPCNT, XEPCNT, all given in volume percentages; (%)

Initial filling-gas pressure, PLPR, (MPa)

Hot plenum temperature, PLTEMP, (^{o}K)

Fuel pellet stack spring force, SPF, (N)

Coolant saturation temperature at specified pressure, TSATW, (^{o}K)

Coolant average pressure, AWP, (MPa)

Coolant inlet temperature, TWIN, (^{o}K)

Coolant outlet temperature, TWOUT, (^{o}K)

Coolant flow rate, CFLOW, (kg/s)

Coolant average film heat transfer coefficient, HCFILM, (W/m^{2o}K)

Initial fuel linear heat rating, QLINIT, (W/cm)

Initial overall temperature (equal to the initial outer cladding surface temperature or coolant bulk temperature), TFW, (^{o}K). (TFW later used to indicate current boundary temperature, see Section A.2 .

4. Fuel Pin Power History:

In order to simulate the given fuel power history, a plot of linear heat rating versus time must be drawn (see Figure A.1). This is then divided into a number of "periods". The variation of power in each of these sub-divisions or periods must be linear, i.e. up-ramp, down-ramp or steady-state. For example the power history given in Figure A.1

can be divided into 13 periods as follows:

1. Up-ramp; 2. steady-state; 3. down-ramp;
4. up-ramp; 5. steady-state; 6. down-ramp;
7. up-ramp; 8. steady-state; 9. steady-state;
10. down-ramp; 11. up-ramp; 12. steady-state;
13. down-ramp.

At the same time the variation of cladding outer surface temperature (or the coolant temperature) versus time, and the variation of coolant pressure with time. For the same duration of power his story must be known and divided into the same number of periods as above (see Figures A.2 and A.3). In this example the cladding temperature variation with time is divided into 13 sub-divisions, so its value at the end of each period can be deduced. The coolant pressure, on the other hand, has constant value for all the periods of this example.

Each period has a time length, PT(I), a linear heat rating (the value at the end of period is taken) QLP(I), and a temperature boundary condition (again at the end of period), i.e. cladding outer surface or coolant temperature TWAT(I). Furthermore, if radial neutron flux (its value at the fuel surface) and axial power shape factors are known, their values can be stored in PHIR(I) and AXFAC(I) (ACFAC stores the axially averaged shape factors for each period or any specific shape factor as required, i.e. if it is desired to perform a calculation at a location of fuel pin where the axial shape factor is 0.40 at all times, then in the example of Figure A.1, AXFAC(1) = 0.40, AXFAC(2) = 0.40, ... AXFAC(13) = 0.40). The maximum number of periods presently

Figure A.1
DIVISION OF A POWER HISTORY INTO PERIODS

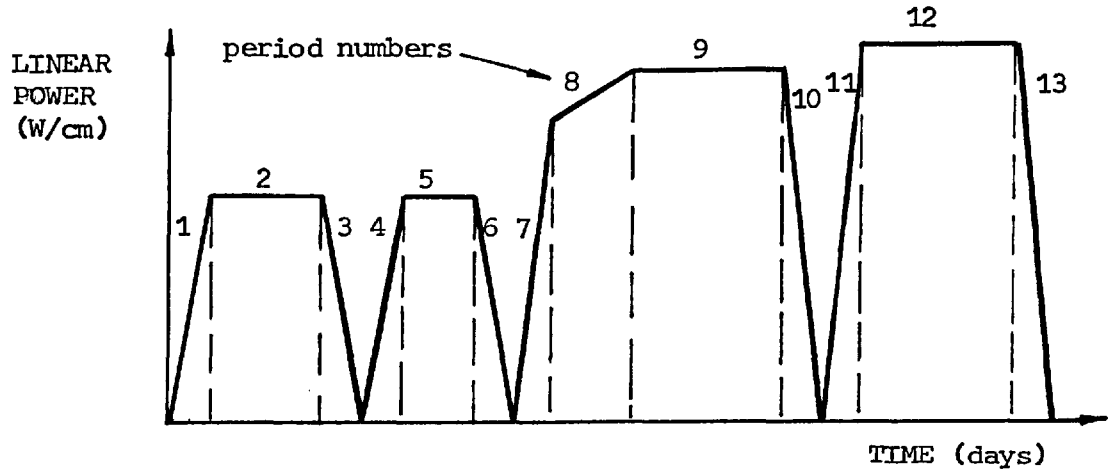


Figure A.2
OUTER SURFACE TEMPERATURE

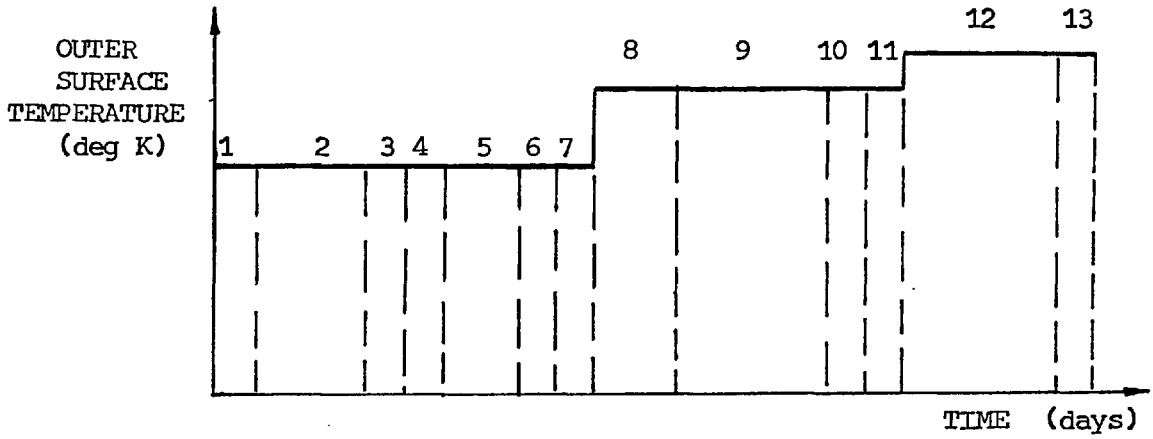
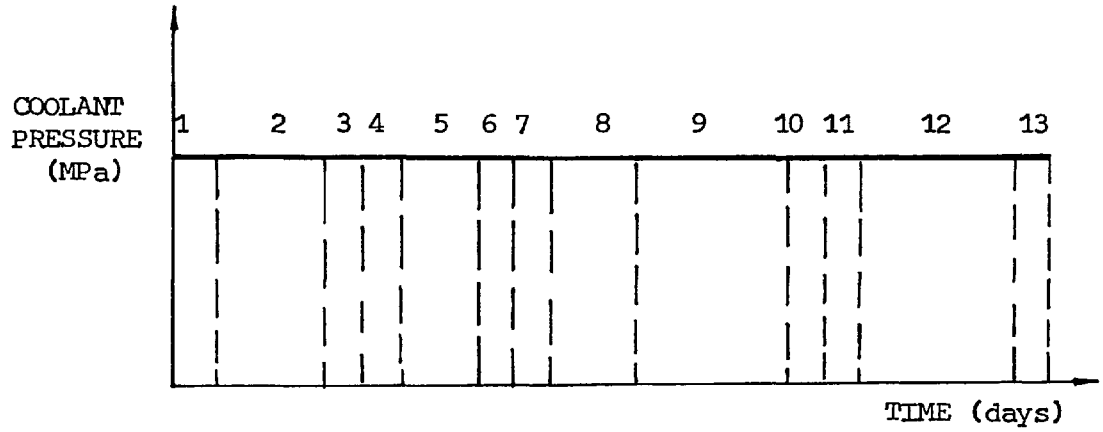


Figure A.3
COOLANT PRESSURE



is 50, i.e. the argument I in PT(I), QLP(I) etc. varies from 1 to 50.

In order to define the type of periods, several "key-words" are used as follows:

URPERIOD for up-ramp periods;

SSPERIOD for steady-state periods;

DRPERIOD for down-ramp periods;

USPERIOD for transient periods, where there is a very fast change in power;

BOPERIOD for burn-out (film-boiling) periods, if such a case is studied (not used currently).

A number of other keywords are also used to identify the particular type of input data and to store them in the right place. These are all used in the subroutine called PROBLM, which reads all the input data, classifies them and prints them out for reference at the beginning of each output print list. Each of these keywords is punched in the first eight columns of a data card which represents the first card in a particular set of data, e.g. periods data etc. Column 10 of the same card is used to punch an integer number, stored as JUST, (also a keyword but = 0-9) and columns 11 to 80 are used to punch up to five real values (with a FORMAT of F14.6) stored as floating-point variables in CONSTS(I), J = 1,5. The input keywords are stored in KEYWRD. A READ statement reads the values of KEYWRD, JUST and CONSTS(I) from each data card and then compares the value stored in KEYWRD with a variable called

GUIDE(K) which contains all the available keywords (20 altogether, i.e. K = 1,20). Then, every time KEYWRD equals one of the keywords the control is sent to a certain part of the subroutine PROBLM and an appropriate action is taken, e.g. some data are read in and stored. Current keywords apart from those given for period identification are:

SECONDS: used to specify time scale in seconds;

DAYS: used to specify time scale in days;

DIVISION: means next card(s) will constain the number divisions in fuel and cladding;

PROPERTY: means next card(s) will contain some fuel or cladding properties (not used currently);

PARAMETR: means next card(s) will contain a list of variables which are desired to be printed out after calculations are performed (optional);

TITLE: print the title of the program and other relevant information about the program (optional);

FUELDATA: store the data given as fuel data;

CLADDATA: store the data given as clad data;

BONDGAS: data read contains information relevant to the fill-gas composition;

FUELCRCK: fuel cracking option, if desired an input fracture stress can be specified;

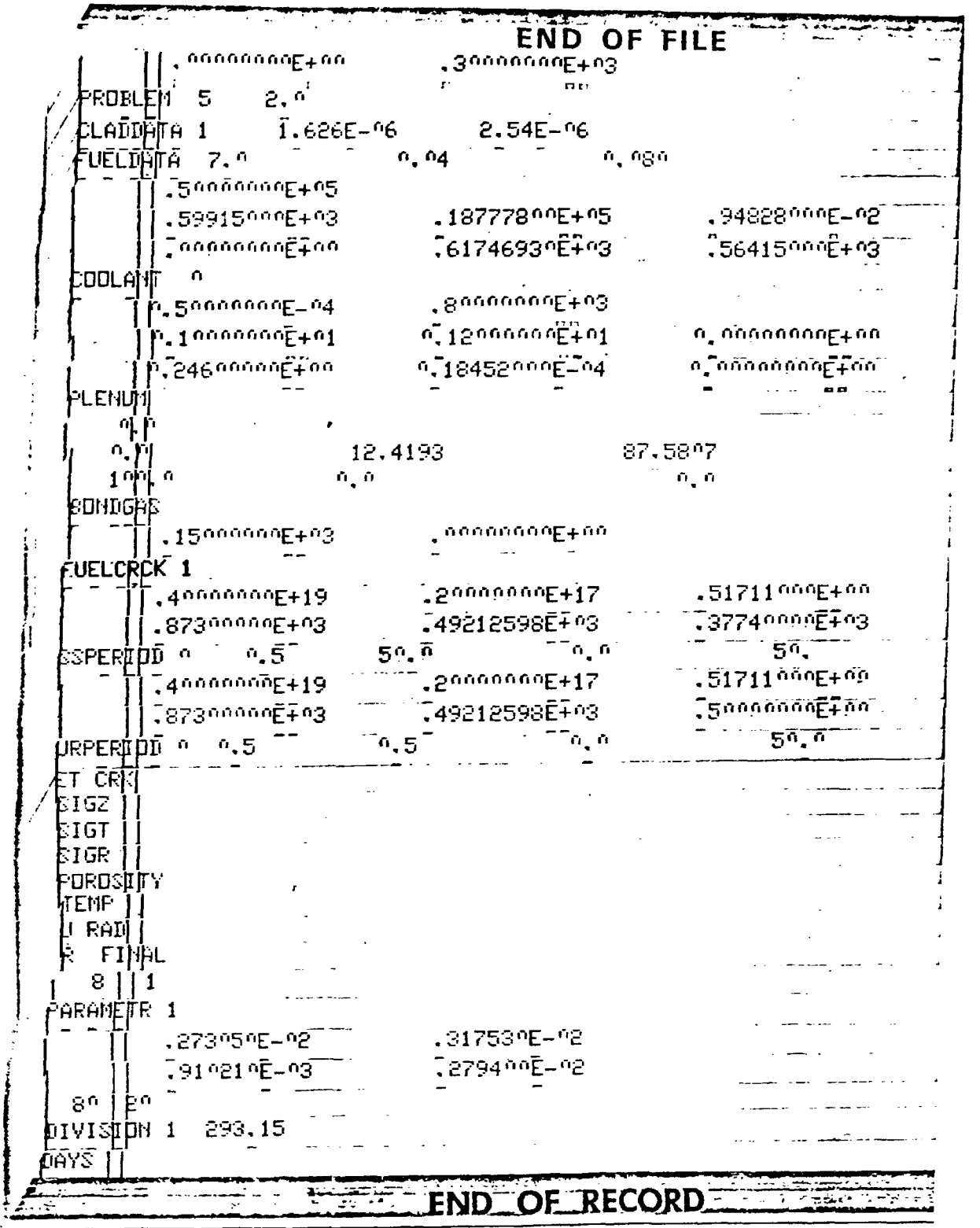
PLENUM: next card(s) will contain plenum data;

COOLANT: next card(s) will contain coolant data;

PROBLEM: definition of problem; giving the initial values.

Figure A.4

ARRANGEMENT OF A TYPICAL INPUT CRAD DECK



A set of typical data is given in Figure A.4 for reference purposes and to show how the values ought to be punched on data cards. More user's information may be found in the list of SAMURA parameters and arrays presented in the next sub-section.

A.2 DEFINITION OF MAJOR ARRAYS AND PARAMETRS IN SAMURA

A list of major variables as used in different sub-routines of SAMURA and transferred through the program by a single unlabeled COMMON statement, is provided here to help program users.

LIST OF SAMURA VARIABLES

A(3,7,200)*	General coefficients of matrix used in the mechanical analysis (see Eqs.(3.144) and (3.243)). These coefficients are defined and calculated in subroutine SASAN.
AA(18,200)	Coefficients defined by Eqs.(3.131) as calculated in SASAN.
AAS(5)	Auxiliary variable to store some of the AA(1,200) coefficients to be used later in SASAN.
ALFA(200)	Coefficients of heat conduction equation matrix as defined in Eq.(3.12), used in HEATRN.
ALOW(200)	Same as above, A(i) in Eq.(3.28).
ALOWN(200)	Same as above, A(i) in Eq.(3.28).
ALOWP(200)	Same as above, A'(i) in Eq.(3.28).
ALT(200)	The value of $(\alpha T)_i$ at any node i; calculated by subroutine THERMX.
AN(200)	Coefficient of heat conduction equation matrix as defined by B(i) array in Eq.(3.28) and used in HEATRN.

*The argument indicates the maximum DIMENSION allocated to the variable in FORTRAN programming of SAMURA.

AP(200)	Coefficient in heat conduction matrix equation defined by B'(i) in Eq.(3.28), used in HEATRN.
ARPCNT	Volume percentage of Argon in fill-gas.
AUP(200)	Coefficient in heat conduction matrix equation defined by C(i) in Eq.(3.28), used in HEATRN.
AUPP(200)	As above, but for C'(i) in Eq.(3.28).
AWP	Average coolant pressure (MPa).
AXFAC(50)	Axially averaged or local value of axial power sharp factor for period 1 to 50.
B(3,200)	Coefficients of axial strain, ZZ(1), ZZ(2) components in the matrix Eq. (3.243).
BETA(200)	Coefficient in heat conduction matrix equation defined by Eq.(3.12), used in HEATRN.
BREF(12)	Variable which stores some of the parameters to be printed out as "brief outputs".
BU	Accumulative fuel burn-up for the current time-step (MWd/teU).
BUOLD	Same as above but for the previous time-step (MWd/teU).
C(3,200)	Constants on the right hand side of matrix Eq.(3.243), defined in SASAN.
CED	Coolant channel equivalent diameter (m).
CFLOW	Coolant flow rate (kg/s).
CLEN	Cladding initial length (m).
CON(200)	Nodal point thermal conductivity as calculated in HEATRN.
D(10)	Coefficient of axial strain component in axial equilibrium equation. See Eqs. (3.136) and (3.244).
DELT	Current time-step (days or seconds).
DELTL	Last time-step.

DENSI(10)	Theoretical density of any region (kg/m^3).
DISHVL	Fuel stack total dish volume (m^3).
DTMAX(50)	Maximum permissible length of time-step for periods 1 to 50.
DTMAXP	Same as above for the current step.
DTPR(50)	Length of the first time-step of each period.
E(10)	Right hand side constants of the axial equilibrium equation, calculated in SASAN (see D(10)).
ECR	Error criterion for the current step.
ERR(50)	Error criterion for periods 1 to 50.
ERRORL	Calculated error (%) for the last time-step.
ER(200)	Total radial elastic strain.
ET(200)	Total tangential elastic strain.
ETA(1,200)	Total tangential cracking strain.
ETA(2,200)	Total radial cracking strain.
ETA(3,200)	Total axial cracking strain
ETHA	Parameter used in SASAN and is equal to 1-THETA.
EZ(200)	Total axial elastic strain.
F(1,200)	Coefficients of radial displacement component in the axial equilibrium equation (see Eq.3.137).
F(2,200)	Same as above but for γ_r.
F(3,200)	Same as above but for γ_θ.
FAXL(10)	Total axial force in regions 1 to 10.
FDEP(200)	See FLUX(200).
FGS	Fuel pellet grain size (μm).
FLUX(200)	Radial flux shape factors calculated in FLXDEP. Equivalent to FDEP(200).

FISSPR	Total internal pin gas pressure (MPa).
G(3)	G(1), G(2) and G(3) are the values of GAR(I), GAT(I), GAZ(I), I = 1,200, as calculated from the Taylor series approximation of creep equations, i.e. $G(p) = Q(p,I) + P(p,1,I).\sigma_r(I) + P(p,2,I).\sigma_\theta^r(I) + P(p,3,I).\sigma_z^\theta(I)$ where p = 1,2,3 and I = 1,200.
GAP	Current value of fuel/cladding radial gap (m).
GAPCON	Current value of fuel/cladding gap conductance calculated in HGAP.
GAR(200)	Current value of total radial non-elastic strain as defined in Eq.(3.116).
GARL(200)	As above but for the previous step.
GASPR(6)	Partial pressures of fill gas components in the pin. The argument indicates He, Ar, Kr, Xe, H_2, N_2 respectively.
GAT(200)	Current value of total tangential non-elastic strain as defined in Eq.(3.117).
GATL(200)	As above but for the previous step.
GAZ(200)	Current value of total axial non-elastic strain as defined in Eq.(3.118).
GAZL(200)	As above but for the previous step.
GGG(200)	The sum of GARL(I) + GATL(I) + GAZL(I) I = 1,200; used to simplify Eq.(3.124).
GPWD	Initial value of fuel-cladding radial gap (m).
H(200)	Coefficients of heat conduction matrix equation equivalent to B(i) coefficients of Eq.(3.28).
H2PCNT	Volume percentage of H_2 in fill-gas.
HCFILM	Input coolant film heat transfer coefficient ($W/m^2\ ^oK$).
HEPCNT	Volume percentage of He in fill-gas.

IAXL	A control parameter used if more than one axial section is chosen.
ICWZR	Parameter that specifies the type of Zircaloy texture; i.e. if ICWZR = 1, cold-worked, if ICWZR = 0 annealed material. Currently used only in Zr yield model (subroutine SIGMAY).
ICOOL	Parameter that specifies the type of outer boundary temperature to be used. If ICOOL = 1, then input TWAT(50)'s are coolant temperatures; if ICOOL = 0 then input TWAT(50)'s are outer cladding surface temperatures.
IDS(50)	Parameter that specifies the units to be used for time i.e. seconds or days. If IDS(K) = 1, K = 1,50 (max. no. of periods), then "seconds" is used. If IDS(K) = 2, K = 1,50, "days" is used.
IPD	Indicates period number that is considered currently.
ISOLID	Paramter that specifies the type of pellets. If ISDL1D = 1, pellets are "solid". If ISOLID = 0, pellets are "hollow".
ITAPE	Control parameter used to specify the option of writing output onto several TAPES if required; if ITAPE = 1 output on specified TAPES. With ITAPE = 0 no output on TAPES.
IWDGAP(10)	Control parameter used to indicate the conditions of the radial gap between regions. If IWDGAP(J) = 1, J = 1,10, gap is open; if IWDGAP(J) = 2, J = 1,10, gap is closed.
IY	Control parameter that specifies the Zircaloy creep model option to be used. If IY = 0, use the EPRI Phase III Zr creep model; if IY = 1, use A.D.HOWl Zr creep model; and if IY = 2, use J. Gittus et al Zr creep model (see SAMURA listing for details).
JOP(50)	Parameter that specifies the number of steps after which an output should occur. This is input for each period and can vary from 1 to any integer number.

KRAK	Parameter that specifies the fuel fracture stress option to be used. If KRAK = 1, SAMURA's internal data is used. If KRAK = 0, users input value is used. KRAK can be used to model the case of uncracked fuel by putting KRAK = 0 and specifying a very large value (10^{20}) as input for fracture stress.
KRPCNT	Volume percentage of Kr in fill-gas.
LR(200)	Parameter that is used to identify different nodes by setting it equal to certain integers, i.e. general nodes have an LR(I), I = 1,200, of zero; but strategically important nodes like the first and second nodes, surface node, gap node etc. have other integers assigned to their LR(I) parameter.
LS(200)	As above and for the same purpose (see SASAN for details).
MC(200)	Control parameter that is used to identify the mode of cracking. If a node I in the fuel cracks then MC(I) = +1; if this node does not crack or heals then MC(I)= 0. MC(I) is also used to identify a plastically yielding node. In such a case no cracking can occur and MC(I) = -1.
MCL(200)	Old value of MC(200).
MOP(50)	Control parameter used to specify the type calculation that is being performed for each period, i.e. transient, steady-state, up-ramp, down-ramp, etc; e.g. if MP = 1 then steady-state period is considered and steady-state head conduction equation is solved. But if MP = 0 a transient calculation is performed.
MP	Value of MOP(K), K = 1,50 for the current period.
NAX	Number of axial sections in the fuel pin (currently equal to 1).
NB	Total number of nodes used in all the regions.
NBOUND(10)	Total number of nodes in each region; NBOUND(K), K = 1,10 (max. no. of regions).

NBREF	Control parameter used to specify if a "brief output" is needed for any time-step. NBREF = 1 provides such an output. NBREF = 0 suppresses brief output.
NCRKT	Total number of rings cracked in the radial direction (η_θ cracks).
NCRKZ	Total number of rings cracked in the axial direction (η_z cracks).
NEVER	An integer that is not used presently (in PROBLM). Can be used as a control parameter.
NOFISS	Integer used to specify the option of gas release model as follows: NOFISS = 1, SAMURA's option 1 gas release model; NOFISS = 2, SAMURA's option 2 gas release; NOFISS = 3, the EPRI Phase III gas release model; NOFISS = 4, input internal gas pressure values are used and no fission gas release calculation is performed; and NOFISS = 5, user's own fission gas release used (must be added to FISGAS).
NNODS	Total number of variables required to be printed out on the "detailed output" list, i.e. the index of the DO loop that reads the names of these variables and stores them in YPRINT(24).
NOUT(50)	Control parameter used to specify for each period the option of having the output at certain times. If NOUT(K) = 0, K = 1,50 (max.no. of periods). this parameter and its associated parameters, i.e. TPRNT(100) and NPRNT(50) are ignored. Otherwise NOUT(K) must be put equal to the number of "specified times" that an output is desired for period K; e.g. if output is required at times 0.1, 0.2 and 0.5 days for a period K, then NOUT(K) = 3.
NPRNT(50)	Parameter used in conjunction with NOUT(50) and stores the number of period that uses the option described in NOUT(50).
NREDO	Integer that counts the number of repeat calculations with a new time-step (max. = 6; see RESAN).

NREG	Total number of regions; currently equals 2.
NRI(10)	Number of "rings" required in each region for finite difference idealisation of the problem; NRI(J), J = 1,10 (max.no. of regions).
NSTEP	Accumulative value of the total number of time-steps used.
NU(10)	Current value of a region's Poisson's ratio calculated for each node according to its temperature.
NUMBR	Integer that counts the number of repeat calculations until an equilibrium state is reached (used in SASAN only). Maximum value = 25.
NWGAP(10)	Current value of IWDGAP(10) stored to be compared with its new value at the end of each calculation.
NWSTEP	Keyword used to indicate that a repeat calculation with a new time-step must be performed if NWSTEP = 1. If the calculation is accepted NWSTEP = 0.
P(3,3,200)	Coefficients used in the equation describing Taylor expansion of creep rates; see Eq.(3.121).
PC235	Fuel enrichment, (%)
PHIR(50)	Radial neutron flux at the surface of pin for each period.
PLPR	Partial pressure of initial fill-gas, (MPa); i.e. He, N_2, etc. Initially equal to the fill gas pressure and then changing with temperature.
PLVL	Fuel pin plenum volume, (m^3).
PLTEMP	Plenum hot temperature, (^oK).
POROS(200)	Nodal value of fuel porosity for the current time-step.
POROSL(200)	Previous values of POROS(200).
PP(3,200)	Variable used to store the current values of non-elastic strains and calculated in RESAN by using the new stresses and the actual creep rate equation for each node. PP(1,I) indicates node I and radial direction, PP(2,I) indicates θ direction and PP(3,I) axial direction.

PPL(3,200)	Previous values of PP(3,200).
PROML(1,10)	Solidus temperature in regions 1-10, (^{o}K).
PROML(2,10)	Liquidus temperature in regions 1-10,(^{o}K).
PROML(3,10)	Latent heat in regions 1-10, (J/kg).
PT(50)	Specified length of each period (days or seconds).
PW(50)	Coolant pressure associated with any period K (K = 1,50).
PYR(200)	Total radial plastic yield strain for the current step for node I (I = 1,200).
PYRL(200)	Previous values of PYR(200).
PYT(200)	Total tangential plastic yield strain for the current step (PYT(I),I = 1,200).
PYTL(200)	Previous values of PYT(200).
PYZ(200)	Total axial plastic yield strain for the current step (PYZ(I),I = 1,200).
PYZL(200)	Previous values of PYZ(200).
Q(3,200)	Coefficients used in the equation describing Taylor expansion of creep rates (see Eq.(3.121).
QLP(50)	Linear heat rating reached at the end of period K (K = 1,50); (W/cm).
QLPL	Linear heat rating at the end of previous period; used as the starting linear heat rating for current period.
QLINIT	Initial linear heat rating (at time zero); (W/cm).
QNEW	Current value of linear heat rating, (W/cm).
QOLD	Previous value of linear heat rating.
QQ(200)	Nodal value of total volumetric heat generation rate in the fuel; (J/m^{3}day).
R(200)	Current value of nodal point radius, (m).
RIN(10)	Innermost radius of any region J, J = 1,10, at time zero, (m).

RINIT(200)	Nodal point radius at time zero, (m).
RMS	Root mean square roughness of the fuel and cladding, (m); RMS = $(\frac{1}{2}R_f^2 + \frac{1}{2}R_c^2)^{\frac{1}{2}}$, where R_f and R_c fuel and cladding roughnesses, respectively.
ROA	The value of ρA, (pellet density x pellet cross-section area), used in convertion of W/cm to W/g, (g.u/cm).
ROCP(200)	Nodal value of ρC_p, (density x heat capacity), used in HEATRN; ($J/m^3\ ^oK$).
ROUT(10)	Outermost radius of any region J, J = 1,10 at time zero.
RRG	Arithmetic mean roughness of the fuel and cladding; RRG = $R_f + R_c$, (m). Ross and Stoute (133) have used: $RRG = 1.2(R_f + R_c)$
RT(200)	Current value of nodal point radius used only in HEATRN (for difference between RT(200) and R(200) see Figures 3.3 and 3.7 in the text).
RTIN(200)	Values of RT(200) at time zero.
SDOT(200)	Fuel swelling rate at any node I; I = 1,200, for the current time-step.
SDOTL(200)	Previous values of SDOT(200).
SHRMOD(10)	Shear modulus of any region J; J = 1,10, calculated in ELMOD for nodal points according to their temperature (i.e. similar to Nu(J), SHRMOD(J) is used to store the nodal point values at any particular time-step. Thus in fact it will take up to a maximum of 200 x 10 values for J = 1,10 (max.no. of regions); (MPa).
SIF(1,10)	Value of fracture stress in the radial direction in region 1 to 10, (MPa).
SIF(2,10)	As above but in the tangential direction.
SIF(3,10)	As above but in the axial direction.
SIFR(1,10)	Residual stress in the radial direction in a cracked region, as used in Sub-Section 3.4.4; (MPa).
SIFR(2,10)	As above but in the tangential direction.

SIFR(3,10)	As above but in the axial direction.
SIGEQ(200)	Nodal point equivalent stress, (MPa)
SIGRES	Initial value of residual stress in a cracked region. Given as input and read in PROBLM.
SIR(200)	Nodal point radial stress for the current step, (MPa).
SIRL(200)	As above but for the previous time-step.
SIT(200)	Nodal point tangential stress for the current step, (MPa).
SITL(200)	As above but for the previous step.
SIZ(200)	Nodal point axial stress for current step, (MPa).
SIZL(200)	As above but for the previous step.
SF	Input value of fuel fracture stress. Used if KRAK = 1. Otherwise internal code data is used.
SPF	Force exerted on fuel stack by the spring located on top of the pin. Included in total axial force; see Eq.(3.104), (N).
STEAM	Volume percentage of steam (or water) in fill-gas.
SW(200)	Nodal point swelling strain.
T(200)	Nodal point temperature, (^{o}K).
TBGN(200)	Nodal point temperature at the beginning of HEATRN calculations.
TBMJ(200)	Average ring temperatures used in HEATRN. See Fig. 3.3 for definition.
THETA	Parameter θ used in the approximation of creep equations $0 \leq \theta \leq 1$. See Eqs. (3.115) to (3.118).
TFW	Initial overall fuel pin temperature. Also used to represent the current value of outer boundary temperature; current value of TWAT (50).
TIME	Total time elapsed from the start of any period. Set to zero at the start of each period, (days or sec.).

TMJ(200)	Interpolated nodal point temperature as defined by Eq.(3.10).
TOLD(200)	Previous values of nodal point temperature.
TOTAL	Total accumulative time from the start of power history, (days or seconds).
TPRNT(100)	Variable used in conjunction with NOUT(50) and NPRNT(50) which stores the times at which an output is desired during any period. TPRNT(JJ), JJ = 100, is read from the input data cards, separated for each period, (days or seconds).
TREF	Initial reference temperature, used for thermal expansion calculations. If different from initial TFW, then a correction is made to densities at the start of calculation (see SAMURA) and TREF is set equal to TFW (the initial overall temperature).
TSATW	Saturation temperature of coolant at its specified pressure.
TWAT(50)	Outer boundary temperature (caldding surface or coolant) at the end of any period K (K = 1,50).
TWATL	Value of TWAT(K), K = 1,50 for the last period used as the starting boundary temperature for the new period (see COOLAN).
TWIN	Coolant inlet temperature, (^{o}K).
TWOUT	Coolant outlet temperature, (^{o}K).
U(200)	Nodal point radial displacement for the current step.
UL(200)	Previous value of U(200).
XEPCNT	Volume percentage of Xenon in the fill-gas.
XI(200)	Constants used in the right hand side of Eq.(3.30) of heat conduction matrix (XI(I), I = 1,200).
XIN(200)	As above but for the cladding region.

XT(10)	Parameter used in thermal expansion calculations as weighting factors (r, θ and z). Currently CT(J) = 1.0 for J = 1,10. This can be used to model anisotropic effects in Zr thermal expansion.
YPRNT(24)	Parameter that stores the code name of variables which are required on the list of detailed output (defined in a DATA statement of SAMURA MAIN program). It includes stresses, temperature, radius, strains, etc. The output as arranged by PRINTX is printed in eight columns, each column giving the nodal point values of any of the 24 variables defined in SAMURA. There is an option of having either 8 or 16 or 24 variables printed out (see Fig.A.4).
YS(200)	Nodal point values of yield stress, (MPa).
ZZ(10)	Total axial strain in any region J (J = 1,10) for the current time-step.
ZZL(10)	Previous values of ZZ(10).

APPENDIX B

APPENDIX B

B.1 PARTIAL DERIVATIVES OF Fp IN EQ.(3.119)

There are nine partial derivatives in the form of $(\partial F_p/\partial \sigma_p)$; $p \equiv r, \theta, z$, in Eq.(3.119) which can be determined through the definition of F_p; Eq.(3.100):

$$F_p = \frac{3}{2} \frac{\dot{g}(\sigma_e)}{\sigma_e} s_p \quad , \quad p \equiv r,\theta,z; \tag{B.1}$$

or its general form:

$$F_p = \frac{\partial \sigma_e}{\partial \sigma_p} \dot{g}(\sigma_e) \quad , \quad p \equiv r,\theta,z; \tag{B.2}$$

Since anisotropy should be included in SAMURA later, the derivatives will be given for an anisotropic material. The conversion to isotropic case (as currently used in SAMURA) would be straightforward. According to Hill (181) if the loading of cylindrical tube is in the principal directions the equivalent stress with anisotropy will become:

$$\sigma_e = \left[F(\sigma_\theta - \sigma_z)^2 + G(\sigma_z - \sigma_r)^2 + H(\sigma_r - \sigma_\theta)^2 \right]^{\frac{1}{2}} \tag{B.3}$$

where F, G and H are the anisotropic parameters and will be discussed later (note that if material is isotropic F=G=H=½; see Appendix C).

Now using Eq.(B.3), one may determine $\partial\sigma_e/\partial\sigma_p$ values for $p \equiv r,\theta,z$:

$$\frac{\partial \sigma_e}{\partial \sigma_r} = \frac{H(\sigma_r - \sigma_\theta) - G(\sigma_z - \sigma_r)}{\sigma_e}$$

$$\frac{\partial \sigma_e}{\partial \sigma_\theta} = \frac{F(\sigma_\theta - \sigma_z) - H(\sigma_r - \sigma_\theta)}{\sigma_e} \qquad \text{(B.4)}$$

$$\frac{\partial \sigma_e}{\partial \sigma_z} = \frac{G(\sigma_z - \sigma_r) - F(\sigma_\theta - \sigma_z)}{\sigma_e}$$

The partial derivatives of F_p are expressed as follows; using (B.2):

$$\frac{\partial F_p}{\partial \sigma_p} = \dot{g}(\sigma_e) \frac{\partial}{\partial \sigma_p} \left(\frac{\partial \sigma_e}{\partial \sigma_p}\right) + \frac{\partial \sigma_e}{\partial \sigma_p} \times \frac{\partial \dot{g}(\sigma_e)}{\partial \sigma_p} \qquad \text{(B.5)}$$

In order to determine the above expression, one needs the first order partial derivatives $\frac{\partial \sigma_e}{\partial \sigma_r}$, $\frac{\partial \sigma_e}{\partial \sigma_\theta}$, $\frac{\partial \sigma_e}{\partial \sigma_z}$, given in (B.4), and the second order partials

$$\frac{\partial^2 \sigma_e}{\partial \sigma_r^2}, \frac{\partial^2 \sigma_e}{\partial \sigma_\theta^2}, \frac{\partial^2 \sigma_e}{\partial \sigma_z^2}$$

$$\frac{\partial^2 \sigma_e}{\partial \sigma_r \partial \sigma_\theta}, \frac{\partial^2 \sigma_e}{\partial \sigma_\theta \partial \sigma_z}, \frac{\partial^2 \sigma_e}{\partial \sigma_z \partial \sigma_r}$$

which are obtained from (B.4):

$$\frac{\partial^2 \sigma_e}{\partial \sigma_r^2} = \frac{HF + FG + HG}{\sigma_e^3} (\sigma_\theta - \sigma_z)^2$$

$$\frac{\partial^2 \sigma_e}{\partial \sigma_\theta^2} = \frac{HF + FG + HG}{\sigma_e^3} (\sigma_z - \sigma_r)^2 \qquad \text{(B.6)}$$

$$\frac{\partial^2 \sigma_e}{\partial \sigma_\theta^2} = \frac{HF + FG + HG}{\sigma_e^3} (\sigma_r - \sigma_\theta)^2$$

$$\frac{\partial^2 \sigma_e}{\partial \sigma_r \partial \sigma_\theta} = \frac{HF + FG + HG}{\sigma_e^3} (\sigma_z - \sigma_r)(\sigma_\theta - \sigma_z)$$

$$\frac{\partial^2 \sigma_e}{\partial \sigma_\theta \partial \sigma_z} = \frac{HF + FG + HG}{\sigma_e^3} (\sigma_r - \sigma_\theta)(\sigma_z - \sigma_r)$$

$$\frac{\partial^2 \sigma_e}{\partial \sigma_z \partial \sigma_r} = \frac{HF + FG + HG}{\sigma_e^3} (\sigma_r - \sigma_\theta)(\sigma_\theta - \sigma_z)$$

Substitution of (B.4) and (B.6) expressions in (B.5) provides all the nine partial derivatives required in the Taylor expansion of F_p. Using the definitions of F_p as given in Eq.(B.1) and Eqs.(B.6), one may easily deduce the following general expression for isotropic materials as in SAMURA:

$$\frac{\partial \sigma_e}{\partial \sigma_p} = \frac{3}{2}\frac{S_p}{\sigma_e}$$

$$\frac{\partial F_p}{\partial \sigma_p} = \frac{\dot{g}(\sigma_e)}{\sigma_e} + \left[\frac{3S_p}{2\sigma_e}\right]^2 \left[\frac{\partial \dot{g}(\sigma_e)}{\partial \sigma_e} - \frac{\dot{g}(\sigma_e)}{\sigma_e}\right] \qquad \text{(B.7)}$$

$$p \equiv r,\theta,z$$

These expressions are then used to obtain the coefficients Q(p,i) and P(p,q,i) in Eq.(3.121) of the text (p = 1,3, q = 1,3 and i = 1,200):

$$P(p,1,i) = \theta.\Delta t.\frac{\partial F_p}{\partial \sigma_r}$$

$$P(p,2,i) = \theta.\Delta t.\frac{\partial F_p}{\partial \sigma_\theta}$$

$$P(p,3,i) = \theta.\Delta t.\frac{\partial F_p}{\partial \sigma_z}$$

$$Q(p,i) = \bar{\gamma}_i + \Delta t\,[\,.P_i + (1-\theta)\bar{P}_i\,]$$

$$+ \Delta t\,[\theta.F_p + (1-\theta)\bar{F}_p\,]$$

$$- \Delta t.\theta\left\{\left[\frac{\partial F_p}{\partial \sigma_r}\right]\bar{\sigma}_{r,i} + \left[\frac{\partial F_p}{\partial \sigma_\theta}\right]\bar{\sigma}_{\theta,i}\right.$$

$$\left. + \left[\frac{\partial F_p}{\partial \sigma_z}\right]\bar{\sigma}_{z,i}\right\}$$

where variables with a bar indicate their value at previous time-step.

APPENDIX C

APPENDIX C

C.1 DERIVATION OF EQUATIONS FOR ANISOTROPIC CASE

Zircaloy has hexagonal (HCP) crystal lattice and exhibits a pronounced anisotropy, so that the existence of preferred orientation (texture) in a tube will confer variations in elastic constants. In a material with hexagonal symmetry there are five independent elastic constants (compliances). The elastic strains are then:

$$\{\varepsilon^e\} = [S]\{\sigma\} + [\alpha]\{\Delta T\} \tag{C.1}$$

where

$$[S] = \begin{bmatrix} S_{11} & S_{12} & S_{13} \\ S_{12} & S_{11} & S_{13} \\ S_{13} & S_{13} & S_{33} \end{bmatrix} \tag{C.2}$$

and S_{ij} constants can be defined in terms of the Zircaloy elastic moduli E and ν (obviously these also vary with direction). Equation (C.1) can then be expanded as:

$$\begin{cases} \varepsilon_r^e = S_{11}\,\sigma_r + S_{12}\,\sigma_\theta + S_{13}\,\sigma_z + \sigma_r.\Delta T \\ \varepsilon_\theta^e = S_{12}\,\sigma_r + S_{11}\,\sigma_\theta + S_{13}\,\sigma_z + \sigma_\theta.\Delta T \\ \varepsilon_z^e = S_{13}\,\sigma_r + S_{13}\,\sigma_\theta + S_{33}\,\sigma_z + \sigma_z.\Delta T \end{cases} \tag{C.3}$$

Equations (c.3) can be solved for the stresses :

$$\sigma_r = (\varepsilon_r^e - \alpha_r.\Delta T)\left(\frac{S_{11}\,S_{33} - S_{13}^2}{\|S\|}\right) - (\varepsilon_\theta^e - \alpha_\theta.\Delta T)\left(\frac{S_{12}\,S_{33} - S_{13}^2}{\|S\|}\right) + (\varepsilon_z^e - \alpha_z.\Delta T)\left(\frac{S_{12}\,S_{13} - S_{11}\,S_{13}}{\|S\|}\right)$$

or

$$\sigma_r = A^r.\varepsilon_r^e + B^r.\varepsilon_\theta^e + C^r.\varepsilon_z^e - (A^r.\alpha_r + B^r\alpha_\theta + C^r\alpha_z)\Delta T \tag{C.4}$$

where

$$A^r = \frac{S_{11} \cdot S_{33} - S_{13}^2}{\|S\|}$$

$$B^r = \frac{S_{12} \cdot S_{33} - S_{13}^2}{\|S\|} \qquad (C.5)$$

$$C^r = \frac{S_{12} \cdot S_{13} - S_{11} \cdot S_{13}}{\|S\|}$$

Similarly for σ_θ and σ_z:

$$\sigma_\theta = A^\theta \varepsilon_r^e + B^\theta \varepsilon_\sigma^e + C^\theta \varepsilon_z^e - (A^\theta \alpha_r + B^\theta \alpha_\theta + C^\theta \alpha_z)\Delta T \qquad (C.6)$$

$$\sigma_z = A^z \varepsilon_r + B^z \varepsilon_\theta + C^z \varepsilon_z - (A^z \alpha_r + B^z \alpha_z + C^z \alpha_z)\Delta T \qquad (C.7)$$

where A^θ, B^θ, C^θ, A^z, B^z and C^z have similar definitions as those of A^r, B^r and C^r. Naturally these coefficients are related and can be simplified in terms of Ep and νp ($p \equiv r,\theta,z$).

Now using Eqs.(3.111), ε_r^e, ε_θ^e and ε_z^e are eliminated from Eqs.(C.4), (C.6) and (C.7) the stresses are then expressed in terms of radial displacements, $\gamma_{r,i}$, $\gamma_{\theta,i}$ and Z for a radial node i:

$$\sigma_{r,i} = A_i^r \left[\frac{U_{i+1} - U_i}{\Delta r_i} - \gamma_{r,i}\right] - B_i^r \left[\frac{U_i}{r_i} - \gamma_{\theta,i}\right]$$

$$+ C_i^r\{Z - 3\Delta t\,[\theta.P_i + (1-\theta)\bar{P}_i] + \gamma_{r,i} + \gamma_{\theta,i} - \sum_p \bar{\gamma}_{p,i}\}$$

$$- (A_i^r.\alpha_r - B_i^r.\alpha_\theta + C_i^r.\alpha_z)\Delta T;$$

$$= \left(\frac{A_i^r}{\Delta r_i}\right)U_{i+1} - \left(\frac{B_i^r}{r_i} + \frac{A_i^r}{\Delta r_i}\right) U_i + (C_i^r - A_i^r)\gamma_{r,i}$$

$$+ (C_i^r + B_i^r)\gamma_{\theta,i} + C_i^r Z$$

$$- \{C_i^r(3\Delta t\,[\,\theta.P_i + (1-\theta)\bar{P}_i\,] + \sum_p \bar{\gamma}_{p,i})$$

$$+ (A_i^r.\alpha_r - B_i^r.\alpha_\theta + C_i^r.\alpha_z)\Delta T_i\} \qquad (C.9)$$

$$\sigma_{\theta,i} = (\frac{A_i^\theta}{\Delta r_i})U_{i+1} - (\frac{B_i^\theta}{\Delta r_i} + \frac{A_i^\theta}{r_i})U_i + (C_i^\theta - A_i^\theta)\gamma_{r,i}$$

$$+ (C_i^\theta + B_i^\theta)\gamma_{\theta,i} + C_i^\theta\, Z$$

$$- \{C_i^\theta(3\Delta t\,[\,\theta.P_i + (1-\theta)\bar{P}_i\,] + \sum_p \bar{\gamma}_{p,i})$$

$$+ (A_i.\alpha_r - B_i^\theta.\alpha_\theta + C_i^\theta.\alpha_z)\Delta T_i\} \qquad (C.10)$$

$$\sigma_{z,i} = (\frac{A_i^z}{\Delta r})U_{i+1} - (\frac{B_i^z}{r_i} + \frac{A_i^z}{\Delta r_i})U_i + (C_i^z - A_i^z)\gamma_{r,i}$$

$$+ (C_i^z - B_i^z)\gamma_{\theta,i} + C_i^z\, Z$$

$$- \{C_i^z(3\Delta t\,[\,\theta.P_i + (1-\theta)\bar{P}_i\,] + \sum_p \bar{\gamma}_{p,i})$$

$$+ (A_i^z.\alpha_r - B_i^z\alpha_\theta + C_i^z.\alpha_z)\Delta T_i\} \qquad (C.11)$$

Comparisons of these expressions with those in Eqs.(3.130) of the text provides the coefficients a_k (k=1,18); and the rest of analysis will be as before.

Finally, as discussed in Appendix B, some other equations must be changed for the case of anisotropic material as follows:

Equivalent stress:

$$\sigma_e = \left[F(\sigma_\theta - \sigma_z)^2 + G(\sigma_z - \sigma_r)^2 + H(\sigma_r - \sigma_\theta)^2\right]^{\frac{1}{2}} \tag{C.12}$$

Equivalent strain:

$$\varepsilon_e = \frac{\left[H(F\varepsilon_r - G\varepsilon_\theta)^2 + F(G\varepsilon_\theta - H\varepsilon_z)^2 + G(H\varepsilon_z - F\varepsilon_r)^2\right]^{\frac{1}{2}}}{(HF + FG + GH)} \tag{C.13}$$

The Levy-von Mises equations:

$$\begin{aligned}
\dot{\varepsilon}_r^p &= \frac{\dot{\varepsilon}_e}{\sigma_e}\left[G(\sigma_r - \sigma_z) + H(\sigma_r - \sigma_\theta)\right] \\
\dot{\varepsilon}_\theta^p &= \frac{\dot{\varepsilon}_e}{\sigma_e}\left[F(\sigma_\theta - \sigma_z) + H(\sigma_\theta - \sigma_r)\right] \\
\dot{\varepsilon}_z^p &= \frac{\dot{\varepsilon}_e}{\sigma_e}\left[F(\sigma_z - \sigma_\theta) + G(\sigma_z - \sigma_r)\right]
\end{aligned} \tag{C.14}$$

Some authors use only two anisotropic parameters R and P as follows:

$$\sigma_e = \frac{1}{(RP + P)^{\frac{1}{2}}}\left[R(\sigma_r - \sigma_\theta)^2 + RP(\sigma_\theta - \sigma_z)^2 + P(\sigma_z - \sigma_r)^2\right]^{\frac{1}{2}}$$

where the relation between these parameters is

$$R = \frac{F}{1 - F} \quad , \quad P = \frac{F}{H} \tag{C.15}$$

This is because in practice one extra equation must be provided to calculate the third parameter, these are:

$$F + G = 1.0 \tag{C.16}$$

or

$$F + G + H = 1.5 \tag{C.17}$$

Either of (C.16) or (C.17) is used in conjunction with the rest of the equations to find the anisotropy factors.

C.2 TYPICAL VALUES OF ANISOTROPIC PARAMETERS

The results of experiments performed by Hunt (182) (out-of-reactor) have provided the following values for three types of Zircaloy tube texture (Table C.1).

Reference (11) has used the following values of R and P for Zr cladding:

R = 1.6 Cold-worked, high or low neutron flux;

R = 2.3 Annealed, high or low flux;

P = 10.0 Cold-worked or annealed, high flux;

P = 2.6 Cold-worked, low flux;

P = 3.3 Annealed, low flux.

With R and P from the above results and Eq.(C.16) one may calculate F, G and H values:

Low flux, cold-worked:

F = 0.615

G = 0.385

H = 0.237 (0.0615 high flux).

Low flux, annealed:

F = 0.697

G = 0.303

H = 0.211 (0.0697 high flux).

Recently a new set of Zr data have been used in a code which does consider anisotropy of cladding (175); see Table C.2.

The obvious conclusion from the data discussed so far is that the values provided for F, G and H do not agree with each other. The data in Table C.2 are the most recent values and are therefore recommended at this stage until more results become available.

TABLE C.1

HUNT'S RESULTS FOR F, G AND H

Parameters		TYPE(I) TEXTURE(*)		TYPE(II) TEXTURE		TYPE(III) TEXTURE	
		Eq.(C.16)	Eq.(C.17)	Eq.(C.16)	Eq.(C.17)	Eq.(C.16)	Eq.(C.17)
COLD-WORKED Zr TUBE	F	0.644	0.773	0.556	0.738	0.702	0.829
	G	0.356	0.532	0.444	0.588	0.298	0.354
	H	0.162	0.195	0.131	0.174	0.268	0.312
ANNEALED Zr TUBE	F	0.759	0.956	0.743	0.956	0.375	0.416
	G	0.241	0.304	0.257	0.331	0.625	0.692
	H	0.191	0.240	0.165	0.211	0.353	0.392

(*) See Reference 182 for details.

TABLE C.2

ANISOTROPIC PROPERTIES OF ZIRCALOY

Zircaloy Properties	Thermal Expansion Coefficient ($10^{-5}/^{o}K$)			Young's Modulus (10^{3} MPa)			Poisson's Ratio	Anisotropic Parameters		
Model	α_r	α_θ	α_z	E_r	E_θ	E_z	$\nu_r=\nu_\theta=\nu_z$	F	G	H
Anisotropic	0.871	0.4441	0.6721	82.32	68.60	65.17	0.325	0.52	0.48	0.87
Isotropic	0.66	0.66	0.66	68.6	68.6	68.6	0.325	0.50	0.50	0.50

APPENDIX D

APPENDIX D

D.1 URANIUM-DIOXIDE FUEL PROPERTIES AND MODELS

The UO_2 fuel properties and models recommended by EPRI (170) are reproduced here in Table D.1:

TABLE D.1

STANDARDISED PROPERTIES AND MODELS FOR UO_2 FUEL - PHASE III

Fuel Property or Model	Units	Recommended Value or Function
Static Modulus, E_f	psi	For $T \leq 1700°C$: $E_f = 15.268\ (1.671 \times 10^6 - 924.4T)\ (1-2.28P)$; For $T > 1700°C$: $E_f = 1.52 \times 10^6$; where T = temperature of the fuel in °C, and P = volume fraction of porosity in the fuel.
Poisson's Ratio, ν_f	None	When plasticity is not treated and T is between 25 and 1700°C: $\nu_f = 0.32 - 1.791 \times 10^{-5}\ (T-25)$; When plasticity is not treated and $T \geq 1700°C$: $\nu_f = 0.29$; When plasticity is treated: $\nu_f = 0.5$; where T = temperature of the fuel in °C.
Maximum Restructured Density, ρ_R	% TD	$\rho_R = 98$, for fuel temperatures high enough to cause columnar grain formation.
Specific Heat, C_{p_f}	cals/(gm-°K)	$C_{p_f} = 3.702 \times 10^{-3}\left[\frac{A D^2 \exp(D/T)}{T^2 [\exp(D/T) - 1]^2} + 2BT + \frac{CE}{RT^2}\exp(-E/RT)\right]$; where: A = 19.145(cal/mole-°K), B = 7.847×10^{-4} (cal/mole-°K^2), C = 5.644×10^6 (cal/mole), D = 535.285 (°K), E = 3.7695×10^4 (cal/mole), T = temperature, 298 to 3073°K, and R = 1.987 (cal/mole - °K).
Surface Emissivity, E_{s_f}	None	$E_{s_f} = 0.85$

TABLE D.1 (cont.)

Fuel Property or Model	Units	Recommended Value or Function
Thermal Conductivity, κ_f	Watts/(cm-°C)	$\kappa_f = (\kappa_{95})(F_p)$; where κ_{95} = thermal conductivity of 95% TD fuel, F_p = porosity correction factor, κ_f = thermal conductivity of fuel, $\kappa_{95} = \frac{33.24}{(402.4+T)} + 6.12 \times 10^{-13}(T + 273)^3$, T = local fuel temperature in °C, $F_p = \frac{1.1316\ (1-P)}{1+(P+10P^2)}$, and P = fractional fuel porosity.
Linear Thermal Expansion, $(\Delta L/L)_f$	Fractional	For $T \leq 26$°C: $(\Delta L/L)_f = 0.0$; For T between 26 and 2175°C: $(\Delta L/L)_f = -1.723 \times 10^{-4} + 6.797 \times 10^{-6}T + 2.896 \times 10^{-9}T^2$; For $T \geq 2175$°C: $(\Delta L/L)_f = 2.04 \times 10^{-3} + 3 \times 10^{-6}T + 2 \times 10^{-9}T^2 + 1 \times 10^{-12}T^3$; where T = fuel temperature in °C.
Theoretical Density, ρ_f	gm/cm^3	$\rho_f = 10.96$
Initial Fuel Density as Heavy Metals, ρ_m	$(gm\text{-metal})/cm^3$	ρ_m = 9.66 for 100% TD, 9.18 for 95% TD, and 8.69 for 90% TD fuel. Linear interpolation is applicable.
Restructuring Temperature for Columnar Grains, T_R	°C	$T_R = 1700$
Plasticity Temperature, T_p	°C	$T_p = 1400$
Unrestrained Fuel Volume Swelling, $(\Delta V/V)_f$	%	For $T \leq 1200$°C: $\%(\Delta V/V)_f = 0.4$ per 10^{20} fissions/cm^3; For T between 1200 and 1700°C: $\%(\Delta V/V)_f = 3.2$ per 10^{20} fissions/cm^3; For $T \geq 1700$°C: No Swelling; where T = local fuel temperature.

TABLE D.1 (cont.)

Fuel Property or Model	Units	Recommended Value or Function
Total Creep Rate, $\dot{\varepsilon}_f$	in/(in-hr)	For $T \leq 1200°C$: $\dot{\varepsilon}_f = (1 + 20.38 t^{-0.37})\ \dot{\varepsilon}_s$; For $T > 1200°C$: $\dot{\varepsilon}_f = (1 + 7.8\ t^{-0.26})\ \dot{\varepsilon}_s$; where $\dot{\varepsilon}_f$ = total fuel creep rate, $\dot{\varepsilon}_s$ = steady-state creep rate, t = irradiation time from BOL in hours, T = local fuel temperature, $\dot{\varepsilon}_s = A\sigma \exp(-90{,}000/RT) + B\sigma^{4.5} \exp(-132{,}000/RT) + 3.7 \times 10^{-23} \sigma \dot{F}$, $A = (9.73 \times 10^6 + 3.24 \times 10^{-6} \dot{F})/(D-87.7)G^2$, $B = 1.38 \times 10^{-4}/(D-90.5)$, σ = equivalent uniaxial compressive stress, psi, $\dot{F}$ = fission rate, fissions/cc-sec, D = fuel density in % TD (if less than 92% then 92% is used), R = 1.987 cals/mole-°K, T = temperature, °K, and G = grain size, microns.
Brittle Fracture Stress, σ_{F_f}	psi	$\sigma_{F_f} = 14.22\ (1164 + 0.223T)$; where T is the local fuel temperature in °C.
Melting Temperature	°C	2840
Local Fission Gas Release, R_i (*)	fractional	R_i, Ti pairs are: 0.0, 0.0; 0.0065, 800.; 0.0315, 1000.; 0.1085, 1200.; 0.2712, 1400.; 0.7394, 1800.; 0.8975, 2000.; 0.9710, 2200.; 1.0, 2600. and above; where R_i is the fractional release of the local fission gas inventory in the fuel at temperature T_i in °C. These values were obtained by an interpolated fit between the models of the References given. Linear interpolation is applicable. The above table of R_i, Ti pairs was obtained from the following equation:

*Reference 170 provides a discussion of the use of this model with certain restrictions on its application.

TABLE D.1 (cont.)

Fuel Property or Model	Units	Recommended Value or Function
Local Fission Gas Release (continued)		$R_i = 1.3025 \times 10^{-2} \sum_{i=0}^{m} \exp(-Z_i^2/2)$; where R_i = the fraction of the local fission gas inventory released at temperature T, $Z_i = (10i/320)-5$, i = an integer from 0 to m, in steps of one, m = T/10, and T = the local temperature, rounded to values of 10, from 0 to 2600°C (e.g., 1532 becomes 1530°C).

D.2 ZIRCALOY CLADDING PROPERTIES AND MODELS

Table D.2 provides the recommended Zircaloy properties and models:

TABLE D.2

STANDARDISED PROPERTIES AND MODELS FOR ZIRCALOY

Zircaloy Property or Model	Units	Recommended Value or Function
Static Modulus, E_c	psi x 10^6	$E_c = 15.48712 - .014984(T)$; where T is the local cladding temperature from 21 to 427°C.
Poisson's Ratio, ν_c	---	$\nu_c = 0.29838 - 0.12645 \times 10^{-3}(T)$; where T is the local cladding temperature from 21 to 399°C.
Density, ρ_c	Grams/cc	$\rho_c = 6.55$ at 21°C; $\rho_c = 6.52$ at 316°C.
Specific Heat, C_{p_c}	Cal/gm	$C_{p_c} = 0.06805 + 2.3872 \times 10^{-5}(T)$; where T is the local cladding temperature from 0 to 635°C.
Diamond Pyramid Hardness, Y	kg/mm^2	$Y = (44013.74 - 200.2689T + 0.47503T^2 - .41618 \times 10^{-3}T^3)^{0.5}$
Surface Emissivity, E_{s_c}	---	E_{s_c} = 0.751 at 850°C; significant data base not available for lower temperatures.
Thermal Conductivity, κ_c	Watts/(cm-°C)	$\kappa_c = 0.13959 + 0.98522 \times 10^{-4} T$
Linear Thermal Expantion, $(\Delta D/D)_c$ and $(\Delta L/L)_c$	fractional	Diametral ($\times 10^{-6}$): $Ln(\Delta D/D)_c = 5.5153 + 2.8426(Ln(T)) + 0.10407 (Ln(T))^2$; Axial: $(\Delta L/L)_c = 42.5323 + 3.96753 T$; where T is the local cladding temperature from 21 to 429°C.

TABLE D.2 (cont.)

Zircaloy Property or Model	Units	Recommended Value or Function
Shear Modulus, G_c	psi x 10^6	$G_c = 0.49\ (10.97225 - .1226 \times 10^{-1}T + .1515 \times 10^{-5}T^2)$; where T is the local cladding temperature from 21 to 427°C.
Yield Stress, σ_{y_c} (Typical cold-worked stress-relief annealed)	ksi	$\sigma_{y_c} = (7944.319 - 35.98934T + .85010 \times 10^{-1}T^2 - .74316 \times 10^{-4}\ T^3)^{1/2}$; where T is the local cladding temperature from 21 to 482°C.
Corrosion Rate, C	Mg/(dm^2-day)	$C = 1.8920 \times 10^{13}$ exp (-40820/RT), the corrosion rate until transition; $Ln(D) = 71.19862 - 11.27444\ Ln\ (T-273)$, the days to transition; $C = 1.7677 \times 10^{10}$ exp (-31300/RT), the corrosion rate beyond transition; where T = temperature, in °K, R = 1.987 cals/(mole-°K), D = days, and C = corrosion rate in mg/(dm^2-day).
Plasticity Stress, σ_{f_c}	psi	$\sigma_{f_c} = k\ \varepsilon_{f_c}^{n}$; where σ_{f_c} = effective stress of cladding (ksi), ε_{f_c} = effective strain of cladding (in/in), $k = \sigma_{y_c} + 33\ (\phi t/10^{21})^{0.40}$, σ_{y_c} = yield stress in ksi as described above as a function of temperature, $n = 0.030\ (\phi t/10^{21})^{0.54}$, and ϕt = fast neutron fluence (n/cm^2, E > 1 Mev). The engineering stress-strain curve may be modeled as a whole by using the lesser of the elastic and plastic stresses as a function of strain.
Stress Free Axial Growth Rate, $\dot{\varepsilon}_g$	in/(in-hr)	$\dot{\varepsilon}_g = 2.52\ (\phi t/10^{21})^{-0.3}\ (\phi/10^{21})$; where $\dot{\varepsilon}_g$ = Zircaloy axial elongation rate due to growth, ϕt = fast neutron fluence (n/cm^2, E > 1 Mev), and ϕ = fast neutron flux (n/cm^2-sec), E > 1 Mev). The following guidelines are to be applied with use of the above axial growth equation: a) Ignore growth in the radial and tangential directions.

TABLE D.2 (cont.)

Zircaloy Property or Model	Units	Recommended Value or Function
Stress Free Axial Growth Rate (cont'd.)		b) Application of the anisotropic creep law recommended herein to an externally pressurized tube also results in axial elongation. The magnitude of this elongation is similar to that predicted independently for stress-free growth. Since both the creep and growth equations were based on data in which independent creep and growth could not be separated, it must be assumed that each equation predicts total deformation under certain circumstances. Therefore, the greater of either the instantaneous axial creep or growth rate is to be used in calculating axial strain for the time or strain increment under consideration. c) If the directions of creep and growth are opposing in the axial direction, total deformation is to be taken as the algebraic sum of creep and growth.
Anisotropic Total Creep Rate Components, $\dot{\varepsilon}_z$, $\dot{\varepsilon}_\theta$, $\dot{\varepsilon}_r$ (*)	in/(in-hr)	Separate expressions for thermal and irradiation creep rates are provided. The greater of either thermal or irradiation creeprates at any time should be used in accumulating creep strain with time. These equations apply at temperatures to 400°C and effective stresses up to the cladding yield stress; $\dot{\varepsilon}_{TH} = [(100/\sigma_y)(\sinh(0.6s))$ $+(1.36 \times 10^{10} \exp(-.008t) + 10^8)$ $(\sinh(0.0966s))][\exp(-40000/RT)]$; $\dot{\varepsilon}_{IRR} = [\phi s(\exp(-8000/RT))]$ $[8.48 \times 10^{-20}(\exp(-0.004t))+(1.14 \times 10^{-18})]$; where $\dot{\varepsilon}_{TH}$ = effective thermal creep rate (hr^{-1}), $\dot{\varepsilon}_{IRR}$ = effective irradiation creep rate (hr^{-1}), $\dot{\varepsilon}_f$ = the greater of either $\dot{\varepsilon}_{TH}$ or $\dot{\varepsilon}_{IRR}$, σ_y = axial 0.2% yield stress in ksi, t = time in hours, R = 1.987 cal/(mole-°K), T = temperature in °K, s = effective stress in ksi, $s = \{0.67(\sigma_z - \sigma_\theta)^2 + 0.26(\sigma_\theta - \sigma_r)^2 + 0.33(\sigma_r - \sigma_z)^2\}^{0.5}$, σ_z, σ_θ and σ_r = principal stresses in ksi, ϕ = fast neutron flux (n/(cm^2-sec), E > 1 Mev), $\dot{\varepsilon}_z$, $\dot{\varepsilon}_\theta$ and $\dot{\varepsilon}_r$ = the principal components of the strain rate, $\dot{\varepsilon}_z = (\dot{\varepsilon}_f/s)(0.67(\sigma_z - \sigma_\theta) - 0.33(\sigma_r - \sigma_z))$, $\dot{\varepsilon}_\theta = (\dot{\varepsilon}_f/s)(0.26(\sigma_\theta - \sigma_r) - 0.67(\sigma_z - \sigma_\theta))$, and $\dot{\varepsilon}_r = (\dot{\varepsilon}_f/s)(0.33(\sigma_r - \sigma_z) - 0.26(\sigma_\theta - \sigma_r))$.

*Reference 170 provides a discussion of the use of this model with certain restrictions on its application.

TABLE D.2 (cont.)

Zircaloy Property or Model	Units	Recommended Value or Function
Isotropic Total Creep Rate Components, $\dot{\epsilon}_z$, $\dot{\epsilon}_\theta$, $\dot{\epsilon}_r$ (*)	in/(in-hour)	Separate expression for thermal and irradiation creep rates are provided. The greater of either thermal or irradiation creep rate at any time should be used in accumulating creep strain with time. These equations apply at temperatures to 400°C and effective stresses up to the cladding yield stress; $\dot{\epsilon}_{TH} = 0.962\,[(100/\sigma_y)\{\sinh(0.4947s)\} + \{1.36 \times 10^{10} \exp(-0.008t) + 10^8\}\{\sinh(0.0796s)\}][\exp(-40000/RT)]$; $\dot{\epsilon}_{IRR} = 0.793[\phi s(\exp(-8000/RT))][8.48 \times 10^{-20}\{\exp(-0.004t)\} + \{1.14 \times 10^{-18}\}]$; where $s = \{0.5(\sigma_z - \sigma_\theta)^2 + 0.5(\sigma_\theta - \sigma_r)^2 + 0.5(\sigma_r - \sigma_z)^2\}^{0.5}$, $\dot{\epsilon}_z$, $\dot{\epsilon}_\theta$ and $\dot{\epsilon}_r$ = the principal components of the strain rate, $\dot{\epsilon}_z = \{\dot{\epsilon}_f/s\}\{\sigma_z - 0.5(\sigma_\theta + \sigma_r)\}$, $\dot{\epsilon}_\theta = \{\dot{\epsilon}_f/s\}\{\sigma_\theta - 0.5(\sigma_r + \sigma_z)\}$, $\dot{\epsilon}_r = \{\dot{\epsilon}_f/s\}\{\sigma_r - 0.5(\sigma_z + \sigma_\theta)\}$, and other parameters are as defined for anisotropic creep.

D.3 MIXED-OXIDE FUEL PROPERTIES AND MODELS

EPRI (170) have also provided a set of data for the mixed-oxide fuel (3-5%) which is reproduced here in Table D.3 :

*Reference 170 provides a discussion of the use of this model with cetain restrictions on its application.

TABLE D.3

STANDARDISED PROPERTIES AND MODELS FOR MIXED-OXIDES

Mixed-Oxide Fuel Property or Model	Units	Recommended Value or Function
Static Modulus	psi	Same as for UO_2 fuel
Poisson's Ratio	None	"
Restructured Density for Columnar Grains	% TD	"
Specific Heat	Cal/(gm-°K)	"
Surface Emissivity	None	"
Linear Thermal Expansion	fractional	"
Restructure Temperature for Columnar Grains	°C	"
Plasticity Temperature	°C	"
Unrestrained Volume Swelling	%	"
Thermal Conductivity	w/(cm-°C)	Same as for UO_2 fuel, except for the fuel porosity correction factor, F_p: $F_p = [(1.025/0.95)\rho)] / [1.0 + 0.5(1.0-\rho)]$; where ρ is the fraction of theoretical density of the fuel.
Theoretical Density, ρ_f	gm/cm^3	$\rho_f = 10.96 + 0.005 \times W$; where W is the weight percent of PUO_2.
Initial Fuel Density as Heavy Metals, ρ_m	$(gm\text{-}Metal)/cm^3$	$\rho_m = 0.88 \times \rho_I \times \rho_f$; where ρ_I is the initial density in fraction of theoretical, and ρ_f is the theoretical mixed-oxide density as calculated above.
Total Creep Rate, $\dot{\epsilon}_f$	in/(in-hr)	$\dot{\epsilon}_f = 0.2([1.0 + 2.11(97.0-\rho)]\ \dot{\epsilon}_{TL} + [1.0 + 0.22(97.0-\rho)]\ \dot{\epsilon}_{TH} + \dot{\epsilon}_{FT} + \dot{\epsilon}_{FA})$, where $\dot{\epsilon}_f$ = total creep rate of the mixed-oxide fuel, ρ = local fuel density in %TD (if greater than 97%, use 97%), $\dot{\epsilon}_{TL} = [(2.23 \times 10^7)/G^2][\sigma][\exp(-92500/RT)]$, $\dot{\epsilon}_{TH} = [1 \times 10^{-3}][\sigma]^{4.4}[\exp(-136000/RT)]$, $\dot{\epsilon}_{FT} = [1.96 \times 10^{-19}][\sigma][\exp(-13700/RT)]$, $\dot{\epsilon}_{FA} = [3.7 \times 10^{-23}][F][\sigma]$,

TABLE D.3 (cont.)

Mixed-Oxide Fuel Property or Model	Units	Recommended Value or Function
Total Creep Rate (continued)		G = fuel grain size in microns, σ = stress in psi, R = 1.987 cal/(mole-°K), T = fuel temperature in °K, and $\dot{F}$ = fission rate in fuel, in $f/(cm^3\text{-sec})$.
Fracture Stress, σ_{F_f}	psi	$\sigma_{F_f} = 6304 + 8.4\ T$; where T is the fuel temperature in °C.
Melting Temperature, T_m	°C	$T_m = 2820.$
Fission Gas Release Fraction, F	fractional	$F = 0.12X_1 + 0.50X_2 + 0.80X_3$; where F = the total fraction of gas released, X_1 = fractional amount of fission gas produced in fuel volume operating at or below 1400°C, X_2 = fractional amount of fission gas produced in fuel volume operating between 1400 and 1700°C, and X_3 = fractional amount of fission gas produced in fuel volume operating at or above 1700°C.

APPENDIX E

APPENDIX E

E.1 MODELLING OF CC-7 EXPERIMENT (EPRI PHASE III STUDIES)*

The CC-7 irradiation experiment was conducted by the Commissariat a l'Energie Atomic (CEA) in 1964 in the EL3 experimental heavy water reactor (170). The experiment consisted of 16 short fuel pins of similar design but different initial cold gaps. Each pin was segmented into two fuel zones; each segment having an active fuel column length of $\sim$ 12.3 cm and ten pellets with no dishing. The pellets were fabricated from UO_2 and the cladding was Zr-2 with a high thickness ($\sim$ 7 mm).

Fuel segments 4113-AE1 and 4112-BE1 from the experiment are evaluated by EPRI. These segments were irradiated for a total time of 1690 hours (70.4 days) and rod averaged burn-ups achieved during this time were 3200 and 2900 MWd/teU in the AE1 and BE1 segments respectively (the segments were positioned in different reactor cells in the core). As-fabricated radial gaps in the AE1 and BE1 sebments were 150 μm and 44.5 μm respectively. The AE1 segment generated much higher specific power than did the BE1 segment. According to EPRI (180), the BE1 pin is in the category of pins

*This experiment, as well as the WR1-206 experiment, of the EPRI Phase III studies (170) had originally been modelled and prepared to be presented in the main text. Unfortunately most of the results, graphs and computer outputs related to these studies were lost during a burglary at Imperial College. Due to many difficulties as well as limitation in time it was not possible to reproduce all the results. However, it was decided to present all that was left for the sake of completeness.

with least influence of gap size and/or fission gas release on fuel temperature calculation (small as-fabricated gap and low EOL gas release). But the AE1 pin is considered to be among the category of pins with a strong interdependence of gap conductance, fission gas release and fuel temperature (large as-fabricated gap and high EOL gas release).

Table E.1 provides the general code input requirements for the AE1 segment. Table E.2 provides the dimensions of the BE1 segment. The rest of the general code input requirements for the BE1 are the same as those of the AE1 segment. Tables E.3 and E.4 present the irradiation histories assumed for each segment (see also Fig. E.1). Only one axial fuel segment is specified for the calculation, since the axial variations of the thermal and neutron flux are reported to be insignificant over these short pin segments.

The AE1 and BE1 pins were modelled by SAMURA using the above information. In the light of SAMURA results for the Maine Yankee pin (see Sub-Section 4.5.2) and especially the somewhat unexpectedly low temperatures obtained by SAMURA when using the cracked pellet gap conductance model, it was thought that the AE1 and BE1 pins could provide further evidence for the evaluation of this model. These test pins have also been regarded by EPRI to be excellent benchmarking exercise for pellet behaviour at high powers (the large cladding wall thickness and low pressure differentials excludes its involvement with gap closure). The code parameterisation was the same as described for the Yankee pin modelling. Furthermore, only one SAMURA run was made for each segment

using the cracked pellet gap conductance model*, the EPRI Phase III Zircaloy creep and the SAMURA option 2 gas release model (see Sub-Section 3.5.10).

As in the previous case study, comparisons are made between the predicted and measured fuel centreline temperatures, EOL fission gas release, EOL cold radial gap, and EOL fuel central foid radii. The results are presented in Tables E.5 through E.7.

The comparisons of predicted and measured temperatures are given in Table E.5 and Figs. E.2 and E.3 . Since all the codes (including SAMURA) predict peak centreline fuel temperature during the first 23 hours of the third irradiation cycle (52.12 days), EPRI have assumed that this is the experimental time for the maximum extension of columnar grain-growth in the fuel of the two pin segments modelled. A temperature of 1872^{o}K has been assigned as the minimum temperature for the formation of equiaxed grain structure in accordance to the EPRI guidelines (180). Experimental peak centreline temperatures have then been inferred considering the range in heat ratings achieved in each segment during the 23 hours of power peaking (170). Results presented in Table E5 for the 4113-AE1 pin show that all codes underpredict the fuel centreline temperature, with COMETHE-IIIJ providing the largest underprediction (- 232^{o}K). SAMURA underpredicts the temperature by 153^{o}K, which is quite acceptable. Other codes' temperature predictions are within the $\pm$ 139^{o}K

*Test runs made for the AE1 pin with the use of Ross and Stoute model produced very high temperatures and therefore were disregarded.

uncertainty band established for this pin (170). Results presented for the 4112-BE1 pin in the same table show that SAMURA, BEHAVE-4 (with either the Phase II or Phase III EPRI gas release model), COMETHE-IIIJ and LIFE-THERMAL-1 provide fuel temperature in good agreement with the experimental temperatures, i.e. within the $\pm$ 111^{o}K uncertainty band. GAPCON-THERMAL-2 has calculated a temperature that is high by 366^{o}K with respect to the measured value.

The graphs in Figures E.2 and E.3 of calculated fuel centreline temperature over the life of each of the pins in the experiment, help in the understanding of models. Figure E.1 provides a means of relating these graphs to the power history of each pin. Due to lack of experimental data against which to compare time-dependent temperatures, little can be said about whether code predictions of the temperature are accurate or not. It can, however, be seen that SAMURA temperature predictions are well within the range of temperature predictions by the other codes. The maximum differences ($\pm$ 160^{o}K) occur during the first cycle of irradiation for the AE1 pin; Figure E.2 , and during the second cycle for the BE1 pin, Figure E.3 .

The reported relative amounts of fission gas released in the two pins are consistent with the observed differences in restructuring. According to EPRI report (170), columnar grains formed in the 4113-AE1 pin, and the fission gas released was 26.7%. The lower-power 4112-BE1 showed only equiaxed grains and a fission gas release of 7.9%. The best prediction of fission gas release in each rod is provided by

LIFE-THERMAL-1 as seen in Table E.6. COMETHE-IIIJ is a little high on the high-powered pin and a little low on the low-powered pin. SAMURA overpredicts the gas release for both pins (41.7% for AE1 and 28.8% for BE1). GAPCON-THERMAL-1 predictions are too high for both pins.

Calculated cold radial gaps are compared in Table E.7 with the cold gaps measured for each pin from photomicrographs (170). BEHAVE-4 and GAPCON-THERMAL-2 provide EOL cold gaps that are slightly larger than measured values for each pin. COMETHE-IIIJ, LIFE-THERMAL-1 and SAMURA provide EOL cold gaps that are slightly smaller than measured for each pin.

The measured and calculated EOL central void radius of the pins is also listed in Table E.7. The high-powered AE1 pin had a central void of 406.4 μm radius, and the calculated values range from 25.4 to 901.3 μm. Considering the uncertainties in the measurement (± 102 μm) and the nature of this calculation, the values of 508.0 μm by COMETHE-IIIJ, 863.6 μm by GAPCON-THERMAL-2 and 813.0 μm are thought to be in good agreement with the observed value. SAMURA provides a slightly higher central void radius (901.3 μm) which in comparison with others is the largest predicted boid. LIFE-THERMAL-1 has been reported to have difficulty in forming a central void in all Phase III cases where a void is present experimentally (170,180). The low-powered pin (BE1) did not form columnar grains and, accordingly no central void. The small central void predicted by COMETHE-IIIJ is said to be a result of crack volume transferred to centre by the radial relocation of pellet segments (170). The large central void

calculated by GAPCON-THERMAL-2 is the result of high temperatures. SAMURA has also calculated a large central void for BE1 pin due to its overprediction of temperature and pore migration rates.

TABLE E.1

CC-7 EXPERIMENT - GENERAL CODE INPUT FOR

PIN SEGMENT 4113-AE1

General Input Requirements	Value	Units
Fuel Pellet O.D.	13.0505	mm
Fuel Pellet I.D.	0.0	mm
Fuel Pellet Length	12.2936	mm
Fuel Density	95.1	% TD
Fuel Enrichment	2.98	% U-235
Fuel O/U Ratio	2.004	- - -
Fuel Grain Size	18	μm
Fuel Dish Volume (none)	- - -	- - -
Fuel Densification by 4000 MWd/teU	1.5	% TD
Active Fuel Column Length	122.9360	mm
Axial Clearance	6.2484	mm
Fuel Surface Roughness	1.016×10^{-6}	m,RMS
Cladding Surface Roughness	2.54×10^{-7}	m,RMS
Cladding I.D.	13.3502	mm
Cladding O.D.	27.0002	mm
Fill Gas Composition	He	- - -
STP Fill Gas Pressure	3.034×10^{-2}	MPa
Plenum Hot Temperature	700	^{o}K
Cold Plenum Void Volume	8.751×10^{-6}	m^3
Coolant Pressure	0.3447	MPa
Coolant Inlet Temperature	313	^{o}K
Coolant Outlet Temperature	323	^{o}K
Coolant Film Coefficient	11527	$W/m^{2o}K$
Ramp Rates:		
Start-ups	262.5	W/cm-hr
Shutdown	(Instantaneous)	-

TABLE E.2

CC-7 EXPERIMENT - GENERAL CODE INPUT FOR PIN SEGMENT 4112-BE1*

General Input Requirements	Value	Units
Fuel Pellet O.D.	12.9794	mm
Cladding I.D.	13.0683	mm
Cladding O.D.	26.9977	mm
Cold Plenum Volume	8.39×10^{-7}	m^3

*The rest of input data is the same as given in Table E.1 .

TABLE E.3

CC-7 EXPERIMENT - IRRADIATION HISTORY OF THE 4113-AE1 PIN SEGMENT

Period Length (days)	Linear Power (W/cm)	Clad Surface (^{o}K)	Neutron Flux ($\times 10^{16}$) (n/m^2s)
0.1000	629.92	352.2	1.0667
0.9583	602.03	350.5	1.0194
0.9583	583.99	349.4	0.9889
1.0000	586.94	349.6	0.9939
1.8750	583.00	349.3	0.9872
1.8750	576.12	348.9	0.9755
0.9583	567.91	348.4	0.9617
1.0833	570.87	348.6	0.9667
0.9583	567.91	348.4	0.9617
1.0833	570.87	348.6	0.9667
0.9583	562.99	348.1	0.9533
0.9583	562.01	348.1	0.9517
0.9583	563.98	348.2	0.9550
0.9583	567.91	348.4	0.9617
0.8750	558.07	347.8	0.9450
2.0417	550.85	347.4	0.9277
0.8750	542.98	346.9	0.9194
1.9167	538.06	346.6	0.9111
2.0000	536.09	346.5	0.9078
5.7083	534.12	346.4	0.9044
1.0417	535.11	346.4	0.9061
0.0100	0.0	313.7	0.0
0.0902	567.91	348.4	0.9617
0.8333	532.15	346.2	0.9011
1.0417	543.96	347.0	0.9211
0.9583	523.95	345.7	0.8872
0.9167	527.89	346.0	0.8939
1.0000	523.95	345.7	0.8722
1.7917	530.84	346.2	0.8989
0.9583	523.95	345.7	0.8872

TABLE E.3 (cont.)

Period Length (days)	Linear Power (W/cm)	Clad Surface (^{o}K)	Neutron Flux (x 10^{16}) (n/m^2s)
0.9167	527.89	346.0	0.8939
1.0000	523.95	345.7	0.8722
1.7917	530.84	346.2	0.8989
0.9583	523.95	345.7	0.8872
8.7083	525.92	345.9	0.8905
3.7917	527.89	346.0	0.8939
4.0000	527.89	346.0	0.8939
0.9167	525.92	345.9	0.8905
0.0090	0.0	313.7	0.0
0.1124	708.00	357.0	1.1989
0.9583	639.11	352.8	1.0822
0.9167	626.97	352.0	1.0617
1.8750	628.94	352.2	1.0650
4.7917	629.92	352.2	1.0667
5.7500	599.08	350.3	1.0144
0.6250	567.91	348.4	0.9617
3.5000	562.01	348.4	0.9517
0.0112	0.0	313.7	0.0

TABLE E.4

CC-7 EXPERIMENT - IRRADIATION HISTORY

OF THE 4112-BE1 PIN SEGMENT

Period Length (days)	Linear Power (W/cm)	Clad Surface Temp. (^{o}K)	Neutron Flux ($\times 10^{16}$) (n/m^2s)
0.0787	496.06	344.0	0.8400
0.9583	508.86	344.8	0.8617
0.9583	502.95	344.5	0.8517
1.0000	511.81	345.0	0.8667
1.8750	508.86	344.8	0.8617
1.8750	517.06	345.3	0.8755
0.9583	519.03	345.4	0.8789
1.0833	523.95	345.7	0.8872
0.9583	521.00	345.6	0.8822
0.9583	526.90	346.0	0.8922
0.9583	524.93	345.8	0.8889
0.9583	524.93	345.8	0.8889
0.8750	528.87	346.0	0.8955
2.0417	511.81	345.0	0.8667
0.8750	507.87	344.8	0.8600
1.9167	508.86	344.8	0.8617
2.0000	515.09	345.2	0.8722
5.7083	511.15	345.0	0.8655
1.04o7	511.81	345.0	0.8667
0.0078	0.0	313.7	0.0
0.0729	459.00	341.8	0.7772
0.8333	467.85	342.3	0.7922
1.0417	486.88	343.5	0.8244
0.9583	465.88	342.2	0.7889
0.9167	478.02	343.0	0.8094
1.0000	467.85	342.3	0.7922
1.7917	475.07	342.7	0.8044
0.9583	469.82	342.4	0.7955

TABLE E.4 (cont.)

Period Length (days)	Linear Power (W/cm)	Clad Surface Temp. (^{o}K)	Neutron Flux (x 10^{16}) (n/m^2s)
8.7083	487.86	343.5	0.8261
3.7917	499.02	344.2	0.8450
4.0000	498.03	344.2	0.8433
0.9167	496.06	344.0	0.8400
0.0073	0.0	313.7	0.0
0.0921	580.05	349.2	0.9822
0.9583	511.15	345.0	0.8655
0.9167	511.15	345.0	0.8655
1.8750	467.85	342.3	0.7922
4.7917	499.02	344.2	0.8450
5.7500	508.86	344.8	0.8617
0.6250	479.00	343.0	0.8111
3.5000	469.82	343.4	0.7955
0.0092	0.0	313.7	0.0

TABLE E.5

CC-7 EXPERIMENT - PREDICTED vs EXPERIMENTAL PEAK CENTRELINE TEMPERATURES

Rod Segment	Date Source	Experiment Time in Life (days)	Range in Linear Heat Rating (W/cm)	Range in Peak Centreline Temperature (°K)	Average[2] Centreline Temperature (°K)	Average[4] Temperature Difference (°K)
4113-AE1	Experiment	52.24 to 53.20[1]	708.7-639.3	3039 - 2944	2991	-
	BEHAVE-4[3]			2923 - 2834	2879	- 112
	BEHAVE-4			2956 - 2859	2908	- 83
	COMETHE-IIIJ			2798 - 2719	2759	- 232
	GAPCON-THERMAL-2			2968 - 2935	2952	- 39
	LIFE-THERMAL-1			2995 - 2809	2902	- 89
	SAMURA[5]			2881 - 2795	2838	- 153

TABLE E.5 (cont.)

Rod Segment	Data Source	Experiment Time in Life (days)	Range in Linear Heat Rating (W/cm)	Range in Peak Centreline Temperature (°K)	Average[2] Centreline Temperature (°K)	Average[4] Temperature Difference (°K)
4112-BE1	Experiment	52.24 to 53.20[1]	580.7 -511.8	2200 - 2166	2183	-
	BEHAVE-4[3]			2180 - 1971	2075	- 108
	BEHAVE-4			2191 - 1989	2090	- 93
	COMETHE-IIIJ			2259 - 1987	2123	- 60
	GAPCON-THERMAL-2			2680 - 2418	2549	+ 366
	LIFE-THERMAL-1			2436 - 1979	2207	+ 24
	SAMURA[5]			2360 - 2145	2253	+ 70

(1) Beginning of the third irradiation cycle (see Figure E.1).
(2) Experimentally inferred temperature by grain-growth analysis; uncertainties are ± 139 and ± 111°K on the rods, respectively.
(3) With use of the Phase II and Phase III gas release models, respectively.
(4) With respect to inferred average experimental temperatures.
(5) With cracked pellet gap conductance, the EPRI Phase III Zr creep and SAMURA option 2 gas release.

TABLE E.6

CC-7 EXPERIMENT - PREDICTED vs

EXPERIMENTAL FISSION GAS RELEASE

Rod Segment	4113-AE1	4112-BE1
Experiment Fission Gas Released by EOL, %	26.7	7.9
Predicted Fission Gas Released by EOL, %		
BEHAVE-4 (1)	44.5, 55.2	8.9, 16.0
COMETHE-IIIJ	34.3	2.9
GAPCON-THERMAL-2	51.3	35.9
LIFE-THERMAL-1	25.9	7.2
SAMURA (2)	41.7	28.8

(1) With the EPRI Phase II and Phase III gas release models, respectively.

(2) With cracked pellet gap conductance, the EPRI Phase III Zr creep, and SAMURA option 2 gas release models.

TABLE E.7

CC-7 EXPERIMENT - PREDICTED vs EXPERIMENTAL COLD RADIAL GAPS AND PELLET CENTRAL VOID AT EOL

Rod Segment	Data Source	EOL Cold Radial Gap (m)	EOL Cold Central Void Radins in Fuel (m)
4113-AE1	Experimental	124.5 (3)	406.4 (5)
	BEHAVE-4 (1)	130.8, 132.1	813.0, 813.0
	COMETHE-IIIJ	97.8	508.0
	GAPCON-THERMAL-2	125.7	863.6
	LIFE-THERMAL-1	102.9	25.4
	SAMURA (2)	112.2	901.3
4112-BE1	Experimental	59.7 (4)	0.0
	BEHAVE-4 (1)	71.1, 74.9	304.8, 228.6
	COMETHE-IIIJ	50.8	203.2(crack volume only)
	GAPCON-THERMAL-2	87.6	812.8
	LIFE-THERMAL-1	43.2	0.0
	SAMURA (2)	49.3	773.4

(1) With the EPRI Phase II and Phase III gas release models, respectively.
(2) With cracked pellet gap conductance, the EPRI Phase III Zr creep, and SAMURA option 2 gas release models.
(3) As-fabricated gap was 150 μm; uncertainty on the EOL gap is ± 10 μm.
(4) As-fabricated gap was 44.5 μm; uncertainty on the EOL gap is ± 10 μm.
(5) Uncertainty on the EOL central void radius is ± 102 μm.

Figure E.1

MODELLING OF CC-7 EXPERIMENTAL TEST PINS

FUEL LINEAR HEAT RATING VS. TIME FOR THE PIN SEGMENTS

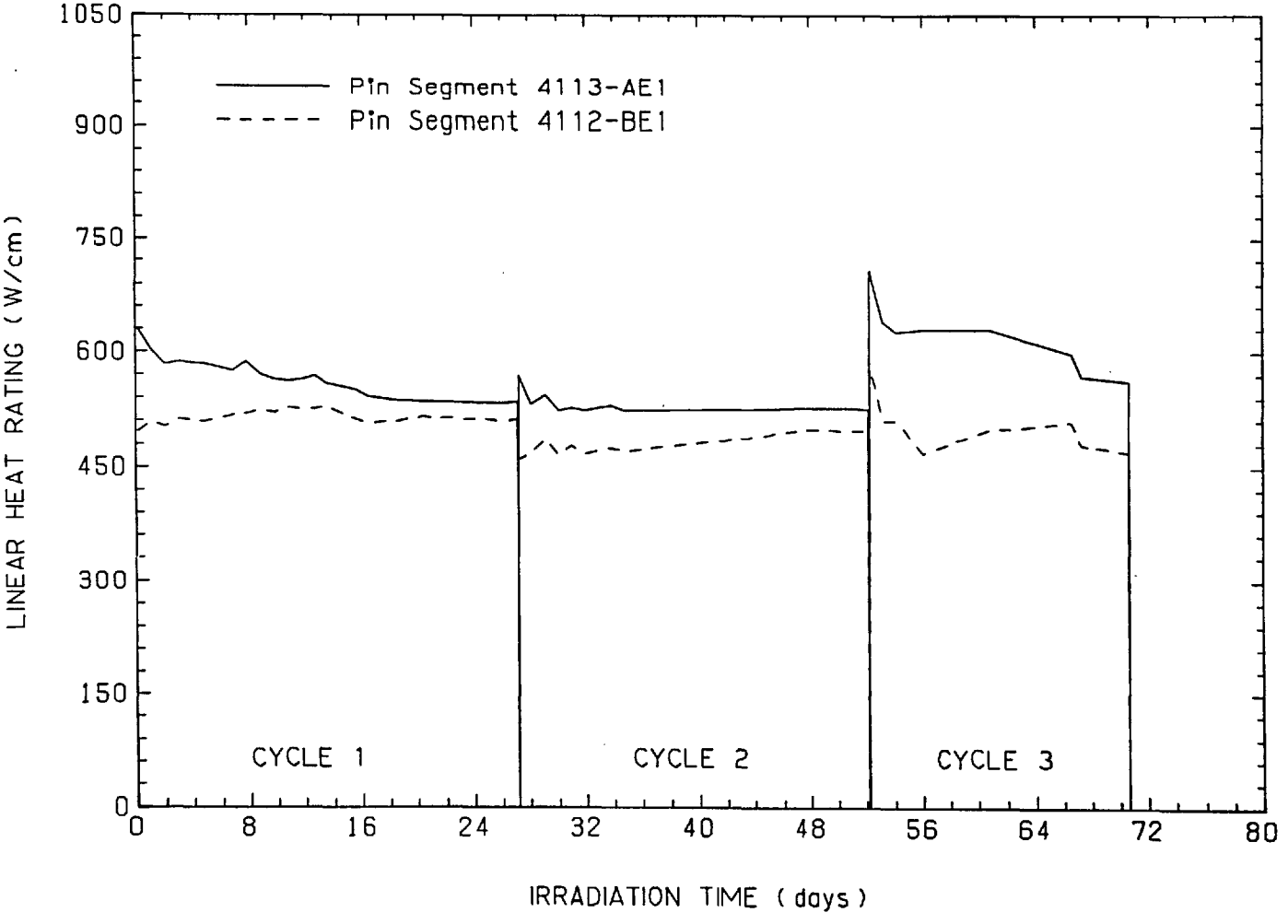


Figure E.2

MODELLING OF CC-7 EXPERIMENTAL TEST PINS

FUEL CENTRELINE TEMPERATURE VS. TIME FOR SEGMENT 4113-AE1

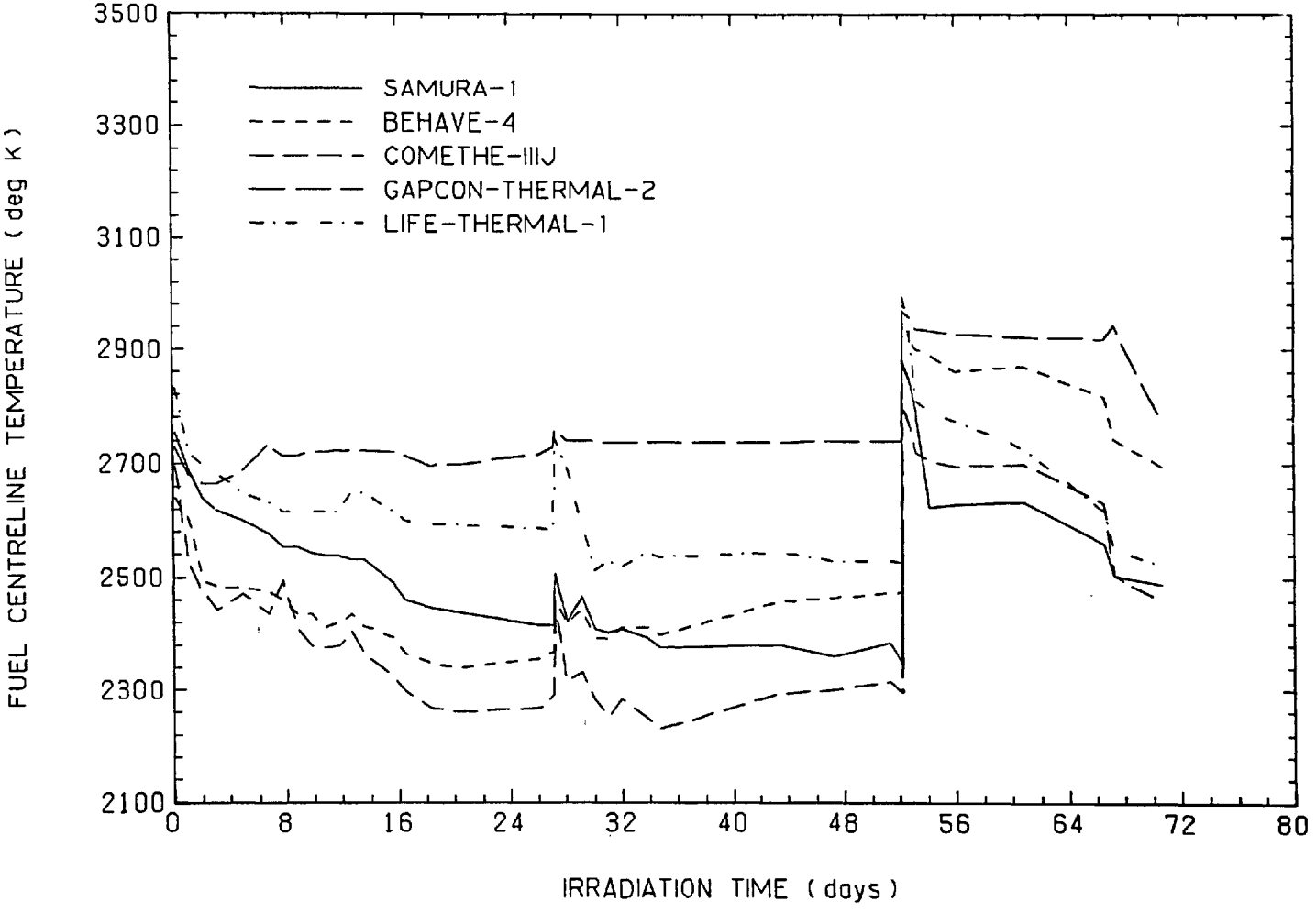
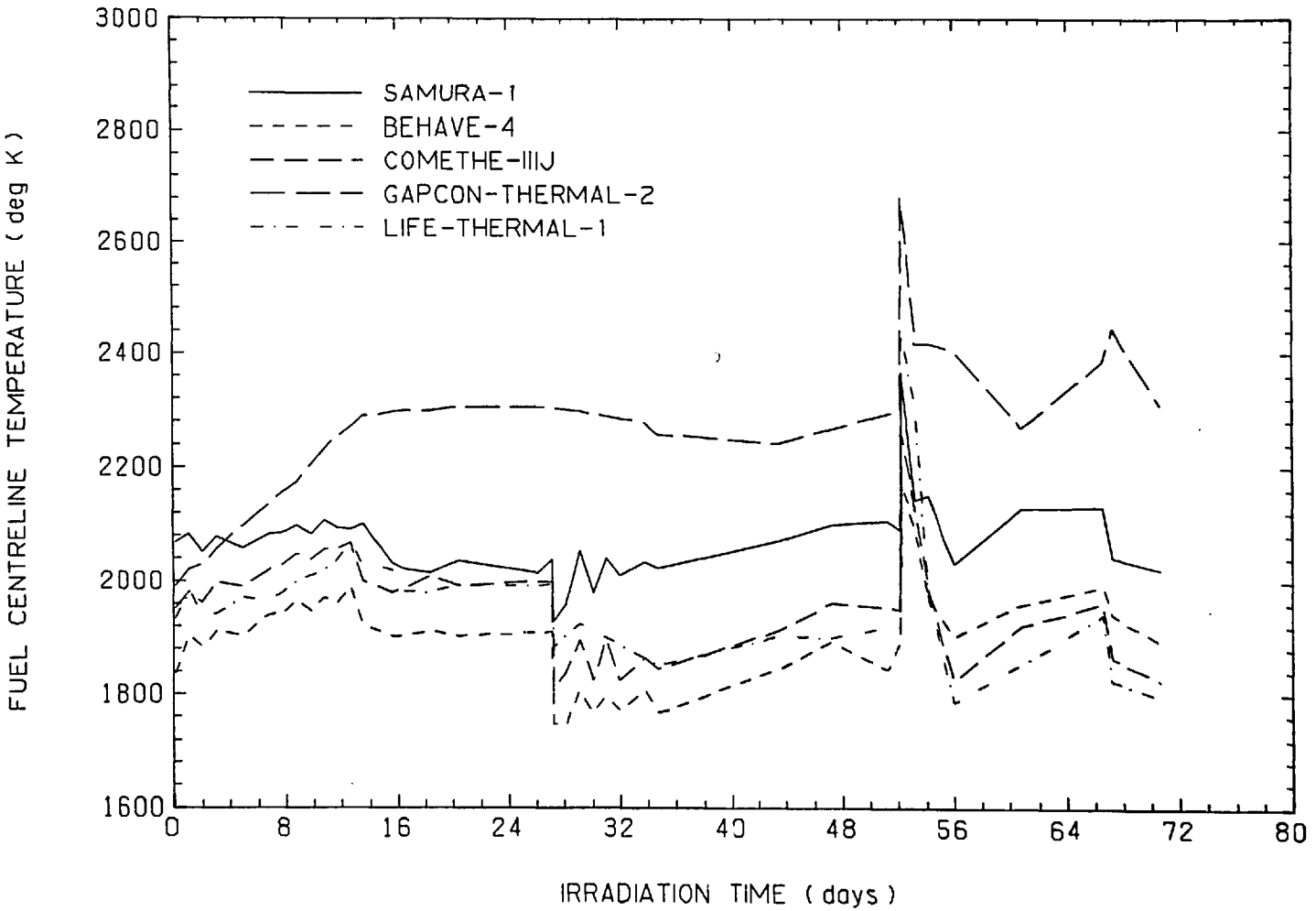


Figure E.3

MODELLING OF CC-7 EXPERIMENTAL TEST PINS

FUEL CENTRELINE TEMPERATURE VS. TIME FOR SEGMENT 4112-BE1



E.2 DISCUSSION OF SAMURA RESULTS

Results presented for the two test pins, 4113-AE1 and 4112-BE1, have clearly demonstrated the ability of SAMURA in handling such high-powered pins. It has also provided further ground for the verification of the cracked pellet gap conductance model. As suggested in the main text this model has very good potentials for further use in SAMURA.

Table E.5 shows that SAMURA has underpredicted the high-power AE1 centreline temperature by 153^{o}K at the beginning of power cycle 3, while it has overpredicted the low-powered BE1 centreline temperature by 70^{o}K during the same period. The differences are within the uncertainty band of temperature measurements. One reason for the underprediction in the case of AE1 is the large central void radius predicted by SAMURA (901.3 μm) as compared to the measured value (406.4 μm). In the case of BE1, however, SAMURA appears to be penalising the gap conductance by the feedback of high gas release (28.8% calculated versus 7.9% measured for this pin), while taking little credit for contact conductance in the BE1 pin. In fact SAMURA provides consistently one of the lowest gap conductances for this pin (which all the codes have predicted to have zero or very small hot gap during most of its life) when compared to the rest of the codes. For instance the values of gap conductance during the same period, for which the temperatures were presented earlier (Table E.5), are given in Table E.8 (170) for comparison (note that the gap is predicted to be closed only by SAMURA, COMETHE-IIIJ and LIFE-THERMAL-1).

TABLE E.8

CC-7 EXPERIMENT - CONTACT GAP CONDUCTANCE VALUE

FOR THE PERIOD 52.24 to 53.20 DAYS

FOR THE 4112-BE1 PIN

Code		Gap Conductance Range ($W/m^2{}^oK$)
BEHAVE-4	($\sim$ 5 μm gap)	17,035 - 56,730
COMETHE-IIIJ	(zero gap)	22,442 - 62,640
GAPCON-THERMAL-2	($\sim$10 μm gap)	3,407 - 3,976
LIFE-THERMAL-1	(zero gap)	28,011 - 34,069
SAMURA	(zero gap)	10,101 - 15,653

The differences between the predictions may be explained by looking back at the definition of contact gap conductance, h_c, as given in Sub-Section 3.3.4, Eq.(3.42). The first term, k_{mix}/δ, is due to gas heat conduction and the second term, C.P/H, is due to contact pressure. The former is usually the dominant term and since the values of k_{mix} (gas mixture conductivity) are greatly influenced by the amount of fission gases and the correction made due to the effects of Knudsen domain, each code would have a different value of k_{mix}. The root mean square of the surfaces, δ, would further change the gas heat conduction term. SAMURA is using an average value of $\delta = 4.39 \times 10^{-6}$m as discussed in Section 3.3. in conjunction with the cracked pellet model. This value is obtained from commercial LWR pins whereas for the AE1 and BE1 experimental pins it is about 1.27×10^{-6}m (according to Ross and Stoute (133) $\delta = a(R_f + R_c)$ where

a ≃ 1.2; R_f and R_c fuel and cladding surface roughness, respectively). So the k_{mix}/δ values as calculated by the other codes could be as high as $4.39 \times 10^{-6}/1.27 \times 10^{-6}$ or ∿ 3.5 times those calculated by SAMURA. As for the second term, since all the codes have used similar parameterisation, H (Meyer hardness) and C (C ≃ constant, see Sub-Section 3.3.4) would be almost the same and only the contact pressure P could alter its values. Since the magnitude of the contact pressure calculated by SAMURA is probably much lower than that of the other codes which take into account fuel/cladding friction effects as well, the second term, C.P/H, is also much smaller for SAMURA.

Gas release quantities predicted by SAMURA are much higher than the measured values, especially in the case of BE1. Basically this is due to the simplicity of fission gas model in SAMURA. It may be interesting to note that the other codes are also somewhat inconsistent with their temperature and gas release predictions. For example COMETHE-IIIJ has actually overpredicted the AE1 gas release but underpredicted the temperature by 232°K. SAMURA, nevertheless, requires a more reliable gas release model which should also be linked to a fuel swelling model.

The EOL cold gap and central void predictions listed in Table E.7, provide further evidence to check the treatment of physical behaviour by code models. The predicted EOL cold radial gaps by SAMURA are in good agreement with the measured values. The central voids calculated by SAMURA are, however, on the large side; which once again

emphasises the need for revision of the pore migration model adopted here.

In summary, the modelling of the CC-7 experiment, as well as the results reported in the main text, have proved that overall predictions made by SAMURA are well within the range of calculations made by the four major codes evaluated by the EPRI program. With some further development, basically in its physical models and material data, SAMURA could become a most valuable tool for the thermal and mechanical analysis of fuel pins.

REFERENCES

REFERENCES

1. F.A. Nichols. "Theory of columnar grain growth and central void formation in oxide fuel rods". J. of Nuclear Materials, 22, (1967), 214-222.

2. D. Freund and C. Sair. "A new simulation method for investigation of UO_2 fuel in a thermal gradient corresponding to reactor conditions". Proc. of Int. Meeting on Fuel Elements, Karlsruhe, 28-30 September, 1970, 78-94.

3. V.Z. Jankus and R.W. Weeks. "LIFE-II - A computer analysis of fast-reactor fuel-element behaviour as a function of reactor operating history". Nuclear Engineering & Design, 18, (1972), 83-96.

4. F.J. Homan, W.J. Lackey and C.M. Cox. "FMODEL - A FORTRAN-IV computer code to predict in-reactor behaviour of LMFBR fuel pins". Oak Ridge National Laboratory, ORNL-4825, (1973).

5. S. Oldberg. "BEHAVE-2: Oxide fuel performance code in two spatial dimensions and time". General Electric Company, GEAP-13788, (1972).

6. H. Kämpf et al. "Das Rechenprogramm SATURN 1a für Brennstäbe". Kernforschungszentrum Karlsruhe, KFK-1575, (1972).

7. E. de Meulemeester. "Review of work carried out by BELGNUCLEARE and CEA on the improvement and verification of the COMETHE computer code". BNES Conf., Paper 92, October 1973.

8. K. Lassmann. "URANUS - A computer program for the thermal and mechanical analysis of the fuel rods in a nuclear reactor". Nucl.Eng.Design, 45, (1978), 325-342.

9. M.R. Hayns and D. Wilmore. "FRUMP - A computer program for the calculation of stresses in reactor fuel pins". AERE-R 7380, (1973).

10. E.D. Hicks and H. Hughes. "Fast reactor pin modelling". BNES Conference, Paper 2, November, (1972).

11. E. Duncombe et al. "An analytical model for the prediction of in-pile behaviour of oxide fuel rods". WAPD-TM-961, (March 1970).

12. S. Levy and J.P.D. Wilkinson. "A three-dimensional study of nuclear fuel rod behaviour during start up". 2nd Int.Conf. on Structural Mechanics in Reactor Technology, Berlin, (1973), Paper D1/5.

13. R.B. Poeppel. "An advanced gas release and swelling subroutine". Proc. of Conf. on Fast Reactor Fuel and Fuel Elements, Karlsruhe, (1970), 78-94.

14. M.G. Andrews et al. "LWR fuel rod modelling code evaluation". Electric Power Research Institute, Phase I Report, CENPD-209, (1975) and Phase II Report, CENPD-218, (1976).

15. J.R. Matthews . "Methods for calculating stress in cylindrical nuclear fuel elements". AERE-R 6585, (1970).

16. C.R. Hann et al. "GAPCON-THERMAL-1, a computer program for calculation of gap conductance in oxide fuels". BNWL-1778, (1973).

17. Gittus et al. "Theoretical analysis of cladding stresses and strains produced by expansion of cracked fuel pellets". Nucl.Appl. & Tech., Vol.9, (1970).

18. A. Garlick. "Fracture of Zircaloy cladding under simulated power ramp conditions". Proc.Conf. on Physical Metallurgy of Reactor Fuel Elements, U.K., Sept.(1973).

19. D.H. Locke. "Review of experience with water reactor fuels 1968-1973". Nucl.Eng.Des., 33, (1975), pp.94-124.

20. "Steam generating and other heavy water reactors". The British Nuclear Energy Society Conference, 14 May 1968, London.

21. L.R. Haywood et al. "Fuel for Canadian power reactors". Atomic Energy of Canada Ltd. Report, AECL-3979, (1971).

22. D.H. Locke. "A U.K. view of fuel densification and clad stability in oxide fuel pins". Nucl.Eng.Intl., December, (1972).

23. M.F. Lyons et al. "UO_2 properties affecting performance". Nucl.Eng.Des., 21, (1972), p.167.

24. F.H. Megarth. "Zircaloy-clad UO_2 fuel rod evaluation program". Quarterly Progress Report, No.3, GEAP-5667, (1968).

25. R.C. Daniels et al. "Effects of high burn-up on Zircaloy-clad bulk UO_2 plate fuel element samples". WAPD-263, (1962).

26. J.A. Christensen et al. "Melting point of irradiated uranium dioxide". ANS Trans., 7, (1964), 390.

28. J.A. Christensen. "Irradiation effects on UO_2". HW-69234, (1962).

29. M.D. Freshley. "Operation with fuel melting". Nucl.Eng. & Des., 21, (1972), pp.254-263.

30. I.A.E.A. "Thermal conductivity of UO_2: report of a panel". Vienna, 1965, IAEA Rep. Series No.59, (1966).

31. D.R. De Halls. "Understanding UO_2 thermal conductivity. Nucleonics, Vol.21, No.10, (1963), pp.92-94.

32. L.A. Goldsmith and J.A. Douglas. "Measurements of the thermal conductivity of UO_2". (1970), TRG-2103(W).

33. J.P. Stora et al. "Conductibitite thermique de l'oxyde d'uranium fritte dan les conditions d'utilisation en pile". (1964), CEA-R-2586.

34. V.C. Howard and T.F. Gulvin. "Thermal conductivity determinations on uranium dioxide by a radial flow method". (1961), IG-Report (RD/C).

35. M.J.F. Notley et al. AECL-2143, (1964).

36. A.S. Bain. AECL-2588, (1966).

37. V.C. Janvier et al. CEA-R 3358, (1967).

38. C.N. Craig et al. GEAP-5748, (1969).

39. R.D. Legget et al. Trans.Amer.Nucl.Soc., 17, (1973), p.175.

40. L.A. Lawrence. Trans.Amer.Nucl.Soc., 15, (1972), p.223.

41. L.A. Lawrence. Trans.Amer.Nucl.Soc., 17, (1973), p.175.

42. B. Brozoska and F. Wunderlich. Dent.Atomforum, Reactor Conference, Nuremberg, April 1975.

43. F.A. Nichols. "Theory of Columnar grain growth and central void formation in oxide fuel rods". J.Nucl.Mat., 22, (1967), 214-222.

44. J.R. MacEwan. J.Amer.Ceram.Soc., 45, (1962), p.37.

45. J.R. MacEwan and V.B. Lawson. J.Amer.Ceram.Soc., 45, (1962), p.42.

46. H. Stehle. Ber.Deut.Keram.Ges., 40, (1963), p.129.

47. H.R. Warner and F.A. Nichols. "Proc. of Conf. on Fast Reactor Technology", (1971), pp.267-289.

48. C. Li et al. Nucl.Appl. & Tech., 9, (1970), pp.188-194.

49. R.M. Caroll. Nucl.Safety, 12, (1971), 297.

50. S.R. Pati et al. J.Nucl.Mater., 50, (1974), 227.

51. J.A. Turnbull and M.O. Tucker. J.Nucl.Mater., 50, (1974), 53.

52. J.W. Dias and K.R. Merckx. "Theories of fission gas behaviour". Annals of Nuclear Energy, Vol.3, (1976), pp.41-53.

53. J.R. Matthews, (Harwell, UKAEA). M.Sc. Course Lecture Notes, Nucl. Power Sec., Mech.Eng.Dept., Imperial College, (1975).

54. R. Hargreaves and D.A. Collins. "A quantitative model for fission gas release and swelling in irradiated uranium dioxide". J.Br.Nucl.En.Soc., (1976), 15, No.4, pp.311-318.

55. H. Assmann and H. Stehle. Deut.Atomforum, Proc. Reactor Conf., Karlsruhe, (1973), p.409.

56. J.B. Ainscough. "In-reactor densification of oxide fuels". UKAEA TRG Rep. 1937(S), (1969).

57. R.L. Coble. J.Appl.Phys., 32, (1961), pp.787-798.

58. USAEC, Technical report on densification of light water reactor fuel. NDV, (1972).

59. D.A. Collins et al. BNES Conf., (1973), Paper 49.

60. H. Stehle and H. Assmann. "The dependence of in-reactor UO_2 densification on temperature and micro-structure". J.Nucl.Mater., 52, (1974), pp.303-308.

61. W. Chubb et al. "Observations relating to the mechanisms of swelling and gas release in uranium dioxide at high temperatures". J.Nucl.Mater., 44, (1972), pp.136-152.

62. M.O. Marlowe. General Electric Rep., NEDO-12440, (1973).

63. R.L. Coble. J.Appl.Phys., 32, (1961), p.787.

64. M.D. Freshley et al. "Irradiation-induced densification of UO_2". J.Nucl.Mater., 62, (1976), pp.138-166.

65. O.L. Anderson. Phys.Rev., 144, (1966), p.553.

66. J.B. Wachtman et al. Phys.Rev., 122, (1961), p.1754.

67. J. Boocock et al. UKAEA Rep. AERE-M 2565, (1973).

68. N. Igata and K. Domoto. J.Nucl.Mater., 45, (1972/73), p.317.

69. A.G. Evans and R.W. Davidge. J.Nucl.Mater., (33), (1969), p.249.

70. R.F. Cannon et al. J.Am.Ceram.Soc., 54, (1971), p.105.

71. F.R.N. Nabarro. Report of a conference on the strength of solids, Phys.Soc., London, (1949), p.75.

72. C. Herring. "Diffusional viscosity of a poly-crystalline solid". J.Appl.Phys., 21, (1950), p.437.

73. J. Weertman. "Steady-state creep based through dislocation climb". J.App.Phys., 28, (1957), p.362.

74. M.V. Speight. "Enhancement of diffusion creep under irradiation". CEGB, U.K., RD/B/N-2402, (August 1972).

75. D. Brucklacher and W. Dienst. "Creep behaviour of ceramic nuclear fuels under irradiation". J.Nucl.Mater., 42, (1972), pp.285-296.

76. R. Scott et al. "The plastic deformation of uranium oxides above 800°C". J.Nucl.Mater., 1, (1959), pp.39-48.

77. W.M. Armstrong and W.R. Irvine. "Creep deformation of nonstoichiometric UO_2". J.Nucl.Mater., 9, (1963), p.2.

78. L.E. Poteat and C.S. Yst. "Grain boundary reactions during deformation". ORNL-P-2371, Oak Ridge National Laboratory, (1965).

79. R.A. Wolfe and S.F. Kaufman. "Mechanical properties of oxide fuels". WAPD-TM-587, Bettis Atomic Power Laboratory, (1967).

80. P.E. Bohaby et al. "Compressive creep characteristics of stoichiometric UO_2". GEAP-10054, General Electric Company, (1969).

81. B. Burton and G.L. Reynolds. "The diffusional creep of UO_2; its limitation by interfacial processes". Act.Met., 21, (August 1973), pp.1073-1078.

82. B. Burton and G.L. Reynolds. "The influence of deviations from stoichiometric composition on the diffusional creep of UO_2". Act.Met., 21, (1973), pp.1641-1647.

83. A.A. Solomon et al. "Fission induced creep of UO_2 and its significance to fuel element performance". ANL-7857, Argonne National Laboratory, (1971).

84. D. Brucklacher et al. "Creep behaviour of oxide fuels under neutron irradiation". ANL-Trans-942, Argonne National Laboratory, (1973).

85. K.P. Steward and B.A. Cheadle. Trans.Metallurgical Soc. of AIME, 239, (1967), p.504.

86. L.M. Howe, J.L. Witton and J.F. McGurn. "Observations of dislocation movement and interaction in zirconium by transmission electron microscopy". Acta.Met., 10, (1962), p.773.

87. L.J. Rapperport and C.S. Hartley. "Deformation modes of zirconium at 77, 575 and 1075^{o}K". Trans.Amer.Inst. Min.Eng., 218, (1969), p.86.

88. R.F. Reed-Hill. "The role of deformation twinning in the plastic deformation in zirconium". Proc.USAEC Symp. on Zirconium Alloy Development, GEAP-4089, II, (1962).

89. C.D. Williams and R.W. Gilbert. "Fast neutron damage in zirconium based structural alloys". AECL-3308, (1973).

90. P.M. Kelly. "Strain-ageing in zirconium-oxygen alloys". J.Nucl.Mater., 46, (1973), p.1.

91. G.R. Piercy. "Mechanisms for the in-reactor creep of zirconium alloys". J.Nucl.Mater., 26, (1968), p.18.

92. S.N. Buckley. "Properties of reactor materials and effects of radiation damage". Ed. W.J. Littler, Butterworth, London, (1962), p.413.

93. R.V. Hesketh et al. "Radiation damage in reactor materials". Vol.I, I.A.E.A., Vienna, (1969), p.365.

94. E.F. Ibrahim and J.E. Winegar. "Dimensional changes of unstressed Zircaloy-2 and Zr-2.5% N6 specimens in a fast neutron flux". J.Nucl.Mater., 45, (1973), p.335.

95. V. Fidleris. "The effect of cold-work and stress relieving on the irradiation growth behaviour of zirconium alloys". J.Nucl.Mater., 46, (1973).

96. P.M. Kelly. "Irradiation growth in zirconium". Conf. on Phys.Metall. of Reactor Fuel Elements, CEGB, Berkeley, U.K., (1973).

97. G.V. Ranjan and E. Smith. "Fracture of Zircaloy cladding as a consequence of power increase in water reactor fuel rods". Paper C2/1. 4th SMiRT Conf., (1977).

98. D.O. Pickman. "Properties of Zircaloy cladding". Nucl.Eng. & Des., 21, (1972), p.212.

99. J.E. Irvin. "Zirconium and its alloys". Electrochem. Soc.Int., 144, (1966), p.240.

100. A.L. Bement, Jr. AEC Res. & Dev. Report, BNWL-SA-672, May, (1962).

101. M.L. Howe and W.R. Thomas. "The effect of neutron irradiation on the tensile properties of Zr-2". J.Nucl.Mater., 2, (1960), p.248.

102. D.O. Hobson et al. "Comparison of rupture data from irradiated fuel rods and unirradiated cladding". Nucl.Technol., August (1963).

103. D.G. Hard. "High temperature expansion and rupture behaviour of Zircaloy tubing". Paper to National Topical Meeting on Water-Reactor Safety, Salt Lake City, Utah, U.S.A., 26-28 March, (1973).

104. K.M. Emmerich et al. "Failure of pressurised Zircaloy tubes during thermal excursions in steam and in inert atmospheres". ASTM-STP-458, (1964).

105. E.F. Juenke and J.F. White. "Physical-chemical studies of clad UO_2 under reactor accident conditions". GEMP-731, (1970).

106. E.R. Gilbert. J.Nucl.Mater., 26, (1968), p.105.

107. J.J. Holmes et al. "In-reactor creep of cold-worked Zircaloy-2 in flow and fracture of metals and alloys in nuclear environments". Am.Soc.Testing & Mats., No.380, (1965), p.385.

108. V. Fidleris and C.W. Williams. "Influence of neutron irradiation on the creep of Zircaloy-2 at 300°C in Zirconium and its alloys". Ed. J.P. Pemsler et al, Electrochemical Soc., New York, (1966), p.258.

109. C.R. Woods. "Properties of Zircaloy-4 tubing". Report WAPD-TM-585, Bettis Atomic Power Laboratory, (1966).

110. P.A. Ross-Ross. Trans.Amer.Nucl.Soc., 10, (1967) p.114.

111. R.J. Holicky and J. Schroeder. J.Nucl.Mater., 33, (1969), p.52: J.Nucl.Mater., 39, (1971), p.27; and J. Nucl.Mater., 44, (1972), p.31.

112. P.A. Ross-Ross, V. Fidleris, D.E. Fraser. Canadian Metal Quarterly, 11, (1972), p.101.

113. A.H. Cottrell. "Vacancies and other point defects in metals and alloys". The Inst. of Metals, London, (1958), p.1.

114. A. Seeger. Proc. 2nd U.N.Int.Conf.Peaceful Uses Atom, Energy, 6, (1958), p.250.

115. J.E. Lesurf and P.E.C. Bryant. "The effect of water chemistry on the oxidation of zirconium alloys under reactor irradiation". AECL-2797, (1968).

116. A.B. Johnson, Jr. "Corrosion and hydriding response and oxide properties of six irradiated zirconium alloys". BNWL-1719, rer., (1968).

117. E. Hillner. "Hydrogen absorption in Zircaloy during aqueous corrosion effect of environment". WAPD-TM-411, (1964).

118. M.G. Balfour and J.F. Mellor. "Post-irradiation examination of CVTR fuel assemblies - final report". WCAP-3850-4, August, (1969).

119. K.D. Knudsen and E.B.M. Majoor. "A compilation of test fuel data of the 1964-1966 test fuel programme". OECD Halden Reactor Project, (HPR-81), December 1967.

120. D.O. Pickman. "Fuel performance in the prototype SGHWR power station". TRG Rep.1943(S), (1969).

121. H.S. Rosenbaum et al. "Interaction of iodine with Zircaloy". GEAP-5100-5, (1966).

122. A. Garlick. "Stress corrosion cracking of zirconium alloys in iodine vapour". Proc. of Int.Conf. on Corrosion, BNES, Paper 3, (1971), p.21.

123. R.C. Nelson. "The corrosion of Zircaloy-2 fuel element cladding in a boiling water reactor environment". GEAP-4089, II, (1969).

124. G.J. Baroch et al. "Comparative performance of Zircaloy and stainless steel clad fuel rods operated to 10,000 MWd/tU in the VBWR". GEAP-4849, (1966).

125. B. Lustman and F. Kerze. "The metallurgy of zirconium". McGraw Hill, (1955).

126. A.S. Bain and J.E. Lesurf. "Oxidation and hydriding of Zircaloy in the NPD reactor". AECL-3065, (1969).

127. W. Evans and G.W. Parry. Electrochem.Tech., 4, (1966). p.225.

128. F. Garzarolli et al. "Corrosion and hydriding of Zr-2 and other zirconium alloys in BWR's". Int.Conf. on Corrosion, Paper 2, BNES, (1971), p.15.

129. W.T. Grub and M.H. Morgan. Proc. ANS Topical Meeting on Water Reactor Performance, May (1977), p.295.

130. B. Cox. "Environmentally induced cracking of zirconium alloys". AECL-Report 3551, (1970.

131. S. Banerjee et al. "A model for analysis of fuel behaviour in transients". Nucl.En. & Des., 42, (1977), pp.319-355.

132. M. Lees. "An extrapolated Crank-Nicholson difference scheme for quasi-linear parabolic equations". Proc.Symp. Non-Linear Partial Differential Equations, Ed. W.F. Ames, Academic Press, (1966).

133. A.M. Ross and R.L. Stoute. "Heat transfer coefficient between UO_2 and Zircaloy-2". CRFD-1075, (1962).

134. J. Dearien. "Modelling for normal operations vs. accident transients". Seminar held in conjunction with the 4th SMiRT Conf., August (1977).

135. I. Cohen et al. "Measurement of thermal conductivity of metal-clad uranium oxide rods during irradiation". WAPD-228, (1960).

136. G. Kjaerheim and E. Rolstad. "In-pile determination of the thermal conductivity and density effects and gap conductance". HPR-80, (1967).

137. I. Devold. "A study of temperature distribution in UO_2 reactor fuel elements". Report AE-318, Aktiebolaget Atomenergi, Sweden, (1968).

138. E.T. Laats et al. USNRC-OECD Halden Project Fuel Behaviour Test Program, Experimental data report for test assemblies, IFA-226 and IFA-239, ANCR-1270, (1975).

139., B.B. Mikis and W.M. Rohsenow. "Thermal contact resistance". DSR 74542-41, Mech.Eng.Dept., Massachusetts Institute of Technology, (1966).

140. H. Fenech and W.M. Rohsenow. "Prediction of thermal conductance of metallic surface in contact. Paper 62-HT-32, Trans.ASME, J. Heat Transfer, (1963).

141. G. Jacob and N. Todreas. "Thermal contact conductance in reactor fuel elements". Nucl.Sci. & Eng., 50, (1973).

142. R.S. Brokaw. "Alignment charts for transport properties, viscosity, thermal conductivity and diffusion coefficient for nonpolar gases and gas mixtures at low density". Lewis Research Centre, NASA-TR-R-81, (1960).

143. J.M. Gandhi and S.C. Saxena. "Correlated thermal conductivity data of rare gases and their binary mixtures at ordinary pressures". J.Chem. & Eng.Data, 13, 3, (1968).

144. "Thermodynamic and transport properties of steam". New York, Am.Soc.Mech.Engs., (1968).

145. R.A. Dean. "Thermal contact conductance between UO_2 and Zircaloy-2". Westinghouse Electric Co., CVNA-127, (1962).

146. R.L. Gibby et al. "Analytical expressions for enthalpy and heat capacity for uranium-plutonium oxide". J.Nucl.Mat., 50, 155, (1974).

147. H.W. Dean and E.A. Eldridge. "Specific heat measurements". Progress Relating to Civilian Applications during August 1963, USAEC Rep.BMI-1644, pp.V-1 to V-2.

148. J.N. Chirigos et al. "Development of Zircaloy-4". Fuel Element Fabrication, New York, Academic Press, (1961), pp.19-55.

149. A.E. Feith. "Thermal conductivity and electrical resistivity of Zircaloy-4". High Temperature Materials Program, Progress Rep. No.61, USAEC Rep.GEMP-61, (1966), pp.153-155.

150. D.B. Scott. "Physical and mechanical properties of Zircaloy-2 and Zircaloy-4". USAEC Rep.WCAP-3269-61, (1965), pp.5-8.

151. J. Belle. "Uranium dioxide, properties and nuclear applications". U.S.Gov.Printing Off., (1961).

152. E.F. Juenke and L.H. Sjodahl. "Physical and mechanical properties; emittance measurements". AEC Fuels and Materials Development Program, USAEC Rep.GEMP-1008, (1968).

153. J.B. Conway et al. "The thermal expansion and heat capacity of UO_2 to 2200°C". TM63-6-6, General Electric (1963).

154. J.A. Christensen. "Thermal expansion and change in volume of uranium diozide on melting". J.Am.Ceram.Soc., 46, 12, (1963), p.607.

155. M. Hoch and A.C. Momin. "High temperature thermal expansion of uranium dioxide and thorium dioxide". High Temperature-High Pressures, 1, 4, (1969).

156. P. Murray and R.W. Thackray. "The thermal expansion of sintered UO_2". HERE M/M 22.

157. R.L. Mehan and G.L. Cutler. "Thermal expansion of Zircaloy-2 between room temperature and 1000°C". USAEC Report KAPL-M-RLM-15, (1958).

158. D. Vollath. "Mechanical properties of unirradiated oxide fuels". Fuel Rod Model Theory, Karlsruhe Nuclear Research Centre, EURFNR-968, (1971).

159. J.R. Matthews. "Mechanical properties and diffusion data for carbide and oxide fuels. AERE-M 2643.

160. R.L. Mehan. "Modulus of elasticity of Zircaloy-2 between room temperature and 1000°F". USAEC Report, KAPL-M-RLM-16, (1958).

161. C.S. Olsen. "Steady-state creep model for UO_2". Trans.Amer.Nucl.Soc., Vol.22, (1975), pp.210-211.

162. J.H. Gittus. Int.Conf. on Physical Metallurgy of Reactor Fuel Elements, Berkeley Nuclear Lab., (1973).

163. C.E. Clement. "The movement of lenticular pores in UO_2 nuclear fuel elements". J.Nucl.Mater., 68, (1977), pp.63-68.

164. C. Ronchi and C. Sari. "Properties of lenticular pores in UO_2, $(U,Pu)O_2$ and PuO_2". J.Nucl.Mater. 50, (1974), pp.91-97.

165. N.C. Small. "Continuum dilation model for creep analysis of ceramic nuclear fuels with applications". WAPD-TM-649, (1967).

166. C.J. Baroch et al. "Effects of irradiation in a thermal reactor on the tensile properties of Zircaloy 2 and 4 and borated stainless steel". ASTM STP 484, American Society for Testing and Materials, (1970), pp.176-193.

167. C.J. Baroch. "Effect of irradiation at 130, 650 and 775°F on tensile properties of Zircaloy-4 at 70, 650 and 775°F". ASTM STP 570, American Society for Testing and Materials, (1975), pp.129-142.

168. A.R. Curtis and J.R. Reid. "MA18A, FORTRAN subroutine for the solution of sparse sets of linear equations. AERE- 6844.

169. H. Hoffman. "Crack formation, crack healing and porosity redistribution during irradiation of UO_2 and $(U,Pu)O_2$". J.Nucl.Mat., 54, (1974).

170. H.R. Freeburn et al. "Light water reactor fuel rod modelling evaluation". EPRI-NP-369, Electrical Power Research Institute, (1977).

171. E.E. Lewis. "A transient heat conduction model for reactor fuel elements". Nucl.Eng. & Design, 15, (1971), pp.33-40.

172. D.E. Lamkin. "Analytical stress analysis for a simplified model of a reactor fuel element". Ph.D. dissertation, Univ. of Arizona (1974).

173. E.M. Smith. "Primary creep behaviour of thick tubes". Proc.Inst.Mech.Engrs., 1963-64, Paper 20.

174. R.W. Bailey. "The utilization of creep test data in engineering design". Proc.Inst.Mech.Engrs., 1935.

175. S. Harriague et al. "The BACO fuel rod analysis computer program". SMiRT 5, Paper D1/2, (1979).

176. E. Smith and G.V. Ranjan. "American Nuclear Society Topical Meeting on Water Reactor Fuel Performance". St. Charles, Illinois, U.S.A., May 1977, p.337.

177. E. Smith. "Thermal reactor fuel elements". Review of SMiRT 4, Nucl.Energy, 17, No.3, (1978), pp.203-209.

178. E. Smith. "The fuel-cladding interfacial friction coefficient in water-cooled reactor fuel rods". SMiRT 5 Conference, Berlin, (1979), Paper D2/6.

179. A.E. Jhonson and B. Khan. "Creep of metallic thick-walled cylindrical vessels subject to pressure and radial thermal gradient". Proc.Inst.Mech.Engrs., 1963-64, Vol.178, Pt.31.

180. N. Fuhrman et al. "Evaluation of fuel rod performance in Maine Yankee Core I - task C". EPRI-NP-218, (1976).

181. R. Hill. "A theory of the yielding and plastic flow of anisotropic metals". Proc.Roy.Soc.A., 193, (1948).

182. C.E.L. Hunt. "Anisotropic theory and the measurement and use of the anisotropic factors for Zr-4 fuel sheaths". Paper C2/9, SMiRT 3, (1975).

183. R.M.Guha, J.L. Head, J.R. Matthews "Analysis of crack patterns in fast reactor fuel pellets". TP719, AERE Harwell.